MARIN

NuTTS'17
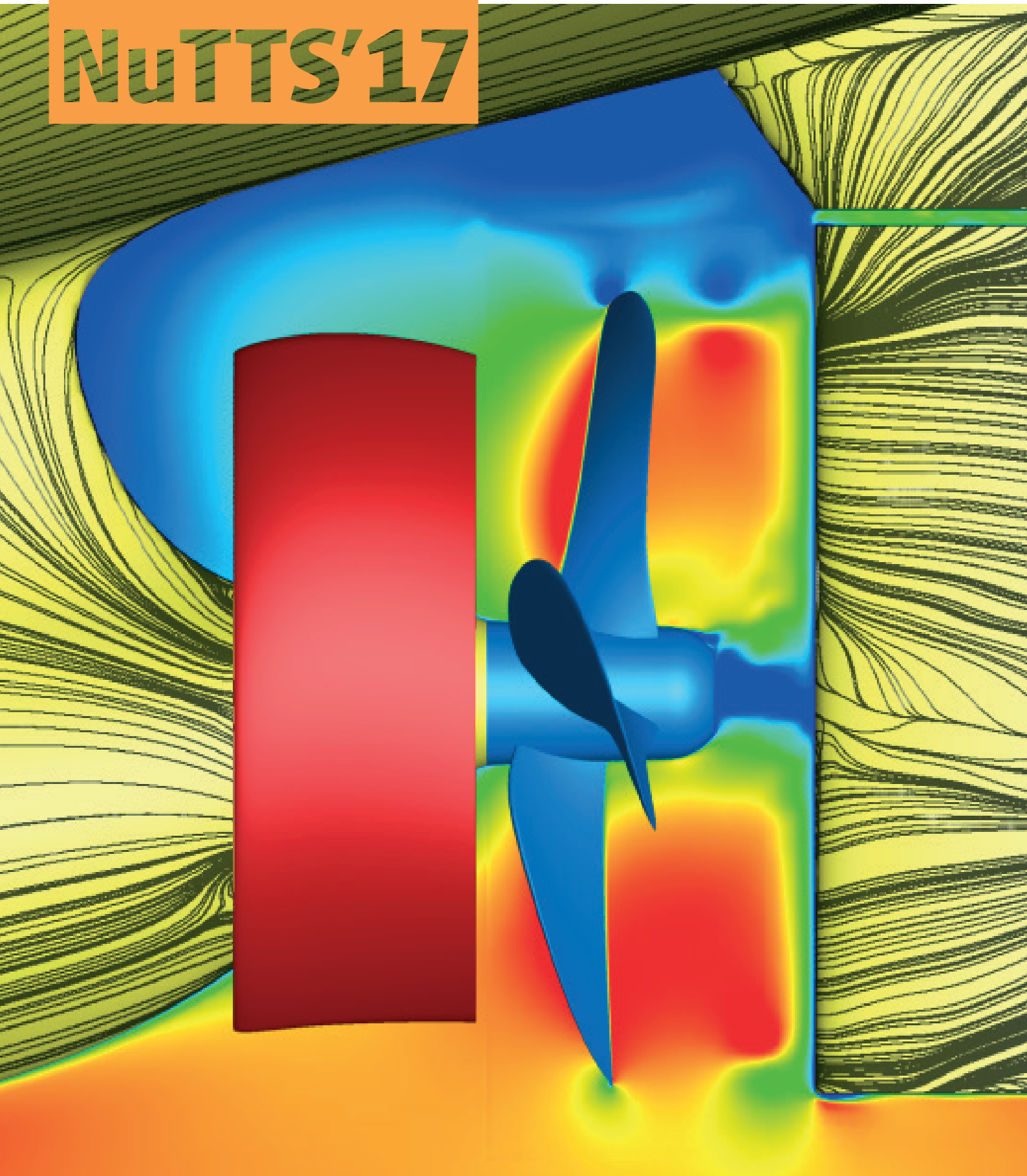
20th Numerical Towing Tank Symposium
1 - 3 October 2017 | Wageningen, the Netherlands

Thomas Lloyd and Auke van der Ploeg (Eds.)

NuTTS'17 is sponsored by

Preface

This document is composed of the extended abstracts presented at the 20th Numerical Towing Tank Symposium, held at Hotel De Wageningsche Berg, Wageningen, the Netherlands, between the 1st and 3rd of October 2017.

Thomas Lloyd and Auke van der Ploeg, MARIN (editors)

Table of Contents

Code Verification exercise of a Navier-Stokes solver for Compressible Flows in the Laminar and Subsonic Regimes

Hugo Abreu[*], Luís Eça[*] and Christiaan M. Klaij[†]

[*]IST Técnico Lisboa, Lisbon/Portugal, [†]MARIN Maritime Research Institute Netherlands,
Wageningen/The Netherlands
hugo.abreu@tecnico.ulisboa.pt

1 Introduction

Many of the flows of interest to the naval and offshore industries deal with fluids that are usually assumed to be incompressible, i.e. their equation of state is $\rho = const$. However, there are several phenomena, as for example slamming, sloshing or cavitation where the fluid compressibility must be taken into account. All these applications involve compressible two-phase flows, which are the ultimate goal of the present development of the flow solver ReFRESCO.

The first step in this development is the implementation of the solution procedure for a laminar, subsonic flow of a perfect gas based on the current version of ReFRESCO. The updated solver is checked using the Method of Manufactured Solutions, Roache and Steinberg (1984), Roache et al. (1990) to perform a Code Verification exercise. The selected Manufactured Solution is based on the work presented in Roy et al. (2004) and Eça et al. (2012). This first step relies on proven methods documented in the open literature for both single phase Ferziger and Perić (2002) and multiphase Moukalled and Darwish (2006) and Miller et al. (2013) flows. The energy equation is already available in ReFRESCO although it is seldom solved in incompressible flow solutions. Its formulation must be update for a compressible fluid. However, in this paper the focus is on the extra terms included in diffusion for the momentum equations and on handling compressibility effects in the determination of the pressure, which is based on the solution of the mass balance equation using the SIMPLE algorithm.

2 Governing equations

The equations that express mass, momentum and energy balances for a three-dimensional flow are given by

$$\frac{\partial \rho}{\partial t} + \frac{\partial (\rho u_i)}{\partial x_i} = 0 \, , \tag{1}$$

$$\frac{\partial (\rho u_i)}{\partial t} + \frac{\partial \left(\rho u_j u_i\right)}{\partial x_j} = -\frac{\partial p}{\partial x_i} + \frac{\partial}{\partial x_j}\left(\sigma_{ij}\right) \, , \tag{2}$$

$$\frac{\partial \left(\rho c_p T\right)}{\partial t} + \frac{\partial \left(\rho u_j c_p T\right)}{\partial x_j} = \left(\frac{\partial p}{\partial t} + u_j \frac{\partial p}{\partial x_j}\right) + \sigma_{ij}\frac{\partial u_i}{\partial x_j} - \frac{\partial q_j}{\partial x_j} \, , \tag{3}$$

where the viscous stress tensor σ_{ij} and the heat conduction vector q_j are defined as

$$\sigma_{ij} = \mu\left(\frac{\partial u_i}{\partial x_j} + \frac{\partial u_j}{\partial x_i}\right) - \frac{2}{3}\mu\left(\frac{\partial u_k}{\partial x_k}\right)\delta ij, \quad q_j = k_T \frac{\partial T}{\partial x_j} \, . \tag{4}$$

Here, $u_i, \rho, p, T, c_p, \mu$ and k_T represent the velocity components, density, pressure, temperature, specific heat at constant pressure, dynamic viscosity and thermal conductivity coefficient, respectively. δ_{ij} is the Kronecker delta and summation is implied over repeated indices. For a compressible fluid that obeys the perfect gas equation of state we also have:

$$\rho = \frac{p}{RT} \, , \tag{5}$$

where R is the gas constant.

Designating a generic dependent variable by ϕ, it is possible to write a general transport/balance equation as

$$\frac{\partial (\rho \phi)}{\partial t} + \frac{\partial \left(\rho u_j \phi\right)}{\partial x_j} = \frac{\partial}{\partial x_j}\left(\Gamma^\phi \frac{\partial \phi}{\partial x_j}\right) + q^\phi, \tag{6}$$

where the definitions of Γ^ϕ and q^ϕ can be deduced from the mass, momentum and energy equations. Equation (6) includes four terms that correspond to the time-derivative at a fixed point in space, convection, diffusion and production/dissipation effects. In fact, all terms not explicitly accounted for in the first three terms are included in the source term q^ϕ.

3 Modification to ReFRESCO solver

ReFRESCO uses the finite volume method for discretization, which means that the governing equations are written in integral form. The domain is discretized by a finite number of contiguous control volumes (CVs) or cells of arbitrary shape. ReFRESCO uses a collocated arrangement for all variables, which means that unknowns are determined at the center of the CVs. Each CV is bounded by a number of cell faces that define the CV surface.

Mass, momentum and energy balances are written for a Cartesian coordinate system in strong conservation form (convection and diffusion terms written as the divergence of a vector field), which leads to volume and surface integrals that must be determined for each CV. Picard linearization is applied to the convective terms of all transport equations, which means that mass fluxes at the boundaries of the CVs are taken from a previous iteration. Solution of mass and momentum balances may be coupled or segregated, whereas solution of the energy equation is always segregated. In this work, we will focus only on the segregated approach.

The discretization techniques are described for the generic transport equation (6). However, determination of the pressure field based on mass conservation requires a different treatment and so it will be described separately.

When equation (6) is integrated over a CV and Gauss's theorem is applied to the terms written in divergence form we obtain

$$
\underbrace{\int_V \frac{\partial (\rho\phi)}{\partial t} \, dV}_{\text{time derivative term}} + \underbrace{\int_S (\rho\phi\mathbf{v}) \cdot \vec{\mathbf{n}} \, dS}_{\text{convective term}} = \underbrace{\int_S \left(\Gamma^\phi \nabla\phi\right) \cdot \vec{\mathbf{n}} \, dS}_{\text{diffusion term}} + \underbrace{\int_V q^\phi \, dV}_{\text{source term}} \; . \tag{7}
$$

The surface S corresponds to the sum of the boundary faces of a CV with volume V.

Equation (7) includes four distinct integrals: the volume integral that quantifies the rate of change of quantity ϕ in volume V (transient or unsteady term); the surface integral that quantifies the balance of the convective fluxes (fluxes out minus fluxes in); balance of diffusive fluxes quantified by a surface integral and a volume integral that quantifies the sources and sinks existing in volume V. All the integrals included in equation (7) are approximated with the second-order mid-point rule.

ReFRESCO contains a module (solve_phi) that solves the general transport equation (7) for specific values of Γ^ϕ and q^ϕ, which have to be determined separately for the momentum and energy balances. On the other hand, there is another module (pressure) that handles the mass balance that it is used for the the determination of the pressure field.

In the present development the module (solve_phi) remains unchanged. Modifications required to include compressibility effects[1] have been performed in the calculation of the right-hand side of the momentum equations[2] and in the pressure correction obtained from the SIMPLE algorithm.

3.1 Momentum equations

Naturally, in compressible flows the density ρ is no longer constant and so ρ at the face centres must be determined from the cell centre values where the dependent variables are stored. However, such requirement is already present for multiphase flows in ReFRESCO. On the other hand, the fact that $\nabla \cdot \mathbf{v} \neq 0$ produces extra terms in diffusion that are equal to a volume integral of $\mu\nabla(\nabla \cdot \mathbf{v}) + \nabla(\lambda\nabla \cdot \mathbf{v})$. For constant[3] μ and $\lambda = -2/3\mu$, this term is equivalent to the volume integral of $\mu/3\nabla(\nabla \cdot \mathbf{v})$.

---

[1]Assuming laminar flow at low Mach numbers simplifies significantly the inclusion of compressibility effects.

[2]The energy equation has not been addressed yet and so we use the temperature field of the manufactured solution imposed at the cells centre.

[3]The extension for variable μ is similar and unnecessary for the present manufactured solution.

This extra term of diffusion must be handled explicitly and its calculation is straightforward because its similar to the pressure gradient term. Therefore, the proposed strategy is:

- Define an array that contains $\nabla \cdot \mathbf{v}$ at the cells centre.

- Determine the gradient of this quantity using Gauss's theorem.

- Calculate the volume integral with the mid-point rule.

3.2 Pressure equation

The determination of pressure from the mass equation follows the SIMPLE algorithm that is described in Klaij and Vuik (2013) when velocity and pressure at iteration $k+1$ are written as $\mathbf{v}^{k+1} = \mathbf{v}^* + \mathbf{v}'$ and $p^{k+1} = p^k + p'$. $\mathbf{v}^*$ stands for the velocity vector obtained from the solution of the momentum equations using the pressure gradient of the previous iteration

$$Q\mathbf{v}^* = f - Gp^k \tag{8}$$

and $\mathbf{v}'$ and p' are the velocity and pressure corrections, respectively. Q is the matrix obtained from convection and diffusion, f is the right-hand side and G stands for the gradient matrix. Satisfying momentum at iteration $k+1$ requires

$$Q\mathbf{v}^{k+1} = f - Gp^{k+1} . \tag{9}$$

The difference between equations (9) and (8) and the SIMPLE approximation that retains only the diagonal terms to obtain Q^{-1} leads to the relation between u' and p'

$$\mathbf{v}' = -\mathrm{diag}(Q^{-1})Gp' . \tag{10}$$

Equation (10) assumes that ρ is constant, i.e. it is the same for equations (8) and (9), which is not true because it should be ρ^k for equation (8) and ρ^{k+1} for equation (9). A simple way to obtain an equation similar to (10) is to use $\rho\mathbf{v}$ as the dependent variable of the momentum equations. However, at this stage, we have just performed the update of ρ at the end of iteration $k+1$ and so equation (10) remains unchanged.

The equation that determines p' is derived from satisfaction of mass conservation at iteration $k+1$, which for an incompressible fluid leads to

$$D\mathbf{v}^{k+1} + Cp^{k+1} = g , \tag{11}$$

where D stands for the divergence matrix, C is the matrix that includes the pressure weighted interpolation Miller and Schmidt (1988) that avoids oscillations in collocated grids and g is the right-hand side[4]. Replacing u^{k+1} and p^{k+1} in equation (11) and using the SIMPLE approximation for Q^{-1} leads to

$$\left(C - D\mathrm{diag}(Q^{-1})G\right) p' = g - Du^* - Cp^k . \tag{12}$$

Naturally, equation (12) is not valid for a compressible fluid because mass conservation includes also ρ derivatives. Inclusion of the effect of these derivatives in the determination of p' are discussed in the open literature, as for example in Ferziger and Perić (2002). However, in the present study we have just added the contribution of these terms explicitly to g, i.e. there is a volume integral of the term[5]

$$-\frac{1}{\rho^k}\nabla\rho^k \cdot \mathbf{v}^*$$

added to g. Obviously, this option cannot lead to a robust solution procedure. Nonetheless, it serves as the starting point for the implementation of algorithms that include the effect of ρ^{k+1} in the determination of $\mathbf{v}^{k+1}$ and p^{k+1}.

---

[4]For a flow with ρ equal in the complete domain it includes only explicit contributions from boundary conditions.
[5]The present study is performed for steady flow.

4 Manufactured Solution

Manufactured solutions provide an excellent framework to perform Code Verification. The present solution does not have any resemblance with a realistic flow. However, the purpose of this solution is to provide the means to check the development of a pressure based compressible flow solver.

4.1 Domain definition

The domain is a square of side L, which means that in dimensionless terms we have $0 \le x/L \le 1$ and $0 \le y/L \le 1$. Cartesian equally-spaced grid are used in the present exercise and so the grid refinement ratio is defined as:

$$r_i \equiv \frac{h_i}{h_1} = \frac{NX_1 - 1}{NX_i - 1} = \frac{NY_1 - 1}{NY_i - 1} \ , \tag{13}$$

where NX and NY are the number of grids nodes in the horizontal and the vertical direction, respectively.

4.2 Manufactured Dependent Variables

The definition of the analytically solution of all the dependent variables of a subsonic, laminar flow requires the definition of several fluid properties. In the present work, we have selected the following values: ratio of specific heats $\gamma = 1.4$; specific gas constant $R = 287.0 m^2/\left(s^2\,K\right)$; constant dynamic viscosity $\mu = 10 kg/\left(m\,s\right)$ and a Prandtl number $Pr = 1$.

The present manufactured solution is an adaptation of solutions available in the open literature. The main differences to the solutions proposed by Roy et al. (2004) are related to the boundary conditions, which are inspired by Eça et al. (2012). The analytical solutions of the dependent variables of a two-dimensional, steady, laminar, subsonic flow take the form:

$$\phi\left(x, y\right) = \phi_0 + \phi_x f_{s_x}\left(\frac{a_{\phi x}\pi x}{L}\right) + \phi_y f_{s_y}\left(\frac{a_{\phi y}\pi y}{L}\right) + \phi_{xy} f_{s_{xy}}\left(\frac{a_{\phi xy}\pi xy\left(x-1\right)\left(y-1\right)}{L^4}\right) \ , \tag{14}$$

where ϕ_i represents any of the primitive variables (ρ, u, v, p) and the function f_s represents sine or cosine functions. Table 1 presents the constants ϕ_i and functions f_s defined for each variable.

Table 1: Constants and functions for the definition of a manufactured solution for a two-dimensional, laminar, subsonic flow.

Equation,ϕ	ϕ_0	ϕ_x	ϕ_y	ϕ_{xy}	f_{s_x}	f_{s_y}	$f_{s_{xy}}$	$a_{\phi x}$	$a_{\phi y}$	$a_{\phi xy}$
$\rho\left(kg/m^3\right)$	1	0.1	0.15	-0.08	cos	cos	cos	0.5	0.5	0.5
$u\left(m/s\right)$	70	4	-12	7	cos	sin	cos	0.5	0.5	0.5
$v\left(m/s\right)$	90	-20	4	-11	sin	sin	cos	0.5	0.5	0.5
$p\left(N/m^2\right)$	1×10^5	-0.3×10^5	0.2×10^5	-0.25×10^5	cos	cos	cos	0.5	0.5	0.5

The ϕ constants have the dimensions of the primitive variable and the a constants are dimensionless. The temperature is obtained from the ρ and p solutions and the equation of state of a perfect gas (5).

4.3 Boundary Conditions

The boundary conditions for the selected domain are given in Table 2. The goal of this choice is the ability to use standard choices of practical flow calculations, which include Inflow and Fixed Pressure conditions. In table 2, Dirichlet stands for a prescribed value and Neumann for a zero normal derivative.

5 Code verification

Two different exercises were performed for the selected manufactured solution: determination of the formal and observed orders of grid convergency. The first case is performed from the determination of the residual of the discretized equations with the exact solution specified at the cells centre, whereas the latter one requires the numerical solution of the discretized system of equations.

Table 2: Boundary conditions of a manufactured solution for a two-dimensional, laminar, subsonic flow.

Variable	Left	Right	Top	Bottom
ρ	Neumann	Dirichlet	Dirichlet	Neumann
u	Dirichlet	Neumann	Neumann	Dirichlet
v	Dirichlet	Neumann	Neumann	Dirichlet
p	Neumann	Dirichlet	Dirichlet	Neumann

In the present study, we have not solved the energy equation. Temperature is defined at the cells centre using the exact solution. Finest grid includes 256×256 cells and the coarsest 8×8 cells covering a grid refinement ratio of $r_i = 32$.

5.1 Determination of the formal order of accuracy of grid convergence

The pressure weighted interpolation is not included in the calculation of the residuals of the continuity and momentum equations for the determination of the formal order of grid convergence.

Table 3: Formal orders of grid convergence obtained from the L_2 and L_∞ norm of the normalized residuals of the continuity and momentum equations.

r_i	L_2			L_∞		
	p_{f_u}	p_{f_v}	p_{f_p}	p_{f_u}	p_{f_v}	p_{f_p}
1	2.47	2.49	2.48	1.95	1.98	1.97
2	2.44	2.49	2.46	1.91	1.97	1.93
4	2.36	2.49	2.43	1.80	1.95	1.87
8	2.21	2.53	2.37	1.57	1.95	1.78
16	2.02	2.67	2.27	0.85	2.00	1.63

The formals order of grid convergence p_f obtained are presented in table 3. The results obtained from the L_2 norm of the normalized residual lead to values close to 2.5, which are likely to be a consequence of regions of the domain where the residual is too small. On the other hand, the L_∞ norm leads to values of p_f that converge to 2 as expected.

5.2 Determination of observed order of accuracy

A meaningfull determination of the observed order of grid convergency p_o requires solutions that exhibit iterative errors that are negligible when compared to the discretization. With the present solution procedure, it was not easy to achieve such result in the finest grid. Nonetheless, the results presented in table 4 are determined from the numerical error of solutions that were converged to (almost) machine accuracy for $r_i \geq 4$.

Table 4: Observed orders of grid convergence obtained from the L_2 and L_∞ norm of errors of the velocity and pressure fields.

r_i	L_2			L_∞		
	p_{f_u}	p_{f_v}	p_{f_p}	p_{f_u}	p_{f_v}	p_{f_p}
1	1.52	2.09	1.11	1.61	1.74	0.69
2	2.16	2.04	1.04	1.35	1.57	0.46
4	1.98	1.92	0.96	0.96	1.36	0.30
8	1.78	1.90	1.00	0.33	1.31	0.65
16	1.93	1.96	1.14	1.67	1.45	0.52

The results presented in table 4 suggest that the velocity components converge with second order accuracy, whereas the pressure field exhibits only fist order accuracy. However, the iterative error obtained

in the finest grids (that exhibit the smallest discretization errors) is not sufficient to determine asymptotic orders of grid convergence.

6 Final remarks

This paper presents the first step of the adaptation of ReFRESCO to the solution of multiphase, turbulent, compressible flows. It includes a Code Verification exercise performed for a manufactured solution of two-dimensional, laminar, subsonic flow that includes the determination of the formal and observed orders of grid convergence.

Although the present solution procedure handles density updates explictly, the present manufactured solution provides an excellent framework to test/develop robust approaches for pressure based algorithms for the solution of compressible flows.

References

P.J. Roache and S. Steinberg (1984). Symbolic manipulation and computational fluid dynamics. *AIAA Journal*, **22**(10), 1390–1394.

P.J. Roache, P.M. Knupp, S. Steinberg, and R.L. Blaine (1990). Experience with benchmark test cases for groundwater flow. In 1990 Spring Meeting of the Fluids Engineering Division, Toronto, Ontario, Canada.

C.J. Roy, C.C. Nelson, T.M. Smith and C.C. Ober (2004). Verification of Euler/Navier-Stokes codes using the method of manufactured solutions. *International Journal for Numerical Methods in Fluids*, **44**, 599–620.

L. Eça, M. Hoekstra and G. Vaz (2012). Manufactured solutions for steady-flow Reynolds-averaged Navier-Stokes solvers. *International Journal of Computational Fluid Dynamics*, **26**(5), 313–332.

J.H. Ferziger and M. Perić (3rd ed.) (1996). *Computational Methods in Fluid Dynamics.* Springer-Verlag, Berlin, Heidelberg, New York.

F. Moukalled and M. Darwish (2006). Pressure based algorithms for single-fluid and multifluid flows. *In: Minkowycz, W.J., Sparrow, E.M. and Murthy J.Y. (eds) Handbook of numerical heat transfer (2nd ed.). Wiley*, 325–367.

S.T. Miller, H. Jasak, D.A. Boger, E.G. Paterson and A. Nedungadi (2013). A pressure-based, compressible, two-phase flow finite volume method for underwater explosions. *Computers & Fluids*, **87**, 132–143.

C.J. Roy, T.M. Smith and C.C. Ober (2004). Verification of a compressible CFD code using the method of manufactured solutions. *AIAA Journal, AIAA Paper 2002-3110*.

W.L. Oberkampf and C.J. Roy (1st ed.) (2010). *Verification and Validation in Scientific Computing.* Cambridge University Press.

C.M. Klaij and C. Vuik (2013). SIMPLE-type preconditioners for cell-centered, colocated finite volume discretization of incompressible Reynolds-averaged NavierâStokes equations. *International Journal of Numerical Methods in Fluids*, **71**, 830-849.

Miller T and Schmidt F (1988). Use of a pressure-weighted interpolation method for the solution of the incompressible Navier-Stokes equations on a nonstaggered grid system. *Numerical Heat Transfer*, **14**, 213-233.

Full-scale Unsteady RANSE CFD Seakeeping Simulations of a High-Speed Craft

Batuhan Aktas[†], Federico Prini[*], Simon Benson[*]
[†]University of Strathclyde, [*]Newcastle University
batuhan.aktas@strath.ac.uk
federico.prini@ncl.ac.uk
simon.benson@ncl.ac.uk

1 Introduction

This paper presents a series of RANSE-based seakeeping simulations on a 17m high-speed monohull. The study is performed on the Severn Class all-weather search and rescue lifeboat, designed and operated by the Royal National Lifeboat Institution (RNLI). The Severn is a planing craft with a maximum operational speed of 25 knots, although it often operates at semi-planing and displacement speeds in different situations and weather conditions.

The work in this paper is an independent follow-up study from the EDSARC project (Enhanced Design of Search and Rescue Craft), a collaboration between Newcastle University, the Royal National Lifeboat Institution (RNLI) and Lloyd's Register (LR). The EDSARC project aims to develop improved methods to predict the structural loads on lifeboats including wave bending moments, pressure and slamming loads. The EDSARC project has assessed the structural response of the Severn in different operating conditions from full-scale trial data, segmented model tests in a towing tank and finite element analysis (FEA). Comparative data from EDSARC is presented in this paper.

Table 1: Severn Class main particulars.

Length overall	Loa	17.00	m
Length waterline	Lwl	15.50	m
Beam max	Boa	5.62	m
Draught	T	1.37	m
Displacement (full load)	Δ	42.0	t
Speed max	V	25	kn

Seakeeping measurements of the Severn were also completed in the EDSARC project to verify the structural response results. In particular, wave pressures were predicted using several frequency domain potential flow codes and mapped directly onto a global finite element model of the vessel (Fig.1). Three different linear codes were used: a panel method, a 2D strip theory and a 2.5D strip theory (Prini et al. 2015). In comparison to the model test results for heave and pitch over a range of wave encounter frequencies, better results were achieved with the 2D strip theory at low speed (up to 10 knots or Fn = 0.4) and a 2.5D strip theory at high speeds (from above 10 knots). The latter code includes a forward speed correction term, which makes it suitable for running cases at Froude numbers above 0.4.
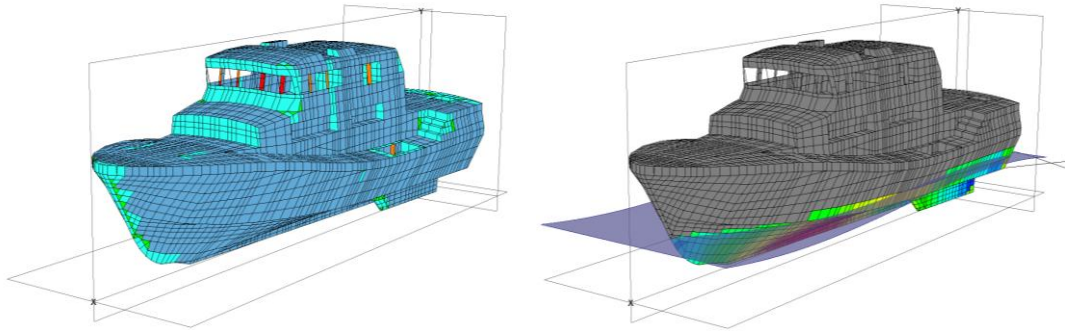
Fig. 1: Global structural finite element (FE) model.

A series of small-scale seakeeping experiments were conducted to validate the CFD results. Two scaled models of the Severn Class were built and tested at Newcastle University's towing tank (Fig. 2). Motions and hull girder loads were measured during tests conducted at varying speeds and in a range of regular waves. Details of the models, the test apparatus and preliminary motion results are detailed in Prini et al., (2016).

The seakeeping analyses presented an opportunity for us to make a further comparative study using a non-linear RANSE-based CFD model. We also discuss the potential use of the CFD model for the prediction of motions and pressure loads of a high-speed craft in waves.
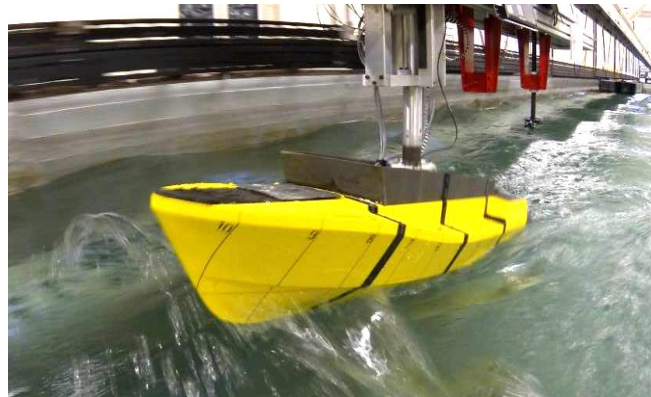
Fig. 2: Small-scale seakeeping experiment.

2 RANSE CFD model

The dynamics of the fluid flow around the RNLI's Severn Class lifeboat was simulated by using a numerical approach. The CFD package STAR-CCM+ finite volume stress solver was used to solve the governing continuity and momentum equations. The setup of the RANS simulations necessitated the determination of a number of crucial settings. Within this framework, the turbulence model selected was a standard "k–ε model" and "Volume of Fluid" (VOF) method was used to model and position the free surface. Dynamic Fluid Body Interaction (DFBI) model was utilized to simulate realistic ship behaviour. The vessel was set free to move in pitch and heave modes. The DFBI module simulates the motions of a rigid body based on the pressure and shear forces exerted by the fluid as calculated by the RANSE solver.

Only half of the vessel hull is modelled within the numerical domain by using a symmetry plane to provide savings from computational time. The computational domain used for the simulations is presented in Fig. 3. Thus, inlet boundary was placed $1L_{BP}$ forward, outlet was placed $3L_{BP}$ backward, side was placed $2L_{BP}$ port and the symmetry plane was located at the centreline of the hull.
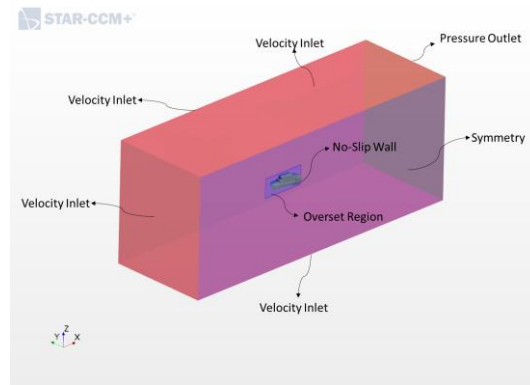
Fig. 3: Numerical domain and boundary conditions.

The Severn surface mesh is shown in Fig. 4. The model incorporates all the underwater hull appendages and details of the deckhouse. Overset meshes, also known as "Chimera" or overlapping meshes, were used to facilitate the motions of the full-scale lifeboat model. The overset region contains the hull body and moves with the hull over a static background mesh of the whole domain. The overset mesh method ensures accurate mesh density in the free surface region both in areas near the hull as well as in the far field regions such as inlet, outlet and ship wake regions.
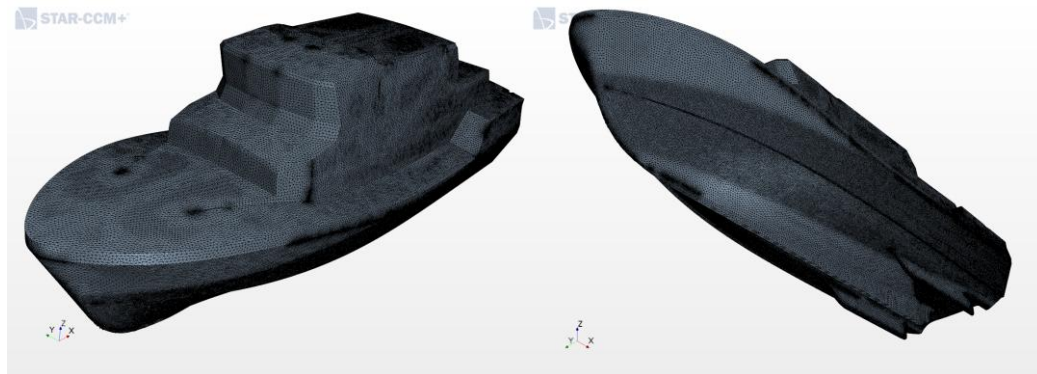
Fig. 4: RNLI's Severn Class Lifeboat surface mesh.

In order to capture the severe free surface flows incidents, a minimum of 150 grid points per wavelength was used near the hull free surface in both the downstream and upstream directions. For the free surface region, a minimum of 20 cells was used in the vertical direction to ensure accurate representation of the wave steepness (Tezdogan et al., 2015). These cell sizes corresponding to above guidelines are calculated for the worst case scenario (i.e. for the shortest wave) and used for all the cases. Overall, with the wake mesh refinement and volumetric mesh enhancements, the domain and the vessel were meshed with 12.5 Million cells as in Fig. 5. While the overset region is meshed with 6 million cells, the background region comprises 6.5 million cells.
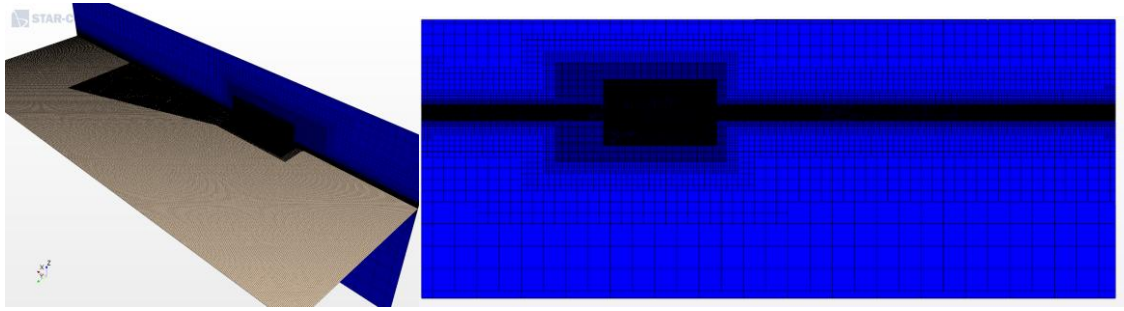
Fig. 5: Volume mesh overview.

The simulations were performed for 32 different conditions incorporating two different wave heights (1m and 2m), two speeds (15kn and 20kn) and eight different wavelengths as outlined in **Error! Reference source not found.**. A standard simulation took 48 hours to converge using 16 processors of the N8 High Performance Computing (HPC) facility. The free surface wave profile for a 2m wave height condition when the simulation is initialized is presented together with the wave profile produced by the numerical solver by Fig. 6

Table 2: Test matrix.

HEADING		SPEED		WAVE HEIGHT	λ/LOA
	[deg]	[kn]	[m/s]	[m]	
head waves	**180**	**15 & 20**	**7.72 & 10.29**	**1 & 2**	**1.4, 1.8, 2.2, 2.6, 3.0, 3.4, 3.8, 4.2**
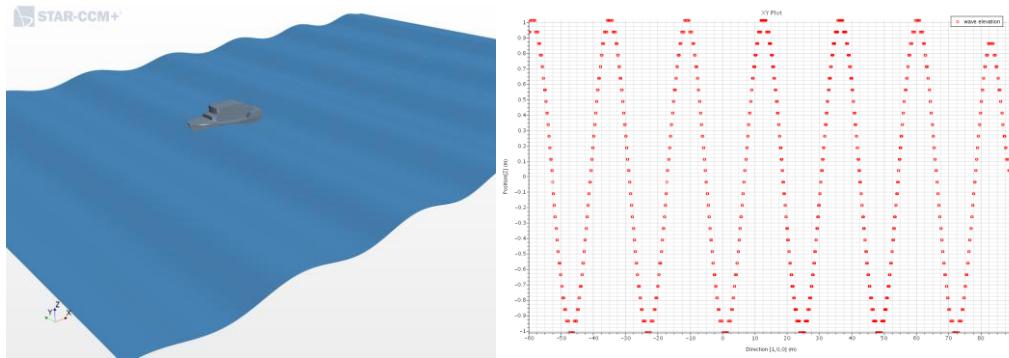
Fig. 6: Free surface wave profile (Left) and wave elevation plot (Right).

The convective CFL number introduced in STAR-CCM+ v11.06 helped significantly to satisfy keeping the CFL number at an average of 1 for the overall domain and increasing the time step when possible. While the minimum time-step was initially set to 256 time steps per wave encounter period, for certain λ/L_{OA} regions shorter time steps ($T_e/1024$) showed better agreement when compared with experimental findings, as discussed in detail within the Results section.

3 Results

Qualitative visual comparisons were made between towing tank video captures and RANSE CFD simulations. While video comparisons are rather more insightful for this purpose, Fig. 7 shows a sequence of snapshots taken during a typical wave encounter from CFD simulations and towing tank tests.
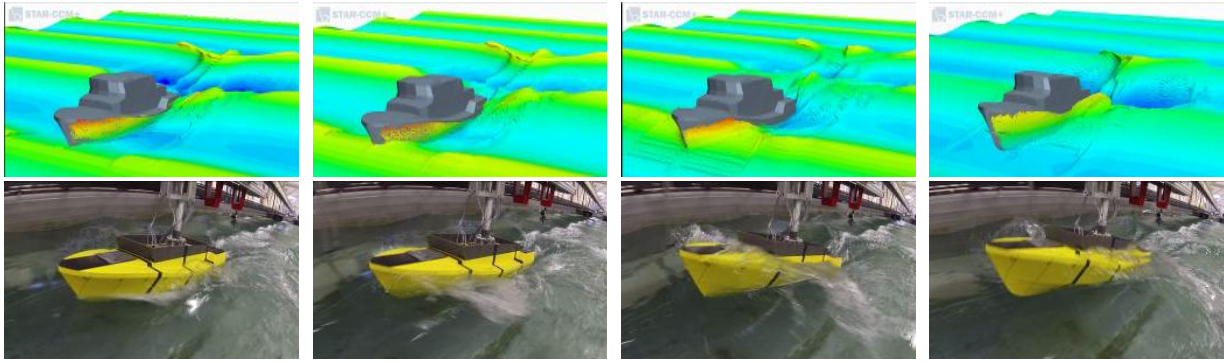
Fig. 7: Image sequence comparison of CFD simulation predictions and experimental observations.

All the motion results are presented in terms of response amplitude operators (RAOs) with the mean motion amplitudes normalised per mean wave amplitude. Both the experimental tests and the STAR-CCM+ simulations produced results in the time domain. A peak-to-peak analysis was conducted to compute the mean values for motion and wave amplitudes.

With the minimum time-step set at $T_e/256$ it was found that the simulations were over-predicting the heave and pitch responses at wavelengths $\lambda/L_{OA}=2.4$ to 3.6. Further simulations were completed with refined time-step settings to enable smaller time-steps with feasible the simulation time. An initial simulation stage was run at $T_e/256$ for seven wave encounters to balance the model. A second stage with a reduced time-step of $T_e/1024$ was then completed. The results were extracted from the second stage. Fig. 8 shows heave and pitch RAOs in regular head waves at 15 and 20 knots for the standard ($T_e/256$) and the refined ($T_e/1024$) time-steps.
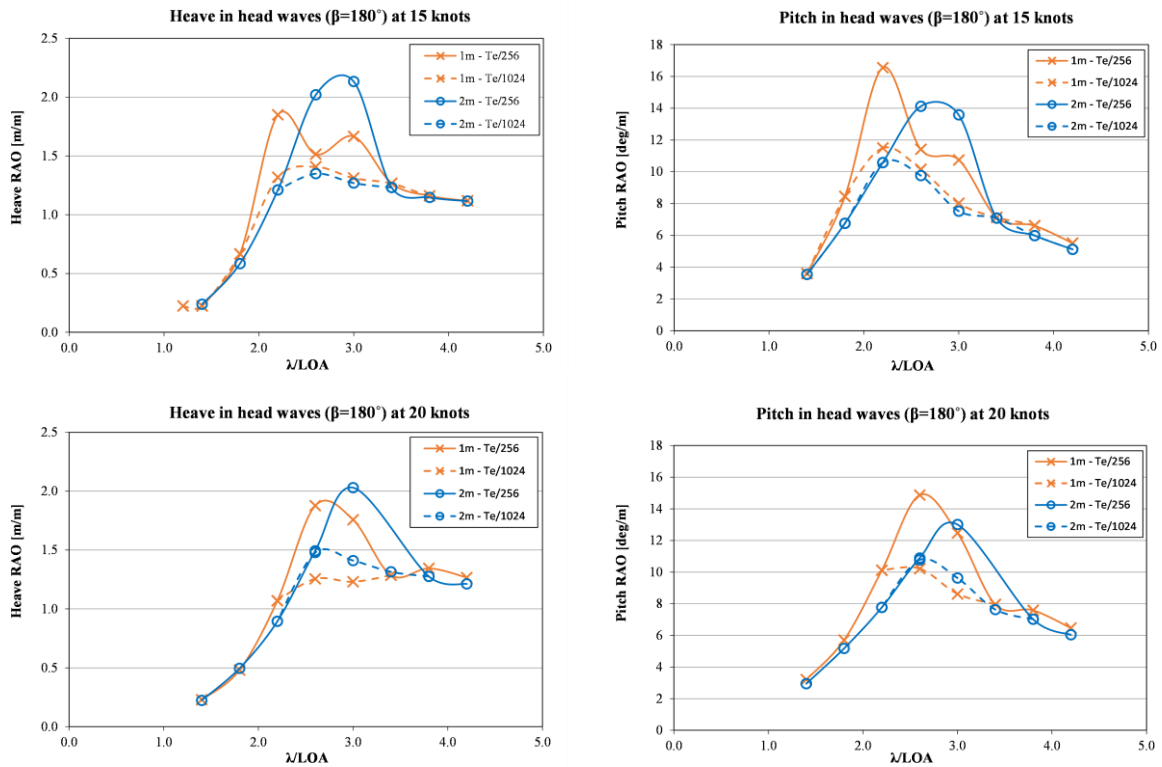
Fig. 8: Heave and Pitch RAOs for the standard and the refined time-steps.

The results obtained with the finer time-step were compared against those predicted by the potential flow solver MAESTRO-Wave and from the towing tank tests. Fig. 9 shows the heave and pitch RAOs in head waves at 15 and 20 knots from the three different methods.
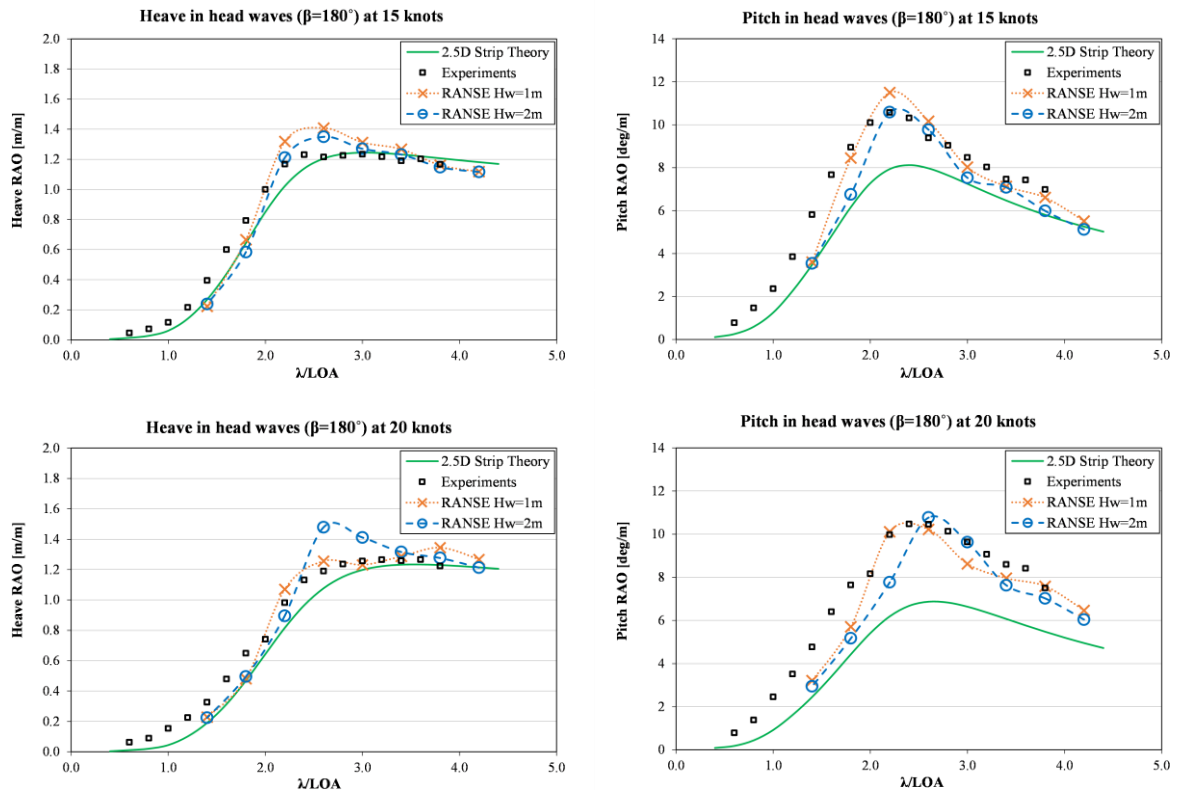
Fig. 9: Heave and Pitch RAOs from experiments, 2.5D Strip theory and RANSE CFD simulations.

4 Conclusions

Fully nonlinear unsteady RANS simulations are conducted at full scale to investigate the seakeeping performance of the RNLI's Severn Class lifeboat. For the majority of the simulations, a standard time-step, given by the ITTC as a guideline, has shown good correlation against the experimental results. However, in the range of wavelengths λ/L_{OA} =2.4 to 3.6, a finer time step has shown to improve the results. Further simulations in different wave heights are being conducted. The results will inform on the effect of the wave height on the seakeeping performance of the Severn. They will also help investigating the effect of the wave steepness on the time-step required to accurately capture the vessel's response in waves.

Acknowledgements

References

Prini, F., Benson, S., Birmingham, R., Dow, R. S., Phillips, H. J., Sheppard, P. J., & Mediavilla Varas, J. (2015). Seakeeping Analysis of a High-Speed Search and Rescue Craft by Linear Potential Theory. In *International Conference on Lightweight Design of Marine Structures*. Glasgow, UK.

Prini, F., Birmingham, R. W., Benson, S., Phillips, H. J., Sheppard, P. J., Mediavilla Varas, J., … Dow, R. S. (2016). Motions and Loads of a High-Speed Craft in Regular Waves: Prediction and Analysis. In *24th International HISWA Symposium on Yacht Design and Yacht Construction*. Amsterdam, NL.

Tezdogan, T., Demirel, Y. K., Kellett, P., Khorasanchi, M., Incecik, A., & Turan, O. (2015). Full-scale unsteady RANS CFD simulations of ship behaviour and performance in head seas due to slow steaming. *Ocean Engineering*, **97**, 186–206.

Virtual Captive Tests with a destroyer hull form

Martin Alexandersson,Kadir Burak Korkmaz and Gabriele Mazza
SSPA Sweden AB, Gothenburg/Sweden
martin.alexandersson@sspa.se, burak.korkmaz@sspa.se, gabiele.mazza@sspa.se

1   Introduction

This extended abstract presents results from a research project carried out at SSPA where Virtual Captive Tests (VCT) have been investigated. Expertise on CFD and manoeuvring model tests have been involved in the project. The abstract presents how the VCT have been conducted and the results are compared to captive model tests and free sailing model tests. The usage of VCT in commercial ship design projects is also discussed.

1.1   Definition

There are generally two different model test methods used to investigate manoeuvring performance of a vessel. Model tests with a free sailing model or model tests with a captive model.

Model test with a free model is the most accurate and widely used method. The model is free to move in all directions. Forces and moment are applied to the model by propeller(s) and rudder(s) and the resulting motions are measured.

In captive model tests, the hydrodynamic forces acting on a ship model are measured at various speeds, drift angles, yaw rates etc. The ship model is held captive, which means that it is forced to move in simple predefined motions and the resulting hydrodynamic forces are measured by a captive balance. The measured hydrodynamic forces are then used in a manoeuvring simulations model, in order to predict the ship motions. This methods implies some assumptions that may introduce errors in certain conventional trial manoeuvre tests and it is therefore not so frequently used today.

Using CFD in the time domain, to simulate a test with a free model, is however considered too advanced, time-consuming and expensive. Which is why a combination of captive test, CFD calcualtions and manoeuvring simulations presents a more feasible option. VCT presents a faster and cheaper way to conduct captive tests. Figure 1 shows an example of rudder angle captive test with CFD.
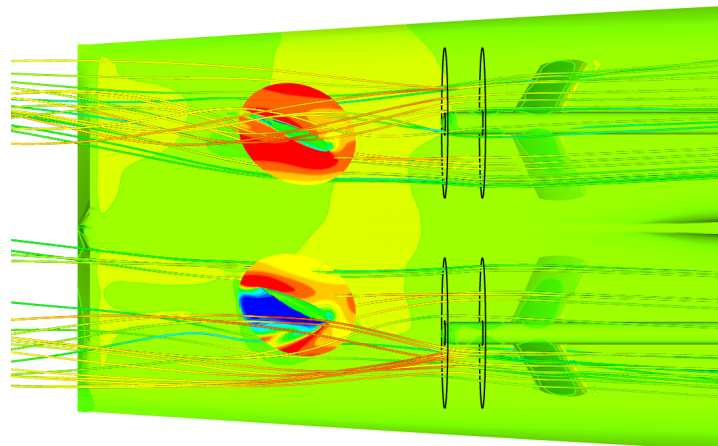
Fig. 1: Example of rudder angle variation captive test with CFD.

1.2 Commercial usage

Manoeuvring performance is of great importance in the design of a new ship. Much effort is spend to fullfill the IMO Standards for ship manoeuvrability (2002). From experience in many commercial model test projects conducted at SSPA, it is the authors belief that manoeuvring performance are generally verified too late in the design process. As a consequence shipyards have sometimes to face costly and time-consuming last-minute changes to the design, in order to improve poor manoeuvring performance. In other situations, the manoeuvring performance is "too good", which means that the ship design is not optimal, perhaps the rudder could have been smaller? There has not been any cost and time-efficient method to investigate manoeuvring performance at an early design stage, with sufficient accuracy and the ability to capture small design changes. This is probably the reason why manoeuvring is usually addressed at the end of the design process, as final validation rather than as part of the optimization process. VCT might be a method that can fill this gap, which would enable a more optimal design process.

2 VCT Calculations

The VCT calculations have been conducted with a destroyer hull form that was previously tested at SSPA. The hull has a complex set of appendages (2 sets of bilge keels, 2 sets of stabilizer fins, shafts, V brackets and full spade rudders) as shown in Figure 2. This hull was chosen since results from model test with both a free and captive model were available.
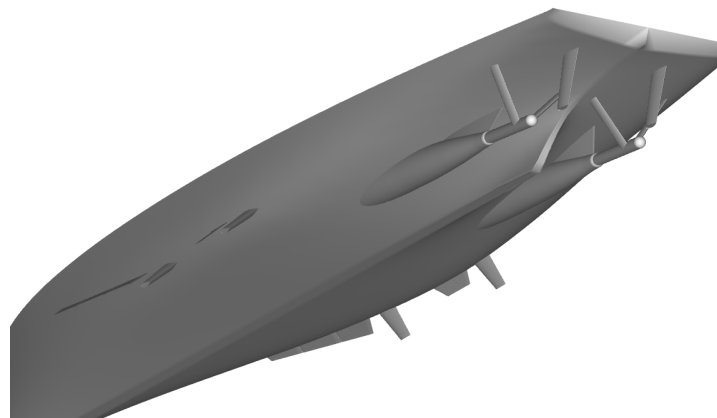
Fig. 2: Appended hull

The calculations have been conducted according to Table 1. The test matrix includes only captive tests with static flow. The dynamic tests: pure sway, pure yaw and roll decay, which are used to derive added mass, were excluded because they were considered too difficult to calculate with CFD. The VCT calculations have been compared with corresponding captive model tests. Figure 4 and Figure 5 shows an examples of this.

2.1 Numerical Computation

The study concerns hull form at 18 knots corresponding to Fn = 0.24 at design draught. The computations were carried out at model scale which corresponds to physical model produced at SSPA. Including the grid dependence study, all simulations were performed fully appended as can be seen at Figure 1.

2.2 Numerical Method

Two of the flow solver modules of SHIPFLOW have been used for the current study: the potential flow solver (XPAN) and the viscous RANS solver (XCHAP).

Potential flow computations were carried out with XPAN, which is a first order panel method with non-linear free-surface boundary conditions. Wave making resistance, sinkage and trim for the bare hull were then obtained.

Viscous flow computations for all cases were carried out using the XCHAP module. Sinkage and trim were fixed to the values from the potential flow solution, but with symmetry conditions applied on the free-surface (double model simulation). The EASM turbulence model was used and no-slip conditions were applied on the hull surface as well as the appendages. No port-starboard symmetry condition were applied since all viscous simulations included operating propellers and some deflected rudders or drift angle. XCHAP is a steady state solver using structured, overlapping grids. Therefore bilge keels, stabilizer fins, shafts, shaft bossings, shaft brackets and rudders were introduced trough overlapping grids. The solver for steady incompressible flow is based on a Roe scheme for discretization of the convective terms while a central scheme is used for the diffusive fluxes. An explicit flux correction is applied in order to achieve second order accuracy.

Self propulsion is performed by body forces applied in a cylindrical grid component at the location of the propeller accoring to Broberg, L., & Orych, M. (2012). The body forces are calculated within Lifting Line (LL) propeller analysis program. The flow passing through the propeller disk is accelerated by the forces in the axial and tangential directions as if it had passed a propeller with an infinite number of blades (Zhang, D (1990)). This is an iterative process, the body forces are updated every tenth iteration in XCHAP. Once the simulation is converged the total wake and the lifting line method should match in the selected propeller plane (Broberg, L., & Orych, M. (2012)). In order to find the required propeller turning rate for the VCT tests, self propulsion mode have been used. Wave resistance have been introduced by a negative towing force since the simulations neglected the wave resistance.

The XCHAP computations were performed with the computational domain that consists of six boundaries as shown in Figure 3. The distance between inlet and fore-perpendicular (FP) is $0.5L_{PP}$. The outflow plane however is located at $0.8L_{PP}$ behind the aft-perpendicular. Radius of the cylindrical outer boundary is $3L_{PP}$ in order to prevent the blockage effect as much as possible. For the drift angle and circle tests the slip (the side of the half cylinder), inflow and outflow boundary conditions are modified and a body force is applied to the flow in order to provide an onset flow to the hull.

A grid dependence study have been performed with the drift angle of 6 degrees. In total, five body-fitted structured grids are generated systematically where total number of cells ranging between 25M to 4.3M. A uniform refinement ratio $r = h_{i+1}/h_i = \sqrt[4]{2}$ is applied in the three directions of the domain. No wall functions are introduced and employed y^+ values are refined with the same ratio. K_T and K_Q values of both propellers are monotonically converged.
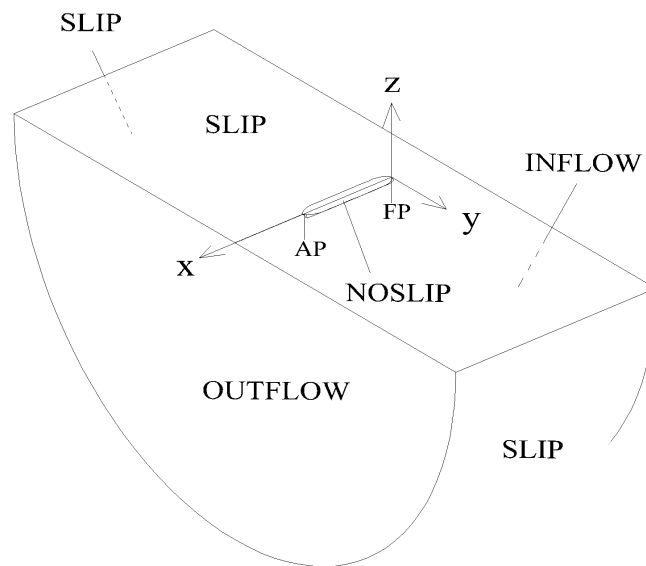
Fig. 3: Viscous flow computational domain

Table 1: Test program for the VCT calculations

Test type	speed	heel angle	rudder angle	drift angle	rpm ratio	Turning radius
		Φ	δ	$\beta = \psi$	$\eta = \eta/\eta_0$	L_{pp}/R
	[knots]	[deg]	[deg]	[deg]	[-]	[-]
Straight line	18				1	
Rudder angle	18				1	
			5		1	
			10		1	
			15		1	
			25		1	
			35		1	
rpm	18		15		0.8	
					0.9	
					1.1	
					1.2	
Drift angle	18			2	1	
				4	1	
				6	1	
				8	1	
				10	1	
Circle	18				1	0.1
					1	0.2
					1	0.3
					1	0.4
					1	0.5
Circle + Drift	18			2	1	0.2
				3	1	0.2
				4	1	0.2
				5	1	0.2
				6	1	0.2
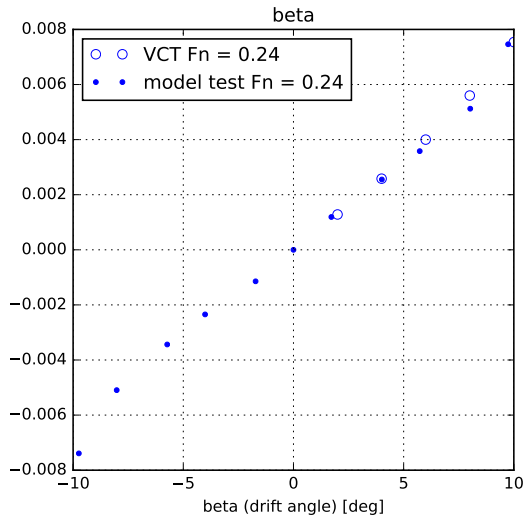
Fig. 4: Comparison of yawing moment between VCT and captive model tests.
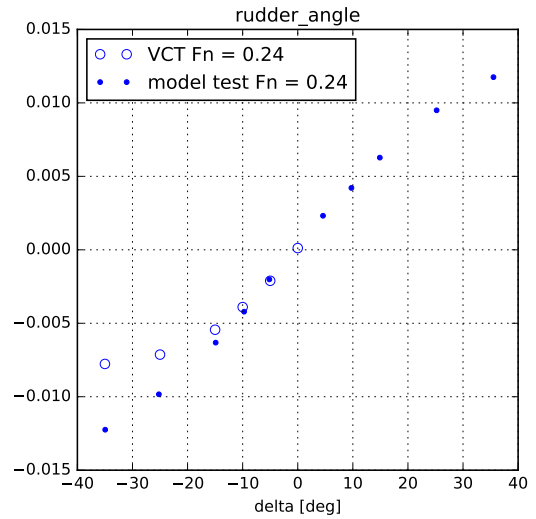
Fig. 5: Comparison of transverse force between VCT and captive model tests.

3 Manoeuvring simulations

Manoeuvring simulations are conducted in the time domain with a slow-motion derivatives model similar to Norrbin (1970). This is done in order to turn the static forces from the VCT calculations into dynamic manoeuvres. This approach does not attempt to model the physics of the complicated flow over the manoeuvring hull. It is simply assumed that the forces are dependent upon the motion variables, their time derivatives, hull geometry and the rudder angle. A Taylor series expansion of forces (from VCT) is used and equations of motion are solved.

Simulations were conducted according to the standard tests defined in Table 2. Missing added mass

coefficients from VCT where taken from the corresponding captive model tests. Comparison between model tests with free model, captive model tests with manoeuvring simulation and VCT with manoeuvring simulation are shown in Figure 6 and Figure 7.

Table 2: Test program for the simulations

Series	Run	Test type	Rudder angle	Direction	Speed
			[deg]		[knots]
2	15	Turning circle	35	stbd	18
2	1	Zig-zag	10	stbd	18
2	3	Zig-zag	20	stbd	18
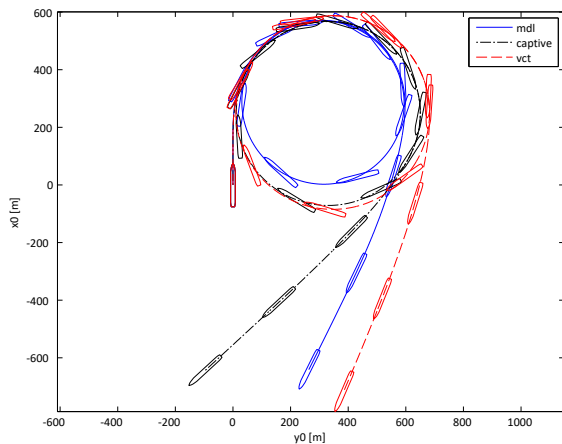
Fig. 6: Comparison of turning circle: model tests with free model (mdl), captive model tests with manoeuvring simulation (captive), VCT with manoeuvring simulation (vct).
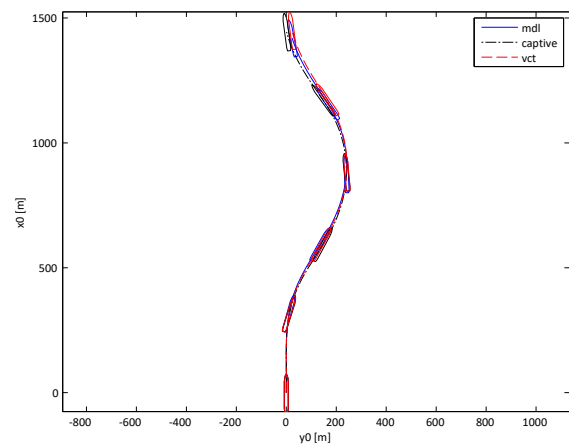
Fig. 7: Comparison 20/20 zig-zag: model tests with free model (mdl), captive model tests with manoeuvring simulation (captive), VCT with manoeuvring simulation (vct).

4 Conclusion

The CFD calculations made in this project has been compared with model test results (both with free and captive model). For some cases (for instance drift angle tests, Figure 4) the agreement between calculations and model tests has been very good. For some cases (for instance rudder angle tests, Figure 5) the agreement has not been so good at high rudder angles. The rudder angle tests showed that stalling behaviour of the rudders was not captured well in the CFD calculations.

A second phase of the research project will be carried out with the purpose of improving the VCT capabilities. It will be possible to conduct captive model tests specifically for the research project. New CFD calculations and captive model tests will be conducted with a tanker hull form. The benefits will be that the captive model tests program can be tailor-made to answer questions raised in the first phase of the project. For instance, the stalling behaviour of the rudders will be investigated more closely. The tests will be conducted at much lower Froude numbers (than for the destroyer in the first phase) and with a simpler set of appendages. This should validate some of the assumptions made in the CFD calculations.

Acknowledgements

References

Nils H. Norrbin (1970). Theory and observtions on the use of a mathemtical model for ship manoeuvring in deep and confined waters. *Proc Eight Symposium on Naval Hydrodynamics Pasadena.*

IMO (2002). Interntional Maritime Organiztion, *Standards for ship manoeuvrability, MSC.137(76).*

Broberg, L., & Orych, M. (2012), *An Efficient Numerical Technique to Simulate the Propeller Hull Interaction., International Journal of Innovative Research & Development, 14.*

Zhang, D (1990), *Numerical Computation of Ship Stern/Propeller Flow (Doctoral dissertation)., Department of Shipping and Marine Technology, Chalmers University of Technology, Gothenburg.*

A Methodology to Identify Erosive Collapse Events in the Incompressible Simulation of Cavitating flows

Mohammad Hossein Arabnejad[*] , Rickard Bensow[*],
[*]Department of Mechanics and Maritime Sciences, Chalmers University of Technology, Gothenburg, Sweden
mohammad.h.arabnejad@chalmers.se

1 Introduction

Cavitation erosion is one of the limiting factor in the design of hydraulic machineries such as propellers, pumps, diesel injectors, etc. The material loss due to cavitation erosion imposes restriction on the performance of hydraulic systems and leads to significant increase in maintenance and repair costs. It is therefore essential to evaluate the risk of cavitation erosion in the design process. In marine applications, the erosion risk is usually assessed by experimental investigations on model scale. Visual assessment of collapsing cavities using high speed video (Bark et al.,2004) complemented by paint test and/or acoustic measurement(van Rijsbergen et al.,2004) has been used for this purpose. As the experimental assessment of cavitation erosion are usually applied on the model scale, the risk of erosion on the full scale are assessed by calibrating the risk of erosion on model scale using ad hoc correlations.
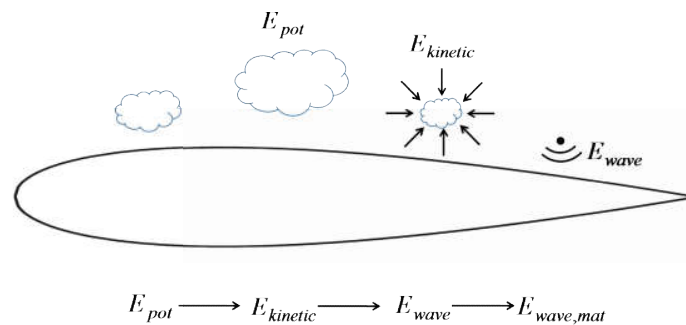
Fig. 1: A sketch of cavitation erosion mechanism based on a concept of energy cascade

Over past decade, a significant progress has been made in numerical modelling of cavitating flows. Several numerical studies have shown that current numerical methodologies are capable of reproducing the main feature of cavitating flows (Bensow and Bark (2010) and Asnaghi et al.(2017)). It is thus becoming feasible to develop numerical erosion indicators models that can predict the risk of erosion based on the result of numerical simulation. van Terwisga et al.(2009) reviewed several erosion models and concluded that the erosion models by Bark et al.(2004) and Fortes-Patella et al. (2004) are suitable for numerical prediction of cavitation erosion. These models are based on the concept of hydrodynamic energy cascade which considers an energy balance between the potential energy of collapsing vapour structures and surface material damage. Based on this energy balance, Bark et al.(2004) introduced the concept of kinematic focusing of collapse energy which describes that the energy of collapsing cavities is focused into small area of the surface material in an erosive collapse(Fig. 1). According to Bark et al.(2004), when a cavity expands in the low pressure region, the surrounding liquid gains potential energy. This potential energy is transformed into kinetic energy when the cavity collapses in the pressure recovery region. At the end of collapse, the kinetic energy of liquid is then converted into acoustic energy which is radiated through pressure waves in the surrounding liquid. Fortes-Patella et al.(2004) provided a similar description for erosive events and

described that some part of the acoustic energy is absorbed by the material when the emitted pressure waves hits the surface. If the absorbed energy exceeds a certain threshold which is a function of material properties, cavitation erosion can occur.

The aim of this study is to present a numerical tool that can identify the erosiveness of a macro-scale collapsing cavity, based on the concept of hydrodynamic energy cascade introduced in the EroCav Handbook (Bark et al., 2004). The proposed numerical method is applied for the cavitating flow over a 3D NACA0015 foil. Erosive collapse events are identified and their locations are compared with experimental erosion pattern by Rijsbergen et al. (2012).

2 Methodology

The potential energy of a cavity at the start of the collapse is defined as

$$E_{pot} = V_0 \,\triangle p \tag{1}$$

where $\triangle p = P_\infty - P_v$, P_v is the vapor pressure, P_∞ is the liquid pressure at infinity, and V_0 is the initial volume of the cavity. Based on the concept of energy cascade. Fortes-Patella et al(2004) proposed that the aggressiveness of a collapsing cavity can be assessed by a parameter called the collapse efficiency, η. This parameter determines what percentage of the potential energy of a cavity, E_{pot}, is transformed into acoustic energy E_{wave} and is defined as

$$\eta = \frac{E_{wave}}{E_{pot}} \tag{2}$$

Fortes-Patella et al. (2013) found that the collapse efficiency is a strong function of liquid pressure at infinity, P_∞, and initial gas pressure inside bubbles, P_{g0}, and can be expressed as

$$\eta = 0.029 (\frac{P_\infty}{P_{g0}})^{0.54} \tag{3}$$

If hydrodynamic conditions (P_∞, V_0, P_{g0}) of a collapsing cavity are known, equations(1)-(3)can be used to estimate aggressiveness of collapse events. However, it is difficult to derive the liquid pressure at the infinity, P_∞ and the initial volume V_0 for a collapsing cavity in the simulation results. An alternative approach could be to estimate these two parameters according to the kinematics of collapsing cavities. This approach is based on the EroCav handbook(Bark et al., 2004) which has hypothesized that the kinematic feature of a collapsing cavity controls the aggressiveness of the collapse. Here maximum collapse rate, $\dot{V}_{max}$ and the volume of the bubble at maximum collapse rate, $V_{\dot{V}max}$, are considered as the collapse kinematic features of interest. In order to apply the EroCav handbook approach, equations should be derive to relate potential Energy E_{pot}, collapse efficiency η and the kinematic feature of the collapse($\dot{V}_{max}$,$V_{\dot{V}max}$). In this study, these equations are derived from a parametric study on the collapse of spherical bubbles using the Rayleigh-Plesset equation(Rayleigh, L.,1917). .If we substitute these equations in equation (2) and (3), the final equation for E_{wave} as a function of kinematic feature of collapse($V_{\dot{V}max}$, $\dot{V}_{max}$), liquid density, ρ_l, and initial gas pressure inside bubbles, P_{g0}, can be derived as

$$E_{wave} = 2.06 \times 10^{-3} P_{g0}^{-0.54} \rho_l^{1.27} V_{\dot{V}max}^{-1.053} \dot{V}_{max}^{3.08} \tag{4}$$

We assume that acoustic energy E_{wave} propagates from the collapse centre by a spherical wave. When this spherical wave hits the surface, some part of the acoustic energy is absorbed by the material. The amount of acoustic energy absorbed by the surface element with area ΔS can be calculated from

$$E_{wave,mat} = e_{wave}(r)\Delta S = \frac{E_{wave}}{4\pi d^2}\Delta S \qquad (5)$$

where d is the distance between surface element and the collapse center. In this study, the maximum value of $E_{wave,mat}$ for each surface element are used to predict areas with high risk of cavitation erosion.

In order to obtain the maximum collapse rate of a collapsing cavity, it is required to evaluate the collapse rate of each cavity before the final collapse. This task is done by a numerical tool that can track each cavity and save its maximum collapse rate. The methodology used in this numerical tool is similar to the one presented in Silver and Wang (1998). At each time step, cavities are extracted from the list of cells with vapor fraction larger than a threshold and negative vapor mass transfer. These cavities are tracked between consecutive time steps by finding the best match for the cavities in time t+1 from the list of cavities in time step t. The criterion for finding the best match is based on the overlap checking. Cavities in time step t that cannot be matched with cavities in time step t+1 are considered as collapsed cavities. The kinematic feature of these cavities and their collapse points are written into a file as an output of the tracking tool. A post-processing tool reads this file and calculates the E_{wave} for each collapsed cavity and the maximum value of $E_{wave,mat}$ for each surface element based on equation (**4**) and (**5**).

3 Results

The above described erosion indicator is applied to estimate the erosion pattern in a cavitating flow over a NACA0015 foil. The flow configuration is the same as the one used in the experimental study by Rijsbergen et al(2012). A summary of flow condition is presented in Table 1. For this flow condition, the experimental study has shown that the cavitating flow has a periodic shedding of cloud cavitation due to a re-entrant jet mechanism; shedding frequency of 188Hz was observed in the experiment. For this simulation, the incompressible interPhaseChangeFoam solver from the OpenFOAM framework is used for the simulation. The mass transfer is modelled using the Schnerr-Sauer model and turbulence is considered using an implicit LES approach where the numerical dissipation acts as the sub-gird scale model.

Table 1 Flow condition

Cavitation Number	2.01
Reynolds Number	9.5×10^5
Inlet Velocity	17.3 m/s
Chord Length	0.06 m
Angle of Attack	8°

The computational domain is a 3D channel with height of 0.08m and width of 0.02m. To decrease the computational cost, the computational domain includes only the half span of the 3D NACA0015 foil and asymmetry condition is applied to the middle plane. The channel is extended 3 chord lengths upstream of the foil leading edge and 5 chord lengths behind of the trailing edge. Fig. 2 shows the mesh topology used in this simulation. The domain is divided into two regions where the region near the foil is discretised with a structure hexahedral O-type mesh and the outer region is discretised with an unstructured mesh. The average value of y+ around the foil is less than 1 and the maximum value of x+ on the upper surface of the foil is around 150. In the span-wise direction, the z+ is less than one close to the channel side wall and around 300 near the symmetry plane.
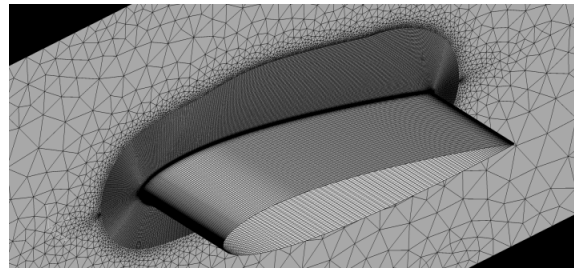
Fig. 2 Mesh topology used for the simulation of cavitating flows over NACA0015 foil

Cavitation pattern

Fig. 3 shows the comparison between the breakup of the sheet cavity and the shedding of cloud cavitation in the numerical simulation and the experimental observation. Numerical results compare well with the experimental observations. In Fig. 3-a, the re-entrant jet moves upstream and cuts the interface of the sheet cavity close to the leading edge. As a result, a cloudy cavity structure is formed with circular motion due to interaction between the re-entrant jet flow and bulk flow(Fig. 3-b). This circular motion gives the cloud cavity a cylindrical shape(Fig. 3-c). As the cloud goes downstream, it breaks up into two structures(Fig. 3-d).Structure 1, which is located in the centre, is transformed into horse-shoe shape and the legs of this horse-shoe shape is attracted toward the surface due to vortex stretching. Structure 2 in Fig. 3-d travels downstream and remains close to the side walls.

a) $t = t_1$ b)$t = t_1 + \frac{3}{20}T$ c)$t = t_1 + \frac{6}{20}T$ d)$t = t_1 + \frac{9}{20}T$
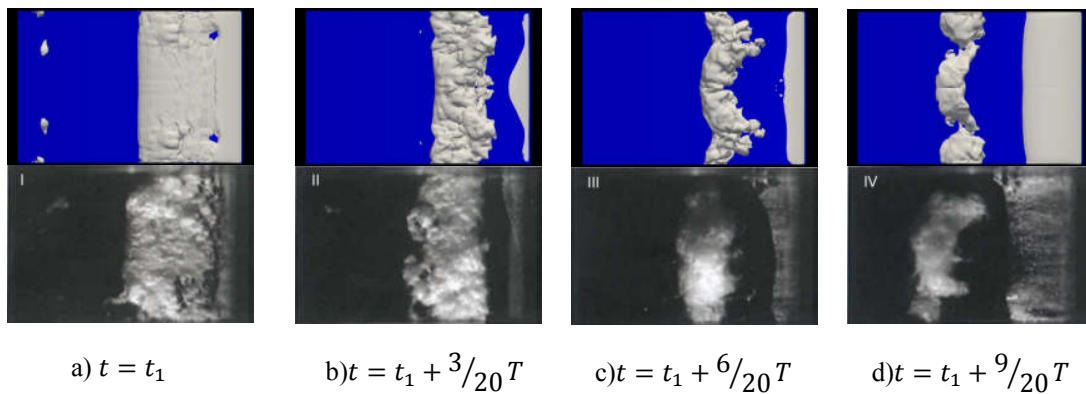
Fig. 3: Cloud shedding in one cycle: Top) Numerical simulation results; Bottom) experimental observation taken from Li(2012)

Fig. 4shows the comparison between the erosion assessment using of the developed methodology as described in this study with the experimental results of van Rijsbergen et al(2012). The erosion obtained by the soft paint shows that areas with high risk of erosion are located mainly in the

downstream half of the foil where the cloud cavity collapses, and in the regions close to the tunnel walls. The location of collapse points and their emitted acoustic energy are shown in Fig. 4-a where each sphere is a collapse point and its size and colour represents its emitted acoustic energy, E_{wave}, estimated by equation(4). The collapse points with high emitted acoustic energy are from the collapse of horse-shoe structure and the structures close to side walls (Fig. 3). The locations of these collapse points agree well with the erosion pattern from the paint test. Fig. 4-d shows the maximum value of acoustic energy absorbed by each surface element of the foil, $E_{wave,mat}$, as computed using equation (5). The maximum value of $E_{wave,mat}$ on the foil surface is located on the leading edge where the collapse of the sheet cavity occurs. As no paint was applied in the area close to the leading edge in the experimental paint test, the predicted erosion on the leading edge absorbed acoustic energy on foil cannot be compared with the experiment. Although there are some collapse points with high emitted acoustic energy in the areas close to the trailing edge in Fig. 4-a and Fig. 4-c, Fig. 4-d shows that the calculated maximum $E_{wave,mat}$ is small in these areas. The reason might be that the collapse point in these areas are far away from the surface, therefore $E_{wave,mat}$ due to these collapses are underestimated by equation (5). The erosiveness could also be influenced by some other focusing mechanisms not considered in this implementation

(a)

(b)

(c)

(d)
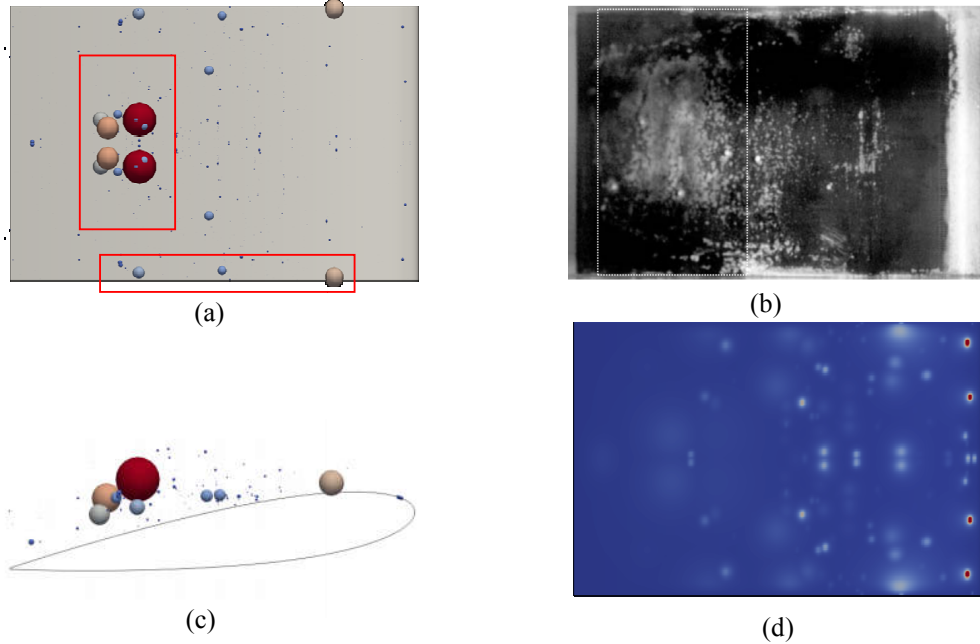
Fig. 4: a and c) The location of collapse points and their emitted acoustic energy, b) experimental erosion pattern obtained by the soft paint, d) the erosion pattern predicted by the maximum value of absorbed acoustic energy on foil.

4 Conclusions

In this study, a new methodology is presented that can identify areas with high risk of cavitation erosion in the incompressible simulation of cavitating flows. The methodology is based on the concept of hydrodynamic energy cascade which considers an energy balance between the energy of collapsing cavities and erosion damage. Using this concept, the emitted acoustic energy of each collapse event is estimated as function of kinematic features of the collapse. The proposed numerical method is applied for the cavitating flow over a 3D NACA0015 foil. The collapse points with high

emitted acoustic energy are indentified and their locations are compared with experimental erosion pattern by Rijsbergen et al(2012). The comparison shows that the location of these collapse points agrees well with the erosion pattern from the paint test. However, the erosion pattern predicted by the maximum value of absorbed acoustic energy on the foil shows discrepancies when compared with the experimental erosion pattern. The reason for this discrepancy might be that collapse event with high emitted acoustic energy are predicted to occur at wrong distance to the surface, therefore their erosiveness are underestimated. Other reasons might be a too simplistic relation for the attenuation of the emitted pressure wave.

References

Asnaghi, A., Feymark, A., and Bensow, R.E., (2017). Improvement of cavitation mass transfer modeling based on local flow properties. *International Journal of Multiphase Flow*, Vol. 93.

Bark, G., Berchiche, N., and Grekula, M., (2004). Application of principles for observation and analysis of eroding cavitation, EROCAV observation handbook. Ed. 3.1, Chalmers University of Technology, Sweden.

Bensow, R. E., and Bark, G., (2010). Implicit LES Predictions of the Cavitating Flow on a Propeller. *Journal of Fluids Engineering*, Vol. 132.

Fortes-Patella, R., Challier, G., Reboud, J.L., Archer, A., (2013). Energy Balance in Cavitation Erosion: From Bubble Collapse to Indentation of Material Surface. Journal of Fluids Engineering, Vol. 135.

Fortes-Patella, R., Reboud, J.L., and Briancon-Marjollet, L. ,(2004). A phenomenological and numerical model for scaling the flow aggressiveness in cavitation erosion. EROCAV Workshop, Val de Reuil.

Rayleigh, L.,(1917). On the Pressure Developed in a Liquid During the Collapse of a Spherical Cavity. Philos. Mag., 34(200), pp. 94–98.

van Rijsbergen, M., Fitzsimmons, P., Foeth, E.-J., and Boorsma, A., (2012), High-speed video observations and Acoustic-impact measurement on a NACA 0015 foil, Proc. of 8th International Symposium on Cavitation, Singapore.

Silver, D., and Wang, X., (1998), Tracking Scalar Features in Unstructured Datasets, Proceedings of the IEEE Visualization 98 (VIZ'98).

van Terwisga, T.J.C., Li, Z., Fitzsimmons, P.A., and Foeth, E.-J., (2009), Cavitation erosion - A review of physical mechanisms and erosion risk models, Proc. of 7th Inter- national Symposium on Cavitation, Ann Arbour, Michigan, United States.

Li., Z. ,(2012), .Assessment of Cavitation Erosion with a Multiphase Reynolds-Averaged Navier-Stokes Method. PhD thesis, Delft TU.

Surge Decay Simulations of a Semi-Submersible Floating Offshore Wind Turbine

Simon Burmester[*], **Sebastien Gueydon**[†], **Guilherme Vaz**[†*], **and Bettar el Moctar**[*]

[*]University Duisburg-Essen, Duisburg/Germany, [†]MARIN (Maritime Research Institute Netherlands),
Wageningen/The Netherlands
simon.burmester@uni-due.de

1 Introduction

In this paper the focus lies on the prediction of the hydrodynamic damping of the surge motion of a semi-submersible floating offshore wind turbine (FOWT). It is assumed that the hydrodynamic damping consists of wave radiation damping and viscous damping. The viscous damping cannot be predicted by potential flow based methods. The viscous flow solver ReFRESCO[1] is used to simulate the surge decay test of the FOWT. A linear stiffness matrix is used in the equations of motion, i.e. the non-linear behaviour and the drag of the mooring lines are not considered in the current study. Several surge decay simulations are performed to understand the effects of scaling, wave radiation and coupled motions on the hydrodynamic damping. This work includes also a verification study. The numerical results are compared with experimental data.

2 Description of Model Tests

The model tests were conducted at 1/50th scale. The semi-submersible floater used was originally developed within the DeepCwind consortium (Robertson et al. (2017)). In the model tests a performance-matched wind turbine, the so-called MARIN Stock Wind Turbine (MSWT), was mounted on top of the floater. Information about this turbine can be found in de Ridder et al. (2014). Since the rotor was not rotating during the surge decay tests, solely the floater geometry is presented (Fig. 2). A right-handed coordinate system is used for the work: the x coordinate points in forward (surge) direction, the y coordinate in transfers (sway) direction, and the z coordinate vertically upwards (heave). The system's origin is set to the centre of gravity of the floating structure. The properties of the investigated system (floater, tower and rotor) are summarized in Tab. 1. The diagonal values of the linear restoring matrix are applied as listed in Tab. 2. More details can be found in Robertson et al. (2017).

Table 1: Main particulars of the floating structure at full scale.

Designation	Full scale value
Draft	$20.0\,\text{m}$
Mass	$1.3958 \cdot 10^7\,\text{kg}$
Centre of Gravity above keel	$11.93\,\text{m}$
Roll radius of gyration	$32.63\,\text{m}$
Pitch radius of gyration	$33.38\,\text{m}$
Yaw radius of gyration	$31.32\,\text{m}$

Table 2: Stiffness properties of the mooring lines at full scale; the values are given with respect to the centre of gravity.

Designation	Full scale value
Surge	$8.46 \cdot 10^4\,\text{N/m}$
Sway	$7.35 \cdot 10^4\,\text{N/m}$
Heave	$1.94 \cdot 10^4\,\text{N/m}$
Roll	$7.63 \cdot 10^8\,\text{Nm/rad}$
Pitch	$1.06 \cdot 10^9\,\text{Nm/rad}$
Yaw	$1.198 \cdot 10^8\,\text{Nm/rad}$

The hydrodynamic damping is analysed by the PQ-method of van der Vegt (1984). This method uses successive amplitudes to determine the relative decrement of the decay test. A line can be fitted through these data points to obtain the intercept (p-value) and slope (q-value). In Fig. 1 the decrement of motion amplitude as a function of the mean motion amplitude is plotted for the model tests. The linear B_1 and quadratic damping coefficients B_2 can be obtained as follows:

$$B_1 = p \cdot \frac{T_n \cdot C}{2\,\pi^2} \ , \quad B_2 = 3q \cdot \frac{T_n^2 \cdot C}{32\,\pi^2} \ . \tag{1}$$

Here, the natural period is denoted by T_n and the stiffness coefficient by C. This method is used to compare the hydrodynamic damping obtained by the experiments and numerical simulations.

---

[1]http://www.refresco.org/
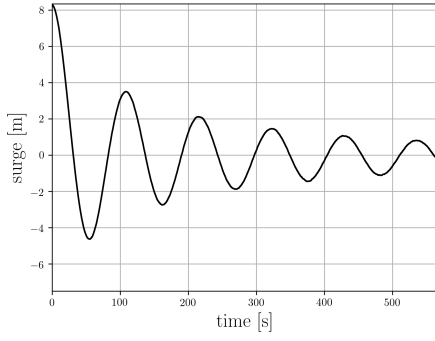
(a) History of surge motion.
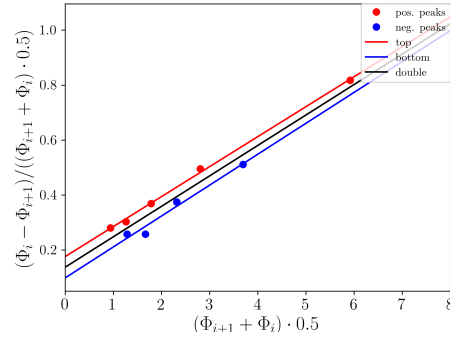
(b) PQ-analysis for surge decay; Φ denotes the oscillation amplitudes.

Fig. 1: Example of a PQ analysis using the experimental data.

3 Numerical Methods and Settings

The numerical simulations are performed with community based open-source CFD code ReFRESCO[1]. The code solves multiphase (unsteady) incompressible viscous flows using the Navier-Stokes equations, complemented with turbulence models and volume-fraction transport equations for different phases, see Vaz et al. (2009). The equations are discretized using a finite-volume approach with cell-centered collocated variables, in strong-conservation form. Time integration is performed implicitly with a second-order backward scheme. The code is parallelized using MPI. State-of-the-art CFD features such as moving, sliding and deforming grids, and automatic grid adaption are also available. Coupling with structural equations-of-motion is possible and done for this work. The free surface is modelled with the volume of fluid (VOF) method. The numerical settings used for the equations are shown in Tab. 3. The applied turbulence model is the KSKL (k-$\sqrt{k}L$) turbulence model (Menter and Egorov (2010)).

The equations of motion for a rigid body enable the description of this body's attitude to external loads, see Rosetti and Vaz (2017). The considered external loads are the hydrodynamic force $\vec{f}_H$, the restoring force $\vec{f}_C$ and the linear viscous mechanical damping force $\vec{f}_B$. With a state vector for three degrees-of-freedom $\vec{r} = \{X_G, Z_G, \Theta_G\}^T$ the dynamic equations are written as:

$$\mathbf{M}\ddot{\vec{r}} + \mathbf{B}\dot{\vec{r}} + \mathbf{C}\vec{r} = \vec{f}_H \ . \tag{2}$$

In this equation $\mathbf{M}$ denotes the inertia, $\mathbf{B}$ the damping and $\mathbf{C}$ the stiffness matrix. The matrices are positive and diagonal. As the body is assumed totally rigid, the mechanical damping matrix is set to 'zero'. Together these equations form a second-order non-linear initial value problem. The problem is non-linear because the hydrodynamic forces, $\vec{f}_H$, keep a non-linear relation with $\vec{r}$ via the Navier-Stokes equations. In the present work, a strongly coupled scheme is applied to avoid numerical instabilities due to low mass ratios and added-mass constraints. The scheme is based on the predictor-corrector second-order Adams-Bashforth-Mouton scheme.

4 Sensitivity Study

The computational domain used in the numerical simulations is modelled as a semi-cylinder in such a way that it forms a symmetric half with respect to the xz plane. At full scale the domain has a total height of $h = 230$ m, a water depth of $d = 200$ m and a radius of $r = 245.22$ m. At the bottom and top of the domain a static pressure is prescribed. The boundaries of the semi-submersible are represented with no-slip conditions. For the xz plane a symmetry condition is used. The curved surface area is modelled as a non-reflecting boundary condition of Sommerfeld type (Sommerfeld (1949)).

To investigate the influence of the grid and time step size on the solution, a sensitivity study is performed using three degrees-of-freedom (DOF) surge decay simulations with free surface. This means that the structure is displaced initially in x direction and can move freely in z and rotate around y axis. The

Table 3: Numerical settings used.

Equation	Preconditioner	Solver	Convection discretization scheme
Momentum	JACOBI	GMRES	QUICK
Pressure	BJACOBI	CG	-
Free Surface	BJACOBI	GMRES	ReFRICS
Turb. model	BJACOBI	GMRES	1st Order UPWIND

Table 4: Grid study

Grid	Total amount of cells
G1	2.75M
G2	5.6M
G3	9.9M

computational domain and grid are generated using Hexpress, a trimmed hexahedral unstructured grid generator software. An example of the grid topology is shown in Fig. 2. The grids are refined towards the semi-submersible and towards the free surface. To reduce the amount of hanging nodes in vertical direction, the refinement at the free surface is kept constant in this direction. The grid is also refined on the curves and surfaces of the semi-submersible. The structure above the water line is refined as much as needed for snapping purposes. The viscous layer cells are generated to guarantee a non-dimensional wall distance value of $y^+ < 1$. The three grids used for the sensitivity study are summarized in Tab. 4.
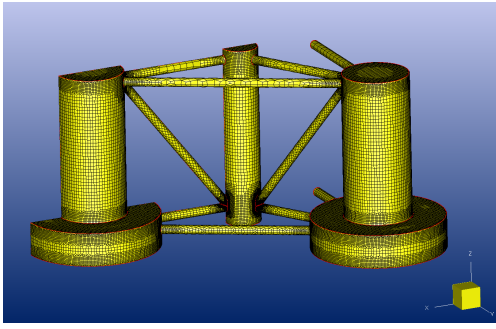
(a) Grid refinement on the semi-submersible.
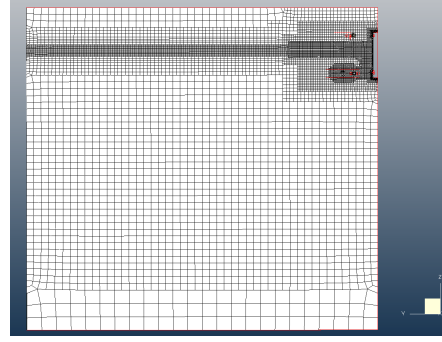
(b) Refinement at the yz plane.

Fig. 2: Grid topology and refinement.

Moreover, three time steps are studied. These time steps are defined in ratio of the oscillation period $T \approx 110s$: $dt = T/3200$, $dt = T/6400$ and $dt = T/12800$. Results of the surge motion are shown on the left of Fig. 3. For each simulation the maximum number of outer-loop iterations is fixed to 60. This number leads to iterative convergence of $< 1 \cdot 10^{-3}$ in $L2$-norm for all equations. The simulations with $G1$ and coarser time steps obtained slightly larger residuals ($< 5 \cdot 10^{-3}$). The large residuals are located at the free surface.

Because of the small differences noticeable in the time history plot, values for each simulation of the first maximum are listed in Tab. 5. In addition, a difference in percentage from the finest grid and time step for each simulation is presented in the last column.

Table 5: Negative maximum of first oscillation cycle

Grid	Time step as T/x	Negative maximum	Difference in %
	3200	−6.44185	2.10
G1	6400	−6.56265	0.27
	12800	−6.68499	1.59
	3200	−6.55113	0.44
G2	6400	−6.54077	0.45
	12800	−6.54902	0.47
	3200	−6.57268	0.11
G3	6400	−6.57739	0.04
	12800	−6.58022	0.0

For the first maximum an uncertainty analysis is performed according to Eça and Hoekstra (2014) (on the right of Fig. 3). A fitted plane is calculated based on the data provided. Then, the uncertainty of one point towards the fitted plane can be determined. Based on this procedure a discretization uncertainty [2] of about 9.5 % of the finest grid and time step is estimated. Inspecting the data points, it can be seen that the coarsest grid provides outliers, whereas the medium and fine grid are almost exactly on the fitted plane. An uncertainty of only 0.5 % more is estimated using the medium grid and time step than using the finest configuration. More-

---

[2]Iterative and statistical convergence are not considered here.

over, the difference between the finest, and the medium grid and time step is of 0.45 %. Therefore, the medium configuration is used for the final computations to save computational costs.

(a) Time history of surge motion.

(b) Numerical uncertainty estimation.
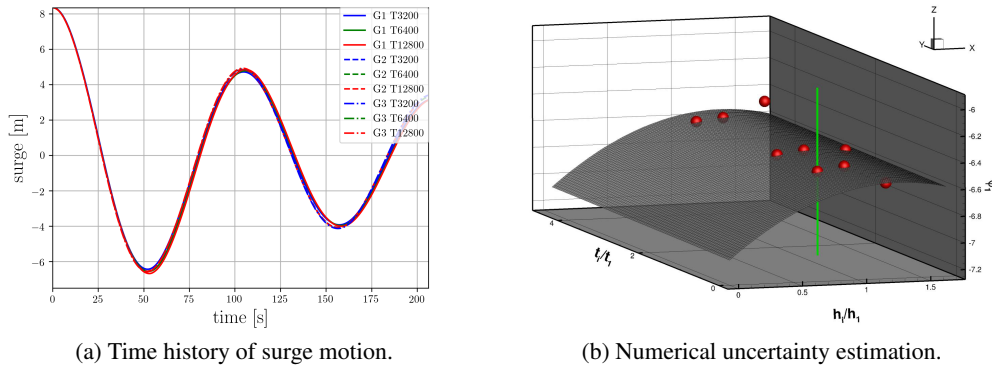
Fig. 3: Results of the numerical sensitivity study.

5 Results and Discussion

Two double body simulations (DB), one at full scale (fs) and one at model scale (ms) are used to investigate the influence of scaling on the viscous damping. In addition, a simulation at model scale with free surface and for 1DOF is performed to study the effect of the free surface on the hydrodynamic damping. Finally, a simulation with free surface and for 3DOF is done to analyse the influence of coupled motions on the damping. The results for the different simulations compared to the experiments are shown in Fig. 4. For the 3DOF simulation an additional vertical force $\vec{f_C}$ is applied to account for the submerged weight of the moorings.

The surge decay motion presented in Fig. 4 is categorized as 'under damped' oscillation. From this figure a large difference in oscillation amplitude between the full scale and model scale double body simulation can be seen. This difference increases with time. The result of the PQ-analysis presented in Tab. 6 shows a dramatic difference in quadratic damping between these two simulations and a significant increase of linear damping. The increase of damping can be explained by the larger boundary layer at model scale in relation to the boundary layer at full scale. Moreover, the PQ analysis of these two simulations shows that the viscous damping is mainly quadratic.

The difference between the 1DOF at ms and the 1DOF DB at ms simulation is the additional free surface. The difference of the oscillation amplitude is hardly noticeable in the beginning of the simulation. After
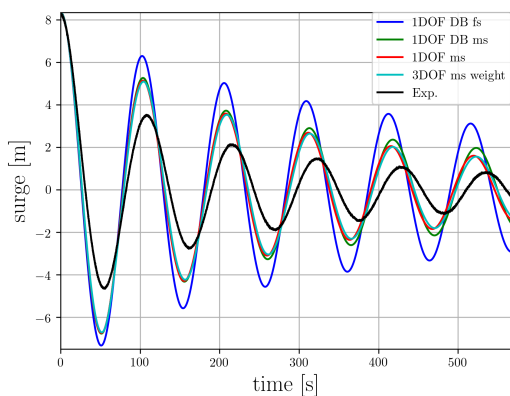
Fig. 4: Comparison of surge decay simulations with model test.

Table 6: Results of PQ analysis of model tests and CFD simulations

Simulation	Period [s]	Damping Coeff. (linear, p) (quadratic, q)
Model test	107.68	0.1372, 0.11075
1DOF DB at fs	103.35	0.0, 0.04012
1DOF DB at ms	104.05	0.0292, 0.0683
1DOF at ms	103.46	0.1245, 0.0545
3DOF at ms	104.51	0.1335, 0.0548

about 300 s this difference increases. The PQ analysis reveals a significant increase of linear damping for the simulation with free surface. This supports the hypotheses that the damping due to wave radiation is a potential damping.

The last simulation presented in this paper is a surge decay simulation with enabled heave and pitch motion. This 3DOF simulation leads to slightly increased linear and quadratic damping. Comparing this 3DOF simulation with the model tests reveals a difference of 2.7 % in linear damping and of 50.5 % in quadratic damping. It shows that the quadratic damping is more dominant for the model tests than for the numerical simulation. Compared to the model tests, this 3DOF computation misses the 6DOF motion, the non-linear behaviour and drag of the mooring lines, the influence of the connected electrical power cable and the possible aerodynamic damping effect of the parked rotor. Each of the numerical simulations is performed with the same structural mass and inertia. Based on these CFD simulations, the observed natural period in surge is influenced by the damping, too. This follows the physical laws as the observed period corresponds to the damped natural period.

The numerical results shown in Fig. 4 and Tab. 6 possess uncertainties of about 10 %. For the model test data no uncertainty estimation was done. Therefore, no formal validation is possible.

(a) 1DOF DB at fs.

(b) 1DOF DB at ms.

(c) 1DOF at ms.

(d) 3DOF at ms.
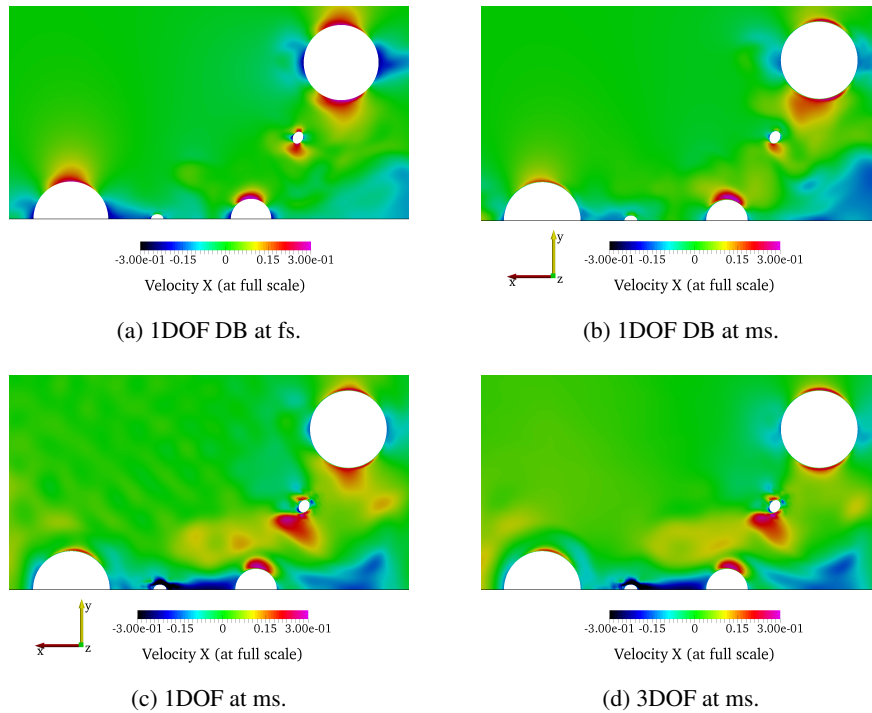
Fig. 5: Velocity $[m/s]$ in x direction during surge decay motion at $t = 220$ s, measured 1 m below SWL and around the floater.

In the figures 5a - 5d the four numerical simulations are presented with full scale values. The velocities in x direction are shown at the height of 1 m below the still water line (SWL). A time instant is chosen shortly after the second oscillation amplitude ($t = 220$ s). Thus, the semi-submersible moves in negative x direction, i.e. to the right of the figures.

The magnitude of the velocity around the elements is larger at full scale (Fig. 5a) than at model scale (Fig. 5b). The velocity profile around the cross brace connecting the top right column with the main column in the symmetry plane is visible on one side at model scale and on both sides at full scale.

The free surface affects the velocity in x direction in particular around the two visible cross braces (Fig. 5c). The cross brace in the symmetry plane and in the shadow of the main column is surrounded by negative flow velocities. The non-symmetric behaviour of the velocities around the cross brace between main and top right column is more pronounced than for the model scale simulation without free surface. The column in the top right corner of the figure is located in free stream. The velocity magnitude in

x around this column decreases with the influence of coupled motions (Fig. 5d). The velocities around the large column in front stays almost constant for the 3DOF simulation. However, an increase of the velocities is observed in the vicinity of this column.

The increase of linear damping in the numerical simulations seems to be associated with a decrease of the velocities in the boundary layer around the large cylinder on the left of the figures and the rise of the non-symmetric flow pattern around the cross brace between the other two columns. To check this conjecture, more flow patterns need to be studied.

6 Conclusions

Grid generation for simulations with the DeepCwind semi-submersible is not an easy task. In particular the refined areas around the connection points of pontoons and braces add a huge amount of cells. These additional cells are not expected to improve the accuracy of the simulations significantly. Therefore, a simplification of these connections are recommended for future investigations.

Linear damping is largely affected by the free surface, but also viscous damping at model scale is partly linear. Moreover, coupled motions increase the linear damping slightly. It can be concluded that wave radiation is mainly a linear/potential damping.

Quadratic damping is largely influenced by scaling. At model scale, when the boundary layer is unrealistically large, the quadratic damping increases. The largest quadratic term is the viscous damping. This quadratic term is also slightly increased due to coupled motions. However, this term is significantly more dominant for the experimental than the numerical results.

The size and orientation of the structural elements of the floater determine whether the flow pattern affects the linear or quadratic damping. For a check of this conjecture, the flow needs to be analysed at more locations and time instances.

The remaining differences in the hydrodynamic damping are expected to decrease for simulations accounting for the drag and non-linear behaviour of the mooring lines, and motion coupling of more than 3DOF. These two aspects are planned for further studies.

References

EJ. de Ridder, W. Otto, GJ. Zondervan, F. Huijs, and G. Vaz (2014). Development of a Scaled-Down Floating Wind Turbine for Offshore Basin Testing. Proceeding of *OMAE* 2014

L. Eça and M. Hoekstra (2014). A procedure for the estimation of the numerical uncertainty of CFD calculations based on grid refinement studies. *Journal of Computational Physics*, 262:104-130.

S. Gueydon (2015). Numerical study of OC5 semi - Calibration of hydrodynamic properties. MARIN Report: 28503-MSG-1, Wageningen, The Netherlands.

F.R. Menter and Y. Egorov (2010). The Scale-Adaptive Simulation Method for Unsteady Turbulent Flow Predictions. Part 1: Theory and Model Description. *Flow, Turbulence and Combustion*, 85 (1), 113-138.

A.N. Robertson, F. Wendt, J.M. Jonkman, W. Popko, H. Dagher, S. Gueydon, et al. (2017). OC5 Project Phase II: Validation of Global Loads of the DeepCwind Floating Semisubmersible Wind Turbine. In Submission to *Energy Procedia*. Elsevier.

G. Rosetti and G. Vaz (2017). On the Numerical Simulations of Captive, Driven and Freely Moving Cylinder. *Journal of Fluids and Structures,* DOI: http://dx.doi.org/10.1016/j.jfluidstructs.2017.06.013.

A. Sommerfeld (2017). Partial Differential Equations in Physics. *Elsevier*.

J.J. van der Vegt (1984). Slinger gedrag van schepen. *KIVI-Lecture on Seakeeping*.

G. Vaz, F. Jaouen, and M. Hoekstra (2009). Free-Surface Viscous Flow Computation - Validation of uRANS code ReFRESCO. Proceedings of *OMAE* 2009, Honolulu, Hawaii, USA.

A Novel Fitting Method for Steady Free Surface Flow

Toon Demeester, Joris Degroote, Jan Vierendeels

Department of Flow, Heat and Combustion Mechanics, Ghent University, Belgium

toon.demeester@ugent.be

1 Introduction

Computational methods to simulate water-air flows around ships can be divided in two categories: surface capturing and surface fitting methods. Capturing methods reconstruct the position of the free surface (FS) to apply the boundary conditions. An example is the volume-of-fluid method, which is usually multi-phase. In fitting methods the mesh lies along the free surface and deforms with it, so that its position is always known. The air phase is often neglected, leading to one phase flow with simpler FS boundary conditions. The dynamic boundary condition (DBC) which requires continuity of the stresses, reduces to a constant pressure condition. The kinetic boundary condition (KBC) requires that the FS is impermeable.

For steady FS flows, two clearly different fitting methodologies can be found in literature. Both consist of an iterative process with two steps that are repeated until convergence is reached: first calculation of the flow field with a fixed FS position and suitable boundary conditions, then update of the FS position. The first methodology uses the DBC in the first step and the KBC in the second (Tzabiras (1997); Muzaferija and Perić (1997)). Using the KBC for updating the surface results in a time-stepping method, which is not efficient for steady cases due to the large number of time steps before transient phenomena have disappeared. Van Brummelen et al. (2001) describe a steady iterative fitting method which uses a combined boundary condition (KBC + DBC) in the flow solver and the DBC for the surface update. This method is efficient but requires a dedicated solver, making it less flexible.

The goal of this paper is to test a novel fitting method which combines a steady iterative approach with a black box flow solver. This requires that the boundary conditions in the flow solver are easy to implement (only KBC) and that the update procedure is time-independent (only DBC).

2 Theory

2.1 Modal analysis

The KBC is easily enforced in the flow solver by setting the FS boundary as a free slip wall. When the flow field is solved, the pressure at the FS will not be constant, yielding a pressure error $\tilde{p}$. To satisfy the DBC, the FS must be updated in an attempt to compensate this error $\tilde{p}$. If a relationship can be found between the known pressure error $\tilde{p}$ and the unknown position error $\tilde{\eta}$, such an update procedure can be established.

A relatively general relationship is obtained by doing a modal analysis of these errors for the inviscid flow over a flat bottom as shown in Fig. 1. In this case the solution is known (a horizontal FS) so that a relation between $\tilde{\eta}$ and $\tilde{p}$ can be found by calculating the flow field for a given error mode $\tilde{\eta}$. This derivation was done using potential flow theory, but the details are skipped here for the sake of brevity. The result is a proportional relation between $\tilde{\eta}$ and $\tilde{p}$

$$\tilde{\eta} = K \cdot \tilde{p} \qquad \text{with} \qquad K = \frac{1}{\rho g \left(\text{Fr}^2 \frac{kh}{\tanh kh} - 1 \right)} \tag{1}$$
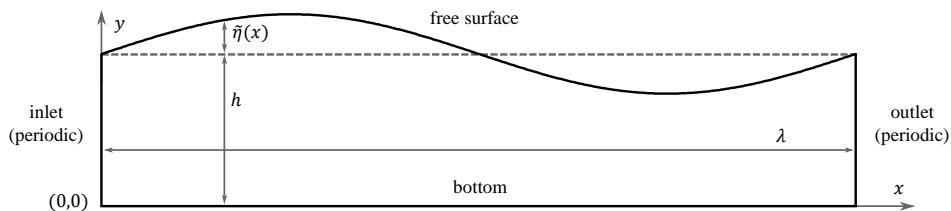

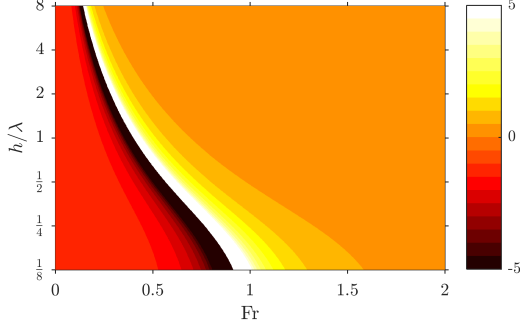Fig. 1: Domain studied in modal analysis
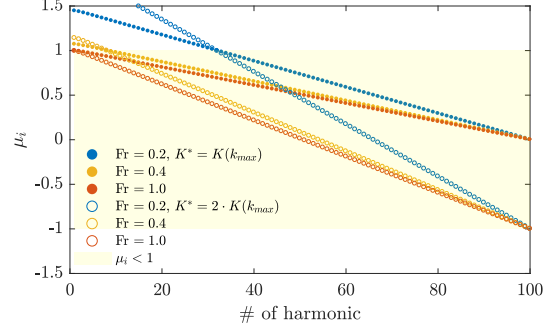
Fig. 2: The proportional factor $\rho g K$

Fig. 3: Amplification μ of Gauss-Seidel iterations for 100 harmonics for two values of K^*

where K is a function of the wavenumber $k = 2\pi/\lambda$ and the Froude number $\mathrm{Fr} = U/\sqrt{gh}$. In these formulas, ρ is the density, g the gravitational acceleration, h the undisturbed water depth, λ the wavelength and U the average flow velocity. The validity of Eq. (1) was checked with numerical experiments.

Two dimensionless parameters are present in Eq. (1): Fr and $h/\lambda = kh/2\pi$. A visual representation of K in function of these two parameters is shown in Fig. 2. h/λ is the aspect ratio of the domain: small values signify shallow water with respect to the wavelength, large values deep water. The Froude number describes the relative importance of inertial to gravitational forces. At low Fr, gravitational forces dominate, so that the flow is governed by the hydrostatic effect: if $\tilde{\eta} > 0 \Rightarrow \tilde{p} < 0 \Rightarrow K < 0$. At high Fr, inertial forces dominate, so that the flow is governed by the Bernoulli effect: if $\tilde{\eta} > 0 \Rightarrow v \searrow \Rightarrow \tilde{p} > 0 \Rightarrow K > 0$. In Fig. 2, these two regions are clearly present and separated by an asymptote. Close to this asymptote, the opposing effects of gravity and inertia on $\tilde{p}$ balance each outer out, leading to a very small $\tilde{p}$ and therefore large K.

2.2 Iterative procedure

The relation in Eq. (1) can now be used to asses the theoretical performance of the iterative procedure mentioned in the introduction: in the first step the flow is calculated for a FS position η with a flow solver $\mathcal{F}(\eta)$, in the second step the surface position is updated with the procedure $\mathcal{S}(p, \eta)$, forming the system

$$\begin{cases} p & = \mathcal{F}(\eta) \\ \eta & = \mathcal{S}(p, \eta) \end{cases} \tag{2}$$

The update procedure is now defined as

$$p = \mathcal{F}(\eta) \qquad \text{and} \qquad \eta = \mathcal{S}(p, \eta) = \eta - K^* \cdot p \tag{3}$$

where K^* is calculated as in Eq. (1) for a wavenumber k^* which is chosen further on. With this definition of $\mathcal{F}(p)$, the residual $\mathcal{R}(\eta)$ of the system (2) is found as

$$\mathcal{R}(\eta) \overset{\Delta}{=} \mathcal{S}(\mathcal{F}(\eta), \eta) - \eta = -K^* \cdot \tilde{p} \tag{4}$$

which gives the Gauss-Seidel (GS) iteration (without underrelaxation) for iteration n as

$$\eta^{n+1} = \eta^n + \mathcal{R}(\eta^n) = \eta^n - K^* \cdot \tilde{p}^n \tag{5}$$

The new position error $\tilde{\eta}^{n+1}$ is found by subtracting the correct position from both sides. If $\tilde{\eta}$ is composed of multiple Fourier modes i, the amplification μ_i of each mode $\tilde{\eta}_i$ is

$$\mu_i = \frac{\tilde{\eta}_i^{n+1}}{\tilde{\eta}_i^n} = 1 - K^* \frac{\tilde{p}_i^n}{\tilde{\eta}_i^n} = 1 - \frac{K^*}{K_i} \tag{6}$$

where relation (1) is used in the last step to model the flow solver. Only if $|\mu_i| < 1$, error mode $\tilde{\eta}_i$ will damp out during Gauss-Seidel iterations and is stable. If modes are present in the left region of Fig. 2
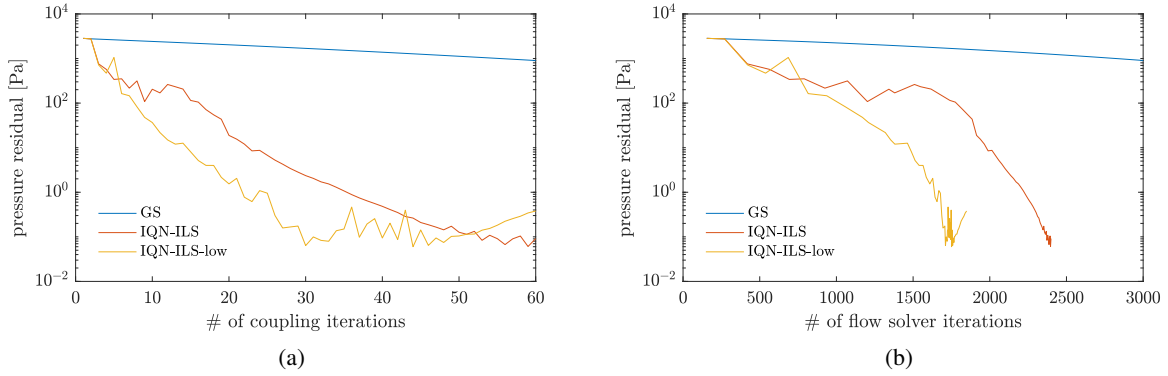
Fig. 4: Pressure residuals for flow over flat bottom

(low Fr), it is not possible to choose a K^* for which all modes are stable, because K_i changes sign when the asymptote is crossed. However it is possible to make all high wavenumber modes stable by choosing $k^* = k_{max}$ in calculating K^*, leading to a limited number of unstable low wavenumber modes. The amplification of the highest mode is then 0. Alternatively, K^* may be chosen twice as large, leading to an amplification of the highest mode of -1. To illustrate these two choices, μ_i is plotted for both of them in Fig. 3 for a structured 200×200 mesh which has 100 harmonics. The base mode corresponds to $h/\lambda = 1/8$, so that quite some unstable modes are produced for low Fr. If the base harmonic has a higher h/λ or the Froude number is higher, the number of unstable modes reduces quickly.

For the cases which have one or more unstable modes, Gauss-Seidel iterations will diverge because those error modes grow while iterating. In the fluid-structure interaction community, similar iterative processes with a limited number of unstable modes are often stabilized and accelerated using a quasi-Newton coupling algorithm such as IQN-ILS (Interface-Quasi-Newton with Inverse Jacobian from a Least-Squares model, Degroote et al. (2009)). Such an algorithm gives a better prediction of the new FS position η^{n+1} based on information from the previous iterations.

In short, the workings of IQN-ILS can be explained as follows. For all previous Gauss-Seidel steps, both the residual $r = \mathcal{R}(\eta)$ and the result of the Gauss-Seidel iteration $\hat{\eta} = \mathcal{S}(\mathcal{F}(\eta), \eta)$ are stored. The differences of these variables between two consecutive time-steps is denoted respectively as Δr and $\Delta \hat{\eta}$. To get from the current position η^n to the new position η^{n+1}, the update $\Delta \eta^n$ must be calculated. From the definition of the residual in Eq. (4) this can be rewritten as

$$\Delta \eta^n = \Delta \hat{\eta}^n - \Delta r \tag{7}$$

Ideally, the iterations should converge in the next time-step, i.e. have $r^{n+1} = 0$, so that Δr^n is known. Δr^n is now written as a least squares approximation of old Δr's. An estimate of $\Delta \hat{\eta}^n$ can then be constructed by taking the same linear combination of old $\Delta \hat{\eta}$'s.

If a mode appears in the residual which has been encountered in one of the previous iterations, the algorithm predicts how the system reacts to this error, and is able to efficiently damp this mode. After a number of iterations, the algorithm knows all the unstable modes and the solution converges. Stable modes may also be recognized by the algorithm and damped faster than would be the case during Gauss-Seidel iterations.

3 Numerical experiments

The iterative procedure discussed in the previous section is tested on two academic test cases in 2D. Viscous forces are not taken into account in the calculations. Three different coupling algorithms are used: Gauss-Seidel, IQN-ILS and a slightly adapted version of the last which is explained later. For the Gauss-Seidel iterations, deviations between experiments and theory are to be expected.

First of all, the actual K_i for the highest frequencies on a given mesh will certainly be different from the values predicted with Eq. (1), because these modes are not well discretized. For example, the highest
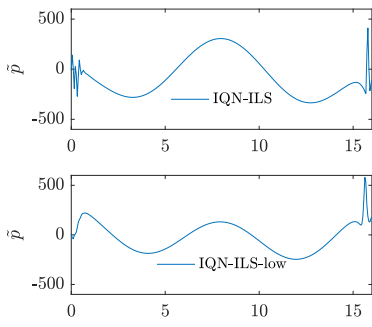
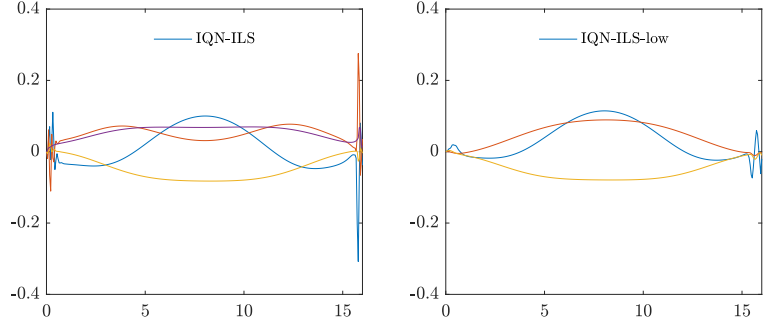Fig. 5: Pressure error $\tilde{p}$ in coupling iteration 7

Fig. 6: Normalized modes Δr in coupling iteration 7

frequency will be a triangle wave instead of a sinusoid. By doing numerical experiments, the correct K_i could be determined for these modes, but it is hard to find a generally valid result as K_i heavily depends on the mesh resolution perpendicular to the surface (y-direction).

Next, the potential theory derivation from which the formula for K was derived, is based on the assumption that $\tilde{\eta}$ is a small perturbation. As this is not the case in the experiments, this may also lead to different values of K. In addition the modes may influence each other so that the relation between $\tilde{\eta}$ and $\tilde{p}$ is in fact non-linear.

Finally, the choice of boundary conditions in the flow solver will play a role: the correct boundary values of the free surface flow are not known so that the implemented values are only an approximation. A fixed inlet velocity is used in combination with a constant pressure at the outlet, instead of periodic boundary conditions in the potential theory.

3.1 Supercritical flow with bottom

The first case is very similar to the one used in the modal analysis (Section 2.1), for which the domain is shown in Fig. 1. The initial error $\tilde{\eta}^0$ consists only of the base harmonic. A cosine is used instead of a sine to make the implementation of the boundary conditions easier.

$$\tilde{\eta}^0 = \frac{\lambda}{10}(1 - \cos kx) \tag{8}$$

A hexahedral mesh of 300×70 cells is used which means there are 150 error modes. The aspect ratio of the domain is $h/\lambda = 1/16$. The flow is chosen to be supercritical (Fr = 2) because in that case K_i does not change sign and Gauss-Seidel iterations are stable. For the surface update, $K^* = 2 \cdot K(k_{max})$ is chosen, because simulations showed better convergence than for $K^* = K(k_{max})$. This choice is case-dependent, it is yet unknown what the optimal value would be in general.

The Gauss-Seidel iterations converge slowly as can be seen in Fig. 4a. The initial error $\tilde{\eta}^0$ is also the harmonic with the worst amplification, in theory $\mu_1 = 0.973$ for $K_1 = 0.31$. As no other modes are present (nor appear), the iterations should converge with the same rate as predicted with μ_1. The experimental result is quite close: on average K is around 0.40, but the value is getting closer to the predicted one while the error decreases.

When the IQN-ILS coupling algorithm is used, convergence is much faster as seen in Fig. 4a. However, after 50-60 iterations the pressure residual stagnates, not converging past 10^{-1}. When the evolution of $\tilde{p}$ is monitored, it is observed that high frequency modes start to appear after a few iterations, unlike what is seen during GS iterations. These sharp peaks in $\tilde{p}$ first appear at both the inlet and outlet due to the boundary conditions, gradually polluting the whole domain. This behavior is shown in an early stage in Fig. 5 (top). As $r = -K^*\tilde{p}$, these peaks immediately appear in the modes Δr which are used in the IQN-ILS algorithm for the least squares approximation of the residual r^n. Theses modes are shown in Fig. 6 (left) for iteration 7. As $\tilde{p}$ is getting more polluted with high frequencies, so are the modes Δr. The
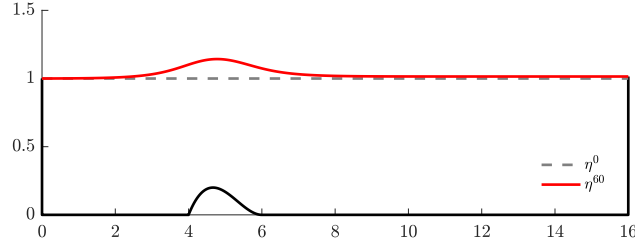
Fig. 7: Initial and final solution for supercritical flow over bottom topography

performance of IQN-ILS deteriorates due to these noisy modes and convergence of the residual stops after a while.

In an attempt to solve this issue, the IQN-ILS algorithm is altered. The error $\tilde{p}$ is split into lower and higher frequency parts. The low frequency part of $\tilde{p}$ is used to construct an IQN-ILS update $\Delta\eta$. The high frequency part is used for a simple GS update, but in theory these modes should converge fast enough due to their low μ_i. The total update is the sum of these two parts. To split $\tilde{p}$ a moving average filter with five points is used (the new value is the average of the point itself and its four closest neighbors). In terms of filtering performance this is a poor choice, but it was chosen only as proof of concept. This procedure will be referred to as *IQN-ILS-low*.

During the first coupling iterations, IQN-ILS-low behaves the same as IQN-ILS. When high frequencies start to appear, IQN-ILS-low starts to converge faster. Fig. 5 shows that $\tilde{p}$ is less prone to develop high frequency peaks, Fig. 6 shows that the modes Δr at that point are much smoother. However, high frequencies do develop slowly and convergence stops at about the same residual size as for standard IQN-ILS. At this point the modes have indeed developed a lot of high frequency noise at inlet and outlet. A better filter is certainly needed to counteract this, but it may also be necessary to find a way to prevent high frequencies to appear at inlet and outlet in the first place.

The number of coupling iterations given in Fig. 4a does not give an accurate view of the total computational cost as the flow calculation becomes cheaper when the coupling iterations are converging. As the flow solver iterations are the dominant time-cost in the iteration process, the pressure residual is also given in function of the number of flow solver iterations in Fig. 4a. Quasi-Newton coupling is clearly very advantageous and IQN-ILS-low is even faster than the original algorithm in this case.

3.2 Supercritical flow with bottom topography

The other case that is studied is an academic case for which experimental data was collected by Cahouet (1984), but this data is not available for public download. It consists of the supercritical flow (Fr = 2.05) over a bottom topography described by the equation

$$y = \frac{27}{4} \frac{H}{L^3} x(x - L)^2 \qquad \text{with} \qquad H = 0.2, L = 2 \tag{9}$$

A graphical representation of the domain is given in Fig. 7, with the flow from left to right. Both the initial solution η^0 and the solution η^{60} after 60 iterations with IQN-ILS-low are shown. Tzabiras (1997) studied the same case for different Froude numbers to test a surface fitting method. Van Brummelen et al. (2001) demonstrated the steady-iterative approach with this case for subcritical flow.

The same three coupling algorithms are tested on this case: GS, IQN-ILS and IQN-ILS-low. K^* is taken as $K(k_{max})$ now. As a filter, the moving average smoothing with window 5 is applied twice in a row. Both these choices are made because better convergence is reached. Fig. 8a and Fig. 8b show the pressure residuals: the results are very similar to those for the flat bottom. The mechanism which stops the residuals from converging further is however slightly different. With IQN-ILS, there are initially no problems at inlet or outlet, but high frequencies start to appear around the position of the bottom topography. Later they also appear at the outlet, littering both zones with high frequency components. With IQN-ILS, the first high frequencies only start to appear after 20-25 iterations, justifying the much faster convergence. Two small zones of high frequencies form: at the inlet and over the bottom topography.
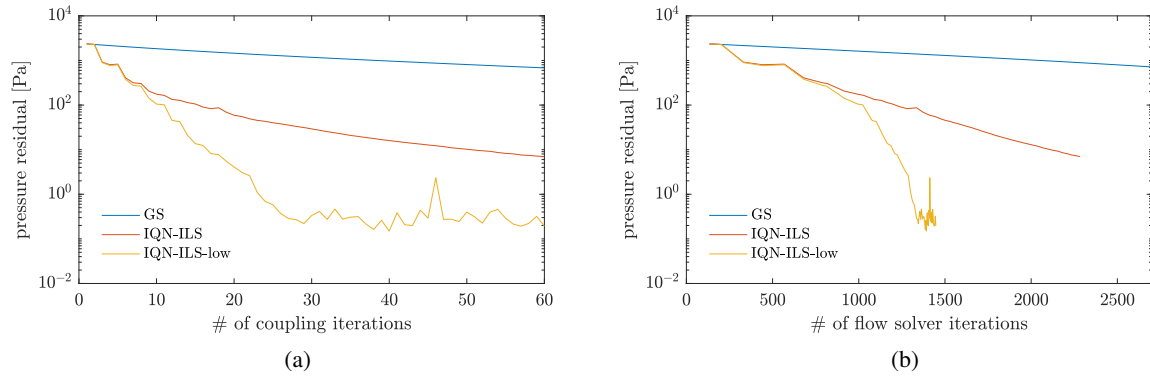
Fig. 8: Pressure residuals for flow over bottom topography

These are not damped out and convergence quickly stagnates. Next to the need for a better filter, it is also necessary to develop a method to get rid of old modes Δr. When the FS changes a lot (which is the case here), some of the old updates may not be relevant anymore. A good criterion must be found for discarding modes.

4 Conclusion

The use of IQN-ILS and IQN-ILS-low gives promising results for solving steady free surface flows. The main issue is currently that high frequency components appear in the pressure error $\tilde{p}$, blocking further convergence at a certain point. Proposed solutions are improvement of the filter for IQN-ILS-low, a good way to remove old information from the algorithm, and a better choice of K^* by studying triangle waves. An other issue that was encountered is the determination of the free surface node pressures from the cell pressures (a FVM solver is used with collocated variables). This becomes problematic when $\tilde{p}$ is getting smaller, because pressure gradients normal to the wall are quite large. Other Froude numbers are also of interest: subcritical flows are currently studied but give convergence problems for the modes with $\mu \approx 1$. For very low Froude flows –such as natural flow in rivers– it is possible that all modes are dominated by gravity ($K < -1$). This will be studied in the future.

References

Cahouet, J. (1984). *Etude numérique et experimentale du probleme bidimensionnel de la résistance de vagues non-linéaire*. Ecole nationale supérieure de techniques avancées.

Degroote, J., Bathe, K.-J., and Vierendeels, J. (2009). Performance of a new partitioned procedure versus a monolithic procedure in fluid–structure interaction. *Computers & Structures*, 87(11):793–801.

Muzaferija, S. and Perić, M. (1997). Computation of free-surface flows using the finite-volume method and moving grids. *Numerical heat transfer*, 32(4):369–384.

Tzabiras, G. (1997). A numerical investigation of 2D, steady free surface flows. *International Journal for Numerical Methods in Fluids*, 25(5):567–598.

Van Brummelen, E., Raven, H., and Koren, B. (2001). Efficient numerical solution of steady free-surface Navier–Stokes flow. *Journal of Computational Physics*, 174(1):120–137.

Iterative Errors in Unsteady Flow Simulations: Are they Really Negligible?

Luís Eça[*], **Guilherme Vaz**[†] **and Martin Hoekstra**[+]

[*]IST Técnico Lisboa, Lisbon/Portugal, [†]MARIN Maritime Research Institute Netherlands,
Wageningen/The Netherlands, [+] Consultant
luis.eca@tecnico.ulisboa.pt

1 Introduction

The numerical solution of a statistically steady flow problem is typically obtained in an iterative process. For a given mathematical model, including boundary conditions, the accuracy of the solution is governed by spatial resolution of the grid, spatial discretisation schemes and the convergence tolerance, which says when the solution is considered to have reached a steady state. Next to hardware quality (round-off error), the discretisation error and the iterative error determine the quality of the solution. For unsteady flow problems matters are more complicated. Temporal and spatial resolution have to be chosen carefully in proper balance. Moreover, in high Reynolds number (turbulent) flows, time integration is usually performed with implicit schemes, which require the solution of a non-linear system of equations at each time step. Again a convergence tolerance is needed to decide on when having solved this non-linear system well enough. Any iterative error propagates to the next time step. How does one guarantee reliability of the results?

A Workshop dedicated to Iterative Errors in Unsteady Flow Simulations was held at the ASME V&V Symposium of 2017. The main goals of this Workshop were to create awareness to the problem and to check if different flow solvers exhbited the same trends in the solution of a laminar, two-dimensional flow of an incompressible fluid around a circular cylinder. Five groups submitted results using respectively ANSYS Fluent, ANSYS CFX, OpenFoam, ReFRESCO and SATURNE. A significant influence of the convergence criteria applied at each time step on the numerical accuracy of the solution was experienced by all participants.

This paper summarizes the main results of this first Workshop on Iterative Errors in Unsteady Flow Simulations. It presents a brief description of the proposed test case and the selected quantities of interest and an overview of some of the submitted data, which are available at Workshop (2017). The paper is also meant as an encouragement for participants of the NUTTS symposium to take part in the second edition of the Workshop that will take place at the ASME V&V Symposium of 2018.

2 Test Case

The selected test case is the laminar flow around a circular cylinder at Reynolds numbers ($Re = \frac{V_\infty D}{\nu}$) based on the incoming velocity V_∞, cylinder diameter D and kinematic viscosity of the fluid ν of $Re = 100$ and/or $Re = 150$[1]. It is suggested to assume that the fluid is incompressible.

The flow is two-dimensional and the calculation domain is a rectangle with the distances of the boundaries to the cylinder centre equal to $20D$ upstream for the inlet, $80D$ downstream for the outlet and $40D$ for top and bottom boundaries. The Cartesian (x, y) coordinate system adopted has the origin at the centre of the cylinder and the x axis aligned with V_∞.

Suggested boundary conditions are: no-slip condition at the cylinder surface ($\sqrt{x^2 + y^2} = D/2$) and normal derivative of the pressure set equal to zero ($\vec{\nabla}p \cdot \vec{n} = 0$); uniform incoming flow at the inlet boundary ($x = -20D$) with horizontal velocity component $V_x = V_\infty$ and vertical velocity component $V_y = 0$; pressure imposed at the outlet boundary ($x = 80D$) and derivatives of the two velocity components in the streamwise direction (x) equal to zero ($\frac{\partial V_x}{\partial x} = \frac{\partial V_y}{\partial x} = 0$); free-slip at the top and bottom boundaries

---

[1]The original proposal included only $Re = 150$. However, a review of the literature showed that there is a lot more published results for $Re = 100$ than $Re = 150$.

($y = \pm 40D$), i.e. normal velocity component equal to zero ($V_y = 0$) and derivatives of the velocity component in the horizontal direction and pressure in the normal direction equal to zero ($\frac{\partial V_x}{\partial y} = \frac{\partial p}{\partial y} = 0$).
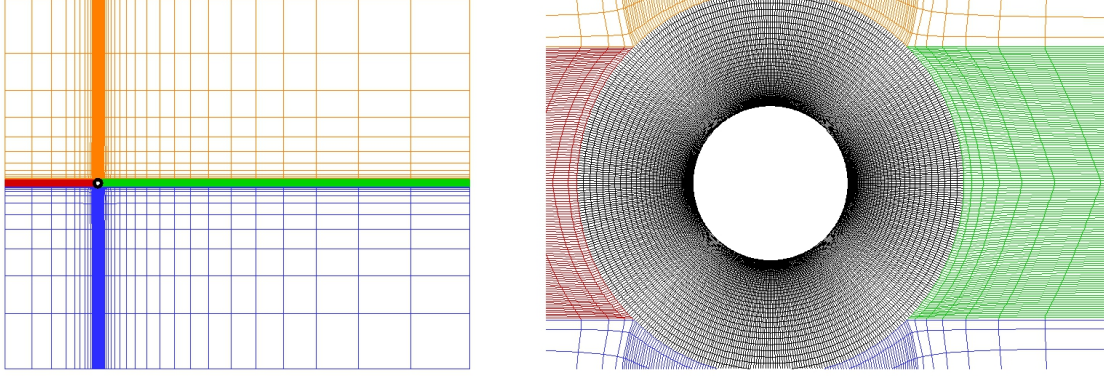

Fig. 1: Illustration of the grids for the calculation domain of the flow around a circular cylinder.

There are four geometrical similar multi-block structured grids available in CGNS, MSH, CFX and OpenFoam formats, which are illustrated in Fig. 1. The grids have clustering of grid nodes in the block of the near-wake. As a consequence, there is a sudden change of cell size at the edge of the inner block, but several preliminary tests were done to guarantee that these grids are suitable for the determination of the quantities of interest. Furthermore, these tests showed that it was important to include a significant increase of the cell-size at the outlet, top and bottom boundaries to avoid pressure reflections. Table 1 presents the total number of cells, the number of faces on the cylinder surface and the grid refinement ratio $r_i = h_i/h_1$ of the 4 grids,

Table 1: Grids available for the Workshop on Iterative Errors in Unsteady Flow Simulations.

Grid	Number of Cells	Number of Faces on Cylinder Surface	r_i
4	125910	960	2
3	196266	1200	1.6
2	282174	1440	1.3(3)
1	503640	1920	1.

3 Selected Quantities of Interest

The selected quantities of interest include time-averaged results of functional and local flow quantities, the standard deviation of force coefficients and the Strouhal number $St = \frac{fD}{V_\infty}$, which quantifies the frequency $f = 1/T$ of the vortex shedding.

Time-averaging of a requested flow quantity ϕ should be determined from

$$(\phi)_{avg} = \frac{\int_0^{nT} \phi(t)dt}{nT} \, ,$$

where T is the period of the lift coefficient C_L time history and n is the number of cycles ($n \geq 5$) used to determine the average value. The beginning of the cycle corresponds to the instant where $C_L = 0$ when the lift coefficient is increasing. Standard deviation of ϕ is obtained from

$$(\phi)_{std} = \sqrt{\frac{\int_0^{nT} \left(\phi(t) - (\phi)_{avg}\right)^2 dt}{nT}} \, .$$

The requested time-averaged flow quantities are: lift $(C_L)_{avg}$ and drag $(C_D)_{avg}$ coefficients with $C_D(t)$ and $C_L(t)$ obtained from the integration of the pressure and shear-stress on the surface of the cylinder and the reference force per unit width equal to $1/2\rho V_\infty^2 D$; base pressure coefficient $(C_{p_b})_{avg}$ that corresponds to the pressure coefficient $C_p = \frac{p - p_\infty}{1/2\rho V_\infty^2}$ at $x = 0.5D, y = 0$ with p_∞ obtained from the largest pressure value at the inlet of the domain $x = -20D$; the flow separation angle $(\theta_{sep})_{avg}$, where θ_{sep} is obtained from the point with shear-stress at the wall equal to zero $\tau_w = 0$. $\theta = 0$ corresponds to the stagnation point of the time-averaged flow and θ increases in the clockwise direction. Standard deviations are requested for the lift $(C_L)_{std}$ and drag $(C_D)_{std}$ coefficients.

4   Overview of Results

The compilation of the submitted results is available at Workshop (2017). There were 4 submissions for each Reynolds number using the flow solvers mentioned above. As expected, solution strategies, time and space discretization techniques and definition of the iterative convergence criteria at each type step were not identical for all the participants.

Pressure-velocity coupling was performed with five different strategies: SIMPLE, SIMPLEC, PISO, a mixture of PISO and SIMPLE (PIMPLE) and with a fully-coupled solution. Time-discretization was always performed with a finite-difference approach for the time derivatives using first or second-order backward differencing schemes. All submissions used second-order schemes for diffusion, but two different approaches were used for the convective terms: second-order upwind and central differences.

Control of iterative convergence at each time step was performed with the following criteria: maximum (L_∞) or root mean squared value (L_2) of normalized residuals that correspond to the change of dimensionless dependent variables in a simple Jacobi iteration; averaged normalized residuals that correspond to the ratio between the sum of the absolute value of the residuals of all cells and the sum of the absolute value of the product between the main diagonal and the velocity magnitude at the cells centre[2]; global sum of squares of cells residuals, which we could not find the definition in the SATURNE manual; total number of non-linear iterations performed at each time step and finally the global imbalance of the discretized continuity and momentum equations. In some submissions, more than one criterion was used at each time step.

The application of different strategies to control the iterative convergence criteria at each time step makes the comparison between the data obtained from the different submissions troublesome. Furthermore, the definition of the time step also varied between the different participants. Most of the submitted calculations used a fixed time step. However, the selected values were significantly different. On the other hand, there was one submission that used the maximum Courant number to adjust the time step. Therefore, in this paper we will restrict ourselves to the results obtained with ReFRESCO. Nonetheless, comparisons of all submitted data are available at Workshop (2017).

In order to give an idea of the influence of the different iterative convergence criteria and time steps, Fig. 2 presents the average values of the number of iterations performed at each time step N_{iter} and the ratio between the L_∞ and L_2 normalized residuals[3] as a function of the tolerance used at each time step Tol_{it}. The data corresponds to calculations performed with $Re = 100$ and second-order time integration in the coarsest (4) and finest (1) grids. The time steps are 0.025, 0.01 and 0.0025 dimensionless time units for grid 4 and half of these values for grid 1 corresponding in both cases to the maximum Courant numbers given in the plots.

Naturally, N_{iter} increases with the decrease of Tol_{it}. However, the growth rate is significantly dependent on the time step and on the grid density. The smallest time step leads to the lowest increase of N_{iter} with Tol_{it} and to the weakest dependency on the grid density. On the other hand, the three plots show that the average value of the L_2 residual is consistently one order of magnitude below the L_∞ residual for the momentum equations and two orders of magnitude for the pressure (continuity) equation. This

---

[2]For the continuity equation there is a different definition, see the manual of ANSYS Fluent.

[3]Maximum value of the first normalized residual described above must be smaller than Tol_{it} for all equations at each time step.
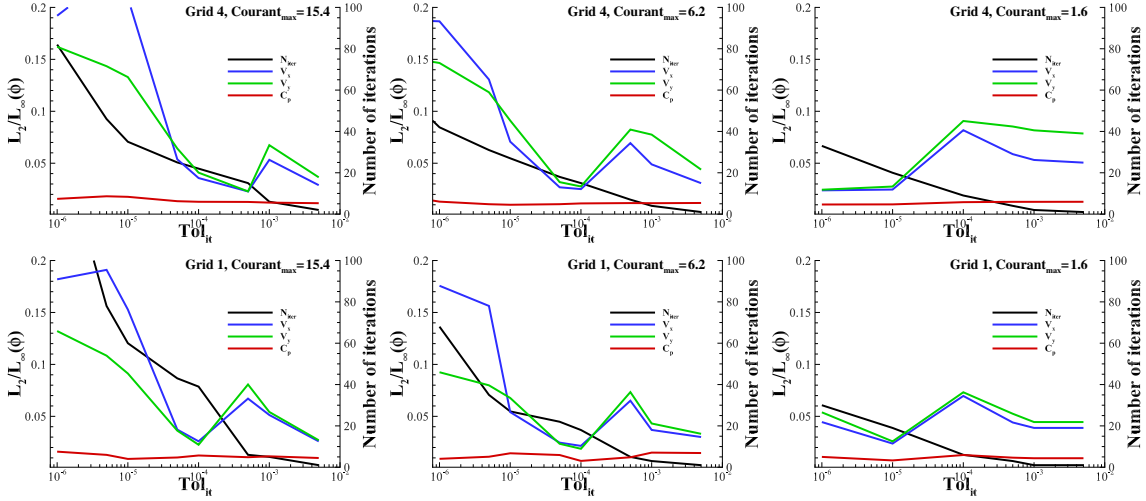
Fig. 2: Average value the number of iterations performed at each time step N_{iter} and the ratio between L_∞ and L_2 normalized residuals as a function of the tolerance used at each time step Tol_{it}. Results obtained in the coarsest (4) and finest (1) grids with second-order integration in time.
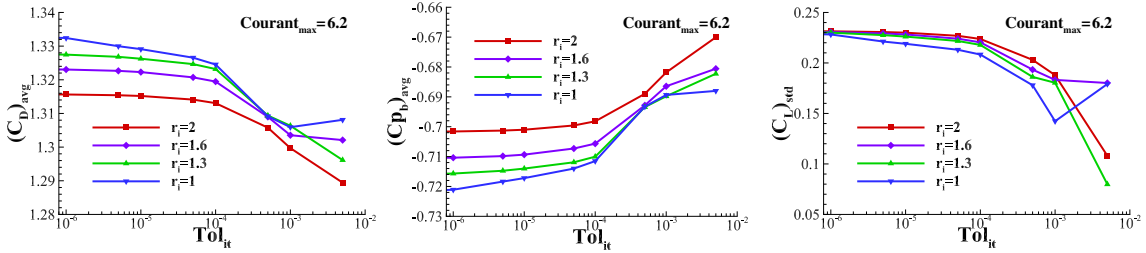

Fig. 3: Time-averaged drag $(C_D)_{avg}$ and base pressure coefficient $(C_{p_b})_{avg}$ and standard deviation of lift coefficient $(C_L)_{std}$ as a function of the tolerance used at each time step Tol_{it}. Results obtained with second-order integration in time.

means that iterative convergence criteria based on the number of non-linear iterations must be dependent on the time step and grid density and that the comparison of solutions based on maximum or root mean squared residual must be performed carefully.

Fig. 3 presents $(C_D)_{avg}$, $(C_{p_b})_{avg}$ and $(C_L)_{std}$ as a function of Tol_{it} for calculations performed with second-order time integration and a refinement of the time step that matches the grid refinement ratio, i.e. $r_i = h_i/h_1 = \Delta t_i/\Delta_1$. This choice of simultaneous grid and time refinement leads to identical values of the maximum Courant number for the four grids. The results show a significant influence of the iterative convergence criteria on the three flow quantities that may have two consequences: the iterative error cannot be neglected in the estimation of the numerical error and/or the estimation of the discretization error may be contaminated by the iterative error.

As an example of the latter problem, Fig. 4 presents the estimate of the discretization error of $(C_D)_{avg}$, $(C_{p_b})_{avg}$ and $(C_L)_{std}$ using the procedure proposed in Eça and Hoekstra (2014). When its determination is possible, the observed orders of grid/time convergence p are given in the legend. The data corresponds to calculations performed with different tolerances for the iterative convergence at each time step. There is a significant influence of Tol_{it} on the estimated discretization uncertainty for the three flow quantities. For the two time-averaged quantities, the error bars obtained with $Tol_{it} = 10^{-3}$ do not intersect those determined for $Tol_{it} = 10^{-6}$. In both cases, the mismatch between the two error bars is of the order of the uncertainty obtained for $Tol_{it} = 10^{-6}$, which is close to 10^{-2}. On the other hand, the numerical uncertainty (and the results) obtained for $(C_L)_{std}$ with different values of Tol_{it} are significantly different: $0.142 \pm 139.4\%$ for $Tol_{it} = 10^{-3}$ and $0.228 \pm 4.1\%$ for $Tol_{it} = 10^{-6}$.
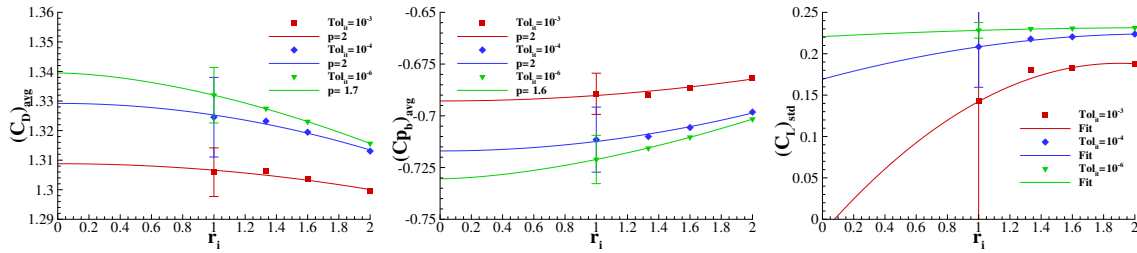
Fig. 4: Estimate of discretization error of the time-averaged drag $(C_D)_{avg}$ and base pressure coefficient $(C_{p_b})_{avg}$ and standard deviation of lift coefficient $(C_L)_{std}$ for different levels of the tolerance used at each time step Tol_{it}. Results obtained with second-order integration in time.

The data of figure 4 also illustrates the importance of the iterative error for the calculations performed with loose iterative convergence criteria. The results obtained for the three select flow quantities in the coarsest grid ($r_i = 2$) with $Tol_{it} = 10^{-6}$ are significantly more (numerically) accurate than those obtained in the finest grid ($r_i = 1$) with $Tol_{it} = 10^{-3}$, which means that iterative errors are actually larger than the discretization errors for the latter simulations.

5   Second Workshop on Iterative Errors in Unsteady Flow Simulations

The second edition of the Workshop on Iterative Errors in Unsteady Flow Simulations will keep the same test case, but only $Re = 100$ will be considered. The proposed domain, boundary conditions, selected flow quantities and grids remain the same of the first Workshop (2017). However, this time simulations will be requested for specific time steps and/or maximum Courant numbers. Furthermore, submissions must include results obtained with at least four levels of iterative convergence criteria.

Detailed information must be submitted about the selected iterative convergence criteria and the number of iterations performed at each time step. For example, calculations performed with convergence criteria based on residuals must report the average number of iterations performed at each time step and vice-versa. Such information is crucial for the comparison of results obtained with different flow solvers.

Finally, we would like to invite all participants of the NUTTS 2017 Symposium meeting to participate in this Workshop that we are sure will provide very useful guidelines for handling iterative errors in unsteady flow simulations.

References

Roache P.J. (2009). *Fundamentals of Verification and Validation.*, Hermosa Publishers, Albuquerque, New Mexico.

Workshop (2017)
`http://web.tecnico.ulisboa.pt/ist12278/Workshop_iterative_2017.htm`

ANSYS Fluent `http://www.ansys.com/Products/Fluids/ANSYS-Fluent`

ANSYS CFX `http://www.ansys.com/Products/Fluids/ANSYS-CFX`

OpenFoam `http://www.openfoam.com/`

ReFRESCO `http://www.refresco.org/`

SATURNE `http://code-saturne.org/cms/`

Eça L. and Hoekstra M. (2014), *A procedure for the estimation of the numerical uncertainty of CFD calculations based on grid refinement studies*. Journal of Computational Physics, **262**:104-130.

Correct Energy Behavior in Two-Fluid Flow

Marco ten Eikelder, Ido Akkerman, Riaan van 't Veer

Delft University of Technology, Department of Mechanical, Maritime and Materials Engineering, P.O. Box 5, 2600 AA Delft, The Netherlands

m.f.p.teneikelder@tudelft.nl

1 Introduction

Two-fluid flow phenomena appear in many engineering fields of which an important one is the shipping industry. One of the main problems in ship hydromechanics involving two-fluid flow is the sloshing of liquefied natural gas (LNG) in cargo tanks. The pitching and roll movement of the ship causes the liquid to move. This creates a high impact pressure on the containing tank which can result in structural damage. Another example of two-fluid flow phenomena occurs in the air lubrication system of ships. This system creates a layer of air under the ship which reduces the resistance of the ship. The behavior of two-fluid flow in these examples physically very complex. This explains the growing interest in two-fluid flow simulations accessed to such problems.

The physical complexity raises high demands on the capabilities of the numerical methodologies employed for the simulations. One of those is linked to the turbulence characteristics of the flows. This asks the employed numerical method to be able to capture multiscale physical phenomena. Furthermore, it occurs to be difficult to accurately describe the two-fluid interface. Many numerical methods unfortunately create artificial energy at the air-water interface. This leads to unphysical behavior.

In this short work we present an approach to tackle these problems. Our methodology uses the variational multiscale approach to capture the detailed complex physical behavior. Within this framework we ensure correct energy behavior to omit artificial energy creation at the interface. Furthermore we employ the novel concept of isogeometric analysis to build a robust and accurate method.

We start off by briefly introducing the several components of our method: the isogeometric analysis framework in Section 2 and the variational multiscale approach in Section 3. In Section 4 we address the energy behavior of the methodology in the two-fluid flow context. We wrap up with conclusions and recommendations in Section 5.

2 Isogeometric analysis

The first building block of our approach is the isogeometric analysis (IGA) methodology. This method proposed in Hughes et al. (2005) shares many features with the finite element method (FEM). A conceptual difference is that the finite element methodology uses polynomial basis functions, whereas IGA employs NURBS (non-uniform rational B-splines) basis functions. Figure 1 shows some C^1-continuous NURBS.
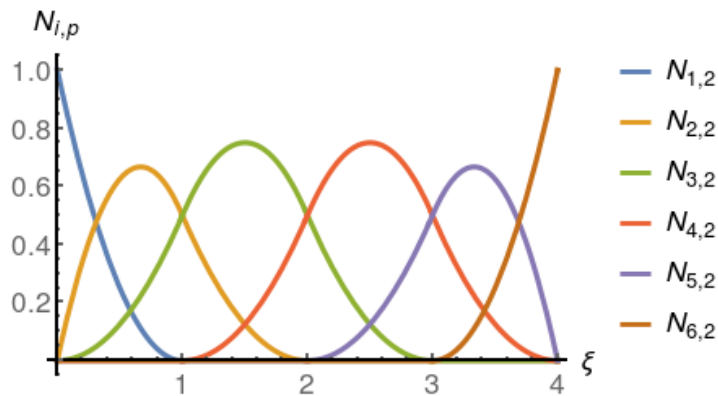

Fig. 1: NURBS basis functions.

One of the main advantages of IGA is its ability to *exactly* represent the geometry under consideration. This is not linked to the level of fineness of the taken discretization or the complexity of the geometry. Figure 2 illustrates the different geometry description of FEM and IGA.

(a)   (b)

Fig. 2: Discretization of a curved geometry. (a) Finite element nodes do not exactly described the surface whereas (b) the NURBS geometry exactly covers the surface. The figure is adapted from Hughes et al. (2005).

IGA can be viewed as the relation between Computer-Aided Design (CAD) and Computer-Aided Engineering (CAE). It significantly speeds up the mesh generation and mesh refinement procedures by employing the NURBS functions from CAD. Apart from this, compared with FEM, IGA shows higher-order convergence behavior and higher-continuity properties on complex domains. The main reason to employ it in two-fluid flow simulations is its ability to *exactly* have a solenoidal velocity field. Furthermore, the higher continuity property of IGA fits our method (more details can be found in ten Eikelder and Akkerman (a)). Various numerical methods employing the IGA framework appear in different fields, see for example Akkerman et al. (2011), Bazilevs et al. (2006) and Bazilevs et al. (2012).

3   Variational multiscale approach

The second ingredient of our approach is the variational multiscale (VMS) framework. This concept, which was proposed in Hughes (1995) and Hughes and Stewart (1996), creates a framework which allows to deal with multiscale phenomena present in nature and engineering. The classical Galerkin finite element approach incorporates that part of the solution living on the discretization grid and ignores the fraction not represented on the grid. This disregards the small-scales and hence the Galerkin methodology is an unsuitable choice for computations involving multiscale effects. The VMS framework aims to correct this deficiency by incorporating the contribution of the small-scales not living on the grid.
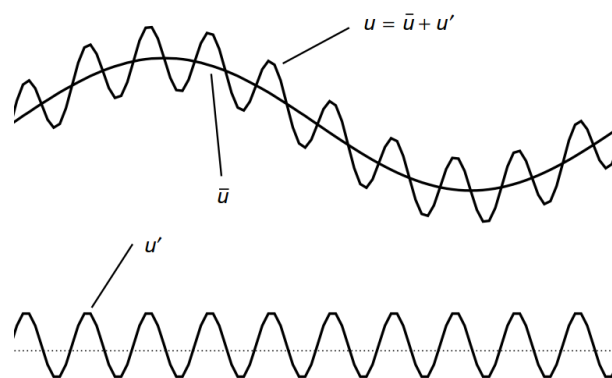

Fig. 3: A multiscale split of the solution. Adapted from Hughes et al. (1998).

The VMS approach uses a projector to split the solution as[1]:

$$u = \bar{u} + u' \tag{1}$$

---

[1]This decomposition is not unique, more details can be found in Hughes (1995).

where $\bar{\boldsymbol{u}}$ are the large- or coarse-scales and $\boldsymbol{u}'$ are the small- or fine-scales not reproduced by the grid, see Figure 3. In the original approach the small-scales are determined as

$$\boldsymbol{u}' = -\tau \mathrm{Res}(\bar{\boldsymbol{u}}), \tag{2}$$

where $\mathrm{Res}(\bar{\boldsymbol{u}})$ is the residual of the fluid flow equation and τ is a stabilization (algebraic) operator. Note that the small-scales scale with the residual, i.e. a small residual implies a small contribution of the small-scales. It is important to emphasize that this approach does not require any *ad hoc* mechanisms like eddy viscosity terms.

4 Correct energy behavior

The isogeometric context allows us to deal with exactly divergence-free velocity fields, i.e. we have exact mass conservation. Unfortunately, this exact behavior does not directly apply to the energy. When employing the (standard) variational multiscale method of Bazilevs et al. (2007) artificial energy can be created. A numerical energy inconsistency might highly influence the numerical results. An example of incorrect behavior caused by energy inconsistencies is described in Akkerman et al. (2012). In that work a dam break problem with an obstacle is presented. A column of water, which is initially at rest, slams into a stationary object. In this test case huge problems occur when employing the traditional approach of staggering the fluid and interface description algorithms[2]. A simultaneous solution approach significantly improves the stability, see Figure 4.
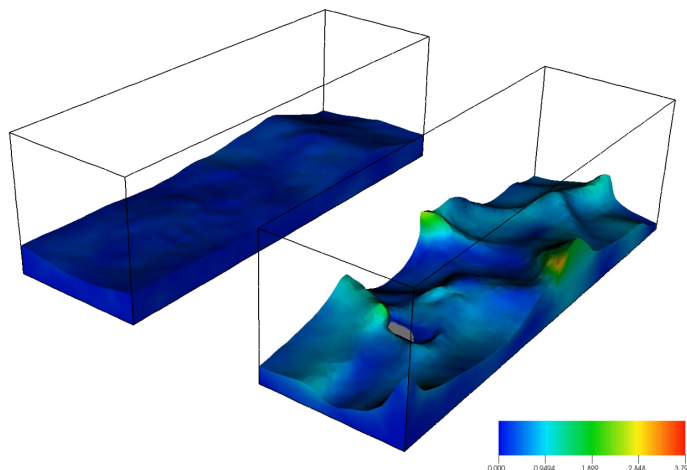

Fig. 4: A dam break problem with an obstacle. Illustration of artificial energy creation. Left: coupled simulation, right: staggered simulation. From Akkerman et al. (2012).

This raises the task to construct a method ensuring correct energy behavior. The discrepancy of the unwanted energy creation vanishes for the proper variational multiscale method. This is described in the recent work ten Eikelder and Akkerman (a) in the convection-diffusion context and ten Eikelder and Akkerman (b) for the incompressible Navier-Stokes equations. By employing the proper small-scale behavior undesired energy creation disappears. The energy evolution in the numerical formulation then closely resembles the continuous case in which the energy changes by viscous effects, external forcing and flow through the boundary. The temporal evolution of the continuous case reads:

$$\frac{\mathrm{d}}{\mathrm{d}t}E_\Omega = -\|\nu^{1/2}\nabla\boldsymbol{u}\|_\Omega^2 + (\boldsymbol{u}, \boldsymbol{f})_\Omega - (1, F_\Omega)_\Gamma. \tag{3}$$

Here E_Ω represents the kinetic energy in the domain Ω, $-\|\nu^{1/2}\nabla\boldsymbol{u}\|_\Omega^2$ the decrease in kinetic energy by viscosity, $(\boldsymbol{u}, \boldsymbol{f})_\Omega$ the change in kinetic energy by external forcing and the latter term $-(1, F_\Omega)_\Gamma$ the flow of kinetic energy through the boundary Γ.

---

[2]The air-water interface is described by a level-set method. This requires a consistent level-set method to obtain correct energy behavior within this setting Akkerman (2017).

The precise formulation of the various terms in the fluid flow equations is of great importance. To illustrate this, we consider a dam break problem, just like in Akkerman et al. (2012), only this time without the stationary object. Let us take the contribution by convection in isolation. Therefore we distinguish the three options: (i) a *conservative* formulation, (ii) a *convective* formulation and (iii) and an alternative formulation to which we refer to as *Lagrange-Multiplier* (LM). Figure 5 displays stable behavior for the latter two options, whereas the first one breaks down.
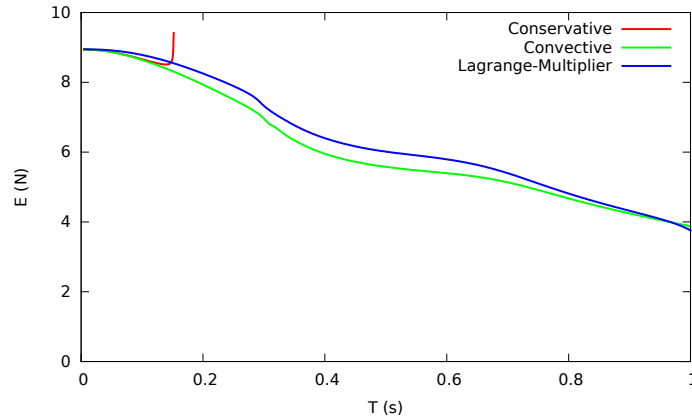
Fig. 5: Dam break problem without obstacle. Energy behavior in the numerical formulation. The conservative, convective and the Lagrange-Multiplier options are employed.

For the two methods that do not break down (method (ii) and (iii)) we provide a mesh convergence study in Figure 6. Here we see that a simulation of the convective approach with a fine mesh delivers a very similar result as the Lagrange-multiplier option on a course mesh.
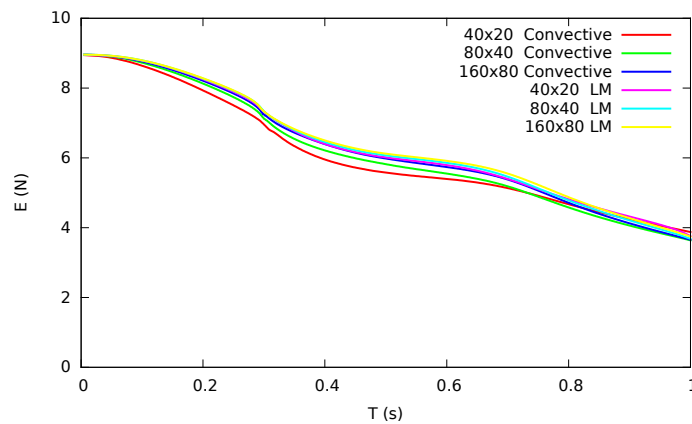
Fig. 6: Dam break problem without obstacle. Mesh convergence of the energy behavior in the numerical formulation. The convective and the Lagrange-Multiplier options are employed.

5 Conclusion

In this work we have seen that the actual numerical formulation of two-fluid flow is very sensitive. A small inconsistency in the capturing of physical laws can highly influence the results and even a breakdown of the methodology is unfortunately possible. To eliminate this danger, a constructive step-by-step approach is demanded. Therefore, we tackle the problem in each of the single fluids first. The mass conservation is automatically fulfilled by the isogeometric approach and we correct the energy behavior.

Combining the various ingredients we construct a powerful tool capable of capturing multiscale physics in two-phase flow behavior. The methodology solves the full incompressible Navier-Stokes equations, does not contain any *ad hoc* mechanism, enjoys exact mass conservation and displays correct energy behavior.

Acknowledgements

References

I. Akkerman (2017). Monotone level-sets on arbitrary meshes without redistancing. *Computers & Fluids*, **146**, 74–85.

I. Akkerman, Y. Bazilevs, D. Benson, M. Farthing, and C. Kees (2012). Free-surface flow and fluid-object interaction modeling with emphasis on ship hydrodynamics. *Journal of Applied Mechanics*, **79**, 010905.

I. Akkerman, Y. Bazilevs, C. Kees, and M. Farthing (2011). Isogeometric analysis of free-surface flow. *Journal of Computational Physics*, **230**, 4137–4152.

Y. Bazilevs, V. Calo, J. Cottrel, T. J. R. Hughes, A. Reali, and G. Scovazzi (2007). Variational multi-scale residual-based turbulence modeling for large eddy simulation of incompressible flows. *Computer Methods in Applied Mechanics and Engineering*, **197**, 173–201.

Y. Bazilevs, V. Calo, Y. Zhang, and T. J. R. Hughes (2006). Isogeometric fluid-structure interaction analysis with applications to arterial blood flow. *Computational Mechanics*, **38**, 310–322.

Y. Bazilevs, M.-C. Hsu, and M. Scott (2012). Isogeometric fluid–structure interaction analysis with emphasis on non-matching discretizations, and with application to wind turbines. *Computer Methods in Applied Mechanics and Engineering*, **249**, 28–41.

T. J. R. Hughes (1995). Multiscale phenomena: Green's functions, the Dirichlet-to-Neumann formulation, subgrid scale models, bubbles and the origins of stabilized methods. *Computer Methods in Applied Mechanics and Engineering*, **127**, 387–401.

T. J. R. Hughes, J. Cottrell, and Y. Bazilevs (2005). Isogeometric analysis: CAD, finite elements, NURBS, exact geometry, and mesh refinement. *Computer Methods in Applied Mechanics and Engineering*, **194**, 4135–4195.

T. J. R. Hughes, G. Feijóo., L. Mazzei, and J. B. Quincy (1998). The variational multiscale method – A paradigm for computational mechanics. *Computer Methods in Applied Mechanics and Engineering*, **166**, 3–24.

T. J. R. Hughes and J. Stewart (1996). A space-time formulation for multiscale phenomena. *J. Comput. Appl. Math.*, **74**, 217–229.

M. F. P. ten Eikelder and I. Akkerman. Correct energy evolution of stabilized formulations: The relation between the variational multiscale approach and the Galerkin/least-squares method via dynamic orthogonal small-scales and isogeometric analysis. I: The convective-diffusive context. *submitted*.

M. F. P. ten Eikelder and I. Akkerman. Correct energy evolution of stabilized formulations: The relation between the variational multiscale approach and the Galerkin/least-squares method via dynamic orthogonal small-scales and isogeometric analysis. II: The incompressible Navier-stokes equations. *under construction*.

Towards Nonlinear Time–Spectral Seakeeping Simulations in foam–extend

Inno Gatin*, Filip Volarić, Vuko Vukčević, Hrvoje Jasak
University of Zagreb, Zagreb/Croatia,
inno.gatin@fsb.hr, fv190377@stud.fsb.hr, vuko.vukcevic@fsb.hr, hrvoje.jasak@fsb.hr

1 Introduction

As the continuation of the development of the Harmonic Balance (HB) method applied to the problems of surface gravity waves in `Naval Hydro` pack in foam–extend [Gatin et al., 2016], body motion is included in the effort aimed towards seakeeping simulations in frequency domain. Using HB, the transient problem which is temporally periodic can be transformed into a set of coupled steady state problems. HB method has been successfully applied on the problem of wave diffraction, while in this paper the extension for general 6–degrees–of–freedom (6–DOF) motion is shown, with preliminary test results.

Application of Finite Volume–based CFD methods for calculation of seakeeping characteristics of floating objects presents an active field of research. The computational price of CFD is a large concern for seakeeping simulations, since a large number of periods is needed for the simulation to reach periodic steady–state. By applying HB to the problem of seakeeping, it becomes a set of coupled steady state equations, each representing one time instant along the period of oscillation, which presumably take smaller amount of time to converge. It is shown previously that a savings by a factor of two or more can be achieved for a realistic diffraction problem [Gatin et al., 2016]. Hence, a similar savings can be expected for seakeeping simulations.

In order to couple 6–DOF equations and the HB method, the body motion equations need to be formulated and solved in the frequency domain. Since the steady state equations are solved in time–domain [Cvijetić et al., 2016], the forces and moments calculated from the simulations are first transformed using Fourier transformation in the frequency domain, where they are used in order to integrate the 6–DOF equations. The translational and rotational motion of the body calculated in frequency domain is than transformed back into the time–domain and applied on individual time–instances. To allow an elegant Fourier transform of rotation, a geometric method for integrating body motion [Müller and Terze, 2016] is applied, assuming second order accuracy of integration. Since the discretisation accuracy in time and space is up to second order, this is considered justified.

In this work the 6–DOF equations are coupled to the HB method which is applied to two–phase flow, where SWENSE (Spectral Wave Explicit Navier–Stokes) solution decomposition method [Vukčević et al., 2016], Ghost Fluid Method (GFM) [Vukčević et al., 2017], and and implicitly redistanced Level Set (LS) interface capturing method [Sun and Beckermann, 2007] are employed.

An overview of the mathematical model of the 6–DOF motion coupling with the HB steady state equations is given in this paper, where the HB method itself is omitted as it is described in the previous publication [Gatin et al., 2016]. Following the mathematical model, a preliminary two–dimensional simulation of a heaving and pitching submerged body is presented.

2 Coupling body motion and Harmonic Balance

In the time–domain, general 6–DOF motion of a rigid body can be described with two equations:

- Equations of translational motion:

$$\frac{\partial \mathbf{u}}{\partial t} = \frac{\mathbf{f}}{m}, \tag{1}$$

  where $\mathbf{u}$ stands for the translational velocity of the centre of gravity, $\mathbf{f}$ stands for the forces acting on the body, while m stands for the body mass.

- Equations of rotational motion:

$$\frac{\partial \boldsymbol{\omega}}{\partial t} = \mathbf{I}^{-1}\left(\mathbf{t} +^* (\mathbf{I}\boldsymbol{\omega})\boldsymbol{\omega}\right), \tag{2}$$

where $\boldsymbol{\omega}$ represents angular velocity vector, $\mathbf{t}$ represents torque acting on body and $\mathbf{I}$ is moment of inertia tensor.

Before they can be coupled with the HB method, the above equations must be transferred into the frequency domain by using Fourier series expansion. By expanding every term in Eq. (1) and Eq. (2) into Fourier series, and equating the corresponding harmonics, the following equation set is obtained:

$$in\omega\mathbf{U}_n = \frac{1}{m}\mathbf{F}_n, \quad n = 1,\ldots,N \quad , \tag{3}$$

$$
\begin{aligned}
\Omega_{x_n}in\omega &= \frac{1}{I_{xx}}\left[M_{x_n} + \left(I_{yy} - I_{zz}\right)\sum_{k=1}^{n}\Omega_{y_k}\Omega_{z_{(n-k)}}\right] \\
\Omega_{y_n}in\omega &= \frac{1}{I_{yy}}\left[M_{y_n} + (I_{zz} - I_{xx})\sum_{k=1}^{n}\Omega_{x_k}\Omega_{z_{(n-k)}}\right], \quad n = 1,\ldots,N \quad , \\
\Omega_{z_n}in\omega &= \frac{1}{I_{zz}}\left[M_{z_n} + \left(I_{xx} - I_{yy}\right)\sum_{k=1}^{n}\Omega_{x_k}\Omega_{y_{(n-k)}}\right]
\end{aligned}
\tag{4}
$$

$\mathbf{U}$ and $\mathbf{F}$ present complex numbers standing for the velocity and force vectors in the frequency domain, respectively. Ω_x, Ω_y and Ω_z are the components of the complex rotational velocity in frequency domain, while M_x, M_y and M_z stand for the complex components of torque in the frequency domain. ω is the base frequency of oscillation, while N stands for the finite number of harmonics. Integration of Eq. (3) and Eq. (4) provides the translational and rotational velocity of the body in frequency domain. To obtain the new position of the body, equations defining the position vector and rotational matrix have to be integrated as well. The position vector is obtained from:

$$\frac{\partial\mathbf{x}}{\partial t} = \mathbf{u}, \tag{5}$$

where $\mathbf{x}$ presents the position vector. When transformed into frequency domain Eq. (5) becomes:

$$in\omega\mathbf{X}_n = \mathbf{U}_n, \quad n = 1,\ldots,N \quad , \tag{6}$$

where $\mathbf{X}$ denotes the complex position vector amplitude in frequency domain. Hence, the position vector in time domain is readily available by transforming $\mathbf{X}$ into time domain, i.e. $\mathbf{x}$, by using Fourier transform. The new solution of the position of the rigid body can than be updated in steady state equations presenting individual time instances.

Rotational orientation of a rigid body is defined by a rotation matrix $\mathbf{R}$. By using the geometric method for rotational integration proposed by [Müller and Terze, 2016], the rotation matrix can be correlated to the rotational velocity ω with a nonlinear function. This whey, the conventional integration using quaternions is avoided, which are cumbersome when it comes to Fourier transformation. Furthermore, by limiting the accuracy of integration to second order, the correlation between the rotation matrix and rotational velocity becomes linear and easy to evaluate. Limiting the 6–DOF integration to second order accuracy is justified since the numerical discretisation of governing equations of the fluid flow is expected to be up to second order accurate. The rotation matrix and vector of angular velocity are correlated through vector $\mathbf{b}$:

$$\mathbf{R} = \mathbf{I} + \frac{\sin(|\mathbf{b}|)}{|\mathbf{b}|}\tilde{\mathbf{b}} + \frac{1 - \cos(|\mathbf{b}|)}{|\mathbf{b}|^2}\tilde{\mathbf{b}}^2, \tag{7}$$

where $\tilde{\mathbf{b}}$ stands for the skew–symmetric matrix corresponding to vector $\mathbf{b}$. Assuming the second order accuracy, vector $\mathbf{b}$ is easily computed from the rotational velocity:

$$\dot{\mathbf{b}} = \omega. \tag{8}$$

Above equation is easily transformed into frequency domain giving:

$$in\omega\mathbf{B_n} = \boldsymbol{\Omega}_n \quad n = 1,\ldots,N, \tag{9}$$

where **B** stands for the complex vector representing **b** in frequency domain. Hence, matrix **R** can be easily obtained by calculating vector **B** and transforming it into time domain. With matrix **R** and **x** the position and orientation of the rigid body are fully defined.

3   Preliminary test case

As a preliminary test, heave and pitch motion of a submerged body is calculated in regular waves with current. Since the simulation is performed in 2D, the body is submerged in order to avoid high frequency violent free surface flow in front of the bow, which deteriorates the convergence of HB method. The spectral space is discretised using two harmonics, giving five coupled steady state equations.

The base frequency is set to the encounter frequency of the incoming waves, $\omega = 3.34$ rad/s. Wave height is set to 0.196 m, and the stream velocity is $U = 2$ m/s. The body has a simple slender shape to avoid flow separation or similar higher frequency flow characteristics. Length of the body is $L = 5$ m, height $H = 0.6$ m, and it is submerged to a depth of 2.65 m below the calm free surface level. In two separate simulations, heave and pitch motion are calculated to check whether the proposed approach yields any physical results.

A two–dimensional grid is used with 13 300 cells. Figure 1 shows the computational grid in the vicinity of the submerged body, where the refinement on the free surface and near the body can be seen. Figure 2 shows the converged volume fraction field, total velocity field, and diffracted component of velocity in one of the time instances. Figure 3 shows the convergence of first order of heave force and heave motion, while on Figure 4 convergence of first order amplitude of pitch torque and pitch motion can be seen. The convergence of all items seems satisfactory, and the values are physical. However, further study is required in order to verify and validate the approach.
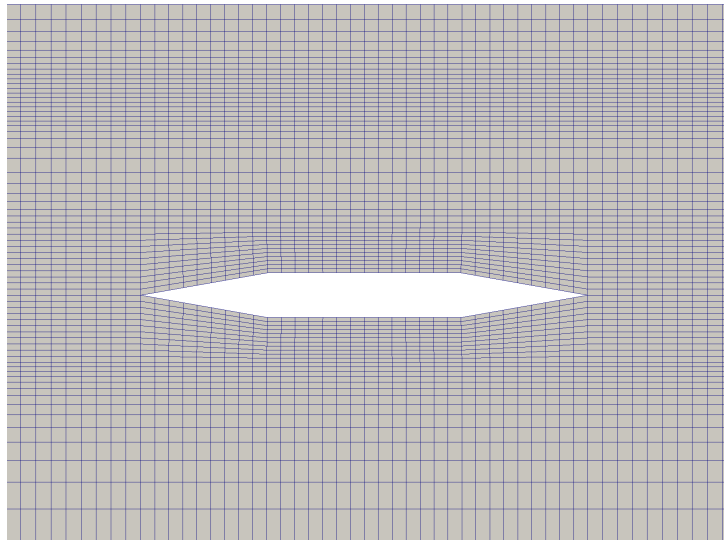
Fig. 1: Computational grid in the vicinity of the submerged body.

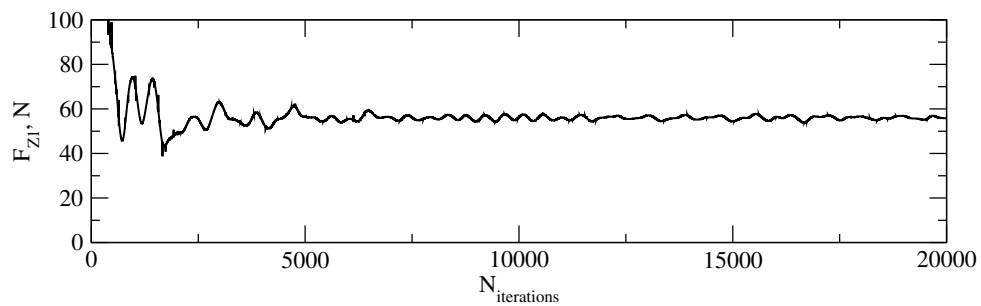(a) Volume fraction field for time instant $t = T/3$,
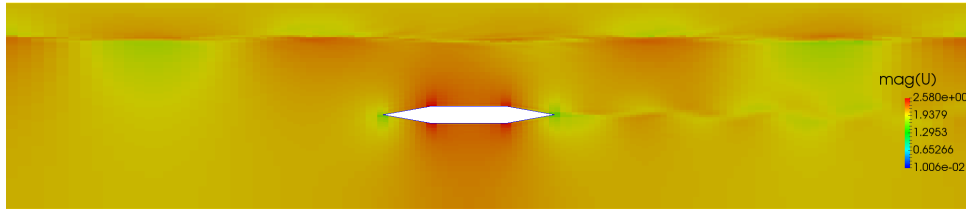
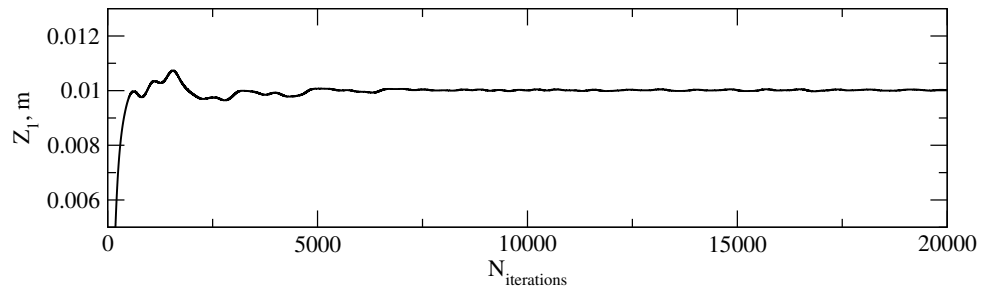(b) Velocity field for time instant $t = T$,
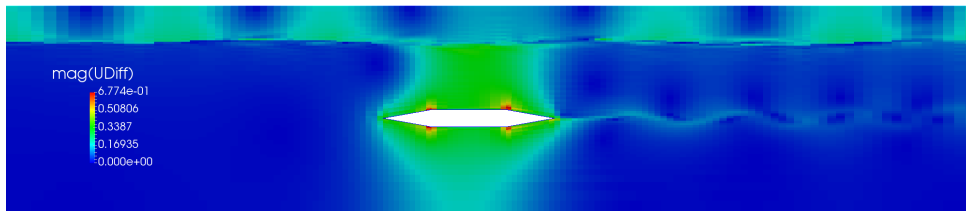
(c) Diffracted velocity field for time instant $t = T$.

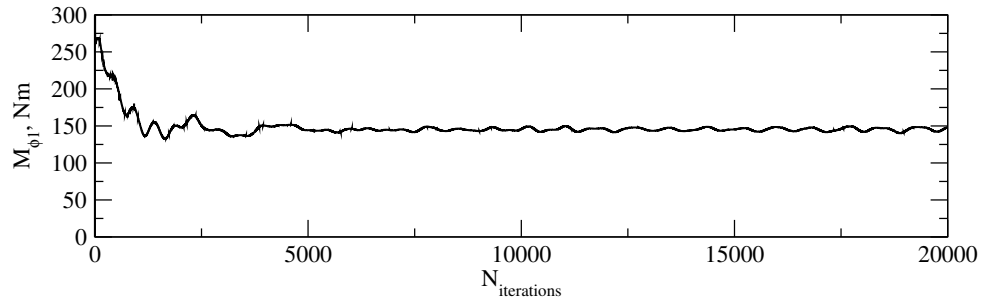Fig. 2: Flow field in the submerged body motion test case.
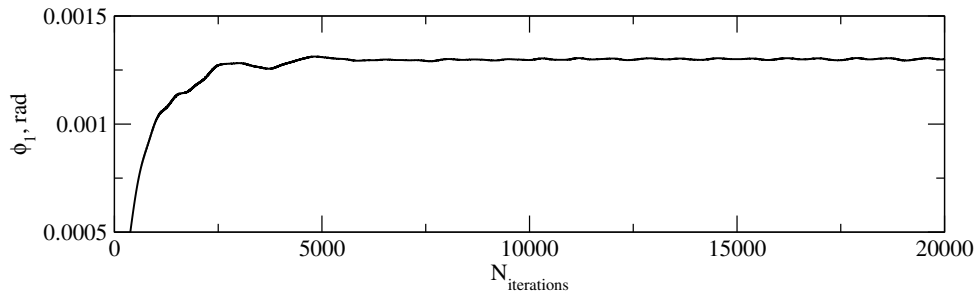

(a) First harmonic of heave force,

(b) First harmonic of heave motion.

Fig. 3: Convergence of heave force and motion in the submerged body test case.

(a) First harmonic of pitch torque,

(b) First harmonic of pitch motion.

Fig. 4: Convergence of pitch torque and motion in the submerged body test case.

4 Conclusion

Time–spectral method for conducting seakeeping simulations using Finite–Volume based CFD is presented. Harmonic Balance method is used to project a transient temporally–periodic problem into a set of coupled steady state equations. Rigid body motion is calculated by integrating the motion equations in the frequency domain.

Rotational motion of the rigid body is handled by limiting the accuracy of 6–DOF motion integration to second order, enabling a simple linear link between the rotational velocity vector and rotation matrix. This approach avoids the use of quaternions, which are cumbersome for performing Fourier transformation.

The method is demonstrated on a simple two–dimensional case of a submerged body free to pitch and heave. Convergence is shown to be stable for the proposed case, however further research is needed to quantify the accuracy and efficiency of the method in terms of CPU time.

References

Cvijetić, G., Jasak, H., and Vukčević, V. (2016). Finite volume implementation of the harmonic balance method for periodic non–linear flows. In *54th AIAA Aerospace Sciences Meeting*, page 0070.

Gatin, I., Cvijetić, G., Vukčević, V., and Jasak, H. (2016). Wave Diffraction CFD Nonlinear Time–Spectral Simulations in foam–extend. In *19th Numerical Towing Tank Symposium*.

Müller, A. and Terze, Z. (2016). Geometric methods and formulations in computational multibody system dynamics. *Acta Mechanica*, 227(12):3327–3350.

Sun, Y. and Beckermann, C. (2007). Sharp interface tracking using the phase–field equation. *J. Comput. Phys.*, 220:626–653.

Vukčević, V., Jasak, H., and Gatin, I. (2017). Implementation of the Ghost Fluid Method for free surface flows in polyhedral Finite Volume framework . *Computers & Fluids*, 153:1 – 19.

Vukčević, V., Jasak, H., and Malenica, S. (2016). Decomposition model for naval hydrodynamic applications, Part I: Computational method. *Ocean Eng.*, 121:37–46.

Comparison of Free Surface Capturing Approaches in OpenFOAM for Ship Resistance Prediction

Muye Ge, Rickard E. Bensow

Chalmers University of Technology, Mechanics and Maritime Sciences

muye.ge@chalmers.se, rickard.bensow@chalmers.se

1 Introduction

The prediction of calm water ship resistance by computational fluid dynamics (CFD) has matured considerably in recent years. For displacement ships, accurate prediction of the free-surface is normally reasonably robust, provided the mesh resolution is sufficient. For more complex situations, such as for high speed vessels where spray becomes important or when in situations where the transom is only partially dry on medium speed ships, the numerical schemes to be used are still in development; even more so perhaps if ship motions and ocean waves are considered. Thus, in the open source package Open-FOAM, there are a wide range of options to choose from when setting up the free-surface simulation, all with different impact on performance. Thus, in the present study, free-surface prediction by different interface capturing are presented for the KCS (KRISO Container Ship) hull resistance simulation. Focus is on some of the options available in OpenFOAM, but also the commercial package Star-CCM+ has been investigated. All simulations have been performed by considering incompressible RANS and the $k - \omega S S T$ turbulence model.

All tested methods are based on the Volume of Fluid (VoF) approach, where an indicator function α is used, and its evolution is modeled by a transport equation. In Star-CCM+, a HRIC (High Resolution Interface Capturing) discretization scheme is the default option available. In OpenFOAM, the FCT (Flux Corrected Transport) method based solver MULES has been developed and has been tested together with several higher order discretization schemes; also a special compressive treatment is available in Open-FOAM. Further, the NVD based high resolution schemes CICSAM and HRIC was also used to solve the α equation directly. A newly published method, isoAdvector, where geometrical interface reconstruction is performed with the potential to be able to predict a sharper and more accurate free surface interface, was also tested. Besides, development performed at the University of Applied Sciences in Kiel within the framework of OpenFOAM, a modified solver with reconstruction of pressure field at the interface where discontinuity exits was also compared.

2 Approaches

In VoF, the transport equation of α is a hyperbolic equation,

$$\frac{\partial \alpha}{\partial t} + \nabla \cdot \alpha \mathbf{u} = 0. \tag{1}$$

In OpenFOAM, a FCT (Flux Corrected Transport) based method was used to solve this equation to guarantee boundedness and accuracy, MULES (MUlti-dimensional Limiter for Explicit Solution). A later version, CMULES, is a semi-implicit approach, which firstly solve Eq. (2) using a diffusive implicit approach (implicit Euler time stepping and upwind convection) and then solve Eq. (3) explicitly with higher order schemes.

$$\frac{\alpha_{i(upwind)}^{n+1} - \alpha_i^n}{\Delta t} V + t F_{upwind}^n = 0, \tag{2}$$

$$\frac{\alpha_i^{n+1} - \alpha_{i(upwind)}^{n+1}}{\Delta t} V + \lambda(t F_{highOrder}^n - t F_{upwind}^n) = 0, \tag{3}$$

where $t F^n$ represent the summation of the face normal flux of α in a cell transported by the velocity. The CMULES maintains boundedness and stability at large Courant number. In the present study, van Leer, SuperBee, HRIC and CICSAM were used to calculate the high order flux in the framework of CMULES.

The High Resolution Schemes (HRS), such as HRIC and CICSAM, can be used outside of the framework of FCT. These two HRS were designed based on Normalised Variable Diagram (NVD), which can switch between high order schemes and inherent bounded schemes. This switch makes the capture of sudden gradient change possible, thus the sharp interface would be captured. For these high resolution schemes, since they already fulfil the boundedness, Eq. (1) could be solved directly. In practice, however, the CICSAM show some unstable behaviours including unboundedness, and is thus here only used with FCT. For the HRIC scheme though, the MULES in *interFoam* was replaced with equation below and discretized using the HRIC scheme,

```
fvScalarMatrix alpha1Eqn
(
    fvm::ddt(alpha1)
  + fvm::div(phi, alpha1, alphaScheme)
  + fvm::div(phirb, alpha1, alpharScheme)
)
```

In OpenFOAM, a compression term $\nabla \cdot (\alpha(1 - \alpha)\mathbf{u}_r)$ is added into the α transport equation. For all the simulations in present study, the *interfaceCompression* scheme was used to calculate $\mathbf{u}_{rf}$.

The isoAdvector by Roenby et al. (2016) is a newly developed solver for complex free surface flows, which can also be used for ship resistance prediction. It is also based on the VoF method, but the transportation is treated differently. In isoAdvector, first a geometric surface inside a cell based on node α values is reconstructed, and secondly the motion of the face-interface intersection line is modelled to obtain the time evolution of the submerged face area. This makes isoAdvector able to give a sharper and more accurate interface capture. A drawback for the ship resistance simulation is the requirement that interface Courant number should below 1 in order to avoid that the interface "advect" across many cells in a time step; this makes the approach computational expensive for the steady state simulations considered here.

Another approach considered in the present study is the development of *interFoam* by the Yacht Research Unit Kiel Janek et al. (2016). This solver deals with the multi-phase problem by improved reconstruction of the pressure field when discontinuity exists based on Queutey and Visonneau (2007). Mainly, the approach establishes a way to calculate two terms used in the momentum equation, $(\nabla p)_f$ in the Laplacian term and p_f in the velocity correction source term, when a sudden change of pressure exists, and avoids the numerical smearing of $(\nabla p)_f$ as well as velocity over-prediction in the air phase in the following velocity correction step.

Finally, Star-CCM+ is a widely used commercial package. Here, a hybrid scheme of upwind differencing and a HRIC is default for the discretization of the α transport equation; in the present study, the switch criteria of Courant number between UD and HRIC was modified to use purely HRIC.

3   Settings

The KCS, Kriso Container Ship, is a widely used validation case for the free surface prediction of merchant vessels. The KCS hull in model scale was used in the present simulations (Fr = 0.26) with Lpp of 7.2786 m. The simulation domain extends about 1.5 Lpp upstream, 2 Lpp downstream, 2.5 Lpp on the portside direction, 1.25 Lpp to the upper boundary and 2.5 Lpp to the bottom. Half of the hull was simulated with symmetry condition on the center line. The mesh was generated using Star-CCM+ with trimmer and prism layer insertion with y^+ value in the range of 30-50. 40 cells near the free-surface on the vertical direction were applied to capture the induced waves. The mesh contains 1.56 million cells in total, which is a little bit on the low side but then also challenges the free surface schemes more. The $k - \omega SST$ turbulence model with wall functions was used for all the simulations. First order accurate time schemes (Euler and Local Euler) and PIMPLE algorithm were used for all the simulations as steady state solution will be expected. Second order schemes were used for velocity and turbulence terms.
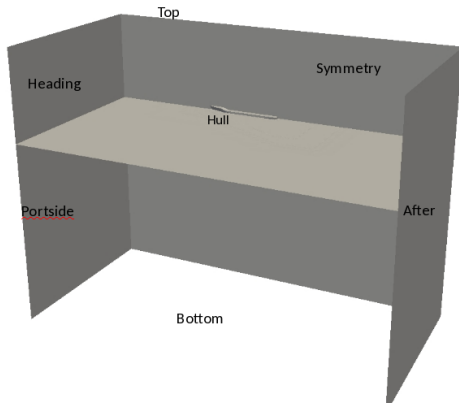
Fig. 1: Simulation domain
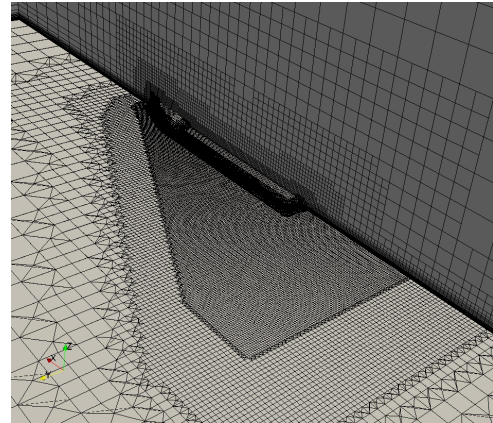
Fig. 2: Refinement near the freesurface

4 Results

The predicted wave patterns are displayed in figures 3 to 10 and compared to experimental data from Kim et al. (2001). Star-CCM+ and CMULES with SuperBee predicted sharpest wave patterns, even overly-sharp compared to the experimental measurements. CMULES with vanLeer and CICSAM, isoAdvector, and Kiel interFOAM predicted similar and reasonable results. For the HRIC related approaches in Open-FOAM, the predicted wave patterns are quite diffusive, no matter using CMULES or solving the alpha equation directly, with high Courant number or low Courant number. The secondary wave generated from the ship shoulder was predicted by all the approaches.
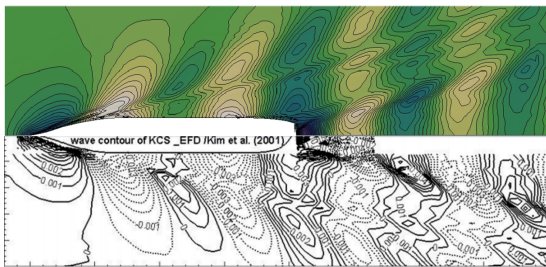
Fig. 3: Star-CCM+
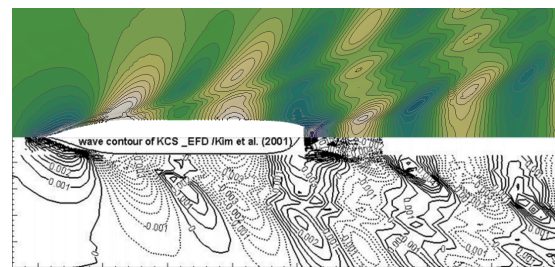
Fig. 4: CMULES with SuperBee
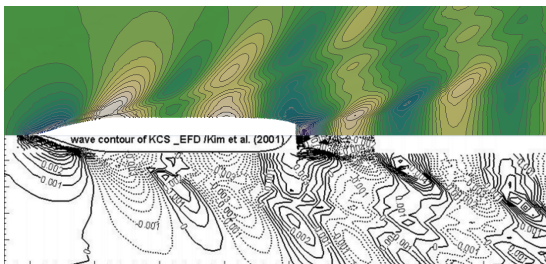
Fig. 5: CMULES with vanLeer, LTS
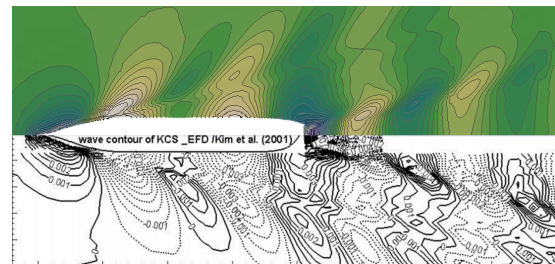
Fig. 6: CMULES with HRIC, Low Co
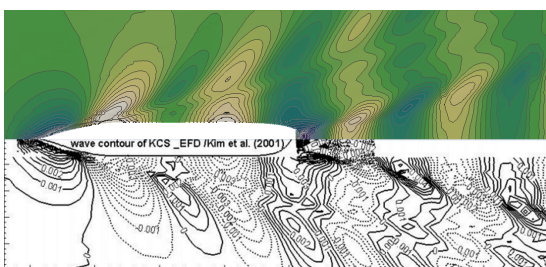
Fig. 7: CMULES with CICSAM, Large Co
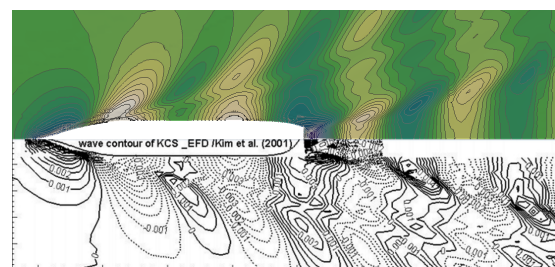
Fig. 8: CMULES with CICSAM, Low Co
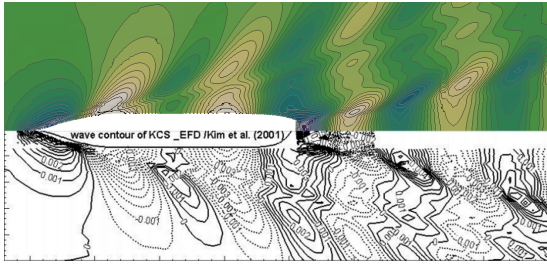
Fig. 9: IsoAdvector, max Co = 0.5
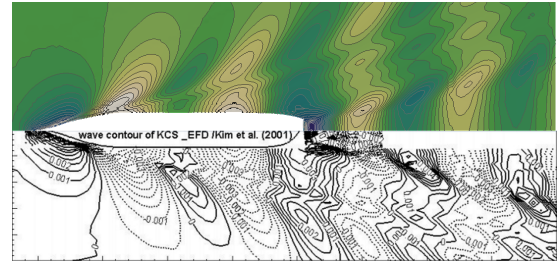
Fig. 10: Kiel interFoam

The predicted water lines on the hull and wave cuts (y/Lpp =0.0741, 0.1509, 0.424) are displayed in figures 11 to 14. Generally all the approaches predicted quite reasonable results compared to the experimental data, except the approaches using HRIC scheme, which are displayed as green lines. In the framework of CMULES, the HRIC related results show no significant difference between high Courant number (~ 40) and low Courant number (~ 0.5); and without CMULES the HRIC scheme with low Courant number predicted almost the same results. These HRIC related approaches predicted almost the same water line on the ship hull compared to other approaches, but with increasing distance away from the hull, the wave pattern show a very diffusive behaviour, as displayed in Figures 12, 13, and 14. The two HRS related approaches also show wavy predictions close to the ship hull, as displayed in Figures 11 and 12.

The differences between isoAdvector, Kiel interFoam, CMULES with Van-leer and SuperBee are quite small. The SuperBee predicted slightly overly sharp wave profile at y/Lpp = 0.4224. As displayed in Figure 15, the isoAdvector and Kiel interFoam predicted a more compact interface (3 cells from $\alpha \sim 0$ to $\alpha \sim 1$) than other schemes (5 cells from $\alpha \sim 0$ to $\alpha \sim 1$) which would be more realistic, but the improvement is limited on the overall wave pattern in this application.
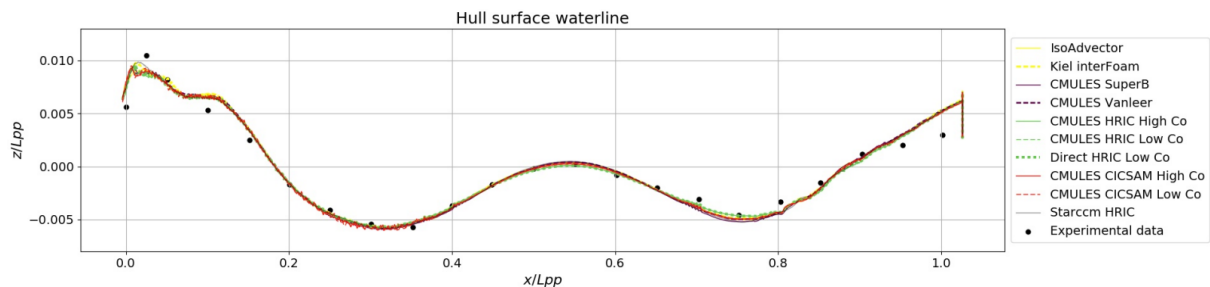
Fig. 11: Waterlines on the ship hull
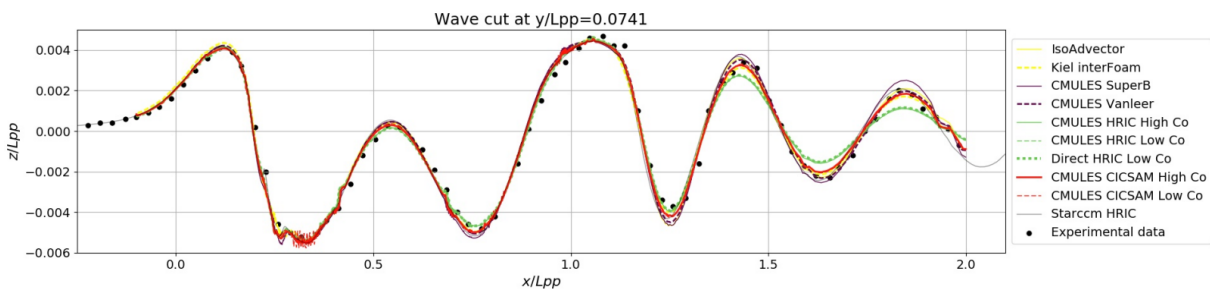
Fig. 12: Wave cuts at y/Lpp = 0.0741
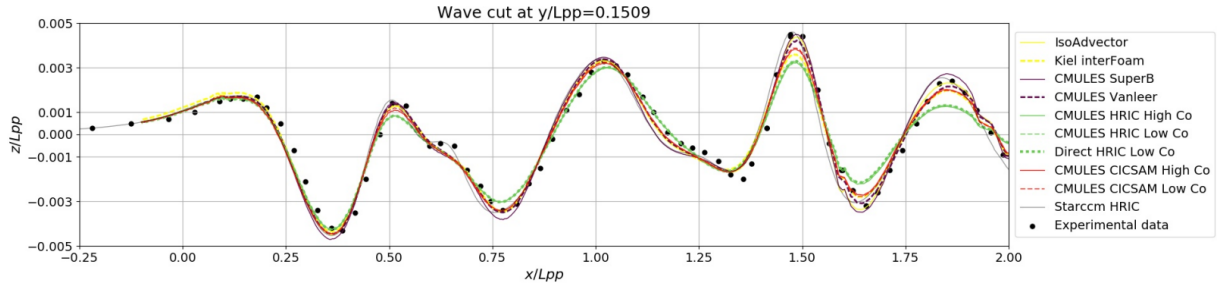
Fig. 13: Wave cuts at $y/Lpp = 0.1509$
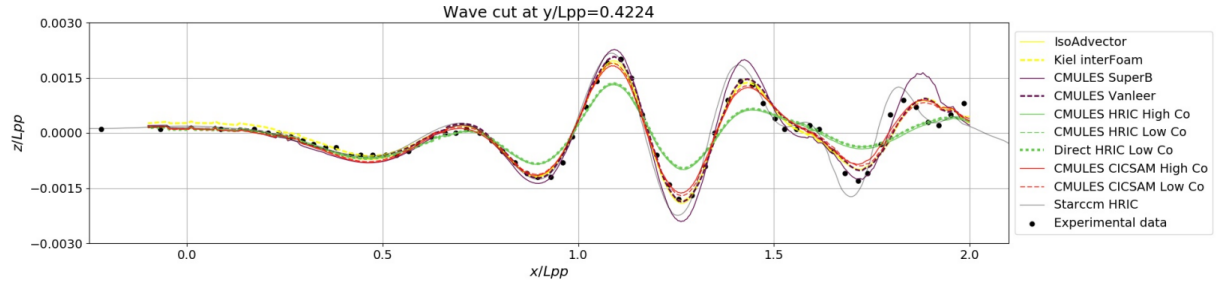
Fig. 14: Wave cuts at $y/Lpp = 0.4224$

| IsoAdvector | CMULES vanLeer | Kiel interFoam |
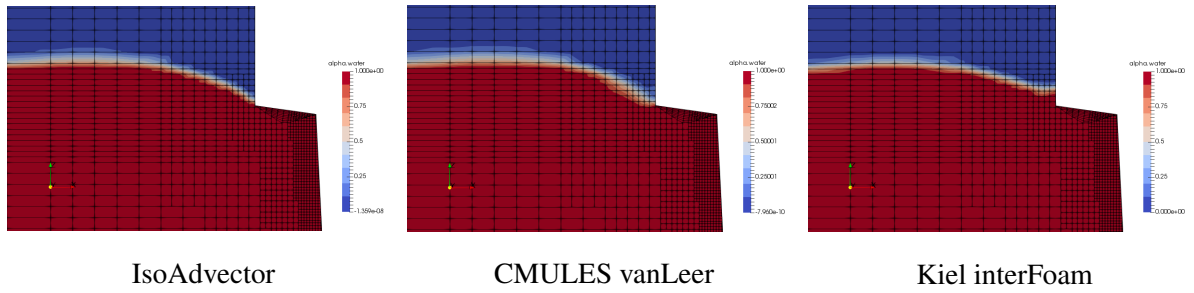
Fig. 15: α field near the ship stern

The summary of predicted force coefficients are listed in Table 1. All the approaches under predicted the total forces acting on the ship hull with relative difference ranging from −3% to −5.5%. Star-CCM+ and OpenFOAM predicted friction resistance coefficient (Cf) with relative difference of about 3% but quite different predictions of residual resistance coefficients (Cr) could be found between the different approaches. The differences between residual resistance coefficients show clearly a trend that depends on the discretization scheme.

Case	Cr $\times 10^3$	Cf $\times 10^3$	Ct $\times 10^3$	Relative Difference(%)
Exp.	-	-	3.577	-
Star-CCM+ HRIC	0.705	2.76	3.46	-3.3
CMULES vanLeer	0.740	2.67	3.41	-4.7
CMULES SuperBee	0.728	2.66	3.38	-5.5
CMULES HRIC	0.790	2.66	3.45	-3.6
CMULES HRIC(Low Co)	0.795	2.67	3.46	-3.3
HRIC direct(Low Co)	0.801	2.67	3.47	-3.0
CMULES CICSAM	0.755	2.66	3.42	-4.4
CMULES CICSAM(Low Co)	0.755	2.67	3.42	-4.4
isoAdvector	0.745	2.66	3.41	-4.7
Kiel interFoam	0.759	2.70	3.45	-3.6

Table 1: Summary of force coefficients with different settings

For the prediction of trim and sinkage, the 6Dof motion solver was used together with SuperBee and Van

Leer in the framework of CMULES. The predicted trim and sinkage are listed in Table 2. As displayed in Figure 16, the trim and sinkage became less oscillating after about 60s simulation.

Case	Trim(deg) [rd%]	Sinkage(cm) [rd%]	Drag(N)	Ct [rd%]
Exp.	-0.169 [-]	-1.394 [-]	-	0.003711 [-]
vanLeer	-0.161 [-4.7]	-1.378 [-1.1]	82.46	0.003583 [-3.5]
SuperBee	-0.152 [-10]	-1.340 [-3.9]	86.19	0.003745 [0.9]

Table 2: Predicted ship motions and force coefficients with different settings

Drag history, SuperBee   Motion history, SuperBee
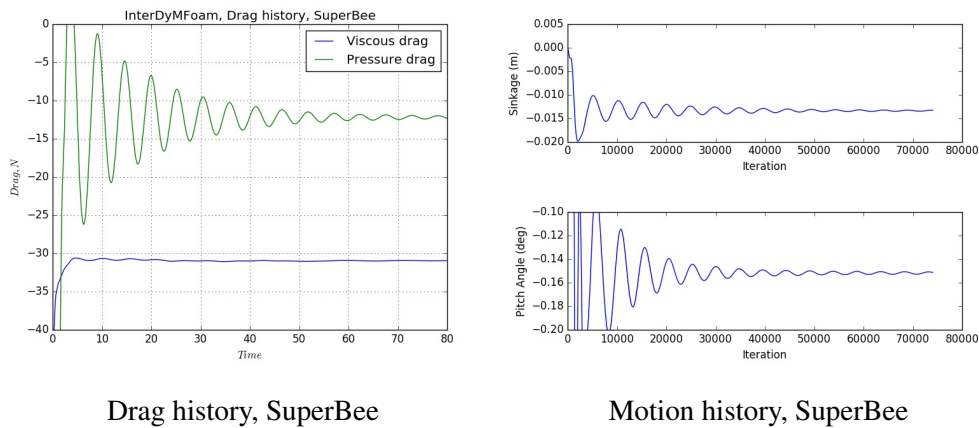
Fig. 16: Predicted forces and motions with SuperBee scheme in OpenFOAM

5 Conclusion

In the present study, several different approaches regarding ship resistance simulation were applied and tested. Some high order scheme, like van Leer and SuperBee, and two high-resolution schemes, CICSAM and HRIC, were employed for the discretization of the convective term in the phase equation under the framework of CMULES; the HRIC was also tested with a modified *interFoam* in which the CMULES was removed to solve the phase equation directly; a newly developed method IsoAdvector and the modified solver from Yacht Research Unit Kiel were also tested.

The predicted wave patterns and wave cuts were compared to the experimental data. Even though the mesh is on the coarse side, most of the approaches show good agreements with the measurement, although Star-CCM+ (HRIC) and SuperBee with CMULES predicted somewhat overly sharp wave patterns and the HRIC related approaches in OpenFOAM predicted diffusive wave patterns. The isoAdvector and Kiel interFoam predicted sharper α field but the computation cost significantly increased using isoAdvector because of the restriction of interface Courant number.

Acknowledgements

References

Janek et al. (2016). Janek, M., Hannes, R., Kai, G., and Slawig, T. Advanced CFD-Simulations of free-surface flows around modern sailing yachts using a newly developed OpenFOAM solver. The 22nd Chesapeake Sailing Yacht Symposium.

Roenby et al. (2016) Roenby, J., Bredmose, H., & Jasak, H. A computational method for sharp interface advection. *Royal Society Open Science*, **3**(11), 160405.

Queutey, P. and Visonneau, M. (2007). An interface capturing method for free-surface hydrodynamic flows. *Computers & fluids*, **36**(9), 1481–1510.

Kim et al. (2001). Measurement of flows around modern commercial ship models. *Experiments in Fluids*, **31**(2001), 567–578.

Coupling of the cavitation mixture model with the discrete bubble model

Ebrahim Ghahramani, and Rickard E. Bensow
Chalmers University of Technology, Gothenburg/Sweden
ebrahim.ghahramani@chalmers.se

1 Introduction

Cavitation is in many cases an undesirable and unavoidable occurrence in industrial hydraulic systems, such as marine propulsion systems and fuel injectors. Cavitation erosion is believed to be the result of violent collapses of the flowing micro-bubbles. Also, cavitation has significant effects on performance and efficiency of the system. Computational Fluid Dynamics (CFD) simulation is an an advancing approach to estimate different characteristics of cavitating flows, and in the last decade it has gained in popularity due to advances in computational resources and modelling. However, due to the various length and time scales present in this complex phenomenon, numerical prediction of cavitation is still a highly challenging task in engineering applications.

Different numerical methods are used to simulate cavitating flows (selectively Bensow and Bark (2010), Giannadakis et al. (2008), Hsiao et al. (2017), Schnerr et al. (2008) and Yakubov et al. (2015)); these models can be categorized in two general approaches. The first approach is based on the mixture equation of state, assuming the thermodynamic equilibrium. As this group of models use compressible solvers, they require very small timesteps to simulate cavitation. Therefore, even if there are suitable models that can adequately estimate the behaviour of cavitation structures, their application in large scale industrial problems is limited, as they require considerably higher computational resources.

The second approach is based on a transport equation for vaporization and condensation. Various numerical models are included in this general classification and the transport equation can be developed in Lagrangian or Eulerian viewpoints. One of the most common Eulerian models is when the flow is treated as a single fluid mixture and mass transfer between the phases is defined by explicit source terms. A limitation to this model (as well as other Eulerian approaches) is that the vapour structures smaller than the grid size, e.g. cavitation nuclei and bubbles, cannot be handled exactly. Also, the mass transfer source term in this model is based on a simplified form of Rayleigh-Plesset equation, in which the cavity inertia is underestimated by neglecting the second derivative of bubble radius (Abdel-Maksud et al., 2010). As cavity inertia becomes more important in the last small scale and fast steps of bubble collapse, this simplification can decrease model accuracy in capturing bubble collapse and rebound. The Lagrangian models, on the other hand, enable more detailed formulations for transport, dynamics and acoustics of discrete vapour bubbles. In this viewpoint the bubble sizes can be much smaller than the grid size and the bubble dynamics is described using a more accurate form of Rayleigh-Plesset equation. However, these models are sometimes quite computationally expensive, and cannot represent large non-spherical vapour structures of the size of computational cells or larger.

Considering the abovementioned capabilities and limitations of the Eulerian and Lagrangian formulations, a solution can be to develop a hybrid multi-scale model that is capable in both resolving the large vapour structures and capturing the small-scale bubbles. There are a few studies in the literature that follows this method, primarily Vallier (2013) and Hsiao et al. (2017). In the current study a multi-scale model is implemented in OpenFOAM. In this model, the large vapour structures are handled using the Eulerian single fluid mixture method and the small scale spherical bubbles are tracked in the Lagrangian framework. Also, a criterion for transition between the Eulerian and Lagrangian vapour structures is defined. The new model is developed in the open source C++ package OpenFOAM by improving the interPhaseChangeFOAM solver and coupling it with the Lagrangian library. This model is similar to the work of Vallier (2013) but with improvements in some features such as in the treatment of the continuity and volume fraction equations.

In the following sections a more detailed expression of the developed model and a qualitative validation of its performance are presented.

2 Method

A multi-scale model that uses the strength of both the Lagrangian and Eulerian formulations is developed. In this model, for the continuum liquid phase, the continuity and Navier-Stokes equations are solved and the vapour phase can be treated by solving a transport equation which can be in either a Eulerian or a Lagrangian framework based on the length scale of the structure. One feature of the Eulerian mixture is that it treats the structures that are smaller than the grid size as a homogenous mixture, thus sparse vapour clouds or subgrid inhomogeneity in cavitation clouds are not well treated. Therefore, to capture small scale cavitation bubbles an extremely high mesh resolution is required. As an alternative less expensive solution, we here combine the Eulerian mixture formulation with a Lagrangian model to account for evolution of individual bubbles aiming for a more realistic estimation of the whole range of cavity sizes. At each timestep, small cavity structures, which cannot be resolved by enough number of computational cells, are transformed to Lagrangian bubbles and the corresponding void fraction of the relative cells (α) is set equal to 1. This transition is shown schematically in Fig. 1 for a simple grid. The grid cells which are occupied by Eulerian cavities are coloured in blue with $\alpha < 1$. Two of the cavities that are resolved by only four cells will be transformed to Lagrangian bubbles. If a bubble becomes large enough afterwards, it is transformed back to a Eulerian structure.
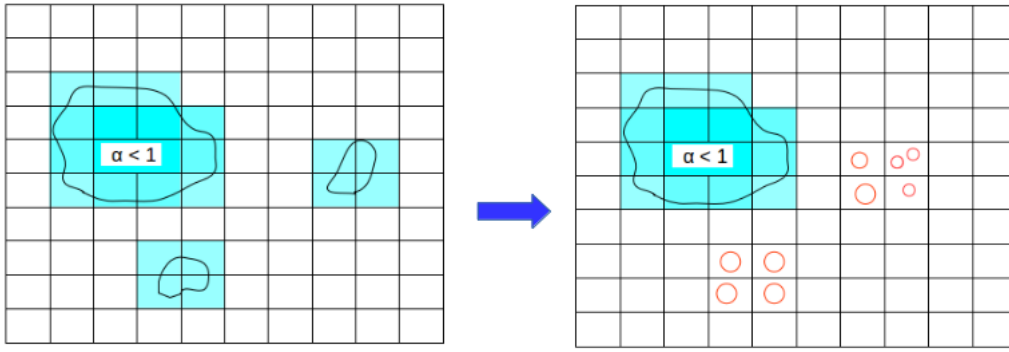
Fig. 1: Transition of small cavities to Lagrangian bubbles

The continuity equation is given by

$$\frac{\partial u_i}{\partial x_i} = (\frac{1}{\rho_l} - \frac{1}{\rho_v})\dot{m}. \qquad (1)$$

The equation source term in 1 models the effect of cavity generation on continuity due to condensation, vaporization or cavity transfer. Here, $\dot{m}$ is the rate of mass transfer, and it is here modelled using the well-known Sauer-Schnerr method (Schnerr and Sauer, 2001). Moreover, ρ_l and ρ_v are densities of liquid and vapour.

In the Eulerian formulation a scalar equation is solved for the transport of the liquid volume fraction quantity,

$$\frac{\partial \alpha}{\partial t} + \frac{\partial (\alpha u_i)}{\partial x_i} = \frac{\dot{m}}{\rho_l}, \qquad (2)$$

where α is the liquid volume fraction and hence vapour volume fraction equals $1 - \alpha$. The RHS term is the phase change source term.

Finally the flow properties (density and viscosity) formula should be corrected to consider the presence of bubbles in the domain. In the mixture approach the flow density is given by

$$\begin{aligned} \rho_f &= \alpha \rho_l + (1 - \alpha)\rho_v, \\ \mu_f &= \alpha \mu_l + (1 - \alpha)\mu_v \end{aligned} \qquad (3)$$

As mentioned before, when a small cavity structure is replaced by a bubble, the α value should be set to 1 to delete the cavity structure in the Eulerian mixture model. According to the above equation, a sudden change of α can cause a drastic change in the fluid density which leads to spurious pressure pulses

in the domain. To avoid this phenomenon, the bubble contribution should be considered in the density formula (3). This contribution can be specified based on the bubble volume fraction in each grid cell. In other words, the bubble volume fraction should replace the Eulerian cavity volume fraction to avoid drastic changes in flow properties. The cavitation source term in the continuity equation should also be revised in the hybrid solver. Since the Eulerian cavity structures are removed, the continuity source term (Eq. 1) vanishes after transition which may lead to spurious pressure pulses and negative pressures in the flow domain. As a solution to this problem the Lagrangian bubble contribution should be added to continuity source term. In other words, the source term of bubbly cells, $\dot{m}$, should be calculated based on bubble volume fraction rather than the cavity volume fraction. These improvements in continuity and flow property equations are new contributions of the current study.

The Lagrangian bubbles are tracked by solving a set of ordinary differential equations along the bubble trajectory,

$$\frac{dx_{b,i}}{dt} = u_{b,i},$$

$$m_b \frac{du_{b,i}}{dt} = F_d + F_l + F_a + F_p + F_b + F_g. \tag{4}$$

The RHS of the second equation includes various forces that are exerted on the bubbles which are, from left to right, drag force, lift force, added mass, pressure gradient force, buoyancy force and gravity. Also, the variation of bubble size is calculated by solving the well-known Rayleigh-Plesset equation,

$$R(t)\ddot{R}(t) + \frac{3}{2}\dot{R}^2(t) = \frac{P_B - P_f}{\rho_m} - 4\nu_m \frac{\dot{R}(t)}{R(t)} - \frac{2\sigma_{st}}{\rho_m R(t)}, \tag{5}$$

where R is the bubble radius, P_B is the bubble inside pressure, P_f is the fluid pressure, and σ_{st} is the surface tension.

An important issue with this approach is to consider when bubble size is in the order of grid cell length scale or larger; sometimes a bubble can occupy a number of cells. In OpenFOAM, when a particle hits a wall, the wall boundary condition is applied correctly only if the particle size is smaller than the wall cell height. When a large particle, which occupies several cells, hits a wall the collision of particle with the wall face may not be detected and the particle-wall boundary condition is not applied correctly. Besides that, to solve bubble transport and dynamic equations (Eqs. 4 and 5) the flow properties should be calculated at particle location. In OpenFOAM these parameters are estimated at the center of bubbles. When a bubble diameter is small relative to local grid size, such an estimation is satisfactory; however, when a bubble diameter is in the order of local grid size or larger, calculating flow properties at the bubble center will yield too low accuracy. Therefore, to have a more accurate prediction in bubble transport and dynamics as well as wall boundary condition, a second coarser grid, called Lagrangian grid, is used for bubble tracking. At each timestep, the Eulerian quantities are calculated by solving continuity, Navier-Stokes and Eulerian cavity transport equations in the finer grid. Then, these properties are transformed to the coarser Lagrangian grid to solve bubble transport and dynamic equations. Finally the bubble contributions on the Eulerian flow are calculated and transformed to the finer grid for next timestep. The coupling procedure between the two grids is similar to the utilized one in OpenFOAM *mapFields* function and the mesh to mesh addressing method is *cellVolumeWeight*.

It should be emphasized that the solver is four-way coupling, which means that the effect of bubbles on the flow field as well as bubble-bubble interaction are considered. Bubble-bubble collisions can be of either coalescence or bouncing type based on their diameters and relative velocities. Also the bubble-bubble interaction function is implemented for parallel simulations as well, which means that bubbles in different processors may interact with each other.

3 Results

In this section the performance of the hybrid multi-scale solver in solving a 2D cavitating flow is shown qualitatively. In Fig. 2.a the cavity structures over a 2D NACA0015 hydrofoil is shown. For solving the flow field two grids are generated. The finer grid used for solving the Eulerian equations is composed of

36244 cells while the coarser Lagrangian grid includes only 550 cells. It should be noted that since the Lagrangian cavitation bubbles are present only near the hydrofoil upper surface, the grid cells in other regions can be made quite large to avoid unnecessary computational expenses, resulting in that only 550 grid cells are needed for solving bubble transport and dynamic equations. The small cavity structure in Fig. 2.a should be transformed to Lagrangian bubbles. In Figs. 2.b and 2.c the initial pressure field before transition and the pressure field after transition are depicted respectively. In this case the original governing equations (similar to Vallier, 2013) are used to calculate the flow field. As can be seen, a spurious pressure pulse is generated and the pressure gets negative around the transition region. As mentioned before, this is a result of drastic change in fluid density and sudden change in continuity equation source term. The same flow field is solved using the improved governing equations (as discussed in the previous section) and the resulting pressure field after the transition is shown in Fig. 2.d. As can be seen neither negative pressures nor spurious pressure pulses are generated in this case. It should be noticed that the pressure contours are plotted on a logarithmic scale.
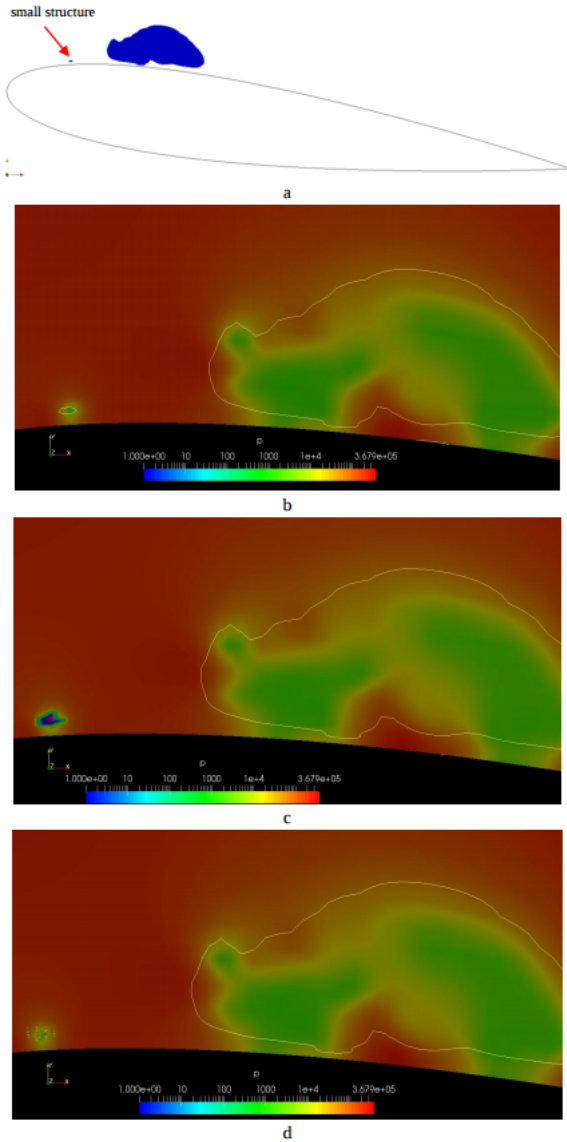
Fig. 2: Transition of small cavities to Lagrangian bubbles

In Fig. 3 different cavity structures including Eulerian cavities and Lagrangian bubbles over the hydrofoil is depicted at 4 different timesteps. Eulerian-Lagrangian transition and evolving of Eulerian structures can be seen in this figure. It should be mentioned that the bubble sizes are enlarged twice to increase the visibility.
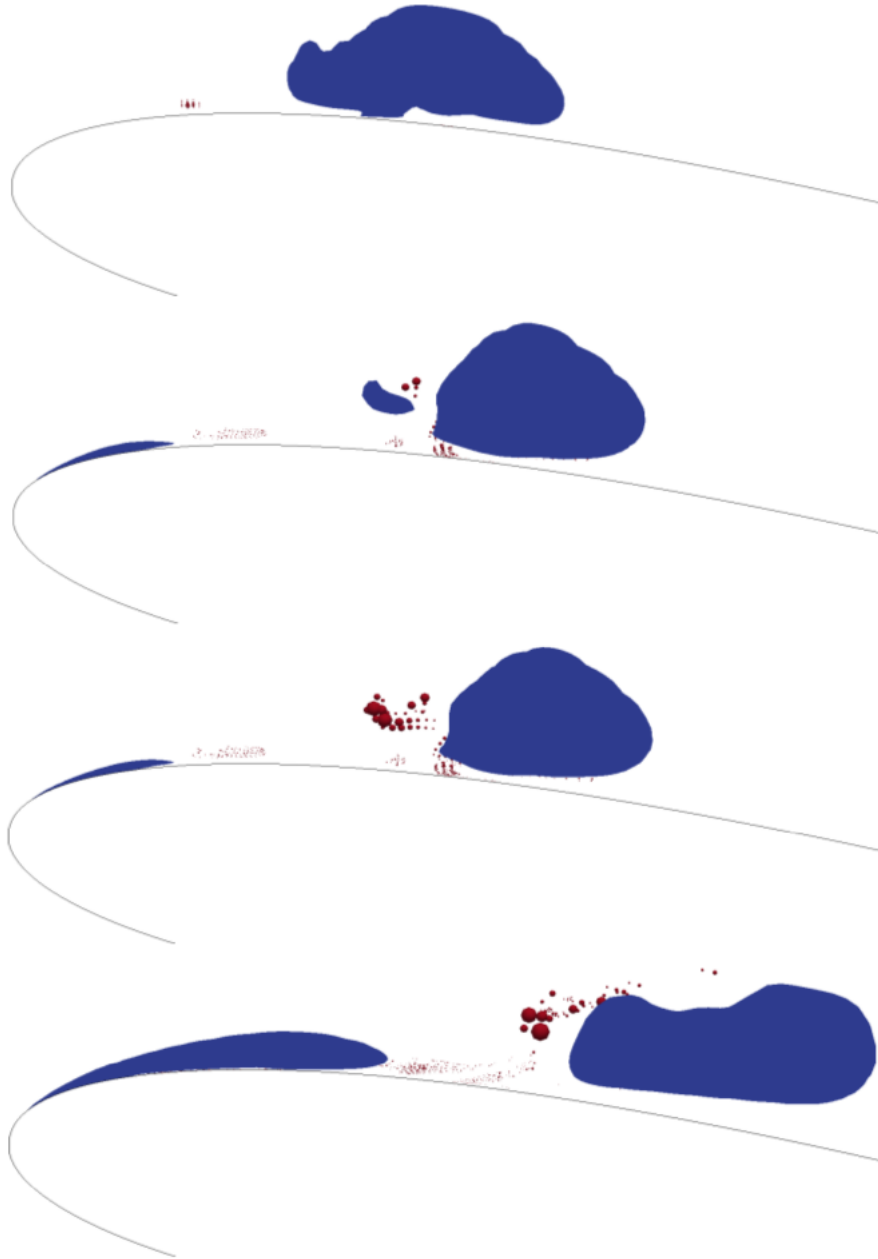
Fig. 3: Eulerian cavities and Lagrangian bubbles on a 2D hydrofoil

4 Conclusion

In this study the negative pressure and spurious pressure pulse problems during Eulerian-Lagrangian transition are fixed. It is shown that this problem is caused by sudden variation of flow properties and source term of continuity equation. However, considering the bubble contribution in Eulerian equations avoids such drastic variations and solves the problem. The hybrid multi-scale solver still needs more improvements to be suitable for simulating complex cavitating flows. In fact, the reverse transition process from Lagrangian bubbles to Eulerian cavities should be corrected so that large groups of bubbles be transformed into Eulerian structures to reduce computational expenses and increase accuracy. Also a more accurate method should be used to overcome OpenFOAM limitations in tracking large bubbles. In this study a second coarser grid was used, however, in a coarser grid some important flow details are missed. In addition to these improvements, the solver performance should be assessed quantitatively as well.

Acknowledgements

References

R.E. Bensow, G. Bark (2010) Implicit LES predictions of the cavitating flow on a propeller.*Journal of Fluids Engineering*, 132(4), 041302

E. Giannadakis, M. Gavaises, and C. Arcoumanis (2008) Modelling of cavitation in diesel injector nozzles. *Journal of Fluid Mechanics*, 153-193.

C-T Hsiao, J Ma and G. Chahine (2017) Multiscale tow-phase flow modeling of sheet and cloud cavitation. *International Journal of Multiphase Flow*, 90, 102-117

S. Yakubov, T. Maquil and T. Rung (2015) Experience using pressure-based CFD methods for Euler-Euler simulations of cavitating flows. *Computers and Fluids*, 111, 91-104.

A. Vallier (2013) *Simulations of cavitation from the large vapour structures to the small bubble dynamics*. PhD thesis, Lund University, Lund, Sweden, 2013.

G. H. Schnerr and J. Sauer (2001) Physical and Numerical Modeling of Unsteady Cavitation Dynamics. Proc. 4th International Conference on Multiphase Flow, New Orleans, 2001.

Numerical Analysis of Local and Global Hydroelastic Response to Wetdeck Slamming Events on Multihull Vessels

Matt Graham and Kevin Maki
University of Michigan, Ann Arbor/USA
grahmatt@umich.edu

1 Introduction

Oceangoing vessels in heavy seas experience slamming events due to large relative vertical motions of the vessel and sea surface. Slamming events most often occur near the bow region in head seas and sometimes occur at the stern in following seas. For catamarans, these slamming events lead to large structural loads on the wetdeck area located between the two hulls. Slamming events can produce the maximum structural loads that a vessel will see during its service life. If the maximum loads are not properly designed for, plastic deformation or failure to the structure occurs. Slamming events also cause fatigue to a vessels structure through a higher frequency whipping response.

Wetdeck slamming events on a catamaran are highly nonlinear and include complex three dimensional effects. Fluid structure interactions (FSI) are important for capturing the correct structural loads. Simplified analytical models have allowed designers to predict slamming loads in the early design stage. However, these simplified analytical models are not able to capture the nonlinear and three dimensional effects. A state-of-the-art high-fidelity FSI solver was developed by Piro, 2013 with the ability to solve nonlinear slamming events. This research uses this new state-of-the-art solver to study idealized problems for wetdeck slamming on catamarans in order to understand the effects of assumptions made when using simplified models.

One advantage of catamarans are their ability to offer a large flat deck area. The deck area between the two hulls is called the wetdeck. In some cases the wetdeck may be flat as seen in Figure 1(a) and may experience wetdeck slamming loads in a large sea state. Figure 1(b) shows a popular design for catamarans involving the use of wave-piercing bows to reduce the added resistance due to a sea state. Although the wave-piercing bows provide a reduction in resistance, the reduced buoyancy in the front of the bow makes the vessel more susceptible to wetdeck slamming. For this reason, a wedge-shaped wetdeck was designed to reduce the impulse force on the wetdeck structure. This wedge shape adds weight and air resistance to the catamaran taking away from the design advantage of a catamaran.

(a) X-craft naval catamaran showing the design of a flat wetdeck circled in red.

(b) The naval HSV catamaran with wave piercing bows and a wedge shaped wetdeck to mitigate slamming loads.

Fig. 1: Catamaran wetdeck examples.

Slamming forces on a wetdeck cause large structural loads and may cause a whipping response which can lead to global structural fatigue. Accurately predicting the slamming forces on a wetdeck structure is important in early stage design. Current methods are not able to model the nonlinear interactions that occur during a wetdeck slamming event. This research uses a state-of-the-art high-fidelity solver to study the interactions between the fluid and the structure during a wetdeck slamming event.

2 Background

This research focuses on expanding a new numerical technique that couples a CFD Volume of Fluid (VoF) approach for the fluid domain to a *modal* decomposition of the structure domain using FEA. This new numerical technique is a high-fidelity FSI solver that can be used to model wetdeck slamming on catamarans with realistic geometries. Common techniques in industry to model fluid structure interactions uses Computational Fluid Dynamics (CFD) with a one-way coupling to the Finite Element (FE) structure to perform a Rigid-Quasi Static (RQS) analysis. Maki et al., 2011 performed a one-way coupling with a 10 degree deadrise angle for wedge drops. Wet natural frequencies were modeled with acoustic elements on the FE structure. The difference in maximum displacement of the wet and dry natural frequencies showed the importance of capturing the correct wetted length of the wedge during impact.

Piro and Maki, 2011 studied the FSI of a wedge during entry and exit using CFD Volume of Fluid (VoF) approach coupled to a *modal* decomposition of a FE structure using beam elements. This two-way couple technique was studied for an exact boundary condition with a deforming mesh and an estimated boundary condition with no deformations and only structure velocity information is given to the fluid. For small deflections, the estimated boundary condition had good comparisons with the exact boundary condition. Camilleri et al., 2015 also looked at wedge drops by coupling two commercial codes, CFD with Star CCM+ and FEM with Abaqus. A large computational expense was needed to converge the fluid and structure solutions using this two-way coupled method. The full structure model was used adding to the computational expense of the method.

Two-way coupling of CFD and FEM has been used to model FSI interactions due to ship slamming in head seas. Seng, 2012 coupled VoF CFD with Timoshenko beam elements to model bow flare slamming for a segmented model test. Piro, 2013 used a similar technique to study slamming with green water on the deck of a segmented JHSS model. A *modal* decomposition was used for the FEM to reduce the degrees of freedom and allow the FSI solver to run at similar computational expense as the rigid body simulations. Higher frequencies in the structural responses were not fully captured, but the lower frequencies that correspond to the primary bending modes showed good agreement with experiments. Two-way coupled CFD and FEM provide a way to model realistic three dimensional geometries and capture non-linear effects; however, there is a significant computational expense and should only be used when three dimensional and non-linear effects are important.

Wetdeck slamming on catamarans is a non-linear process that is three dimensional in nature. The proper modeling of entry and exit is important when it comes to wetdeck slamming (Faltinsen, 2015). Hydroelastic effects are important to capture during a slamming event. In some cases, multiple slamming events, or slamming clusters, can occur before the whipping response has damped out from previous slamming events (Dessi and Ciappi, 2013). This research uses a state-of-the-art high-fidelity FSI solver to study wetdeck slamming on catamarans. This solver has the ability to capture the non-linear free-surface interactions coupled with the structural interactions for realistic geometries.

There are several challenges when it comes to modeling wetdeck slamming on catamarans. First, real sea states have short-crested three dimensional waves as well as breaking waves. Second, the catamaran experiences large accelerations and motions that are determined by the severity of the sea state. The mass distribution and moments of inertia of a catamaran are important for capturing the correct motions in a given sea state. Finally, fluid structure interaction is important for the hydroelastic response of the catamaran and the free-surface deformations. The fluid structure interaction is also coupled to the motion of the vessel. These challenges make modeling wetdeck slamming on catamarans highly non-linear and complex.

Numerical models have the ability to capture complex geometries, non-linear free-surfaces with breaking waves, and fluid structure interactions for both global and local loads. The current numerical research for wetdeck slamming on catamarans has focused on rigid body interactions with simple wave profiles. Fluid structure interactions are modeled with simple beam elements and do not include the interactions between global and local loads. This research uses a high-fidelity numerical model to capture the non-linear and three dimensional effects of wetdeck slamming on catamarans to investigate the local and global hydroelastic effects.

3 Method

The state-of-the-art high-fidelity FSI solver was developed by Piro, 2013. The solver uses CFD with a VoF surface capturing techniques for the fluid domain, coupled with a FEA *modal* decomposition for the structure domain. The solver was validated with elastic wedge drops and segmented model tests of a JHSS hull in head seas.

3.1 Fluid Solution

The fluid solution is solved using the OpenFOAM CFD library. OpenFOAM uses an arbitrary-polyhedral discritization that allows for the modeling of realistic and complex geometries. The governing fluid equations are the incompressible Navier-Stokes equations. An arbitrary Lagrangian-Eulerian finite volume discritization is used to allow for a moving and deforming mesh. A two-phase flow is captured using the VoF technique with the alpha equation,

$$\frac{\partial \alpha}{\partial t} + \nabla \cdot (\alpha \vec{u}) + \nabla \cdot (\alpha(1-\alpha)\vec{u_r}) = 0. \tag{1}$$

The volume fraction variable, α, tracks the two-phases which is 0 for air and 1 for water. This method allows for the tracking of a nonlinear free-surface. Fluid discritization schemes are second order for both space and time.

3.2 Structure Solution

The structure is modeled using the Finite Element Method (FEM). The homogeneous equations of motion for the FEM are written as,

$$[M]\{\ddot{u}\} + [K]\{u\} = 0 \tag{2}$$

where $[M]$ is the global mass matrix, $[K]$ is the global stiffness matrix, and $\{u\}$ is the displacement vector for the nodes. Assuming small deflections and sinusoidal vibrations, Equation 2 can be written as a determinate problem and the eigenvalues and eigenvectors of the system can be found which correspond to the natural frequencies and mode shapes of the structure. The *modal* equations of motion including damping and forcing are,

$$[I]\{\ddot{q}\} + [2\xi\omega_n]\{\dot{q}\} + [\omega_n^2]\{q\} = \{f\} \tag{3}$$

where $[I]$ is the identity matrix, $[2\zeta\omega_n]$ is the *modal* viscous damping matrix, $[\omega_n^2]$ is a diagonal matrix containing the squared natural frequencies of the structure, $\{q\}$ is a vector containing the *modal* amplitudes, and $\{f\}$ is the *modal* force vector.

An advantage to using the *modal* equations of motion is reducing the number of degrees of freedom in the structural system by neglecting the high frequencies. This can be done since the majority of energy is contained in the lower frequencies which corresponds to the first set of mode shapes.

3.3 Fluid Structure Interaction

The solver tightly couples the fluid and structure solutions to capture the fluid structure interactions. The fluid solution is solved first and the pressure forces are interpolated to the Gauss points on the structure through a weighted distance function. The structural forces are then interpolated to nodes and transformed to modal forces. The *modal* equations of motion are then solved and transformed back to structural velocities and displacements. The structural velocities and displacements are given to the fluid solution and the fluid solution is solved again. This iterative process is repeated until the fluid and structural solution has converged for the current time step.

Two boundary conditions are possible for the fluid solution. The exact boundary condition uses the structure displacements to deform the mesh. The approximate boundary condition only uses the structure velocities on the body boundary to impart the structure velocity on the fluid without deforming the mesh. The second boundary is chosen which gives a good approximation for the assumption of small deflections as shown in Piro and Maki, 2013.

Using the approximate boundary condition and the reduced frequencies *modal* equations of motion for the structure allows for a large reduction in computational expense. Piro, 2013 found that for complex ship slamming simulations using only the first 100 frequencies, the FSI solver had similar computational times to the rigid body simulations.

4   Flat Plate Drops

A simplified slamming case is used to compare the high-fidelity FSI solver to experiments and other slamming models. Flat plate drop tests were conducted at the MARINTEK wave basin in Norway. Descriptions of the tests setup and some results were published by Faltinsen et al., 1997. A steel and stiffened aluminum section were tested, but detailed results were only given for the steel section. Dummy plate sections were placed on either side of the test plate section to reduce the three dimensional effects for comparisons with two dimensional slamming models. Pressure, acceleration, strain, and displacement measurements of the test section were taken at several locations. The plates were dropped on flat free-surfaces as well as the top of waves with varying radius of curvatures. The dry structural natural frequencies and torsional rigidity of the plate connection points were experimentally determined before the flat plate drops. The total weight of the rig setup was 500kg to model a constant velocity impact which is widely used in two dimensional slamming models. Data for comparative studies was only provided for a drop height of 0.5m and a wave radius of curvature of 10.2m for the steel test section.

(a) Top view.   (b) Profile view.   (c) Test plates.
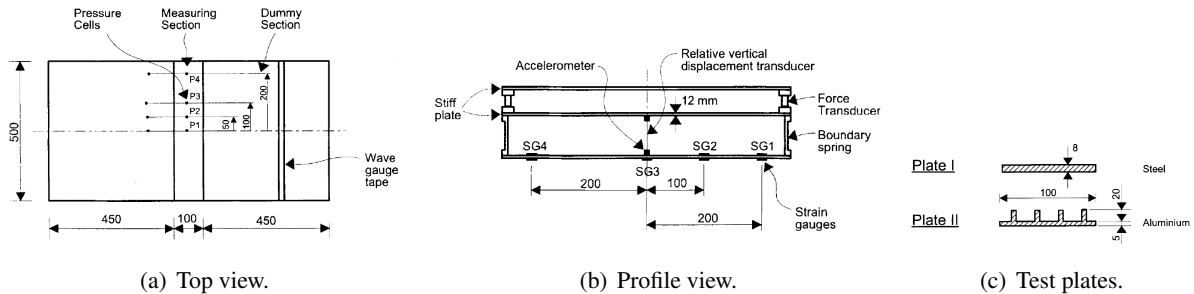
Fig. 2: Flat plate drop test setup (Faltinsen et al., 1997).

Three dimensional effects are assumed negligible for the flat plate drops, so the FSI solver uses a 2D fluid grid with euler beam elements representing the plate structure. A constant velocity impact, which is common in slamming models, and a free drop impact were solved and the vertical deflections at the center of the plate and the strain at the center of the plate are shown in Figure 5(a) and 5(b) respectively. The free drop impacts are similar to the constant velocity impacts, but the constant velocity impact under-predict the maximum deflections. The constant velocity was chosen as 2.5m/s by averaging the velocity time history during impact from the experiment. The two boundary conditions, exact and approximate, for the FSI solver show similar results when looking at the deflections at the center of the plate. The strains show differences in the higher frequency oscillations between the two boundary conditions, but the maximum strains are similar. This shows, that for small deflections, the approximate boundary condition can be used which avoids the high computational cost in morphing the mesh at each iteration when using the exact boundary condition.

Comparing the FSI solver to Faltinsen et al., 1997 asymptotic solution, the maximum deflections for the FSI solver are closer to the experiments than the asymptotic solution. When looking at the strains, higher frequencies oscillations are present in the asymptotic solution that are not present in the experiments. Although the FSI solver does not have the higher frequencies oscillation, it over predicts the strains at the center of the plate by a factor of two. The reason for the similar deflections, but different strains are in the proper modeling of the structural boundary conditions and pressure loading. The torsional stiffness at the ends of the plate were experimentally measured and assumed to be symmetric. The middle of the plate was assumed to impact the wave crest first while neglecting the horizontal wave velocity which would assume symmetric pressure loading. In the experiments the real structural boundary conditions would not be symmetric and the wave crest impacts never hit the center of the plate first. This

on top of possible plastic deformations in the structure would give different strains for similar deflections at a point on the structure. The asymmetries in boundary conditions and pressure loading would also attribute to the difference in the frequency response of the structure. These issues highlight the sensitivity of the structural model to the structural stresses and strains developed during a slamming event.

(a) (b)
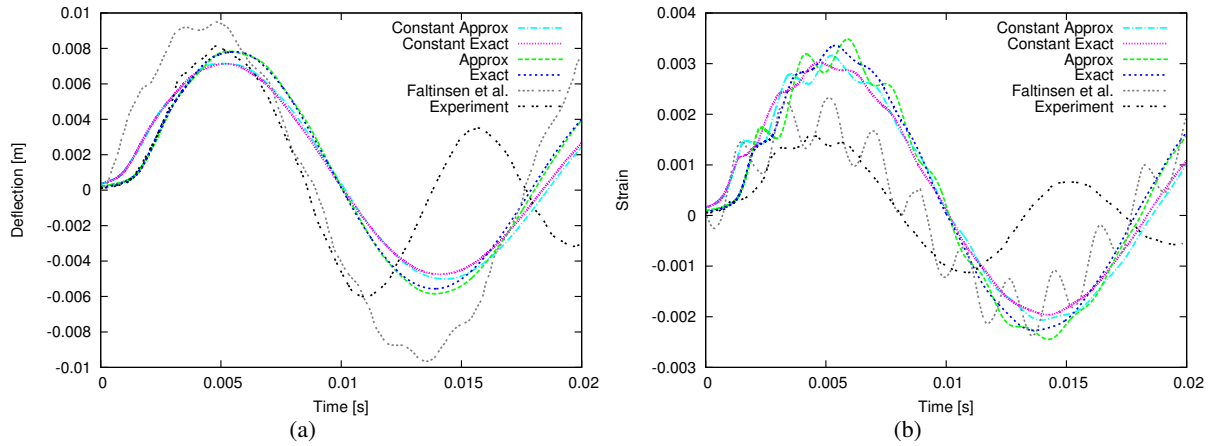
Fig. 3: Comparisons of deflection and strain at the center of the plate.

5 Wetdeck Slamming on SES

To model wetdeck slamming on catamarans, a segmented model for a Surface Effect Ship (SES) operating without the skirt was tested for head seas with and without forward speed at MARINTEK in Norway. The body plan for the SES in Figure 4(a) shows a typical flat wetdeck for catamarans. The backspline layout for the segmented SES is shown in Figure 4(b). The backspline models the scaled global frequencies and mode shapes of the full scale vessel. The wetdeck is cut into four segments and connected to the rest of the structure through the backspline. This allows for the wetdeck slamming effects on the global structure to be assessed.

(a) Body plan (b) Backspline layout
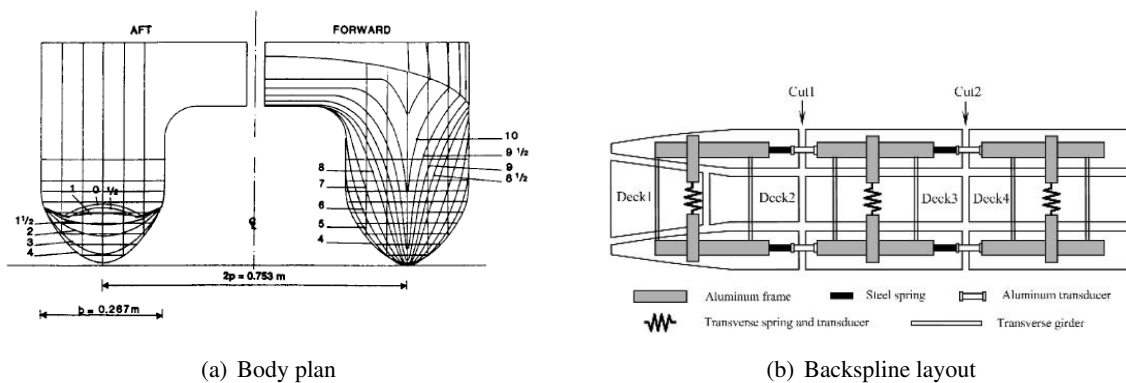
Fig. 4: Surface effect ship segmented model without the skirt from by Ge, 2002.

Økland, 2002 experimentally measured the Response Amplitude Operators (RAO) for the SES in head seas with no forward speed. The RAOs measured from the optical sensor and Motion Reference Unit (MRU) for the expriements are shown in Figure 5. Rigid CFD simulations were run to compare against the experimental measurements. Confidence in the experimental measurements for heave at the lower frequencies is low due to the differences in the RAOs for the optical sensor and MRU. The largest slamming event analyzed by Ge, 2002, occured for a wave period of 1.8 seconds. For this wave period our CFD model is the closest to the experimentally measured heave RAO and the pitch RAO closely follows the trend from the experiments at this frequency. Further CFD runs will be conducted for slamming

events with forward speed with the FSI solver to compare with Ge's results.
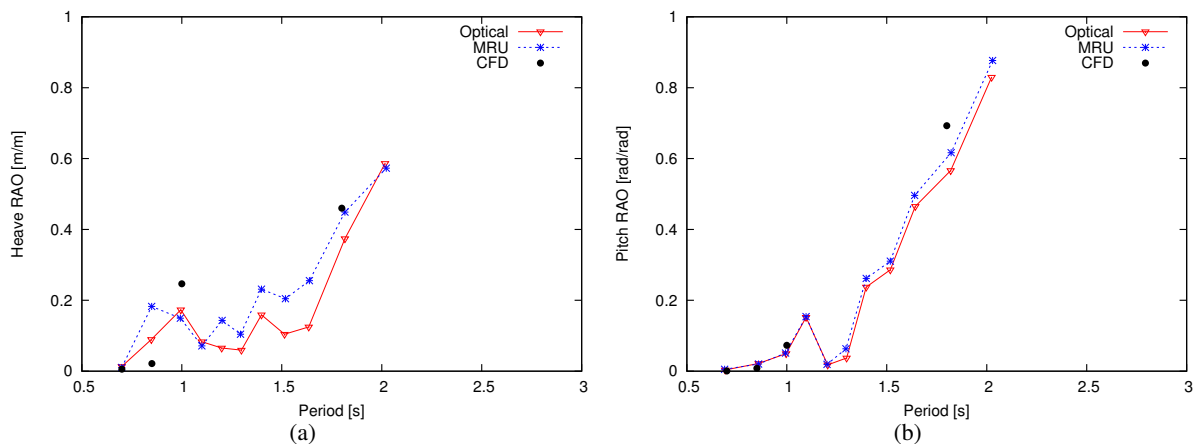
Fig. 5: RAOs for head seas with zero forward speed.

Simulations of extreme slamming events will be compared between rigid body and FSI simulations. Using the high-fidelity FSI solver will allow for the hydroelastic effects to be studied for global and local structural loads during wetdeck slamming on a catamaran. Multiple slamming events and realistic wave geometries can also be modeled using the high-fidelity FSI solver. The experimental simulations for the SES geometry that are still to be run before the conference are:

- Rigid slamming simulation with one-way coupling

- Flexible simulations modeling only the backspline for global structural loads.

- Flexible simulations modeling the backspline for global structural loads and plate elements on the wetdeck to model local structural loads.

6 Conclusion

To be added

Acknowledgements

To be added

References

Camilleri, J., Temarel, P., and Taunton, D. (2015). Two-dimensional numerical modelling of slamming impact loads on high-speed craft. In *7th International Conference on Hydroelasticity in Marine Technology*, pages 43–54, Split, Croatia.

Dessi, D. and Ciappi, E. (2013). Slamming clustering on fast ships: From impact dynamics to global response analysis. *Ocean Engineering*, 62:110–122.

Faltinsen, O. M. (2015). Hydrodynamics of marine and offshore structures. *Journal of Hydrodynamics*, 26(6):835–847.

Faltinsen, O. M., Kvlsvold, J., and Aarsnes, J. V. (1997). Wave impact on a horizontal elastic plate. *Journal of Marine Science and Technology*, 2(2):87–100.

Ge, C. (2002). *Global Hydroelastic Response of Catamarans Due to Wetdeck Slamming*. PhD thesis, Norwegian University of Science and Technology, Trondheim, Norway.

Maki, K. J., Lee, D., Troesch, A. W., and Vlahopoulos, N. (2011). Hydroelastic impact of a wedge-shaped body. *Ocean Engineering*, 38(4):621–629.

Økland, O. D. (2002). *Theoretical and experimental analysis of wetdeck slamming*. PhD thesis, Norwegian University of Science and Technology, Trondheim, Norway.

Piro, D. J. (2013). *A Hydroelastic method for the analysis of global response due to slamming events*. PhD thesis, University of Michigan.

Piro, D. J. and Maki, K. J. (2011). Hydroelastic Wedge Entry and Exit. *FAST 2011 11th International Conference on Fast Sea Transportation*, (September).

Piro, D. J. and Maki, K. J. (2013). Hydroelastic analysis of bodies that enter and exit water. *Journal of Fluids and Structures*, 37:134–150.

Seng, S. (2012). *Slamming and Whipping Analysis of Ships*. PhD thesis, Technical University of Denmark.

Investigation into the Tip Gap Flow and it's Influence on Ducted Propeller Tip Gap Noise Using CFD

Adam Higgens[*]**, Phillip Joseph**[†]**, and Stephen Turnock**[*]

[*]Fluid-Structure Interactions research group, University of Southampton, SO16 7QF,
[†]Institute of Sound and Vibration Research group, University of Southampton, SO17 1BJ
a.d.higgens@soton.ac.uk

1 Introduction

Propeller noise can be classified into several components including: turbulence ingestion, trailing edge noise, cavitation and tip gap interaction noise. While there has been extensive research into the first three mechanisms, the mechanism which generates noise from the tip vortex is less well understood. The noise generated by an aerodynamic fan in a duct has been the focus of a significant amount of research for aircraft engines and wind turbines, due in part to requirements near airports for maximum sound levels for the comfort of nearby (human) residents. However, the research into the noise of marine propellers has been far less extensive, perhaps because the affect of marine noise is not felt by the majority of the human population, the research regarding marine propeller noise is driven mainly by the military.

While a high proportion of the aerodynamic research has involved experimental procedures, producing empirical results, this research hopes to analyse the flow regime between the tip of the blade and the duct, and understand the flow geometry in this region, allowing the prediction of effective noise mitigating designs. In order to understand the complex tip gap flow region, simulations have been performed using a simplified arrangement of a single foil of constant cross section with a square tip, using a range of tip gap sizes. A schematic representation of the investigation is given in Figure 1.
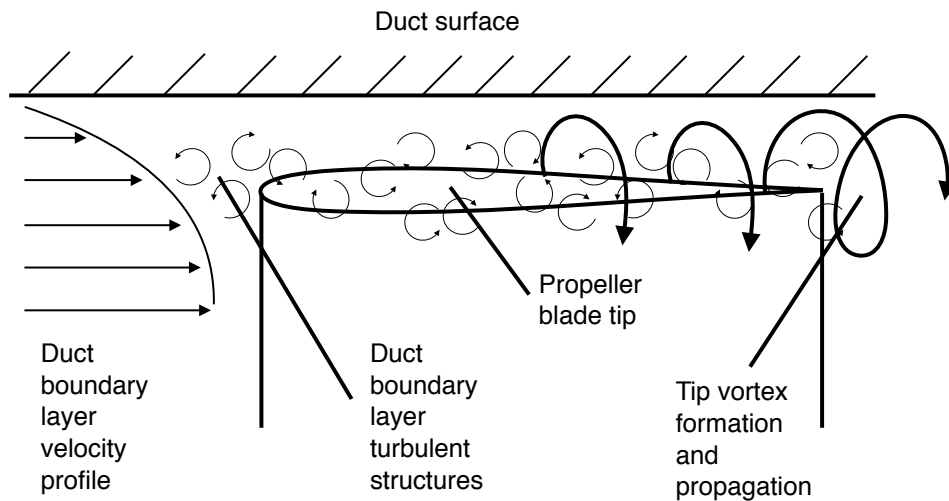
Fig. 1: Schematic representation of tip vortex interaction with the turbulent boundary layer of a surface near the tip.

The CFD program being used for this research is `OpenFOAM`, an open source CFD software based on finite volume methods. `OpenFOAM` offers the ability to split or decompose jobs across multiple processors and therefore is easy to use with high powered computing clusters for greater efficiency in simulation time. The open source nature of `OpenFOAM` also offers greater flexibility in the set up of simulations.

The future aim of this work is to develop the unsteady simulations to allow the identification of noise sources within the flow, and predict the noise radiated to the far field.

2 Initial steady simulations in RANS

An initial CFD case was generated using a NACA0020 foil in a domain with the same dimensions as the R.J. Mitchell wind tunnel at the University of Southampton. This initial case was chosen as the exper-

Table 1: RANS numerical model settings

Parameter	Unit	Setting
Rudder span	m	1
Rudder chord	m	0.667
Mesh Type	-	Unstructured (Hex)
No. of Elements	-	$\approx 8 - 10$m
y^+	-	$\approx 1 - 2$
Inlet	-	Freestream velocity (10m/s)
Outlet	-	Zero gradient
Tunnel floor/side walls	-	Slip
Tunnel roof	-	Slip
Rudder	-	No slip
Duct	-	Slip
Reynolds' Number	-	4×10^5
Turbulence Model	-	$k - \omega$ SST Turbulence
Solver	-	SIMPLE

Table 2: Test matrix detailing tip gaps to be investigated, shown in SI units as well as relative to characteristic dimensions.

h / mm	500	400	300	200	100	50	40	30	20	10
h/c [%]	75	60	45	30	15	7.5	6.0	4.5	3.0	1.5

imental data was available from Molland and Turnock, 1991, as well as the results from a comparable CFD study by Badoe et al., 2012. This validation would provide confidence in the simulation set up, and allow the study of the tip vortex formation in detail to better understand the effects of the tip gap. Table 1 shows the numerical setup of this case, following the work by Badoe et al., 2012.

The preliminary investigation was developed to investigate the effect of introducing a boundary near the free tip of the rudder on the tip flow and vortex generation. The flow through the finite gap around a foil has not seen much investigation due to the difficulty which comes with the experimental set-up. The NACA0020 case and the range of pressure data available allows for validation of the CFD set-up and therefore gives confidence to the findings made with the adapted arrangement. Ducted propellers are widely accepted to produce lower noise levels but this evidence has largely been obtained experimentally, without a thorough understanding of why that is. The initial stages focussed on investigating the effect of the tip gap by introducing a large test matrix to identify the threshold past which tip gap size begins to play a role in the tip leakage flow and vortex generation. This understanding will provide a good basis of knowledge to hypothesise about the influence of the tip gap on noise generation mechanisms, and also allow the development of the chosen simulation to lead into noise predictive simulations in the future.

Table 2 shows the range of tip gaps and foil thickness investigated by the RANS simulations. The NACA0020 foil used has a span of $1m$ with an aspect ratio of 1.5, so a chord, c of 0.667m. The gap height, h, has been non-dimensionalised by the chord length, as is common within the literature, and the gaps will be referred to as % chord values in this paper. Figure 2 shows the effect of the tip gap on the lift and drag coefficients of the foil. It can be seen that the lift increases even with relatively large gaps when compared to the open tipped simulation, while the drag only sees significant reduction in gaps of less than 7.5% chord. This implies that at these smaller tip gaps, the boundary surface begins to interfere with the formation of the tip vortex and so reduce the induced drag.

The λ_2-criterion was used to illustrate the interaction of the tip vortex with the boundary surface by creating a contour surface of $\lambda_2 = 0$, as shown in Figure 3, with flow direction from right to left, and lift being produced vertically upwards. The λ_2-criterion compares the vorticity tensor with the strain rate
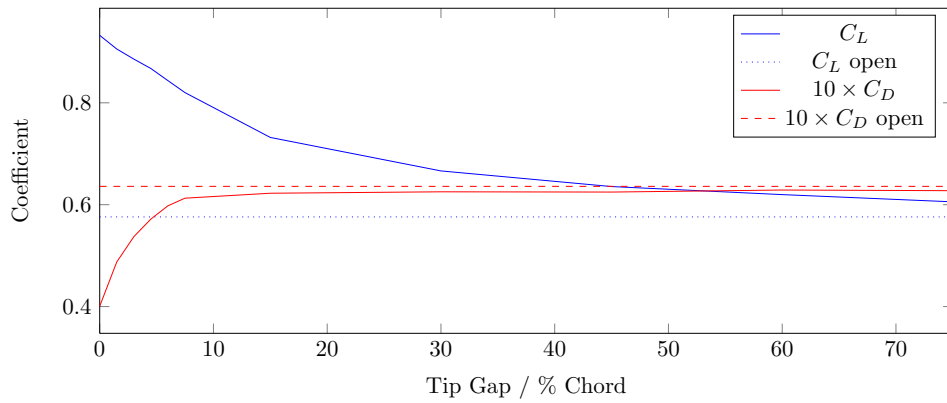
Fig. 2: Variation of C_L and C_D with varying tip gap

(a) Open tip

(b) $h/c = 7.5\%$

(c) $h/c = 6.0\%$

(d) $h/c = 4.5\%$

(e) $h/c = 3.0\%$

(f) $h/c = 1.5\%$
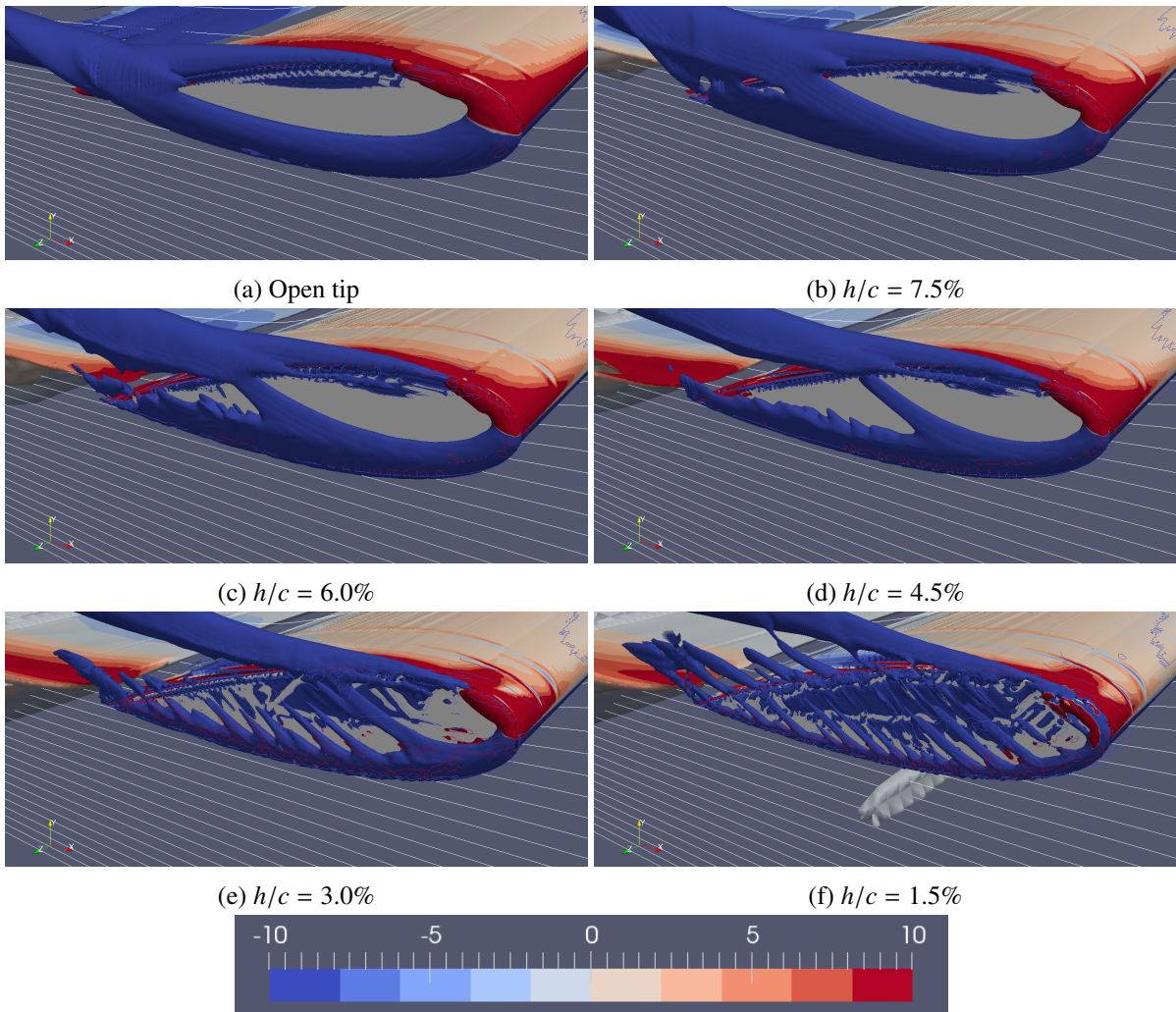
Fig. 3: The effect of tip gap size on the formation and propagation of the tip vortex, shown by the contour $\lambda_2 = 0$. Flow is in the $-x$ direction relative to the axes in each figure, and the contour is coloured by vorticity in the x direction to show the direction of rotation of the vortices.

tensor to identify if vorticity is dominant, and therefore infer the presence of a vortex core. Figure 3a shows this contour on the open tipped foil to illustrate the formation of the uninhibited tip vortex. Two distinct vortices can be seen forming, one on the top of the tip caused by flow over the pressure side (PS) edge, and on the suction side (SS) of the foil, caused by the tip leakage flow over that edge. These vortices stay attached to their respective tip edges until they reach the trailing edge of the foil where they coalesce and propagate downstream. Figures 3b to 3f show that as the tip gap reduces, the tip leakage flow becomes the dominant component, and the separation point moves forward on the tip. Inspection of these contours also shows that at these small gap sizes the RANS simulation and λ_2 contour are no longer showing reliable results as relatively large vortex structures seem to dissipate very quickly after being formed implying that to get an accurate understanding of the flow, unsteady simulations are required.

3 Unsteady simulations

The flow in the tip gap region is likely to contain highly unstable structures, and these structures will be likely to have a strong influence on the noise sources within the region. In order to simulate these structures directly, Large Scale Eddy (LES) simulations were carried out using a Wall Adapting Local Eddy (WALE) viscosity model. LES was chosen because it has been shown to outperform unsteady RANS (uRANS) acoustic predictions for complex flows, while still having a significant saving in computational cost when compared with Direct solution of the Navier Stokes equations (DNS).
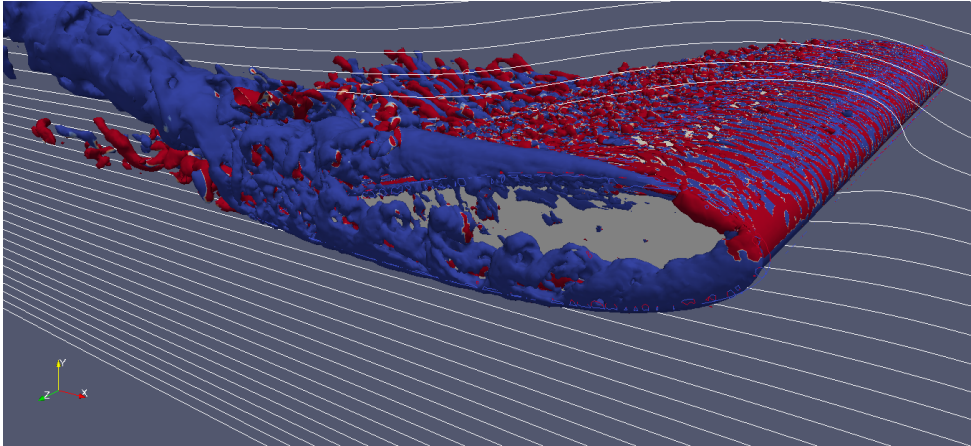

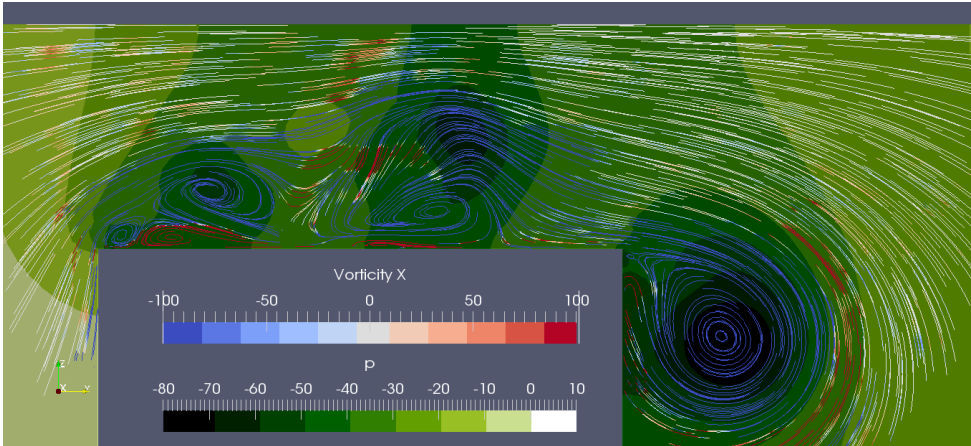Fig. 4: Snapshot from LES simulation of $h/c = 7.5\%$ simulation

Fig. 5: Snapshot from LES simulation of $h/c = 7.5\%$ simulation showing a transverse slice through the centre of the foil in line with the mean flow.

Using the λ_2 contour analysis on a snapshot from the converged LES solution for the $h/c = 7.5\%$
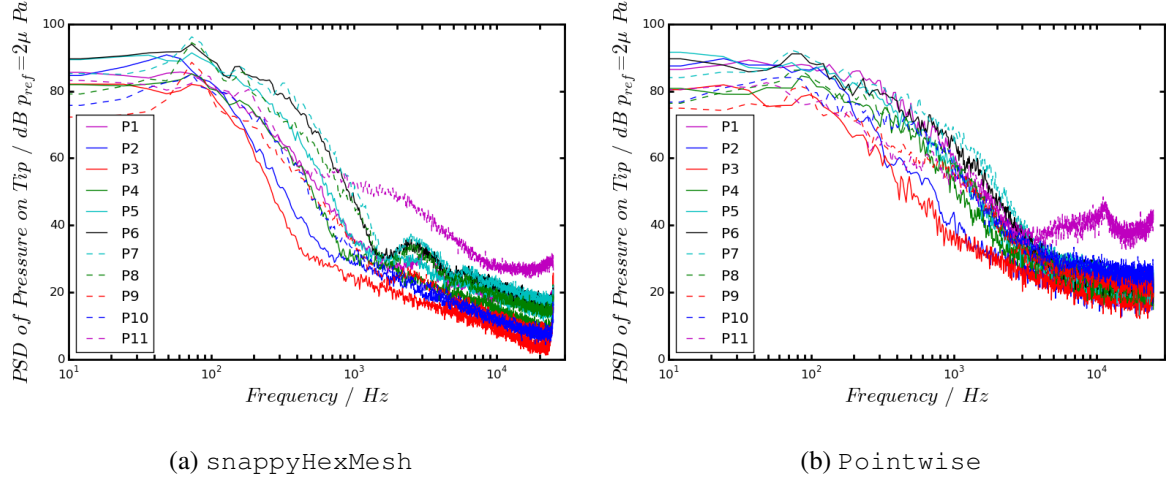
(a) `snappyHexMesh` (b) `Pointwise`

Fig. 6: PSD analysis of pressure samples from the tip of the NACA0020 foil for both mesh techniques

case confirms the unstable nature of the structures produced by the RANS simulation. Figure 4 shows the smooth vortex seen on the PS edge in Figure 3b is actually made up of smaller helical structures which can be seen to propagate downstream when viewed as an animation from a series of subsequent time steps. This suggests a more unstable shedding of smaller vortices is responsible for the continuous vortex indicated by the RANS simulation.

The analysis of the transverse flow through the tip gap region is achieved by taking a transverse slice through the mid chord of the rudder at the saved time steps. The surface vectors on that slice are then calculated and visualised as streamlines which represent the velocity components in the yz-plane, Uy and Uz. The slice can be coloured by vorticity about the x-axis ω_x, which will indicate the direction of rotation for any vortices present with either positive or negative values.

Figure 5 shows snapshots from this analysis for the $h/c = 7.5\%$ case. This figure is looking in line with the flow direction, as indicated by the axes shown and the grey area shows the rudder cross-section at this location. The SS is on the right and the PS is on the left, so the tip leakage flow is generally from left to right, in the positive y-direction. The upper limit of the figure is 50mm above the rudder tip, i.e. at the edge of the domain for the $h/c = 7.5\%$ case. The slice has been coloured by relative pressure to show the pressure drop caused by the complex flow, and the stream vectors have been coloured by vorticity, ω_x to indicate the direction of rotation.

The vortex on the SS edge was observed to remain highly stable throughout the animation. The formation of this vortex is due to the total tip leakage flow, which remains stable in the y-direction due to the pressure gradient between the sides of the rudder. The vortex on the PS edge can be seen to build in strength and shed periodically by viewing the animation, and Figure 5 shows the series of counter rotating vorticies, along with areas of low pressure being shed through the tip gap.

4 Mesh comparison and suitability

The mesh generation software used for these initial cases was `snappyHexMesh` (sHM), an unstructured castellated grid generator which is packaged with `OpenFOAM`. While has a utility to generate layers on the surface of a solid body, it can be unstable if the edges of the feature do not align well with the background grid. This caused difficulties in reliably creating the high fidelity grids required for LES simulations. The $h/c = 0.75\%$ case produced a mesh which met the requirements of the LES methods but the other small gap arrangements could not reliably generated to meet the requirements. For this reason the mesh generation was migrated to `Pointwise` (PW), a commercial meshing software which can produce unstructured tetrahedral meshes, with layers of prisms to produce the boundary layer mesh. In order to assess the suitability of this software a series of LES simulations were run using the $h/c = 7.5\%$ case to compare against the existing simulations.
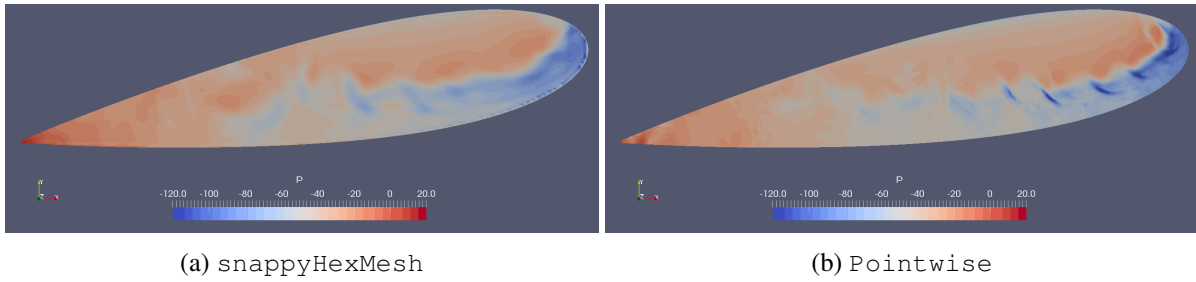
(a) `snappyHexMesh` (b) `Pointwise`

Fig. 7: Comparison of snapshots of unsteady tip pressure for the two different mesh techniques.

To investigate the difference in the meshing techniques with regard to future noise predictions, a number of sampling points were placed along the chord line of the foil tip. Applying a spectral analysis of the pressure samples on these points produced the plots shown in Figure 6. It can be seen that the shape of these is quite different, with the PW grid predicting higher power levels in the medium to high frequencies, but sHM produces more distinct frequencies, shown by sharp features in the PSD.

The tetrahedral structure of the PW grid could potentially cause numerical noise due to the non orthogonal nature of the cell surfaces, however the highly turbulent structure of the flow should mitigate these effects. In order to establish if the PW grid is introducing small turbulence structures, the pressure map on the tip of the foil was compared for the two mesh techniques as shown in Figure 7. This shows that the small structures present in the PW simulation are confined to the region of the propagating vortex, but are not present in the more stable region near the SS edge. This gives confidence to the PW mesh technique, suggesting that the small structures being captured are caused by the unsteady flow, and are not being captured by the castellated mesh from sHM.

5 Conclusion

In regions of highly complex flow, an unstructured tetrahedral grid seems to be capable of capturing small structures well, without introducing a great amount of numerical noise. This mesh technique will be taken forward and developed, to facilitate the production of noise predicting simulations using Ffowcs Williams-Hawkins analogy to predict the noise levels radiated into the far-field. These simulations will follow the techniques by Lidtke et al., 2016 and Lloyd et al., 2015 by investigating the noise radiated by the solid surface of the foil, as well as using a control surface within the fluid to capture the sources from within the fluid. The current simulation setup will be validated by producing simulations to model the experimental work by Jacob et al., 2010, providing an experimental case to validate the numerical predictions.

Acknowledgements

References

Badoe, C., a.B. Phillips, and Turnock, S. (2012). Numerical propeller rudder interaction studies to assist fuel efficient shipping.

Jacob, M. C., Grilliat, J., Camussi, R., and Gennaro, G. C. (2010). Aeroacoustic investigation of a single airfoil tip leakage flow. *International Journal of Aeroacoustics, Multi-Science Publishing*, 9(3):253–272.

Lidtke, A. K., Turnock, S. R., and Humphrey, V. F. (2016). Characterisation of sheet cavity noise of a hydrofoil using the Ffowcs Williams-Hawkings acoustic analogy. *Computers and Fluids*, 130:8–23.

Lloyd, T. P., Rijpkema, D. R., and van Wijngaarden, E. (2015). Propeller acoustic modelling: comparing CFD results with an acoustic analogy approach. *Proceedings of the 4th International Symposium on Marine Propulsors*, (November 2016).

Molland, A. F. and Turnock, S. (1991). Wind tunnel investigation of the influence of propeller loading on ship rudder performance. Technical report.

Stabilization of a Fluid-Deforming Structure Partitioned Coupling

S.M. Hosseini Zahraei[*]**, P.R. Wellens**[*]**, A.E.P. Veldman**[†]

[*] Technical University of Delft, The Netherlands,

[†] University of Groningen

s.hosseinizahraei@tudelft.nl

1   Introduction

It is generally accepted that strong partitioned coupling of the fluid-structure systems encounters instability under certain conditions. For the problems which are inherently one-way, this will not occur. While the problem undergoes a two-way physical phenomena, the amount of interaction between fluid and structure increases. As a consequence through the procedure the required rate of exchange of information increases as well. If the coupling is strong, this can be taken care of with sub-iterations, which is the iterations between fluid and structure at each time step until convergence. It is clear that the cost bottleneck of this type of simulations is the number of required sub-iterations. less sub-iterations the better. On the other hand, physics can be even more unfavourable. The rate of information exchange is directly related to the ratio of added mas over structural mass. The amplification factor of the sub-iterative loop should not exceed one, if so the rate need to be relaxed. This is generally called, under-relaxation method. This will automatically slow down the convergence and therefore increase in computation time. This paper is an overview of the aforementioned problem and describing the method proposed to remedy it. The simple two dimensional flexible bottom container case is the numerical test cae.

2   Coupling Scheme

Partitioned fluid-structure system consists of both fluid and structural solver. Those models are independent and only the motion and the loads are exchanged at the interface. In this research the fluid solver is ComFLOW a free surface flow solver developed in university of Groningen and technical university of Delft. ComFLOW is based on finite volume method. The mathematical and numerical methods is comprehensively explained in Wellens, 2012. The structural solver is a one dimensional Euler-Bernoulli beam using Hermite shape functions. In this section, the conventional and the new proposed method are elaborated.
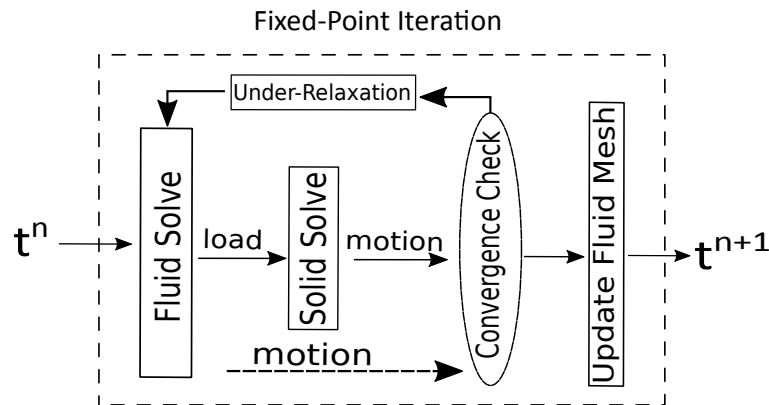
Fig. 1: THE SCHEMATIC VIEW OF PARTITIONED FLUID-STRUCTURE NUMERICAL ALGORITHM.

2.1   Conventional Method

The method of fixed-point iteration is commonly used for the fluid-structure interaction problems. As illustrated in Fig. 1 the so called sub-iterative loop between fluid and the structure continues until convergence is achieved. The convergence criteria is based on the velocities at the interface of fluid and the structure(FS). For in-compressible flows the amount of under-relaxation is related to the ratio of added

mass to structural mass as explained in van Brummelen, 2009 . When problems encounters more two-way interaction, more under relaxation need to be applied. The number of sub-iterations per time step directly make the computation more expensive. According to S.M. Hosseini Zahraei, 2017, the origin of this instabilities are the large eigen values of the added mass operator.
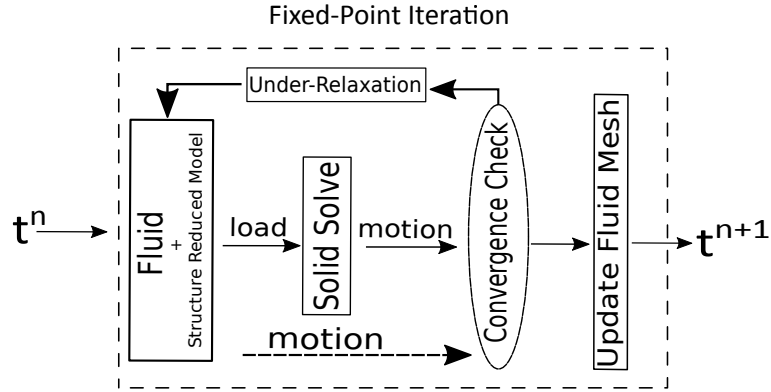

Fig. 2: THE SCHEMATIC VIEW OF QUASI-SIMULTANEOUS PARTITIONED FLUID-STRUCTURE NUMERICAL ALGORITHM.

2.2 Quasi-Simultaneous Method

The new method tries to make most of the advantages of the monolithic approach, while still keeping the system partitioned. This method then can be called quasi-simultaneous. The idea is to make an approximate of the structure, as here it's reduced order model. As illustrated in Fig. 2 this approximate is then solved with the fluid at the same time. The idea of approximate model or also called as interaction law is also present in the work of Veldman, 2009 to couple viscid and in-viscid flows.

According to S.M. Hosseini Zahraei, 2017, the origin of instability is within the most dominant modes of the structure. As those dominant modes are solved with the fluid simultaneously, under-relaxation relief is achieved. this is the moment when the next largest eigen-value of the system takes over, or in other words, the next dominant mode of the structure rules the structural response. Consequently, the amount of under-relaxation required will lower and therefore the convergence will be achieved with less number of sub-iterations.

3 Numerical test Model

One by one meter fluid domain is considered which is 80 percent filled with water. At the bottom of the domain an Euler-Bernoulli beam is placed. The domain dimensions are illustrated in fig3. The beam density is $900\frac{kg}{m^3}$ and it is divided into 101 1D elements. Added mass of the beam can be approximated by the mass of the column of water above the beam which is $0.8 \times 1000 = 800$. Mass per length of beam is $0.05 \times 900 = 45$, therefore the initial ratio of the added mass to the structural mass approximately is $\frac{800}{45} = 17.8$. The beam is initially horizontal and has no deflections. The interaction between fluid and the beam is then simulated. Fluid domain has 101×41 grids. The solver for pressure Poisson is SOR and the beam fem solver is CG. The time step is 10^{-4} for both fluid and beam. Convergence criteria for the interaction is based on residual of the computed velocities at the interface at each step, as :

$$\frac{u^{n+1} - u^n}{u^1 - u^0} \qquad (1)$$

4 Results

In this section, first the solution in terms of beam midpoint deflection and total force acting on beam is presented. Next, the relaxation factor required and the effect of it on convergence history is elaborated. In the next part, the interaction law, it's requirements and it's performance under different settings is shown
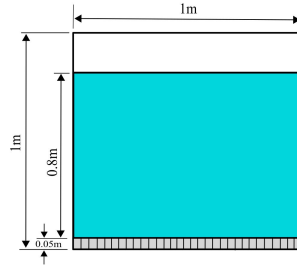
Fig. 3: Dimensional properties of numerical test case

and discussed.

4.1 Coupled Fluid-Beam System Solution

The beam vibrates under the forcing of fluid, as shown in Fig. 4 the midpoint starts to go down and then oscillate until it reaches it's steady deflection under fluid forcing. The force on the beam increases gradually from zero at the beginning and it increase until the beam experiencing it's maximum defection. It oscillates as well as beam deflection until it reaches its final constant value. In the results sown below the simulation is done only for 0.05 seconds.
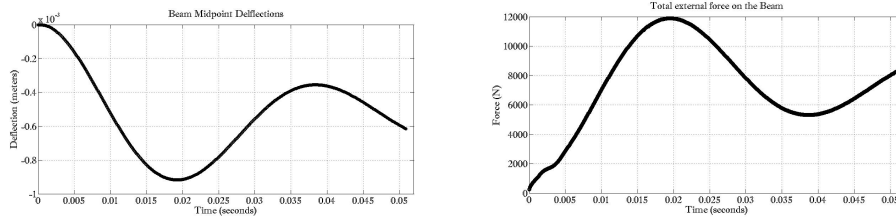
Fig. 4: Beam midpoint defection (top) and tota forrce acting on it(bottom)

4.2 Coupled Fluid-Beam System Convergence

In order to solve for this problem under relaxation should be applied to the rate of load and motion transfer between these two partitions. The added mass ratio as approximated in section one is 18. Theoretically, maximum value for relaxation which can give a stable solution is $\frac{1}{18} = 0.05$. According to simulations, 0.03 already brings a lot of instability. This is due to the fact that the added mass is approximated and the height of the water above the beam varies from one element to the other and also in time. In other words, added mass is also function of time and also fluid free surface. The approximated value of 18 is not exact. The convergence history of the first time step is shown in fig 5. The convergence criteria is as equation 1 and the threshold is set to be 10^{-3}. It is shown that by increasing the relaxation the number of iterations required for the convergence is decreased but also instabilities increased.
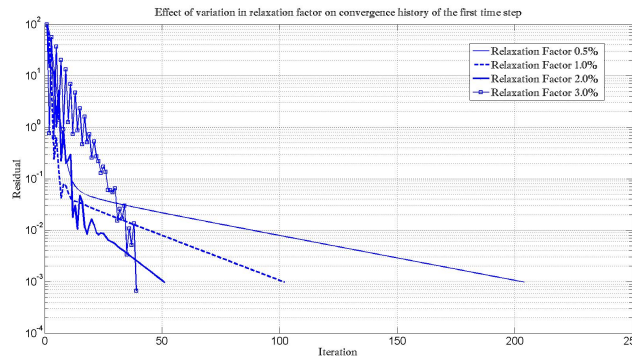
Fig. 5: The effect of relaxation factor on the convergence history for the first time step

4.3 Mode shapes of the beam

All structural eigen-values and eigen-modes are extracted by using the mass and stiffness matrices of the beam and constructing $K^- M$ matrix. As an example, the first five mode shapes as well as two higher ones, 101 and 102 are shown in figure 4.3. The shape of higher mode shapes seems to be affected by numerical accuracy of method used to compute them.
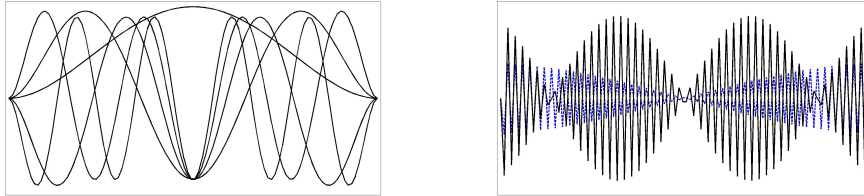
4.4 Boundary of Instability

In this section, by keeping the relaxation factor to be 0.03 and plugging in the interaction law with different levels of accuracy, again the convergence history is observed. As illustrated in figure 6, the coupling convergence is affected by the interaction law. It is more stable and the number of iterations is slightly less only for the first time step.
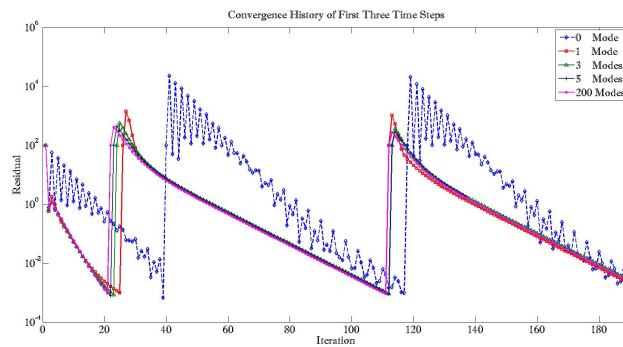
Fig. 6: Convergence history or the first three time steps for different levels for the interaction laws

4.5 Higher relaxation values

In this section the focus is on the number of sub-iterations and the interaction law's influence on reducing the number of iterations. Using the first five modes and applying different relaxation factors, starting from boundary of instability i.e. 0.03, leads in reduction o sub-iterations. The sub-iteration history for first 15 time steps is shown in figure 7 .
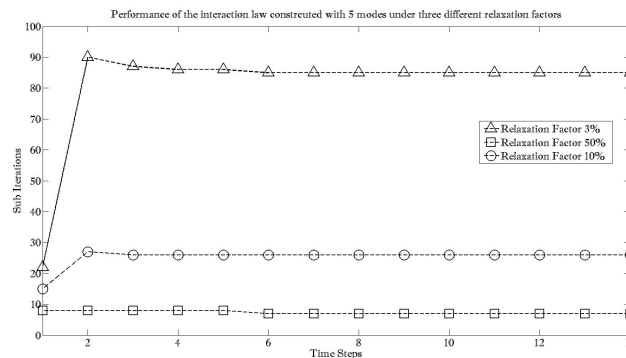
Fig. 7: Interaction law constructed with 5 modes for three different relaxation factors

Using 5 modes, instabilities starts to play a role using 0.50 as relaxation factor, therefore the number of modes is increased to 10. This is sufficient to set the relaxation factor to one. Basically in this case no relaxation is applied. Since the approximate beam inside interaction law is not the same as external beam, still few sub-iterations is needed to achieve convergence. It is also observe that in the first few time steps the number of sub-iterations required is more and that is because more instabilities will occur. The coupling gets more stable as time advances and therefore the number of sub-iterations decreases.
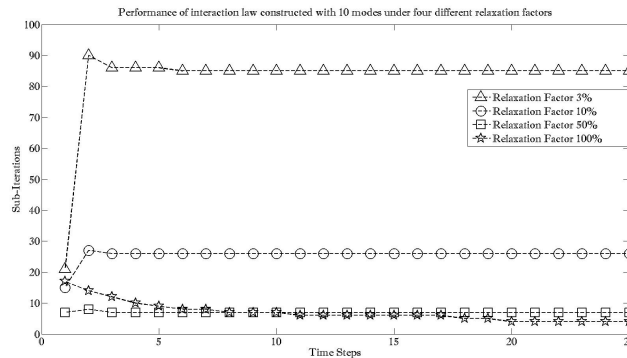
Fig. 8: Interaction law constructed with 10 modes for four different relaxation factors

Adding more modes to the interaction law and keeping the relaxation to be one does not decreases the number of iterations to one. The reason is because of the fact that higher modes are not computed precisely, as shown in figure 5.

It is observed that by decreasing the size of problem and less number of elements the mode shapes are accurate enough to decrease the number of sub-iterations to one. That case will be documented as well.

5 Conclusion

By solving the fluid-structure interaction problem partly simultaneous and choosing the interaction law or the approximate model to be base on dominant structure mode shapes, the coupling scheme speeds up. Specially when there is a strong interaction between fluid and the structure, the quasi-simultaneous method decreases computation time drastically.

NWO | Applied and Engineering Sciences

References

S.M. Hosseini Zahraei, P.R. Wellens, I. A. A. v. R. H. (2017). The role of a structural mode shape based interaction law to suppress added mass instabilities in partitioned strongly coupled elastic structure-fluid systems. *OMAE Conference, Tronheidm, Norway*.

van Brummelen, E. H. (2009). Added mass effects of compressible and incompressible flows in fluid-structure interaction. *Journal of Appl. Mech.*, 76.

Veldman, A. E. P. (2009). A simple interaction law for viscous-inviscid interaction. *Journal of Eng. Math.*, 65:367–383.

Wellens, P. R. (2012). *Wave Simulation in Truncated Domains for Offshore Applications*. Phd thesis, Technical university of Delft. http://resolver.tudelft.nl/uuid:d64907ac-4420-4026-b36d-95b4e24ef421.

Physics-Based and Learning-Based Roll-Damping Predictions

Ian Hubbard, Gabriel D Weymouth
University of Southampton, Southampton, UK
G.D.Weymouth@soton.ac.uk

1   Introduction

Computational fluid dynamics (CFD) has become prevalent not only in analysis of ship hydrodynamics but also in ship hull design optimization. The use of CFD in an optimization loop is a promising method to develop more energy efficient future ships but computational cost is still, and will always be, the limiting factor. Given practical limits on computational time and the large number of adjustable parameters for a given design, only a small number of CFD simulations can be run, making it very unlikely to obtain a unique global optimum or a complete optimal Pareto front (Schmitz et al., 2002). Because of these limitations it may be advantageous to avoid traditional design search and optimization methods in favour of more advanced machine learning approaches. In other words, while local gradient-based approaches may suffice when using simulations measured in seconds, once the computational cost of each simulation is measured in hours it is only prudent to seek any means available to reduce the number of evaluations required.

Moreover, in order to obtain even a modest number of simulations, a host of numerical and modelling assumptions are made which introduce corresponding numerical and modelling errors and which can easily invalidate the entire optimization process. The classic example of *modelling* error is the use of a turbulence model, such as RANS, which is not capable of capturing the flow effects relevant to the system of interest. In this case a more computationally intensive turbulence modelling such as LES or DNS would have to be employed, which will quickly deplete the feasible computational budget of any design. The classic example of *numerical* error is insufficient numerical resolution of the flow features. A more subtle numerical error is introduced when automatically developing grids which conform to the changing hull geometry as it is optimized. Errors in this process are common and can cause entire regions of the search space to be unexplored.

In this work we will examine the utility of including CFD in the process of optimizing roll damping keels. A roll-damping keel is an ideal candidate system for the inclusion of CFD as it is dominated by viscous effects. The particular physics of roll damping differ substantially to those of the remaining degrees of freedom of ship motions, where motions such as heave, sway and pitch may be easily and sufficiently accurately obtained from potential flow methods in the form of strip theory. The viscous nature of roll-damping results in substantial non-linearity in roll responses for various hull shapes, ship operational types and requirements, and of course, intensity of the forced roll responses due to irregular seas (Ikeda et al., 1978).

This work focuses on two elements of viscous roll-damping predictions. First, we will investigate the modelling errors introduced by turbulence models and two-dimensional flow restrictions into CFD simulations of roll-damping keels. By doing so, we seek to determine the fidelity required to make design predictions and therefore required within an optimization framework. Second, we investigate the use of machine learning to build an accurate surrogate model to the non-linear physics of roll-damping. Such a model could be used as a rapid way to establish the global design optima, potentially reducing the overall cost of the optimization and enable higher-fidelity simulations and/or greater exploration of the design space.

2   Case study and physics-based predictions

The first objective of this work is to determine a suitable case-study problem. While the full 6DOF seakeeping problem is fundamental to Naval Architecture and there are important coupling effects on the degrees of freedom, we choose to focus solely on the prediction of optimal design of keels for 1DOF roll-damping. Our test geometry is chosen to mimic a midship-section; a rectangular body, uniform in the longitudinal direction and mirrored around the nominal waterline. This system does not feature the damping effects of forward speed and wave radiation, allowing us to focus on the viscous roll-damping
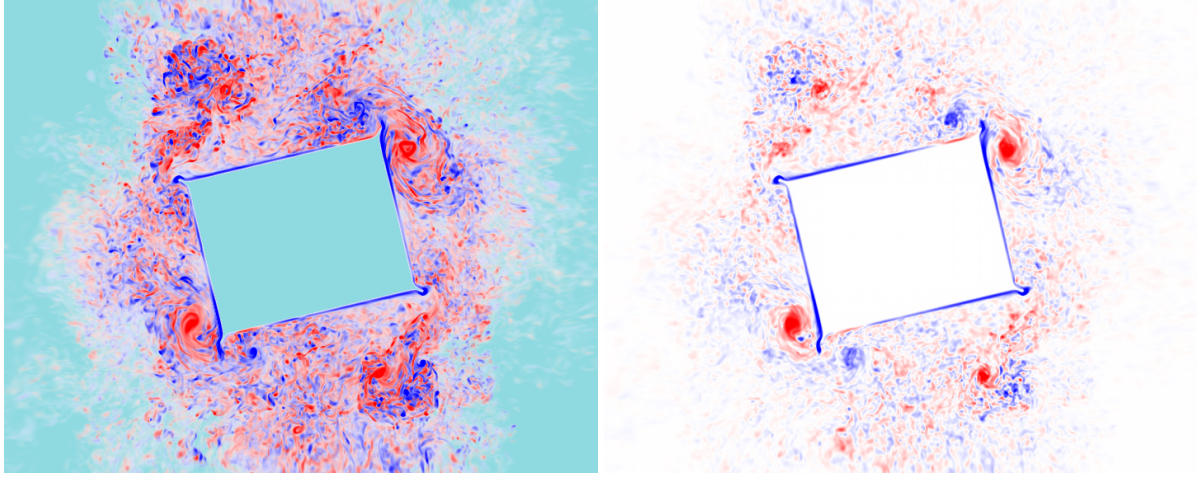
Fig. 1: Instantaneous in-plane vorticity predictions for the model roll-damping system. The rectangular geometry and four keels are seen in the negative space in the center of the images. The left image is a volume rendering and the right image shows the vorticity averaged longitudinally through the domain to highlight the primary vortex structures; two vortex pairs being shed off the top-right and bottom-left keels, and two older and less organized vortex pairs which are shed off the other corners in the first half of the roll period.

effects for which CFD simulations are most crucial. Similar systems have been used in experimental and numerical studies previously (Ikeda et al., 1978, Jaouen et al., 2011a) enabling model validation and comparison of results.

The next objective of this work is to develop an efficient computational framework to run general roll-damping simulations. To isolate modelling errors from numerical errors, we choose to use the Boundary Data Immersion Method (BDIM, Maertens and Weymouth, 2015) to solve the full Navier-Stokes equations on a Cartesian-grid. Immersed boundary approaches are ideal for design optimization as the exact same background grid can be used for every design evaluation; even when changing discrete geometric properties of the design such as the number of keels. The BDIM method in particular is capable of accurately predicting surface stresses even for in the case of thin boundary layers and large amplitude motions (Maertens and Weymouth, 2015). For this study we have utilized the Lotus flow solver, an in-house implementation of BDIM developed at the University of Southampton which has been extensively validated and can be run efficiently on HPC systems if needed.

An initial set of simulated roll damping results for this test case are present in Figure 1. For this test case the mirrored section geometry has an aspect ratio $B/2D = 1.25$ with four plate keels oriented at 45 deg with a length of $l/B = 0.04$. The body is given prescribed roll motion of the form

$$\phi(t) = \phi_0 \sin(\omega t)$$

Note the roll amplitude ϕ_0 is proportional to the Keulegan-Carpenter number K. As there is no free-surface or cross flow in this test case there can be only *one* additional physical non-dimensional parameter. In this work, we choose the Stokes number which we define as

$$Stk = \sqrt{\frac{B^2 \omega}{2\nu}}$$

The Stokes number compares the time scale of motion to the viscous time scale. Based on the laboratory experiments of Ikeda et al., 1978, with $B = 0.28m$ and roll period $T = 1s$, we use $Stk = 490$ and $\phi_0 = 0.232$ (which gives $K = UT/l = 24.8$ where U is the keel tip velocity magnitude).

The numerical parameters in the simulation are the domain size, a $20B$x$20B$x$0.5B$ prism, the grid spacing, a uniform grid with $h = 0.0042B$ near the body and a 3% grid expansion rate in the far field, and
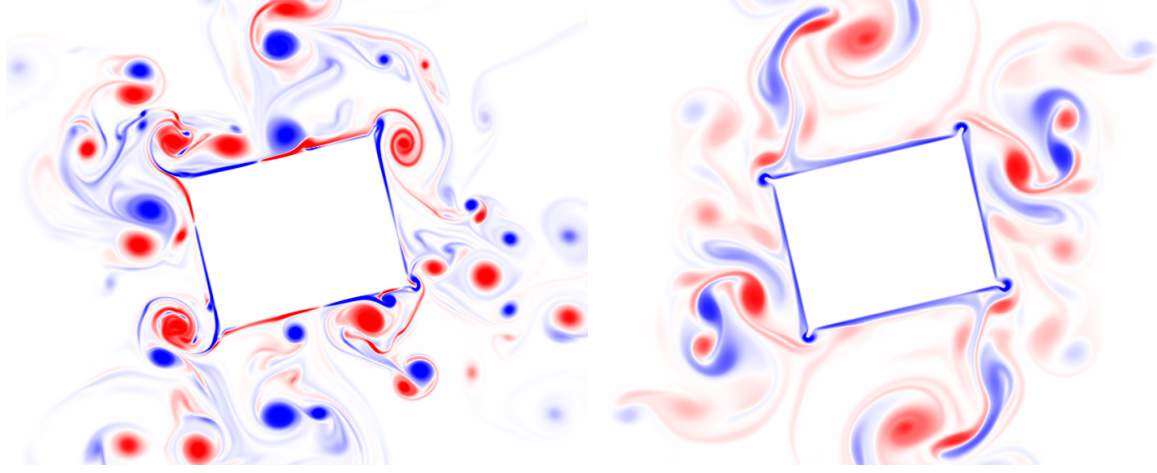
Fig. 2: Instantaneous in-plane vorticity predictions for the 2D flows; compare to Figure 1. The left image shows the iLES model which is essentially obtaining a direct solution of a 2D turbulent wake. The large and energetic vortex structures illustrate the significantly differences between 2D and 3D turbulence. The right image shows the Smagorinsky LES model which damps out the vortex structures. This doesn't improve the match to the details of the 3D simulation, but does produce reasonable damping coefficients.

the boundary conditions which are no-slip on the body and free-slip the domain boundaries. The effect of subgrid scale convection is included through the use of an implicit Large Eddy Simulation (iLES) model, which requires no modelling parameters and has been extensively validated (Margolin et al., 2006).

The instantaneous vorticity field, Figure 1, shows the development of a fully turbulent wake near the rolling body. Large vortex pairs are formed on the keels every cycle which then propagate into the domain and quickly break down due to turbulent mixing. The non-dimensional damping coefficient during the roll motion is defined as

$$M^* = \frac{M}{\rho \phi_0 \omega^2 B^3 D}; \quad b_\phi^* = Re(\hat{M}^*(\omega))$$

where M is the integrated moment on the body per unit span, M^* is the dimensionless moment, and the coefficient b_ϕ^* is the real part of the Fourier transform of the time signal at the excitation frequency. The moment (not shown) is essentially periodic and the damping coefficient b_ϕ^* matches the experiments of Ikeda et al., 1978 to within 2%.

Considering the approximately 38M points used, these results have been obtained fairly quickly, requiring only around 12 hours of computational time on a 16 core machine. However, this is still far too slow to be included in an optimization cycle. The importance of viscous effects has made physics-based roll-damping predictions notoriously difficult (Jaouen et al., 2011b). As such, roll-damping also serves as a stringent test for the impact of model errors on the ability to identify optimal ship hull designs. We next evaluate two alternative models to speed up the roll-damping prediction; 1) 2D simulations using the same iLES model, 2) 2D simulations using an explicit Smagorinsky LES model with an eddy-viscosity coefficient of $C = 0.2$. Other than using a 2D domain, these simulations are identical to the previous case. As shown in Figure 2, neither option captures the details of viscous roll-damping particularly well, however Figure 3 shows that the LES damping coefficient is adequate for use in a design optimization process, with errors generally less than 10% compared to the experiments of Ikeda et al., 1978.

3 Machine learning application

To enable a study of the applicability of machine learning methods to roll-damping problems, a database of T-type bilge-keel roll-damping simulations is generated using the 2D LES simulations. The bilge keels are placed on a round bilge, double-hull mid-ship section and parameterized with four geometric variables; keel angle relative to the bottom, keel length, keel T upper length, and keel T lower length. The
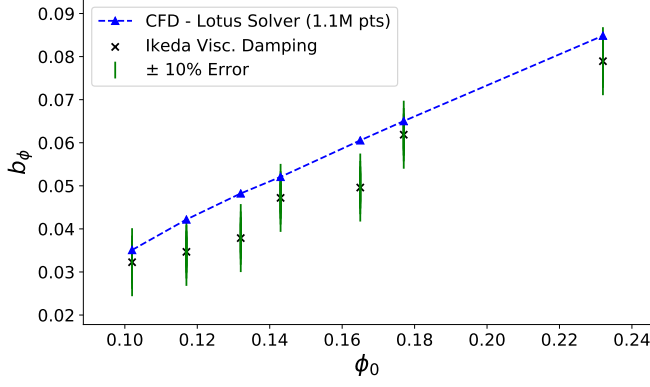
Fig. 3: Validation of the damping coefficient from the 2D Smagorinsky LES model.
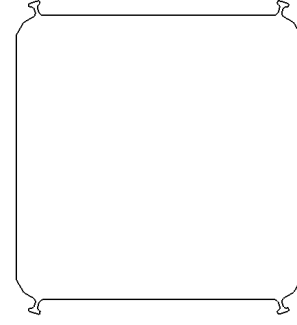
Fig. 4: Example T-type keel geometry.
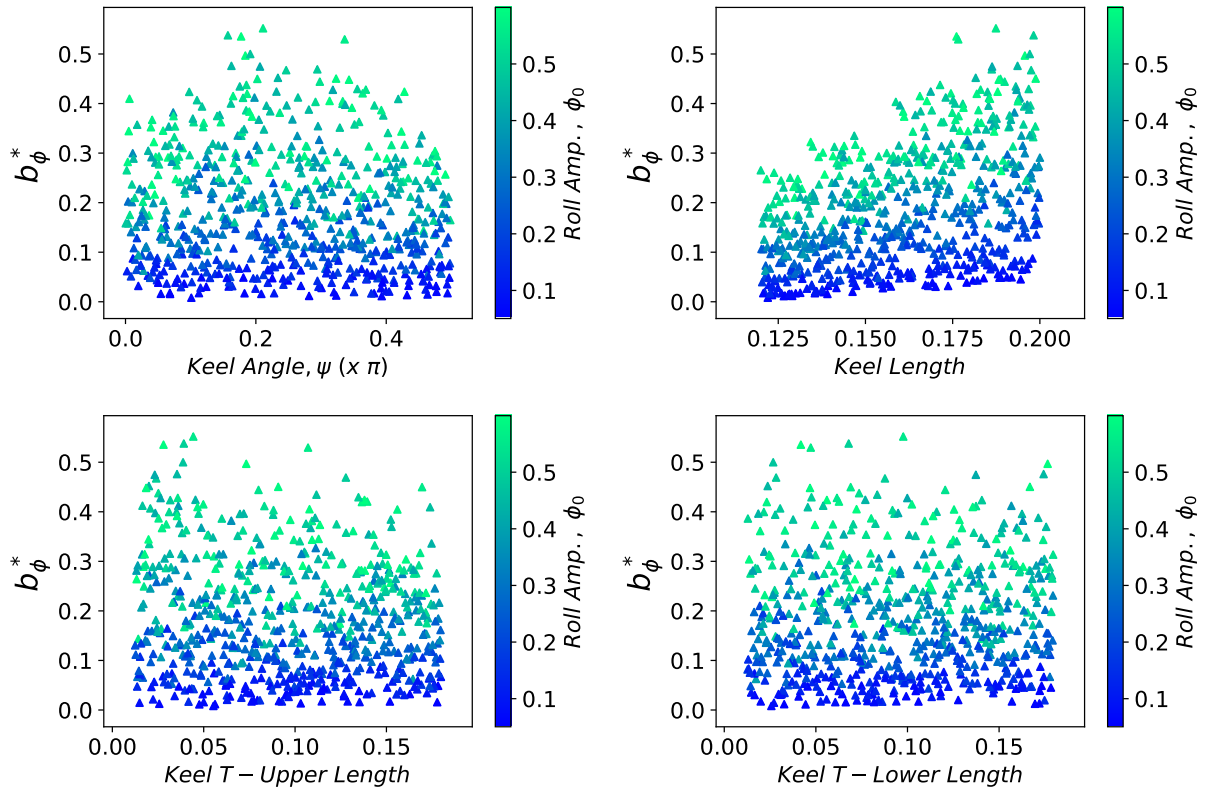
Fig. 5: The damping coefficient from all 660 simulations plotted against all four design variables.

roll amplitude ϕ_0 is included as a fifth variable to study nonlinear effects. Figure 4 shows an example geometry. A Latin Hypercube sampling plan is used to maximize the variety of the simulations data-set, and the damping coefficient results for the 660 simulations are shown in figure 5. The results show that the roll amplitude, keel length, and the keel angle have a strong impact on the damping coefficient in general agreement with expectation. It is difficult to determine the influence of the T size.

Next, the machine learning approach is described. The database is split into training and test sets using the machine learning python library scikit-learn (Pedregosa et al., 2011). scikit-learn provides various resources for efficiently preprocessing datasets to array formats required for the input layers of the neural networks in TensorFlow (Abadi et al., 2015). The data-set of 660 samples is split in a training/testing ratio of 0.2, hence allocating a maximum of 528 data points for training and 132 data points for testing. Before splitting, the rows of the dataset are randomly shuffled to make the data points
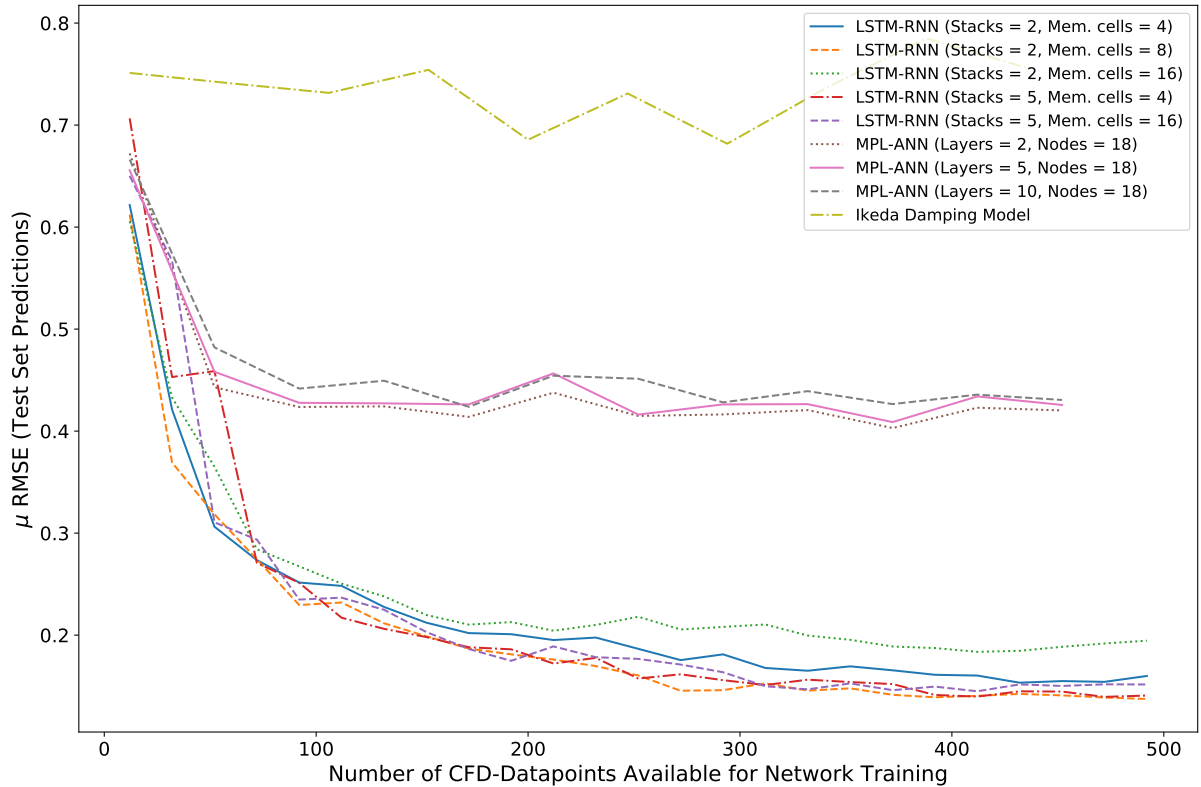
Fig. 6: Mean error in learning as a function of training set size.

allocated for testing as stochastic as possible. After splitting the data the StandardScaler function from the scikit-learn library is used to scale the data to zero mean and unit deviation.

Next, two deep learning models are investigated for their candidacy as surrogate models. These are the Multi-Layered Perceptron (MPL) and the Long Short-Term Memory-Recurring Neural Network (LSTM-RNN). The models are built separately using TensorFlow (Abadi et al., 2015), a library developed by Google Deepmind and can utilize GPU acceleration on CUDA capable hardware if required, depending on the size of the data-set and network depth. The primary difference between the networks is that the MPL learns from the inputs of each training sample, whilst the RNN learns in a recurring loop, feeding the output prediction from the previous training sample as an additional input to the following sample and retaining memory. In the case of both MPL and RNN, there is no definite guide to setting their hyper-parameters and it is usually a tuning art, however a good upper-bound for the number of neurons in an MPL is roughly four times the number of neurons as there are inputs (Kanellopoulos and Wilkinson, 1997). Here 18 neurons will be used. For the number of memory units or hidden states in the LSTM layer, 4 is initially used, 1 for each gate in the LSTM memory cell and will be incremented by 4 units at a time as a hyper-parameter investigation. The number of layers and network depth is also explored within this work. Finally, the adam (Kingma and Ba, 2014) stochastic optimizer algorithm was used to train the network weights. The algorithm has been implemented in the TensorFlow python library and was used directly when compiling the neural network run script, using RMSE as the minimization objective.

The results of the machine learning approach to predicting roll-damping is shown in figure 6. This figure shows both types of network and a number of hyper-parameters options. The results of the LSTM are generally much better than the MPL, with minimum mean errors of 12% and 43%, respectively. The test error is less strongly dependent on the model's hyper-parameters within the range of options shown. As a base-line, we have also plotted the mean error of the semi-empirical roll-damping formula proposed by Ikeda, which results in error levels of around 70% against the randomly selected test sets.

A crucial factor studied in figure 6 is the dependence on the number of data points in the training set.

These results were achieved by reshuffling and splitting the database, keeping the test set size constant but progressively decreasing the training set size. For very sparse data set of $O(10)$ examples, the error rates for both method are very high (though still better than the semi-empirical model) and of similar magnitude. As more data is included, the error decreases until the MPL model's improvement stops at around 50 training samples. Despite the much improved performance of the LSTM model, many hundreds of examples are required before the error level drops to around 15%.

These results indicate the potential gains for concepts such as transfer learning and Physics-Based Learning Models (PBLM, Weymouth and Yue, 2013) to reduce the dependence on the number of training points. Our initial attempt to use the Ikeda model within a PBLM failed to provide significant improvement, likely because of the model's poor performance on this test set. Further research in this direction is ongoing.

Acknowledgments

References

Abadi, M., Agarwal, A., Barham, P., Brevdo, E., Chen, Z., Citro, C., Corrado, G. S., Davis, A., Dean, J., Devin, M., Ghemawat, S., Goodfellow, I., Harp, A., Irving, G., Isard, M., Jia, Y., Jozefowicz, R., Kaiser, L., Kudlur, M., Levenberg, J., Mané, D., Monga, R., Moore, S., Murray, D., Olah, C., Schuster, M., Shlens, J., Steiner, B., Sutskever, I., Talwar, K., Tucker, P., Vanhoucke, V., Vasudevan, V., Viégas, F., Vinyals, O., Warden, P., Wattenberg, M., Wicke, M., Yu, Y., and Zheng, X. (2015). TensorFlow: Large-scale machine learning on heterogeneous systems. Software available from tensorflow.org.

Ikeda, Y., Himeno, Y., and Tanaka, N. (1978). Components of roll damping of ship at forward speed. *Journal of the society of Naval Architects of Japan*, 1978(143):113–125.

Jaouen, F., Koop, A., and Vaz, G. (2011a). Predicting roll added mass and damping of a ship hull section using cfd. In *OMAE*, volume 49085, page 2011.

Jaouen, F., Koop, A., Vaz, G., and Crepier, P. (2011b). Rans predictions of roll viscous damping of ship hull sections. In *5th Int. Conf. on Computational Methods in Marine Engineering, MARINE 2011*.

Kanellopoulos, I. and Wilkinson, G. (1997). Strategies and best practice for neural network image classification. *International Journal of Remote Sensing*, 18(4):711–725.

Kingma, D. and Ba, J. (2014). Adam: A method for stochastic optimization. *arXiv preprint arXiv:1412.6980*.

Maertens, A. P. and Weymouth, G. D. (2015). Accurate cartesian-grid simulations of near-body flows at intermediate reynolds numbers. *Computer Methods in Applied Mechanics and Engineering*, 283:106–129.

Margolin, L., Rider, W., and Grinstein, F. (2006). Modeling turbulent flow with implicit les. *Journal of Turbulence*, 7.

Schmitz, A., Besnard, E., and Vives, E. (2002). Reducing the cost of computational fluid dynamics optimization using multi layer perceptrons. In *Neural Networks, 2002. IJCNN'02. Proceedings of the 2002 International Joint Conference on*, volume 2, pages 1877–1882. IEEE.

Weymouth, G. D. and Yue, D. K. (2013). Physics-based learning models for ship hydrodynamics. *Journal of Ship Research*, 57(1):1–12.

Simulation of Acoustic Stream with a Sonotrode

Byoung Guk Kim, Philip Wilson, Stephen Turnock
Fluid Structure Interactions group, Faculty of Engineering and Environment,
University of Southampton, Southampton SO16 7QF
bgk1g15@soton.ac.uk

1 Introduction

Cavitation is the name of a phenomenon that describes a phase change from the liquid to the vapour without supply of heat energy. Acoustic pressure waves are generated from the rapid collapse of these vapour bubbles and a portion of the energy contained in the acoustic pressure waves is transferred to its nearby boundary surface to cause plastic deformations. Eventually this is thought to cause material loss in a similar manner as the fatigue failure of metals. This process of plastic deformation and eventual loss of material is called 'erosion'.

Because cavitation erosion can cause a catastrophic structural failure of marine propellers, it is an important aspect of marine propeller design (ITTC, 2005). Unfortunately, the currently available model test methods such as paint test or high-speed video image analysis are all qualitative and not universally reliable in assessing such a risk. Therefore, it is desirable to have a new quantifiable and more reliable model test method to replace the existing methods. Boorsma and Fitzsimmons (2009) reported that acoustic emission (AE) signal peaks were concurrently occurred as the cavity structure collapsed on the surfaces of propeller blades or rudders, and it could be used as an index of the intensity of cavitation impacts. Therefore, it appears the AE has a good potential as a quantitative index for cavitation erosion, provided the signal amplitude show a correlation with the cavitation impact loads.

A joint research is under way among Lloyd's Register EMEA, SSPA Sweden AB and DSME to develop a new erosion test method to replace the existing paint erosion test, which is arguably difficult to reproduce in general. A sonotrode is an ultrasonic vibratory cavitation device that is commonly used to investigate cavitation erosion process in the laboratories in an accelerated and controlled manner. It is intended to be used to investigate a correlation between the cavitation intensity and the erosion rate in this research work (see Fig. 1). The aim of the study reported is to investigate suitable approaches to simulate the acoustic stream generated by the vibrating disk on a sonotrode and the subsequent unsteady wall pressure signal. A series of simulation of this device has been carried out to support analysis of the experimentation results for this research.

The acoustic cavitation is known to oscillate at a certain sub-harmonic frequency rather than at the driving acoustic excitation frequency (Müller et al., 2013, Žnidarčič et al., 2015). Furthermore, the cavitation impact frequency of hydrodynamic cavitation and the acoustic cavitation will be obviously different from each other. Therefore, numerical simulation of the experiment will be very helpful to plan the experiment and analyse its results providing the simulation is physically accurate enough. To find such a proper numerical model for the acoustic cavitation simulation, a number of simulation have been carried out with different cavitation models by the authors (Kim et al., 2016). This paper discusses results with a barotropic cavitation model in comparison with the experimental results obtained by Rahimi et al. (2017).
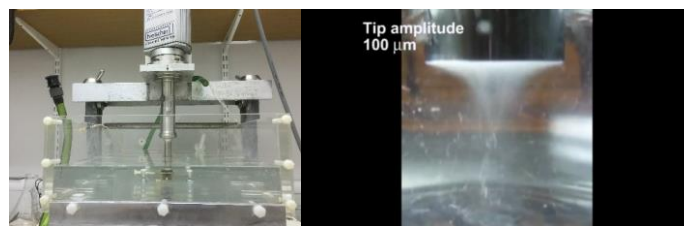

Fig. 1: A sonotrode installed for the experiment and an example image of the acoustic cavitation
(https://youtu.be/qGSioE58YjA)

2 Numerical modelling

Rahimi et al. (2017) carried out PIV measurements to validate their ultrasonic reactor simulation. The PIV measurements had been performed with a high-speed camera with exposure time ranging from 1 μs up to 5 s. Unfortunately, no further detailed information was provided such as exact time interval between the images or the number of images used for their analysis. According to the writing author's personal communication (Movahedirad, 2017), their acoustic stream velocity measurements data were compared with a 2-D pressure-based solver with Singhal cavitation model (Singhal et al., 2002). They modified the cavitation model to include the proposed modification by Žnidarčič et al. (2015). In this paper, their experimental results of the PIV measurements were compared with 2-D and 3-D simulation results.

A model was created according to Rahimi et al. (2017) except for the cross-sectional shape of the water bath. Meanwhile the actual basin was a rectangular one having sectional area of 0.04 x 0.04 m^2, it was modelled as a cylinder having the same diameter as the edge length of the square section. The horn tip was submerged into the water by 0.01 m at the centre of the bath. The acoustic oscillation amplitude and frequency were set to 40 μm (peak-to-peak) and 20 kHz.

Numerical simulation was performed using 'cavitatingFoam' that is a compressible, viscous multiphase flow solver provided with an open source CFD software suite, OpenFOAM (version 3.0.1). A deforming mesh scheme was used to mimic the ultrasonic horn tip oscillation. Initial study had been carried out with a 2-D cylindrical slice model as reported in Kim et al. (2016). Since the 2-D simulation exhibited very high magnitude of acoustic stream and the mesh quality becomes poor as one gets closer to the symmetry axis, a full 3-D model was used later to see any difference from the better mesh quality of the 3-D model.

A time-dependent RANS (Reynolds Averaged Navier-Stokes) equations with a barotropic equation of state were solved based on a homogeneous equilibrium mixture model. The solver provides several options of barotropic compressibility models such as linear (Delannoy, 1990), Wallis (Wallis, 1969) or Chung (Chung et al., 2004). Wallis model was developed for very low flow velocity compared with the sound wave in a given medium and known as prone to get unstable (Karrholm, 2008). In this study 'linear' barotropic compressibility model was used as the first step. The compressibility of the mixture was assumed to be a weighted sum of disperse and continuous phases in proportion to the volume fraction of each phase. The pressure equation was solved by PISO (Pressure Implicit with Separating Operators) algorithm. Finally, to investigate whether it is appropriate to use unsteady RANS with a turbulence model, an LES simulation was carried out and compared with the RANS simulation results.

The boundaries of the calculation domain were defined as Fig. 2. 'piston' patch was modelled as a sinusoidally oscillating boundary. 'bottom', 'wall' and 'piston side' patches were all modelled as the no-slip walls. k-ω SST turbulence wall functions were applied to all the boundaries except 'outlet'. For 'outlet', two different boundary conditions were tried for the pressure boundary condition at 'outlet' patch to investigate the effect of it on the acoustic stream velocity. Firstly, a Dirichlet type boundary condition was tried and then, a non-reflecting boundary condition was applied to mimic an unbounded space. The velocity boundary condition for all the boundary patches was given as Neumann type.

A second order upwinding scheme was used for temporal discretisation and the central differencing scheme applied for spatial discretisation. The model consisted of 1.63 M cells in total and y^+ on the piston boundary was mostly about 50 or less. However, where there occurred high magnitude of vorticity e.g. near the interface of both phases on the boundary, y^+ increased up to an order of 200. Typically, y^+ is supposed to be roughly in a range of 40 ~ 120 to apply a turbulence wall function. Therefore, the accuracy of the simulation may have been slightly degraded where y^+ became higher than 120. The meshes near the piston boundary needs to be finer for future simulation works. Time step was automatically controlled to keep the acoustic Courant number less than 50. The actual average time step size was in the order of $7x10^{-7}$ sec.
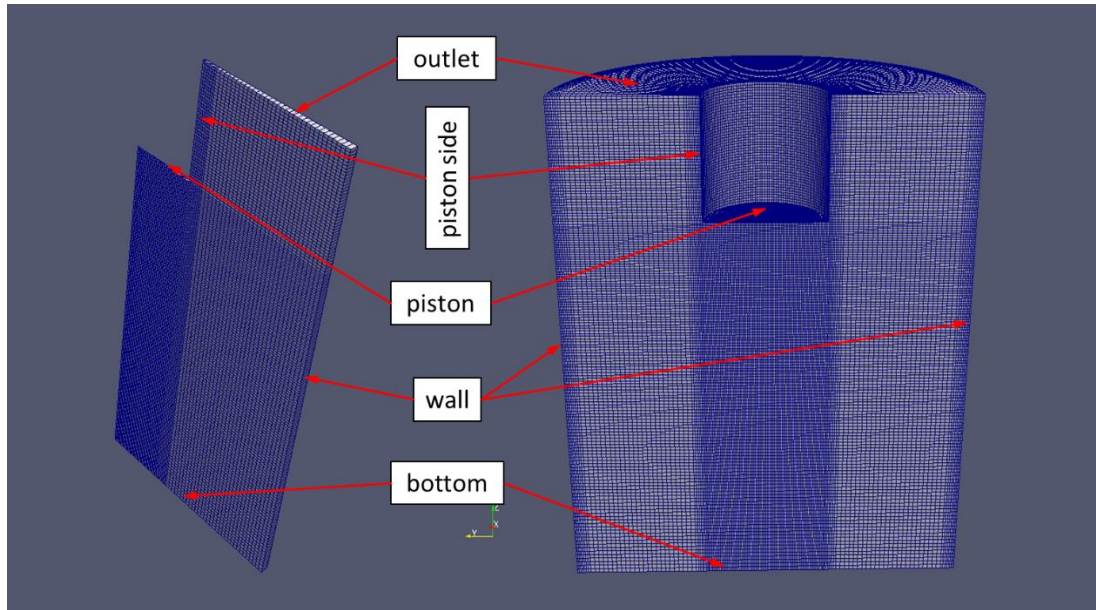
Fig. 2: 2-D model (left) and 3-D model (right) of the fluid domain.

3 Results

The initial 2-D simulation results produced a similar flow pattern as that with full 3-D simulation, which is shown in *Fig. 3*. However, the acoustic stream velocity was predicted approximately 5~6 times higher than the experimental results. The reason was believed to be related to two weak spots of the simulation. One was the unrealistic flow domain volume change by the piston oscillation that should have been compensated at the outlet boundary, but, kept as a fixed pressure outlet in the model. The second was the absence of energy dissipation mechanism via small gravity waves generation at the free surface, which was modelled as a fixed pressure outlet. To overcome this, a non-reflecting pressure boundary condition (Grote and Keller, 1995) for the pressure outlet was introduced instead of a fixed pressure value. Although the flow velocity exaggeration was somewhat released by the non-reflecting boundary condition, it was still higher than the experiment. Finally, a full 3-D model was tried to see if any differences would be made by it.

With the 3-D model, the main flow feature of the acoustic stream and the magnitude of the vertical velocity component of the stream were compared with the PIV measurement results.

To compare the overall flow feature predicted by the simulation, the flow velocity vector plots were produced at a tenth time interval of the excitation period (5 x 10^{-5} s) for 3 excitation cycles. The vector plots were almost unchanged during the whole excitation cycles except for the fluid region very close to the ultrasonic horn tip. This agrees very well with the other research works on the acoustic streaming (Brennen et al., 1988, Schenker et al., 2013). *Fig. 3* shows one of the plots in comparison with a PIV image from the experiment. The characteristic jet-like acoustic stream underneath the ultrasonic horn tip and a large re-circulating flow structures (marked in red circles in the figure.) are visible. A closer look of the plot shows smaller eddy structures along the acoustic stream, which shows how the kinetic energy of the sonotrode is convected downstream forming the acoustic stream in the liquid.

The velocity profiles of the vertical flow component are compared with the PIV measurements in *Fig. 4*. The figure shows a vertical and horizontal profiles of the average magnitude of the vertical flow velocities at different time stages, which were extracted at the locations marked in *Fig. 3*. The overall predicted velocity magnitude tended to reduce as time passes keeping largely the same profile shapes. The most significant departures from the experiment were that, first, the decay of the acoustic stream along the axis was significantly slower than the measured data, second, the width of the jet-like stream was predicted to be much wider. For example, with the PIV measured data, the velocity magnitude reduces to a half at a radial position of about slightly less than 30 % of the ultrasonic horn tip radius in

x = 0 mm (axis)

Z = 5 mm

Z = 10 mm

Acoustic streaming

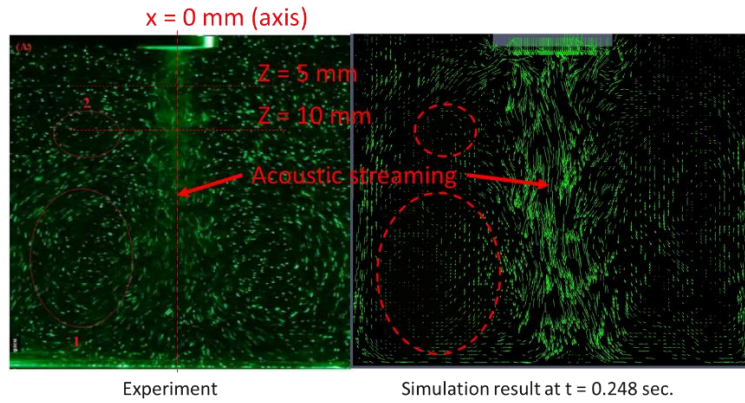Experiment   Simulation result at t = 0.248 sec.

Fig. 3: Comparison of a PIV image from the experiment and a plot of flow velocity vectos.

the right figure below, meanwhile, the simulation predicted it to be at slightly beyond 60 %. However, considering the fact that there are some uncertainties associated with the PIV measurement and the manner in which the flow field is averaged from multiple images that may tend to smear out peaks, the peak value could be regarded reasonably realistic. The decay profile of the acoustic stream needs to be further investigated whether it was caused by the cylindrical bath shape or some neglected physics in the model. With the current cylindrical bath, a focusing of acoustic pressure seemed to happen at a lower section of the bath as a result of the acoustic pressure wave reflections from the walls.
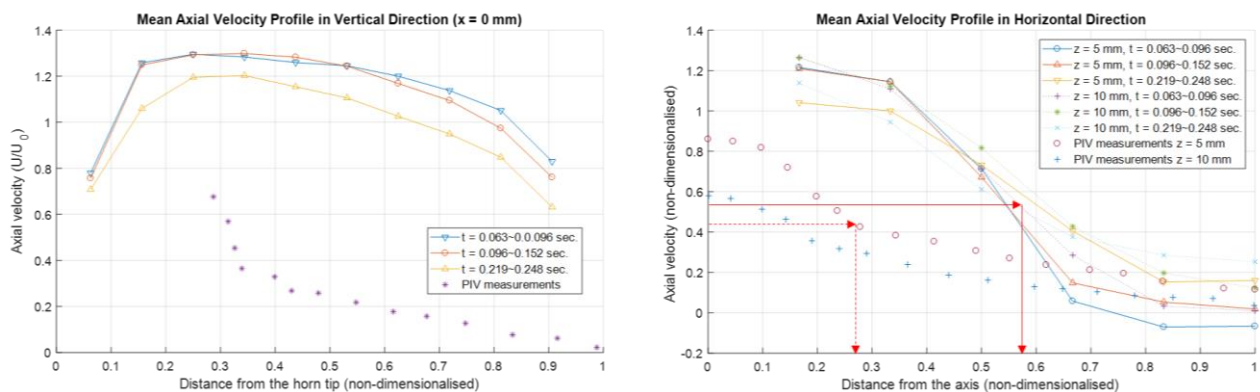
Fig. 4: The acoustic stream velocity profiles.The magnitude of velocities were non-dimensionalised based on the maximum velocity of the ultrasonic horn tip, U_0=2.5133 m/s.

Sub-harmonic oscillation of the acoustic cavitation on the ultrasonic horn tip is one of the most prominent phenomenon in this kind of experimentation. According to Brennen et al. (1988), it was expected a sub-harmonic oscillation at a half the excitation frequency even in an unbounded fluid domain provided the acoustic excitation was strong enough. Therefore, although there was no report of such phenomenon from Rahimi et al. (2017), harmonic analysis of the force acting on the ultrasonic horn tip was carried out to see if such sub-harmonic oscillation was predicted. The analysis was performed with the force data of the horn tip surface for the time duration of 0.192 ~ 0.248 s. Fig. 6 shows the result and it did not show any significant sub-harmonic components. Survey of the vapour volume fraction indicated a weakly alternating cavity oscillation as shown in Fig. 7. The figure shows formation of cavity in alternating manner during a sequence of four oscillation cycles. A part of the horn tip surface is covered with vapour (Fig. 7a), then, in the next cycle (Fig. 7b), the vapour structure is formed on the other part. Similar pair of events continue at another sites as shown in figures 7c and 7d. The sites where cavity was formed appear rather random. Lastly, a comparison between the time-dependent RANS simulation and an LES simulation was carried out which did not create any noticeable differences in the results. Note that the LES simulation had been performed with the same mesh as the RANS case.
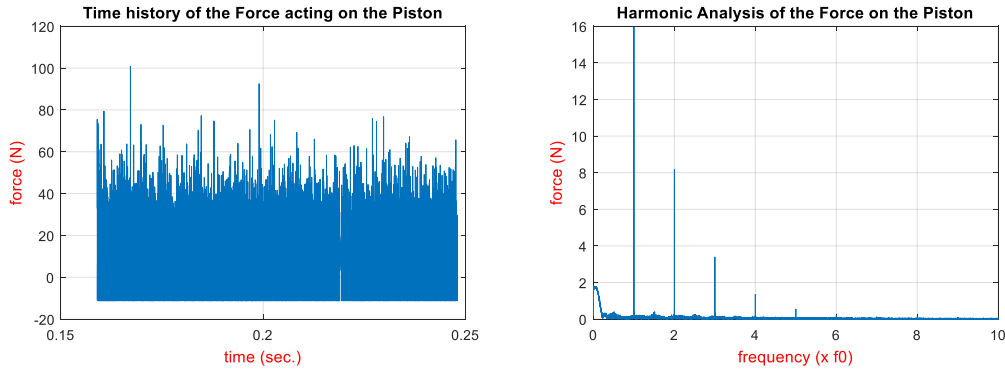
Fig. 5: The force acting on the ultrasonic horn tip in time and frequency domains.
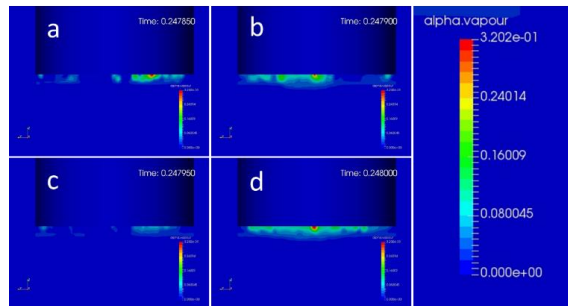
Fig. 6: Vapour volume fraction.

4 Discussion

The acoustic streaming simulation with a barotropic cavitation model appears to agree with the experimental results of Rahimi et al. (2017) in view of general flow features such as forming a consistent acoustic streaming underneath the ultrasonic horn tip which is independent of the vibratory excitation motion. However, comparison of the flow velocity profiles shows a bit wider jet formation and much less dissipation of the kinetic energy of the stream compared with the experimental results.

Another potential issue is a sub-harmonic oscillation of the acoustic cavity and the resulting pressure pulses. Not reported such a behaviour by Rahimi et al. (2017), it is well known to occur in this kind of cavitation events. *Fig. 6* indicates the cavitation events for four consecutive acoustic oscillation cycles. The cavity was formed in such an alternating manner that a cavity was formed on a part of the ultrasonic horn tip surface in one cycle and then formed on the other part in the next cycle. However, the result of the harmonic analysis of the force acting on the sonotrode tip showed only a negligible amount of contribution from it. This may be accounted for the current barotropic cavitation model that does not include any bubble dynamics consideration in connecting the density change to the pressure change.

5 Conclusion

An open source CFD software OpenFOAM provides a compressible viscous multiphase flow solver 'cavitatingFoam'. The solver includes a barotropic cavitation model with several barotropic compressibility models as linear, Wallis and Chung. The linear model was tested to compare with the experimental results of the acoustic stream velocity profiles measured by Rahimi et al. (2017).

The prediction results appear to agree with the experimental result in view of main flow features such as formation of a consistent acoustic stream underneath the acoustic excitation source and the location of forming several number of recirculating flows. However, the current simulation results predict too small turbulence kinetic energy dissipation resulting in too high acoustic streaming barely with any decay in strength. Secondly, it does not appear to be capable of predicting the sub-harmonic oscillation of the acoustic cavitation and the resulting pressure pulses. It is supposed to be due to lack of bubble

dynamics inclusion in the barotropic cavitation model. It will be worth of testing the current multiphase flow solver with a bubble dynamics included in the model to see if the new model could improve the fidelity of the pressure pulses from the sub-harmonic oscillation of the acoustic cavitation. The reasons of the two potential flaws of the simulation will be further investigated.

Acknowledgements

References

A. Boorsma and P. Fitzsimmons (2009). Quantification of Cavitation Impacts with Acoustic Emissions Techniques. 7th International Symposium on Cavitation, Ann Arbor, Michigan, USA.

C.E. Brennen, T. Colonius and F.d. Auria (1988). Computing shock waves in cloud cavitation. Third International symposium on Cavitation, Grenoble, France.

M.S. Chung, S.B. Park and H.K. Lee (2004). Sound speed criterion for two-phase critical flow. *J Sound Vib*, 276(1), 13-26.

Y. Delannoy (1990). Two phase flow approach in unsteady cavitation modelling. Proc. of Cavitation and Multiphase Flow Forum, 1990,

M. Grote and J.B. Keller (1995). Exact Nonreflecting Boundary Conditions for the Time Dependent Wave Equation. *Siam J Appl Math*, 55(2), 280 - 297.

ITTC (2005). The Specialist Committee on Cavitation Erosion on Propellers and Appendages on High Powered/High Speed Ships - Proceedings of the 24th International Towing Tank Conference. International Towing Tank Conference, Edinborough, U.K.

B.G. Kim, P.A. Wilson and S.R. Turnock (2016). Numerical Simulation of An Ultrasonic Vibratory Cavitation Device. 19th Numerical Towing Tank Symposium, St. Pierre d'Ole'ron.

S. Movahedirad (2017). *RE: Interested in your recent work; M. Rahimi et al., "CFD study of the flow pattern in an ultrasonic horn reactor: introducing a realistic vibrating boundary condition", Ultrason. Sonochem. (2016)*. Personal Communication.

M. Rahimi, S. Movahedirad and S. Shahhosseini (2017). CFD study of the flow pattern in an ultrasonic horn reactor: Introducing a realistic vibrating boundary condition. *Ultrasonics sonochemistry*, 35(Pt A), 359-374.

M.C. Schenker, M.J. Pourquie, D.G. Eskin and B.J. Boersma (2013). PIV quantification of the flow induced by an ultrasonic horn and numerical modeling of the flow and related processing times. *Ultrason Sonochem*, 20(1), 502-9.

A.K. Singhal, M.M. Athavale, H. Li and Y. Jiang (2002). Mathematical Basis and Validation of the Full Cavitation Model. *Jounal of Fluid Engineering*,

G.B. Wallis (1969). One dimensional two-phase flow.

A. Žnidarčič, R. Mettin and M. Dular (2015). Modeling cavitation in a rapidly changing pressure field - application to a small ultrasonic horn. *Ultrason Sonochem*, 22(482-92.

Modelling of the Plume of a Submerged Exhaust System

Maarten Klapwijk[*], **Gem Rotte**[*], **Maarten Kerkvliet**[†], **and Tom van Terwisga**[*†]

[*]Delft University of Technology, Delft/Netherlands, [†]MARIN, Wageningen/Netherlands

m.d.klapwijk@hotmail.com

1 Introduction

The Royal Netherlands Navy (RNN) currently operates four diesel-electric Walrus class submarines. The submarines sail submerged on electric engines and periodically recharge the batteries with diesel engines at periscope depth. While recharging, air is taken in with a snorkel mast and exhaust gases are dispelled at the back of the sail, below water level. Figure 1 shows a situation sketch and photograph of this. During the sea trials of the current class of submarines in the nineties, a disturbance on the surface behind the sail was observed, due to rising exhaust gases. The surface elevation was substantial (Fig. 1a) which caused a limited backward visibility, water occasionally flooding the air intake and an increased signature. The elevation was deemed unacceptable and model tests were performed to modify the design and reduce the surface elevation with success. However, the Walrus class is scheduled for replacement around 2025, and a similar power configuration could be used for the new class. To enable evaluating several exhaust configurations the Defence Material Organisation (DMO), responsible for the design and maintenance of the fleet of the RNN, has expressed desire in a numerical model to predict the surface elevation.

(a) Photograph of the sea trial of a Walrus class submarine. The snorkel is the left most mast, on the left of that the surface elevation is visible, Ministerie van Defensie (1990)

(b) Situation sketch

Fig. 1: A photograph and situation sketch of a submarine sailing while using a snorkel.

The numerical modelling is divided in two sections. First a turbulent jet is modelled to determine the required numerical settings, secondly the submarine simulations are performed. This article describes the influence of different turbulence models on the turbulent jet, the verification of the turbulent jet, and the validation of the submarine simulations with experimental data obtained by the Maritime Research Institute Netherlands (MARIN).

The numerical solver used for all simulations is ReFRESCO, which is a multiphase (unsteady) incompressible viscous flow solver using the RANS equations, complemented with turbulence models, cavitation models and volume-fraction transport equations for different phases. For turbulence modelling, both RANS/URANS and Scale-Resolving Simulations (SRS) models such as SAS, DDES/IDDES, XLES, PANS and LES approaches can be used, MARIN (2017).

2 Computational settings turbulent jet

In order to find the required settings for the submarine exhaust case first a single turbulent jet is modelled. The jet is modelled in a three dimensional cylindrical domain, with a round nozzle at the bottom through which air flows with a constant inflow velocity. An overview of the main settings can be found in Table 1, and the domain with boundary conditions as well as the applied computational grid are shown in Figure 2. A QUICK scheme is used for the momentum and the turbulence equation and the transport equation for the volume fraction is handled by a SUPERBEE scheme, which is flux limited, compressive and

TVD. Furthermore, the diffusion terms are treated by central schemes and the time derivatives use an implicit 2nd order backward scheme. A time step is chosen such that the Courant number is lower than 1 in the domain, except in the region immediately above the nozzle where higher Courant numbers occur due to local grid refinement and high velocity of the jet. The effects of surface tension are not implement in ReFRESCO, however based on a dimensional analysis it can be argued that these effects are negligible for this case, see the Bond number in Table 1. Both the surface elevation and the spread of the plume (at four different heights) are investigated. The spread is determined based on the magnitude of the vorticity

$$|\omega| = \sqrt{\omega_x^2 + \omega_y^2 + \omega_z^2} \tag{1}$$

which is compared with a threshold value of 1 Hz. Since the water in the tank is stationary the precise value of the threshold is irrelevant as long as it is larger than 0. To reduce the statistical uncertainty the start-up behaviour is not taken into account, and a time of at least thrice the start-up time is simulated.

Table 1: Main settings for the turbulent jet.

Description	Symbol	Value	Unit
Tank diameter	D	1	[m]
Tank height	H	1	[m]
Nozzle diameter	d	0.01	[m]
Waterlevel height	H_0	0.5	[m]
Inflow velocity gas	V_{gas}	2.64	[m/s]
Reynolds number	Re	$8.3 \cdot 10^3$	[-]
Bond number	Bo	$1.3 \cdot 10^3$ - $2.1 \cdot 10^4$ *	[-]

* Calculated using a surface tension coefficient $\gamma = 0.063$ N/m.

(a) Computational domain   (b) Grid   (c) Nozzle detail
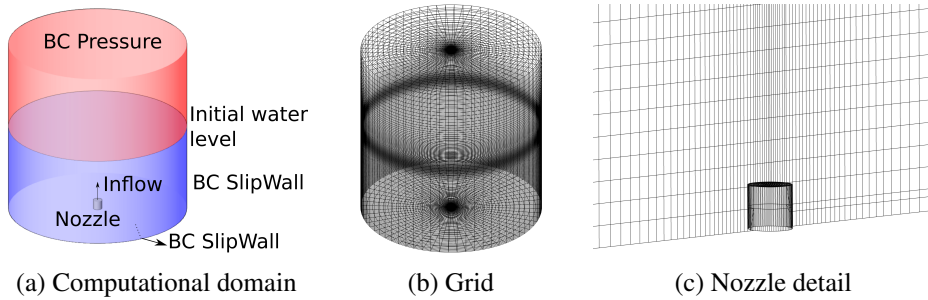
Fig. 2: Computational domain and grid for the turbulent jet.

3 Turbulent jet results

Figure 3 shows the sensitivity of the shape and air distribution in the plume to the applied turbulence model. For visualisation a value of the air volume fraction of 10% used, as is common practice for cavitation modelling. It can be observed that the choice of turbulence model influences the distribution of air in the domain. The Spalart-Allmaras and $(k - \omega)$ SST 2003 model suffer from an over-prediction of eddy-viscosity around the air-water interface (Fig. 3a and 3b). This leads to a stiff (viscous) interface, consequently the air is trapped in the centre of the plume, rather than spread out in the domain. The over-prediction can possibly be remedied with an eddy-viscosity correction, as described by Reboud et al. (1998). The correction is an ad-hoc correction of the eddy-viscosity, given by

$$\mu_t = f(\rho) \frac{C_\mu k^2}{\epsilon} \tag{2}$$

in which $f(\rho)$ is the correction factor, defined as

$$f(\rho) = \rho_g + \left(\frac{\rho_g - \rho}{\rho_g - \rho_l} \right)^n \left(\rho_l - \rho_g \right). \tag{3}$$

In this function ρ_g is the density of the gas, ρ_l is the density of the liquid and ρ is the local cell density. The correction factor is determined by the reduction factor n, which is often taken as 10 in cavitation modelling. The application to the SST 2003 model, with a reduction factor $n = 5$, leads to more instabilities at the interface and a more spread out plume (Fig. 3c). It is questionable to what extent the instabilities on the interface are physical, since they are related to the selected correction method. Therefore the effect of two more advanced turbulence models is investigated.

First the $k - \sqrt{k}L$ (KSKL) model as proposed by Menter et al. (2006) is used. This model is stated to have Scale-Adaptive properties, the model produces an eddy-viscosity small enough to allow the formation of smaller eddies until the grid limit. It is said that the model leads to a LES-like behaviour in unsteady flow regions, and a RANS capability in attached regions. If the KSKL model is applied to the turbulent jet it is observed that the interface is more unstable than for a SST 2003 case and the air spreads out in the domain (Fig. 3d). The inclusion of an eddy-viscosity correction for this model is also tested, this does little to the shape and spread (Fig. 3e). Since the KSKL model leads to an increased spread, the density in the entire domain is close to the density of pure water. Consequently the correction factor $f(\rho)$ is close to 1 and has little influence. The model also has a satisfactory convergence behaviour, the L_∞ norm for all residuals is usually around or below 10^{-6} except for the volume transport equation. The convergence in some time steps stagnates after which the convergence is resumed. This stagnation is usually when a large pocket of air rises from the nozzle. The convergence can be improved by using a parabolic velocity profile instead of a uniform outflow, to reduce the local velocity gradients, Klapwijk (2017).

Secondly, the Explicit Algebraic Reynolds Stress Model (EARSM) by Dol et al. (2002) is used. In this model also the anisotropic nature of turbulence is taken into account, in contrast to the other turbulence models, based on the Boussinesq assumption. The interface is again unstable (Fig. 3f). However the model is accompanied by poor convergence. L_∞ norms of the residuals are generally in the order 10^{-2}, occasionally 10^{-5} is reached. Next to that the convergence stagnates in a large number of time steps.

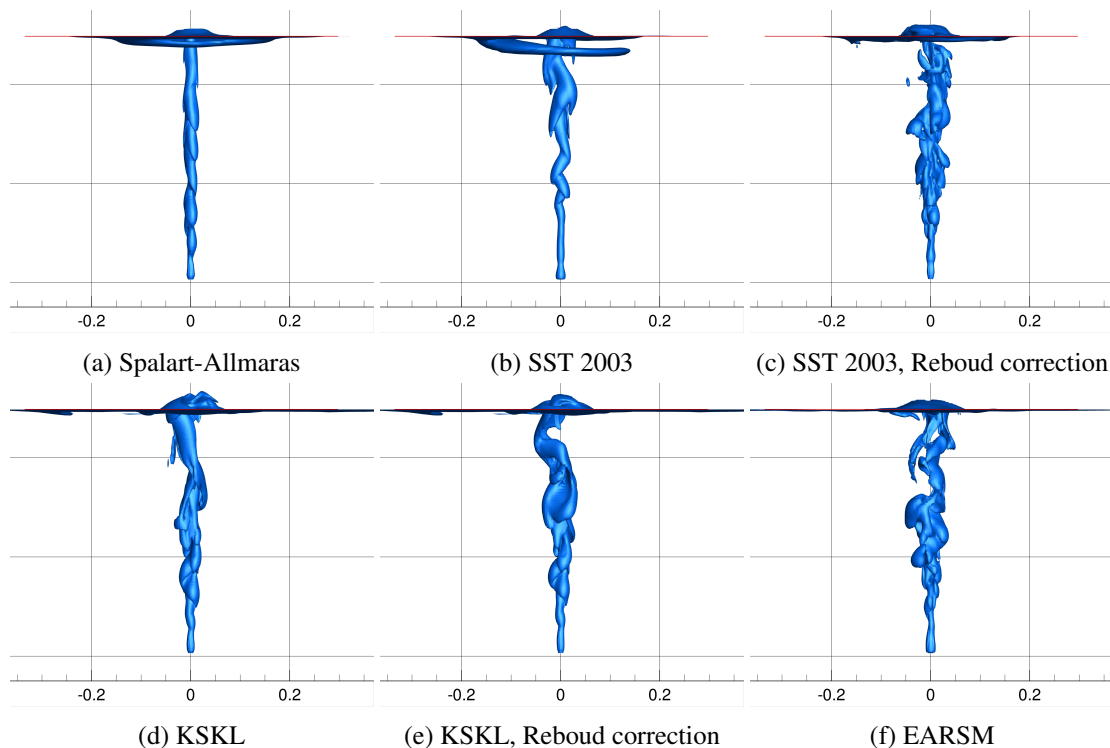|		
(a) Spalart-Allmaras	(b) SST 2003	(c) SST 2003, Reboud correction
(d) KSKL	(e) KSKL, Reboud correction	(f) EARSM

Fig. 3: Isosurfaces of the air volume fraction at $AVF = 0.1$ for the different turbulence models. The horizontal red line indicates the free surface.

Figure 4a shows the influence of the turbulence models on the spread based on vorticity. All models produce results for the mean surface elevation between 2 and 3 cm.

Based on the more physical spreading of air in the domain, the lack of influence on the spread and surface elevation, and the satisfactory convergence behaviour it is concluded that, based on this selected model study, the KSKL model is a suitable choice for this application.

4 Verification

To verify the results, the numerical uncertainty is determined. For this verification study the KSKL turbulence model is used. Numerical uncertainty consists of a round-off error, an iterative error and a discretization error, Roache (1998). Due to double-precision arithmetic the round-off error is negligible compared to the other error sources, Eça and Hoekstra (2006, 2014). It is assumed that the convergence behaviour as described earlier, is acceptable such that the iterative error is negligible compared to the discretization error.

The discretization error is estimated using the method by Eça and Hoekstra (2014). To this end 12 simulations are performed on 4 geometrically similar grids and using 4 different time steps. The error is determined for the spread at four heights and for the surface elevation. The uncertainty estimate for the surface elevation is shown graphically in Figure 4b. For the surface elevation the uncertainty is in the order of 12%, for the spread the uncertainty is in the order of 37% near the nozzle and decreases along the plume to 12%. The larger uncertainty at lower heights is attributed to the fact that the difference between the values in general is small, consequently one large deviation leads to a high percentage. The large uncertainty in general can be attributed to the fact that the process is highly unstationary, there is an influence of a statistical uncertainty. This effect can be decreased to some extent by using an increased amount of time steps, due to the limited computational resources this was not done for this study. Of these estimates the value for the surface elevation is the main interest since this is the final goal of this research.

Validation of the results is difficult due to a lack of proper experimental data. The spread is visually compared with results reported in literature, such as Norwood and Chen (2004), and is the same order of magnitude. For the surface elevation no experimental results are available.

(a) Spread versus height   (b) Discretization uncertainty
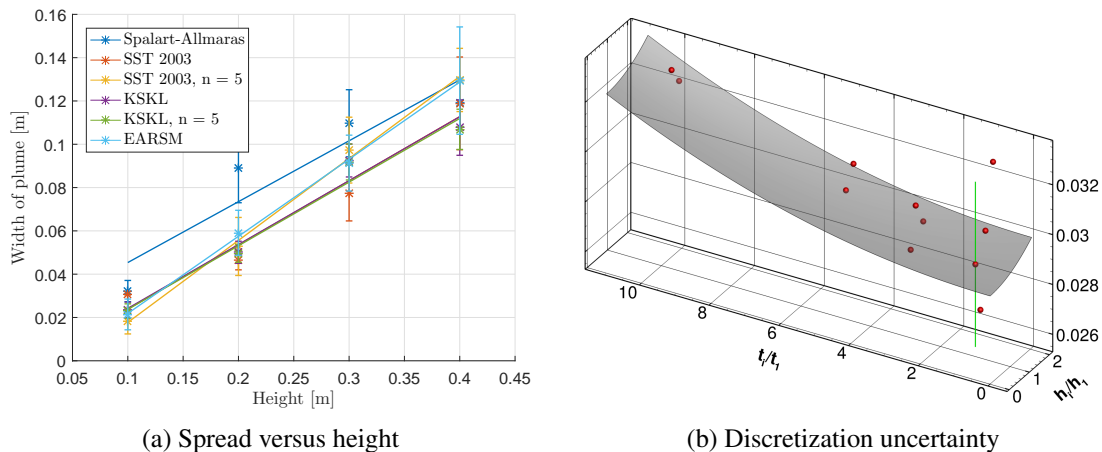
Fig. 4: Spread versus the height for the different turbulence models, and discretization uncertainty for the mean surface elevation for a KSKL turbulence model.

5 Computational settings submarine simulations

Based on the observations for the turbulent jet the original configuration of the Walrus class is simulated and compared with the experimental data as described by Van Hees (1990). Three simplifications are made: only the flow surrounding the sail is modelled (without the hull of the submarine), the control planes on the sail are not modelled, and no incoming waves on the free surface are taken into account. Due to confidentiality reasons in the figures in this section no axes are shown, and no exact values for a number of parameters can be given. Figure 5a shows the computational domain with used boundary conditions.

6 Submarine results and validation

Figure 5b shows a side view of the exhaust plume. Both in the experiments and in the simulations a pulsating behaviour can be observed in the rising air. L_∞ norms for the submarine modelling are generally in the order 10^{-3}, but occasionally less. The decay of the L_∞ norms per time step is around two orders of magnitude. The stagnation of convergence occurs due to the grid refinement in the boundary layer and a high inflow velocity perpendicular to the boundary layer. This yields high Courant numbers near the exhaust. Smaller time steps can improve the convergence behaviour, however they lead to unfeasible long computation times. In this work it is assumed that this convergence is satisfactory to estimate the mean surface elevation. The normalized maximum surface elevation, both numerically and experimentally, are shown in Figure 6.

(a) Computational domain	(b) Side view of the plume behind the sail
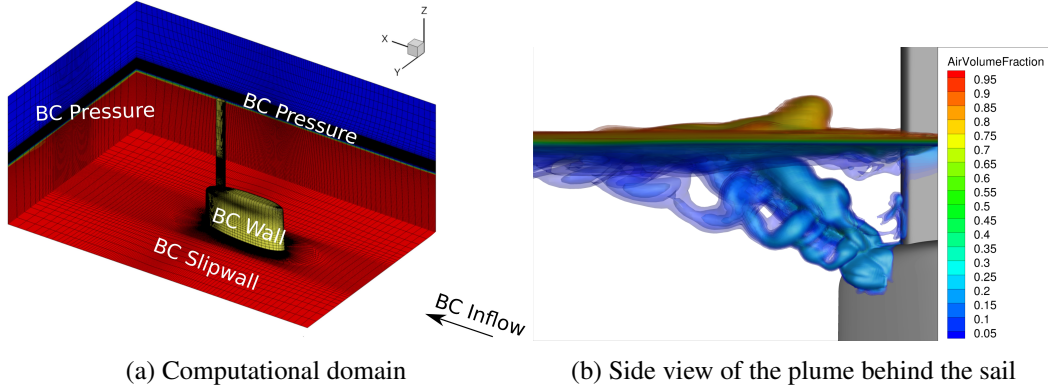
Fig. 5: Computational domain and instantaneous isosurfaces of the air volume fraction of the exhaust plume behind the sail.

(a) Numerical result	(b) Experimental result
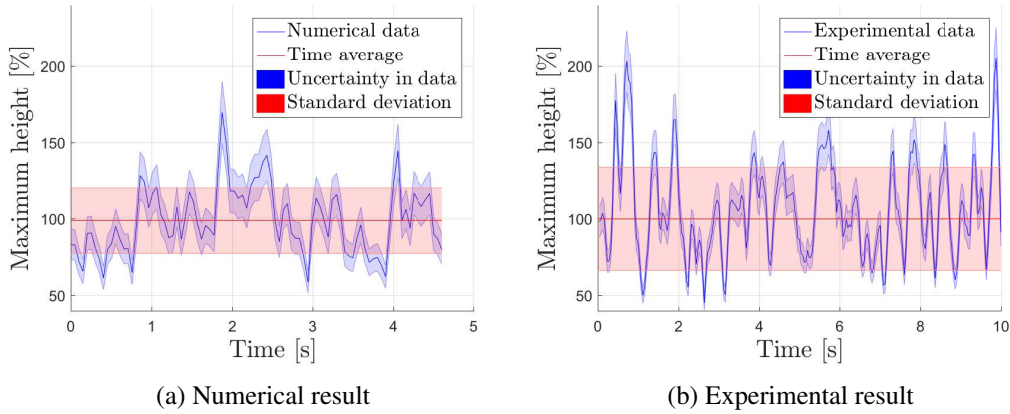
Fig. 6: The development of the mean and standard deviation over time. The results are normalized with respect to the experimental mean height.

The result for the surface elevation is validated with the experiments done by Van Hees (1990) using the method described by Rijpkema and Vaz (2011). Therefore the validation uncertainty

$$U_{val} = \sqrt{U_\phi^2 + U_{inp}^2 + U_{exp}^2} \qquad (4)$$

is compared with the validation comparison error

$$E = \phi_i - \phi_{exp}. \qquad (5)$$

In these equations U_ϕ is the numerical error, which, for the submarine simulations, is assumed to be equal to the error as determined for the turbulent jet. U_{inp} is the input uncertainty, and is assumed to

be negligible. U_{exp} is the experimental uncertainty, and is estimated by the author to be in the order of 10%. Finally ϕ_i is the numerical result, whereas ϕ_{exp} is the experimental result. If $|E| < U_{val}$ the result is validated against the experiments. Table 2 shows the results of the validation process. The mean is validated, the standard deviation is under-predicted and the frequency is over-predicted. This discrepancy is attributed to a difference in definition for the elevation. In the simulations the free surface is defined as an air volume fraction of 0.5, whereas the experimental value is based on camera images. The corresponding air volume fraction for the experimental elevation is difficult to assess.

Table 2: Validation of the numerical results with the experimental results.

	E	U_{val}	Conclusion
Mean	-1.2%	15.6%	$|E| < U_{val}$
Standard deviation	-36.6%	15.6%	$|E| > U_{val}$
Frequency	20.3%	15.6%	$|E| > U_{val}$

7   Conclusion

It is concluded that the code ReFRESCO can be used for the modelling of a submerged exhaust to estimate the mean surface elevation. The estimated uncertainty for the surface elevation result is rather high, in the order of 15%. Based on the tested set of turbulence models, the KSKL model is the most suitable for modelling an exhaust plume. The results for the EARSM also seem promising. For the EARSM it is recommended to investigate whether the convergence can be improved, for instance by using a velocity profile or smaller time steps. Additional experimental results for the turbulent jet are needed to validate the numerical results. For the submarine simulations an additional verification study is recommended, to determine the influence of grid and time step and estimate the numerical uncertainty. This way also the convergence might be improved, which leads to a reduction in iterative error. Finally the experimental uncertainty should be reduced by performing additional experiments, this way the uncertainty in the surface elevation can be reduced. Also by using cameras in multiple viewing directions a better definition of the surface for the validation process can be obtained.

References

Dol, H., Kok, J., and Oskam, B. (2002). Turbulence modelling for leading-edge vortex flows. In *40th AIAA Aerospace Sciences Meeting & Exhibit*, page 843.

Eça, L. and Hoekstra, M. (2006). On the Influence of the Iterative Error in the Numerical Uncertainty of Ship Viscous Flow Calculations. In *26th Symposium on Naval Hydrodynamics*, pages 17–22.

Eça, L. and Hoekstra, M. (2014). A procedure for the estimation of the numerical uncertainty of CFD calculations based on grid refinement studies. *Journal of Computational Physics*, 262:104–130.

Klapwijk, M. (2017). Modeling of the exhaust plume of a submerged exhaust system. *TU Delft Repository*.

MARIN (2017). ReFRESCO description.

Menter, F., Egorov, Y., and Rusch, D. (2006). Steady and Unsteady Flow Modelling Using the $k - \sqrt{k}L$ Model. In *Ichmt Digital Library Online*. Begel House Inc.

Ministerie van Defensie (1990). Movie of the sea trial of Hr. Ms. Zeeleeuw.

Norwood, C. and Chen, L. (2004). Water injection for bubble noise reduction. In *Proceedings of ACOUSTICS*.

Reboud, J., Stutz, B., and Coutier, O. (1998). Two phase flow structure of cavitation: experiment and modeling of unsteady effects. In *Third International Symposium on Cavitation, Grenoble, France*.

Rijpkema, D. and Vaz, G. (2011). Viscous flow computations on propulsors: verification, validation and scale effects. *Proceedings of the Developments in Marine CFD*.

Roache, P. (1998). *Verification and Validation in Computational Science and Engineering*. Hermosa.

Van Hees, M. (1990). Observatieproeven van de onder water uitlaat voor de Walrus-klasse onderzeeboten. Technical report, MARIN.

Shallow water effect for a high block coefficient ship

Hiroshi KOBAYASHI[*]

[*]National Maritime Research Institute, Tokyo/Japan,

1 Introduction

In shallow water condition, forces acting on a hull surface and flow around a hull are different from those in deep water condition. In the paper, numerical simulations based on RANS equation are carried to compute the flow around a high block coefficient ship. The computation is performed with overset grid assembling approach to cope with complex geometries such as a rudder and bilge keels, and to cope with various water depths without re-generating grids around the hull. Brief instructions of numerical procedure, and conditions for an experiment and numerical simulations are described firstly, following the discussion about the computed results comparing with the measured data.

2 Numerical Procedure

2.1 Overset Assembling

Overset grid assembling approach uses a set of grids that enclose the computational domain and overlap each other without requiring face-to-face matching between computational grids. An overset assembling system called UP_GRID (Hiroshi et al. (2016)) is under development in NMRI. The system is based on structured grid approach and covers comprehensive features for overset assembling, i.e., grid generation, grid modification, and computing Domain Connectivity Information (DCI) for overset interpolation. Ferguson spline curve is used to compute curves through grid points and cell centroids for trimming grids and computing DCI robustly and accurately.

2.2 NS Solver

The simulation is carried by a flow solver NAGISA (Ohashi et al. (2014)), which is under development in NMRI. The solver can cope with overlapped grids with DCI generated by UP_GRID. Spatial discretization is based on a finite-volume method and inviscid fluxes are evaluated by the third order upwind scheme based on the flux- difference splitting. The evaluation of viscous fluxes is the second order centered differencing. Artificial compressibility approach is used to velocity- pressure coupling. For free surface treatment, both an interface fitting approach and the level-set method are employed. One and two equations models are available for the turbulence model. In addition, full multi grid method is also available (Ohashi et al. (2016)) not only with a single grid but also with overset grids. Overset interpolation is carried in the finest level because it is hard to avoid occurrence of orphan cells (a cell which does not have appropriate donor cells that can provide values of field variables) in coarser levels due to difficulty of appropriate hole cutting. Cells belonging to coarser grids that include receptor cells of finest grid are treated as receptor cells.

3 Conditions

3.1 Experimental Setup

The experiment in shallow water condition was carried (Fujisawa et al. (2017)) in Middle Towing Tank (width 7.5[m]) in NMRI using a hull called Japan Bulk Carrier (JBC) (Hino et al. (2016)). The particulars of the model of JBC is shown in Table 1. A rudder was installed but no energy saving device was attached. The experiment was carried in four different water depth shown in Table 2. Fig. 1 is a photo of the experiment in Shallow2 case.

Fig. 1: The experiment in shallow water condition

3.2 Computational Conditions

The solution domain is composed of 11 blocks as following list. A coordinate system is right handed and the origin of the coordinate system is located at midship on design water line.
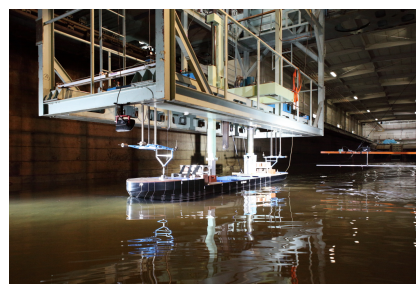
Table 1: Particulars of JBC model				
$L_{PP}[m]$	4.8276	$\nabla[m^3]$	0.9155
$L_{WL}[m]$	4.9138	$S_0[m]$	5.9243
$B[m]$	0.7759	C_B	0.8580
$D[m]$	0.4347	C_M	0.9981
$d[m]$	0.2845	$L_{CB}(\%), fwd+$	2.5475

Table 2: Experimental Condition				
Case	$H[m]$	H/d	$\rho[kgfs^2/m^4]$	$\nu[m^2/s]$
Shallow1	0.405	1.42	101.7990	1.0287
Shallow2	0.615	2.16	101.7909	1.0187
Shallow3	0.790	2.78	101.7909	1.0187
Deep	3.4	11.95	101.7083	0.9326

The axis x is positive streamwise, the axis y is positive from port side to starboard side and the vertical axis z is positive upward. The number of total cells are approximately 21 million. Figs. 2 and 3 show schematic view of grids. Once a set of grids are generated for Shallow 1 case, the set of grids for other H/d cases are easily generated by just adding cells to the bottom of last two rectangular parallelepiped grids without regenerating other grids. This flexibility is the advantage of overset grid approach.

1. An O-O type grid around the rudder.

2. A grid around the stern tube.

3. A rectangular parallelepiped grid behind ship for refinement.

4. An O-O type grid around the bilge keel at starboard side.

5. A rectangular parallelepiped grid for refinement around a bilge keel at starboard side.

6. An O-O type grid around the bilge keel at port side.

7. A rectangular parallelepiped grid for refinement around a bilge keel at port side.

8. An O-O type grid around the hull.

9. A rectangular parallelepiped grid for refinement around water surface. $\Delta_Z/L_{PP} = 1.25 \times 10^{-4}$ at the still water level.

10. A rectangular parallelepiped grid for refinement around the hull grid.

11. A rectangular parallelepiped grid ($-2.5 \leq x \leq 5, -0.777 \leq y \leq 0.777, -z \leq 0.212$) which covers whole domain. The width of the grid corresponds to the one of the Middle Towing Tank, and the minimum value of z should be set corresponding to each water depth.
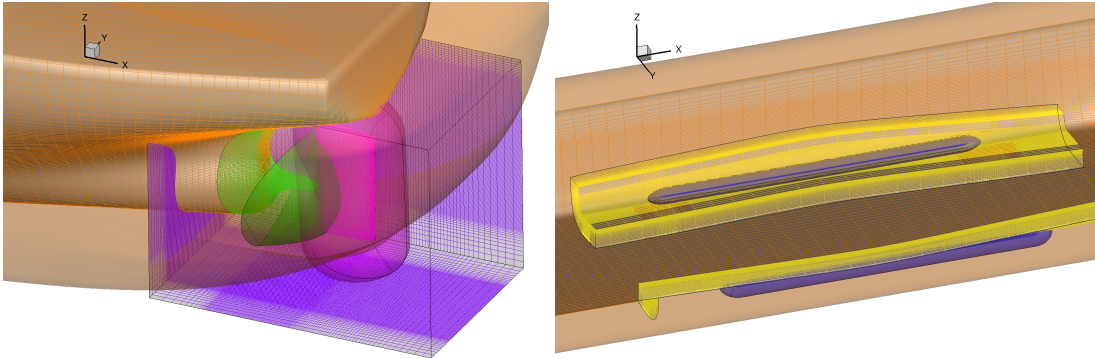

Fig. 2: Left : Computational grids around the rudder and the stern tube. Grid #1(rudder), #2(stern tube), #3(refinement) and #8(hull), Right : Computational grids around the bilge keel. Grid #4,6(bilge keel), #5,7(refinement) and #8(hull)
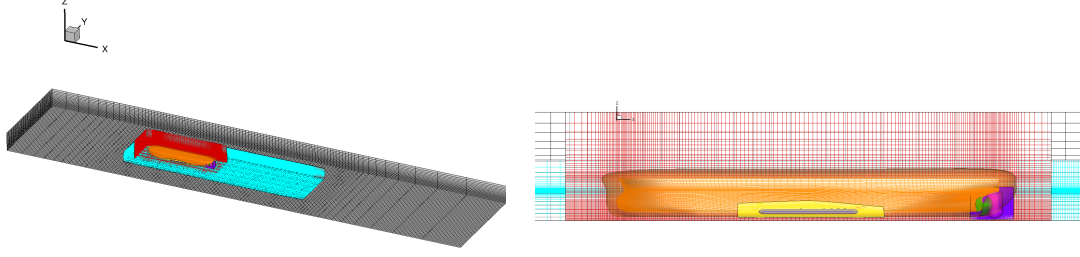
Fig. 3: Left : Computational grids. Grid #8(hull), #9(refinement for free surface), #10(refinement for hull) and #11(solution domain), Right : side view of computational grids(Shallow1)

Boundary Conditions are imposed as Table 3 . p is normalized pressure and u, v, w are normalized velocity components in x, y, z directions, respectively. ϕ is the level-set function for free surface capturing. In the computation, (U, V, W) is set to $(1, 0, 0)$. Level-set approach is adopted for free surface computation. The wall and the bottom of the basin moves with (U, V, W), then the velocity at the boundary should be specified as Dirichlet condition, while the level-set function ϕ should be Neumann condition for reflection.

Table 3: Boundary Conditions

	p	u	v	w	ϕ
Inflow	$\frac{\partial p}{\partial n} = 0$	U	V	W	$-z$
Outflow	$p = 0$	$\frac{\partial u}{\partial n} = 0$	$\frac{\partial v}{\partial n} = 0$	$\frac{\partial w}{\partial n} = 0$	$\frac{\partial \phi}{\partial n} = 0$
Wall and bottom of basin	$\frac{\partial p}{\partial n} = 0$	U	V	W	$\frac{\partial \phi}{\partial n} = 0$
Solid wall	$\frac{\partial p}{\partial n} = 0$	0	0	0	$\frac{\partial \phi}{\partial n} = 0$

Froude number and Reynolds number are $F_n(L_{PP}) = 0.142$ and $R_e(L_{PP}) = 4.596 \times 10^6$, respectively. EASM model is used for turbulence modeling. Full multi grid method with two levels is used to accelerate convergence.

4 Results and Discussions

Table 4 shows the results of integral values. No blockage correction is applied in measured data. For all cases, the hull is fixed to evenkeel condition in the computation. C_T and C_Z are defined as $C_T =$

Table 4: Results of integral values

Case	H/d	Measured	Computed		
		C_T	$C_T \times 10^3$	$1 - w_n$	$C_Z - \frac{\nabla}{0.5 F_n{}^2}$
Shallow1	1.42	8.34	7.67	-0.069	-0.174
Shallow2	2.16	5.65	5.98	-0.053	-0.154
Shallow3	2.78	5.12	5.58	0.245	-0.148
Deep	11.95	4.58	4.68	0.285	-0.137

$\frac{F_X}{0.5\rho U^2 S_0}$ and $C_Z = \frac{F_Z}{0.5\rho U^2 L_{PP}{}^2}$, respectively. The tendency that the resistance increases as H/d decreases is represented in the computed result. The value of nominal wake is negative in small H/d. Fig. 4 shows distribution of axial velocity(u/U) at propeller plane. The large area in which the value of axial velocity is negative, is observed in Shallow1 case. The amplitude of vertical down force due to hydrodynamic pressure ($C_Z - \frac{\nabla}{0.5 F_n{}^2}$) in Table 4 increases as H/d decreases. Fig. 5 shows the pressure distribution on the hull and Fig. 6 shows the distribution of pressure coefficient on the bottom of basin. The pressure distribution around bow on the hull are differ between each case and lower value of C_P is observed in smaller H/d case. These difference of pressure field causes the variation of vertical down force.
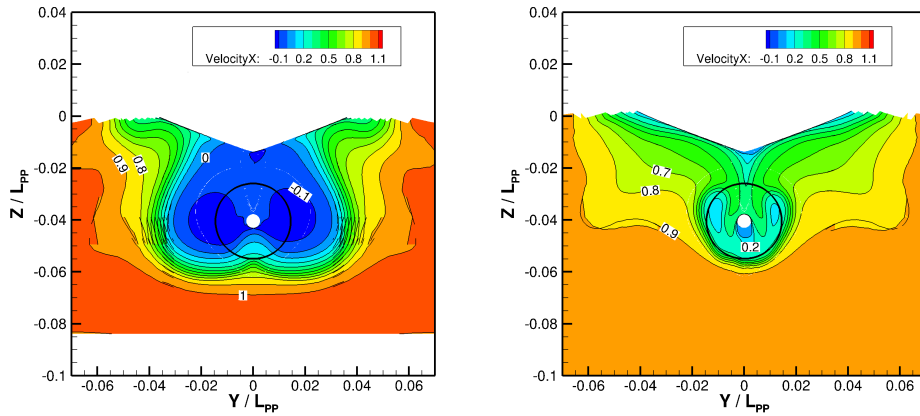
Fig. 4: Axial velocity at propeller plane. $\Delta(u/U) = 0.1$. Left: Shallow1, Right: Deep
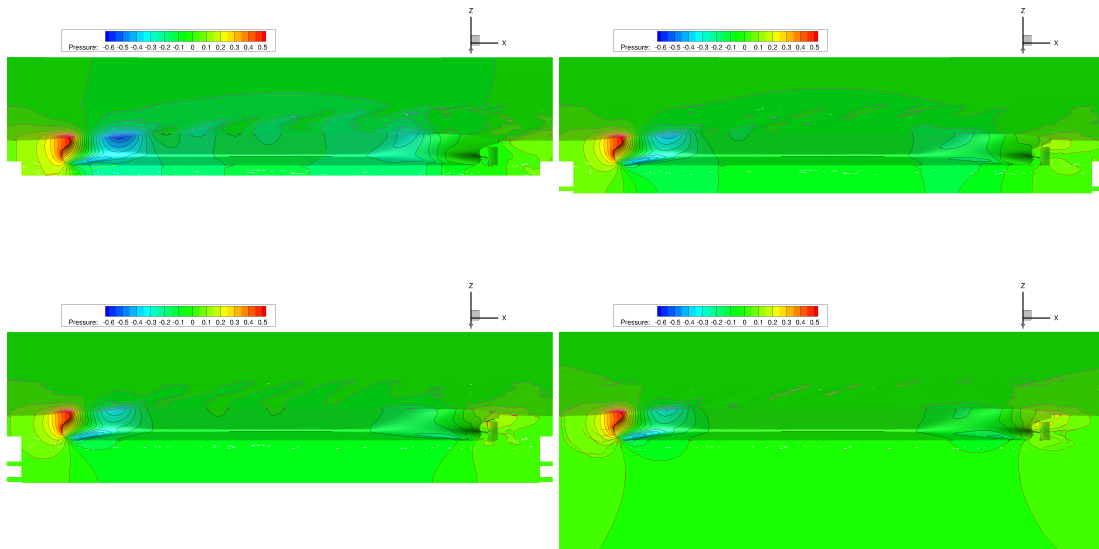
Fig. 5: Pressure distribution on the hull, free surface and sliced plane at $y/L_{PP} = 0$. $\Delta p = 0.05$. Top Left: Shallow1,Top Right: Shallow2, Bottom Left: Shallow3,Bottom Right: Deep

In order to evaluate an effect of sinkage and trim, the computation in given trim condition is carried. Seven blocks around the rudder, the bilge keels, the stern tube and the hull are transformed according to the measured results shown in Table 5 . Fig. 7 shows the values of C_T for measured and computed results. In the most shallow condition ($H/d = 1.42$), computed C_T with given trim condition increased from $C_T = 7.67$ (even keel) to $C_T = 8.67$, while differences between given trim and even keel condition are slight in other H/d . Wave profile on the hull in $H/d = 1.42$ are shown in Fig.8 . Wave height of wave
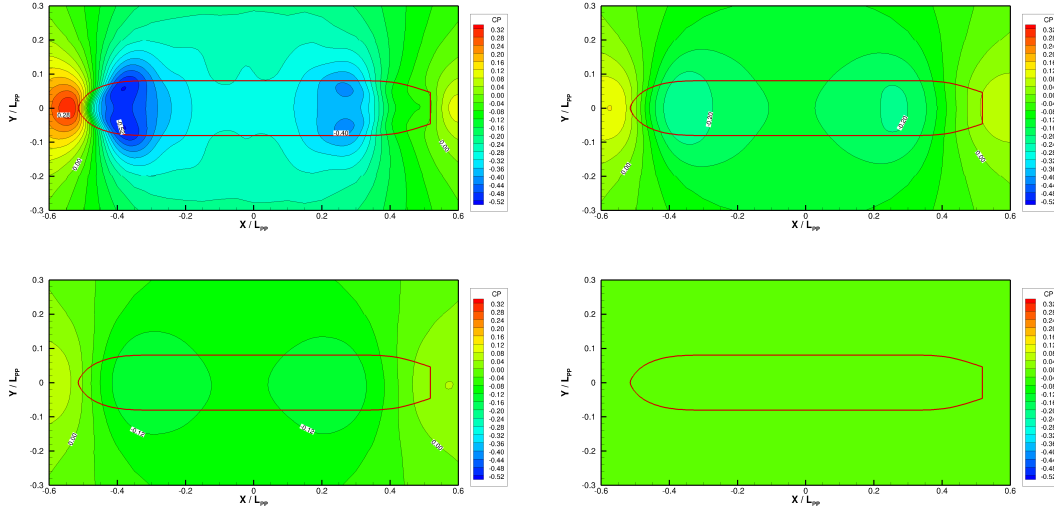
Fig. 6: The distribution of pressure coefficient $C_P = 2p$ on the bottom of basin. $\Delta C_P = 0.04$. Top Left: Shallow1,Top Right: Shallow2, Bottom Left: Shallow3,Bottom Right: Deep

profile on the hull increases in given trim condition corresponding to the increase of C_T . An effect of sinkage and trim is crucial in smaller H/d .

Table 5: Measured results of sinkage and trim

	Shallow1	Shallow2	Shallow3	Deep
sinkage $\sigma/L_{PP} \times 10^3$	5.273	3.199	2.297	0.993
trim τ[deg]	−0.181	−0.114	−0.100	−0.097
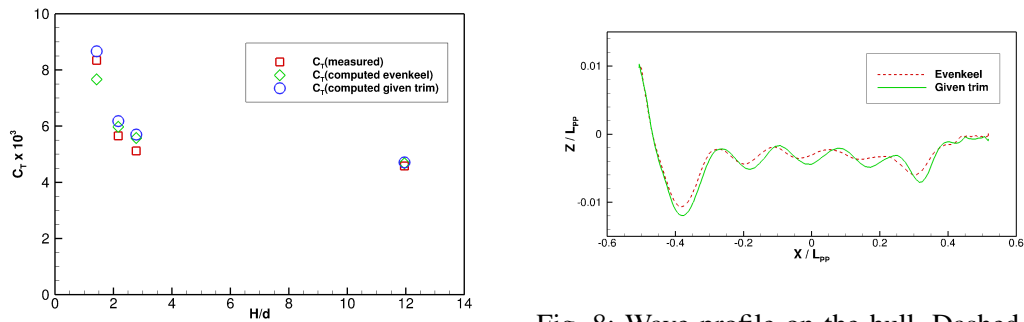
Fig. 7: C_T versus H/d

Fig. 8: Wave profile on the hull. Dashed line: Evenkeel, Solid line: Given trim

5 Conclusion

The computations for high block coefficient ship in various water depth are carried. The computed resistance shows good agreement for tendency depending on water depth. Pressure field around the hull and wake at propeller plane are different between shallow and deep conditions. It is confirmed that the numerical codes have capability to simulate flow field around a ship in shallow water with overset grid approach practically.

References

H. Kobayashi and Y. Kodama. Developing Spline Based Overset Grid Assembling Approach and Application to Unsteady Flow Around a Moving Body. Journal of Mathematics and System Science6 (2016) 339-347, doi: 10.17265/2159-5291, 2016

K. Ohashi, T. Hino, N. Hirata and H. Kobayashi. Development of NS Solver with a structured overset method. Proceedings of 28th CFD Symposium, F06-2, 2014

K. Ohashi, H. Kobayashi. Performance Improvement Of Flow Computations With An Overset-Grid Method Including Body Motions Using A Full Multigrid Method, Proceedings of VII European Congress on Computational Methods in Applied Sciences and Engineering, 2016

J. Fujisawa, R. Fukasawa and M. Tsujimoto, Evaluation of Resistance and Propulsion Performance by Shallow water Tests and Powering in Shallow Water, Journal of the Japan Society of Naval Architects and Ocean Engineers, Vol. 25, pp.47-53, 2017

T. Hino, et. al., Hull form design and flow measurements of a bulk carrier with an energy-saving device for CFD validations, Proceedings of 13th PRADS, 2016

Optimization and Numerical Analysis of "Neighbor Duct" by CFD

**Yosuke Kobayashi[*], Yoshihisa Okada[*], Kenta Katayama[*],
Yasuo Ichinose[†], and Ryohei Fukasawa[†]**

[*]Nakashima Propeller Co., Ltd., Okayama/Japan,
y-kobayashi@nakashima.co.jp, yoshihisa@nakashima.co.jp, ken-katayama@nakashima.co.jp

[†]National Maritime Research Institute, Tokyo/Japan
ichinose@nmri.go.jp, fukasawa@nmri.go.jp

1 Introduction

CFD (Computational Fluid Dynamics) has become large-scale year by year, and it has become possible to solve the flow field around the hull or the propeller accurately in the past few years. For this reason, CFD can be utilized to relatively easily develop energy-saving device. Furthermore, as the demand for energy-saving has increased as a result of the increasing trend of international CO2 reduction such as EEDI regulation. Efficient method by CFD to develop energy-saving hull or device has been required. Under such circumstances, the authors developed a stern duct by utilizing CFD. In the energy-saving device which is set in front of the propellers influences on the propeller revolution speed because of the operation point of the propeller changes. Therefore it is necessary to alter the design of propeller if the affect is large. Moreover, since the behavior of the bilge vortex is difference between the model and the actual ship, it must be to change the geometry of the energy-saving device [1]. However it is difficult to change the geometry of the device between the model and actual ship without numerous actual ship measurement results. In this study, thrust deduction coefficient 1-t was focused on and a duct which improved 1-t due to generate thrust was developed. The optimization method and CFD result of the duct was verified, the performance of the duct was evaluated.

2 Optimization by CFD

Generally, in order to be generated thrust by a stern duct, it is necessary proper angle of attack of a stern duct against an upward flow or a downward flow due to a bilge vortex[2]. On the other hand, "Neighbor Duct" obtains thrust by harnessing flow along sides of hull, the duct has a vertical-long-oval shape so as to be along sides of the hull as much as possible. The shape of the duct was defined by several parameters, and optimization calculation using CFD was performed while changing the parameters. In the optimization, 82,000 DWT Panamax bulk carrier developed by NMRI was used as the target ship. Principal particulars of the hull are shown in Table 1, and the propeller particulars are shown in Table 2. In this study, CFD was carried out on the model scale in order to verify by model test.

Table 1: Principal particulars of hull.

NMRI 82Pana_Max Bulk Carrier			
Condition		Designed Full	
Principal Dimension		Actual	Model
Length Between Perpendiculars	[m]	222	7.631
Length on Designed Load Water Line	[m]	225	7.734
Breadth	[m]	32.26	1.109
Depth	[m]	19.0	0.653
Design Draft	[m]	12.2	0.419
Block Coefficient	[m]	0.87	0.87

Table 2: Principal particulars of propeller.

Principal Dimension		Actual	Model
Diameter	[m]	6.4	0.22
Pitch Ratio		0.6781	0.65
Boss Ratio		0.16	0.16
Expanded Area Ratio		0.495	0.55
Chord Length at 0.7R	[m]		0.0696
Number of Blades		4	4
Shaft Center Line Height	[m]	3.5	0.1203

In this study, SC/Tetra which is a commercial code was used for CFD. The calculation was used the double-body model, and the turbulence model was SST k-ω. Fig.1(a) shows the calculation domain, and (b) the state of mesh around the stern. In the calculation domain, a hull model is placed in a semi-cylindrical watershed, the dimensions of the calculation area are based on the Length of perpendicular (Lpp) of the hull model. The distance from the inlet to the bow equals Lpp, the radius of the cylinder equals Lpp, the distance from the stern to the outlet is twice of Lpp. The propeller thrust and torque were obtained on the propeller disk in Fig.1(b) by infinitely blade propeller theory.
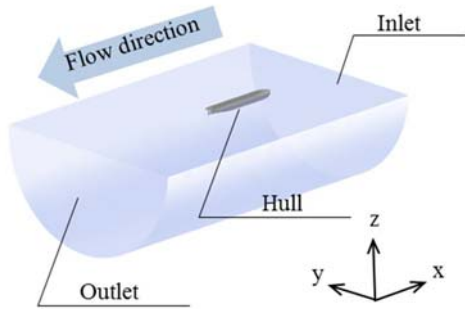

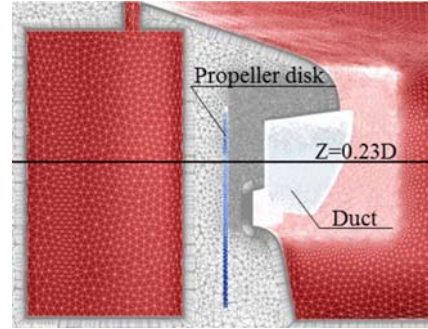Fig. 1(a): Overview of the calculation domain.

Fig. 1(b): The mesh around the stern.

The computational grids were mainly unstructured tetrahedral grids, and the prism grids were used in the boundary layer. The overset grid approach is used for the duct. The grids around the duct are subdivided in order to improve accuracy of the calculation. The total number of cells was 32.6 million, and the dimensionless distance y+ from the wall surface of the first layer of the boundary layer was 1 or less. The coordinates are the center point of the propeller disk as the origin, the x axis in the bow direction, the y axis in the port direction and the z axis in the water surface direction. In the calculation of self-propulsive condition, calculation at 3 different revolution speeds of propeller was performed at design ship speed, and the self-propulsion factor at the self-propulsion point was obtained by interpolation. The hull resistance was calculated without the duct. This resistance was used regardless with or without of the duct when calculate of the self-propulsion factor. Since the double-body model is applied to stabilize the calculation, the wave resistance is evaluated by the tank test results, which obtained from the resistance test conducting at the 400 m towing tank at NMRI. For optimization, self-propulsion factor was calculated for each duct which has difference shape parameter. The ratio of 1-t, 1-w with and without the duct are assumed to be △1-t,   △1-w. The performance of the duct was evaluated of the two values, and other factors were not considered. Fig.2(a) shows the calculation results. The vertical and the horizontal axis represent △1-w and △1-t to plot the values obtained in each self-propulsion calculation on the chart. At the point painted red in Fig.2(a), △1-t is 2.6% and △1-w is -2.9%, and the shape at this point is decided as the optimized duct. Fig.2(b) shows the geometry of the optimized duct.
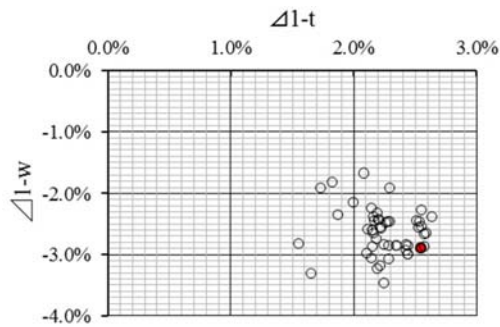
Fig. 2(a): The optimization result.   Fig. 2(b): The geometry of the optimized duct

In the geometric parameters of the duct, having a large influence on the self-propulsion factor were size of the duct, opening angle of the duct and the side projection shape of the leading edge of the stern duct. The side projection shape of the leading edge has a large influence on 1-t. From those, it was found that the mutual position of the leading edge of the duct and the side of the hull is important.

3 Principle of thrust generation by "Neighbor Duct"

The principle of thrust generation was analyzed in the optimized duct by CFD in detail. As Dp is the propeller diameter, and a plane is put on Z = 0.23 Dp as shown in fig.1(b). Fig.3 shows the streamlines and the pressure distribution on the inspection plane in the state with and without the duct. The streamline passes through a point on the inspection plane indicated by purple 'x' mark in fig.3.
As shown in the stream line and the pressure distribution on the plane, the flow along the hull sides flows to the duct with proper angle of attack. Therefore the lift is generated in the duct and thrust is generated. However, since the inside of the duct becomes negative pressure, drag occurs to the stern.
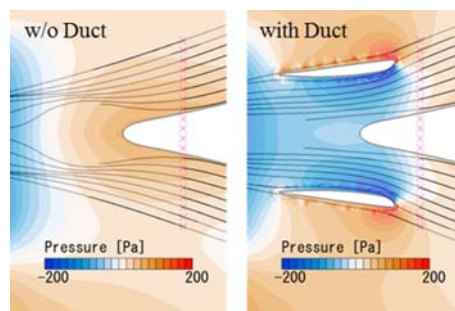
Fig. 3: The stream and the pressure distribution on a plane.

In order to evaluate the force exerted by the pressure in the state of with and without the duct, the normal vector of each surface was multiplied by pressure, and the x direction component Px of them was obtained. Fig.4(a) shows the distribution of Px on the surface of the hull in the state of with and without the duct. A positive value represents thrust and a negative value represents resistance. Comparing Px distribution with and without the duct, Px turns from positive to negative in the region where the surface of the hull is covered with the duct, which indicates that the resistance increased on the surface of the hull with the duct. On the other hand, at the distribution of Px on the surface of the duct shown in fig.4(b) shows a positive value as a whole, and in particular, it can be found that a large thrust is generated at the leading edge from the side portion to the upper portion inside the duct.

In order to compare the resistance and the thrust by the duct, the force Fx which working on the surface of the hull and the duct is obtained from integration Px. Each Fx is shown in Table 3. However, due to the change the flow into the propeller by the duct, the propeller wake flow changes and the resistance value of the rudder changes. The authors focused only on the relation between the hull and the duct, not including the rudder. From Table 3, it can be found that the thrust generated by

the duct is larger than the hull resistance. Therefore the thrust is increased in whole. A relationship between the increase of the hull resistance by the duct and the increase of the thrust by the duct is important for increasing thrust in whole, and the mutual position of the duct and the stern clearly influences to the relationship. This confirms the finding that the influence of the mutual position of the leading edge of the duct and the sides of the hull obtained by the optimization calculation is large. Also, the front edge of the duct side part generates a large thrust and it can be said that increasing the thrust generating part using the vertical-long-oval shape is effective for improving thrust.
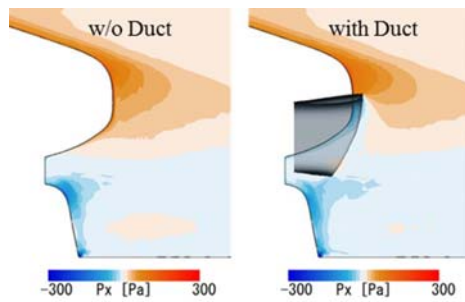
Fig. 4(a): Px distribution on hull surface.
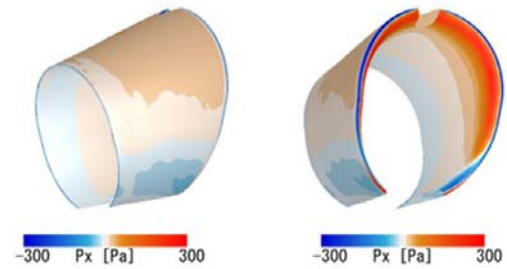
Fig. 4(b): Px distribution on duct surface.

Table 3: The Difference of Fx by the duct.

Region		Hull	Duct	Total
Fx : without duct	[N]	-14.36	-	-14.36
Fx : with duct	[N]	-14.58	0.63	-13.95
Difference	[N]	-0.22	0.63	0.41

4 Model test

In order to verify the results obtained by the optimization calculation, a towing tank test was conducted in a 400 m water tank at NMRI. Regarding the resistance value used for the self-propulsion test, the resistance test value without stern duct was used as a reference regardless of the presence or absence of the duct was same as CFD. Fig.5 shows a photograph around the stern of the model used in the test. The model of the duct was made of resin and made with a 3D printer.

Fig. 5: The hull and the duct model.

Fig.6 shows 1-t and 1-w obtained from CFD and model test at design speed. According to the model test result, $\triangle$1-t and $\triangle$1-w are 2.7% and -0.9%, respectively. Comparing CFD with the results of the model test, the absolute values of 1-t and 1-w are somewhat different, but the trend is consistent. Although $\triangle$1-t is a reasonable calculation result, it proved to be overestimating about $\triangle$1-w.
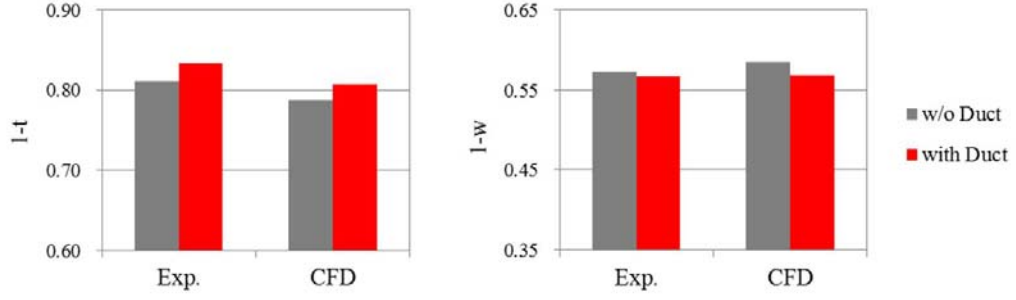
Fig. 6: Comparison of self-propulsion factor.

Fig.7 shows the wake distribution obtained from the CFD and the model test. Comparing the CFD and the result of the model test without the duct, the position of the bilge vortex center and the state of the downwash by the vortex are in good agreement with each other. However at the upper middle part of the propeller disk, 1-w of the CFD result was lower.
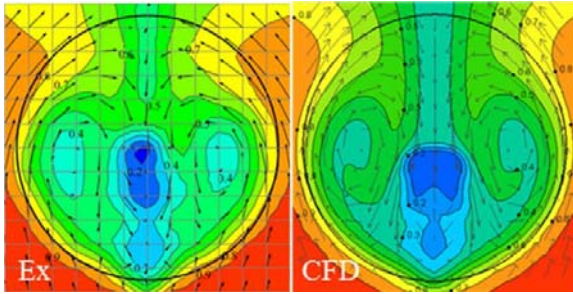
Fig. 7(a): Wake distribution without duct.   Fig. 7(b): Wake distribution with the duct.
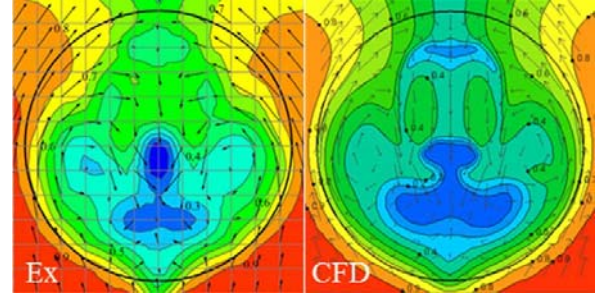
Also, looking at the difference between the two due to the presence or absence of a stern duct, the change of wake by the stern duct is similar, but the degree of decrease of 1-w behind the stern duct is larger for CFD. From these results, it can be said that this calculation method tends to evaluate excessively the deceleration degree of the fluid behind the object, such as a stern end and a stern duct. Therefore, the self-propulsion calculation by CFD seems to overestimate difference of 1-w due to the presence or absence of the duct.

5 The prediction of performance of the actual ship

The performance of the actual ship was predicted based on the model test results. EHP was calculated by three-dimensional extrapolation method from the resistance test result without the duct. The wake coefficient correction 1-Ws with the duct was obtained from Yazaki chart and the following equation[3].

$$1 - W_s = \varepsilon_0 (1 - W_{T0}) - \Delta w \tag{1}$$

$$\varepsilon_0 = (1 - W_s)/(1 - W_T) \tag{2}$$

$$\Delta w = (1 - W_{T0}) - (1 - W_T) \tag{3}$$

W_{T0} : Wake factor without a duct
W_T : Wake factor with a duct
Δw : Influence to wake factor by a duct
ε_0 : Wake correction factor without a duct

Table 4: The prediction of performance of the actual ship.

Condition	Design Draft	
Vs (Knot)	14.2	
Fn	0.1555	
Duct	w/o duct	with duct
EHP (kW)	5,327	5,327
η_R	0.979	0.987
1-t	0.811	0.833
$1-W_T$	0.573	0.567
1-Ws	0.627	0.621
η_H	1.294	1.341
η_{OS}	0.524	0.525
η_S	0.663	0.694
BHP (kW)	8,112	7,752
Ns (RPM)	114.7	113.4

The performance prediction of the actual ship estimation results are shown in Table 4. Effects on each self-propulsion factor by the duct on the actual ship were improved by 2.7% for 1-t, 0.9% for 1-Ws, 3.6% for ηh, 0.9% for ηr and 0.2% for ηo respectively, and BHP is reduced 4.4%. The change amount of 1-Ws is relatively small, therefore there is little influence on the propeller operating point, it can be said that it is not necessary to change the propeller design greatly.

6 Conclusion

Comparison the presence or absence of the duct, 1-t, 1-w, and ηh were improved by 2.6%, 2.9%, and 5.5% respectively in the result of CFD. It was found that not only the size and opening angle of the duct but also the mutual position of the leading edge of the duct and the sides of the hull influences the duct performance. In the model test, 1-t, 1-w, and ηh were improved by 2.7%, 0.9%, and 3.6% respectively by the duct. Comparison the model test and the CFD result, the result of 1-t is a reasonable, however 1-w seems to be overestimate in CFD because of the flow behind the object is excessively decelerated. In this study, although 1-t and 1-w were evaluated equally in optimization, it seems that an evaluation method weighting 1-t is more appropriate. Analysis of the principle of thrust increase of the duct using the CFD result showed that by setting the duct having proper angle of attack regarding to the flow of the side portion of the hull, thrust was found to occur. Therefore, a vertical-long-oval duct which increases the thrust generating part on the side seems to be considered effective for efficiency improvement. The performance of the actual ship was predicted based on the model test results and it was found that the duct reduces BHP of 4.4%. In addition, it is found that 1-w was only decreased 0.9%. The wake flow distribution near the top changes by the duct, therefore it would be considered the influence on cavitation and surface force. In addition, it is necessary to accurately estimation method of the flow behind the duct in order to consider the influence of cavitation by CFD.

References
[1]   Y. Inukai et al., "Energy-Saving principle of the IHIMU semicircular Duct and Its Application to the Flow Field Around Full Scale Ship", IHI Engineering Review., Vol. 50, No.4 pp. 33-38, (2010).
[2]   Universal Shipbuilding Co.,Ltd., "Stern Duct and Ship equipped it", Japan patent 2008-24072, (2008).
[3]   H. Kawashima et al., "Study of Weather Adapted Duct (WAD)", Papers of National Maritime Research Institute, Vol. 14, No.2 pp. 89-104, (2014).
[4]   Y. Ichinose et al., "A Development and Analysis of the New Energy Saving Device USTD", Proceedings of 19th Numerical Towing Tank Symposium, (2016).

Experimental and numerical direct assessment of the weather criterion

Jean-Marc Laurens[*], Shuhaimi Mansor[†], and Arman Ariffin[*]
[*]ENSTA Bretagne/France, [†]UTM/Malaysia
Jean-marc.laurens@ensta-bretagne.fr

1 Introduction

A comprehensive background study of intact stability development was written by Kuo & Welaya (Welaya & Kuo, 1981). Their paper "A review of intact stability research and criteria", stated that the first righting arm curve was proposed by Reed in 1868, but that the application was presented by Denny in 1887. The current Intact Stability (IS) Code 2008 is in force. Except for the weather criterion also called dead ship condition which concerns a ship without motorisation in bad weather, the IS Code 2008 only applies to the hydrostatics of the ship. It does not cover the seakeeping behaviour of the ship and first and foremost, it always considers a ship with a negligible trim angle. In head or following seas, the ship can present a significant angle of trim which may affect the righting arm. To prevent the resulting failure modes, the International Maritime Organisation (IMO) is introducing new generation intact stability criteria (Francescutto & Umeda, 2010). Figure 1 presents the procedure to apply to the second generation intact stability rule.
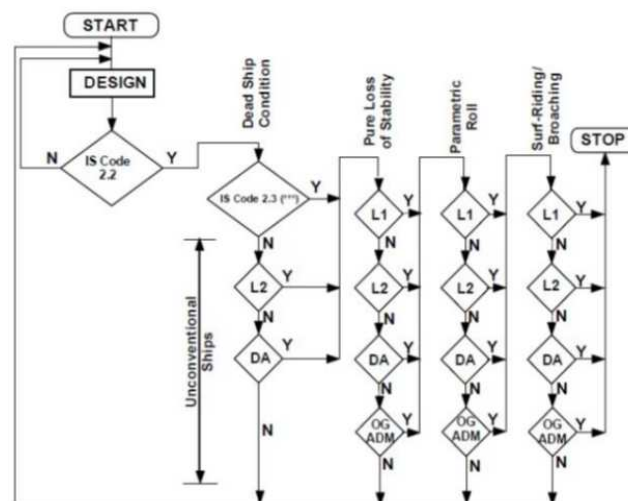
Figure 1. Structure of Second Generation Intact Stability Criteria.

Once the basic criteria have been satisfied, each failure mode has to be verified to satisfaction. Levels 1 and 2 can be verified using a hydrostatic solver only and the Direct Assessment (DA) involves hydrodynamics. While implementing levels 1 and 2 in our existing hydrostatic codes, we wondered what the DA would look like. Discussions among the IMO committee show that we are very far from a satisfactory international agreement on this matter. We therefore decided to design some experimental and numerical procedures to perform a reasonable direct assessment of the existing weather criterion. The weather criterion is item 2.3 of the IS Code 2008 as shown in Figure 1. The ship must be able to withstand the combined effects of beam wind and rolling at the same time. For civilian ships, the conditions are:

   a. *the ship is subject to a steady wind pressure acting perpendicular to the ship's centreline which results in a steady wind heeling lever (lw1).*

b. *from the resultant angle of equilibrium (φ0), the ship is assumed to present an angle of roll (φ1) to windward due to the swell. The angle of heel under the action of the steady wind (φ0) should not exceed 16˚or 80% of the angle of deck edge immersion, whichever is less.*

c. *the ship is then subjected to a gust wind pressure which results in a gust wind heelinglever (lw₂); and under these circumstances, area b shall be equal to or greater than area a, as indicated in Figure 2.*
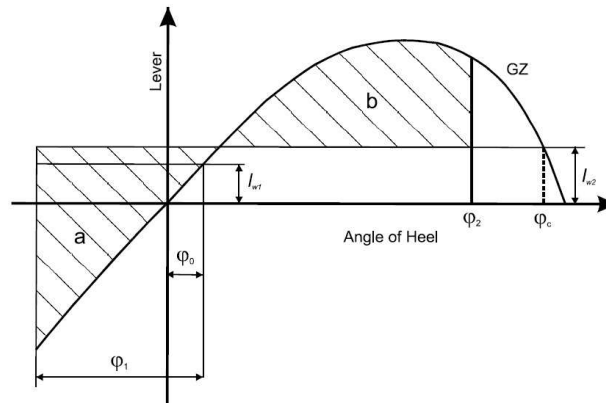
Figure 2. The weather criterion. Civilian rules.
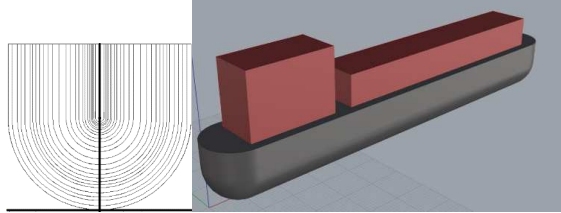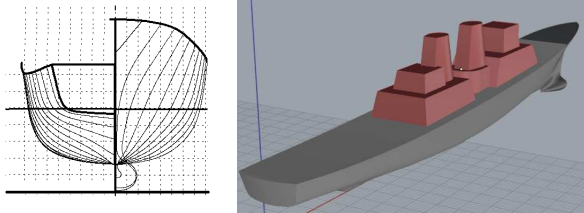
2 The proposed experimental direct assessment

A wind tunnel test was conducted at the low speed wind tunnel facility at Univerisiti Teknologi Malaysia. This wind tunnel has a test section of 2m (width) x 1.5m (height) x 5.8m (length). The maximum test velocity is 80m/s (160 knots). The wind tunnel has a non-uniformity flow of less than 0.15% and a turbulence level of less than 0.06% (Mansor, 2013).

Ship models

Two models were used for the experimental work. The first model is an academic container ship geometry refered to as "ASL shape" in the rest of the paper. The second model is a research ship model, the DTMB 5415 (Molgaard, 2000). The principal characteristics of both models are provided in Table 1.

Table 1. Principal characteristics of both ships

ASL shape		DTMB 5415	
LOA (m)	140.0	LOA (m)	153.3
BOA (m)	20	BOA (m)	20.54
Draft (m)	12	Draft (m)	6.15
Δ (tons)	26,994	Δ (tons)	8,635
VCG (m)	10	VCG (m)	7.555
GM (m)	0.206	*GM* (m)	1.938

Both models were made according to the size of the wind tunnel of the UTM in Johor-Bahru, Malaysia, the scale is 100th. They were constructed at ENSTA Bretagne, France using the Computer Numerical Control (CNC) machine. The material used was polystyrene extrude. Both models designed in 3D drawing and imported to the CNC machine program for fabrication process. The cutting tool forced us to divide the models in several parts. Then, all parts were glued and laminated with fiberglass. The superstructure is made of synthetic glass. The ship models are shown in Figure 3.
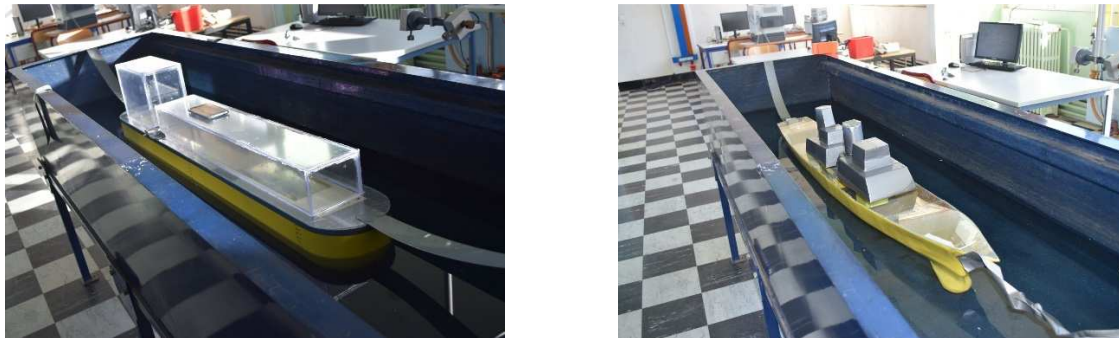
Figure 3. The ASL (left) and the DTMB 5415 (right) models in the righting arm measurement tank.

It was of course essential to verify that they respected the hydrostatic characteristics before shipping the models to Malaysia. The *GM* metacentric heights were verified with the ENSTA Bretagne parallelogram scale by placing the models in a basin. We then measured the natural roll periods of the two models, which were successfully compared with the different formulas proposed in the literature. The experimental design has deliberately been kept simple to be proposed as a direct verification method applicable to the needs of industrial shipbuilding. One does not seek to obtain the rolling movement due to the waves created by the wind. The experimental device must allow the model to be placed in a basin in which it is free to roll. It is placed perpendicularly to the breath. The scale of the models being in the 1/100th, the speed of the wind is the 10th of the real speed. The models had three degrees of freedom (roll, heave and pitch). In a first step, the angle of stability in heel ϕ_0 obtained in the wind tunnel is compared as a function of the wind speed and the angle obtained by the regulatory calculation. For the ASL the experimental curve is above the curve obtained with the rules of the IMO in GHS whereas it is the reverse for the frigate DTMB5415. These are the curves presented in Figure 4. The parabolic shape of the curves for the DTMB5415 is consistent with the fact that the hydrostatic curve is linear over the range of angles considered (0 to 30°) and that the wind pressure follows Bernoulli's rule. The stability curve of the ASL is not linear and the non-parabolic shape of the ϕ_0 curve as a function of the wind speed derives from this characteristic. The origin of the differences between the experimental curves and the curves obtained with the IMO calculations is related to the hydrodynamic force applied to the superstructures. The regulatory calculation used by GHS implies that the aerodynamic drag coefficient of the ship, C_D, is equal to 1.2, regardless of the shape of these superstructures. For the silhouette of the frigate DTMB5415, it is found that the C_D should rather be taken equal to 0.85 which is the case for this type of ship, Luquet 2015. For the ASL shape, which is a simple rectangular parallelepiped, the C_D is greater than 1.2 and decreases when the ship heels. The results are therefore in line with expectations and it is shown that the regulation is not always conservative.
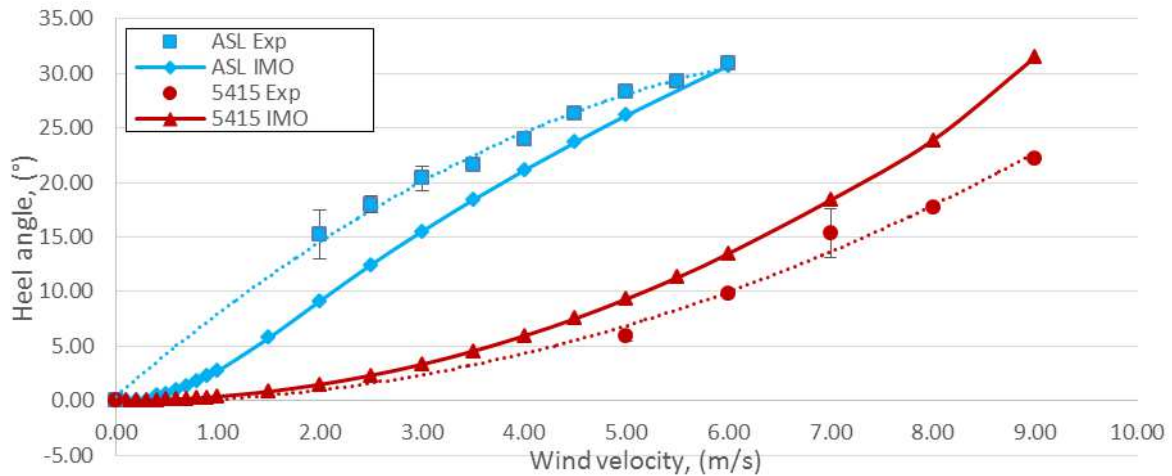
Figure 4 Graph of the angle of stable heel versus wind velocity for the ASL shape and the 5415 shape obtained by experimental results and GHS calculations.

The weather criterion mainly concerns the maximum angle of roll ϕ_2 that the ship will be exposed to during a gust of wind. Since the roll amplitude due to waves, ϕ_1, is not explicitly computed, the intention is to use the value given by the regulatory calculation. The sensitivity of the result to this parameter is checked by examining the result as a function of its value. For both vessels the IMO result is well above the experimental values, which shows that the regulation is very conservative, Figure 5.
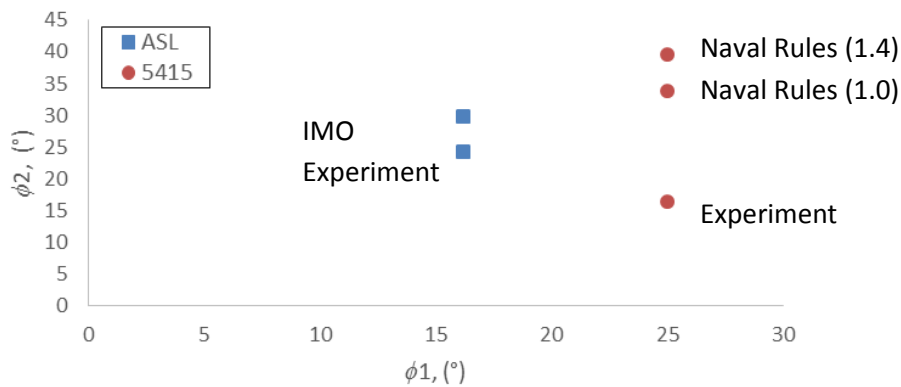
Figure 5. Experimental results versus IMO and naval rules

In the IMO rule, a gust of wind is applied as the ship starts to roll back. Such an event cannot be simulated in the wind tunnel. The wind is applied, ϕ_0 is obtained, the model is placed at a $\phi_0 - \phi_1$ list angle and released, subsequentlythe roll back angle ϕ_2 is measured. Since ϕ_0 is not the IMO value, the vertical scale of Figure 5 is $\phi_2 - \phi_0$, the resulting angle is called $\phi_2{}^*$.

Additional tests have been performed with a bilge keel; we found that the roll back angle is reduced by a little more than 0.7 which corresponded to the allowed reduction for ϕ_1 in the IMO calculation.

3 The proposed numerical direct assessment

If direct verification of the weather criterion can be carried out experimentally, it requires a large wind tunnel, a facility not necessarily available. The other obvious approach is a numerical simulation. The logical sequel of the previous section would be a repetition of the identical procedure using real flow numerical simulation. Ironically, if a wind tunnel was available, the equivalent computer power was not. 3D unsteady Navier-Stokes solvers still require important computer resources which are not yet in the reach of every laboratory. The decision was therefore taken to limit our investigations to 2D calculations. The principle is to show a conservative calculation with respect to reality but less conservative than the regulation in force. The RANSE solver FINE Marine has been used with a k-ω SST turbulence model and the automatic remeshing feature. The models had two degrees of freedom (roll and heave). The roll back angles obtained in the numerical simulations were compared with the experimental results and the IMO rules in Figure 6 for the ASL and in Figure 7 for the DTMB5415. It was first verified that the natural roll period of the 2D shapes was close to that of the 3D shapes. In the IMO rule there is no damping and the drag coefficient is constant and equal to 1.2. The drag coefficient of the 2D shape is higher than the one of the 3D shape and since the ASL should present no other damping than friction, one could expect $\phi 2$ to be higher in the numerical results. The reason why it is not the case is because the drag coefficient of the free rolling shape is very chaotic and on average much lower. The numerical results for the DTMB shape are more difficult to explain and an additional batch of simulations should be carried out.
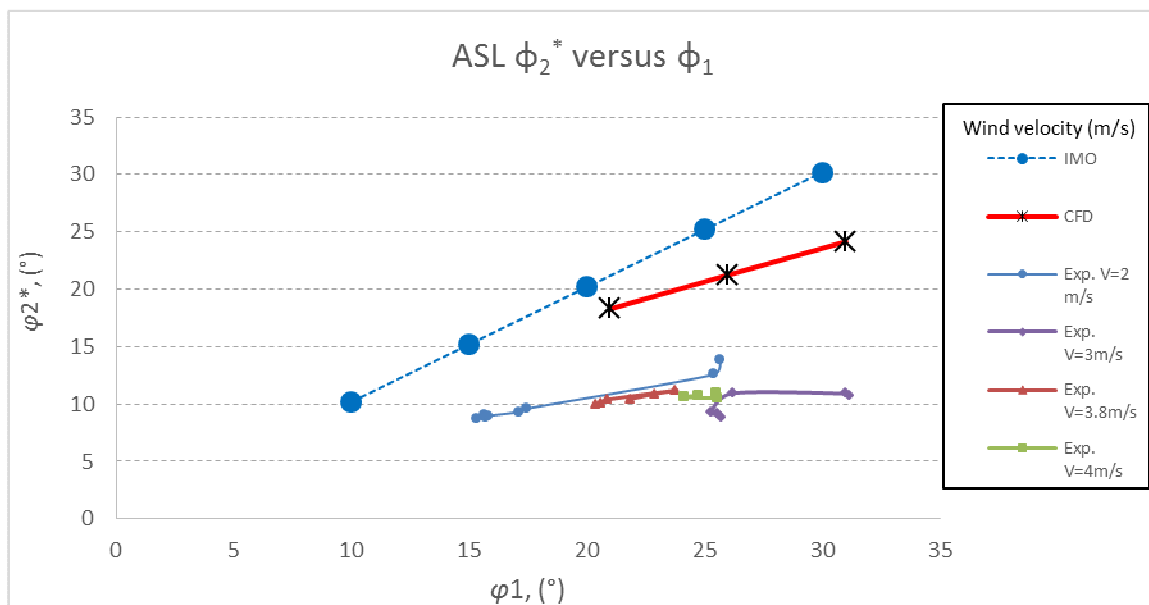
Figure 6. Result comparison for roll back angle ϕ_2* vs roll to windward ϕ_1 for ASL shape
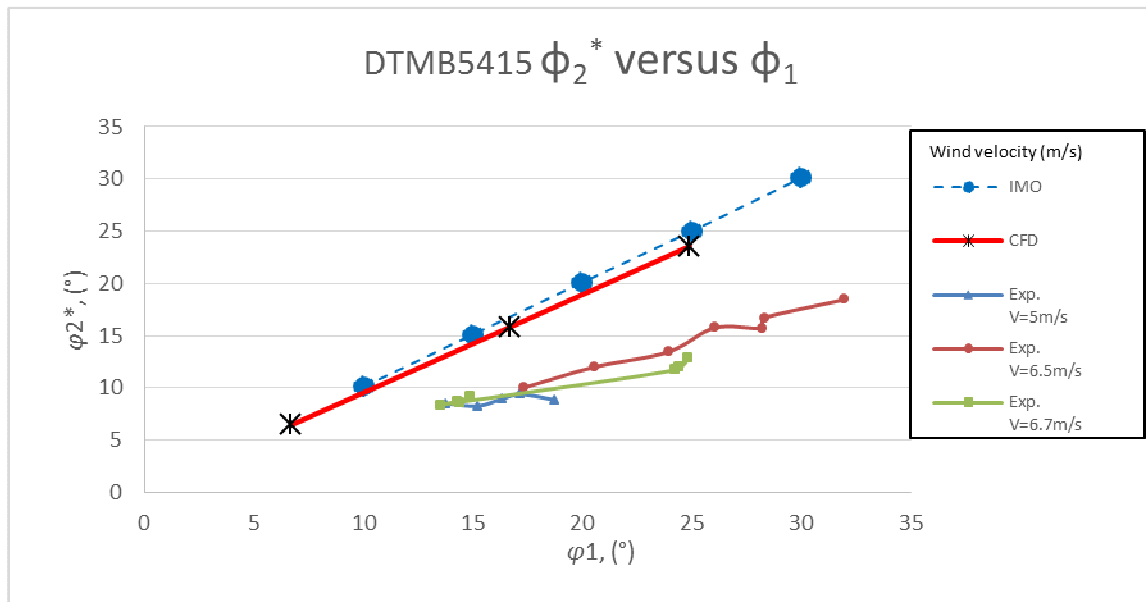
Figure 7. Result comparison for roll back angle ϕ_2^* vs roll to windward ϕ_1 for the 5415 shape

Nevertheless, the hierarchy of the obtained roll back angles shows that both experimental and numerical results are less conservative than the IMO rules.

4 Conclusion

Two direct assessment methods are proposed, a full 3D experimental method and a 2D section numerical method. Results of the experimental method indicate a much lower roll back angle than the IMO rule whilst the numerical simulation results are lower but closer to the IMO rule. 3D simulations would be less conservative and should present results close to the experimental trials. They would also require more important computer resources. As expected the key point for the dead ship condition is the drag coefficient. Some measurements are in progress on the DTMB 5415 shape. Finally, some trials were also conducted with a yaw angle and it was found that a direct beam wind does not necessarily lead to the highest roll back angle. Here again, the drag coefficient of the superstructure is the key point.

References

Welaya, Y, and Chengi Kuo. 1981. "A Review of Intact Ship Stability Research and Criteria." *Ocean Engineering* 8: 65–84.

Francescutto, Alberto, and Naoya Umeda. 2010. "Current Status of New Generation Intact Stability Criteria." In 11th international Ship Stability Workshop. Wageningen, The Netherlands.

Shuhaimi Mansor. 2013. "Measuring Aerodynamic Characteristics Using High Performance Low Speed Wind Tunnel at Universiti Teknologi Malaysia." Journal of Applied Mechanical Engineering 3 (1): 1–7.

Molgaard, Axel. 2000. "PMM-Test with a Model of a Frigate Class DDG-51." Lyngby, Denmark.

Luquet, Romain, Pierre Vonier, Andrew Prior, and Jean François Leguen. 2015. "Aerodynamics Loads on a Heeled Ship." 12th International Conference on the Stability of Ships and Ocean Vehicles, 735-44. Glasgow, UK.

Simulating turbulent transition using Large Eddy Simulation with application to underwater vehicle hydrodynamic modelling

Artur K. Lidtke*, Stephen R. Turnock*, Jon Downes*

FSI Group, University of Southampton, SO16 7QF, Southampton, UK

akl1g09@soton.ac.uk

1 Introduction

Large Eddy Simulation (LES) has been widely used by the aerospace community in order to model laminar separation bubbles (Uranga et al., 2011; Visbal et al., 2009) and other low Reynolds number phenomena.In maritime-related applications this family of turbulence modelling techniques has typically been used to model unsteady cavitation (Bensow, 2011).,Present work aims to apply it to develop first-hand experience with modelling laminar separation bubbles using LES in OpenFOAM, specifically looking at the effects of the choice of the subgrid model. The investigation is carried out on the SD7003 2D foil section, for which PIV flow field measurements, as well as reference CFD results, are available. Four different popular LES models are tested: Smagorinsky, dynamic k-equation, wall-adaptive (WALE), and implicit (ILES). The ultimate goal of this work is to apply the established methodology to model flows on underwater vehicle appendages, as well as propellers, which have been reported to experience noticeable amounts of laminar flow when operating at model-scale Reynolds numbers (Reverberi et al., 2016).These flows experience complex, unsteady hydrodynamic phenomena, such as tip and root vortices, laminar separation bubbles, and are affected by onset turbulence. Thus, studying them with LES could lead to improved predictions compared to the previous work by the authors which relied on using RANS transition models to simulate the flow past underwater vehicle geometries (Lemaire et al., 2016).

2 Methodology

2.1 Smagorinsky model

The turbulent viscosity subgrid model by Smagorinsky (1963) was first introduced in the context of weather modelling and has since seen wide adoption in many spheres of turbulence research. Its OpenFOAM implementation follows a different derivation than typically considered literature. It assumes local equilibrium and then uses the k-equation model formulaiton,

$$\mathbf{B} = \frac{2}{3}k\mathbf{I} - 2\nu_{SGS}\,dev(\overline{\mathbf{S}}). \tag{1}$$

Knowing that $\overline{\mathbf{S}} = \frac{1}{2}\left(\nabla\overline{\mathbf{U}} + (\nabla\overline{\mathbf{U}})^T\right)$, $\nu_{SGS} = C_k\sqrt{k}\Delta$, and $\overline{\mathbf{S}} : \mathbf{B} + \frac{C_e}{2\Delta}k^3 = 0$, the subgrid scale viscosity may be computed. The model thus makes use of two calibration constants, whose values were assumed in this work to be $C_k = 1.048$ and $C_e = 0.094$.

2.2 Wall-adaptive (WALE) model

The WALE model was derived by Nicoud and Ducros (1999) with the purpose of correctly modelling eddy viscosity near solid boundaries without the need for dynamic calculation of proportionality constants, making it attractive from accuracy and efficiency point of view. It has also been used to model transition, which is of particular interest in the present work. where V is the cell volume and $C_w = 0.325$ is a calibration constant. The model defines a modified filter length, $\Delta_S = C_w V^{\frac{1}{3}}$, The eddy viscosity is then computed as

$$\nu_{SGS} = \Delta_S^2 \left(S_{ij}^d S_{ij}^d\right)^{\frac{3}{2}} \left[\left(\overline{S}_{ij}\overline{S}_{ij}\right)^{\frac{5}{2}} + \left(S_{ij}^d S_{ij}^d\right)^{\frac{5}{4}}\right]^{-1}. \tag{2}$$

In Eq. (2) $S_{ij}^d = \frac{1}{2}\left(\left(\frac{\partial u_i}{\partial x_j}\right)^2 + \left(\frac{\partial u_j}{\partial x_i}\right)^2\right) - \frac{1}{3}\delta_{ij}\left(\frac{\partial u_k}{\partial x_k}\right)^2$. The OpenFOAM implementation also requires constants C_k and C_e to be specified but these do not get used in the eddy viscosity computation.

2.3 Dynamic k-equation model

This model by Kim and Menon (1995) differs from the other two models considered so far in that it requires a transport equation for the subgrid turbulent kinetic energy to be solved,

$$\frac{\partial k}{\partial t} + \nabla \cdot (\mathbf{U}k) - \nabla \cdot (D_k \nabla k) = G - \frac{2}{3}k\nabla \cdot \mathbf{U} - \frac{C_e k^{\frac{3}{2}}}{\Delta} + S_k. \qquad (3)$$

In Eq. (3) D_k is the diffusivity constant and C_e is not a constant but is instead dynamically computed based on the filter length and the rate of strain tensor. In the present work the inflow turbulence levels 0.2% were assumed to compute the inflow subgrid turbulence intensity.

2.4 Implicit model

The implicit LES (or ILES) approach does not attempt to formulate an expression for the effect of subgrid-scale eddies on the resolved flow. Instead, it relies on the dissipation provided by the mesh in order to emulate the added viscosity. It has been successfully used in cavitation (Bensow, 2011) and laminar separation (Visbal et al., 2009) modelling contexts and hence is of high relevance here.

3 Simulation set up

The simulation was carried out with chord length and inlet velocity having unit values, which allowed the Reynolds number to be adjusted by changing only the viscosity. This was assigned a value of $1.67{\cdot}10^{-5}$ m^2 s^{-1}, corresponding to a Reynolds number of 60,000, matching conditions in the experiments by Ol et al. (2005) and Burgmann et al. (2008). The angle of attack was set to 4° to match the experimental conditions. All simulations were initialised with a potential flow solution.

Structured meshes of C-grid topology were used, as shown in Figure 1. The grids extended 16 chord-lengths in away from the foil and span of 10% of chord was used, following simulations by Lemaire et al. (2016) who studied the same foil using RANS transition models and found little variation in predicted flow beyond this span-wise domain size. The first grid point away from the wall was located at y$^+$ of 0.2. The stream-wise and span-wise non-dimensional wall spacings were chosen as x$^+$=50 and z$^+$=15, respectively. This follows guidance from the literature which recommends (x$^+$,y$^+$,z$^+$)≤(130, 1, 30) (Choi and Moin, 2012). The resulting mesh constituted of 2.6 million cells, with 250 points placed along the chord and 20 in the span-wise direction. The LES filter length was computed based on the cubic root of the cell volume.

Second-order *fitleredLinear2V* convection and second-order *backward* time derivative schemes were used. Where necessary, additional transport equations were discretised using the first-order upwind scheme. Conservation of momentum and any additional quantities were solved using the preconditioned bi-conjugate gradient (*PBiCG*) solver, and the multigrid (*GAMG*) solver was used for pressure. Implicit pressure coupling algorightm PIMPLE was used to solve the unsteady flow with each of the equations being iteratively solved during several outer loops until L$_1$ norm residual of at most 10^{-7} has been reached. Time advancement was done by fixing the Courant number at 2.5 and letting the solver adjust the time step, which was typically around 0.001 s.

4 Results and discussion

Table 1 shows integral flow coefficients computed using the present simulations in comparison to reference experimental and numerical data. The predicted force coefficients may be seen to diverge by between 8 and 15% from the experimental data in terms of lift and between 30 and 50% for drag, with LES over-estimating both quantities. This trend is consistent for the LES data presented in the literature. Interestingly, the RANS simulations by Lemaire et al. (2016), while also over-predicting the forces, are closer to the measured values with a lift coefficient error of 5% and drag coefficient error of 35%. It may be seen that all the present models predict the location of separation to within 10% compared to each other and reference LES data. However, discrepancies with the experiments are much larger at up to 50% difference. One should note, however, that a very large spread of ±35% from the mean exists within the experimental measurements themselves, making exact quantitative comparison less certain. In terms of the position of reattachment, the range of error magnitudes compared to the experiments is greatly

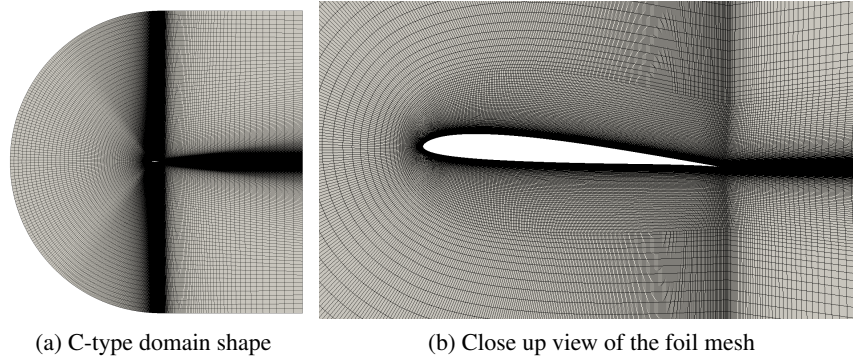(a) C-type domain shape   (b) Close up view of the foil mesh

Fig. 1: Overview of the numerical grid used for all computations.

reduced to between 18 and 32%, while for the reference LES data it varies between 12 and 15%. Notably, the discrepancy between the experiments themselves is also much smaller at approximately ±10%. This much better consistency between the present and published simulations and experiments indicates that the reattachment phenomenon is both better predicted and measured. No experimental data report mean force coefficients, but the present simulations agree well with the published LES data with the lift coefficient errors between 1% and 8%. For the unsteady RANS results by Lemaire et al. (2016) the discrepancy range grows to between 3% and 11%. For the drag coefficient the magnitude of differences between present and published LES data grows to between 9% and 30% and is approximately the same for the reference RANS data. In all cases, the WALE and dynamic k-equation models perform the best to the reference results.

Table 1: Comparison of integral flow coefficients for different tested LES models, as well as experimental and numerical data from the literature. Experimental data from Ol et al. (2005) and Burgmann et al. (2008), reference LES results from Visbal et al. (2009) and Uranga et al. (2011). RANS data with transition modelling from Lemaire et al. (2016).

Data set	$\overline{C_L}$	$\overline{C_D}$	x/c_{sep}	$x/c_{reattach}$	RMS C_L
Present simulations					
ILES	0.6609	0.0342	0.24	0.87	2.6744
Smagorinsky	0.6637	0.0344	0.24	0.88	2.1086
Dynamic k-equation	0.6078	0.0222	0.23	0.67	0.8819
WALE	0.6061	0.0220	0.23	0.65	0.8362
Public domain data					
Selig (Exp.)	0.5575	0.0154			
Burgmann (Exp.)			0.39	0.52	
IAR (Exp.)			0.33	0.63	
TU-BS (Exp.)			0.30	0.62	
AFRL (Exp.)			0.18	0.58	
Lemaire (LCTM URANS)	0.5851	0.0239	0.21	0.73	
Uranaga (ILES)	0.6122	0.0241	0.21	0.67	
Visbal (ILES)			0.23	0.65	
Xfoil	0.6250	0.0190	0.21	0.57	

The origin of these discrepancies may be better understood by analysing the mean distributions of axial velocity and turbulence intensity shown in Figure 2. The Smagorinsky and ILES models may be seen to significantly over-predict the extent of laminar separation, both in terms of the thickness and length of the bubble, compared to the experiments. The remaining two models predict velocity and turbulence iso-contours similar to those measured experimentally. A more quantitative assessment of this behaviour is presented in Figure 3, which depicts velocity cuts along several sections perpendicular

to the chord line of the foil. The data reveal close agreement between the WALE and dynamic k-equation models and the experiment, although the LES results appear to over-estimat the thickness of the laminar separation bubble by approximately 6% consistently over the entire length of the foil.

(a) ILES

(b) Smagorinsky

(c) Dynamic k-equation
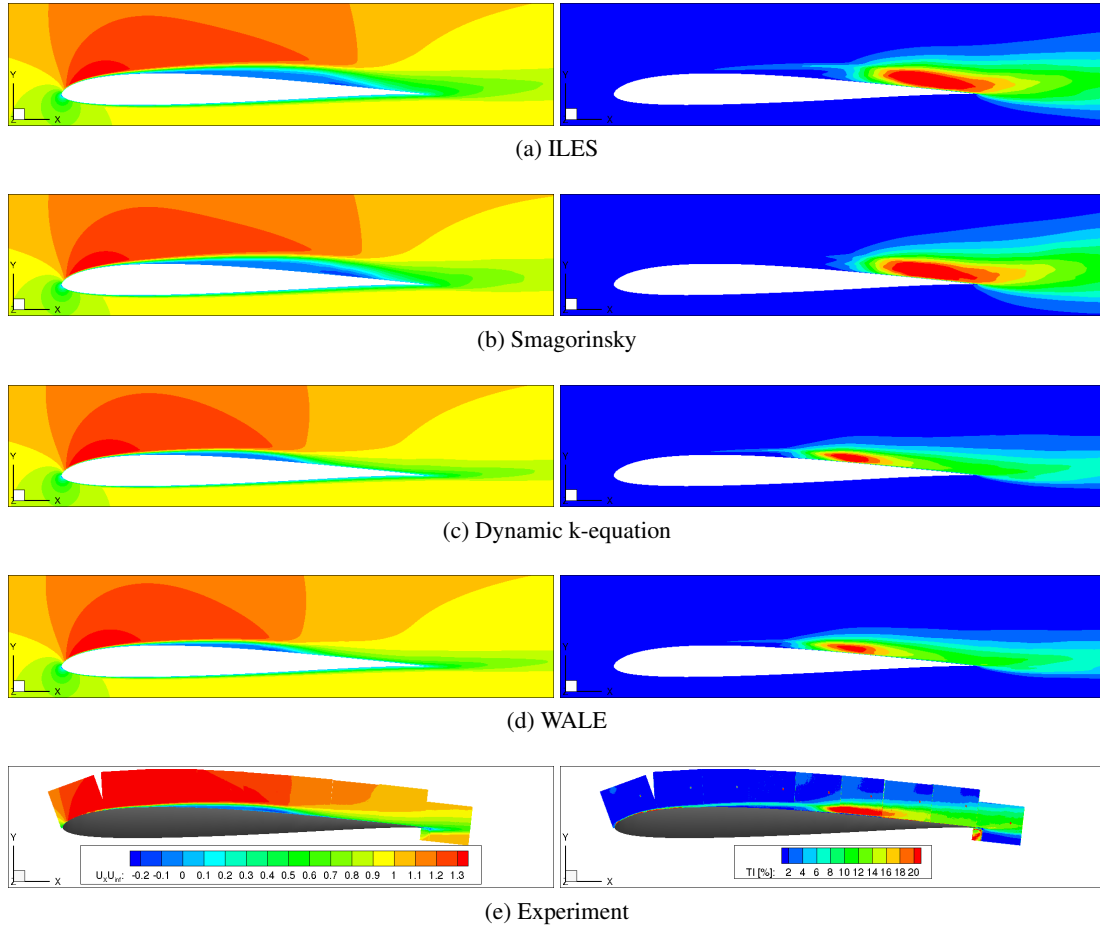

(d) WALE

(e) Experiment

Fig. 2: Mean axial velocity (left) and turbulence intensity (right) contours at the mid-span of the foil for different LES models, including experimental PIV data by Burgmann et al. (2008). All sub-figures use the same colour scales as shown for the experiments. Turbulence intensity computed as $TI = \sqrt{\left|\frac{1}{3}\overline{u_i' u_i'}\right|}$.

It is interesting to note how the over-predicted size of the laminar separation bubble affects the unsteady nature of the flow. Figure 4 presents the time history and power spectral density functions of the predicted lift coefficient. The approximately 8% difference in mean C_L between the two simpler and two more complex considered models is easily discernible. One may also note how all models are affected by frequencies between Strouhal numbers of 0.18 and 0.22. However, the Smagorinsky and implicit methods predict a much more pronounced higher frequency content between St 1 and 4, and also predict prominent peaks at St of 0.55 which are not visible in the WALE and dynamic k-equation model data.

The origin of this behaviour is due to the models predicting larger separation bubbles also computing much larger coherent vortices in the wake of the foil. This may be seen in Figure 5 showing instantaneous iso-contours of the λ_2 criterion. Because the turbulence in the wakes predicted by WALE and dynamic k-equation models is much finer and approaches an isotropic state much faster, the unsteady load variations caused by them have less of an influence on the force coeffcient. This makes the principle shedding frequency at St of approximately 0.2 stand out much more in the energy spectra compared to the ILES and Smagorinsky models.
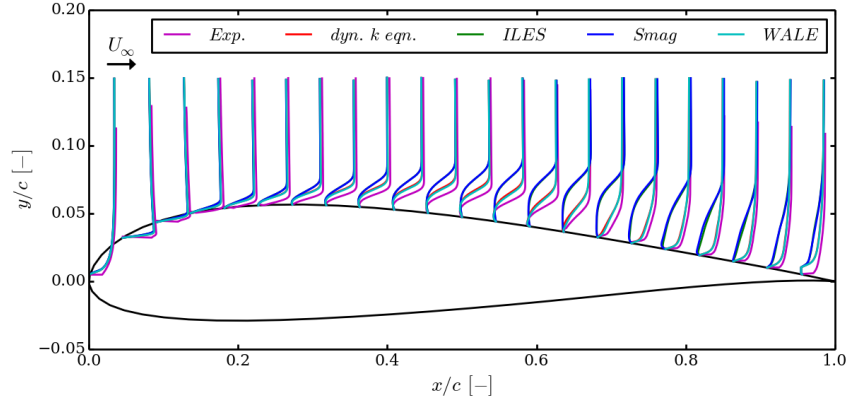
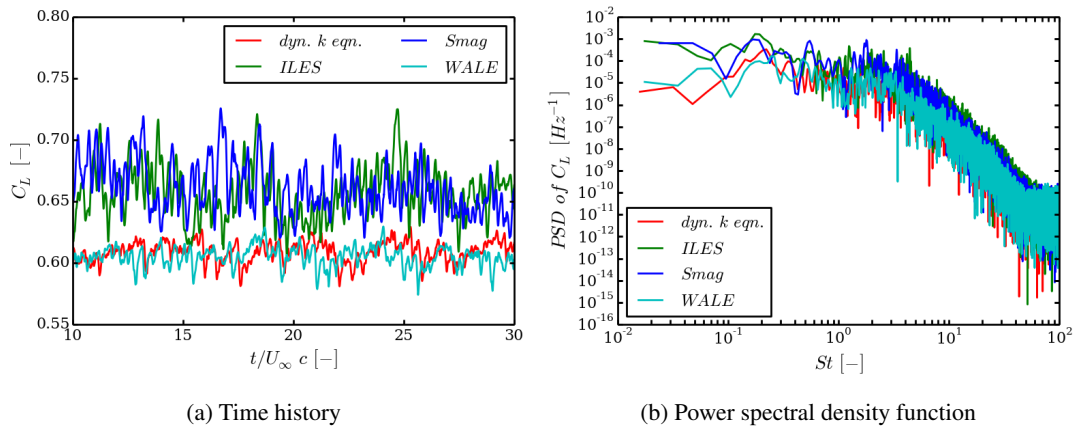Fig. 3: Mean axial velocity at cuts spaced along the chord line of the foil.

(a) Time history

(b) Power spectral density function

Fig. 4: Overview of the numerical grid used for all computations.

5 Conclusions

Comparison of the four different subgrid LES models has shown that the wall-adaptive eddy viscosity (WALE) and dynamic k-equation subgrid models perform better than their Smagorinsky and ILES counterparts at modelling flows undergoing laminar separation. This is evident from the size and position of the separation bubble being better with the former two models. For all models the vortices shed off from the trailing edge of the separation bubble are predicted to stretch the entire span-wise extent of the numerical domain. Due to the much larger size of the recirculating flow region in the case of Smagorinsky and ILES models, the predicted shed vortices are much larger and remain coherent further downstream.

The results have shown poor agreement with the experiments regarding the position of separation which is predicted to occur earlier than in the experiments with errors up to 50%. All of the models methods appear to be in good agreement with each other in this respect. Presence of significant discrepancies among the experimental measurements indicates difficulties in conducting quantitative measurements of this quantity, which somewhat discredits the argument against the accuracy of the numerical methods. Position of the reattachment is predicted better with errors around 20%, although it is found to occur further downstream than what was reported experimentally. The thickness of the recirculating flow region forming the laminar separation bubble is over-predicted by approximately 6% with respect to the measurements. The overall larger size of predicted laminar separaiton bubbles leads to over-estimation of the lift and drag coefficients, leading to errors of approximately 8% for the lift and 30% for the drag.

The computational expense to simulate 100 non-dimensional time units was approximately 120 CPU-hours per 10,000 cells and did not vary significantly between the different turbulence models. This, while

significant, indicates that with sufficient computational resources and mesh resolution the models should be capable of capturing transition and complex three-dimensional flow features on underwater vehicle appendages and model-scale propellers.
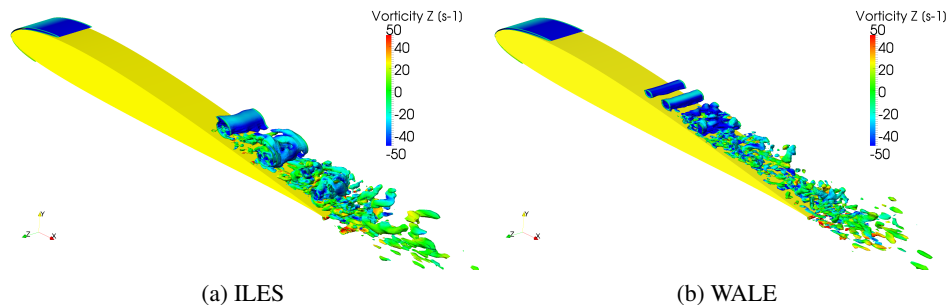

(a) ILES   (b) WALE

Fig. 5: Comparison of instantaneous $\lambda_2 = -150$ iso-contours for two considered LES models showing the different predicted size of vortices shed off the trailing edge of the separation bubble. Coloured by the span-wise vorticity component indicating the amount of turbulent mixing.

Acknowledgements

References

Bensow, R. (2011). Simulation of the unsteady cavitation on the the Delft Twist11 foil using RANS, DES and LES. In *2nd International Symposium on Marine Propulsors*, Hamburg, Germany, June.

Burgmann, S., Dannemann, J., and Schroder, W. (2008). Time-resolved and volumetric PIV measurements of a transitional separation bubble on an SD7003 airfoil. *Experiments in Fluids*, 44(4):609–622.

Choi, H. and Moin, P. (2012). Grid-point requirements for large eddy simulation : Chapman's estimates revisited. *Physics of Fluids*, 24.

Kim, W.-W. and Menon, S. (1995). A new dynamic one-equation subgrid-scale model for large eddy simulations. In *33rd Aerospace Sciences Meeting and Exhibit*, Reno, NV, USA.

Lemaire, S., Lidtke, A. K., Vaz, G., and Turnock, S. R. (2016). Modelling Natural Transition on Hydrofoils for Application in Underwater Gliders. In *19th Numerical Towing Tank Symposium (NuTTS)*, 3-4 October, St Pierre d'Oleron, France.

Nicoud, F. and Ducros, F. (1999). Subgrid-scale stress modelling based on the square of the velocity gradient tensor Subgrid-scale stress modelling based on the square of the velocity gradient tensor. *Turbulence and Combustion*, 62(3):183–200.

Ol, M. V., McCauliffe, B. R., Hanff, E. S., Scholz, U., and Kähler, C. (2005). Comparison of Laminar Separation Bubble Measurements on a Low Reynolds Number Airfoil in Three Facilities. *35th AIAA Fluid Dynamics Conference and Exhibit*, pages 1–11.

Reverberi, A., Lloyd, T., and Vaz, G. (2016). Towards cavitation modelling accounting for transition effects. In *219th Numerical Towing Tank Symposium (NuTTS)*, St Pierre d'Oleron, France.

Smagorinsky, J. (1963). General circulation experiments with the primitive equations I: the basic experiment. *Monthly Weather Review*, 91(3):99–164.

Uranga, A., Persson, P., Drela, M., and Peraire, J. (2011). Implicit Large Eddy Simulation of transition to turbulence at low Reynolds numbers using a Discontinuous Galerkin method. *International journal for numerical methods in engineering*, 87(October 2010):232–261.

Visbal, M. R., Gordnier, R. E., and Galbraith, M. C. (2009). High-fidelity simulations of moving and flexible airfoils at low Reynolds numbers. *Experiments in Fluids*, 46:903–922.

On the Decay of Freestream Turbulence Predicted by Two-equation Eddy-viscosity Models

Rui Lopes[1], **Luís Eça**[1], **and Guilherme Vaz**[2]
[1] Instituto Superior Técnico - University of Lisbon,
[2] Maritime Research Institute Netherlands
rui.a.lopes@tecnico.ulisboa.pt

1 Introduction

As reported before by Spalart and Rumsey (2007), the decay of freestream turbulence in two-equation eddy-viscosity turbulence models is overestimated. In simulations of external flows at high Reynolds numbers that assume "fully turbulent" flow, this excessive decay has a negligible impact on the solution. The laminar regime is confined to a very small region near the leading edge of the body and so the correct prediction of transition is not relevant. On the other hand, in model scale experiments it is common pratice to force transition through the use of trip wires or roughness. Therefore, as illustrated for example in Eça and Hoekstra (2006), the incorrect prediction of the transition location by two-equation eddy-viscosity models becomes an asset instead of a problem.

Nowadays there is an increasing focus on low Reynolds number applications such as underwater gliders, UAVs and wind turbines, which operate in the Reynolds number range of 10^5 to 10^6. In such cases, the correct prediction of transition from laminar to turbulent flow becomes essential and so standard two-equation models are not adequate to perform such simulations.

This known shortcoming of the most common turbulence models led to the development of transition models, as for example the $\gamma - Re_\theta$ model by Langtry and Menter (2009), which supplements the two-equation eddy-viscosity SST $k - \omega$ model proposed in Menter (1984), Menter (2003). Its local formulation and capability to account for several transition mechanisms such as natural transition, bypass transition and separation-induced transition make it an attractive option.

The onset of transition is strongly dependent on the level of the free-stream turbulence intensity, which makes the excessive decay of turbulence predicted by the SST $k - \omega$ model troublesome. In most of the applications of the $\gamma - Re_\theta$ published in the literature, this shortcoming of the SST $k - \omega$ model is overcomed by specifying values of the inlet eddy-viscosity $(\nu_t)_{in}$ significantly larger than the kinematic viscosity ν. It is not unusual to find values of $(\nu_t)_{in} = 100\nu$ or even larger, which is at least questionable. On the other hand, when $(\nu_t)_{in}$ is kept at values smaller or equal than ν, the dissipation terms of the k and ω transport equations must be modified to obtain the desired level of turbulence intensity at the leading edge of the body, as discussed in Spalart and Rumsey (2007) and Eça et al. (2016).

The goal of this work is twofold:

1. Demonstrate that the onset of transition is essentially determined by the local value of the turbulence kinetic energy k.

2. Modify the SST $k - \omega$ turbulence model to obtain a decay of free-stream turbulence that does not require the use of awkward values of $(\nu_t)_{in}$ to obtain the correct location of the onset of transition. This modification requires two steps

   (a) Recalibrate the constants of the dissipation terms of the k and ω transport equations for free-stream turbulence using the data available from the ERCOFTAC database.

   (b) Introduce a new blending function that guarantees the use of the standard constants in the viscous region of the flow and the new constants in the free-stream. Identification of both regions is made from the value of the dimensionless total head.

In this paper we present the first step of this development that is performed for the flow over a flat plate, for which there are experimental data available for transitional flows with different levels of free-stream turbulence in the ERCOFTAC Classic Database.

2 Turbulence Model in a Uniform Flow

For a statistically steady, uniform flow of velocity V_∞ and reference length L, of an incompressible fluid of density ρ and kinematic viscosity ν, the two-equation $k - \omega$ SST turbulence model defines the eddy-viscosity ν_t from

$$\frac{\nu_t}{\nu} = \frac{k^*}{\omega^*} Re \, , \tag{1}$$

where k^* and ω^* are the dimensionless[1] turbulence kinetic energy and specific turbulence dissipation and Re is the Reynolds number $Re = \frac{V_\infty L}{\nu}$. The transport equations of k^* and ω^* reduce[2] to

$$\frac{\partial k^*}{\partial x} = -\beta^* \omega^* k^* \tag{2}$$

and

$$\frac{\partial \omega^*}{\partial x} = -\beta(\omega^*)^2 \, . \tag{3}$$

These equations can be solved analytically (Spalart and Rumsey (2007)) to obtain:

$$k^* = k_{in}^* \left(1 + \beta \left(x^* - x_{in}^* \right) \omega_{in}^* \right)^{-\beta^*/\beta} \tag{4}$$

$$\omega^* = \omega_{in}^* \left(1 + \beta \left(x^* - x_{in}^* \right) \omega_{in}^* \right)^{-1} \tag{5}$$

k_{in}^* and ω_{in}^* are the values specified at the inlet boundary and x_{in}^* is the location of the inlet boundary. Thus, the eddy-viscosity is given by

$$\frac{\nu_t}{\nu} = \frac{(\nu_t)_{in}}{\nu} \left(1 + \beta \left(x^* - x_{in}^* \right) \omega_{in}^* \right)^{1-\beta^*/\beta} \, . \tag{6}$$

These equations show that the decay of ν_t/ν is weaker than that obtained for k^* and ω^*. On the other hand, ω_{in}^* can be replaced in Eq. 4 by k_{in}^* and $(\nu_t)_{in}$ to obtain

$$k^* = k_{in}^* \left(1 + \beta \left(x^* - x_{in}^* \right) k_{in}^* \frac{\nu}{(\nu_t)_{in}} Re \right)^{-\beta^*/\beta} \tag{7}$$

Eq. 7 shows that in external flows the turbulence kinetic energy at the leading edge of a body is dependent on the level of the following variables: turbulence kinetic energy at the inlet k_{in}^*; constants of the dissipation terms of the k and ω transport equations β, β^*; location of the inlet boundary x_{in}^*; inlet eddy-viscosity $(\nu_t)_{in}/\nu$ and Reynolds number Re. Furthermore, Eqs. 4 and 5 may be re-written to obtain the k_{in}^* and ω_{in}^* values that would lead to a given value of k^* at x^*.

$$\omega_{in}^* = \omega^* \left(1 - \beta \left(x^* - x_{in}^* \right) k^* \frac{\nu}{\nu_t^*} Re \right)^{-1} \tag{8}$$

and

$$k_{in}^* = k^* \left(1 + \beta \left(x^* - x_{in}^* \right) \omega^* \right)^{\beta^*/\beta} \, . \tag{9}$$

Eq. 8 shows that for a given pair of values of k^* and $(\nu_t^*/\nu)(1/Re)$ required at x^*, there is a maximum distance to the inlet $(x^* - x_{in}^*)$ that can be used with the two-equation eddy-viscosity model because ω exhibits a singularity at

$$x^* - x_{in}^* = \frac{1}{\beta} \frac{1}{k^*} \frac{\nu_t}{\nu} \frac{1}{Re} \, . \tag{10}$$

There are several possibilities to address this problem. Spalart and Rumsey (2007) suggest to limit k and ω to a minimum value of k_{amb} and ω_{amb} in the free-stream by adding source terms to the k and

---

[1]Reference quantities are ρ, V_∞ and L.

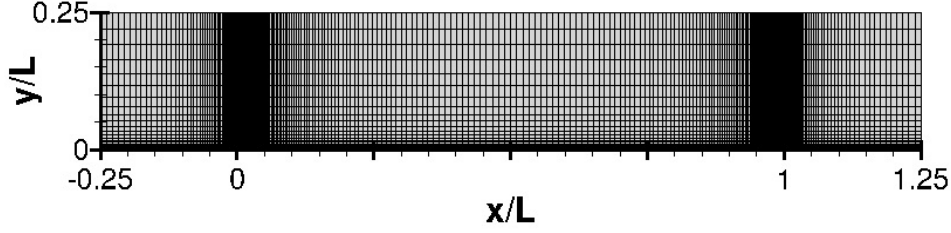[2]The cross-diffusion term in the ω equation is neglected.

Fig. 1: Illustration of the computational domain and grid topology.

ω transport equations that partially cancel diffusion. Suggested values for k_{amb} and ω_{amb} are given by Spalart and Rumsey (2007). However, the main difficulty of the approach is that the additional source terms should not be active in the viscous region of the flow, i.e. in the region where shear-stresses are not negligible.

An alternative approach has been tested in Eça et al. (2016). For[3] $x < x_{tin}$, the dissipation terms of the k and ω transport equations are neglected, which means that the values of k_{in} and ω_{in} are transported to x_{tin}. Naturally, this simple approach might become troublesome in complex geometries. Nonetheless, we will keep it for the present study. However, such modification solves only the problem of the singularity of Eq. 8.

The most common technique to solve the problem of the decay of k for transitional flow simulations is to increase the value of $(\nu_t)_{in}/\nu$ (Langtry and Menter (2009)). As mentionned above, this may lead to values of $(\nu_t)_{in}$ significantly larger than ν. Therefore, in this paper, we propose to keep the standard values[4] of $(\nu_t)_{in}$ and determine values of β_{amb} and β^*_{amb} that adjust the decay of free-stream turbulence to the experimental data. Naturally, this re-calibration of the dissipation terms of the k and ω transport equations should not be used in the viscous flow region and so we propose to define β and β^* from

$$\begin{aligned} \beta &= (1 - F_{amb})\beta_o + F_{amb}\beta_{amb} \\ \beta^* &= (1 - F_{amb})\beta^*_o + F_{amb}\beta^*_{amb} \,, \end{aligned} \tag{11}$$

where F_{amb} is a blending function based on the dimensionless total head.

3   Results

The test case is the statistically steady, two-dimensional, flow over a flat plate of an incompressible fluid. The Reynolds number based on the plate length L is $Re = 10^7$. Reynolds-Averaged continuity and Navier-Stokes equations are solved supplemented by the SST $k-\omega$ eddy-viscosity model (Menter (2003)) and the $\gamma - Re_\theta$ transition model (Langtry and Menter (2009)). The computational domain[5] illustrated in figure 1 is a rectangle of length of $1.5L$ and $0.25L$ width. The inlet is located $0.25L$ upstream of the leading edge of the plate, the outlet is placed $0.25L$ downstream of the trailing edge of the plate and the outer boundary is $0.25L$ away from the plate. Boundary conditions are identical to those described in Eça et al. (2016).

Calculations are performed in stretched Cartesian grids with a finest discretization of 1537×193 cells and a maximum dimensionless near-wall cell size $y^+_{max} \simeq 0.1$. Extra geometrically similar grids are used to estimate the numerical uncertainty of the selected quantities of interest.

All calculations were performed with the flow solver ReFRESCO, Vaz et al. (2009). Second-order accurate discretization schemes are used for all equations with the exception of the convective terms of the turbulence and transition transport equations, which are approximated by first-order upwind. Iterative convergence criteria requires that the L_∞ norm of the normalized residuals[6] of all transport equations

---

[3]Naturally, this definition assumes that V_∞ is aligned with the x axis and that $x_{out} > x_{in}$.

[4]We have used successfully the relation $((\nu_t)_{in}/\nu)(1/Re) = 10^{-8}$ in many applications of the SST $k - \omega$ model.

[5]The present domain and boundary conditions have been checked in many previous studies, as for example Eça and Hoekstra (2006) and Eça et al. (2016).

[6]Normalized residuals are equivalent to dimensionless variables changes in a simple Jacobi iteration.

Table 1: Experimental data for turbulence intensity I at the first measured location from the ERCOFTAC Classic Database. Flow over a flat plate.

Designation	T3AM	T3A	T3B
I [%]	0.874	3.043	5.952
Re_x	1.225×10^5	1.52×10^4	1.51×10^4
x/L	1.225×10^{-2}	1.52×10^{-3}	1.51×10^{-3}

must be below 10^{-6}. The inclusion of the γ and Re_θ equations in the iterative convergence criteria leads to residuals for the remaining transport equations smaller than at least 10^{-8}.

The main quantity of interest is the skin friction C_f distribution, which is one of the flow quantities that identifies the transition location. Nonetheless, we will also present k and ν_t profiles in the transitional flow region.

Three different inlet turbulence quantities have been tested that correspond to the experimental data available in the ERCOFTAC Classic Database. These inlet conditions will be designated by T3AM, T3A and T3B with the turbulence intensity[7] I specified according to the first measurement available from the experiments, as shown in table 1.

The first step of our work is to investigate which is the most important variable for the determination of the onset of transition. To this end we have performed 4 simulations for the T3A case using four different inlet conditions that are summarized in table 2. All cases have the same $k_{in} = 1.4 \times 10^{-3} V_\infty^2$, but four different values of $(\nu_t)_{in}$ and x_{tin}, which are given in table 2.

Table 2: Inlet boundary conditions for the turbulence quantities in the simulation of the T3A flow over a flat plate.

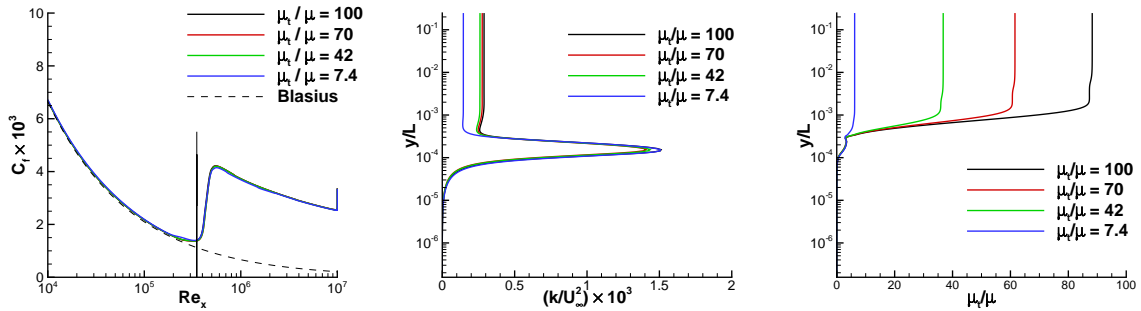| Case	A	B	C	D
$\frac{\mu_t}{\mu}$	100	70	42	7.4
x_{tin}	-0.25	-0.175	-0.1	-0.01

Fig. 2: Skin friction coefficient C_f in the transition region (left) and turbulence kinetic energy k (middle) and eddy viscosity ν_t (right) profiles at $Re_x = 3.5 \times 10^5$.

Fig. 2 presents the skin friction coefficient C_f of the plate near the transition region and the turbulence kinetic energy k and eddy viscosity ν_t profiles at $Re_x = 3.5 \times 10^5$, which is close to the onset of transition, i.e. the location where C_f starts to grow. Although there are significant differences between the ν_t profiles in the outer flow region, the four C_f distributions are very similar and the k profiles are also graphically identical inside the boundary-layer. These results show that k has the stongest influence on the onset of transition and that the high levels of $(\nu_t)_{in}$ are only required to control the decay of free-stream turbulence.

The next step is to calibrate β_{amb} and β^*_{amb} using the data available from the ERCOFTAC database for the three values of I at the inlet (see table 2). Assuming that $\beta_{amb} = \lambda\beta_o$ and $\beta^*_{amb} = \lambda\beta^*$, eq. 7 shows

---

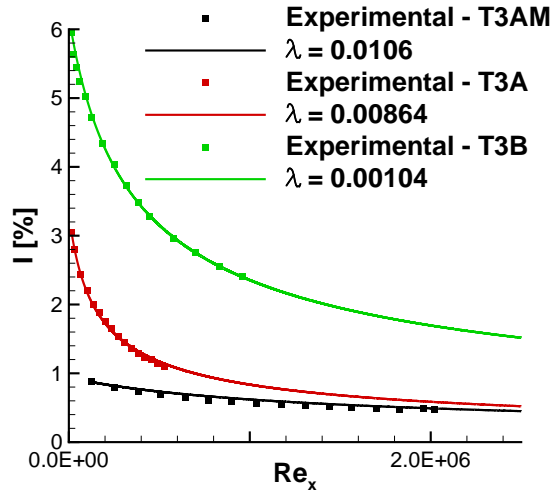[7]Assuming isotropic turbulence we have $k^* = 1.5I^2$.

Fig. 3: Adjusted decay of the turbulence intensity.

that the quantity to detemine is $\lambda \frac{\nu}{(\nu_t)_{in}} Re$. However, for illustration purposes, Fig. 3 presents the fit to the experimental data using $\frac{(\nu_t)_{in}}{\nu} \frac{1}{Re} = 10^{-8}$. There is an excellent agreement between the experimental data and Eq. 7, but the value of λ depends on the level of I at the inlet. Results show a decrease of λ for an increase of I.

Finally, to determine β and β^* from Eq. 11 the blending function F_{amb} is defined using the dimensionless total head p_t^* as the independent variable.

$$p_t^* = \frac{p + \frac{1}{2}\rho U^2}{p_\infty + \frac{1}{2}\rho U_\infty^2} \ . \tag{12}$$

p_t^* is smaller than 1 in the viscous flow region, i.e. where shear-stresses are not negligible and tends to 1 in the free-stream region. At this stage of the development, a simple cubic polynomial is used to define the change from the viscous to the free-stream regions.

$$F_{amb} = \begin{cases} 0 & \Leftarrow \quad p_t^* \le 0.95 \\ 3\xi^2 - 2\xi^3 & \Leftarrow \quad 0.95 \le p_t^* \le 0.995 \\ 1 & \Leftarrow \quad p_t^* \ge 0.995 \end{cases} \ , \tag{13}$$

where

$$\xi = \frac{p_t^* - 0.95}{0.045} \ .$$

Results will be presented for the T3AM, T3A and T3B test cases using the proposed approach to correct the decay of free-stream turbulence.

References

P. R. Spalart, and C. L. Rumsey (2007). Effective Inflow Conditions for Turbulence Models in Aerodynamic Calculations. *AIAA Journal*, **45**(10), 2544–2553.

L. Eça and M. Hoekstra (). The Numerical Friction Line. *31st Symposium on Naval Hydrodynamics*.

R. Langtry, and F. R. Menter (2009). Correlation-Based Transition Modelling for Unstructured Parallelized Computational Fluid Dynamics Codes . *AIAA Journal*, **47**(12), 2894–2906.

F. R. Menter (1984). . *AIAA Journal*, **47**(12), 2894–2906.

F. R. Menter (2003). . *AIAA Journal*, **47**(12), 2894–2906.

L. Eça, R. Lopes, G. Vaz, J. Baltazar and D. Rijpkema (2016). Validation Exercises of Mathematical Models for the Prediction of Transitional Flows. *31st Symposium on Naval Hydrodynamics*.

G. Vaz, F. Jaouen and M. Hoekstra (2009). Free-Surface Viscous Flow Computations. Validation of URANS Code FRESCO. *Proceedings of OMAE2009, Honolulu, Hawaii, USA*.

D. C. Wilcox (1998). *Turbulence Modelling for CFD, 2nd ed.* DCW Industries

Cavitation Prediction Using a URANS Method

Themistoklis Melissaris[*], Norbert Bulten[*] and Tom van Terwisga[†]
[*] Wärtsilä Netherlands BV, Drunen/The Netherlands, [†] Maritime Research Institute Netherlands
(MARIN), Wageningen/The Netherlands
themis.melissaris@wartsila.com

1 Introduction

Cavitation on marine propellers is unavoidable, therefore accepted. As a result, it is of high significance to know the extent to which cavitation is not harmful in operation. To this end, cavitation prediction becomes a prerequisite for induced erosion prediction.

As a continuation of previous work, Melissaris et al. (2017), in two-dimensional flows, there is a current focus on the flow around three-dimensional hydrofoils. First, the flow around the Delft Twist 11 hydrofoil is investigated, focusing on the cavitation dynamics and the shedding frequency. A grid refinement study is conducted and the numerical uncertainty is assessed, Eca and Hoekstra (2014), both in wetted and cavitating flow. The required temporal resolution is also investigated by taking into account the analytical solution of the Rayleigh Plesset equation for the bubble cloud collapse.

Finally, the same numerical set-up is used for cavitation prediction on a model scale propeller in open water condition. The results are compared with experimental data.

2 Mathematical Model

The equations solved are the Reynolds Averaged Navier-Stokes (RANS) equations. An incompressible segregated flow model is selected solving the integral conservation equations of mass and momentum in a sequential manner combined with the SIMPLE pressure-velocity coupling algorithm.

An eulerian multiphase model is used, treating the fluid as a single continuum, assuming a no-slip condition between liquid and vapor phase, with varying properties in space according to its composition . The volume fraction of the components is determined from the condition:

$$a_v + a_l = 1 \tag{1}$$

while density and viscosity are defined as:

$$\rho = a_l \rho_l + \alpha_v \rho_v \quad \text{and} \quad \mu = a_l \mu_l + a_v \mu_v \tag{2}$$

The turbulence model used in this study is the k-ω SST turbulence model developed by Menter (1994). An empirical reduction of turbulence dissipative terms in two-phase regions has been applied, by modifying turbulent viscosity:

$$\mu_t = f(\rho) C_\omega \frac{k}{\omega}; \quad f(\rho) = \rho_v + \frac{(\rho_m - \rho_v)^n}{(\rho_l - \rho_v)^{n-1}}; \quad n \gg 1 \tag{3}$$

where ρ_v is the vapor density, ρ_l the liquid density and ρ_m the mixture density. For the constant n a recommended value n=10 has been used. This modification improves the numerical simulations by taking into account the influence of the local compressibility effects of the vapor/liquid mixture on the turbulent structure.

The conservation equation that describes the transport of vapour is similar to the mass conservation for liquid and is described by:

$$\frac{\partial a_v}{\partial t} + \nabla \cdot (a_v \boldsymbol{u}) = S_{a_v} \tag{4}$$

In equation (4), S_{a_v} represents the source of volume fraction of vapor. In order to close the system of equations formed by the RANS equations and the transport equation for the vapor, a cavitation model should be introduced for the source term of the volume fraction of vapor. The cavitation model used is the model proposed by Schnerr-Sauer (2000) based on a simplified Rayleigh-Plesset equation, which neglects the influence of bubble growth acceleration, as well as viscous and surface tension effects:

$$\frac{dR}{dt} = sign(p_v - p)\sqrt{\frac{2|p_v - p|}{3\rho_l}} \tag{5}$$

Where p_v is the saturation pressure, p is the local pressure around the bubble and ρ_l is the fluid density. According to this rate the source term in equation (4) is defined as:

$$S_{a_v} = \frac{4\pi R^2 n_0}{1 + \left(\frac{4}{3}\pi R^3\right) n_0} \frac{dR}{dt} \tag{6}$$

3 Case Description

The tested hydrofoil is the Delft Twist 11 hydrofoil. The section of the foil is a NACA 0009 hydrofoil with an angle of incidence that changes along the spanwise direction:

$$a(\bar{y}) = a_{max}(2|\bar{y} - 1|^3 - 3(\bar{y} - 1)^2 + 1) + a_{wall} \tag{7}$$

where $a_{max} = 11$ the maximum angle of attack at the mid span, $\bar{y}$ is nondimensionalised with the chord length c and varies over the spanwidth, being twice the chord length (0 < y < 2) with $\bar{y} = 0$ at the wall.

The boundary conditions are listed on the table below:

Boundary conditions	Wetted Flow	Cavitating Flow
Velocity inlet	V_{in} = 6.75 m/s	V_{in} = 6.97 m/s
Angle of incidence	-2 degrees	
Pressure Outlet	P_{out} = 97 kPa	P_{out} = 29 kPa (σ=1.07)
Turbulent Intensity	1%	
Turbulent Viscosity Ratio	10	
Foil	No-slip Condition	
Walls	Slip Condition	
Water Temperature	24°C	

For the grid generation, trimmed hexahedral cells are used with local refinements and prism layers along the wall, with such first cell distance so the average y+ value is well below 1 to resolve the viscous sublayer. Three refinements are applied, one around the hydrofoil, one downstream the trailing edge and a final refinement on the leading edge due to low thickness at this area (Fig. 1). To ensure the

geometrical similarity on the meshes for the assessment of numerical uncertainty, the following formulas where used proposed by Crepier (2017):

$$S_n = S_0 \frac{1 - r_1^{\frac{1}{n}}}{1 - r1} \quad and \quad r_n = r_1^{\frac{1}{n}}$$

(8)

where S_0, r_1 the first cell size and the growth ratio in the initial coarse grid respectively and S_n, r_n the first cell size and the growth ratio for the grid refinement n (n=1 for the coarse grid).
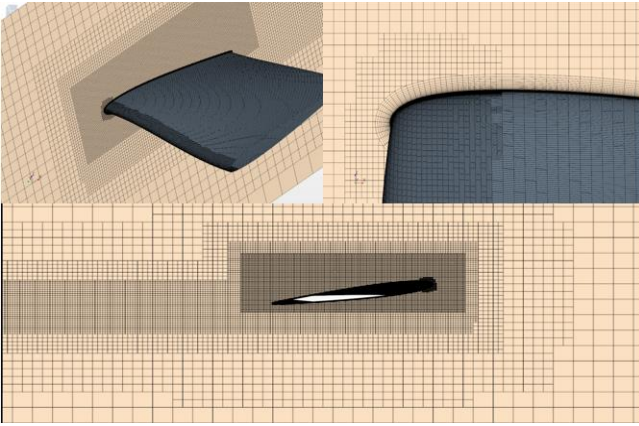

Fig. 1: Grid visualization of the domain and the aditional refinements.
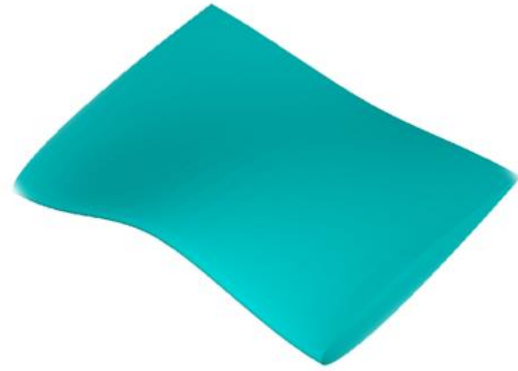

Fig. 2: Representation of the geometry of the Twist 11 hydrofoil.

The collapse time of a shedded cloud can be calculated from the analyrical solution of the Rayleigh-Plesset equation by just estimating the radius of the cloud:

$$T_C^2 = \frac{\xi^2 R_0^2 \rho}{p}$$

(9)

where $\xi \cong 0.915$ is the Rayleigh factor, ρ the liquid density, p the far-field pressure and R_0 the bubbly cloud radius. By calculating the collapse time of the cloud we can regulate the number of time steps during the collapse.

4 Results

The results for the lift coefficient and the pressure distribution in wetted flow are presented and compared with experimental data. Table 1 includes the results for the lift force and the lift coefficient in wetted flow for the different grids. The results show asymptotic behavior diverging from the experimental value, however it should be mentioned that the experimental uncertainty for the lift force is around 10%. To this end the pressure distribution is also calculated in three different planes along the chord of the foil and is compared with experimental data. Fig. 3 shows the planes where the pressure distribution is measured and fig.4-6 show the comparison between the different grid densities and the experimental results at each plane.

Table 1: Number of cells, average Y+ values, Lift force, lift coefficient and the numerical uncertainty for every grid.

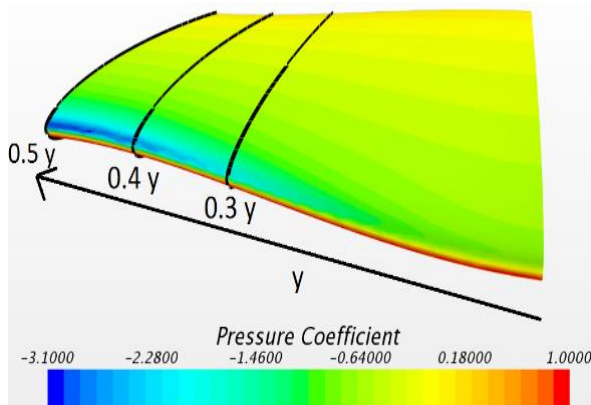| Grid	# Cells	Avg. y+	Lift (N)	C_L	%(CFD-EXP)	U_φ
G1	506,000	0.8	449.1	0.454	1.30	
G2	890,000	0.63	448.3	0.453	1.47	
G3	1,850,000	0.46	446.5	0.451	1.87	
G4	3,150,000	0.39	444.2	0.449	2.37	
G5	5,730,000	0.34	442.6	0.447	2.73	

Fig. 3: Visualization of the planes where the pressure distribution is compared with experimental data.
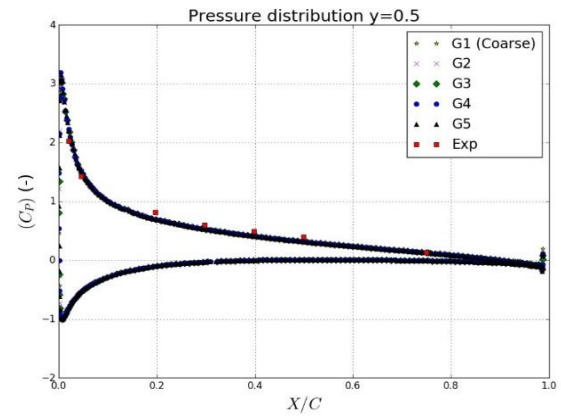

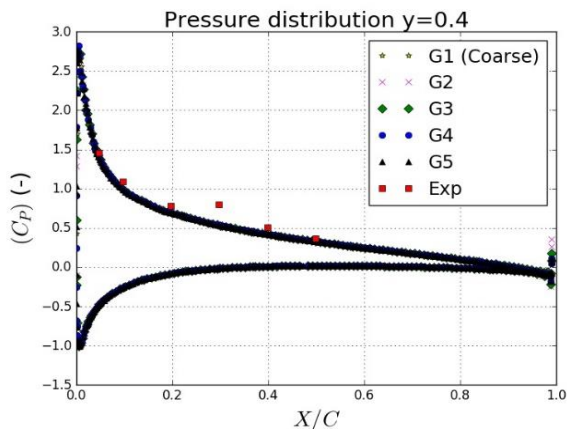Fig. 4: Pressure distribution at the 50% of the span.

Fig. 3: Pressure distribution at the 40% of the span.
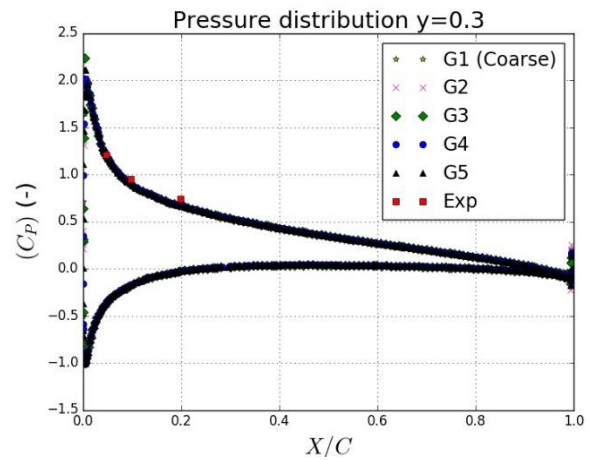
Fig. 4: Pressure distribution at the 30% of the span.

Simulations in cavitating flow for all the grids are conducted, to investigate the impact of grid resolution. A time step sensitivity study is conducted in order to derive the sufficient number of time steps needed to resolve the bubbly cloud collapse. The total vapor volume is calculated and shown in Fig. 7 together with a spectral analysis for deriving the shedding frequency. The shedding frequency is compared between the different grids (only for the first two grids yet, the rest will follow) and also with the experimental data and other numerical studies.

Fig. 5: History of the total vapor volume (top) and its spectral analysis (bottom) for the grid G2.

Table 2: Comparison between the calculated shedding frequency for every mesh, the experimental frequency and the frequency obtained by previous numerical studies.
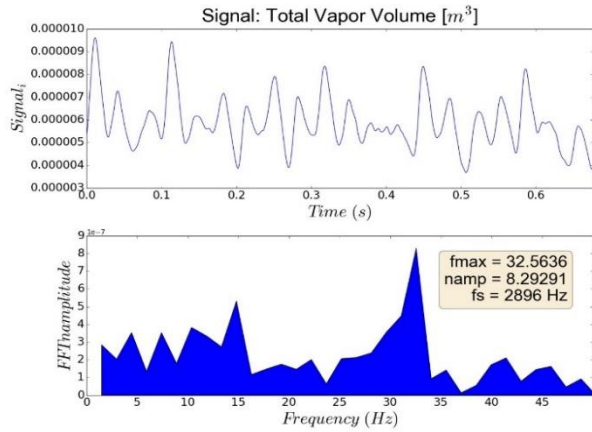
	Shedding Frequency
Foeth (Experiment)	33 Hz
I. Oprea	31 Hz
G1 (Coarse)	30 Hz
G2	33 Hz

The shedding frequency for the grid G1 is around 30 Hz which is lower than the experimental frequency. However, even with grid G2 a good match with the experimental value is obtained. The shedding frequency for the rest of the grids needs to be calculated as well. A typical shedding cycle is shown in Fig. for the G1 and G2 grids.
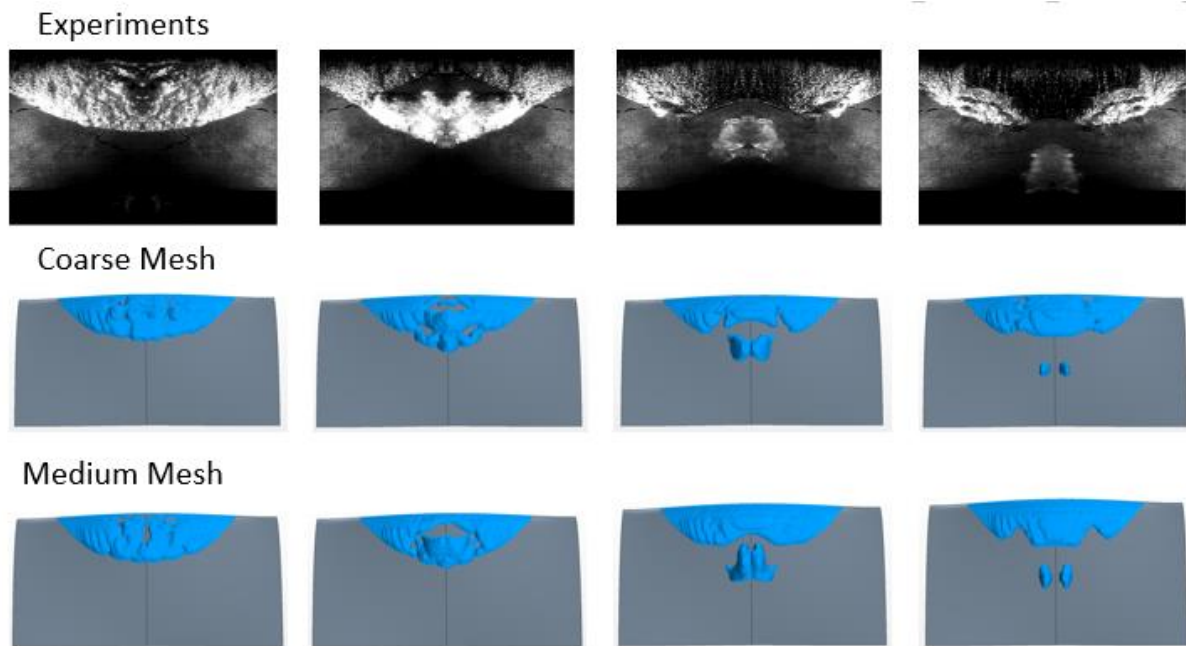
Fig. 6: Typical shedding cycle. Comparison between the experiment (top), the grid G1 (middle) and the grid G2 (bottom).

Computations using finer meshes are planned, to give us a better overview of the grid and the temporal sensitivity. After deriving the required grid density and the required time step, the same procedure will be implemented for prediction cavtation on a model scale propeller.

5 Conclusion

The results in wetted flow show a good agreement with the experiments. In cavitating flow, the shedding frequency seems to be sensitive to the grid density when a time step corresponded to a courant number around 0.75 is used. Grid G2 is fine enough to capture the experimental frequency, however finer meshes should be used to have a more clear conclusion on that. The assessment of the numerical uncertainty will give an overview of the reliability of the results.

Using smaller time steps is expected to simulate the bubbly cloud collapse with higher accuracy and hopefully will capture the convection of the cloud downstream to the trailing edge. Taking into account the conclusions drawn by the simulations around the Twist 11 hydrofoil, cavitation prediction on a model scale propeller is expected. The results will be compared with experimental data.

References

T. Melissaris, N. Bulten, and T. Terwisga (2017). A numerical study on the shedding frequency of sheet cavitation. Proceedings of MARINE 2017, Nantes, France.

L. Eca and M. Hoekstra (2014). A procedure for the estimation of the numerical uncertainty of CFD calculations based on grid refinement studies. *Journal of Computational Physics*, vol. 262, pp. 104-130.

F. Menter (1994). Two-equation eddy-viscosity turbulence modeling for engineering applications. *AIAA Journal*, vol. 32, pp. 1598-1605.

P. Crepier. Ship resistance prediction: verification and validation exercise on unstructured grids. Proceedings of MARINE 2017, Nantes, France.

Analysis of the reduction in resistance for a frigate type vessel with trim control options using CFD

Andrea Mikelic[*],

[*]DAMEN Schelde Naval Shipbuilding, the Netherlands. A.Mikelic@damennaval.com

1 Introduction

A trim wedge optimization was carried in a towing tank in order to improve the powering efficiency of a frigate type hull form at design speed. The results lead to a quite high trim wedge angle and an overall improvement of the powering capacity compared to an initial design. Nevertheless, such a high angle is detrimental for resistance at lower speed.
Alternatives to a trim wedge exist but their effect on a displacement vessel is difficult to quantify.
The present study aims at investigating some of these and their ability to compete with the trim wedge optimum.
Two possible alternatives are studied:
- 		Addition of interceptor plates of various heights to the vessel without trim wedge
- 		Forward ballasting the vessel.

The resistance values of the full-scale bare hull CFD computations are compared for the different alternatives. The optimization was done at design speed (Froude number 0.56) but the resistance curve is also considered to assess the impact at lower speed. In addition, the transom flow is investigated to get a deeper understanding of its interaction with the hull.

All computations are carried out using an unsteady viscous-flow CFD RANS code, ReFRESCO (www.refresco.org). The community based open-usage CFD code solves multiphase (unsteady) incompressible viscous flows using the Navier-Stokes equations, complemented with turbulence models, cavitation models and volume-fraction transport equations for different phases Vaz (2009).

2 Case Pre-processing, geometry, grid and computational settings

2.1 Variant of the studied frigate
The vessel considered for the study is a frigate type vessel equipped with a trim wedge. The 3 alternative geometries considered are the reference vessel:

- without trim-wedge, referred to as "0deg"
- equipped with a high angle trim-wedge, referred to as "Trim wedge"
- equipped with interceptor plates whose heights varied from 0 to 20 cm. Each alternative is referenced with its interceptor plate height.

Some research has been made in the literature to try to estimate the height of the interceptor plate the most likely to lead to an equivalent lift force. If it is assumed that a trim wedge is equivalent to a stern flap, the following Eq. (1), developed by Dawson and Blount (2002) can be applied:
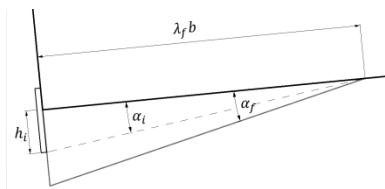
$$\begin{cases} \alpha_i = 0.175 \cdot \alpha_f + 0.0154 \cdot \alpha_f^2 \\ \quad\quad h_i = \lambda_f \cdot b \cdot \sin\alpha_i \end{cases} \quad (1)$$

Fig. 1: Scheme of the terms used in Eq (1)

According to Rijkens (2011), the Eq(1) is limited to 15 deg of flap angle as the original study does not seem to include flare angles higher than 15 deg, therefore for higher flare angles values α_f the corresponding height should be used with caution. The formula predicts a corresponding plate of around

30cm which is considered very high. The approach is then to limit the study to 20cm and to identify the "optimum" plate length. The corresponding stern geometries are shown Fig. 2.
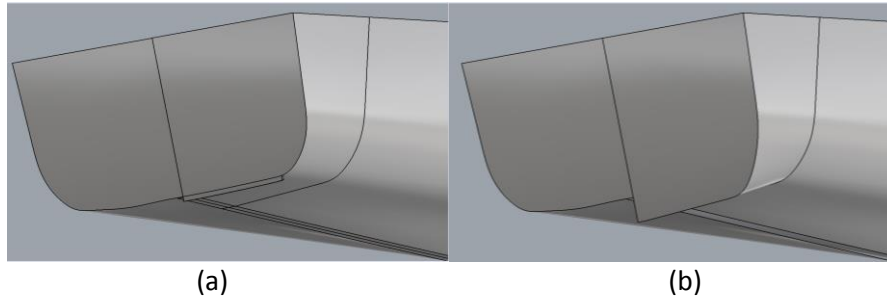

(a)   (b)

Fig. 2: (a) Transom view of the "0 deg" (left) compared with the "10 cm" (right) and (b) transom view of the "0 deg" (left) compared with the "Trim wedge" (right)

2.2 Mesh details
Based on the preliminary results from a grid refinement study and foreseeing the high number of computations needed, a grid of around 5 million of cell has been chosen. For the interceptor plates, a more refined grid has been chosen to ensure that the transom wave is captured as accurately as possible considering its impact on the resistance. In order to allow a fair comparison between the geometries studied, similar grid settings are used. The grid settings were set according to a verification study performed for the Froude number 0.56.

Table 1: Main grid characteristics

Quantity	Value
Domain size in Lpp	8x3x3
Number of cells	~5 million
Target Y+	Around 300
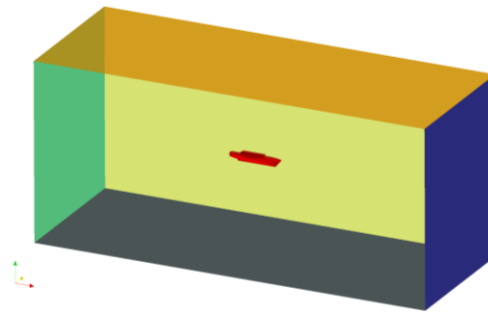
Fig. 3: View of the domain and boundaries

The grids build with Hexpress™ are unstructured grids consisting of hexahedral elements.

2.3 Main computational settings
A view of the domain is given Fig.3. The following boundaries are set: on the bottom (grey) and top (orange) dirichlet BC Pressure set to 0; on the Deck and left wall (yellow) a BC SlipWall, on the mirror plane a BC SymmetryPlane. For the inlet an initial speed of 0 m.s^{-1} was set in the BC Inflow boundary and the outlet is a 0 pressure BC outlet. The vessel walls are defined as BC Wall with automatic wall function.
Table 3 summarizes the settings used for the computations.

Table 3: Main settings

Quantity		Values	units
Scale		Full scale	[-]
Water	Dynamic viscosity	0.00122	[Pa.s]
	Density	1,026.02	[kg/m^3]
Air	Dynamic viscosity	1.85×10^{-5}	[Pa.s]
	Density	1.2	[kg/m^3]
Turbulence model		k-ω SST 2003	[-]

3 Results and discussion

3.1 Forward trim study
The forward trim study has been set up in such a way that the displacement of the vessel is constant and only the Longitudinal Center of Buoyancy (LCB) has been moved backward, as seen Table 4.

Table 4: Variation of hydrostatic parameters with forward trim

Quantity	Value					units
Forward trim angles	0	1	2	2.5	3	[deg]
Ta	100%	85%	70%	61%	55%	[% of T]
Tf	100%	115%	130%	139%	145%	[% of T]
T	100%	100%	100%	100%	100%	[% of T]
LCB	47%	50%	54%	55%	56%	[% of Lpp]

The results in terms of resistance reduction with respect to the vessel without trim-wedge and a forward trim angle of 0 deg are shown Fig. 4. Nominal computations, i.e. with no suction of the propeller, and total computations were performed, i.e. with modelling of the suction of the propeller by means of an actuator disk.

Table 5: Results from the forward trim study. The trim wedge is given as a reference

Trim forward angle (degree)	Dynamic trim (degree)	Dynamic sink-age (m)	Reduction in nominal resistance	Reduction in total resistance
0	-2.60	0.24	0.0%	0.0%
1	-1.42	0.45	0.3%	0.3%
2	-0.38	0.55	0.4%	1.1%
2.5	0.06	0.59	0.1%	0.1%
3	0.47	0.64	-0.1%	-0.3%
Trim wedge	**-0.80**	**0.23**	**11.1%**	**12.8%**

As seen in Table 5 and in Fig.4, the effect of trim forward the vessel is limited.
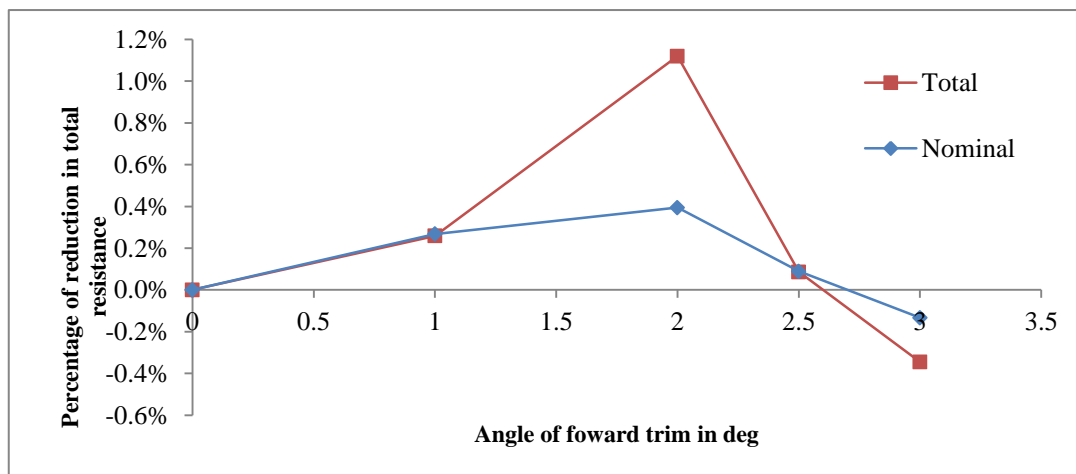

Fig. 4: Resistance reduction for forward trim angle from 0 to 3deg.

The computations were done based on the same grid thus it is supposed that the uncertainty of the gridding is identical in each simulation. Still this represents a small variation compared with the trim wedge 11% of reduction.

3.2 Interceptor study

Another way replace the effect of a trim wedge is to replace it with an interceptor plate. A similar procedure as before is chosen. Table 6 shows the results of the study. The trim wedge values are given for comparison.

Table 6: Results of the interceptor height variation study.

Interceptor plate height (cm)	Dynamic trim (degree)	Dynamic sinkage (m)	Reduction in nominal resistance	Reduction in Total resistance
0	-2.60	0.28	0.0%	0.0%
5	-2.05	0.23	9.0%	10.9%
10	-1.66	0.24	12.7%	14.1%
15	-1.15	0.25	12.2%	14.4%
20	-0.99	0.28	12.5%	14.0%
Trim wedge	**-0.80**	**0.23**	**11.1%**	**12.8%**

Fig.5 shows that if the vessel is equipped with an interceptor plate of about 7 cm, the same reduction in resistance should be reach than in the case of the "Trim wedge".

A clear optimum is not visible as for heights higher than 10 cm the reduction in resistance seems constant near 12.5%, see Fig. 5(a). As the suction of the propeller is modelled and added as body forces to the computation, a clear optimum is still not visible and the resistance seems to remain constant around 14%, see Fig5(b). In terms of vessel balance and resistance reduction, an interceptor height of 15cm seems to be a fair choice.

(a)   (b)
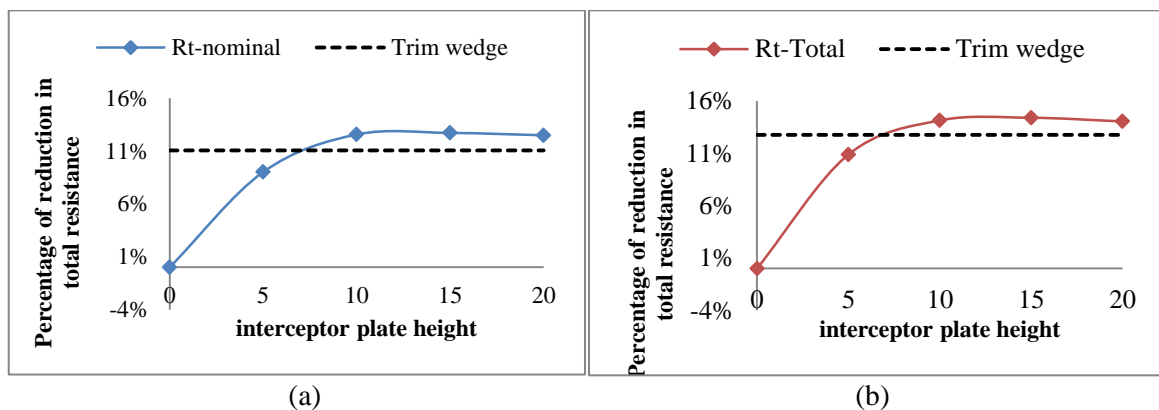
Fig. 5: Evolution of the reduction in resistance with interceptor plate height

Fig.6 gives an overview of the wave pattern for the vessel with no trim wedge ("0deg"), the vessel equipped with a 15cm interceptor plate and the initial trim wedge. The water at the transom is now a crest and not a trough.

Fig. 6: Evolution of the wave pattern at a cut near the vessel

The resistance component (pressure and friction) along the vessel is shown Fig.7. A peak in the pressure component of the resistance is seen Fig7, at the transom in case of the "15cm" interceptor and the

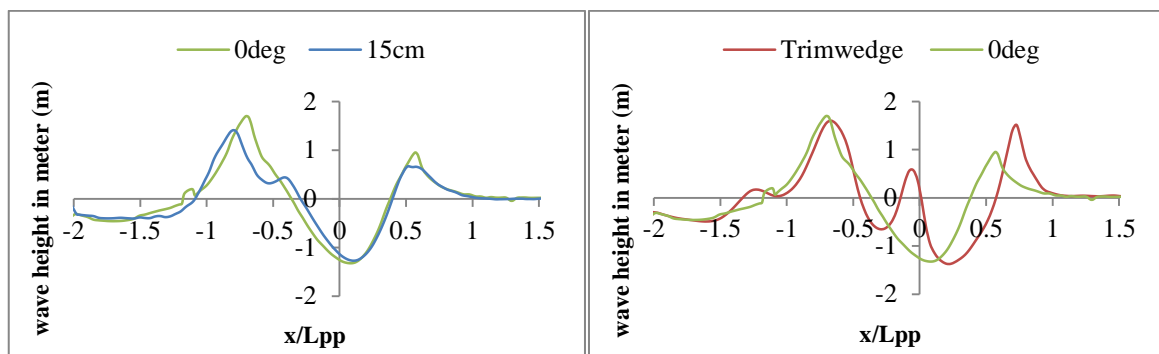"Trim wedge". The new balance of the vessel changes also the overall the pressure distribution. The bow wave is higher with an interceptor plate or a trim wedge but this extra pressure is fully recovered.
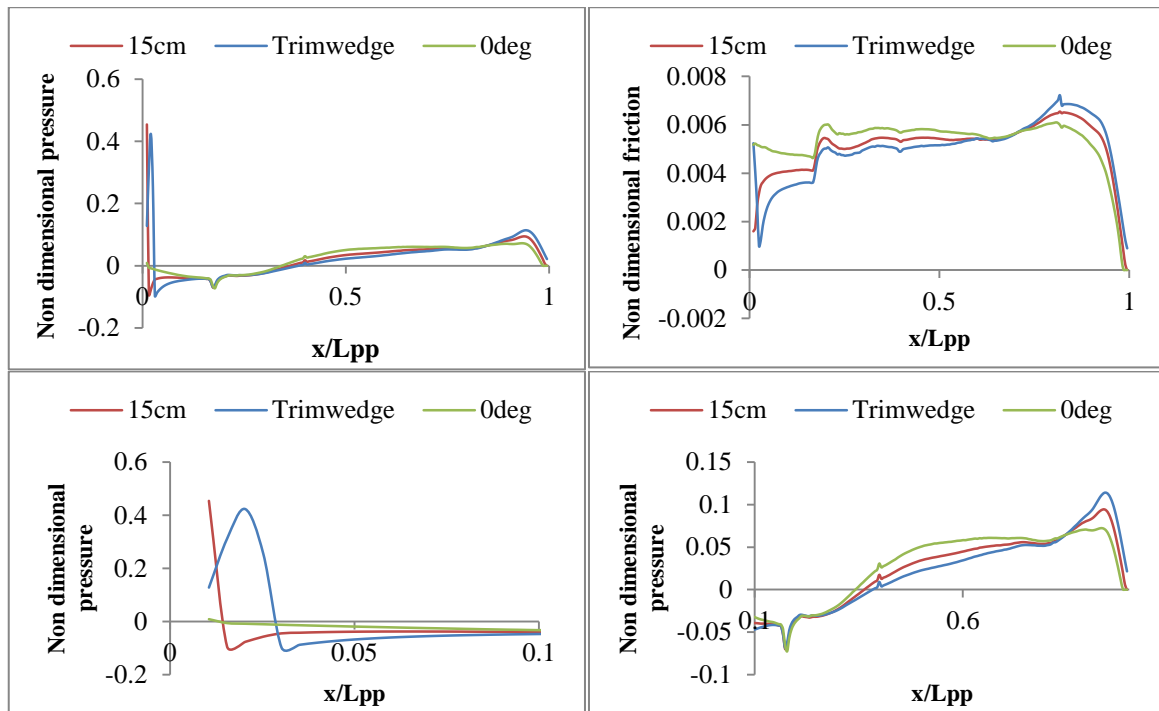
Fig. 7: Pressure and friction along the hull for 3 of the alternatives (top) and zoom on the stern region (left) and bow region (right)

3.2 Resistance curve

In order to assess the application of a 15cm interceptor plate, a resistance curve is evaluated at 5 different speeds. This will give an estimation of the gain at low speed and especially at the range computation speed.

Fig. 8 compares the resistance curve of the vessel with trim wedge ("Trim wedge") and equipped with the 15cm interceptor ("15cm"). Once a roughness correction is added, the improvement between the 2 alternatives increases while the speed decreases and goes from 2% to 17%.

Fig. 8: Non dimensional total resistance comparison for the 15cm interceptor and the trim wedge. The extrapolated experimental data are given in dashed line.

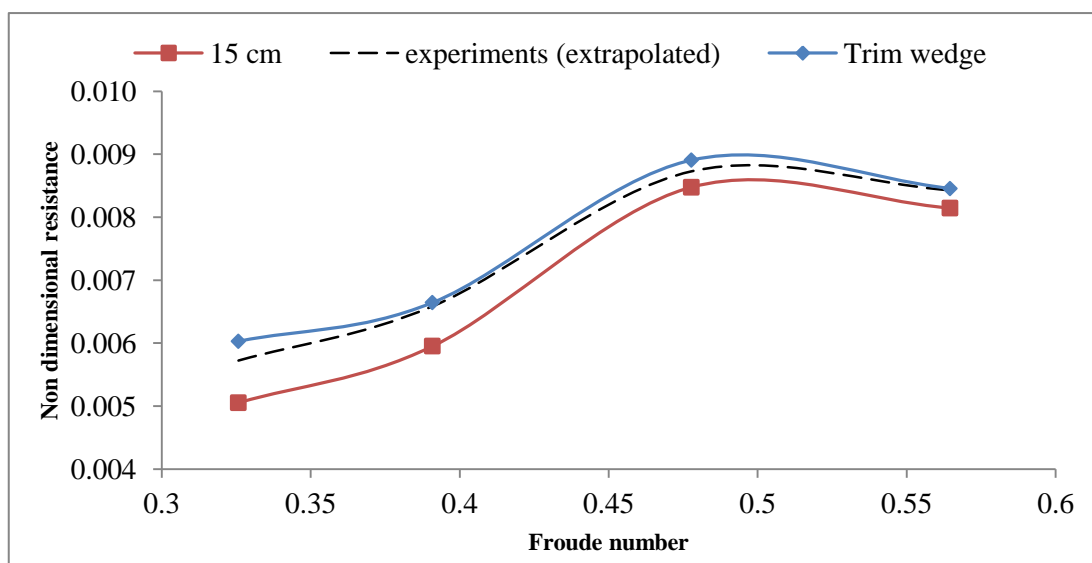The results from the experiments done on the "Trim wedge" are also shown in order to check whether the improvements are in line with the prediction from the tank.

At Froude number 0.33 (range speed) the value obtained from the CFD is 5% higher than the extrapolated resistance from the tests, therefore the overall improvement found may be over predicted. If lower speeds are computed this tendency seems to remain.

Nevertheless, if a similar propulsion system (effective power) is in place, a polynomial interpolation allows us to estimate a gain of 0.31 knots for top speed and 0.94 knots for the economic speed. In terms of range, this corresponds to an extra 6% in nautical miles with the current propulsion configuration.

4 Conclusions

Even though ballasting the vessel forward does compensate the high dynamic trim angle, the reduction of resistance is quite small as no extra lift effect is present.
The use of interceptors instead of trim-wedges seems to have a beneficial impact both on top and low speed for a frigate type fast displacement vessel.
There is some flexibility in the choice of the interceptor plate height as there is no clear optimum. Any length higher than 7 or 8 will insure at least a similar reduction than in the "Trim wedge" case.

The differences with the extrapolated tank test values seem to be increasing with the decreasing speed and therefore the overall uncertainty on the value. It can be argued that the grid used for the resistance curve that was "optimized" for the top Froude number is not valid for Froude number lower than 0.3.

References

D.L.Blount, D.Dawson, and al (2002). Trim control. Professional Boatbuilder,February/March

 A.A.K.Rijkens, J.A.Keuningand, R.H.S.Huijsmans (2011). A computational tool for the design of ride control systems for fast planing vessels. International Shipbuilding Progress, 58,165-190

G.Vaz, F. Jaouen, M. Hoekstra (2009). Free-surface viscous flow computations. Validation of URANS code FRESCO, In Proceedings of OMAE2009, May 31–June 5, Hawaii, USA.

Unsteady Flow Over a Smooth Flat Plate Using DES

Sajad Mozaffari, Michel Visonneau, Jeroen Wackers
LHEEA, Centrale Nantes/CNRS, Nantes/France
sajad.mozaffari@eleves.ec-nantes.fr

1 Introduction

Computations based on Reynolds-Averaged Navier–Stokes (RANS) equations are common in industry today. Although they are very successful in predicting many parts of the flow around a vehicle, a ship or an airplane, they still have some limitations for the high Reynolds number flows. Detached Eddy Simulation (DES) is a modification of a RANS model for the prediction of turbulent flows at high Reynolds numbers. It was first proposed as a solution to the high computational costs of applying Large-Eddy Simulation (LES) to complete configurations at high Reynolds numbers [Spalart et al., 1997], and to improve the predictive capabilities of turbulence models in highly separated regions [Guilmineau et al., 2011].

On the other hand, adaptive mesh refinement (AMR), is a solution to accurately capture flow features. It is a technique to speed up the computation by starting the solution on a coarse grid and refining this grid locally to accurately resolve areas of interest. It is an ideal way to efficiently solve flow problems that have strong local structures whose position is not known a priori without excessive increase in computational effort.

Application of both methods is the subject of many recent studies. One of the issues confronting using AMR method is the creation or destruction of the turbulence at the interface of the coarse and fine grids, where the turbulent properties' conservations are violated. Using the DES model, would make the case more complex, espacially at the vicinity of RANSE/LES interface because of the existence of a *grey area* in which a shear layer, after separation, must generate LES content (random eddies) which it did not possess in the boundary layer upstream [Squires, 2004]. Thus, in our project, first of all, in order to look at the grey zone and its effect, the DES method for a turbulent flow over a smooth flat plate is investigated.

In the section 2, the DES used in the ISIS-CFD flow solver as a part of the FINE™/Marine computing suite, is formulated in detail. Then the physical description, computational domain, grid generation and the numerical setup of the case are explained. In the computation part, RANSE and DES turbulence models are compared, in order to see which one gives a better representation of the physical phenomena.

2 Detached Eddy Simulation (DES)

The DES version used in ISIS-CFD, is based on the k-ω SST model, because it is consistently considered as one of the best two-equation RANS models, particularly for separation prediction. The DES modification is applied to the dissipation term in the k transport equation. In the original model, the dissipation term is written as:

$$\rho\varepsilon = \beta^* \rho K \omega \tag{1}$$

where ε is the dissipation rate, β^* is a constant of the SST model. For the SST-DES, this term is written now as:

$$\rho\varepsilon = \beta^* \rho K \omega F_{DES} \tag{2}$$

with

$$F_{DES} = \max\left(\frac{L_t}{C_{\mathrm{DES}}\Delta}, 1\right) \tag{3}$$

where Δ is the maximum local grid spacing ($\Delta = \max(\Delta x, \Delta y, \Delta z)$), L_t is the turbulent length scale, $L_t = \sqrt{K}/(\beta^*\omega)$ and C_{DES} is a constant. In the initial version of the DES-SST [Menter et al., 2003], C_{DES} was 0.61. For the ISIS-CFD solver, we prefer to use the value $C_{DES} = 0.78$ [Menter and Kuntz., 2003]. According to the above equation, wherever $F_{DES} > 1$, LES is used. In contrast for $F_{DES} \approx 1$, all turbulence is modeled and RANSE is used.

3   Case Setup

The computational domain sizes in the streamwise, wall normal and spanwise directions are respectively $L_x = 0.5m$, $L_y = 0.1m$ and $L_z = 0.005m$. Three meshes were generated according to the data in Table 1. The meshes were refined only in the streamwise direction. Moreover, another domain with a larger size in spanwise direction ($L_x = 0.5m$, $L_y = 0.1m$ and $L_z = 0.05m$) is also taken into consideration to study the possible turbulent effects over the flow in spanwise direction. The parameters of this mesh (called Mesh 4) are tabulated and presented in Table 1. The first layer thickness in wall normal direction is $1.59167 \times 10^{-6}m$ and constant for all the meshes. The free stream velocity is $U_e = 70ms^{-1}$, and the

Table 1: Parameters of the meshes employed in the computation

Mesh name	$N_x \times N_y \times N_z$	y^+	Streching ratio	N_{cells}
Mesh 1	$300 \times 137 \times 50$	0.2	1.05	2 055 000
Mesh 2	$800 \times 137 \times 50$	0.2	1.05	5 480 000
Mesh 3	$1500 \times 79 \times 50$	0.2	1.1	5 925 000
Mesh 4	$1000 \times 94 \times 100$	0.2	1.08	9 400 000

Reynolds number per meter is $Re = 4.72 \times 10^6 m^{-1}$. The computation is unsteady and the time step for all the computations was set to $10^{-4}s$.

4   Results & Discussions

In this part, the results of the computations which have been done according to the previous explainations, are presented. To get a broader view of the grids in the boundary layer, Fig. 1 shows the grid densities scaled using the boundary layer thickness (δ) at $X = 0.5m$ for each mesh.

(a) Mesh 1

(b) Mesh 2

(c) Mesh 3
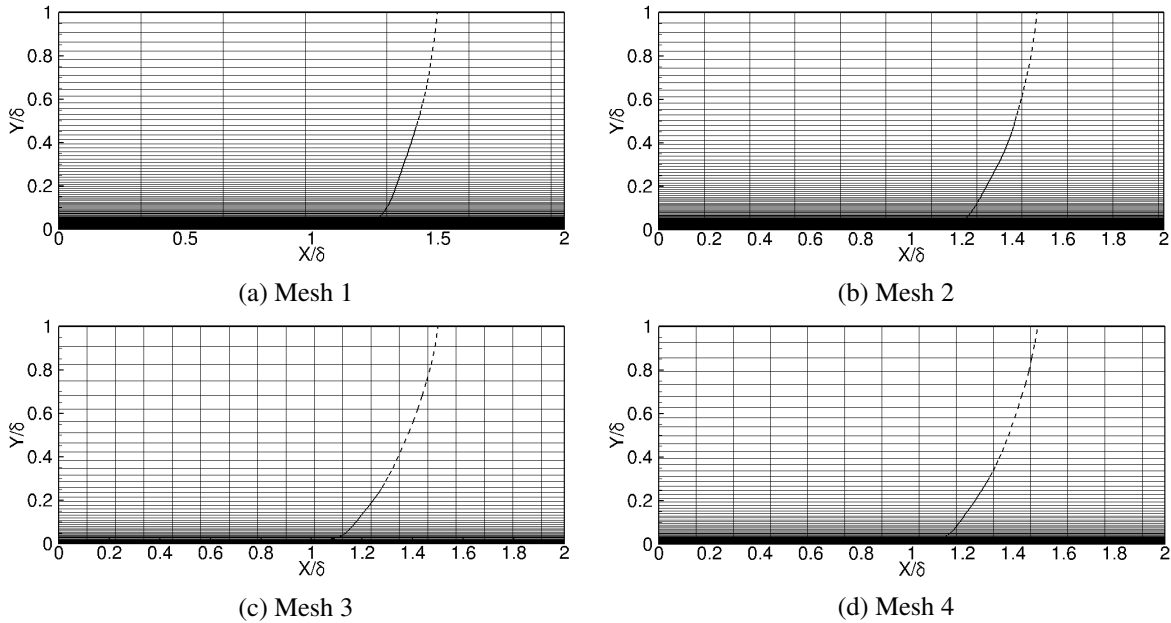
(d) Mesh 4

Fig. 1: Grids in the boundary layer at $X = 0.5m$

It is seen in Table 2 that by refining the gird in streamwise direction, the boundary layer thickness is decreasing, and for Mesh 4, it is almost half of the value computed by the RANSE model. In addition, Fig. 2 shows the instantaneous velocity profile in the streamwise direction. Apart from the boundary layer thickness changes, no unsteadiness and fluctuation was captured.

According to Fig. 3, on finer meshes, the F_{DES} function increases as it should. According to section 2, this switches the turbulence model to LES, so we would expect that the resolved part of the solution

Table 2: Boundary layer thickness evolution (at $X = 0.5m$)

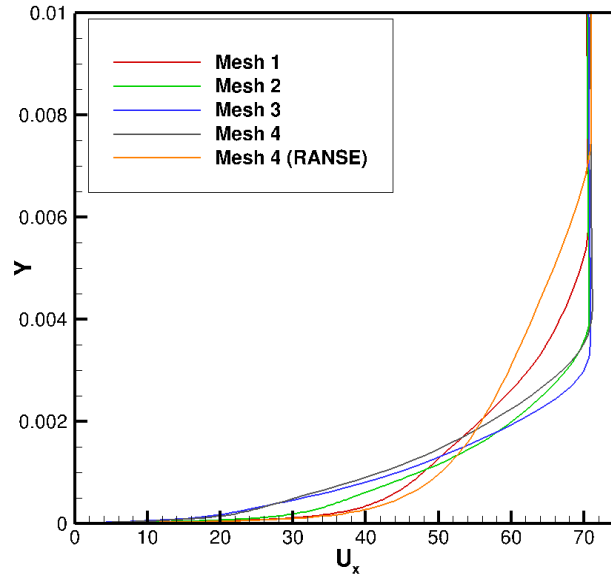| Mesh name	δ(m)
Mesh 1	5.13 E-03
Mesh 2	3.47 E-03
Mesh 3	2.97 E-03
Mesh 4	3.40 E-03
Mesh 4 (RANSE)	6.31 E-03

Fig. 2: Instantaneous Velocity profile in the streamwise direction (at $X = 0.5$)

increases. But this is not the case. For instance, the averaged modeled and resolved Turbulent Stress $u'u'$ for Mesh 4 are illustrated in Fig. 4. It shows that the resolved part of the solution is negligible.

Reviewing the presented results, several obvious deductions can be made:

- No unsteadiness is seen in the results.

- Flow rate is negligible in Z direction (spanwise velocity is zero).

- The averaged resolved turbulent stresses are also zero.

- As the mesh is refined, the boundary layers thickness is reduced.

- For Mesh 4, the boundary layers thickness of RANSE computation is almost two times larger than the one in DES case.

5 Conclusion

A real flat-plate boundary layer is unsteady, but in this case there no unsteadiness was captured by the DES model. It will have impact on grid adaptation. One possibility which should be tested, is imposing unsteadiness into the system. In the next step of the study, using a stochastic approach, at each time-step, an unsteady velocity fluctuation is generated and will be used as the inlet boundary condition of the domain (Fig. 5), to see if it would be helpful to have resolved solution for the part of the part of the domain where the turbulence model is switched to LES.
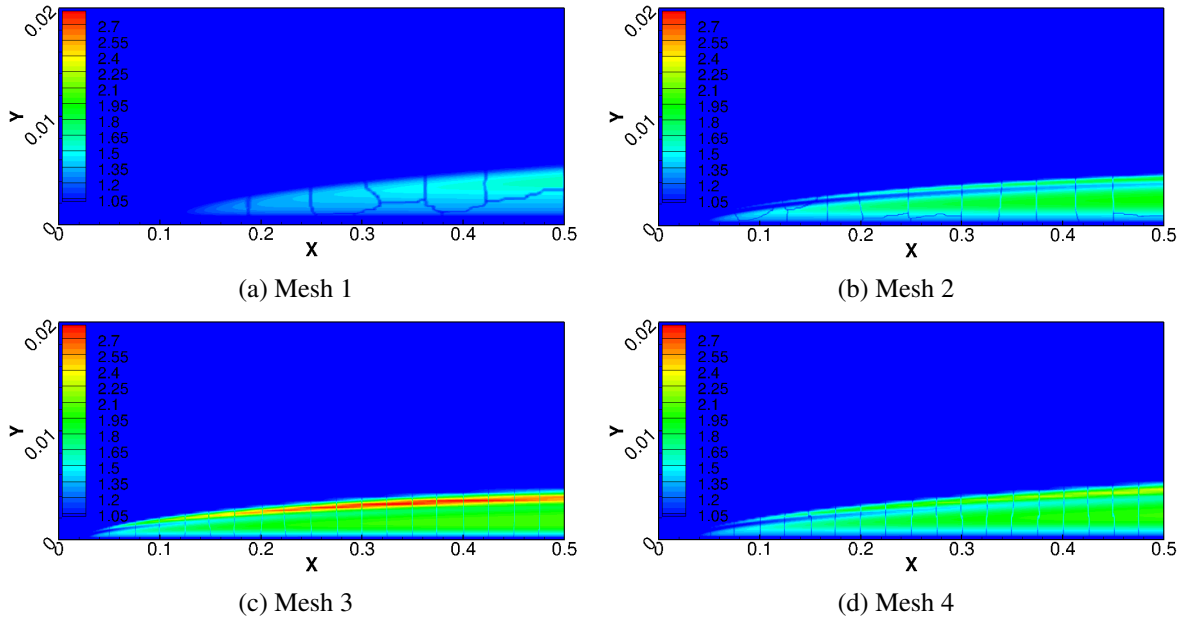
(a) Mesh 1

(b) Mesh 2

(c) Mesh 3

(d) Mesh 4

Fig. 3: F_{DES} Function

(a) modeled

(b) resolved
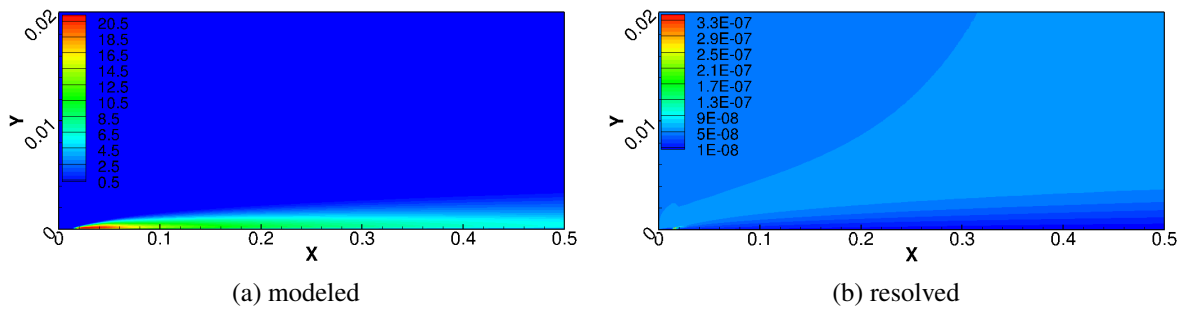
Fig. 4: Averaged Turbulent Stress $u'u'$ of the DES simulation for Mesh 4

References

Guilmineau, E., Deng, G., and Wackers, J. (2011). Numerical simulation with a DES approach for automotive flows. *Journal of Fluids and Structures*, 27(5–6):807 – 816. IUTAM Symposium on Bluff Body Wakes and Vortex-Induced Vibrations (BBVIV-6).

Menter, F. R. and Kuntz., M. (2003). A zonal sst-des formulation. In *DES Workshop, St Petersburg.*

Menter, F. R., Kuntz, M., and Langtry, R. (2003). Ten years of industrial experience with the SST turbulence model. *Turbulence, heat and mass transfer*, 4(1):625–632.

Spalart, P. R., Jou, W., Strelets, M., and Allmaras, S. (1997). Comments of feasibility of les for wings, and on a hybrid rans/les approach.

Squires, K. D. (2004). *Detached-Eddy Simulation: Current Status and Perspectives*, pages 465–480. Springer Netherlands, Dordrecht.

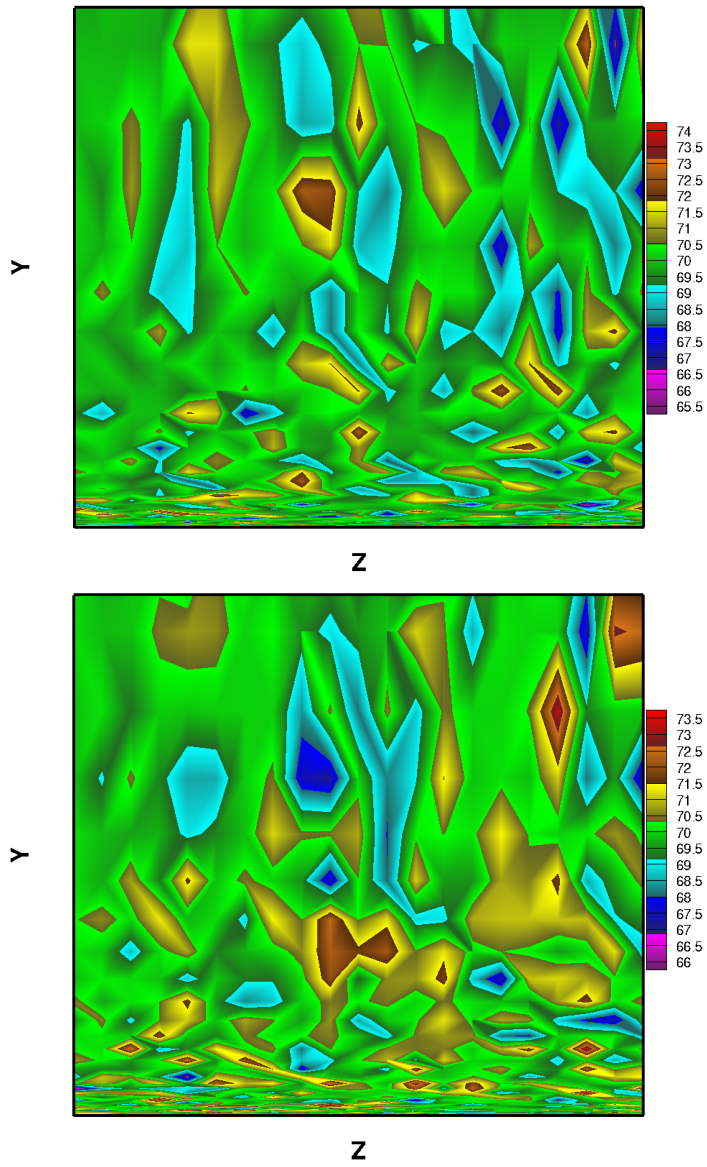Fig. 5: Inlet generated velocity at two different time-step

Analysis of hydrofoil cavitation using Proper Orthogonal Decomposition

Carlo Negrato[*†]**, Tom van Terwisga**[II]**, Rickard E. Bensow**[*]

[*]Chalmers, Gothenburg/Sweden; [†]MARIN Academy, [II]MARIN, Wageningen/Netherlands.

negrato@chalmers.se

1 Introduction

Cavitation is the change of phase from liquid to vapor when the pressure falls below the saturation pressure. For marine propellers, occurrence of cavitation is accepted on modern designs, in order to achieve high propeller efficiency. However, there is a need to keep cavitation under control, because its extent can lead to undesired phenomena such as increased noise and erosion. To understand the dynamics of cavitation, researchers often focus on cavitation on simpler geometries, such as hydrofoils.

In this work, the test case consists of a two dimensional NACA0015 hydrofoil. It has been studied by many authors both numerically (Arndt et al., 2000) and experimentally (Ganesh and Ceccio, 2016). The results from a viscous flow simulation are considered here; the scope is to gain additional insight into cavitation dynamics in a regime of cloud shedding, by applying a Proper Orthogonal Decomposition (POD) technique. POD is used for analysis of experimental data or CFD results and consists of a decomposition of the flow field by a linear combination of basis functions which are representative of flow structures. It was applied to distinguish coherent structures from turbulent fluctuations (Chen et al., 2012) or to detect specific flow patterns (Minelli et al., 2016). POD was also applied to experimental observation of hydrofoil cavitation, Prothin et al. (2016), where the authors analyzed the variations of grey-scale level in high-speed video frames.

This paper provides a description of the numerical setup and the basic theoretical background for POD in section 2. The flow dynamics predicted by the CFD code are shortly discussed in section 3.1. More extensively, section 3.2 is dedicated to the outcome of orthogonal decomposition for two scalar fields: the vapor volume fraction and the pressure coefficient.

2 Methodology

2.1 Numerical setup

The test case investigated is depicted in Figure 1: the two-dimensional NACA0015 foil has a chord length of $c = 0.2\,m$ and the center of the coordinate system is placed at the center of gravity of the foil, at a relative chordwise position of 0.3086. The foil is confined in a water tunnel of height $2.85c$ and nominal width $w = c$. The Reynolds number based on the chord length is $Re = 1.2 \times 10^6$, resulting from the inflow velocity $U_\infty = 6\,m/s$, the water density $\rho_l = 998\,kg/m^3$ and the dynamic viscosity $\mu_l = 1.002 \times 10^{-3}\,kg/(m\,s)$; the vapor density and viscosity are respectively $\rho_v = 0.024\,kg/m^3$ and $\mu_v = 1.02 \times 10^{-5}\,kg/(m\,s)$. The foil operates at an angle of attack of $6°$ and cavitation number $\sigma = 2(p_{ref} - p_v)/(\rho U_\infty)^2 = 1.0$. A pressure pick-up is positioned on the top tunnel wall at $x = 0.5c$.

The viscous solver ReFRESCO is used (http://www.refresco.org/). Flow modeling relies on the unsteady, incompressible RANS equations; the $k - \sqrt{k}L$ model is chosen for turbulence closure. Mixture modeling is used for multi-phase flow, complemented with a modified Sauer (2000) model for mass transfer. The convective terms are discretized with first-order upwind scheme, except for the momentum equation, with QUICK scheme. Implicit Euler scheme is used for time marching, with a normalized time step $t^* = \Delta t U_\infty/c = 10^{-5}$, which results in eight thousands time steps per shedding cycle.
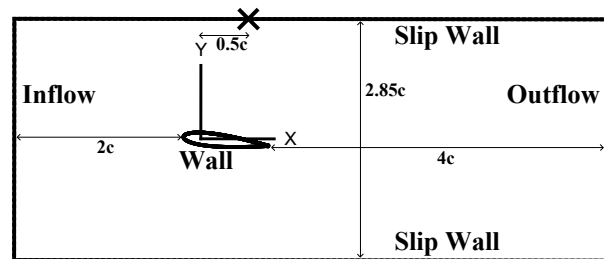

Fig. 1: Domain, boundary conditions and reference system. The cross shows the location of the pressure probe at the top tunnel wall.
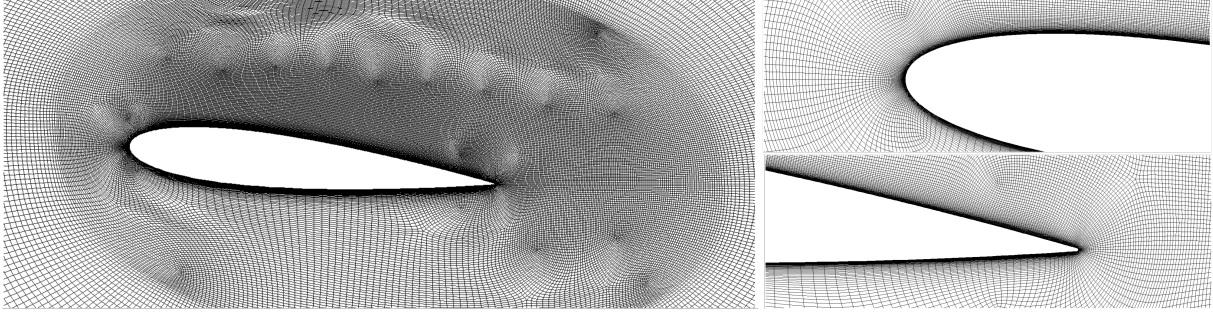
Fig. 2: Overview of the mesh. Zoomed regions at the foil nose and tail.

A block-structured mesh of roughly 118×10^3 cells is produced using the commercial package GridPro® (Figure 2) . A large number of cells are clustered at the foil suction side, where cloud cavitation develops, as well as in the near wake of the foil. The boundary layer is fully resolved, as confirmed by the resulting maximum $y^+_{max} = 1.3$. A complete description of the grid generation, together with a comparison of the results from a fully unstructured grid, is provided in Negrato et al. (2016).

2.2 Proper orthogonal decomposition

The idea behind POD is to decompose the flow (in terms of field variables, e.g. pressure or velocity) into independent spatial distributions which form an orthonormal basis, representative of coherent structures in the flow.

The present analysis employs the Proper Orthogonal Decomposition method described by Chen et al. (2012). The decomposition is carried out using the snapshot method (Sirovich, 1987), which is suitable for cases with a large number of spatial degrees of freedom (the grid points). POD requires saving the numerical solution at a number K of time steps, in other words it requires K snapshots.

POD was applied to two scalar fields: the vapor volume fraction and the pressure coefficient distributions in the entire domain. Let $s^{(k)}$ be the distribution of vapor or pressure for a certain snapshot k. The idea is to approximate $s^{(k)}$ by a linear combination of spatial basis function φ_m (the POD modes), which are not function of time, multiplied by time-dependent coefficients $c_m^{(k)}$:

$$s^{(k)} = \sum_{m=1}^{M} c_m^{(k)} \varphi_m, \tag{1}$$

where M is the total number number of modes used for the approximation, with $M \leq K$. The superscript (k) refers to the snapshot index (hence representative for time dependency) while the subscript m refers to each of the modes. The basis functions must satisfy an orthogonality condition and they are computed by minimizing the L_2 norm of the difference between the actual field $s^{(k)}$ and its reconstruction. The minimization is realized by solving the eigenvalue problem on the spatial correlation matrix for the scalar field distributions (Chen et al., 2012).

The coefficient $c_m^{(k)}$ provides the contribution of mode m to the solution at snapshot k. Therefore, in the framework of modal analysis, the energy associated with each mode i is obtained by summing the square of the coefficients over all K snapshots:

$$KE_i = \frac{1}{2} \sum_{k=1}^{K} (c_i^{(k)})^2. \tag{2}$$

The nomenclature is due to the fact that, whenever the POD is applied to the velocity field, the modal energy is the specific kinetic energy associated with each mode. Although for the vapor fraction field and pressure field there is not a physical counterparts for the modal energy, the same nomenclature is kept.
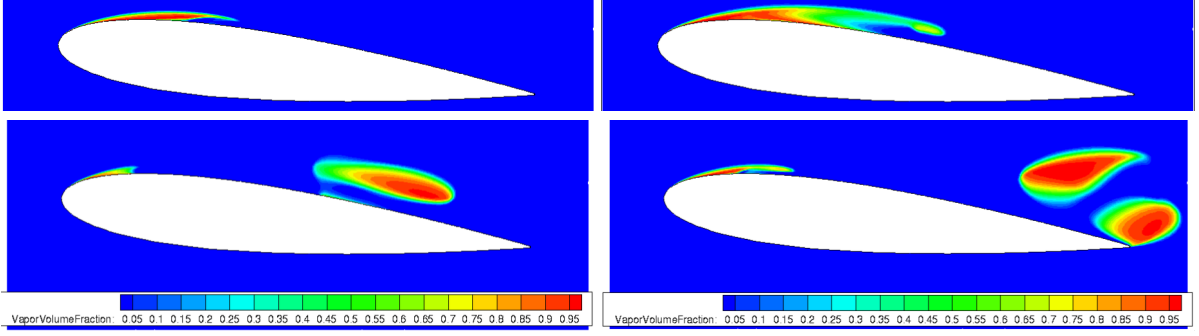
Fig. 3: Instantaneous vapor volume field during one shedding cycle.

Additionally, to compare two scalar distributions $D^{(1)}$ and $D^{(2)}$, the *relevance index* can be employed:

$$R_p = \frac{(D^{(1)}, D^{(2)})}{\left\|D^{(1)}\right\| \cdot \left\|D^{(2)}\right\|}, \tag{3}$$

where $\| \star \|$ denotes the L_2 norm and $(\star, \ast)$ the inner product. R_p represents a normalized projection of distribution $D^{(1)}$ onto $D^{(2)}$, and it provides a quantitative comparison, in addition to a qualitative visual inspection. By definition of orthogonality, $R_p = \delta_{ij}$ when mode i is projected onto mode j. Alternatively, R_p can be used to compare a mode with an instantaneous distribution or to compare two snapshots (for instance at the same phase in the shedding cycle, but from two different cycles in a simulation).

3 Results

3.1 Numerical solution

A complete analysis of cavitating flow results was presented in our previous work, Negrato et al. (2016). In this section, only the main flow features are discussed, in order to provide a description of the data set which is analyzed using POD in section 3.2.

The flow, at the given conditions of $\sigma = 1.0$ and angle of attack of $6°$, is characterized by a regime of unsteady partial cavity (Ganesh and Ceccio, 2016). The pressure drop at the foil suction side is such that cavitation begins; an attached sheet cavity forms, which grows to a maximum length of about 1/4 of the chord length. The re-entrant jet developing at the rear edge breaks the sheet and a vapor cloud is shed, which travels downstream. Once the shed structure approaches the trailing edge of the foil, it strongly interacts with the vortical trailing edge flow, resulting into break up and, partly, condensation. The remaining vapor structures are convected in the near-wake where they eventually collapse. Figure 3 illustrates four stages of a shedding cycle: development of the attached cavity, detachment of a vapor cloud, convection of the cloud over the foil and break up at the trailing edge.

The shedding frequency is computed from the signal of the lift coefficient. The resulting Strouhal number based on the chordlength is $St = fU_\infty/c = 0.134$. The frequency contents in the following sections are plotted as function of harmonics of the shedding frequency.

3.2 Modal and frequency analysis

The Proper Orthogonal Decomposition (POD) method is applied to two scalar fields: the vapor volume fraction α_v and the pressure coefficient $C_p = 2p/(\rho_l U_\infty)$. We emphasize that the POD calculations for the two fields are two independent post-processing analysis, although the results will be correlated. For both fields, the flow is reconstructed using a limited number of modes, giving a low order estimate of the actual field. Concerning the vapor fraction, the modal energy and the frequency contents for the time dependent coefficients $c_i^{(k)}$ are analyzed, whereas for the pressure field the focus is on the pressure signal at the probe on the top tunnel tunnel wall (Figure 1).

The analysis is limited to the flow solution in the last 10 shedding cycles, with 40 snapshots per cycle, which corresponds to a sampling ratio of $\Delta_{t_S}/\Delta_t = 200$. The method provides as many modes as the number of snapshots processed; the modes are here indicated by index i ranging from 0 to 399.

When POD is made on the complete field (without a-prori substracion of the mean value), mode 0 should be equal to the ensemble average, Chen et al. (2012); this property is necessary to exclude that larger modes contain flow features which belong to the average flow. As a confirmation, for the vapor volume the relevance coefficient between the first mode and the ensemble average is $R_p > 0.99$.

Figure 4 shows the energy fraction, i.e. the ratio of modal to total "kinetic" energy for the first 15 modes. The average flow (mode 0-th) account for 68% of the total energy and it is not plotted. The energy contribution is below 2% for modes $i > 5$. Furthermore, the first pair of modes (1,2) has similar energy content, just above 6% of the total energy, which is twice as large as the energy contents of higher modes.

Figure 5 shows how the time dependent coefficients $c_i^{(k)}$ change in the last three cycles for modes $i = 1, 2, 3, 4$. Remarkably, the signals for Mode 1 and Mode 2 are similar but shifted in time; also, their frequency content is dominated by a peak at the shedding frequency. Concerning Mode 3 and Mode 4, the resemblance of the signal is not as clear, but the frequency content still has the same peak, at twice the shedding frequency. The modal energy histogram and the analysis of the temporal coefficients shows that adjacent modes have similar features. It is concluded that the flow is described by pairs of modes, as found in the analytical work of Luchtenburg et al. (2009) and the numerical results of Minelli et al. (2016), with the exception of mode 0, i.e. the ensemble average.
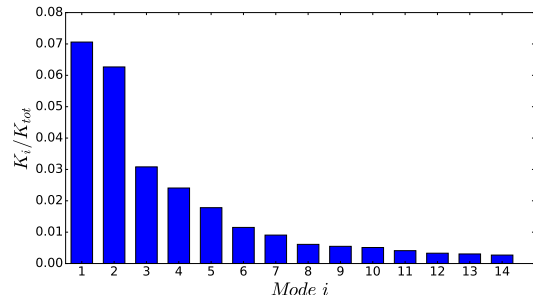

Fig. 4: Modal energy fraction of the modes 1 to 14. Mode 0 (the ensemble average) is not plotted.

Since information on flow structures are carried by pairs of modes, the instantaneous vapor volume fraction field is reconstructed (as of equation 1) using 3 modes ($i = 0, 1, 2$) and 5 modes ($i = 0, 1, 2, 3, 4$) respectively. Figure 6 gives a comparison of the actual solution to the reconstructed ones, for two time steps. The first row shows the instant of detachment of a vapor structure: at the rear edge of the cavity the vapor is more smeared out in the reconstructed fields, which suggests that larger modes are required to reproduce a sharper interface. In both reconstructions the growth of the sheet cavity and the early phase of cloud shedding are captured, hence lower modes $i = 1, 2$ already contain most of the cavitation dynamics. In the second row of Figure 6 the comparison is given for a time instant where the vapor structure breaks up. Here, the 5-modes reconstruction reproduces the location of the primary and secondary vapor structures, although the vapor fraction is smaller than observed in the actual snapshot. More importantly, the secondary structure close to the trailing edge is only marginally captured by the 3-modes reconstruction. Therefore, information on the cavity structure break up (as well as its collapse in the wake) are contained in modes $i > 3$.
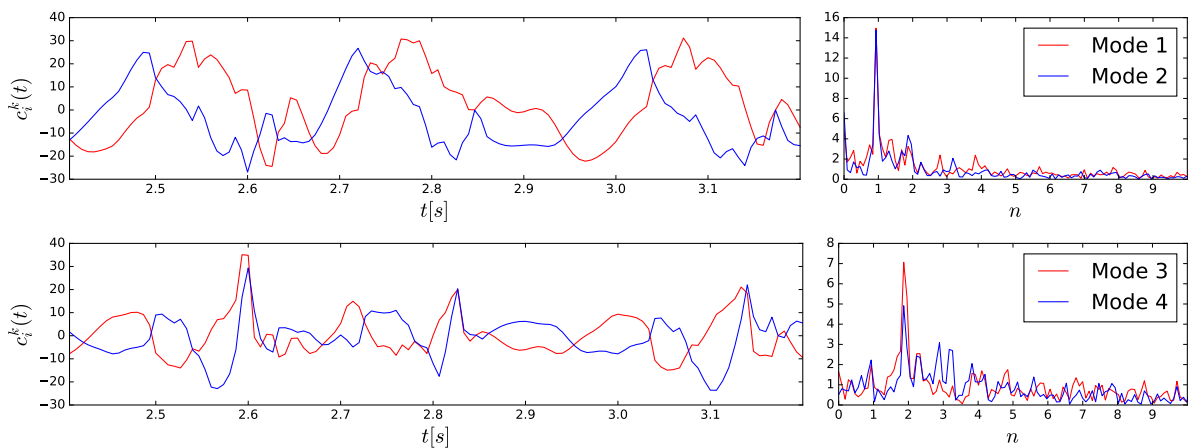

Fig. 5: History of coefficients and frequency contents for modes 1-4 of the vapor volume fraction.
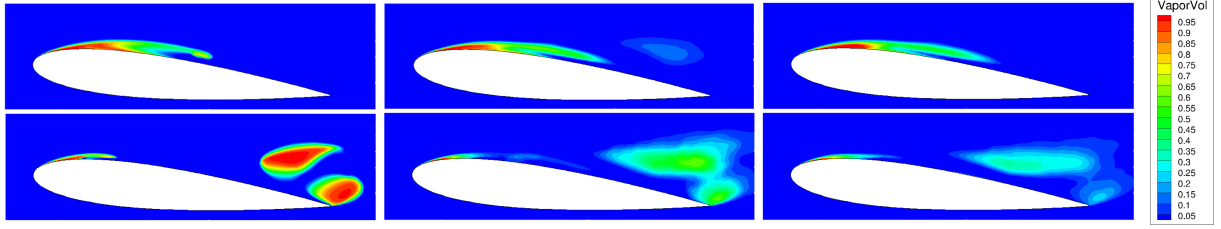
Fig. 6: Instantaneous vapor volume fraction field for two time steps. Left: numerical solution. Center: reconstruction using 5 modes. Right: reconstruction using 3 modes.
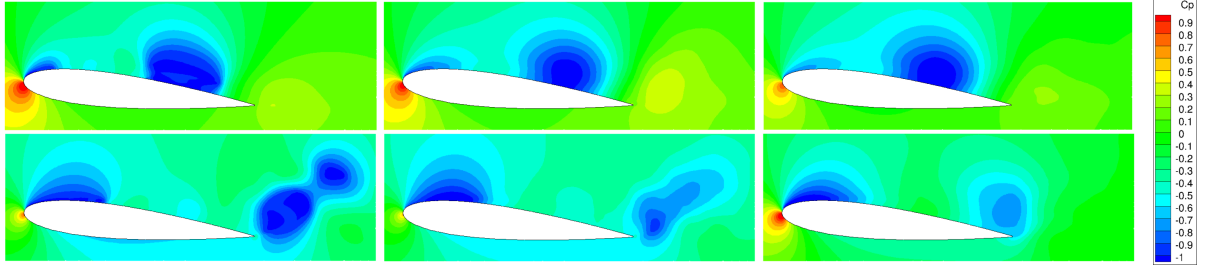

Fig. 7: Instantaneous pressure field for two time steps. Left: numerical solution. Center: reconstruction using 5 modes. Right: reconstruction using 3 modes. (The time steps differ from those in Figure 6).

The POD technique is applied also to the pressure coefficient. The top row of Figure 7 refers to a time instant when the shed cloud lies over the foil suction side, while the second row refers to the final stage before collapse. In the second row the pressure coefficient for the 3-modes reconstruction does not show any low pressure region in the wake: the information on vapor structures traveling in the wake is lost. Therefore, lower modes are sufficient for capturing the early and central stages of the shedding cycles, but only higher modes are representative for the vapor structure convection/collapse in the wake.

Finally, we present the study of the pressure probe at the top wall. First of all, in order to assess the influence of sampling, the signal for the complete simulations (with all time steps) is compared to the signal for a reconstructed field using all the available modes (400). The result is illustrated in the top row of Figure 8. The time history of the full simulation has large peaks corresponding to the instants of the collapse, which is a well-known consequence of spurious pressure oscillations due to the incompressible flow modeling. As a result of sampling, the sharp peaks are not well captured. Nevertheless, the frequency contents only differ for frequencies close to the cut-off frequency of 74.6 Hz, corresponding to $n = 18.6$. The first-harmonic component is dominant, but harmonics up to 7th also contribute significantly.

As a second step, the reconstruction with a limited number of modes is compared with a reconstruction using all modes (bottom row of Figure 8). In both the time and the frequency plots, the differences are small between a full reconstruction and a 5-mode approximation. Hence, most of the dynamics is captured within the first 5 modes. However, with a 3-modes reconstruction the peaks in pressure history are lost, as well as the larger harmonics contribution (as visible in the range $2 < n < 4$).

4 Conclusion

A Proper Orthogonal Decomposition (POD) method is used to analyze the numerical results of cavitating flow over a two-dimensional NACA0015 hydrofoil. The numerical simulation predicts an unsteady, cyclic cavitation: a sheet cavity grows, followed by the detachment of a vapor structure from the rear edge of the sheet cavity. The cloud breaks up in proximity of the foil trailing edge and the vapor structures collapse downstream of the foil.

The POD analysis of the vapor volume fraction reveals that the ensemble average is the most energetic mode (68% energy fraction) while modes $i > 5$ provide negligible contributions. Furthermore, in view of the modal energy and frequency contents of the temporal coefficients, it is shown that adjacent modes have similar features. Hence, the flow is described by pairs of modes, rather than single
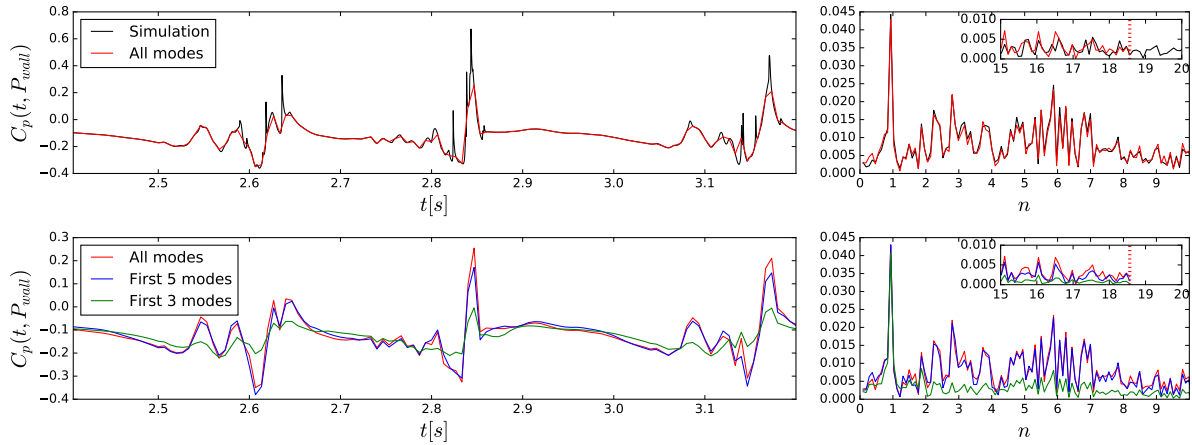
Fig. 8: History and frequency contents of the pressure at the top wall probe. Complete signal for the numerical simulation and reconstruction using all modes, 5 modes and 3 modes.

ones. A reconstruction using 5 or 3 modes proved that different modes contribute to different stages in the shedding cycle. On the one hand, modes 1 and 2 already reproduce the growth of the sheet cavity and the detachments of the vapor cloud. On the other hand, the break-up and the downstream collapse require higher modes to be captured. From the study of the pressure pick-up on the top wall, it is seen that the first harmonic contribution is already captured with 3 modes, while the larger harmonics are only visible from a reconstruction using 5 modes. Hence, the higher frequency contents is attributed to vapor structures' break-up and collapse.

The POD method can be applied equally to two-dimensional slices of three-dimensional domains, given a proper choice of their location. The extension to three dimensions would be a natural continuation of this study. Furthermore, in view of the contribution of the break up/collapse to the higher frequency contents in pressure fluctuations, modeling approaches which resolve a greater spectrum of turbulence (e.g. Large Eddy Simulations) and include compressibility effects are recommended for future studies.

Acknowledgements

References

R.E.A. Arndt, C.C.S. Song, M. Kjeldsen, J. He and A. Keller. *Instability of partial cavitation: a numerical/experimental approach.* 23rd Symp. on Naval Hydrodynamics, Val de Reuil, France (2000).

H. Chen, D.L. Reuss. D.L.S. Hung and V. Sick. *A practical guide for using proper orthogonal decomposition in engine research.* International Journal of Engine Research, 14(4) 307-319 (2012).

H. Ganesh, J. Wu and S.L. Ceccio. *Investigation of Cavity Shedding Dynamics on a NACA0015 Hydrofoil Using Time Resolved X-ray Densitometry.* 31st Symposium on Naval Hydrodynamics, (2016)

D.M. Luchtenburg, B.R. Noack and M. Schlegel. *An introduction to the POD Galerkin method for fluid flows with analytical examples and MATLAB source codes.* Department of Fluid Dynamics and Engineering Acoustics, TU Berlin. Technical Report 01/2009.

G. Minelli, S. Krajnović, B. Basara and B.R. Noack. *Numerical investigation of active flow control around a generic truck A-pillar.* Flow Turbulence and Combustion, 97:1235-1254 (2016).

C. Negrato, T. Lloyd, T.v. Terwisga and R. Bensow. *Influence of grid setup on the prediction of hydrofoil cavitation.* Proceedings of the 19th Numerical Towing Tank Symposium (2016).

S. Prothin, J.Y. Billard and H. Djeridi. *Image processing using proper orthogonal and dynamic mode decomposition for the study of cavitation developing on a NACA0015 foil.* Exp. Fluids 57:157 (2016).

J. Sauer. *Instationär Kavitierende Strömungen - Ein neues Modell, basierend auf Front-Capturing(VoF) und Blasendynamik.* PhD Thesis, University of Karlsruhe, Germany (2000).

L. Sirovich. *Turbulence and the dynamics of coherent structures.* Quart Appl Math; 45: 561-571 (1987).

Numerical Simulation of Flows around Moving Bodies using an Overset Moving Grid Technique

Kunihide Ohashi*, **Nobuaki Sakamoto***

*National Maritime Research Institute, Japan

k-ohashi@nmri.go.jp

1 Introduction

The overset grid method and the moving grid technique are coupled with the structured NS solver. The body motions are obtained by solving motion equations, and taken into account by the grid deformation which depends on the weight function with the distance from the solid surfaces. The regions where the overset relations are composed deform with the body motions to maintain the overset information, and the amount of deformations gradually decrease with the distance from the body surfaces. Such the way is adapted to be able to avoid the computational load with using the dynamic overset grid method. The present method is applied to the computations of flows around the two dimensional single cylinder, and of flows around multiple cylinders.

2 Computational method

2.1 Base solver

The governing equation is 3D RANS equation for incompressible flows. Artificial compressibility approach is used for the velocity-pressure coupling. For unsteady flow simulations, a dual time stepping approach is used in order to recover incompressibility at each time step.

$$\frac{\partial q}{\partial t} + \frac{\partial q^*}{\partial \tau} + \frac{\partial (e - e^v)}{\partial x} + \frac{\partial (f - f^v)}{\partial y} + \frac{\partial (g - g^v)}{\partial z} = 0 \tag{1}$$

$$q = [\ p \quad u \quad v \quad w\ ]^T, \quad q* = [\ 0 \quad u \quad v \quad w\ ]^T$$

The Eq.1 is non-dimensionalized by the reference density ρ_0 , reference velocity U_0, reference length L_0. (u, v, w) are in (x, y, z) directions. Physical time is expressed by t, artificial time is τ.

Convective terms e, f, g, and viscous terms e^v, f^v, g^v are defined as follows.

$$e = \begin{bmatrix} \beta u \\ (u - u_g)u + p \\ (u - u_g)v \\ (u - u_g)w \end{bmatrix}, f = \begin{bmatrix} \beta v \\ (v - v_g)u \\ (v - v_g)v + p \\ (v - v_g)w \end{bmatrix}, g = \begin{bmatrix} \beta w \\ (w - w_g)u \\ (w - w_g)v \\ (w - w_g)w + p \end{bmatrix}, \tag{2}$$

$$e^v = \begin{bmatrix} 0 \\ \tau_{xx} \\ \tau_{xy} \\ \tau_{zx} \end{bmatrix}, f^v = \begin{bmatrix} 0 \\ \tau_{xy} \\ \tau_{yy} \\ \tau_{yz} \end{bmatrix}, g^v = \begin{bmatrix} 0 \\ \tau_{zx} \\ \tau_{yz} \\ \tau_{zz} \end{bmatrix},$$

where (u_g, v_g, w_g) is grid velocities due to the moving grid, β is parameter of the artificial compressibility approach and $\beta = 1.0$ is given in the present computation. τ_{ij} is defined as $\tau_{ij} = \frac{1}{R}\left(\frac{\partial u_i}{\partial x_j} + \frac{\partial u_j}{\partial x_i}\right)$, R is Reynolds number, ν is kinematic viscosity coefficient.

The integrated and discretized form of Eq.1 is expressed as Eq.3 with using the finite volume method and Gauss integral theorem.

$$\frac{\partial V_i q_i}{\partial t} + \frac{\partial V_i q_i^*}{\partial \tau}$$
$$+ [E - E_v]_{i-1/2}^{i+1/2} + [F - F_v]_{j-1/2}^{j+1/2} + [G - G_v]_{k-1/2}^{k+1/2} = 0 \tag{3}$$

where $\pm 1/2$ means directions of each cell faces, E, F, G are convective fluxes, E_v, F_v, G_v are viscous fluxes.

The convective flux E is expressed as follows.

$$E = \begin{bmatrix} \beta U \\ u(U - U_g) + pS_x \\ v(U - U_g) + pS_y \\ w(U - U_g) + pS_z \end{bmatrix} \tag{4}$$

where $U = uS_x + vS_y + wS_z$, $U_g = u_g S_x + v_g S_y + w_g S_z$. The convective flux is evaluated by the third-order upwind scheme based on the flux-difference splitting of Roe.

$$E_{i+1/2} = \frac{1}{2}[E(q^L) + E(q^R) - |A|(q^L - q^R)]_{i+1/2} \tag{5}$$

where q^L and q^R are the left and right interface values of q at the $i + 1/2$ face. $E(q^L)$ and $E(q^R)$ are evaluated by q^L, q^R and $i + 1/2$ face area vector (S_x, S_y, S_z) with grid velocity U_g. $|A|$ is obtained by the following way. A is defined as

$$A = \frac{\partial E}{\partial q} = R\Lambda L \tag{6}$$

R is right eigen vector, and L is left eigen vector. The eigenvector Λ is expressed as follows.

$$\Lambda = diag(U - U_g, U - U_g, U - \frac{U_g}{2} + c, U - \frac{U_g}{2} - c) \tag{7}$$

where c is the pseudo-speed-of sound which is defined as

$$c = \sqrt{(U - \frac{U_g}{2})^2 + \beta(S_x^2 + S_y^2 + S_z^2)} \tag{8}$$

and $|A|$ is expressed by

$$|A| = R|\Lambda|L \tag{9}$$

where $|\Lambda| = diag(|U - U_g|, |U - U_g|, |U - \frac{U_g}{2} + c|, |U - \frac{U_g}{2} - c|)$.

The values q^L and q^R on the $i + 1/2$ face are evaluated by MUSCL approach with the third order upwinding scheme.

$$q^L_{i+1/2} = \frac{2}{6}q_{i+1} + \frac{5}{6}q_i - \frac{1}{6}q_{i-1} \tag{10}$$
$$q^R_{i+1/2} = \frac{2}{6}q_i + \frac{5}{6}q_{i+1} - \frac{1}{6}q_{i+2}$$

The grid velocities are derived from the volume where an each cell face sweeps in the second order accuracy which is same accuracy as the physical time discretization. The flux of F, G are also obtained in the similar way by replacing the suffix i to j, k. The velocity gradient on a face is computed by the divergence theorem to the control volume constructed around the face $i + 1/2$, and utilized to compute the viscous fluxes.

The second order two-step backward scheme is applied to the physical time stepping, and the first order Euler implicit scheme for the pseudo time. The linear equation system is solved by the symmetric Gauss-Seidel method. Multigrid method and local time stepping are employed to get fast convergence.

2.2 Body motion

The body motions are obtained by solving the motion equations. The general form of motion equation is given as follows.

$$\ddot{h} + C\dot{h} + Kh = (C_{force} + F_{ext})/M \tag{11}$$

where h is displacement, C is dumping coefficient, K is the constant of proportionality, C_{force} is hydrodynamic force, F_{ext} is external force, M is the mass of the system. The acceleration of motion is computed by Eq.11, and the velocity of motion is obtained as follows.

$$\dot{h}^{n+1} = \dot{h}^n + \Delta t \ddot{h}^{n+1} \tag{12}$$

The displacement of motion is obtained by third order Adams-Bashforce scheme.

$$h^{n+1} = h^n + \frac{\Delta t}{12}(23\dot{h}^{n+1} - 16\dot{h}^n + 5\dot{h}^{n-1}) \tag{13}$$

In present work, the physical time step takes the small value, and the week coupling method which the displacement is obtained at the first step of the artificial time step is applied.

2.3 Overtset grid method

The weight values for the overset grid interpolation are determined by an in-house system(Kobayashi et al.(2015)). The detail of the system can be found on Kobayashi et al.(2015), the summary is described.

1. The priority of the computational grid is set.

2. The cells of a lower priority grid and inside a body is identified (called as in-wall cell in here).

3. Receptors cells which the flow variables have to be interpolated from donor cells are defined. Two cells on a higher priority grid and facing to the outer boundary are set as receptor cells to satisfy the third order discretization of NS solver. Additionally, two cells neighborhood of in-wall cells, the cells of a lower priority grid and inside the domain of a higher priority grid are also set as the receptor cell.

4. The weight values for the overset interpolation are determined by solving the inverse problem based on Ferguson spline interpolation.

Flow variables of the receptor cell are updated when the boundary condition is set.

3 Computational results

The present method is applied to the computation of the flows around single and multiple two-dimensional cylinders(Yang et al.(2008)).
The motion equation of the cylinder is given as follows.

$$\ddot{h} + 2\zeta\left(\frac{2\pi}{U^*}\right)\dot{h} + \left(\frac{2\pi}{U^*}\right)^2 h = \frac{2}{\pi m^*}C_{force} \tag{14}$$

where h is displacement in each direction, ζ is the dumping coefficient, m^* is mass ratio which is defined as follows.

$$m^* = \frac{m}{m_f} = \frac{m}{\rho_0 \pi (D^2/4)L_c} \tag{15}$$

where D is the diameter of cylinder, L_c is the height of cylinder. $U^* = U_0/f_N D$ and f_N is natural frequency, non-dimensionalized hydrodynamic force $C_{force} = F_{force}/(\frac{1}{2}\rho DL_c U_0^2)$.

3.1 Single cylinder

At first, the computation with the motions of single cylinder by using the overset grid method which the cylinder and rectangular grids are overlapped. The mass ratio m^* is 1.07, U^* is set as 5.0, Reynolds number is $R = 200$, the dumping coefficient is $\zeta = 0.01$. The physical time step Δt is 0.01.

The division number of the cylinder surface is 161, and the minimum spacing on the surface is 1.0×10^{-4}. The distance from the cylinder surface to the grid edge takes 0.25D for the cylinder grid, and divided by 40 cells . The grid points of the rectangular grid near the cylinder are gathered to fit the cylinder grid for the overset grid interpolation.

Fig. 1 shows the computational grids after the grid deformation with the displacement of the cylinder and the axial velocity distribution near cylinder. The grid points within the distance 1.0D from the cylinder surface are deforms with the displacement of the cylinder motions, then the amount of the deformation becomes smaller, and finally take the original grid lines. The velocity contour lines connect smoothly in the two grids, thus the present method which is composed by the overset grid method and moving grid technique works well.
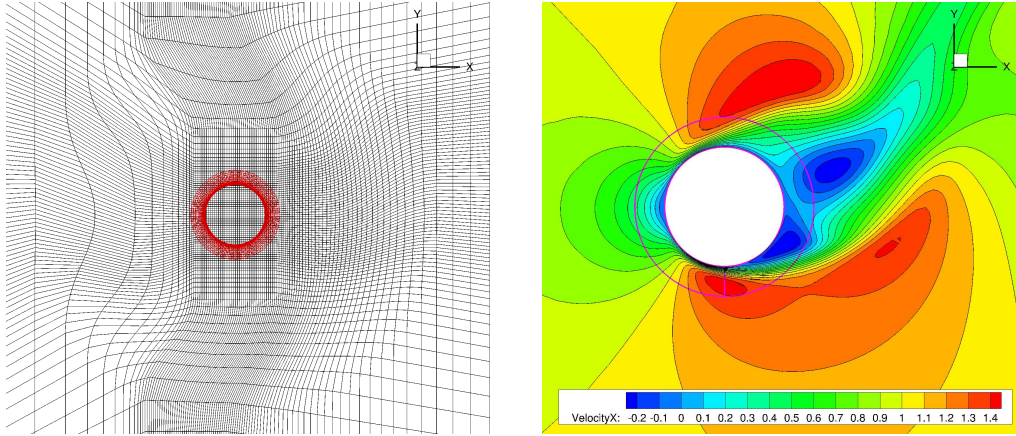
Computational grids after the deformation   Axial velocity u distribution near cylinder

Fig. 1: Results of single cylinder case

Fig. 2 shows the time history of the cylinder motion at the cylinder center. Although the displacement in x-direction has the difference, the present result draws the figure-eight as similar with the reference result.
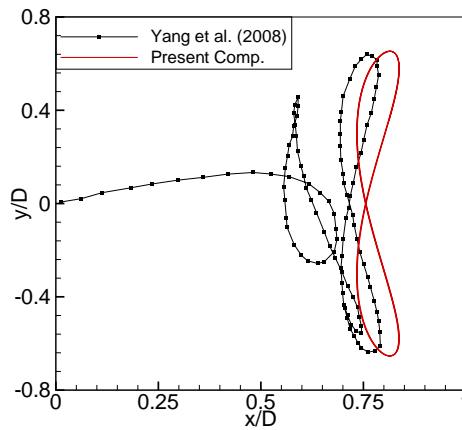
Fig. 2: Comparison of motions at cylinder center

3.2   Multiple cylinders

Next, the computation of flows around multiple cylinders with motions is carried out. 16 cylinder and the rectangular grids are overlapped. The motions of each cylinder is obtained by solving the motion equation individually. The cyclic condition is imposed to the boundary of the rectangular grid.

The same coefficients for the motion equations on the single cylinder case are utilized. The mass ratio m^* is 12.73, U^* is set as 5.0. Reynolds number based on the averaged flow velocity at the inflow boundary and the diameter of cylinder is $R = 200$, the dumping coefficient is $\zeta = 0.03$. The rectangular grid size is 14.0D in the length and width, and equally divided by 296 cells in both directions The grid for the cylinder is as same as the case of the single cylinder.

Fig. 3 shows the computational grids after the grid deformations with the displacement of the multiple cylinders and the vorticity distribution in the plane. The cylinders move individually, and the grid points within the distance 0.3D from the cylinder surface deform with the cylinder motions. The amount of the deformation becomes smaller, and finally take the original grid lines at the distance 0.9D from the cylinder surface. The regions where the grid deformations are lapped are transformed in order of the priority of the overset grid method from lower priority to higher priority. The vortices which come from the flow separation on the cylinder surface are interacted with the other vortices and cylinders, the vortices affect to the cylinder motion. The velocity contour lines connect smoothly in all grids, thus the present method works well on the multiple cylinders with motions using the overset grid method.
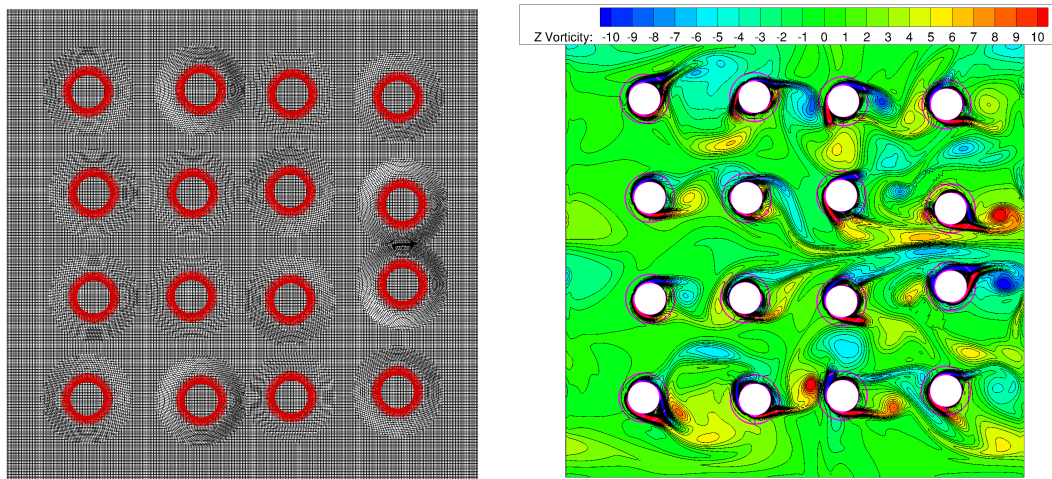
Computational grids after the deformation   Vorticity distribution in the plane

Fig. 3: Results of multiple cylinder case

4 Conclusion

The present method can handle the displacement of the motions using the grid deformation and the overset grid method. The regions where the overset relations are composed deform with the body motions to maintain the overset information, and succeed to reduce the computational load of the dynamic overset grid method.

References

K. Ohashi, N. Sakamoto. (2015). Numerical Simulation of Flows around Moving Bodies using an Overset Moving Grid Technique. Annual meeting of the Japan Society of Fluid Mechanics.

K. Ohashi, T. Hino, N. Hirata, H. Kobayashi. (2014). Development of NS solver with a structured overset grid method. The 28th Computational Fluid Dynamics Symposium.

H. Kobayashi, Y. Kodama. (2014). Developing spline based overset grid assembling approach and application to unsteady flow around a moving body. Proc. of ECCOMAS MARINE 2015.

J. Yang, S. Preidikman, E. Balaras. (2008). A strongly coupled, embedded-boundary method for fluid-structure interactions of elastically mounted rigid bodies. Journal of Fluids and Structures 24:167-182.

RANS Simulation of Self Propulsion of KCS using Simple Body-Force

Pablo Esquivel de Pablo, Janne F. Otzen and Claus D. Simonsen
FORCE Technology, Denmark, cds@force.dk

1 Introduction

The use of actuator disk plays an important role in the use of CFD for flow problems involving propeller-hull interaction. It reduces the computational cost and complexity of the simulations compared to simulations with the rotating geometry. The present work is based on the quasi-steady blade element theory described by Tokgoz (2012) which adds more complexity than simpler actuator disk models.

In the present work, the blade element model developed by Win (2014) in the self-propulsion of the KCS hull is applied. The objective is to demonstrate the capabilities of the propeller model coupled in RANS simulations. In this work, the propeller of the KCS is modelled from its geometric properties. The propeller model is tested in both open water and still water self-propulsion simulations of the 230m KCS. This study includes comparison of the propeller performance with EFD data measured in FORCE Technology towing tank.

The first step consists of the comparison and tuning of the propeller model with experimental data of the open water setup. The original model is modified by introducing two corrections coefficients, one for the thrust and the other for the torque, which are calculated with the EFD open water data. By introducing these coefficients, the accuracy of the self-propulsion simulations remains within the standard CFD margins.

The second step is to check the approach with a comparison with the self-propulsion data from the towing tank. The propeller model is inserted behind the KCS hull with the previously calculated correction coefficients.

2 Computational method

The computations are performed with the Reynolds Averaged Navier-Stokes (RANS) solver StarCCM+. The code solves the RANS and continuity equations on integral form on an unstructured mesh by means of the finite volume technique. Closure of the Reynolds stress problem is achieved by means of the k-ω SST turbulence model with an all Y^+ wall treatment. The effects of the propeller are included as a momentum source.

The setup for the open water simulations is based on two mesh regions (see Fig. 1). The background of hexahedral mesh (in blue) where the shaft used in the open water tests is included (red). The second region is a structured cylindrical mesh around the propeller area (mesh in green). The propeller model is formulated in cylindrical coordinates. The cylindrical mesh simplifies the equations of the body force integrations and gives stability to the solution. The two regions sum up 1.1 million cells and they are linked by the interface included in StarCCM+.
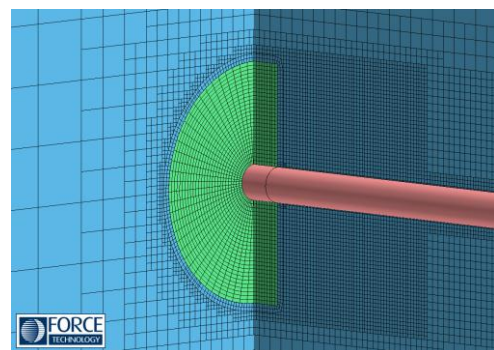

Fig. 1: Mesh for the open water setup

The behind ship setup is also divided in two regions in a similar way. The propeller region is the same cylindrical mesh imported from the previous setup with the local cylindrical coordinates. The second region contains the hull of the KCS in a domain with similar dimensions to a standard resistance simulation. The two regions sum up to 7.5 million cells. The free surface is modeled with the two-phase volume of fluid technique (VOF). The hull can move with two degrees of freedom to include the dynamic sinkage and trim effects. The rudder is included as in the EFD tests.
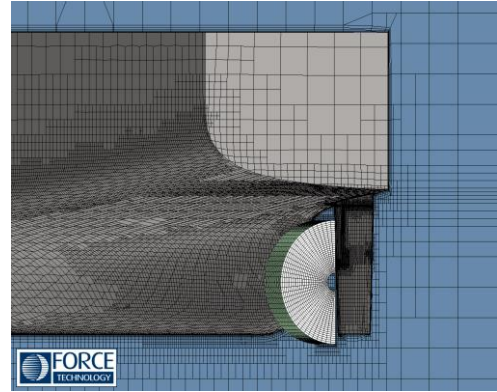
Fig. 2: Mesh for the self-propulsion setup

3 Basic ship configuration

The study is carried out for the 230m KCS in model scale as shown in table 1. Both the tank tests and the computations are done in model scale using a scale of 1:37.89. Finally, one speed condition was chosen for all configurations namely model speed of 2.006 m/s (24.0 knots full scale) corresponding to a Froude number of 0.26.

Table 1: Hull and propeller data.

		Ship	Model
Scale	[-]	1:1	1:37.89
L_{PP}	[m]	230.0	6.0702
B	[m]	32.2	0.8498
T	[m]	10.8	0.2850
∇	[m³]	52061.7	0.9571
C_B	[-]	0.651	0.651
I_{YY}	[kg·m²]	-	2232.6
LCG	[m]	111.6	2.945
D_P	[m]	7.900	0.208
Z	[-]	5	5
$P/D_{0.7}$	[-]	0.997	0.997

The 5 bladed propeller is designed by MOERI. Besides the main dimensions described above, the pitch, thickness and chord distributions along the blade are required in this model.

The rudder of the KCS is also included in the self-propulsion setup. No other appendix is defined for this hull.
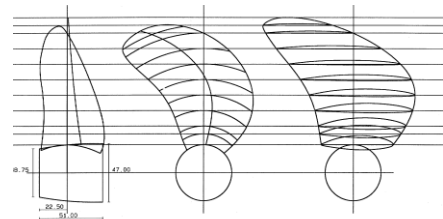
Fig. 3: MOERI's KCS propeller geometry

The geometries of both the propeller and the rudder are available in SIMMAN (2014).

4 Propeller model

The propeller model is developed by Tokgoz (2012) and it is described with high detail in Win (2014). The present work continues directly from that paper and applies the same methodology and equations with the propeller of the KCS. Starting from the blade element theory and developing an infinite-bladed model, the thrust and torque are calculated for the propeller region from the propeller geometry and flow characteristics around the propeller plane.

The equations (1) and (2) give the corrected thrust, dT, and torque, dQ, as in the model by Win (2014), but adding two correction factors, one for the thrust, C_T and one for the

$$dT = C_T \cdot (dL \cos \beta - dD \sin \beta) \cdot F \quad (1)$$
$$dQ = C_Q \cdot (dL \sin \beta + dD \cos \beta) \cdot rF \quad (2)$$

torque, C_Q. If these two correction coefficients were set to 1, the model is identical to Tokgoz and Win method.

The rest of the element are the same: the lift and drag, dL and dD; the hydrodynamic pitch angle, β; the radial distance to the center of the propeller, r; and Prandtl's tip correction factor, F.

The thrust and torque are discretized into the cylindrical propeller grid and added as a momentum source to the flow. The use of a structured cylindrical mesh simplifies the discretization. It also ensures that the same grid is used in both open water and propelled hull simulations.

5 Computational output

The computation of the open water is setup following the EFD tests in the tank. The solution is steady for each advance ratio, J. Therefore the tests can be run by changing the inflow speed to cover the advance ratio from J=0 to J>1. From the results of the original CFD setup (no correction of thrust nor torque, i.e.: C_T and C_Q = 1), the propeller has a deviation from the EFD measurements of around 4% in thrust and up to 16% in torque, see results in figures 4a and 4b. The CFD model has a small deviation of the thrust, when compared to the EFD data. On the other hand, the torque is underpredicted for values of J, below 0.5.
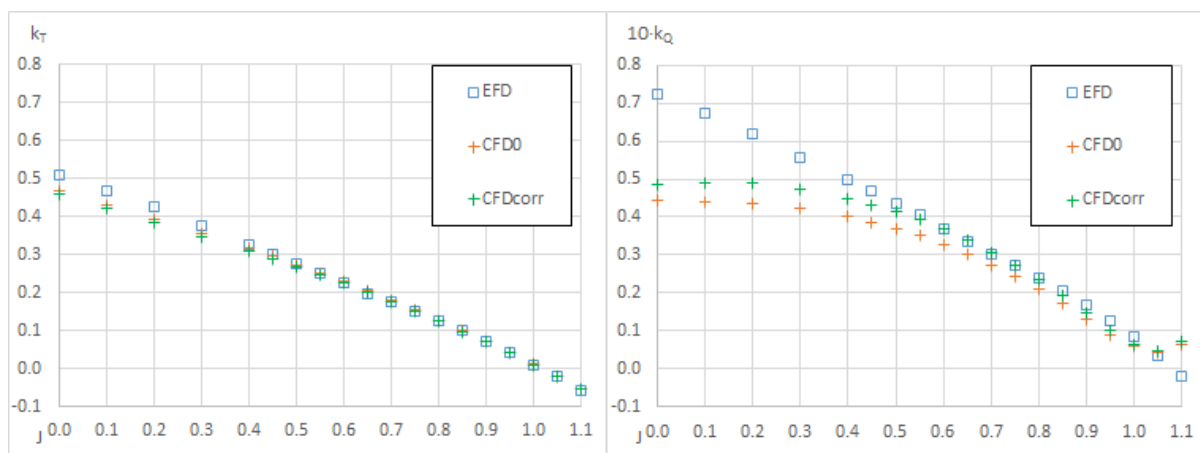

Fig. 4a: k_T results for EFD, CFD_0 (no correction) and CFD corrected

Fig. 4b: k_Q results for EFD, CFD_0 (no correction) and CFD corrected

The use of the correction factors described in equations 1 and 2, allows the model to be tuned to fit closer to the EFD data. To calculate them, it is required the EFD data or some other input of the

propeller measurements. The changes in thrust and torque are mapped for a range of C_T between 1.3 and 1.5 and a range of C_Q between 1.4 and 1.6 and compared to the EFD data. The effect of each coefficient has impact on both thrust and torque, but the combined effects of both coefficients have a planar effect in both thrust and torque, as seen in figures 5a and 5b. By using a 2D least squares method, the mapped thrust creates a plane (Fig. 5a) which means a line by crossing the zero difference with the EFD. By applying the same method with the torque, two line cross in the region at the best fitting correction coefficients, C_T and C_Q, can be calculated for each advance ratio.
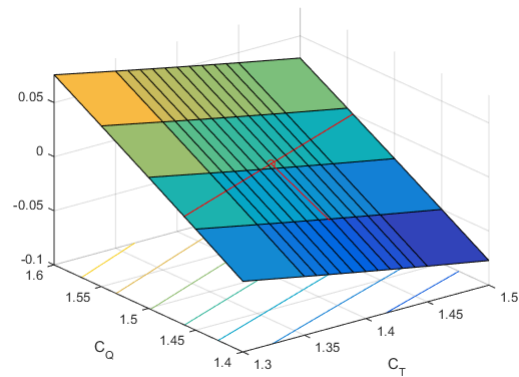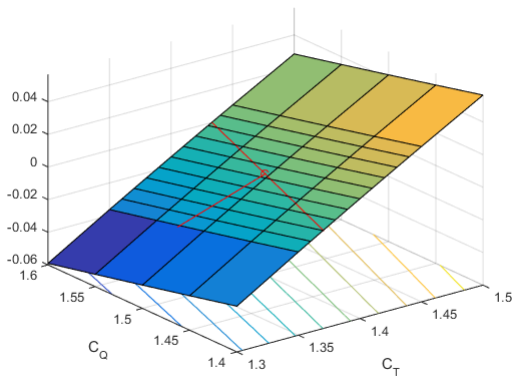
Fig. 5a: Thrust variation from EFD data with the correction factors C_T and C_Q.

Fig. 5b: Torque variation from EFD data with the correction factors C_T and C_Q.

The correction factors are specific for each advance ratio calculated. As the propeller curves deviate more in torque from the EFD measurements for lower J values, the correction factors increase significantly as seen in figure 6. Both C_T and C_Q have a minimum value around the operation point of the propeller. Constant values have been used for the calculation of the open water and for the self-propulsion simulation.
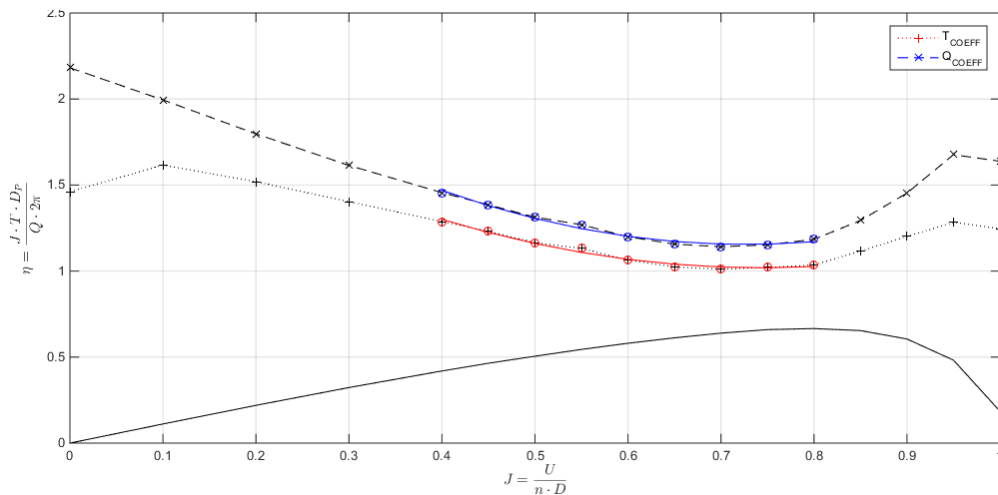
Fig. 6: Correction coefficients C_T and C_Q for the MOERI KCS propeller.

The results of the corrected CFD model in figures 4a and 4b show that the thrust is around 2% off the EFD data and the torque is 8% off for values of J>0.5. The operation point of this propeller is around J=0.6 in the self-propulsion.

6 Self-propulsion results

The corrected propeller model is implemented behind the hull in the setup described above. One speed and three RPMs are compared to the tank self-propulsion results. The model self-propulsion point has a maximum deviation of 1.3% in thrust-resistance and the torque deviates 1.4% from the EFD data.
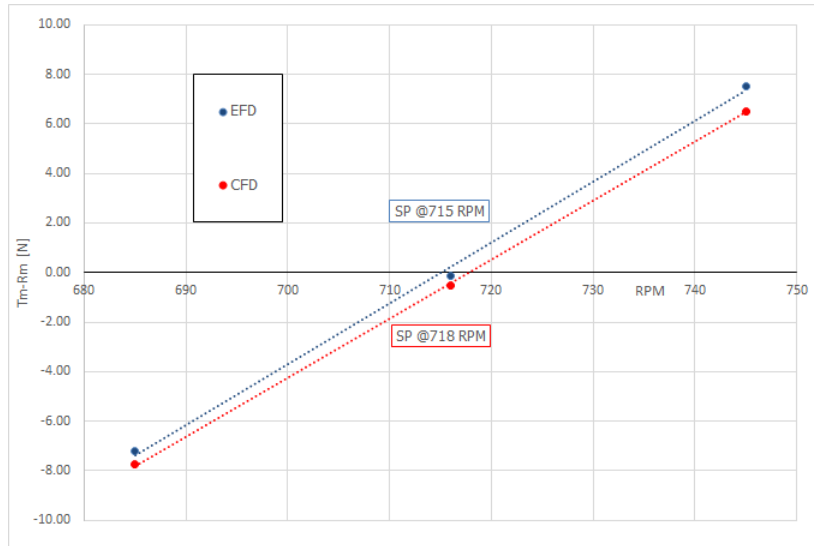
Fig. 7: Self propulsion thrust-resistance equilibrium results of EFD (blue) and CFD (red).

The dynamic sinkage and trim have a constant deviation from the EFD data. The sinkage is underestimated 6.7% from the towing tank results and the trim is 16.7% smaller than the tank, as seen in figures 8a and 8b.
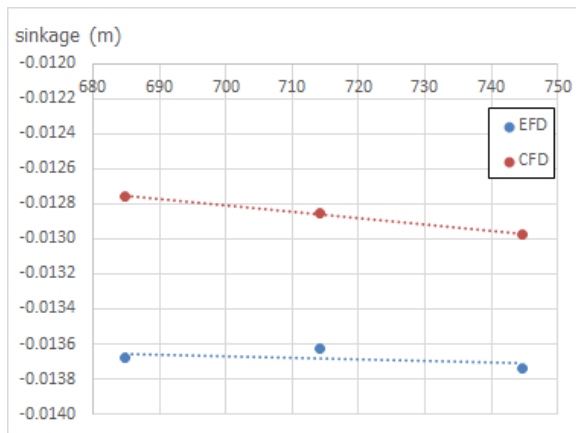
Fig. 8a: Dynamic sinkage of the self-propelled EFD (blue) and CFD (red) tests.
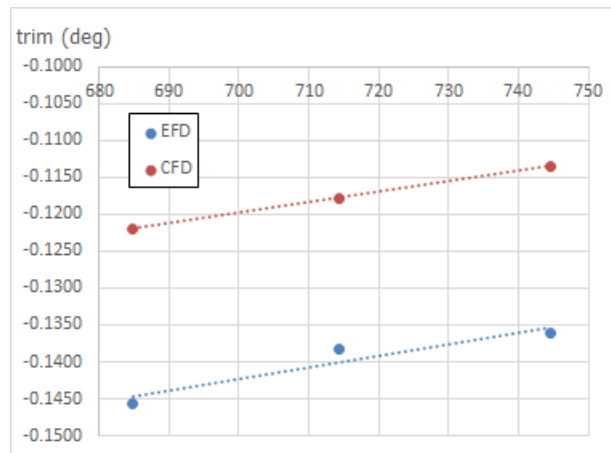
Fig. 8b: Dynamic trim of the self-propelled EFD (blue) and CFD (red) tests. Negative values mean bow down.

The propeller velocity field (fig. 9) when working behind the hull shows qualitatively good results when compared to other measurements as the published in Tokyo (2015).
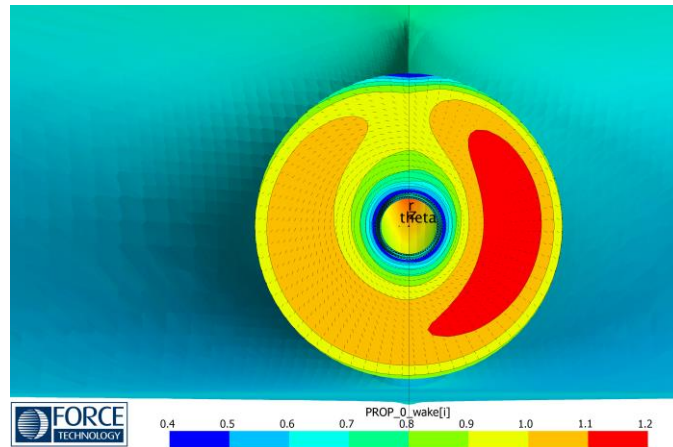
Fig. 9: Velocity field at the propeller plane.

The figures 10 and 11 represent the thrust and torque per volume unit in the disk.
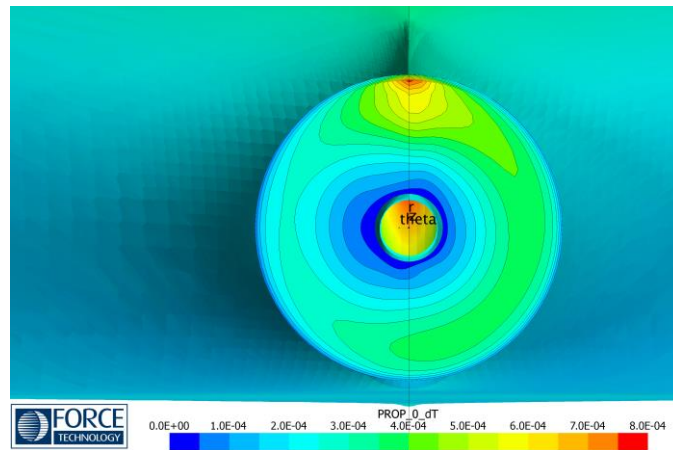
Fig. 10: Thrust distribution in the propeller disk.
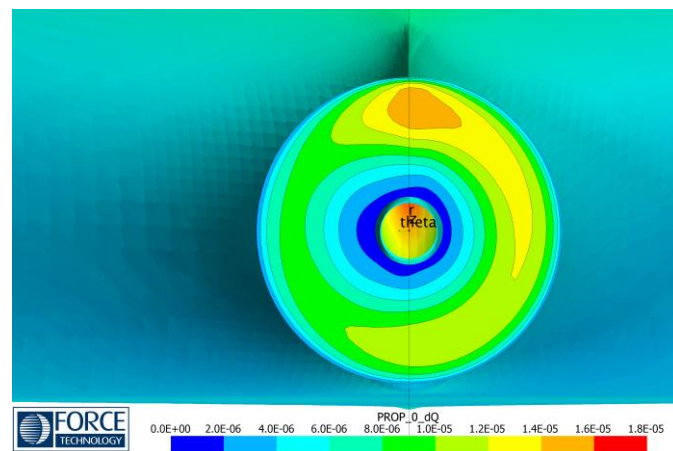
Fig. 11: Torque distribution in the propeller disk.

4 Conclusion

A simplified body force propeller model, based on the blade element theory, has been implemented in StarCCM+ to simulate ships during self-propulsion. Once the propeller model is adjusted based on experimental open water data, it provides self-propulsion results which are in quite good agreement with the data from self-propulsion towing tank tests for the KCS.

In the future, this propeller model will be applied in more tests cases to validate its implementation.

References
Y.N. Win, E. Tokgoz, P.C. Wu, F. Stern and Y. Toda (2014). Computation of Propeller-Hull Interaction using Simple Body-Force Distribution Model. *ISOPE*

Tokgoz, E, Win, YN, Kuroda, K. and Toda, Y. A New Method to Predict the Propeller Body Force Distribution for Modeling the Propeller in Viscous CFD Code without Potential Flow Code. 2nd East Asia International Student Symposium on Maritime Sciences, 2012 Kobe, Japan.

SIMMAN 2014 https://simman2014.dk/

Tokyo 2015. A Workshop on CFD in Ship Hydrodynamics. Proceedings, Volume III. Test Case 2.7. NMRI, December 2015. Tokyo, Japan.

Predicting the Reflection Coefficients of Wave Damping Zones Before Running the Flow Simulations

Robinson Perić and Moustafa Abdel-Maksoud

Institute for Fluid Dynamics and Ship Theory, Hamburg University of Technology (TUHH),
Schwarzenbergstrasse 95 C, 21073 Hamburg, Germany
robinson.peric@tuhh.de

1 Introduction

Undesired wave reflections, which occur at domain boundaries, can lead to significant errors in computational fluid dynamics (CFD) simulations. Such reflections can be reduced by gradually forcing the solution towards the solution for a calm free surface within a 'zone' attached to the corresponding domain boundary. Several such approaches have been presented under various names (e.g. wave damping zone (e.g. Park et al., 1999), sponge layer (e.g. Choi and Yoon, 2009), absorbing layer (e.g. Wei et al., 1999), dissipation zone (Park et al., 1993), ...), which will be called forcing zones in the following.

A key problem when using forcing zones is to judge how much of the wave is reflected back into the domain. This is partly because reflection coefficients are seldom determined in industrial practice, and partly because the forcing function contains user-defined parameters; these parameters must be adjusted case-dependently to ensure reliable wave damping. Since recommendations for selecting these parameters have become available only recently (see Perić and Abdel-Maksoud, 2016), many simulations are still run with default forcing parameters. Thus it is difficult to distinguish between such CFD results, which are contaminated by undesired wave reflections, and those CFD results, in which reflections were sufficiently minimized so that their influence on the results is negligible.

The present paper compares an analytical approach for predicting reflection coefficients, proposed by Perić and Abdel-Maksoud (2017), to CFD simulation results. The theory is found to predict optimum forcing zone parameters and corresponding reflection coefficients with satisfactory accuracy; it can be used for forcing of x-momentum, or z-momentum, or x- and z-momentum combined, or both x- and z-momentum as well as volume fraction α.

2 Wave damping using forcing zones

This work considers fluid flow governed by the following conservtion equations:

$$\frac{\mathrm{d}}{\mathrm{d}t} \int_V \rho \, \mathrm{d}V + \int_S \rho \mathbf{v} \cdot \mathbf{n} \, \mathrm{d}S = 0 \quad , \tag{1}$$

$$\frac{\mathrm{d}}{\mathrm{d}t} \int_V \rho u_i \, \mathrm{d}V + \int_S \rho u_i \mathbf{v} \cdot \mathbf{n} \, \mathrm{d}S =$$
$$\int_S (\tau_{ij}\mathbf{i}_j - p\mathbf{i}_i) \cdot \mathbf{n} \, \mathrm{d}S + \int_V \rho \mathbf{g} \mathbf{i}_i \, \mathrm{d}V + \int_V \rho q_i \, \mathrm{d}V \quad , \tag{2}$$

$$\frac{\mathrm{d}}{\mathrm{d}t} \int_V \alpha \, \mathrm{d}V + \int_S \alpha \mathbf{v} \cdot \mathbf{n} \, \mathrm{d}S = \int_V q_\alpha \, \mathrm{d}V \quad , \tag{3}$$

with volume V of control volume (CV) bounded by the closed surface S, fluid velocity vector $\mathbf{v}$ with the Cartesian components u_i, unit vector $\mathbf{n}$ normal to S and pointing outwards, time t, pressure p, fluid density ρ, components τ_{ij} of the viscous stress tensor, unit vector $\mathbf{i}_j$ in direction x_j, and volume fraction α of water. Unless severe wave breaking occurs, the propagation of ocean waves is an approximately inviscid phenomenon. Thus the results in this work apply regardless which formulation for τ_{ij} is chosen or whether it is neglected altogether.

Undesired wave reflections can be minimized by applying forcing source terms

$$q_\alpha = \gamma b(x) (\alpha_{\mathrm{ref}} - \alpha) \quad , \tag{4}$$

$$q_i = \gamma b(x)(u_{i,\mathrm{ref}} - u_i) \quad , \tag{5}$$

with reference volume fraction α_{ref}, reference velocity component $u_{i,\text{ref}}$, forcing strength γ and blending function $b(x)$. In this work, $u_{i,\text{ref}} = 0$, and α_{ref} corresponds to the volume fraction for calm water surface, thus the 'forcing' can be interpreted as 'damping'. Forcing strength γ regulates the magnitude with which the solution at a given cell is forced against the reference solution. The blending term $b(x)$ regulates how the source term varies within the zone. In this work, exponential blending is used

$$b(x) = \left(\frac{e^{\left(\frac{x - x_{\text{sd}}}{x_{\text{ed}} - x_{\text{sd}}} \right)^2} - 1}{e^1 - 1} \right) \quad .$$

(6)

with start coordinate x_{sd} and end coordinate x_{ed} of the forcing zone; the zone thickness is $x_{\text{d}} = |x_{\text{ed}} - x_{\text{sd}}|$. Zone thickness x_{d} and forcing strength γ are case-dependent and must be adjusted for each simulation. Perić and Abdel-Maksoud (2016) showed that forcing strength γ and forcing zone thickness x_{d} scale as

$$\gamma \propto \omega, \quad x_{\text{d}} \propto \lambda \quad ,$$

(7)

with angular wave frequency $\omega = \frac{2\pi}{T}$, wave period T, and wavelength λ.

3 Simulation setup

In the flow simulations in this work, a regular long-crested free-surface wave train is created and propagates in positive x-direction towards a forcing zone as sketched in Fig. 1, where it is partly reflected and partly absorbed. The wave has height $H = 0.16\,\text{m}$, period $T = 1.6\,\text{s}$, wavelength $\lambda \approx 4\,\text{m}$ and is moderately non-linear (steepness H/λ is $\approx 29\%$ of maximum steepness). Deep water conditions apply (water depth $> 0.5\lambda$).
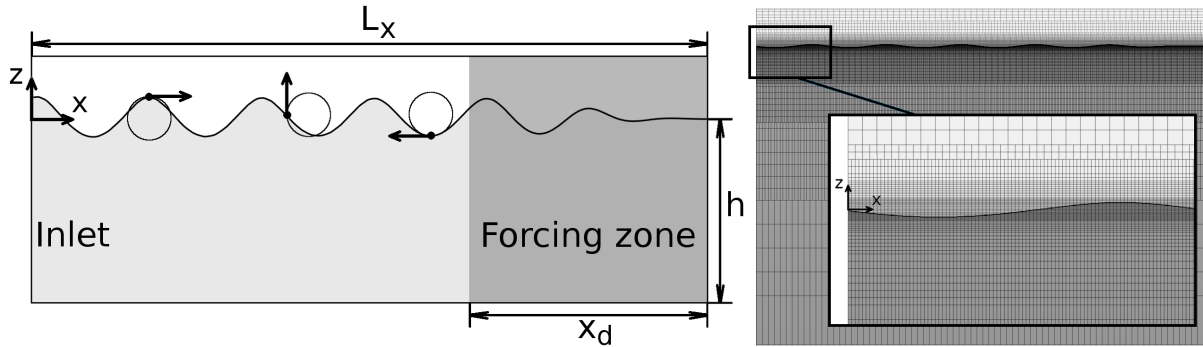
Fig. 1: Left: solution domain filled with air (white) and water (light gray, water depth h), velocity inlet at $x = 0$ and forcing zone (shaded dark gray) with thickness x_{d}; three fluid particles (black dots) are sketched with their particle paths (circles) and velocity vectors (arrows); right: computational grid with close-up, showing the initialized location of the free surface (thick black curve) and of the liquid phase (shaded dark gray)

The finite-volume-based commercial flow solver STAR-CCM+ version 11.06.010-R8 from Siemens (formerly CD-adapco) is used. The volume of fluid (VOF) method accounts for the two phases, liquid water and gaseous air, using the High Resolution Interface Capturing scheme (HRIC) as given in Muzaferija and Perić (1999). All discretization approximations are of second order. The linearized equation system is solved by the iterative STAR-CCM+ implicit unsteady segregated solver, using an algebraic multigrid method with Gauss-Seidel relaxation scheme, V-cycles for pressure and volume fraction of water, and flexible cycles for velocity calculation. The under-relaxation factor is 0.9 for velocities and volume fraction and 0.4 for pressure. Eight iterations are performed per time-step; one iteration consists of solving the governing equations for the velocity components, the pressure-correction equation (using the SIMPLE method for collocated grids to obtain the pressure values and to correct the velocities) and the transport

equation for the volume fraction of water. Further information on the discretization of and solvers for the governing equations can be found in Ferziger and Perić (2002) or the STAR-CCM+ software manual.

The forcing approaches from Sect. 2 are used to reduce wave reflections. Simulations are either run with forcing of x-momentum (q_x), of z-momentum (q_z), of both x- and z-momentum (q_x, q_z), or of volume fraction α and x- and z-momentum (q_α, q_x, q_z).

The domain has dimensions $0 \leq x \leq L_x$ and $-h \leq z \leq 0.5\lambda$, with domain length $L_x = 6\lambda$ and water depth $h = 4.5\lambda$. The simulations are run quasi-2D, i.e. with only one layer of cells in y-direction and symmetry boundary conditions applied to the y-normal boundaries. The wave is generated by prescribing the volume fraction and velocities according to Fenton's (1985) 5th-order Stokes theory at the inlet boundary ($x = 0$). At boundary $x = L_x$, the hydrostatic pressure for a calm water surface is prescribed. All remaining boundaries are no-slip walls. As initial condition, the volume fraction and velocities in the solution domain are prescribed according to Fenton's (1985) Stokes 5th-order theory to reduce the simulation time. The domain is discretized using a rectilinear grid with local mesh refinement around the free surface. The free surface stays at all times within the region of the finest mesh with ≈ 100 cells per wavelength and ≈ 16 cells per wave height. The computational grid, which consists of $\approx 43\,000$ cells, is shown in Fig. 1. The total simulated time is $18\,\mathrm{s} \approx 11.3T$ with a time step of $\Delta t = T/1000$. The free-surface elevation is written to a file at 80 evenly spaced time intervals per wave period. From the elevation in an interval of 1.5λ adjacent to the forcing zone, the overall highest and lowest wave heights are obtained as $H_{\max}$ and $H_{\min}$. From these, the reflection coefficient is calculated as in experiments after the procedure by Ursell et al. (1960) as

$$C_R = (H_{\max} - H_{\min})/(H_{\max} + H_{\min}) \quad . \tag{8}$$

The reflection coefficient gives the ratio of the wave heights of reflected to incoming wave; the ratio of the energy of the reflected (E_{refl}) wave to the incoming (E_{in}) wave is $E_{\mathrm{refl}}/E_{\mathrm{in}} \approx C_R^2$, since according to linear wave theory the wave energy depends on the wave height squared. Thus a reflection coefficient of $C_R = 10\%$ means that the forcing zone reflects 1% of the incoming wave energy.

4 Results and discussion

4.1 Forcing of x-momentum

Flow simulations are carried out with the setup from Sect. 3 and compared to the theory presented in Perić and Abdel-Maksoud (2017). Forcing of x-momentum according to Eq. (5) with exponential blending from Eq. (6) is used to damp the waves. Simulations are run for different forcing strengths ($0.625\,\mathrm{rad/s} \leq \gamma \leq 5120\,\mathrm{rad/s}$) and forcing zone thicknesses ($0.25\lambda \leq x_d \leq 2\lambda$). Comparing simulation results and theory in Fig. 2 shows that the theory can predict reflection coefficient C_R with high accuracy. Although the waves are moderately nonlinear ($\approx 29\%$ of maximum steepness), the deviations are small; this agrees with results from Perić and Maksoud (2016), where deep-water waves up to $\approx 71\%$ of the maximum steepness were investigated, and the influence of wave steepness on the reflection coefficient in this range was found to be negligible for practical purposes ($< 2\%$ difference), except for γ roughly an order of magnitude below optimum, where the damping improved noticeably for the steeper wave. The simulated and theoretical surface elevations agree well as shown in Fig. 3, where boundary $x = 24\,\mathrm{m}$ was set to wall for better comparison (this was also done for the free surface elevation in Fig. 5 and for Fig. 4). The peaks in the partial standing wave have different locations depending on γ, which shows that, with increasing forcing strength γ, the effective reflection location shifts from the boundary, to which the forcing zone is attached (here $x = 24\,\mathrm{m}$), towards the entrance to the forcing zone (here $x = 16\,\mathrm{m}$). The theory predictions for horizontal and vertical velocities also agree well with simulation results and are not plotted here. Figure 4 shows that the forcing creates vorticity (here: $w_{x,j} - u_{z,j}$) in the flow field within the forcing zone. Although the generated amount of vorticity is comparatively small, it is predicted remarkably well. Small amounts of vorticity are also generated at the free surface and at locations where the mesh size changes, as artifacts of the interface capturing scheme and the discretization; however, such a vorticity generation is discretization dependent, i.e. it disappears on infinitely fine grids, whereas the forcing-generated vorticity turned out to be grid-independent.

Fig. 2: Reflection coefficient C_R over forcing strength γ for forcing of x-momentum, given for different forcing zone thickness x_d according to simulation and theory
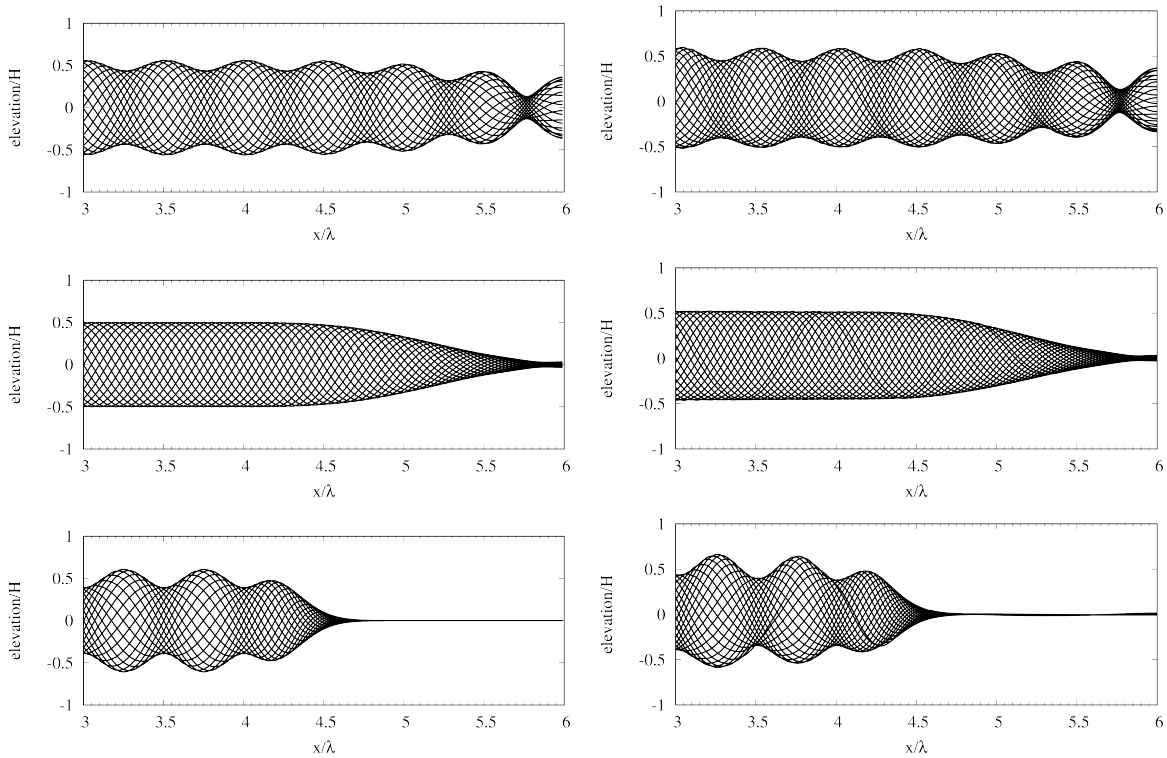
Fig. 3: Theory predictions (left) and simulation results (right) for surface elevation scaled by wave-height H over x-coordinate scaled by wavelength λ for forcing zone thickness $x_d = 2\lambda$; evaluated for equally spaced time intervals during the last simulated period; with forcing strength γ too weak (top, $\gamma = 2.5\,\text{rad/s}$), close to optimum (middle, $\gamma = 10\,\text{rad/s}$), too strong (bottom, $\gamma = 640\,\text{rad/s}$)
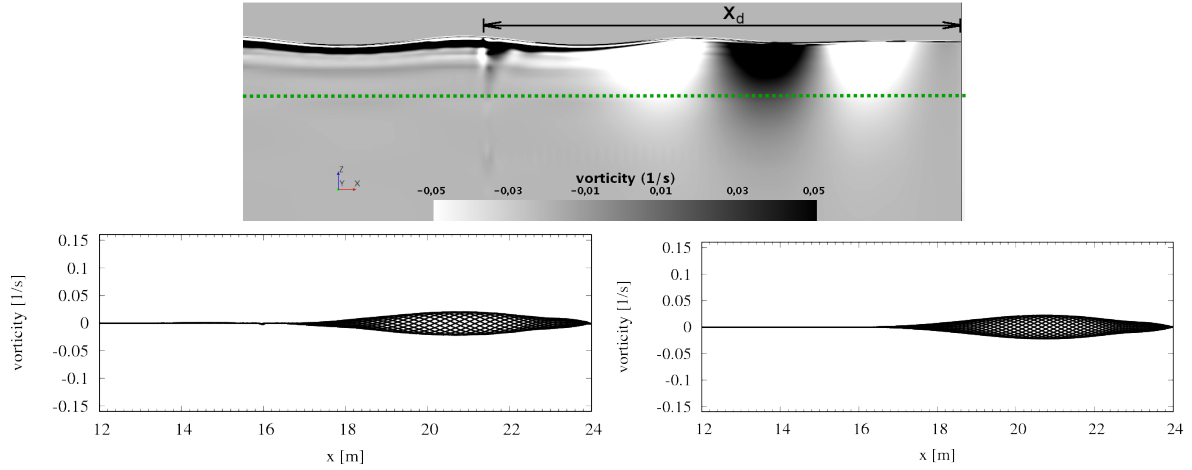
Fig. 4: Top: simulation results at time $t = 18\,\mathrm{s}$ for vorticity in domain section including the forcing zone, for forcing strength $\gamma = 10\,\mathrm{rad/s}$, zone thickness $x_\mathrm{d} = 2\lambda$, and exponential blending according to Eq. (6); bottom: vorticity over x-coordinate for simulation (left) and theory (right); evaluated at $z = -1.2\,\mathrm{m}$ for equally spaced time intervals during the last simulated period

4.2 Forcing of z-momentum

Repeating the simulations from Sect. 4.1 with forcing of z-momentum instead of x-momentum shows that the theory predicts optimum forcing strength and corresponding reflection coefficient C_R reliably. Figure 5 shows that, for optimum or lower values of forcing strength γ, the simulation results agree well with theory predictions. For stronger forcing than optimum (here: $\gamma > 40\,\mathrm{rad/s}$) the theory predictions of C_R are conservative. For such γ-values, forcing of z-momentum leads to a noticeable net mass flux into the forcing zone in the simulation. This becomes more pronounced with increasing γ. In the present case, this mass flux resulted in a lower reflection coefficient C_R compared with x-momentum forcing for the same γ. However, since this effect is negligible for optimum and lower forcing strength, the theoretical prediction is satisfactory for practical purposes.
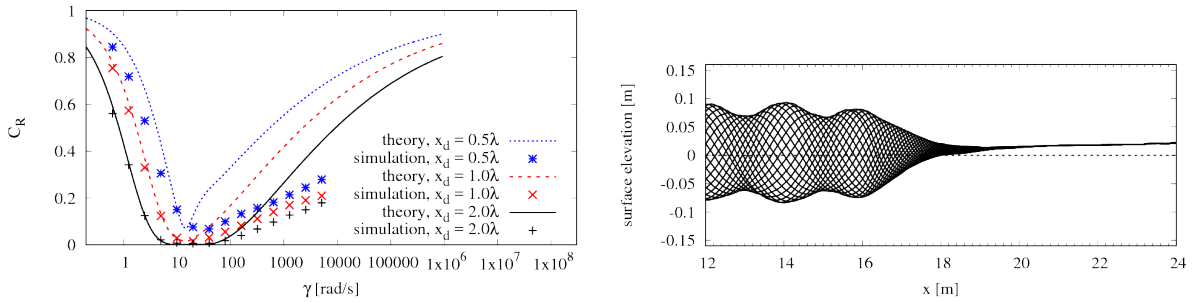
Fig. 5: Left: As Fig. 2, except for forcing of z-momentum; right: Simulation results for surface elevation over x-coordinate for forcing of z-momentum with zone thickness $x_\mathrm{d} = 2\lambda$ and stronger-than-optimum forcing $\gamma = 2560\,\mathrm{rad/s}$; evaluated for equally spaced time intervals during the last simulated period; a rise in water level (dashed line indicates undisturbed free surface) occurs close to the domain boundary at $x = 24\,\mathrm{m}$, which indicates a net mass flux into the forcing zone that was not observed for x-momentum forcing

4.3 Forcing of x- and z-momentum and volume fraction α

The simulations from Sect. 4.1 are repeated with forcing of x- and z-momentum (Eq. (5)), both with and without forcing of volume fraction α (Eq. (4)). The theory predicts the optimum forcing strength γ and the corresponding reflection coefficient C_R satisfactorily. Figure 6 shows that, as in Sect. 4.2, for stronger

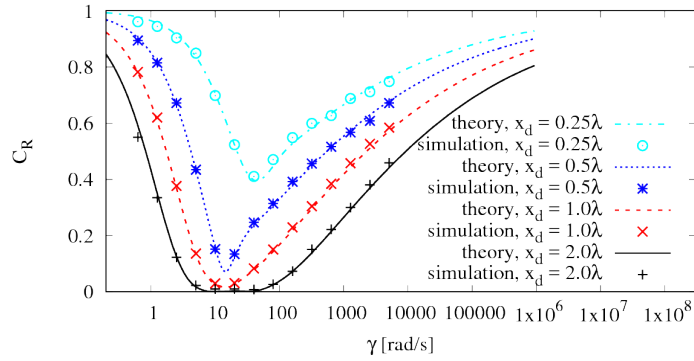than optimum forcing, reflection coefficients in the simulations are smaller than the theory predicts.
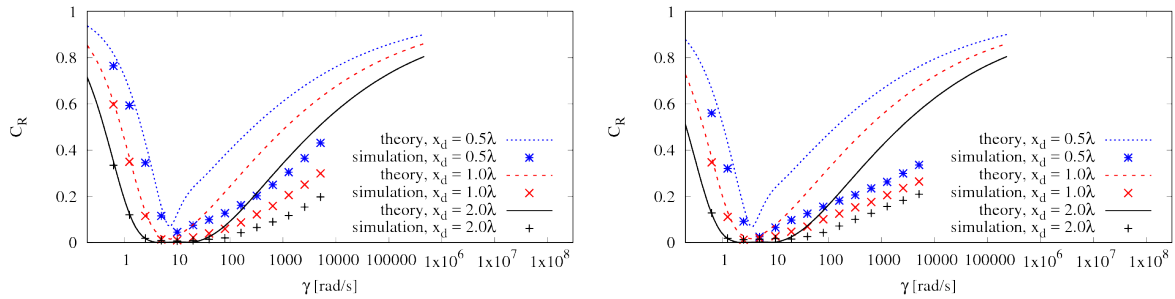
Fig. 6: Reflection coefficient C_R over forcing strength γ given for different forcing zone thickness x_d according to simulation and theory; for forcing of x- and z-momentum (left), and for both forcing of x- and z-momentum and volume fraction α (right)

5 Conclusion

The results show that the theory presented by Perić and Abdel-Maksoud (2017) predicts the optimum parameter settings and corresponding reflection coefficients for wave damping zones with satisfactory accuracy. For engineering practice, the theory can be used to optimally tune the parameters of the wave damping zone *before running the simulation*. Although only results for exponential blending $b(x)$ were shown in this work, the theory can take any arbitrary blending function $b(x)$ as input - thus it can predict reflection for many existing wave damping implementations in CFD codes. The theory can also be useful to assess the influence of reflections on the results from flow simulations that one did not perform oneself. Since it is not common practice in industry to provide reflection coefficients for flow simulations, it is beneficial to be able to obtain the reflection coefficients from theory, and judge whether the settings were appropriate; this is possible for any forcing zone formulation that can be expressed in terms of Eqs. (5) and (4). Literature results are promising that the theory also predicts reflection for damping of three-dimensional waves, irregular waves and highly non-linear waves with satisfactory accuracy; future research will investigate this.

Acknowledgements

References

Choi, J., Yoon, S. B., 2009. Numerical simulations using momentum source wave-maker applied to RANS equation model. Coast. Eng., 56(10), 1043-1060.

Fenton, J.D., 1985. A fifth-order Stokes theory for steady waves. J. Waterway, Port, Coastal, Ocean Eng. 111 (2), 216-234.

Ferziger, J., Perić, M., 2002. Computational Methods for Fluid Dynamics, Springer, Berlin.

Muzaferija, S., Perić, M., 1999. Computation of free surface flows using interface-tracking and interface-capturing methods, in: Mahrenholtz, O., Markiewicz, M. (Eds.), Nonlinear Water Wave Interaction, WIT Press, Southampton, pp. 59-100.

Park, J. C., Kim, M. H., Miyata, H., 1999. Fully non-linear free-surface simulations by a 3D viscous numerical wave tank. Int. J. Numerical Methods in Fluids, 29(6), 685-703.

Park, J. C., Zhu, M., Miyata, H., 1993. On the accuracy of numerical wave making techniques. J. Society of Naval Architects of Japan, 1993(173), 35-44.

Perić, R., Abdel-Maksoud, M., 2015. Assessment of uncertainty due to wave reflections in experiments via numerical flow simulations. Proc. Twenty-fifth Int. Ocean and Polar Eng. Conf. (ISOPE2015), Hawaii, USA.

Perić, R., Abdel-Maksoud, M., 2016. Reliable damping of free-surface waves in numerical simulations. Ship Technology Research, 63(1), 1-13.

Perić, R., Abdel-Maksoud, M., 2017. Analytical Prediction of Reflection Coefficients for Wave Absorbing Layers in Flow Simulations of Free-Surface Waves. Preprint, link: https://arxiv.org/abs/1705.06940

Perić, R., Hoffmann, N., Chabchoub, A., 2015. Initial wave breaking dynamics of Peregrine-type rogue waves: a numerical and experimental study. European J. Mechanics-B/Fluids, 49, 71-76.

Wei, G., Kirby, J. T., Sinha, A., 1999. Generation of waves in Boussinesq models using a source function method. Coast. Eng., 36(4), 271-299.

Adaptive grid refinement for two-phase flow applications

Peter van der Plas[*], **Arthur E. P. Veldman**[*], **Joop Helder**[†], **Ka-Wing Lam**[†]
[*]University of Groningen, Netherlands, [†]MARIN, Wageningen/Netherlands
P.van.der.Plas@rug.nl

1 Introduction

In a previous study (van der Plas et al., 2015) we introduced an adaptive grid refinement method for free-surface flow simulations and presented preliminary results for various offshore applications. In a follow-up study, the grid refinement method has been extended to include support two-phase flow (Wemmenhove et al., 2016) and enable the inclusion of moving objects (Fekken, 2004). In this paper, we highlight some of its properties and its applications.

2 Outline of the numerical method

In the past, the CFD simulation tool ComFLOW (Veldman et al., 2016) has been successfully applied to wave simulations and impact calculations. In many offshore applications, e.g. impact calculations, the grid resolution can be increased efficiently by means of grid stretching or static local refinement. However, when trying to accurately resolve the surface dynamics and kinematics of irregular and breaking waves, the resolution requirements are strongly time-dependent and difficult to predict in advance. Efficient grids can then only be obtained by means of time-adaptive refinement

A Cartesian block-based refinement approach is followed which allows for efficient grid adaptation, with moderate overhead. Upon satisfying a refinement or coarsening criterion grid blocks can be split or merged. Employing fixed-size grid blocks allows for a computationally efficient implementation of the numerical algorithms. Instead of an oct-tree, an array-based data structure is employed which exploits the semi-structured nature of the Cartesian block grid. A simple relation between grid indices of a parent block at level L and its underlying children at level L+1 as shown in Figure 1(a). Missing data (e.g. pressure, velocity, liquid distribution) is reconstructed in so-called guard layers, colored green and blue in Fig. 1(b), which allows to extend the regular discretization methods up to and including the boundaries of the refinement grids.
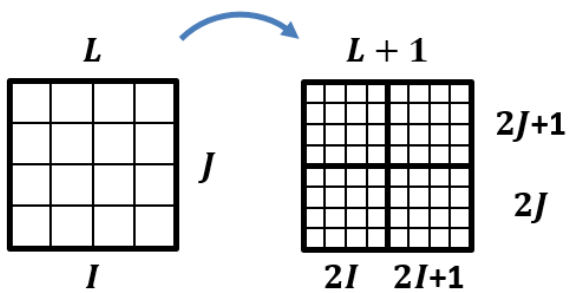
Fig 1(a): illustration of semi-structured indexing on a locally refined Cartesian grid
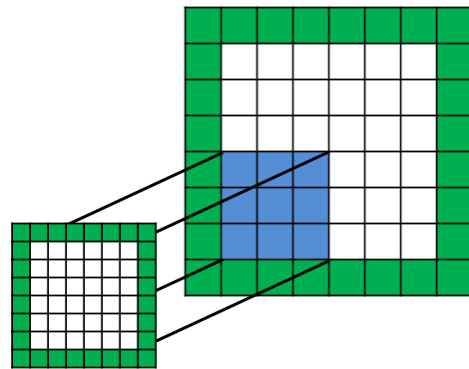
Fig 1(b): guard layers on a block-based adaptive grid

The method was introduced previously for static local grid refinement and proved useful in a variety of offshore applications (van der Plas, 2013). The modified grid data structure and the numerical discretization at interfaces is described in full detail in (van der Plas, 2017). Special attention was paid

to the modified treatment of the Volume-of-Fluid scheme near refinement interfaces. At refinement interfaces the accuracy of the numerical is scheme is lower than in regular parts of the grids (first-order versus second-order). In particular if the cells are cut by the geometry or the free surface the accuracy can degrade even further. This poses no problems as long as the grid interfaces can be placed in smooth parts of the solution, however, depending on the problem at hand this may be difficult to realize. Designing a higher-order and conservative discretization at refinement interfaces is a difficult task. As an alternative, we decided to adapt the computational grid using a surface- and geometry-tracking criterion which ensures that a uniform resolution is maintained around the free surface and the geometry.

3 Wave simulations

An important application area of ComFLOW is the simulation of irregular waves. One example could be the reconstruction of wave conditions as observed in an experimental test setup. In that manner CFD can be used to numerically investigate modifications in the test setup. An iterative procedure is applied in which after each run, the incoming wave signal is modified in order to better reproduce the measured water elevations inside the domain. Once a good representation is obtained, the signal is imposed on a 3-D domain including all features of the experimental setup. A more detailed description of this procedure can be found in reference (Bunnik et al., 2015).
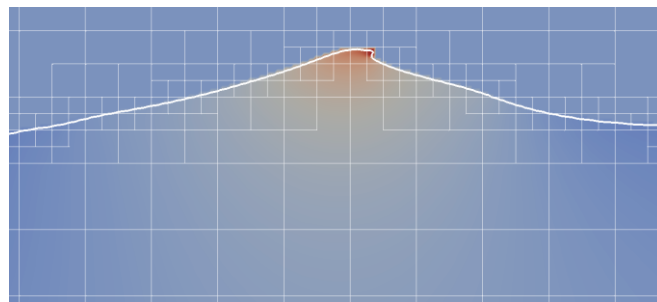
Fig. 2: spilling breaker on an adaptive grid, cross section colored by horizontal velocity

The efficiency of wave simulations can be increased considerably by coarsening the grid away from the free surface. For moderate wave conditions, static local grid refinement can be applied straightforwardly by inserting one or more refinement strips along the entire surface. For these cases, the overhead of grid adaptivity would not pay itself back. However, under more violent wave conditions, e.g. focusing and breaking waves, static refinement becomes less efficient and grid adaptivity starts to become more interesting (see e.g. Figure 2). Block-based (adaptive) grid refinement reduces the number of grid cells, but also introduces overhead due to data exchange and grid adaptation. On block-based grids data has to be exchanged between adjacent blocks, even if located on the same refinement level. Overhead increases with the relative number of grid interface cells, hence becomes more noticeable on smaller blocks. For illustration purposes consider the simulation of a spilling breaker in a 2-D domain using four different types of grids as outlined in Table 1. Similar outcomes were obtained on all grids.

	uniform	*patch*-based local refinement, static	*6x6-block*-based local refinement, static	6x6-block-based refinement, adaptive
#	47k	16k	16k	6k
total time [s]	**1287**	**443**	**746**	**366**
time per grid point [s]	0.03	0.03	0.05	0.06

Table 1: computation times for a 2-D wave simulation on different types of grids. All grids have identical resolution around the free-surface; the patch-based and block-based grids are effectively identical.

As shown in Table 1, employing a 6x6-block-based grid is almost twice as costly as employing a patch-based grid. Grid adaptivity ultimately compensates for this overhead (last column of Table 1) and altogether yields the best performance, but it may be worthwhile to increase efficiency. This could be accomplished, for example, by combining adjacent grid blocks into larger patches so as to reduce the number of interfaces. The example just considered only slightly benefits from introducing grid adaptivity. It is worth noting that larger (3D) problems or problems with more variation in time, show increasing benefit from grid adaptivity. One such example will be given in the following section.

4 Simulation of a free-fall lifeboat drop

In this section, we investigate the applicability of the numerical method by considering the simulation of a free-fall lifeboat drop. Measurements were performed at MARIN, which will be used for comparison. Adaptive grid refinement is used to facilitate grid setup and reduce computational time.

Currently we only consider lifeboat drops in still water, but ultimately it can be combined with incoming (irregular) waves, for example using the method described in the previous section.
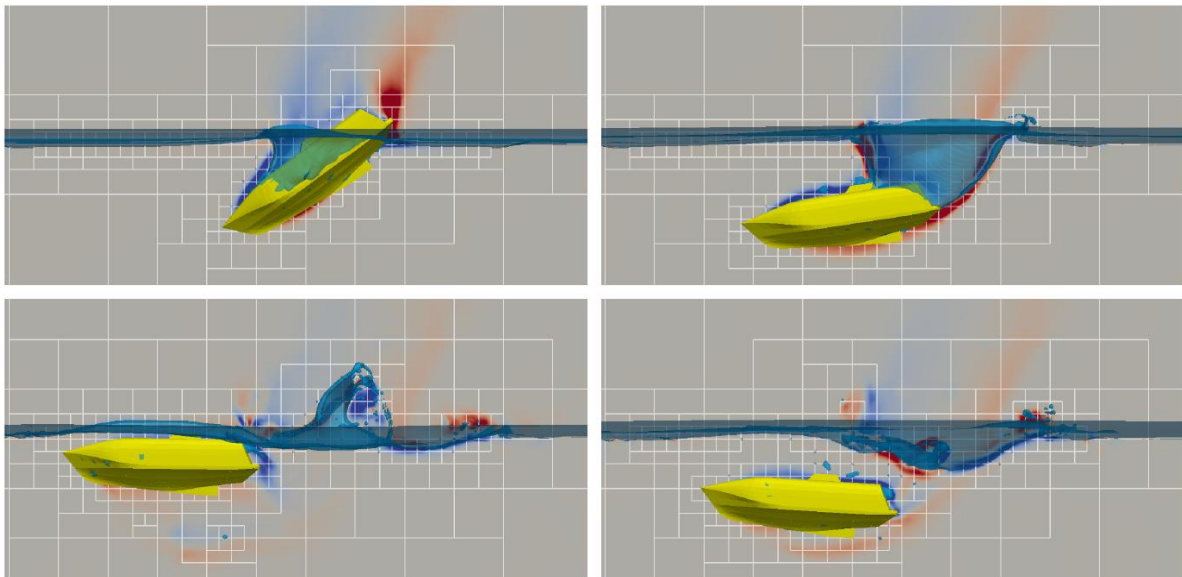

Fig. 3: Simulation of a free-fall lifeboat (snapshots are sorted clockwise, starting from the top-left corner). The grid is adaptively refined by means of a basic surface and geometry tracking criterion. Each visualized block corresponds to 6x6x6 grid cells. Coloring represents the flow vorticity in the *xz*-plane, clipped to the interval [-12; 12].

Here we only present the results obtained with the two-phase flow module and a second-order upwind convection. As a starting point, simulations were also performed using the one-phase flow module of ComFLOW and a first-order upwind discretization of convection. However, the results obtained with these settings resulted in a poor approximation of the measurements in the test basin. It was concluded that two-phase flow effects play a crucial role that cannot be neglected. Furthermore, it was observed that second-order upwind discretization of convection significantly improved results (we hope to further investigate the role of turbulence modeling in the near future).

grid	resolution around surface [m]	resolution around geometry [cm]	#	total computation time [h]
2-1 / FF1000S-*coarse*	50.0	25.0	35k	??
3-2 / FF1000S-*medium*	25.0	12.5	90k	??
4-3 / FF1000S-*fine*	12.5	6.25	320k	??

Table 2: properties of the numerical simulations. NOTE: final paper will mention computational times, including the computational time on a static grid for comparison purposes

Of critical importance is the grid resolution around the object and the free surface. Various grid configurations were investigated with local resolutions ranging between 0.5 m and 0.06 m. The properties of three simulations are listed in Table 2. In the far-field, both in horizontal direction and towards the bottom of the domain, the grid resolution is coarsened down to a resolution of 2 m.

The obtained numerical results are shown in Figure 4, together with the measurements from experiment. Overall, a good agreement is observed between the numerical simulation and the measurements from experiment. Given the small differences between the solutions on the medium and fine grids it is expected that further grid refinement will only have minor effect on the solution. The remaining differences are most visible after 1.5 to 2 seconds, which is when the lifeboat is almost totally submerged and detaches from the air gap (see steps 2 and 3 in Figure 3). It is thought that the results may improve further, by modeling more of the physical aspects at play. One could think of turbulence modeling (in particular behind the lifeboat), surface tension, as well as compressibility (in particular in the region of air inclusion).
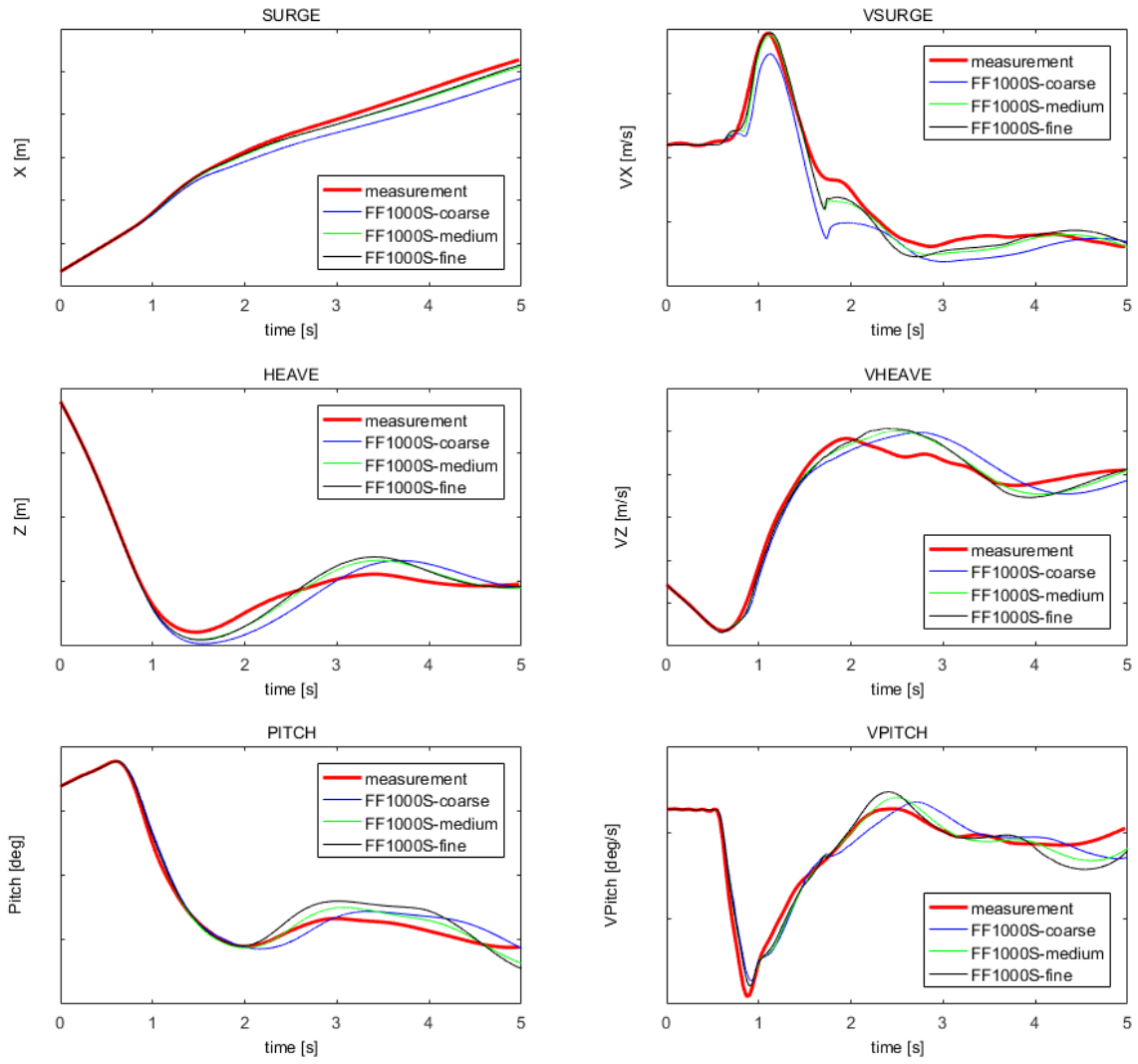
Fig. 3: Comparison of motion time traces obtained from experiment and simulation (positions on the left and velocities to the right).

Conclusions and outlook

Currently we are testing the numerical method to the simulation of lifeboat drops in waves. Ultimately our goal is to combine the functionality described in sections 3 and 4 in order to perform simulations of free-fall lifeboat drops in regular and irregular wave conditions. This poses several challenges such as accurately imposing the incoming waves and modifying the absorbing boundary conditions to support two-phase flow. Furthermore, the computational efficiency will be improved by means of MPI parallelization and further optimization of the adaptive grid refinement method. As mentioned in section 4, we also intend to investigate the role of other physical aspects, such as turbulence, surface tension and compressibility.

References

T. Bunnik, J. Helder and E-J. de Ridder (2015), Deterministic Simulation of Breaking Wave Impact and Flexible Response of a Fixed Offshore Wind Turbine, *Proceedings* OMAE 2015.

G. Fekken: Numerical simulation of free surface flow with moving rigid bodies. *PhD thesis*, University of Groningen (2004).

P. van der Plas, A.E.P. Veldman, et al. (2015), Adaptive Grid Refinement for Free-Surface Flow Simulations in Offshore Applications, *Proceedings* OMAE 2015.

P. van der Plas, et al. (2013), Local Grid Refinement for Free-Surface Flow Simulations, *Proceedings* NuTTS Symposium 2013.

P. van der Plas (2017), Local Grid Refinement for Free-Surface Flow Simulations, *PhD thesis*, University of Groningen

A.E.P. Veldman, R. Luppes, et al. (2016), Locally Refined Free-Surface Flow Simulations for Moored and Floating Offshore Platforms, *Proceedings* ISOPE 2016.

R. Wemmenhove, R. Luppes, A.E.P. Veldman and T. Bunnik (2015). Numerical simulation of hydrodynamic wave loading by a compressible two-phase flow method. Comp. Fluids, 114 (2015)

On the Turbulence Modelling for an Air Cavity Interface

Gem Rotte[*], Maarten Kerkvliet[†], and Tom van Terwisga[*†]
[*]TU Delft, Delft/The Netherlands [†]MARIN, Wageningen/The Netherlands
G.M.Rotte@tudelft.nl

1 Introduction

The use of air lubrication techniques can significantly reduce a ship's fuel consumption by reducing the frictional drag. One of the most promising techniques applicable to ships is the external air cavity technique. An external cavity is created beneath the ship's hull with the help of a cavitator, which is located directly upstream of an air injection point (at the left of figure 1a). The cavitator is extended in the span-wise direction and typically has a rectangular or triangular cross section. It is used to separate the mean water flow from the hull, thereby providing a stable air layer. Air cavity applications are claimed to lead to propulsive power reduction of 10-20% (Gorbachev and Amromin (2012), Zverkhovskyi (2014)). However, a complete understanding of the influence of the ship's hull form on the relevant two-phase flow physics and thereby also on the length and stability of the air cavities is still lacking. This inability to predict the air cavity characteristics hampers the application of air cavity techniques in the shipping industry. Multiphase CFD methods can help us to gain a better understanding of the relevant physics.
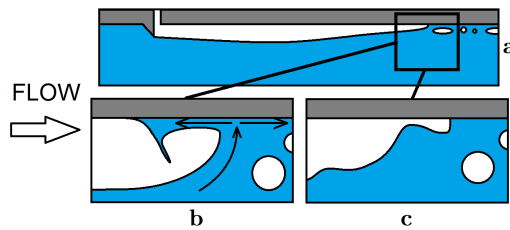
Fig. 1: The external air cavity technique (a) and two possible mechanisms for air discharge: re-entrant jet (b) and wave pinch-off (c)

The largest challenge in predicting the air cavity characteristics lies in correctly modelling the closure region (Shiri et al. (2012), Zverkhovskyi et al. (2015)). Here, the closure region is defined as the region where the stable air layer transforms into a dispersed flow. Both the re-entrant jet mechanism and the wave pinch-off mechanism are cited as possible mechanisms for air discharge from the cavity in the closure region (e.g. Mäkiharju (2012), Shiri et al. (2012), Zverkhovskyi (2014)). The re-entrant jet mechanism for an air filled cavity is provisionally assumed to be similar to the re-entrant jet mechanism responsible for the break-up of vapour sheet cavities as described by Callenaere et al. (2001). In the closure region of a sheet cavity, a region with high adverse pressure gradient is formed. The increase in local pressure forces a thin stream of liquid into the cavity which is called the re-entrant jet (figure 1b). Impingement of this jet with the gas-liquid interface results in that a portion of the attached cavity is being pinched off and transported by the mean flow.

The other mechanism, as illustrated in figure 1c, is governed by waves on the air-water interface. These waves are believed to be formed by turbulence structures interfering with the interface. If the resulting wave amplitudes are of the same magnitude as the cavity thickness, the free surface interface will hit the ship's bottom and a pocket of air will be shed from the cavity.

This article aims to link the physical modelling of the relevant phenomena to their numerical modelling, with an emphasis on the modelling of the re-entrant jet mechanism with a RaNS turbulence model. The numerical solver used for all simulations is ReFRESCO (MARIN (2017)). It is a multiphase (unsteady) incompressible viscous flow solver using the RANS equations, complemented with turbulence and cavitation models. Time integration is performed implicitly with first or second-order backward schemes. For turbulence modelling, both RANS/ URANS and Scale-Resolving Simulations (SRS) models such as SAS, DDES/IDDES, XLES, PANS and LES approaches can be used.

2 Base case simulations

The (2D) simulations are based on the measurements performed in the Delft Cavitation Tunnel by Zverkhovskyi (2014). The cavitation tunnel has a test section length of 2m and a 0.3·0.3m cross-sectional area. The length of the computational domain upstream of the cavity is chosen such that the boundary layer profile in de simulations approaches the one from the measurements. A schematic of the domain including the applied boundary conditions is shown in figure 2. The close-ups show the grid topology in the region including the cavity, with refinement zones in the region around the cavitator, the cavity closure and the expected cavity interface. Close to the wall grid clustering was applied to ensure $y+$ values well below 1. The total number of grid cells is around 185000. Unsteady simulations were carried out with a water tunnel inlet velocity of 1 m/s. Based on current experimental observations in the Delft Cavitation tunnel, this is the free-stream velocity at which the re-entrant jet mechanism is dominant over the wave pinch-off mechanism. All computations were carried out using the $k - \sqrt{k}L$ (KSKL) turbulence model as described by Menter et al. (2006). A second order backward scheme is used for the time discretisation and the time step used in the calculations was 0.04ms to ensure Courant numbers smaller than 0.2 around the air-water interface. The discritisation of both the momentum and turbulence equations is treated by a QUICK scheme and the transport equation for the volume fraction is handled by a SUPERBEE scheme, which is flux limited, compressive and TVD. Regarding the iterative convergence of all the simulations presented; the L_∞ norm is in the order of 10^{-5} for all residuals, except the residual of the momentum equation in x-direction which is in the order of 10^{-3}. It is noted that this is a relatively poor convergence level. However, the regions where these levels are found are very local. It is all condensed to small regions with air inside the cavity and does not translate to the water phase. From the interface and in the water phase all residuals drop below 10^{-7} for the L_∞ norm.
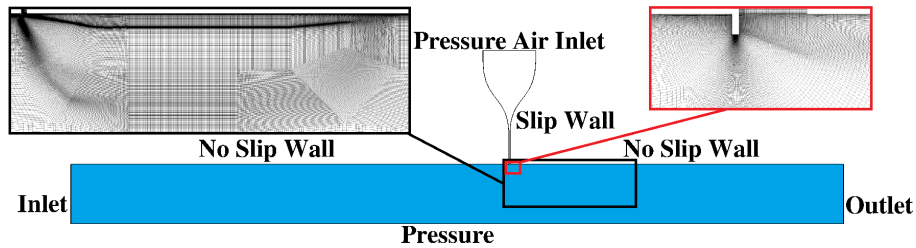
Fig. 2: Computational domain and boundary conditions

Zverkhovskyi et al. (2015) found that prescribing the air flux at the air inflow did not yet give physical solutions. Figure 3 shows instantaneous cavity profiles for simulations with an air inlet pressure of 40, 45, 50, 55 and 60 Pa respectively. The profiles are plotted using the contour where the air volume fraction equals 0.5. Based on linear wave theory and the experiments from Zverkhovskyi (2014) a cavity length 0.32 m and a cavity thickness of around 0.01 m is expected. The pressure at the air inlet for the base case simulation is chosen such that the the cavity profile from the simulations matches the one from the experiment as close as possible, which resulted in an air inlet pressure of 50 Pa.
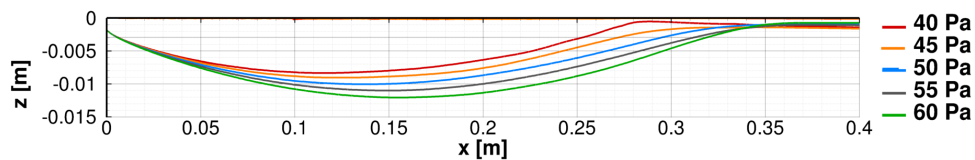
Fig. 3: Cavity profile sensitivity to pressure at the air inflow boundary

The base case simulation did not show correct cavity closure behaviour. A thin layer of air is constantly present at the closure and downstream of the cavity, influencing the computed wall shear stress. Figure 4 shows the ensemble averaged velocity profiles in the boundary layer upstream, in the

middle and downstream of the air cavity. They compare reasonably well with the measured time-averaged profiles. However, the computed upstream profile slightly differs from the experimental one, as seen as well in the middle and downstream of the cavity. As for the profile at the middle of the cavity, the simulations predict higher velocities outside the cavity. This seems a reasonable solution due to the narrowing of the tunnel as a result of the presence of the cavity. Unfortunately the results of the experimental measurements close to the wall are of insufficient resolution to quantitatively compare the viscous sub-layer of the boundary layer, which determines the wall shear stress.

Fig. 4: Ensemble-averaged boundary layer profiles at three different streamwise locations: upstream, in the middle and downstream of the cavity. The 2-phase base case simulations from the current project and the time-averaged experimental data from Zverkhovskyi (2014) are shown

3 Eddy-viscosity correction

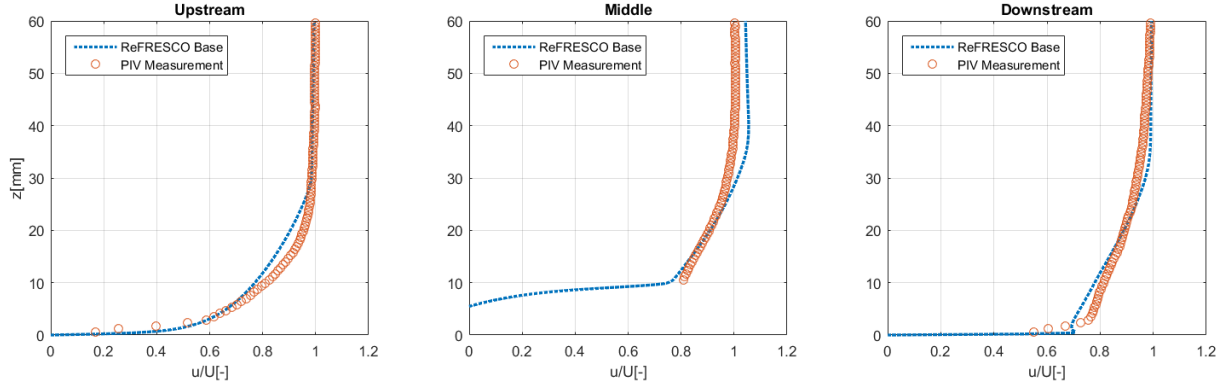For the numerical modelling of the re-entrant jet in the air cavity cases, it was investigated to see whether RaNS methods can be used. Currently, these models are still the most commonly used for application in practical ship design. For the simulation of unsteady vapour sheet cavity dynamics, and in particular the re-entrant jet mechanism occurring in those cases, RaNS methods can already be applied. However, the commonly used two-equation turbulence models, such as the k-ϵ and k-ω models, were originally developed for RaNS simulations of single-phase flows. A frequently encountered problem with these turbulence models that are based on the Boussinesq assumption is the over-prediction of the eddy-viscosity around the liquid-gas interface and thus in and downstream of the cavity closure region. According to Reboud et al. (1998), this over-predicted eddy-viscosity reduces the development of the re-entrant jet and can thus prevent the occurrence of shedding. The above mentioned tendency is not just associated with one specific RaNS solver or cavitation model. A widely used eddy-viscosity correction model that artificially lower the over-predicted eddy-viscosity, is the Reboud-correction. Here, the formulation for the turbulence viscosity is modified. The originally computed turbulence viscosity $\mu_{\mathbf{t}}$ is multiplied by a correction factor based on a function of the local density $f(\rho)$. Computations were carried out using two different correction functions: the function as used by Reboud et al. (1998) and described in Coutier-Delgosha et al. (2001) and a correction based on a Gaussian function which is proposed in this paper. The same numerical settings as given in section 2 are applied.

The function as described by Coutier-Delgosha et al. (2001) is given in Eq. (1). Here, ρ_g is the density of the gas, ρ_l is the density of the liquid, ρ is the local cell density and n influences the amount of reduction. For vapour cavitation problems, n usually has a value of 10. The eddy viscosity correction factor is obtained by dividing $f(\rho)$ by the local cell density, resulting in a value between 0 and 1.

$$f(\rho) = \rho_g + \left(\frac{\rho_g - \rho}{\rho_g - \rho_l} \right)^n (\rho_l - \rho_g) \tag{1}$$

The correction based on a Gaussian curve is proposed in Eq. (2). Here, A and W are the amplitude and width of the peak and have a value between 0 and 1, and p controls the order of the function and thus also the width of the peak. Figure 5 shows the different correction functions for different values of n for

cases of Reboud correction and different values of A, W and p for Gaussian correction cases. It can be observed that the Reboud correction function is asymmetrical and has a bias towards the lower density fluid. It also has large gradients when the mixture approaches pure air or pure water, which can possibly introduce difficulties when numerically solving the problem. For the proposed Gaussian functions the correction only is active when the cell is marked as an interface cell and the function is symmetric.

$$g(\rho) = \left(-Ae^{-\left(\frac{\left(\rho - \frac{1}{2}(3\rho_l - \rho_g) \right)^2}{2(W(\rho_l - \rho_g)/10)^2} \right)} + 1 \right)^p \tag{2}$$
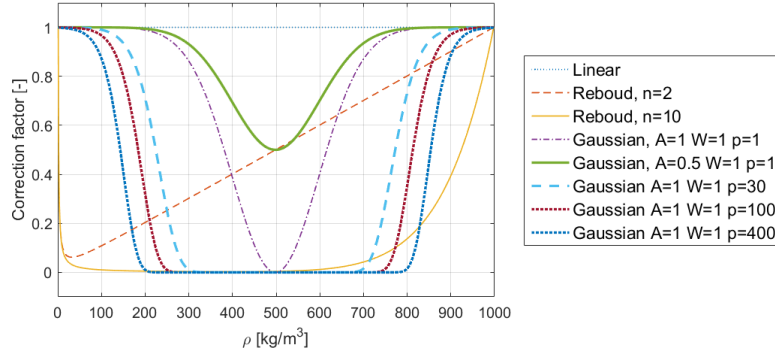

Fig. 5: Eddy-viscosity correction factor as a function of the local density ρ. The computed eddy viscosity is multiplied by this correction factor.

Figure 6 shows the computed cavity profiles for three representative cases: the base case, one case with Reboud correction and one case with Gaussian correction. Most probably, the asymmetric nature of the Reboud correction function is the reason that the cavity profiles as computed including this function are very unstable. This instability is present for all $n > 1$, thus for all cases were the correction function is applied. In all cases including the Reboud correction, the cavity grows to its stable length which is similar to profile of the base case and then becomes unstable. The air volume fraction inside the cavity is equal to or larger than 0.99, but due to the bias of the Reboud correction function towards the low density fluid, all eddy-viscosity ν_t inside the cavity is reduced such that there is no eddy-viscosity at all. The total viscosity difference between inside and outside the cavity is approximately ten times lower for the base case when compared to the the Reboud cases. The total eddy-viscosity outside the cavity is rather high, due to the developed boundary layer upstream of the cavity ($Re_x > 10^6$). Due to the recirculating flow inside the cavity and the lack of eddy-viscosity in the air layer for the Reboud cases, the velocity differences as well as the vorticity are larger in the Reboud case and instabilities are more likely to occur.
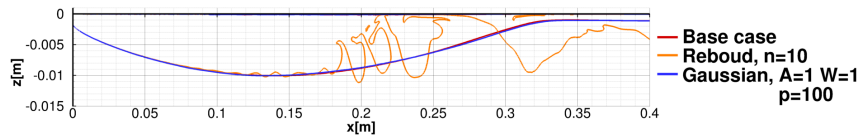
Fig. 6: Cavity profiles for different eddy viscosity correction functions

In contrast to the unstable behaviour which is found for the simulations including the Reboud correction function, all three simulations as carried out using the Gaussian correction produced very stable cavity profiles (figure 6). The Gaussian correction function was applied with A=1, W=1 and p=1, 30 and 100 respectively. All simulations produced more or less the same result as found for the base case calculation, showing incorrect closure behaviour. This lead to the conclusion that the reduction of the eddy-viscosity on the air-water interface is probably not the only requirement for the re-entrant jet to form and the production of eddy viscosity at the cavity interface as well as inside the cavity and

upstream of the cavity have a large influence on the interface stability. Figure 7 shows the regions where the correction function was active for both the Reboud function and Gaussian function. The Reboud function is active in a large region inside the cavity, whereas the Gaussian correction function only acts on the cavity interface.

For the boundary layer profiles, similar profiles were found for all correction cases. Only the simulations including the Reboud correction did show some irregular behaviour behind the cavity closure, most probably due to passing pockets of air-water mixture bubbles.
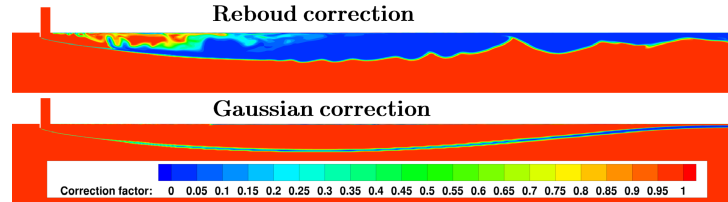
Fig. 7: Regions where the eddy viscosity correction function was active; 1: no reduction, 0: maximum reduction

4   Discussion

Most of this article focuses on the numerical simulation of the re-entrant jet mechanism for air cavity flows with a RaNS model. Solely correcting the eddy-viscosity on the air-water interface appears to be insufficient to initiate the re-entrant jet shedding mechanism. However, the computed eddy-viscosity at the cavity interface as well as inside the cavity have a large influence on the interface stability. In contrast to the RaNS modelling of vapour cavitation problems, there is a developed boundary layer upstream of the cavity in the ventilated cavity cases. The eddy-viscosity produced in this region is transported with the flow, causing a thick band of viscous flow around the cavity. This could also hamper the formation of the re-entrant jet in the simulations. To explore this hypothesis, simulations are carried out with a very short no-slip wall upstream of the cavity, thus almost no boundary layer formation. Figure 8 shows the different cavity profiles for the base case simulations as well as the simulations with a thin boundary layer (BL), with and without Gaussian correction function. The simulations with the thin boundary layer result in a longer and thicker cavity, although the same pressure inside the cavity was prescribed. Apart from the length and thickness difference, which is solely due to the velocity difference and thus pressure difference around the cavity, still no shedding is observed in the closure region.
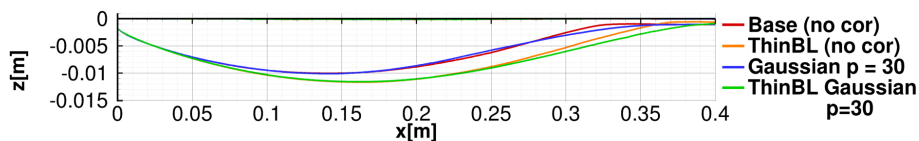
Fig. 8: Cavity profiles for different boundary layer thickness, with and without Gaussian correction

Another difference with respect to natural sheet cavitation modelling is the lack of a condensation term. There is no 'destruction' of gas at the cavity closure in the case of air filled cavities. Additionally, the pressure difference inside versus outside the cavity is around one order of magnitude lower for air cavities when compared to vapour cavities. The question then rises whether this pressure difference is high enough to create the re-entrant jet.

Also, the RaNS modelling of natural cavitation problems usually asks for a low-order and thus diffuse discretisation scheme for the volume fraction equation. Here a higher order scheme is used, since in the current approach the stable cavity interface till the closure should be solved as well, especially when one is also interested in the wave pinch-off mechanism and the total air flux leaving the cavity.

5   Conclusions and further work

To conclude, the simulated velocity profiles at different streamwise locations in the boundary layer around the cavity compare reasonably well with the experimental profiles. However, RaNS two-equation turbulence models like the $k - \sqrt{k}L$ model show serious deficiencies for the modelling of the re-entrant jet mechanism for air cavities. Also after including an ad-hoc eddy-viscosity correction model as proposed by Reboud et al. (1998) and in this paper. Maybe a Reynolds Stress Model (RSM) could improve the simulations, since the isotropic turbulence modelling as used in classical 2-eq. RaNS turbulence models is a violation of the anisotropic nature of the turbulence structures near the interface. The Reynolds stresses across the interface should be close to zero as no significant momentum flux should cross the interface (Hannoun et al. (1988)).

Next to the modelling of the re-entrant jet, the simulation of the wave pinch-off mechanism also needs to be included to be able to capture the cavity closure dynamics. This mechanism is hypothesised to be governed by waves formed by turbulence structures disturbing the interface. A scale resolving or hybrid model such as LES, RaNS-LES or PANS is then required. From a practical point of view, these scale resolving models are not believed to be viable for practical ship design purposes yet. However, these models can first be used to identify the physical conditions in the closure region and to study and identify scaling influences. Thereafter, a practical engineering correction which can be used with RaNS models for the numerical modelling of air cavities could be developed. The dispersion (or diffusion) of the gas phase can then for example be modelled by an extra convection-diffusion term to break up the air layer. This extra term can then be activated when certain conditions characterised by the physics in the closure region are met.

Further work will first focus on a performance study for different RaNS and hybrid RaNS-LES turbulence models around air-water interfaces using a benchmark case such as a Kelvin-Helmholtz stability analysis in the vicinity of a wall with a known disturbance. Thereafter hybrid RaNS-LES, LES or PANS simulations could be carried out to study the physical mechanisms responsible for air discharge in the closure region.

References

Callenaere, M., Franc, J.-P., Michel, J.-M. and Riondet, M. (2001). The cavitation instability induced by the development of a re-entrant jet. *J. Fluid Mech* 444, 223-256

Coutier-Delgosha, O., Fortess-Patella, R. and Reboud, J.L. (2003). Evaluation of the turbulence model influence on the numerical simulations of unsteady cavitation. *J. of Fluids Eng.* 125(1), 38-45

Gorbachev, Y. and Amromin, E. (2012). Ship Drag Reduction by Hull Ventilation from Laval to Near Future: Challenges and Successes. *ATMA 2012*

Hannoun, I.A., Fernando, H.J.S. and List, E.J. (1988). Turbulence structure near a sharp density interface. *J. of Fluid Mech.* 189, 189-209

Mäkiharju, S.A. (2012). The Dynamics of Ventilated Partial Cavities over a Wide Range of Reynolds Numbers ans Quantitative 2D X-Ray Densitometry for Multiphase Flow. *Ph.D. Thesis* The University of Michigan

ReFRESCO (2017) http://www.refresco.org, Online; accessed 23 March 2017

Menter, F.R., Egorov, Y. and Rusch, D. (2006). Steady and unsteady flow modelling using the $k - \sqrt{k}L$ model. *Ichmt Digital Library Online*, Begel House Inc.

Reboud, J., Stutz, B. and Coutier, O. (1998). Two-phase Flow Structure of Cavitation: Experiment and modelling of Unsteady Effects. *Third International Symposium on Cavitation*, Grenoble, France

Shiri, A., Leer-Andersen, M.,Bensow, R.E. and Norrby, J. (2012). Hydrodynamics of a Displacement Air Cavity Ship. *29th Symposium on Naval Hydrodynamics*, Gothenburg, Sweden

Zverkhovskyi, O. (2014). Ship Drag Reduction by Air Cavities. *Ph.D. Thesis*, TU Delft

Zverkhovskyi, O., Kerkvliet, M., Vaz, G. and van Terwisga, T. (2015). Numerical Study on Air Cavity Flows. *Proceedings of NuTTS 2015*, Cortona, Italy

Side wall effects of ship model tests in shallow water waves

Manases Tello Ruiz [1*], Wim Van Hoydonck[2], Guillaume Delefortrie[2], and Marc Vantorre[1]

[*]1Ghent University, Technologiepark Zwijnaarde 904, Ghent 9052, Belgium
[2]Flanders Hydraulics Research, Berchemlei 115, Antwerp 2140, Belgium
[*]manases.ruiz @ugent.be

1 Introduction

Ship model tests in waves are limited to specific combination of model speeds, main wave parameters, and the tank's main dimensions. Side wall effects are major constraints to tests in waves and their effects can be relatively significant (Kashiwagi et al., 1990, Chen, 1994, and Zhu et al., 2011). For tests at zero forward speed, according to Chen (1994), side wall effects are important for both the first and second order quantities. Similar results were found by Zhu et al. (2011) for an open ship in oblique seas. Kashiwagi et al. (1990) studied the non-zero forward speed case for deep water and concluded that, although side wall effects occur, a limiting region where the side wall effects are less than 10% of the quantities obtained in open sea can be determined.

The ITTC–Recommended Procedures and Guidelines, Seakeeping experiments (7.5-02 07-02.1) provides practical guidelines to select test parameters at which side wall effects are avoided. This is obtained by simply selecting ship speeds higher than a critical speed Fr_{hcrit}. This critical speed (assuming the ship is moving on a straight course along the centre line of the tank) results from the time needed for the radiated waves to travel back and forth and the time needed for the ship to move one ship length (see LLoyd, 1989, and ITTC, 2014).

The ITTC speed limits are a function of the tank's width W_T to ship length L_{PP} ratio $r = W_T/L_{PP}$, independently of the waves. This general relationship is possible because deep water is assumed. As wave characteristics depend on the water depth this relationship is not valid for finite water depths. Hence, the speed limits for finite water depths must be estimated including the wave characteristics.

In finite water depths, shallow water from the ship's point of view ($1.5 > h.T_m > 1.2$, PIANC, 2012), the ITTC guidelines are very restrictive, because the required speeds to avoid side wall effects do not necessarily comply with the common practice of low to moderate manoeuvring speeds. The available range of test parameters is then reduced to a few possible combinations of waves and ship speeds. An intuitively solution is to use a wider tank; this is, however, an expensive solution, not only from the experimental point of view but also from computational requirements if CFD studies are performed.

To investigate a possible solution to increase the suitability of model tests in shallow water waves , experimental and numerical studies have been conducted at Flanders Hydraulics Research (FHR) in Antwerp, Belgium (in cooperation with Ghent University). The study includes experimental and numerical results obtained from two container ship models, the KCS and a scale model of an ULCS (referred to as C0W). Model tests included different ship speeds, wave frequencies, and offsets from the tank's centre line. The numerical study was carried out for two different tank widths with the CFD software package FINE™/Marine.

2 Experimental program

2.1 Experimental set-up
The experiments were conducted at the Towing Tank for Manoeuvres in Shallow Water at Flanders Hydraulics Research (FHR) in Antwerp, Belgium (in cooperation with Ghent University). Delefortrie et al. (2016) presented the towing tank's main characteristics. During tests horizontal forces were measured by the load cells LC1 and LC2 and the ship's heave and pitch were obtained by using four potentiometers P1 to P4 (see Figure 1a,b). Wave profiles were recorded with four wave gauges, WG1 to WG3 located at a fixed position along the tank and WG4 attached to the main carriage (see Figure

1c). Positions and orientations during tests are defined by using two coordinate systems, an Earth-bound $O_0x_0y_0z_0$ and a body-bound $Oxyz$, both, North-East-Down oriented, see Figure 1c.
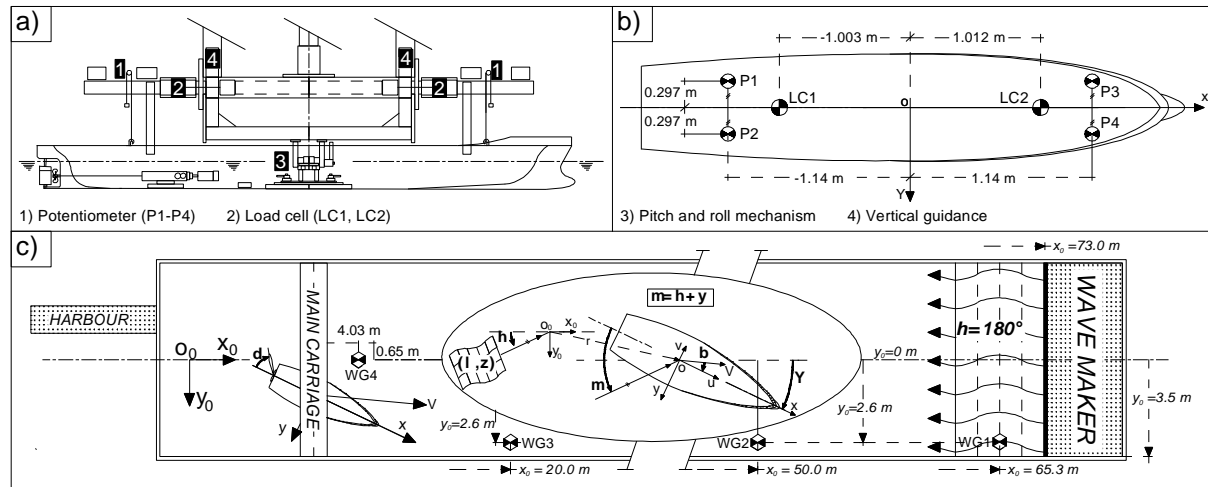

Figure 1 Towing tank at FHR, set-up for semi captive tests for both the C0W and the KCS ship.

The ship models main parameters for the KCS and the C0W are given in Table 1.

Table 1 Container ship models main parameters.

Ship	$L_{pp}(m)$	$B(m)$	$T_m(m)$	Cb	$\nabla(m^3)$	$x_G(m)$	$z_G(m)$	$r_{44}(m)$	$r_{55}(m)$	$r_{66}(m)$
KCS	4.367	0.611	0.205	0.651	0.356	-0.07	-0.03	0.20	1.07	1.09
C0W	4.191	0.627	0.161	0.594	0.258	-0.114	0.00	0.22	1.03	1.05

2.2 Test matrix

The main parameters for the experimental and numerical analysis are presented in Table 2. Wave lengths of regular waves RW are given as a function of the ship length L_{PP}, with wave heights (through to crest) of 0.04 m. and 0.08 m for the C0W and the KCS, respectively. Ship speeds (Fr_h) as a Froude to depth number, and the tank's width W_T to ship length L_{PP} ratio $r = W_T/L_{PP}$ are calculated for each ship. The test matrix leads to sixteen EFD tests for the KCS ship and to two CFD tests for the C0W. The water depths h correspond to 100% and 50% ukc for the KCS and the C0W, respectively.

Table 2 Experimental and numerical parameters for model test in waves.

KCS ship, EFD, $h = 0.410$ (m)								C0W ship, CFD, $h = 0.242$ (m)			
W_T/L_{PP}				Speeds		Waves		W_T/L_{PP}		Speeds	Waves
$r1$	$r2$	$r3$	$r4$	Fr_{h1}	Fr_{h2}	RW_1	RW_2	$r1$	$r2$	Fr_{h1}	RW_1
1.60	1.51	1.37	1.15	0.124	0.424	$0.4L_{PP}$	$0.6L_{PP}$	1.67	3.97	0.352	$0.45L_{PP}$

The sixteen different EFD tests with the KCS were obtained by running the same speed and wave length at four different offsets from the tank's centre line, while the two numerical simulations for the C0W were conducted with CFD with two different tank widths.

3 Experimental analysis and discussions

The critical speeds (based on the ITTC guidelines) obtained with the KCS for the four r ratios are plotted in Figure 2 with continuous lines, while the 16 EFD tests are displayed with square markers. The corresponding ratios between the critical speed and the speeds used during tests are given in Table 3.
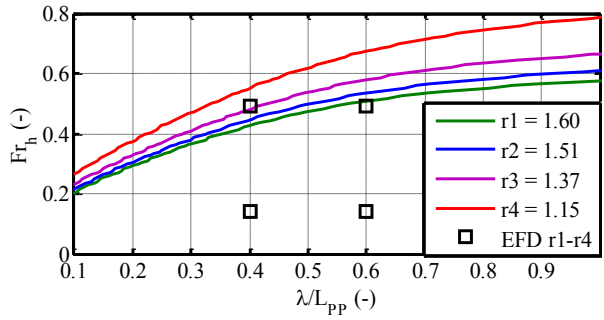
Table 3 KCS ship speed to critical speed ratios.

Speed (-)	$r1$	$r2$	$r3$	$r4$	λ (-)
		W_T/L_{PP} (-)			
Fr_{h1}/Fr_{hcrit}	0.33	0.32	0.29	0.26	$0.4L_{PP}$
	0.27	0.25	0.24	0.20	$0.6L_{PP}$
Fr_{h2}/Fr_{hcrit}	1.17	1.11	1.03	0.91	$0.4L_{PP}$
	0.94	0.90	0.83	0.72	$0.6L_{PP}$

Figure 2 Critical speeds for the KCS ship.

From Figure 2, all tests seem to suffer from side wall interaction (following ITTC guidelines) with the exception of tests at Fr_{h2}, $0.4L_{PP}$, and ratios $r1$ to $r3$ (see Table 3, where $Fr_{h2}/Fr_{hcrit} > 1$). Then, tests at lower Fr_{h2}/Fr_{hcrit} would be principally excluded from the study. To evaluate if side wall effects are present/significant, a Fourier analysis was conducted for all tests. The results are shown together for the same speed and wave length but for the four different ratios r in Figure 3. Results obtained for $0.4L_{PP}$ and $0.6L_{PP}$ are plotted in the first/second and the third/fourth row, respectively.
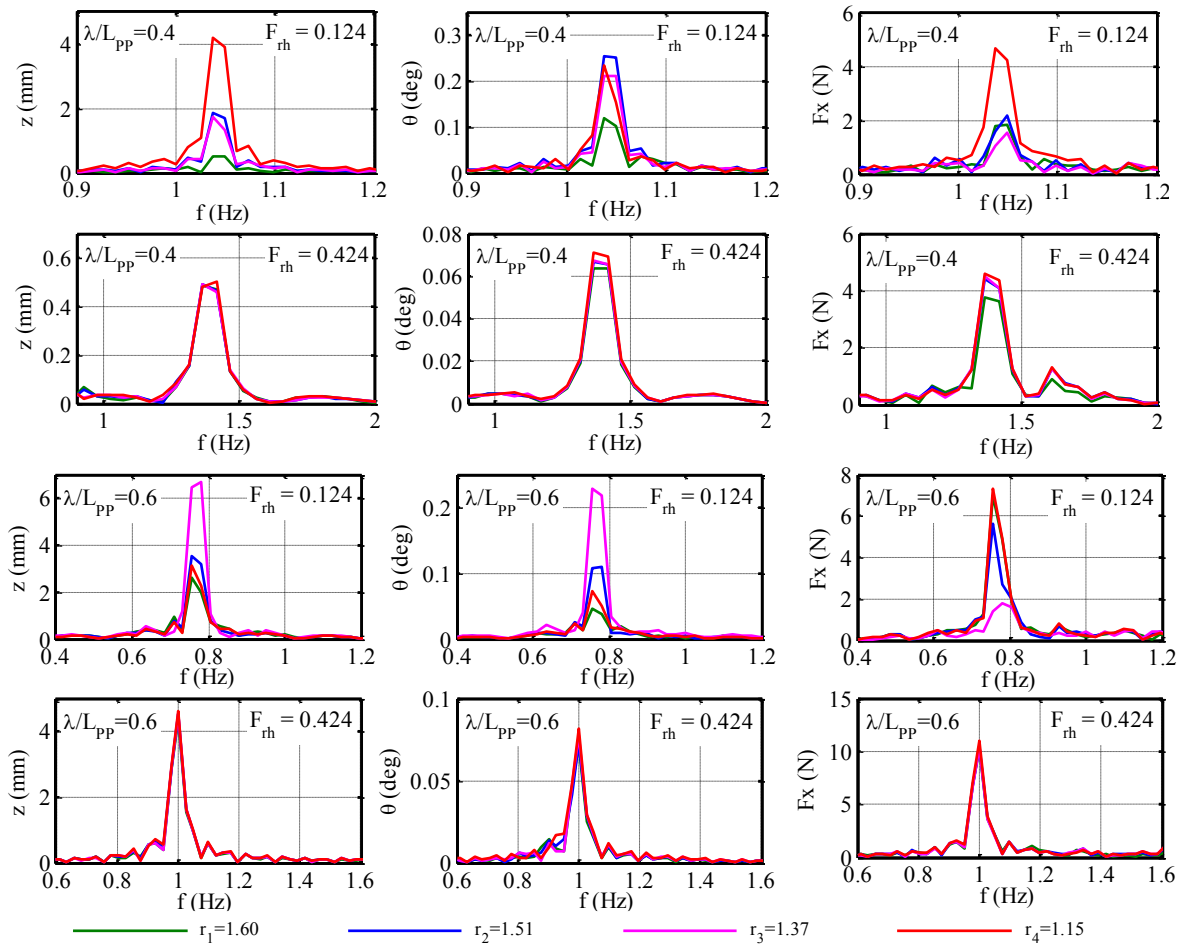
Figure 3 Spectral analysis of the KCS test in waves for four different r ratios.

From Figure 3, significant side wall influence is observed for results obtained at low ship speed to critical speed ratios, Fr_h/Fr_{hcrit} $Fr_h/Fr_{hcrit} < 0.35$ (first and third row in Figure 3, see Table 3). In contrast, for tests at $Fr_h/Fr_{hcrit} > 0.70$ results remain the same, thus indicating negligible side wall effects. This seems to introduce a new limit to define whether tests, expected to suffer from side wall interaction, can yet be performed.

4 Numerical analysis and discussions

To verify the observed speed limit $Fr_h/Fr_{hcrit} > 0.70$, a CFD study was carried out for the C0W ship model with two different tank's width, see Table 2. The ship was set free to heave and pitch. For both tests, the same wave length, ship speed, and water depth were used. The CFD study was conducted with the software package FINE™/Marine.

The corresponding speed limits for these two cases and the numerical solutions are plotted in Figure 4. The respective means (a_0), height (H, trough to crest) and periods (T) of the harmonic signals are given in Table 4.
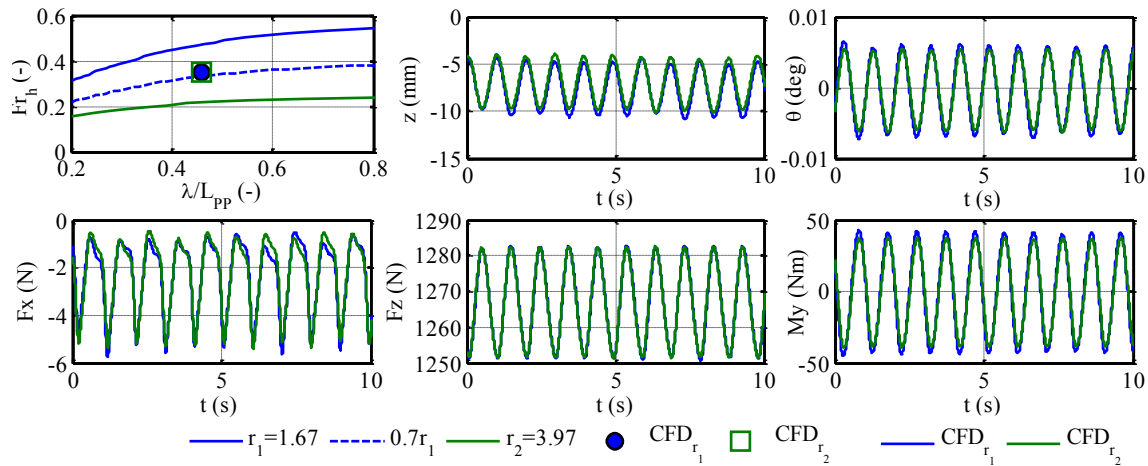
Figure 4 C0W ship model, (top-left) critical speeds, and motion responses from the two CFD studies.

Table 4 Mean and harmonic components of the two CD computations.

Items	z (mm)		θ (deg)		Fx (N)		Fz (N)		My (Nm)	
	r1	r2	r1	r2	r1	r2	r1	r2	r1	r2
a_0	-6.76	-6.25	0.00	0.00	-2.25	-2.19	1267.08	1267.07	0.00	0.01
H	5.78	5.69	0.01	0.01	4.42	4.46	31.55	30.90	83.97	76.08
T (s)	0.16	0.16	0.16	0.16	0.16	0.16	0.16	0.16	0.16	0.16

From Figure 4 and Table 4, the ship's responses, forces and motions, do not show any significant variation between the narrower and wider tank. The largest influence is even less than 8%, obtained for the sinkage (a_0, corresponding to z). Thus the signals appear to not suffer significantly from side wall effects. Although the results are obtained for another ship and a different test configuration, this seems to confirms the limits observed with the EFD tests for the KCS ship.

5 Conclusion

The study shows that side wall interaction does not influence significantly ship model tests in waves for ship speeds higher than 70% of the critical speed (determined based on the ITTC approach expressed in shallow water conditions). Although this is not yet confirmed for other ship types, the reduction of the speed limits seems considerably important. This does not only represent an advantage for experimental analysis only, but also for numerical studies in which reducing the width of the numerical domain would decrease significantly computational time.

References

X. Chen (1994). On the side wall effects upon bodies of arbitrary geometry in wave tanks. Applied Ocean Research, 16(6), 337–345.

G. Delefortrie, S. Geerts, and M. Vantorre (2016). The towing tank for manoeuvres in shallow water. MASHCON 2016. Hamburg, Germany.

ITTC (2014). ITTC – Recommended procedures and guidelines. Seakeeping experiments (7.5-02 07-02.1).

M. Kashiwagi, M. Ohkusu, and M. Inada, M. (1990). Side-Wall Effects on Radiation and Diffraction Forces on a Ship Advancing in Waves. Journal of The Society of Naval Architects of Japan, 1990(168), 227–242.

A.R.J.M. LLoyd (1989). Seakeeping: ship behaviour in rough weather. (Ellis Horwood, Ed.). Ellis Horwood Series in Marine technology.

S. Zhu, M. Wu, and T. Moan, T. (2011). Experimental and Numerical Study of Wave-Induced Load Effects of Open Ships in Oblique Seas. Journal of Ship Research, 55(24), 100–123.

Numerical Prediction of Vortex Dynamics in Inviscid Sheet Cavitation

Sören Schenke[*], **Tom J.C. van Terwisga**[†*]

[*]TU Delft, Delft/ the Netherlands, [†]MARIN, Wageningen/ the Netherlands

s.schenke@tudelft.nl

1 Introduction

Recent studies have indicated that mass transfer models are able to correctly reflect the sheet cavitation dynamics of inertia driven flows, given that the mass transfer model constants governing the source term magnitude are sufficiently large (Koukouvinis and Gavaises 2015) and that enough temporal resolution is provided (Schenke and Van Terwisga 2017). The inertia driven dynamics, characterised by cavity collapse time, shedding frequencies and local pressure impact frequencies, were shown to be insensitive to variations of the mass transfer coefficients in this limit.

This study focuses on an inviscid cavitating flow around a NACA0015 hydrofoil. The flow dynamics are driven by the re-entrant jet as the main mechanism of cavity shedding. A threshold of mass transfer magnitude, temporal and spanwise spatial resolution is identified, beyond which the frequency of local pressure impacts is model parameter independent. Although the excact values of peak pressure loads remain time step size, grid size and model parameter dependent, the sheet cavitation dynamics are considered as well resolved in this regime as far as shedding frequency and characteristic cavity collapse time are concerned. The results are compared to experimental results by Van Rijsbergen et al. (2012). Based on this, the study further focuses on the mechanism of vorticity generation and vorticity break-up, causing potentially erosive cavitating structures such as horseshoe cavities (Dular and Petkovšek 2015).

2 Modelling Approach

The vorticity equation, as derived from the inviscid Navier-Stokes equation for momentum without any non-conservative body forces but with variable density, is given by (Xing et al. 2005)

$$\frac{\partial \omega}{\partial t} + u \cdot \nabla \omega = \omega \cdot \nabla u - \omega \nabla \cdot u + \frac{1}{\rho^2} \nabla \rho \times \nabla p, \tag{1}$$

where $\omega = \nabla \times u$ denotes the vorticity. The term $\omega \cdot \nabla u$ on the right-hand side represents the three-dimensional tilting of vorticity vectors and the divergence term $\omega \nabla \cdot u$ reflects the alteration of vorticity due to density change. The baroclinic term $1/\rho^2 \nabla \rho \times \nabla p$ must always be zero in an ideal barotropic flow (Koop 2008). Mass transfer models, however, typically generate artificial baroclinic torque, because the density-pressure states can not follow unique barotropic states (Schenke and Van Terwisga 2017). Similar to a study on cavitating vortices by Xing et al. (2005), the vorticity Eq. (1) is only employed for post-processing purposes. The flow model itself is based on the inviscid Navier-Stokes equations for momentum and mass continuity:

$$\rho \frac{\partial u}{\partial t} + \rho u \cdot \nabla u = -\nabla p + \rho g \tag{2}$$

$$\frac{\partial \rho}{\partial t} + \nabla \cdot (\rho u) = 0 \tag{3}$$

The velocity field is modeled as divergence free in the incompressible pure liquid and vapour regimes with corresponding densities ρ_l and ρ_v. In the phase transition regime, the local velocity divergence is equal to a mass transfer source term, for which the model by Merkle et al. (1998), slightly modified however (Schenke and Van Terwisga 2017), is employed:

$$\nabla \cdot u = -\frac{1}{\rho}\left(1 - \frac{\rho_v}{\rho_l}\right)(p - p_v) \begin{cases} C_v \gamma & \text{if} \quad p \leq p_v \\ C_c (1 - \gamma) & \text{if} \quad p > p_v \end{cases} \tag{4}$$

With the liquid volume fraction γ given by the linear mixture relation $\gamma = (\rho - \rho_v) / (\rho_l - \rho_v)$, combining Eq. (3) and Eq. (4) gives the liquid volume fraction transport equation:

$$\frac{\partial \gamma}{\partial t} + \nabla \cdot (\gamma u) = -\frac{1}{\rho} \frac{\rho_v}{\rho_l}(p - p_v) \begin{cases} C_v \gamma & \text{if} \quad p \leq p_v \\ C_c (1 - \gamma) & \text{if} \quad p > p_v \end{cases} \tag{5}$$

3 Numerical Set-Up

The numerical set-up is in line with experiments carried out by Van Rijsbergen et al. (2012) and numerical simulations carried out by Li et al. (2014), where the open source CFD package OpenFOAM (2017) is employed in this study. The angle of attack of the NACA0015 hydrofoil is 8° and its cord length is $c = 0.06$ m, with the channel height and width being 0.08 m and 0.04 m, respectively. The inlet is located at $3c$ upstream from the leading edge of the foil and the outflow enters a diffuser section (Fig. 2) at $6.5c$ downstream from the leading edge to avoid pressure fluctuations at the outlet boundary. The ratio between the diffuser outlet patch and the tunnel cross section area is 66. The inflow boundary condition is given by a uniform inflow speed of 17.3 m/s and the downstream pressure in the foil tunnel section is aimed to be 302.295 kPa. The fixed outlet pressure at the end of the diffuser section is derived from the Bernoulli equation and the mass continuity equation. By this means, the aimed downstream tunnel pressure is matched under wetted flow conditions. The vapour pressure is $p_v = 1854$ Pa and the densities of pure liquid and vapour are $\rho_l = 998.85$ kg/m^3 and $\rho_v = 0.01389$ kg/m^3, respectively. Since viscous forces are neglected, any solid wall is treated as a slip wall. The numerical simulation is carried out on an unstructured grid with uniform grid density around the foil. Four refinement levels are applied in the vicinity of the foil (Fig. 1). The refinement factors against the background mesh are 2^n, where $n = 0$ on the base level and $n = 4$ on the finest level around the foil. On the finest level, the cell length in axial direction is $\Delta x = 0.3125$ mm. To investigate the effect of three-dimensional vorticity break-up, the spanwise resolution is varied, where $\Delta z = 8\Delta x$ for the coarse grid, $\Delta z = 4\Delta x$ for the medium grid and $\Delta z = 2\Delta x$ for the fine grid. The mass transfer constants $C_{c,v}$ and time step size Δt have been varied systematically to identify a converged configuration for a given grid density. In all cases, the ratio between C_c and C_v is kept constant at $C_c/C_v = 2$. Local quantities such as pressure and density signals are evaluated at observation points on the foil surface at $0.2c$ and $0.5c$ in the centre plane.
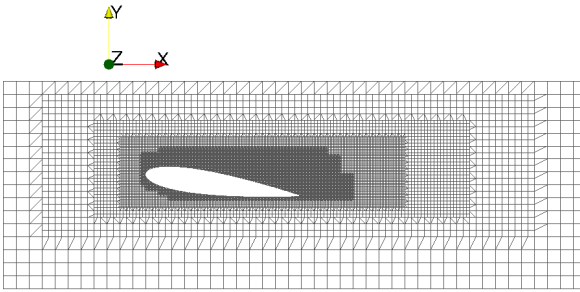
Fig. 1: Unstructered grid with 4 refinement levels
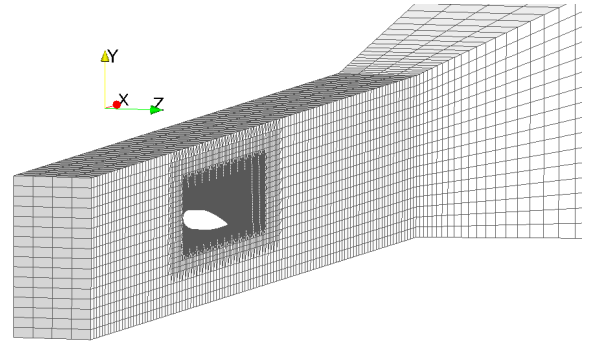
Fig. 2: Foil and diffuser section

4 Results

The local main pressure impacts at $0.2c$ and $0.5c$ (Fig. 3) show strong correlation. The dominating frequency of the cyclic pressure loads is identified from Fast Fourier Transforms of the pressure signals (Fig 4) at $0.2c$. Subfigures A, B and C depict the pressure amplitude spectra for decreasing time step size and three different mass transfer rates each, where the data is obtained from the finest grid ($\Delta z = 2\Delta x$). The dominating frequency gets more pronounced with decreasing time step size. The same effect is observed for variation of the spanwise resolution (subfigure D), where the dominating frequency band is smeared out as the spanwise resolution decreases. From subfigure C we find a model parameter independent pressure load frequency of 193 Hz. This value is in good agreement with the shedding frequency of 188 Hz that was found by Van Rijsbergen et al. (2012) from their experiments. Convergence of the impact frequency is confirmed by Fig. 3, depicting the pressure signals for two different mass transfer constants differing by a factor of 100. While the frequency converges to a model parameter independent value, the impact amplitudes still exhibit strong dependency on the magnitude of the mass transfer constants $C_{c,v}$ and temporal resolution. They increase with increasing C_c and decreasing Δt.
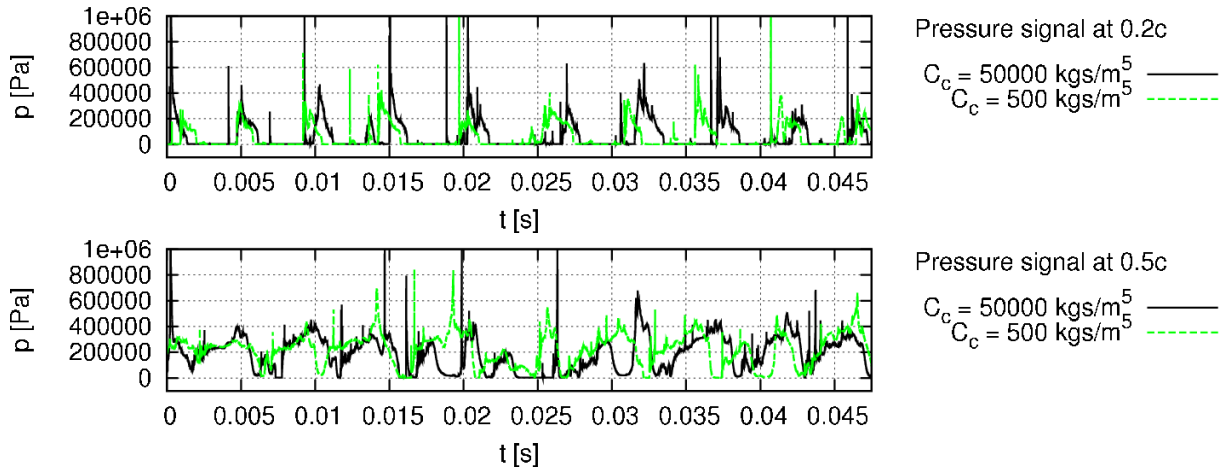
Fig. 3: Pressure signals on the foil surface at $0.2c$ (above) and $0.5c$ (below) in the centre plane for Δt =7.5e-7 s (small time step) and $\Delta x/\Delta z = 1/2$ (fine grid)
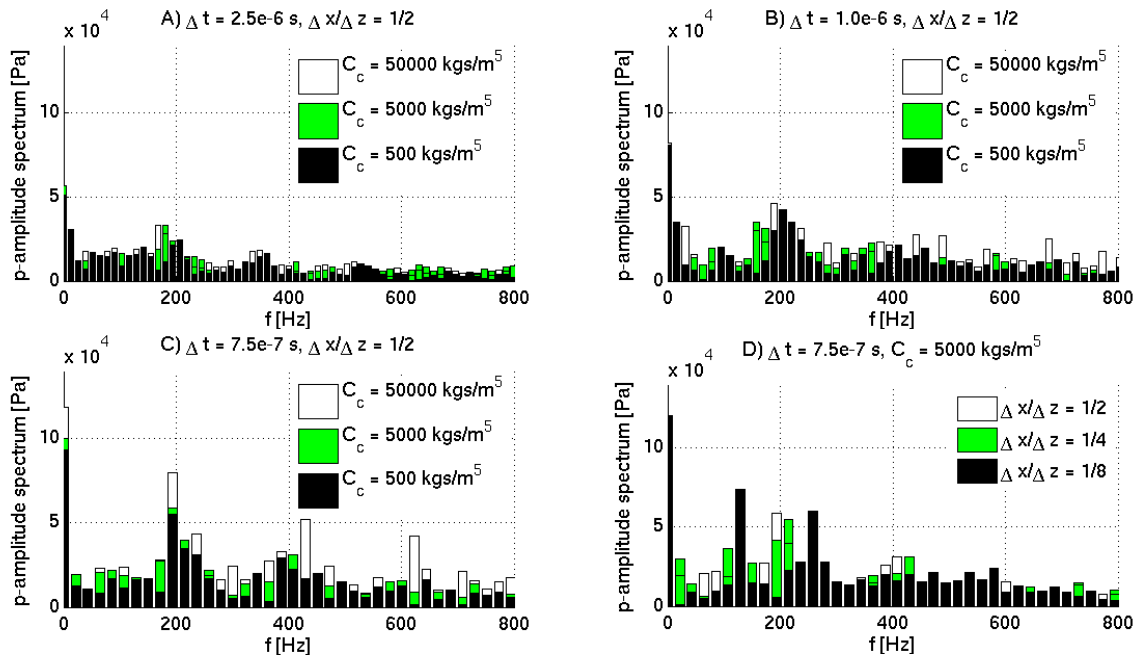
Fig. 4: Pressure amplitude spectra on the foil surface at $0.2c$ in the centre plane
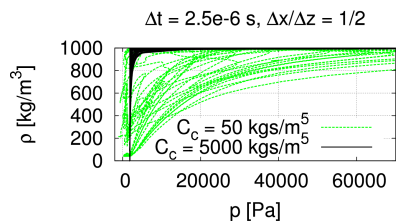
Fig. 5: ρ-p trajectory for large time step and fine grid
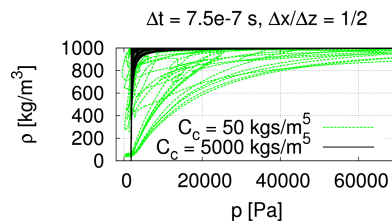
Fig. 6: ρ-p trajectory for small time step and fine grid
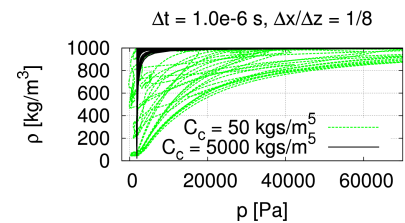
Fig. 7: ρ-p trajectory for medium Δt and coarse grid

Obviously, variation of the mass transfer coefficients does not affect the inertia driven dynamics of the flow as long as they are sufficiently large. Increasing the mass transfer constants $C_{c,v}$ has the effect of increasing the steepness of the density-pressure trajectories (Koukouvinis and Gavaises 2015, Schenke and Van Terwisga 2017). As shown by Fig. 5, 6 and 7, the outline of the area swept by the trajectories on statistical average only depends on the values of the mass transfer constants and is independent from both

time step size (compare Fig. 5 and Fig. 6) and grid density (compare with Fig. 7). Temporal resolution, however, has an influence on the time that it takes to achieve phase transition, hence the time that it takes to cover the same trajectory. With decreasing time step size, this characteristic phase transition time converges to a limit value (Schenke and Van Terwisga 2017).
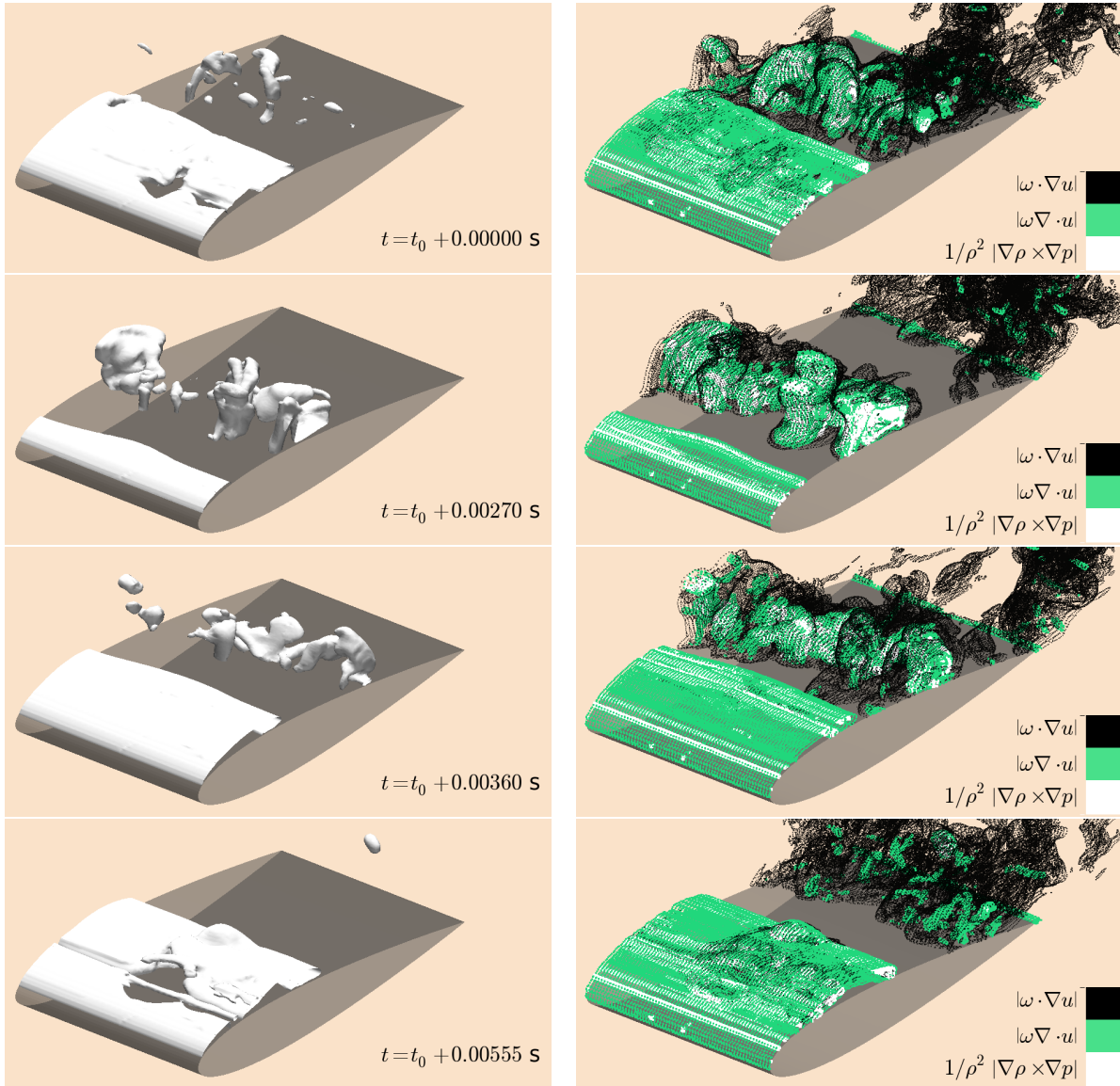
Fig. 8: Instantaneous vapour structures indicated by iso-surfaces at $\gamma = 0.75$ (left) and corresponding iso-surfaces of the vorticity equation source term magnitudes at 1.0e7 s^{-2} (right)
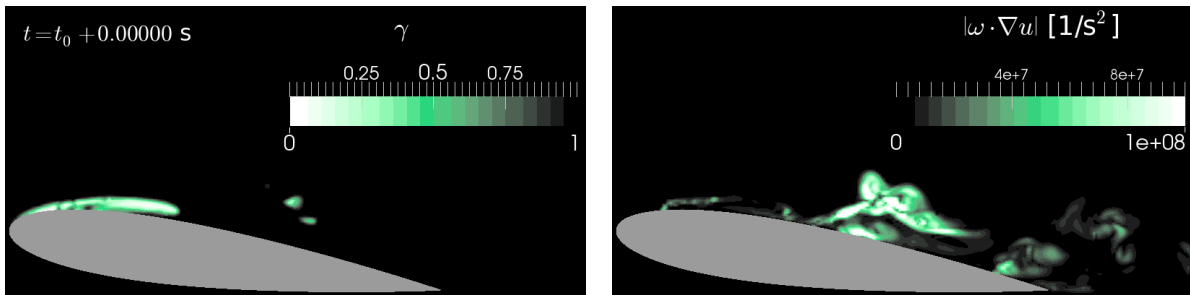
Fig. 9: Instantaneous volume fraction field in the centre plane (left) and corresponding magnitude of the vortex tilting source term $\omega \cdot \nabla u$ (right)
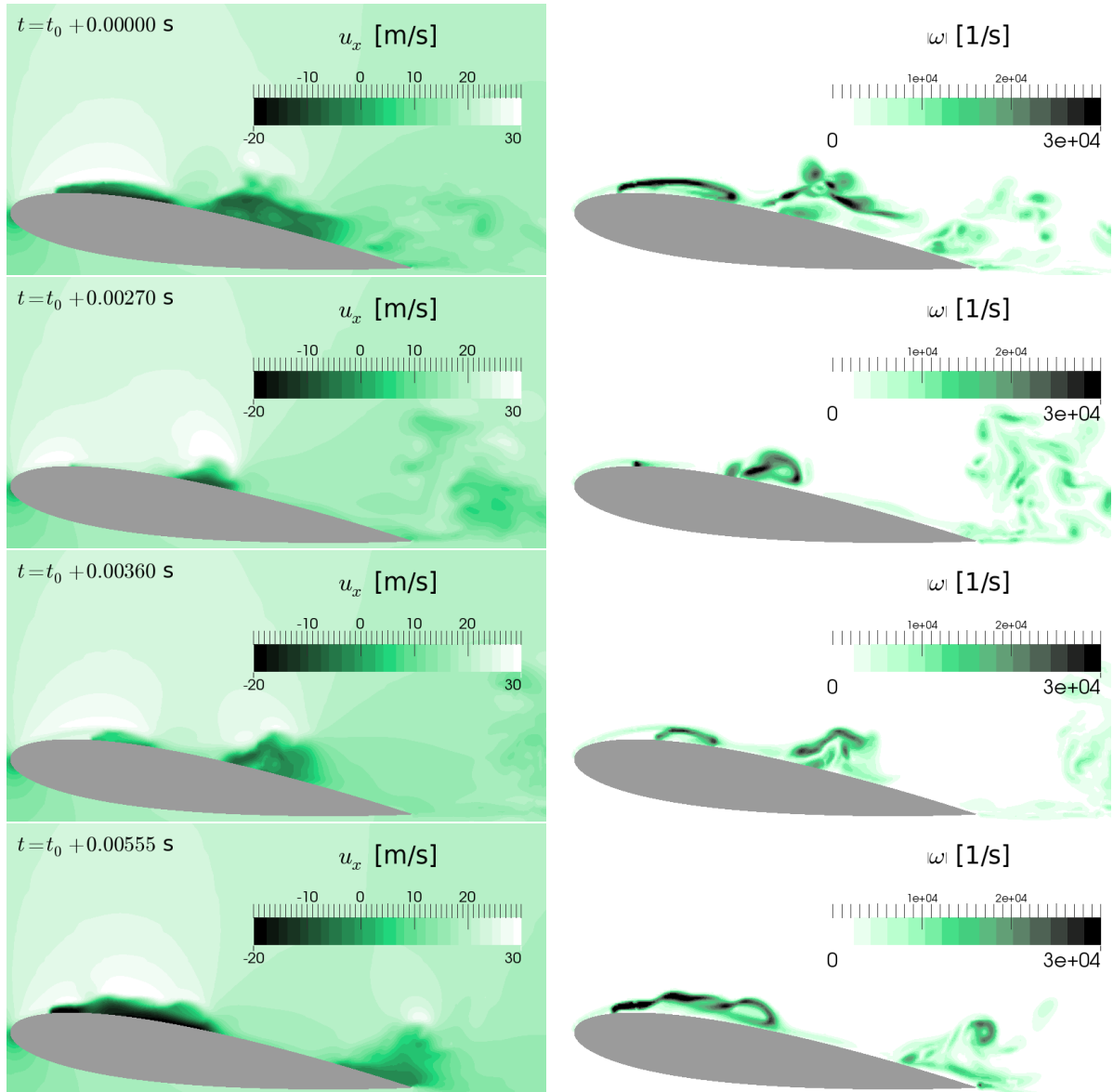
Fig. 10: Axial velocity field in the centre plane (left) and corresponding vorticity magnitude field (right)

The converged simulation for Δt = 7.5e-7 s and C_c = 50000 kgs/m^5 is extended a little further to investigate the formation of cavitating vortical structures. Schmidt et al. (2009) have shown that the formation of vortical structures in sheet cavitation is mainly an inertia driven effect. The alteration of the vorticity field is visualised by evaluating iso-surfaces of the source terms on the right-hand side of the vorticity Eq. (1). Fig. 8 (right) depicts instantaneous iso-surfaces of the source term magnitudes at 1.0e7 s^{-2} for one shedding cycle, from the time instant of cavity pinch-off to the subsequent pinch-off. The white iso-surface represents the artificial baroclinic torque contribution, the green iso-surface the divergence contribution, in this case associated with phase transition, and the black iso-surface the three-dimensional tilting of vorticity vectors. The corresponding instantaneous vapour structures are shown in Fig. 8 (left). During the growing phase at instants t_0+0.00270 s and t_0+0.00360 s, the sheet cavity exhibits two-dimensional behaviour. Spanwise disturbances at the specified iso-surface magnitude are observed downstream from the pinch-off region at instants t_0 + 0.00000 s and t_0 + 0.00555 s. The main three-dimensional break-up, however, occurs as the shed cavities collapse further downstream. The inception region of the spanwise instability, indicated by the formation of vortex tilting in Fig. 9 (right) coincides with the pinch-off region indicated by the volume fraction field in Fig. 9 (left). The vorticity break-up associated with the downstream cavity collapse, however, is significantly larger. Prior to the occurrence of spanwise instabilities, we observe the formation of large in-plane vorticity caused by the re-entering

flow. Fig. 10 (left) depicts the distribution of the axial velocity component in the centre plane and Fig. 10 (right) shows the corresponding distribution of vorticity magnitude. At the moment of pinch-off (instants $t_0 + 0.00000$ s and $t_0 + 0.00555$ s), a re-entrant flow velocity in the order of 20 m/s is observed, going along with the generation of pronounced in-plane vorticity around the sheet. This in-plane vorticity is almost zero during the sheet growing phase at instant $t_0 + 0.00270$ s and builds up as the re-entrant jet starts to form at instant $t_0 + 0.00360$ s. An overview over different mechanisms possibly causing the formation of vorticity in the pinch-off region is given by Dular and Petkovšek (2015). A comparison of Fig. 8 and 10 further shows that the three-dimensional break-up of vorticity goes along with the formation of cavitating ring structures such as horseshoe cavities observed at instants $t_0 + 0.00000$ s and $t_0 + 0.00360$.

5 Conclusion

We have identified a configuration of mass transfer magnitude, temporal and spatial resolution for which the sheet cavitation dynamics around a NACA0015 hydrofoil are not sensitive to variation of the mass transfer model constants, given that the model constants are sufficiently large to provide an overcapacity of mass transfer magnitude which is not fully exploited during phase transition. In this regime the mass transfer constants could be varied by a factor of 100 without having any effect on the dominating frequency of the cyclic sheet cavitation dynamics. The predicted frequency is in good agreement with experimental results by Van Rijsbergen et al. (2012). We conclude that the cavitation dynamics of the larger scale structures are correctly predicted. Local peak pressures, however, remain dependent on both resolution and mass transfer magnitude and are not reliably predicted. The results further suggest that the inception of spanwise instabilities occurs in the cavity pinch-off region, even in the absence of viscous forces, and that the break-up of vorticity is amplified during the collapse of the shed cavities. This confirms the finding by Schmidt et al. (2009), stating that sheet cavitation dynamics are inertia driven.

Acknowledgements

References

M. Dular and M. Petkovšek (2015). On the Mechanisms of Cavitation Erosion - Coupling High Speed Videos to Damage Patterns. *Experimental Thermal and Fluid Science*, **68**(2015), 359–370.

A.H. Koop (2008). *Numerical Simulation of Unsteady Three-Dimensional Sheet Cavitation.* PhD thesis, University of Twente.

P. Koukouvinis and M. Gavaises (2015). Simulation of Throttle Flow with Two Phase and Single Phase Homogenous Equilibrium Model. Proceedings of the 9th International Symposium on Cavitation, Lausanne, Switzerland.

Z. Li, M. Pourquie and T.J.C. van Terwisga (2014). Assessment of Cavitation Erosion With a URANS Method. *Journal of Fluids Engineering*, **136**(4), 041101-1–041101-11.

C.L. Merkle, J.Z. Feng and P.E.O. Buelow (1998). Computational Modeling of the Dynamics of Sheet Cavitation. Proceedings of the 3rd International Symposium on Cavitation, Grenoble, France.

OpenFOAM (2017). OpenFOAM web site, 2017.

M. van Rijsbergen, E.J. Foeth, P. Fitzsimmons and A. Boorsma (2012). High-Speed Video Observations and Acoustic-Impact Measurements on a NACA 0015 Foil. Proceedings of the 8th International Symposium on Cavitation, Singapore, Republic of Singapore.

S. Schenke and T.J.C. van Terwisga (2017). Simulating Compressibility in Cavitating Flows with an Incompressible Mass Transfer Flow Solver. Proceedings of the 5th International Symposium on Marine Propulsors, Espoo, Finland.

S.J. Schmidt, M. Thalhamer and G.H. Schnerr (2009). Inertia Controlled Instability and Small Scale Structures of Sheet and Cloud Cavitation. Proceedings of the 7th International Symposium on Cavitation, Ann Arbor, Michigan, USA.

T. Xing, Z. Li and S.H. Frankel (2005). Numerical Simulation of Vortex Cavitation in a Three-Dimensional Submerged Transitional Jet. *Journal of Fluids Engineering*, **127**(4), 714–725.

A Novel Power-Saving Device for Full-Block Vessels

Lars-Uve Schrader, and Jochen Marzi
HSVA Hamburg Ship Model Basin, Hamburg/Germany
schrader@hsva.de

1 Introduction

The flow conditions in the wake behind a ship play a crucial role for the propulsive efficiency. The shape of the after body determines the inflow into the propeller, with bulky hull forms of full-block vessels suffering from massive losses of axial velocity above the propeller shaft (Fig. 1). These inflow defects cause strong periodic variations of the local angle-of-attack toward the propeller blades along with pressure fluctuations and risk of cavitation. Here, a novel type of hull appendage for improved propulsion is presented, dubbed "BLAD" (boundary-layer alignment/acceleration device).
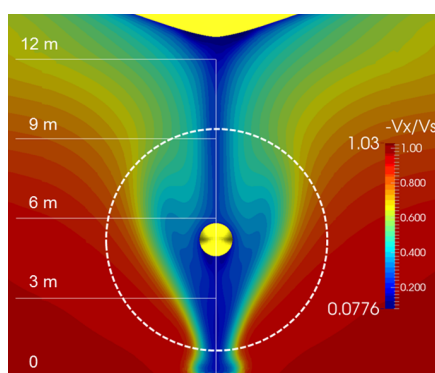
Fig. 1: Normalized axial flow velocity in the propeller plane for a Capesize bulk carrier. Computation at scale $\lambda = 30$ with the RANSE solver FreSCo$^+$

2 Design aspects and test case

The purpose of the BLAD is to deflect the outer streamlines in the after-body flow field towards the hull surface so as to locally accelerate the wake flow and reduce the boundary-layer thickness, yielding a more homogeneous flow through the propeller. Moreover, the BLAD design intends to create a swirl against the propeller rotation such that extra thrust is generated at a given engine power. In contrast to the well-established propulsion-improving devices (e.g. stator fins and ducts), which are attached close to the propeller, the BLAD is mounted far forward of the propeller plane such that a significant upstream portion of the flow field can be manipulated. The upstream placement is also advantageous in that the device is not exposed to the propeller-induced unsteady flow field and the associated dynamic loads. In the present study, the BLAD has been developed and tested for a Capesize bulk carrier with a 8.5m diameter four-bladed screw propeller (Fig. 2). At her design speed of 14 knots, the vessel suffers from significant wake flow defects owing to her bulky hull form (cf. blue regions in Fig. 1).

Capesize bulk carrier		171,199 dwt	
Hull		**Propeller**	
(L_{pp}, B, T)	$(280, 45, 17.62)$ m	n_{blade}	4
$c_B(T)$	0.844	D	8500 mm
U_s	14 kts	$P/D\,(r/R = 0.7)$	0.6619

Fig. 2: Ship hull and propeller considered

3   Numerical methods

Computational Fluid Dynamics (CFD) has been used for designing and optimising the BLAD, considering two sets of simulation: numerical towing tests and numerical propulsion tests. Initially, a viscous free-surface computation has been conducted to determine the wave drag of the vessel. Subsequent simulations have been carried out in a double-body configuration as the wave influence on the flow field around the BLAD is negligible, while the wave drag is included as a constant added force. The double-body CFD meshes for the towing and propulsion tests (Table 1) comprise a well-refined after-body region near the BLAD and the propeller to capture all relevant effects of the hull-BLAD-propeller interaction.

Table 1: Size of unstructured CFD meshes used for double-body (DB) and free-surface setup (FS)

	Bare hull	Hull with BLAD
# cells (DB)	4.4×10^6	5.3×10^6
# cells (FS)	6.3×10^6	7.2×10^6

The numerical towing tests have been conducted using HSVA's viscous-flow code FreSCo$^+$ solving the RANS equations. The turbulent boundary layers on the hull and BLAD surfaces are treated by a k-ω-SST turbulenc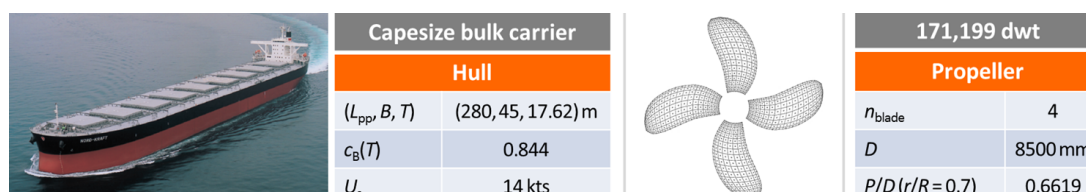e model along with logarithmic wall functions. In the numerical propulsion tests, propeller effects are included in FreSCo$^+$ by an actuator-disk body force model. The propeller forces exerted on the fluid are computed using HSVA's in-house boundary-element code QCM, an implementation of the Vortex-Lattice Method. It is sufficient for a power prediction to impose mean body forces in the propeller zone of the RANS mesh, obtained by averaging the instantaneous loads over six propeller revolutions. Since the wake field from the FreSCo$^+$ computation and the propeller forces from the QCM calculation depend on each other, the two codes are executed alternately in an iterative manner until a converged equilibrium between the propeller thrust and the propulsive hull resistance is reached (Fig. 3).
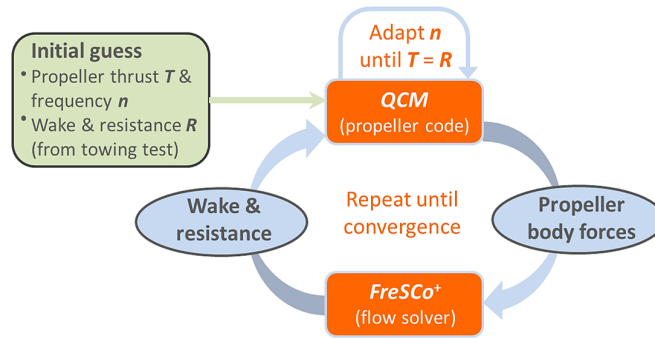
Fig. 3: Iterative procedure of the numerical propulsion tests: alternating update of propeller forces and propulsive wake field up to equilibrium between propeller thrust and propulsive hull resistance

4   Implementation of the BLAD concept

The BLAD consists of two flow deflectors on the port and starboard sides of the ship hull (Fig. 4) which have been created in the CAD design system CAESES based on a NACA wing with integrated struts. Being comparable to the propeller blades in size, the BLAD appendages are placed approximately two propeller diameters upstream of the propeller plane at zero sweep to avoid any cross stream. The wings and struts are at first carefully aligned to the local streamlines, leading to a twisted geometry. Subsequently, they are tilted around their leading edge so as to deflect the streamlines toward the hull surface. The angle-of-attack is adjusted until a significant improvement of the wake uniformity is achieved. Finally, the starboard BLAD deflector is cambered and shifted upward, leading to an asymmetric arrangement along with the desired swirl in the propeller inflow.
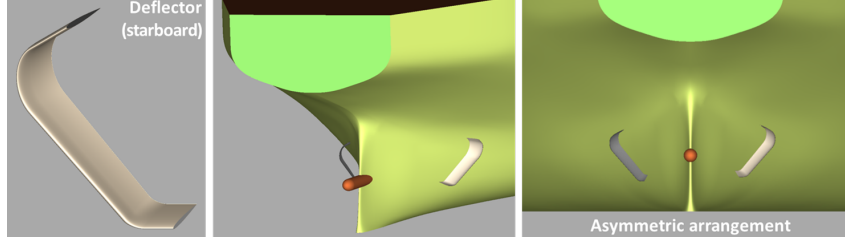
Fig. 4: Close-up view of the starboard BLAD deflector and position of the deflectors on the hull

5 Testing the BLAD

5.1 Numerical towing tests

The numerical towing tests serve to establish the resistance and the wake quality of the bare and appended hulls. The wake quality is characterised in terms of the wake fraction w and a wake-uniformity criterion,

$$C_{\text{wake}} = 1 - A \int_{\Phi} \frac{1}{r} \frac{|U_{\text{ax}}(r, \phi, x) - \overline{U}_{\text{ax}}(r)|}{U_S} \mathrm{d}\Phi, \tag{1}$$

where

$$A = \frac{1}{\int_{\Phi} \frac{1}{r} \mathrm{d}\Phi}. \tag{2}$$

The symbols r, ϕ and x denote the radial, circumferential and axial coordinates in the propeller disk Φ, U_{ax} is the local axial velocity and $\overline{U}_{\text{ax}}$ its circumferential-axial average on the radius r, and U_S is the ship speed. A comparison of the nominal wakes highlights a marked reduction of the axial velocity defect thanks to the BLAD (Fig. 5), reflected by a 21% decrease of the wake fraction w and a 3% increase of the wake uniformity C_{wake} (Table 2). Moreover, the BLAD deflectors create an asymmetric velocity field with a significant swirl against the propeller rotation, as desired.
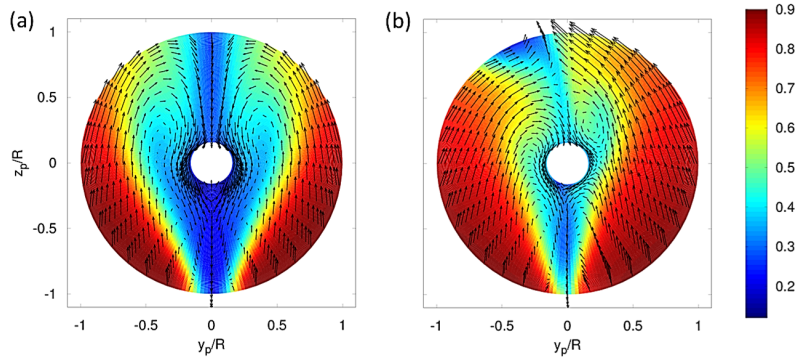
Fig. 5: Nominal wake in the propeller plane (a) without and (b) with the BLAD

Table 2: Wake quantities without and with the BLAD

Quantity	Symbol	Bare hull	Hull with BLAD
Wake fraction	w	0.508	0.403 (-20.7%)
Wake uniformity	C_{wake}	0.869	0.894 ($+2.9\%$)

The numerical towing tests reveal that the BLAD reduces the total resistance of the appended hull model by 0.3% (Fig. 6), thus acting as a passive thruster. This reduction is attributed to a 1.5% drop of the viscous drag, surprising at first and explained by a patch of separated flow above the skeg with positive, forward-pushing axial wall shear stresses (white contour in Fig. 7a). The separation bubble is fortunately limited in size, does not lead to excessive pressure drag and shrinks upon propeller activation

due to suction (Fig. 7b). The pressure resistance of the hull alone drops significantly (−14%, rightmost column of Fig. 6) because the pressure sides of the BLAD deflectors locally enhance the forward-pushing pressure level of the after body. The total hull resistance excluding the BLAD is 4% lower than that of the bare hull; however, most of this benefit is lost to the 3.7% extra resistance of the BLAD deflectors.
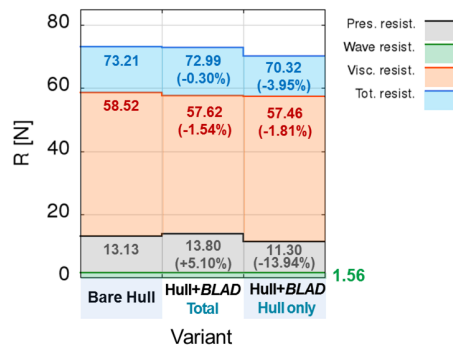
Fig. 6: Wave, pressure and viscous drags plus total resistance of the hull model (scale $\lambda = 30$) without and with the BLAD. For the appended-hull case, the contribution of the hull alone is also shown
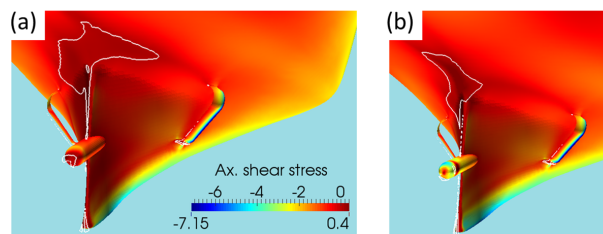
Fig. 7: Patch of separated flow (white contour) on the surface of the appended hull, triggered by the BLAD deflectors: (a) without, (b) with active propulsion

5.2   Numerical propulsion tests

Since the BLAD generates a swirl in the propeller plane (cf. Fig. 5b), the propeller turning rate is expected to drop. To avoid detuning the main engine, the original propeller (Fig. 8a) may need to be modified or even replaced. Two approaches are considered: a propeller modification through clipping and grinding the blade trailing edges (Fig. 8b) and a new propeller (Fig. 8c). The first option represents a low-cost dry-dock retrofit alternative while the second is potentially more beneficial in terms of energy saving. It is pointed out that the modified and new propellers may be more vulnerable to cavitation than the original, although the BLAD is expected to reduce the cavitation risk thanks to the more uniform wake.
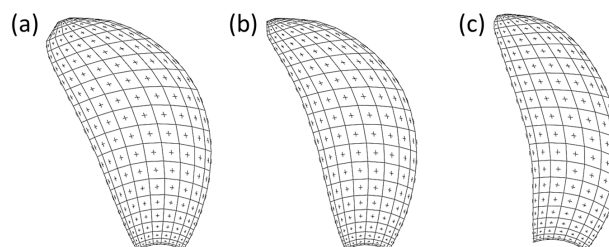
Fig. 8: Propeller blades (vortex lattices) used in the numerical propulsion tests. (a) Original propeller, (b) modified propeller (clipped, ground trailing edge), (c) new propeller

In the following, the baseline setup (bare hull plus original propeller) is compared to the three appended-hull configurations (hull with BLAD plus original, modified or new propeller). If the original propeller operates behind the appended hull, the turning rate drops by almost 1% (Fig. 9), as expected,

whereas the modified and new propellers nearly maintain the original frequency and thus the correct engine operating conditions.
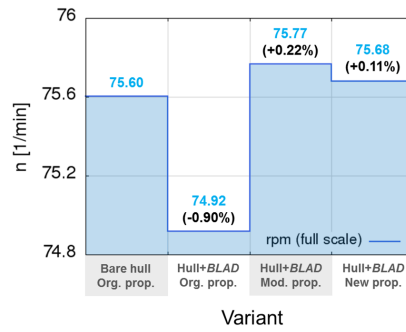
Fig. 9: Propeller frequency (rescaled for full scale) for four cases: (i) bare hull with original propeller; (ii-iv) appended hull with (ii) original, (iii) modified and (iv) new propeller

For all three propellers, the BLAD deflectors reduce the required thrust by some 1% with respect to the baseline case (Fig. 10a). This improvement benefits from two contributions: (i) a slightly lower hull resistance (cf. Fig. 6) and (ii) diminished propeller suction reflected by smaller thrust-deduction coefficients (Table 3). The lowest thrust is observed when combining the BLAD with the new propeller, yielding a 3.7% decrease of the thrust-deduction coefficient. The torque around the propeller shaft also drops thanks to the BLAD (Fig. 10b), becoming manifest in a reduction of the propeller power by 1.5% (original propeller) to 7% (new propeller; Fig. 10c). As a result, the propulsive efficiency increases from 73.3% to 78.5% for the best case (Fig. 10d). A split-up into efficiency components reveals that the improvement is mainly attributed to a higher open-water propeller efficiency (Table 4): the BLAD raises the advance number such that the propeller operating point becomes more favourable; however, the larger advance speed also leads to a loss of hull efficiency. The results indicate that the BLAD performs best in combination with adapted propellers which can make use of the larger advance speed and the higher relative rotative efficiency. On the other hand, these propellers would not perform as well at the lower advance number provided by the BLAD-less hull. Therefore, both components – the BLAD and a propeller modification – are necessary to obtain significant power savings above 4%.
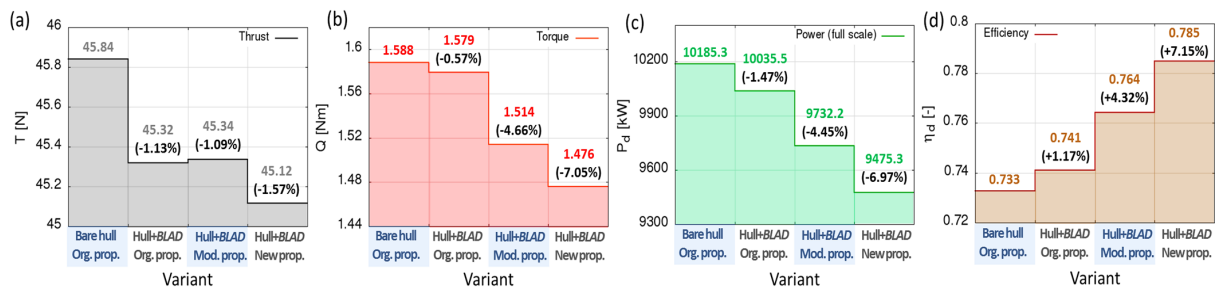
Fig. 10: (a) Thrust, (b) torque, (c) full-scale power and (d) propulsive efficiency for four cases: (i) bare hull with original propeller; (ii-iv) appended hull with (ii) original, (iii) modified and (iv) new propeller

Table 3: Thrust-deduction coefficient for the four cases considered

Quantity	Symbol	Bare hull Org. prop.	Hull + BLAD Org. prop.	Hull + BLAD Mod. prop.	Hull + BLAD New prop.
Thrust deduct. coeff.	t	0.162	0.159 (-1.9%)	0.160 (-1.2%)	0.156 (-3.7%)

A comparison of the thrust distribution across the propeller plane reveals two observations (Fig. 11): (i) the BLAD deflectors cater for a more even propeller-thrust distribution with a smaller peak along the circumferential direction than in the bare-hull case, yielding a more homogeneous propeller loading with

Table 4: Advance number and efficiencies for the four cases considered

Quantity	Symbol	Bare hull Org. prop.	Hull + BLAD Org. prop.	Hull + BLAD Mod. prop.	Hull + BLAD New prop.
Advance number	J	0.331	0.405	0.401	0.401
Open-water prop. eff.	η_0	0.490	0.568 (+15.9%)	0.578 (+18.0%)	0.579 (+18.2%)
Hull efficiency	η_H	1.703	1.409 (−17.3%)	1.407 (−17.4%)	1.414 (−17.0%)
Rel. rotative eff.	η_R	0.878	0.926 (+5.5%)	0.939 (+6.9%)	0.959 (+9.2%)

lower risk of propeller and hull vibrations. (ii) The thrust distribution becomes more symmetric about the mid-ship plane when the BLAD is present. The enhanced symmetry is expected to increase the course stability of the ship such that losses due to corrections of the rudder angle may diminish.
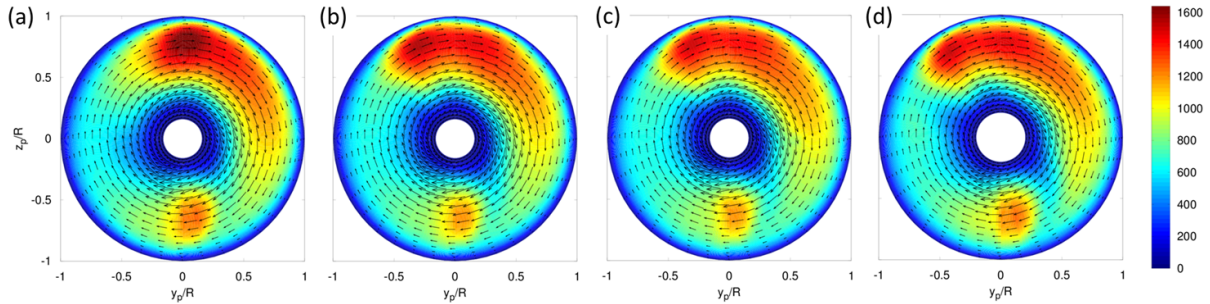
Fig. 11: Distribution of averaged thrust in propeller plane for (a) bare hull with original propeller and (b-d) hull + BLAD with (b) original, (c) modified and (d) new propeller

6 Concluding remarks

A novel propulsion-improving device is proposed, the BLAD. The working principle does not differ from that of existing devices: the recovery of momentum losses in the hull wake and of rotational losses in the propeller slipstream. Well-proven appendages, e.g. the Mewis duct (Guiard et al. (2013)), often need two components (duct and fins) to tackle these two loss sources while the BLAD achieves this with only one type of structure – the deflectors, mounted far upstream of the propeller. This may qualify the BLAD design as simpler, safer against structural failure and more cost-effective than the established devices, although the achievable power savings may be lower. The present findings indicate that the BLAD can considerably increase the propulsive efficiency, rendering it a promising device. The major strength of the concept is seen in its potential to create the necessary flow conditions for more powerful propeller designs. The BLAD is believed to perform even better for ships with distinct bulbous sterns while the present test vessel features comparably sleek lines around the propeller shaft.

It is emphasised that the reported study should be understood as a proof-of-concept. Before a BLAD will be seen on a real cargo vessel (if ever), the following issues should be addressed: (i) How does the BLAD perform outside the design point (different speed, draft, trim) and in seaway? (ii) Can the present CFD results be reproduced in experiments? (iii) What about propeller cavitation? (iv) What are the implications for the rudder? (v) How does the BLAD perform at full scale?

Acknowledgements

References

T. Guiard, S. Leonard, and F. Mewis (2013). The Becker Mewis Duct® – Challenges in Full-Scale Design and new Developments for Fast Ships. Proceedings of smp'13, Tasmania, Australia.

Controlling the added-mass instability in fluid-solid coupling

Henk Seubers and Arthur Veldman
University of Groningen

1 Introduction

Simulating the hydrodynamics of floating structures using a partitioned strategy poses a major challenge when the coupling between the fluid and the structure is strong. The incompressibility of the fluid plays an important role, and leads to strong coupling when the ratio of so-called added mass to structural mass is considerate. Existing fluid-structure interaction procedures become less efficient in such cases, and can even become unstable as shown by Causin et al., 2004. The current paper proposes a coupling method that is unaffected by this instability, and shows its efficient implementation.

2 Stability

The fluid model and the solid model should be in agreement at any point where the fluid meets the solid. Restricting ourselves to mechanical interactions, this agreement requires two conditions to be satisfied at each point. The kinematic condition simply requires that the local fluid and solid motions are the same (i.e. displacement, velocity, acceleration), so each point remains on the interface. The dynamic condition requires that any force on the fluid is equalled by an opposite force on the solid in order to conserve momentum.

Typically these two conditions are enforced by a fixed-point iteration. The fluid and solid models are evaluated in turn, subject to the kinematic and dynamic condition respectively. Assume the interface is discretized into n degrees of freedom. The displacements $\vec{x}(t) \in \mathbb{R} \to \mathbb{R}^n$ and forces $\vec{f}(t) \in \mathbb{R} \to \mathbb{R}^n$ are exchanged between the fluid and the solid. Everything else remaining the same, the stability of this iteration can therefore be expressed in terms of the response of each model to the applied forces and displacements. We denote the fluid response by the function F and the solid response by the function S,

$$\vec{f}(t) = F(\vec{x}(t)), \tag{1a}$$

$$\vec{x}(t) = S(\vec{f}(t)). \tag{1b}$$

Of course these functions depend on the initial state and external forcing of the models as well, but this is understood to be part of F and S since these do not change between iterations. The solid only responds to the fluid force, and the fluid in turn responds to the solid motion. The fixed-point iteration can thus be expressed as

$$\vec{f}_{k+1}(t) = F(S(\vec{f}_k(t))). \tag{2}$$

The asymptotic convergence is determined by the greatest eigenvalue of the Jacobian of $F \circ S$ (at the fixed point),

$$J(t) = \frac{\partial F \circ S(\vec{f}(t))}{\partial \vec{f}(t)} \tag{3}$$

which is a function of time. Only if the magnitude of this eigenvalue is smaller than one, the above fixed-point iteration (2) will converge. Otherwise, one has to resort to relaxation or quasi-Newton methods.

When timestepping an unsteady fluid-solid problem (1), the functions $\vec{f}(t)$ and $\vec{x}(t)$ are converged up to the start t_n of the timestep and are to be determined up to the end of the timestep $t_n + \Delta t$ via a suitable extrapolation. In an incompressible flow, the only nonzero eigenvalues of $J(t_n)$ are related to the inertia of the fluid and solid (Seubers and Veldman, 2017). The ratio of added mass of the fluid to the the solid mass determines these eigenvalues (Förster et al., 2006) and hence the stability. This instability is not controllable by the timestep Δt.
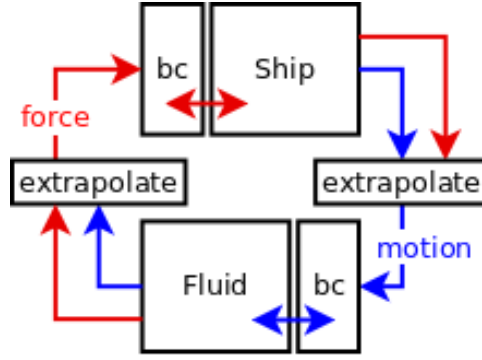
Fig. 1: Fixed point iteration according to Eq. (2).

It is undesirable that the stability of the numerical process depends on a physical parameter that can not be controlled. Therefore we will introduce a modification to the fixed-point iteration (2) that removes the added-mass instability from the system (1). In that system, the fluid is directly subjected to the motion S of the solid. This boundary condition is only realistic when the solid is largely unaffected by the fluid. Instead, we can subject the fluid to a more realistic condition that allows the solid to respond.

The key observation is that the two conditions (kinematic and dynamic) on the two unknowns ($\vec{x}$ and $\vec{f}$) can be linearly combined. However we cannot simply combine (1a) with (1b), since this would require a single monolithic code for the fluid and solid. Instead, we can make a crude approximation of the solid,

$$\vec{x} = S(\vec{f}) \approx S(\vec{f_k}) + D(\vec{f} - \vec{f_k}) \tag{4}$$

where D is a n-by-n matrix. Instead of the pure kinematic condition, this equation becomes the new boundary condition to the fluid equation (1a), resulting in the iteration

$$\vec{f_{k+1}}(t) = F\left(S(\vec{f_k}(t)) + D(\vec{f_{k+1}}(t) - \vec{f_k}(t))\right) \tag{5}$$
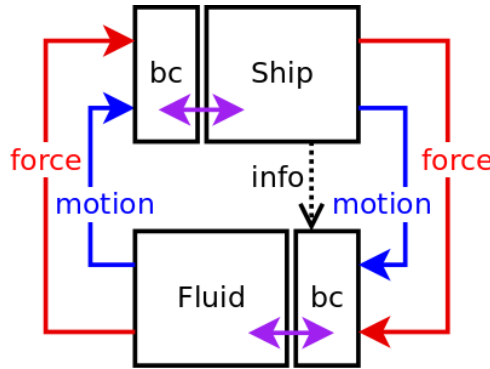
Fig. 2: Fixed point iteration according to Eq. (5).

We wish to point out three properties of the modified iteration (5). First of all, it has exactly the same solutions as equation (2) since these equations are identical at the fixed point $\vec{f_{k+1}} = \vec{f_k}$. This is due to the fact that although (4) can be a crude approximation, it is equal by definition to the exact solid at these fixed points. Secondly, the stability of the fixed points will be different. Comparing the Jacobians of the original (2) and modified (5) iterations, we see that

$$J_{\text{eq. (2)}}(t) = J_F(t) * J_S(t), \tag{6}$$

$$J_{\text{eq. (5)}}(t) = (J_F^{-1}(t) - D)^{-1} * (J_S(t) - D), \tag{7}$$

hence the matrix D can be used to control the stability. Thirdly, if the matrix D equals the linearized solid J_S the method will convergence with second order in the nonlinearity, comparable to Newtons method.

3 Control of stability

Short proof of stability for diagonal D, convergence criteria.

4 Boundary conditions

As noted in the previous section, the boundary conditions to the fluid need to be modified into a linear combination of forces and motions. Consider an incompressible viscous fluid governed by the Navier-Stokes equations,

$$\frac{\partial \vec{u}}{\partial t} + \vec{u}^T \nabla \vec{u} + \frac{1}{\rho} \nabla p = \nu \nabla^2 \vec{u} + \vec{g} \qquad\qquad \nabla^T \vec{u} = 0 \qquad (8)$$

It is clear that a prescribed force leads to a Dirichlet-type boundary condition on the pressure. Similarly, a prescribed acceleration leads to a Neumann-type boundary condition for the pressure, which is just the product of Eq. (8) with the normal vector to the boundary. A combination of forces and motions therefore leads to a generalized Robin-type boundary condition.

Since Eq. (5) was formulated in the discrete setting, we will first discretize the fluid equations as well. Applying the symmetry-preserving finite-volume method (Verstappen and Veldman, 2003) to Eq. (8), we obtain the discrete momentum and continuity equations,

$$\frac{\Omega}{\Delta t}(\mathbf{u}^{n+1} - \mathbf{u}^n) + C(\mathbf{u}^n)\mathbf{u}^n + \frac{1}{\rho}G\mathbf{p} = \nu L\mathbf{u}^n + \mathbf{g} \qquad\qquad G^T\mathbf{u}^{n+1} = 0. \qquad (9)$$

The pressure values are associated to cells, while the velocities are associated to cell faces. Considering a discrete domain with n boundary faces, m interior faces and k cells, the discrete unknowns and operators are of the following dimensions.

symbol	meaning	space
$\mathbf{p}$	pressure	$\mathbb{R}^k$
$\mathbf{u}$	velocity	$\mathbb{R}^{m+n}$
$\mathbf{g}$	gravity	$\mathbb{R}^{m+n}$
C	convection	$\mathbb{R}^{m+n} \to \mathbb{R}^{m+n}$
L	diffusion	$\mathbb{R}^{m+n} \to \mathbb{R}^{m+n}$
G	gradient	$\mathbb{R}^k \to \mathbb{R}^{m+n}$
G^T	divergence	$\mathbb{R}^{m+n} \to \mathbb{R}^k$
Ω	control volume	$\mathbb{R}^{m+n} \to \mathbb{R}^{m+n}$

Table 1: Discrete quantities

The momentum equation applies to all velocities, including those at the boundary of the cut cells as shown in Fig. 3. Note however that only forces *within* the fluid are covered by the above momentum equation, which means that the boundaries are force-free. This is easiest to see by inspecting the gradient operator G at the boundary. It contains only a single pressure contribution from the adjacent cell, because its transpose contains the single contribution of the boundary velocity to the divergence of that cell. To incorporate forced boundaries, a Lagrange multiplier $\boldsymbol{\lambda} \in \mathbb{R}^n$ is introduced.

From the incompressibility condition, we obtain a Poisson equation for the pressure ...

Results

Recommendations

Acknowledgements
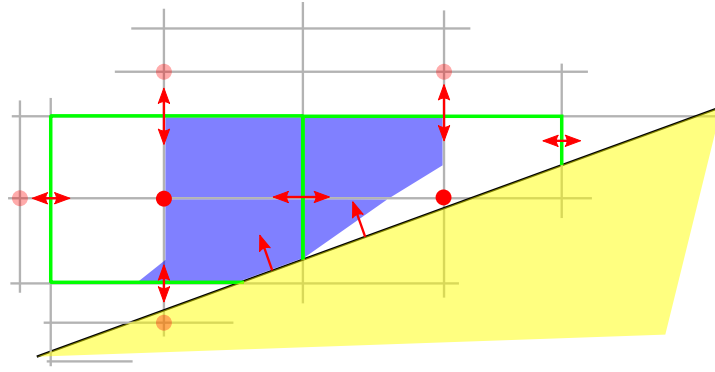
Fig. 3: Finite volume discretization on a staggered grid with cut cells. The solid is shown in yellow, a momentum control volume in blue. Two adjacent continuity cells are outlined in green.

References

Causin, P., Gerbeau, J. F., and Nobile, F. (2004). Added-mass effect in the design of partitioned algorithms for fluid-structure problems. *Computer methods in applied mechanics and engineering.*

Förster, C., Wall, W. A., and Ramm, E. (2006). Artificial added mass instabilities in sequential staggered coupling of nonlinear structures and incompressible viscous flows. *Comput. Methods Appl. Mech. Engng.*, 196(7):1278–1293.

Seubers, J. H. and Veldman, A. E. P. (2017). Acceleration of fluid-structure interaction procedures by anticipatory coupling. In Manolis Papadrakakis, E. O. and Schrefler, B., editors, *Coupled Problems in Science and Engineering VII.*

Verstappen, R. and Veldman, A. (2003). Symmetry-preserving discretization of turbulent flow. *Journal of Computational Physics*, 187(1):343 – 368.

A Verification and Validation Study of CFD Simulations for the Flow Around a Tug

Bastiaan Vink[*]**, Joost Schot**[*]**, Guilherme Vaz**[†]**, Serge Toxopeus**[†]

[*]Damen Shipyards, Gorinchem/The Netherlands, [†]Maritime Research Institute Netherlands (MARIN), Wageningen/The Netherlands

Bastiaan.Vink@Damen.com, Joost.Schot@Damen.com, G.Vaz@Marin.nl, S.Toxopeus@Marin.nl

1 Introduction

An important vessel for the operational process in a harbour is the tug, a vessel built for the specific purpose of assisting and berthing ships. The key features of a tug are the towing and escorting performances under operational conditions, often reached when sailing under drift at high Froude numbers. Performance predictions for these tug operations can be based on free running or captive model tests, which can be expensive, give no thorough insight in flow specifics and although large-scale models are used still suffer from scale effects. An alternative approach is the use of Computational Fluid Dynamics (CFD).

The industrial standard in CFD is modelling the (U)RANS equations with turbulence models, however this is at the cost of accuracy and resolution in space and time compared to directly solving the Navier-Stokes equations. Therefore, multiple numerical errors, e.g. the discretisation, iterative and round-off error as described by Eça and Hoekstra (2006a) and the modelling error must be assessed first, before quantifying the modelling errors. Quantifying these numerical errors is generally known as Verification, where the quantification of the modelling error is known as Validation.

It has already been shown with the use of Verification & Validation for a multitude of cases that time-averaged RANS equations are accurate enough to predict the resistance of both simple and sometimes more complex vessels, e.g. Schot et al. (2017). However, an increase in complexity of the flow, e.g. bluff vessels, drift angles or a combination as is present for tugs, results in more difficulty, Toxopeus (2011).

The validation case used in this research is a reference tug from Damen Shipyards that was found a difficult case for CFD simulations, Schot et al. (2017). A tug is highly affected by flow separation which increases under drift and requires free surface modelling due to the high Froude numbers. Due to the flow separation turbulence modelling and significant grid densities are required for a sufficiently small discretisation error, similar to drift simulations of other vessels found in literature, e.g. Stern et al. (2009). To the authors knowledge no publications exist on the verification and validation of CFD for tugs sailing under drift including free surface. Jahra (2015) and Smoker et al. (2016) presented free surface simulations on unstructured grids compared to model tests. They show that correct trends can be obtained, although with large comparison errors and without presenting numerical or experimental uncertainties.

This present work will estimate the experimental uncertainties from captive model tests to obtain correct validation material. Thereafter a verification and validation exercise of free surface simulations on unstructured grids with the KSKL turbulence model and a drift angle β of 15° will be presented. These are followed by a turbulence sensitivity study and finally simulations at other drift angles will be presented.

2 Validation case

The main particulars of the model scale reference tug are V_s =2.29[kn], L_{pp}=1.847[m], B=1.026[m], T=0.271[m], which correspond to F_n=0.28, Re=2.20E+06. This research uses the model scale dimensions of a barehull tug for validation, where it results in excluding possible scale effects. Experimental results are obtained with captive model tests performed at MARIN.

3 Methodology

3.1 ReFRESCO solver

The CFD code used in this present work is ReFRESCO, Vaz et al. (2009). ReFRESCO is a community based open-source viscous-flow CFD code that solves multiphase (unsteady) incompressible flows using the Navier-Stokes equations, complemented with turbulence models, cavitation models and volume-

fraction transport equations for different phases, (*www.refresco.org*) .

For this present study, the convective fluxes of the momentum equation are discretised using a quadratic upwind discretization (QUICK) with eccentricity corrections, where the time and convective fluxes of the turbulence equations are discretised with a first-order implicit Euler backward scheme. The air volume fraction is discretized using the MARIN inhouse developed ReFRICS scheme and 3 turbulence models and one SRS formulation are used: the KSKL model of Menter et al. (2011), the k−ω SST model of Menter et al. (2003) the EARSM model of Dol et al. (2002) and the k−ω SST based DDES of Gritskevich et al. (2012).

3.2 Domain and boundary conditions

The simulations are performed in a hexahedral domain with a Cartesian coordinate system (x, y, z). The still water line is representing the location of the free surface, located at $z = 0$ as shown in figure 1. The vessel is placed at the origin O, where $x, y, z = 0$ and is modelled by a no-slip boundary condition The exterior of the domain is modelled with two different boundary conditions. The inflow surface of the domain is modelled by an inflow boundary condition, where the rest of the domain is modelled by a Dirichlet pressure boundary condition with the pressure set to the hydrostatic pressure. A view of the imposed boundary conditions on the domain is given in figure 1.
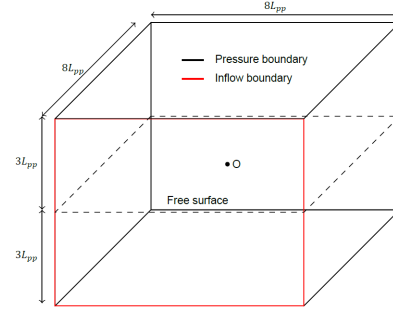
Fig. 1: The computational domain showing the imposed boundary conditions

3.3 Grids

A set of five trimmed hexahedral grids is created using HEXPRESS. The grids are created for wall resolved simulations for the wetted surfaces with corresponding y^+ values as given in table 1, where the boundary layer mesh is forced as much as possible into geometric similarity by adapting the growth ratio and inserting a prescribed number of layers. The grids are further refined by free surface refinement boxes, bow and stern refinement boxes and a refinement around the full vessel, where the refinement level is based on 20 cells over the wave height for grid g_4. A representation of the grid is given in figure 2 where pictures of g_2 are shown. The parameters and number of cells of all grids are shown in table 1.

Table 1: Properties of the grids used: the refinement ratio $r_i = \sqrt[3]{n_5/n_i}$, the target y^+ value, the number of cells along the length of the hull $N_{L_{pp}}$, the number of cells used for the initial domain division N_X, N_Y, N_Z and the total number of cells N_C.

Grid	r_i	y^+	$N_{L_{pp}}$	N_X	N_Y	N_Z	N_C
g_5	1	0.168	480	48	48	36	28424763
g_4	1.5	0.204	400	40	40	30	17649143
g_3	2	0.258	320	32	32	24	9538299
g_2	2.5	0.353	240	24	24	18	4326562
g_1	3	0.557	160	16	16	12	1248936

3.4 Simulation matrix

Fifteen simulations are performed for the verification of the free surface simulations with the KSKL turbulence model at $\beta = 15°$. These simulations involved 3 different time steps and 5 grids. The timesteps used in the verification are based on MARIN in-house guidelines for steady wave pattern simulations. The timesteps are based on a reference timestep $T_{ref} = \frac{L_{pp}}{V_s}$ and are given by $\tau_1 = T_{ref}/50, \tau_2 = T_{ref}/75$ and $\tau_3 = T_{ref}/100$. These timesteps are expected not to be fine enough to correctly resolve a breaking bow wave or correctly resolve turbulence, since the maximum Courant numbers for the simulations are ranging between 20-60 for the finest timestep τ_3.

The investigation into the sensitivity of turbulence modelling is performed with τ_3 and grid g_3 for the SST and EARSM turbulence model, where a DDES calculation is performed on grid g_4.

To obtain lift and drag curves, simulations are performed on grid g_4 with τ_3 and the KSKL turbulence model for $\beta = 0°, 15°, 30°, 45°$ and $90°$.

Fig. 2: Pictures of grid g_2.

3.5 Estimation of the experimental uncertainty

Four quantifiable uncertainty sources are found to be dominating in the performed captive model tests. The first source is the unce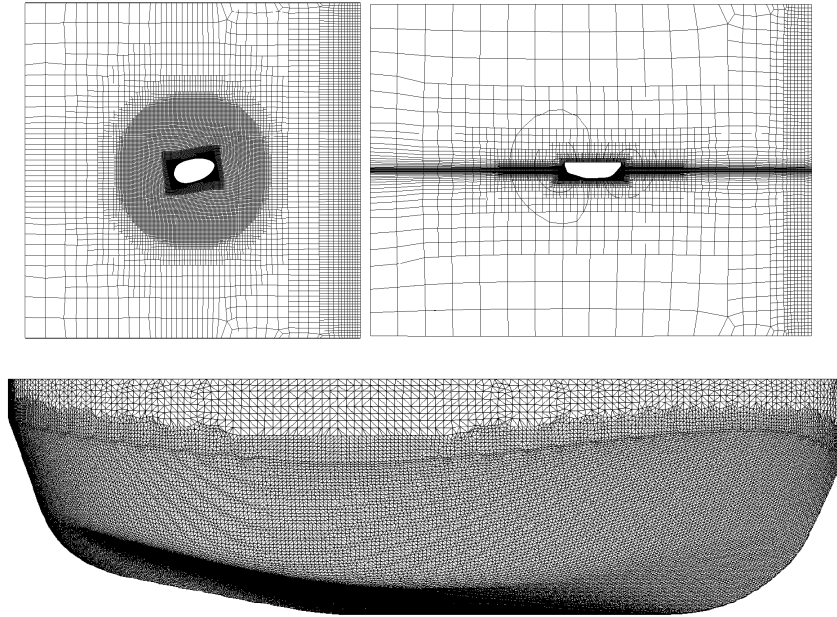rtainty originating from the statistical convergence and is estimated by the Transient Scanning Technique proposed by Brouwer et al. (2013). The second source is the uncertainty originating from the model speed in the towing tank which has two components: the uncertainty of the speed of the towing carriage, which is estimated according to the ITTC guidelines, ITTC (2014), and the uncertainty due to residual flow in the towing tank. The third dominating source is the uncertainty due to the 6-component (6C) force balance frame. This uncertainty is estimated based on known uncertainties of 6C frames with small dimensions. The last source is the uncertainty of the predicted force due to an possibly incorrect set-up of the drift angle.

Three other uncertainties or errors, which cannot be quantified with the available data, are expected to be of significant influence. The first is related to the finite length of the towing tank which results in signals which do not statistically converge and thus no correct estimate of the mean could be obtained. The second expected unquantified error is a constant force measured in Y-direction for the specific case of $\beta = 0°$, which is equal to 50% of the force in X-direction, where for symmetric vessels an oscillating force around a zero mean is expected. This effect is expected to originate from a constant location of a separation region at one side of the vessel. The last source of unquantified uncertainty are the turbulence tripping strips applied to the model during tests. The strips are only located at the front of the vessel which leads to an asymmetric flow pattern in model tests under drift.

Combining the quantifiable uncertainty sources results in uncertaintly levels between 6.8% and 26.8% for the range of drift angels.

3.6 Estimation of the numerical uncertainty and modelling error

The numerical uncertainty in steady CFD simulations consists of three terms, the round-off error, iterative error U_i and the discretization error U_d as described by Eça and Hoekstra (2006a) and computed using their methodology. In unsteady simulations an additional uncertainty arises from the statistical error U_A and the discretization error has two contributions, spatial and temporal.

The round off error arises from the finite precision of computers and is due to the double-precision solvers assumed to be negligible in these simulations Eça and Hoekstra (2006b).

The iterative error cannot be easily estimated due to difficulty of the flow problem, e.g. finer grids, unstructured grids or free surface computations with a VoF approach, which results in the inability of converging the residuals to negligible values. Therefore the iterative error is estimated by performing

eleven simulations on grid g_3 with τ_3, where different convergence criteria are set. The standard deviation of the different obtained results combined with the the statistical uncertainty is taken as the iterative uncertainty.

The total numerical uncertainty U_S is, assuming dependency between the separate components, by summation of the individual uncertainty components as proposed by The American Society of Mechanical Engineers (2009). The total numerical uncertainty is combined with the experimental uncertainty to find the validation uncertainty, where the input parameter uncertainty is assumed negligible.

4   Results

4.1   Verification $\beta = 15°$

The force coefficients in X- and Y-direction on 5 grids and 3 time step sizes are plotted in figure 3 together with the computed fit and the estimated uncertainty. The temporal variation of the results is below 2% and is insignificant in comparison with the variation obtained with spatial refinement. The variation occurs mainly due to difficulties in the convergence of the flow separation region. The free surface interface and flow outside the separation region were converged from grid g_4. The computed uncertainties seem high, especially considering the differences between all values. However, the uncertainty of the force in X-direction, U_d=15.8%, is in the same range as the EFD uncertainty and has a variation of 7.09% in all computed results. The uncertainty of the force in Y-direction, U_d=59.3%, is much higher as an effect of the safety factor of 3 and the result on grid g_5 where numerical air ventilation interacted with the flow separation and significantly affected the forces. The total variation of the results of all simulations 30.5%.

(a)   (b)
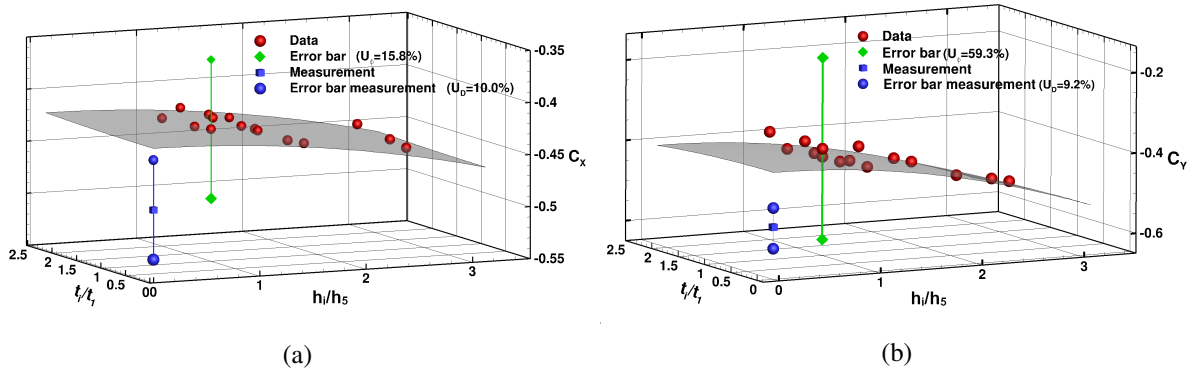
Fig. 3: Discretization uncertainty for the forces in X , **(a)**, and Y direction, **(b)**. Simulation with the KSKL turbulence model. Plotted for temporal refinement ratio t_i/t_3 and spatial refinement ratio r_i/r_5.

4.2   Validation $\beta = 15°$

The results of the validation exercise for timestep τ_3 are shown in table 2. The iterative uncertainty from grid g_3 is applied to all other grids. Firstly, the results show that the comparison error increases with grid refinement. Secondly, they show that the validation uncertainty decrease stagnates from grid g_3, where figure 3 showed that this was due to scatter in these results. Table 2 shows that both EFD and CFD results should be improved before drawing decisive conclusions from the results and quantifying a possible modelling error.

4.3   Sensitivity to turbulence modelling

The simulations with the SST and EARSM turbulence model showed no improvements in the comparison errors as shown in figure 4. Similar results were found with the DDES simulation performed on

Table 2: Validation exercise of the forces simulated with KSKL turbulence model with τ_3 and at $\beta = 15°$ and $Fn = 0.28$. Comparison errors higher than 10% are shown in red.

Mesh		U_d	U_i	U_A	U_S	U_{val}	E
g_1	F_X	26.5%	1.5%	0.0%	10.0%	29.7 %	5.5 %
	F_Y	88.1%	0.9%	0.1%	9.2%	88.6 %	3.7 %
g_2	F_X	27.1%	1.5%	0.0%	10.0%	30.3 %	7.7 %
	F_Y	78.8%	0.9%	0.1%	9.2%	79.4 %	16.7 %
g_3	F_X	21.8%	1.5%	0.0%	10.0%	25.3 %	10.8 %
	F_Y	68.4%	0.9%	0.1%	9.2%	69.1 %	15.8 %
g_4	F_X	29.1%	1.5%	0.0%	10.0%	32.2 %	13.8 %
	F_Y	52.5%	0.9%	0.1%	9.2%	53.4 %	19.3 %
g_5	F_X	15.8%	1.5%	0.0%	10.0%	20.0 %	11.8 %
	F_Y	59.3%	0.9%	0.1%	9.2%	60.1 %	26.2 %

grid g_4 with τ_3.

The KSKL and SST are comparable and are within each others error bars. However the EARSM and DDES results are significantly different. This difference originates from the prediction of the breaking bow wave of the vessel. A visual comparison of the computed free surface interface and the water surface of the model tests is given in figure 5. Here it is concluded that the KSKL and SST model show better resemblance with the water surface of the model tests than the computations with the EARSM turbulence model and the DDES. Difficulties in computing the breaking bow wave are found, resulting in a distortion of the free surface interface and leading to the change in forces. At this moment it is not completely understood were this effect is originating from and additional research is required.
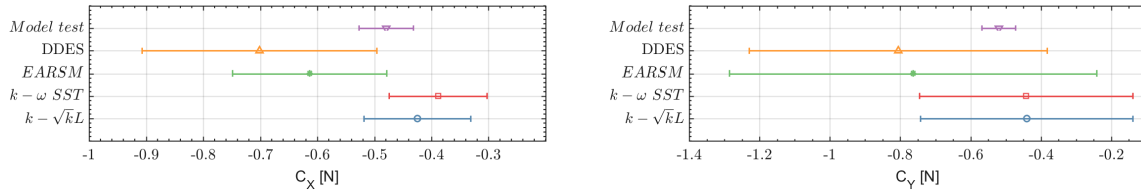
Fig. 4: Comparison between different turbulence models. The force is plotted together with the numerical uncertainty of the KSKL turbulence model assigned to all models.

(a)

(b)

(c)

(d)

(e)
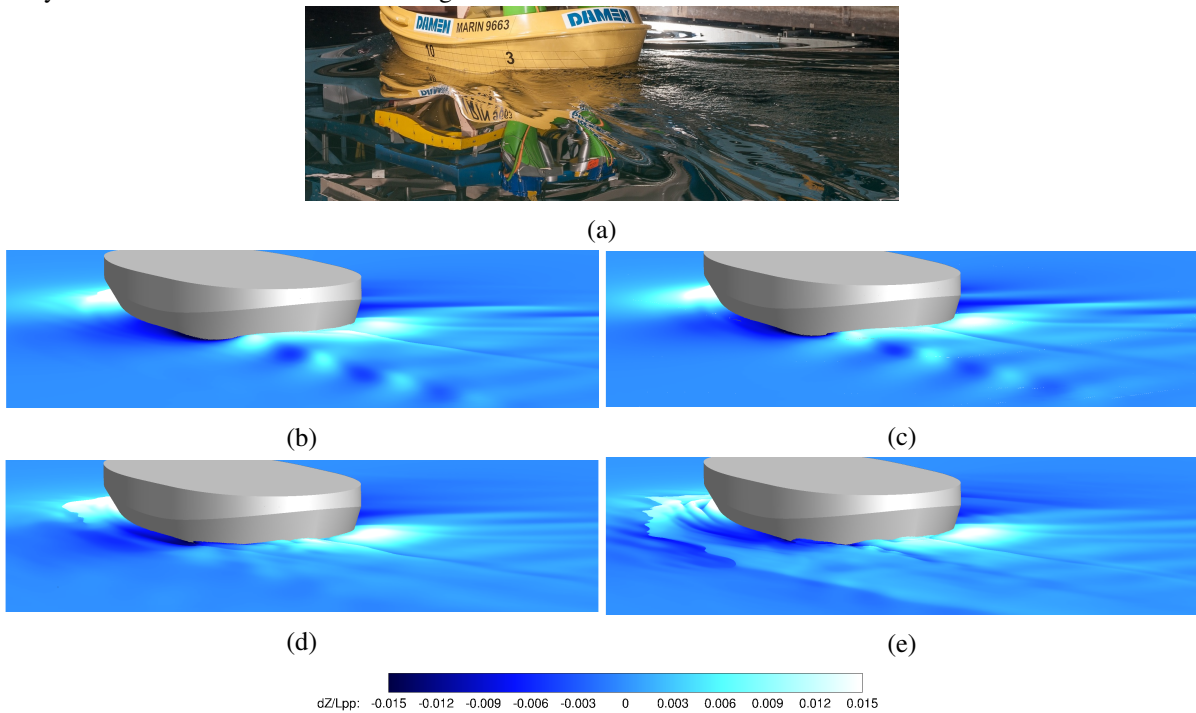
Fig. 5: Stern perspective of the free surface. **(a)** Model test, **(b)** KSKL, **(c)** SST, **(d)** EARSM, **(e)** DDES.

5   Drift angle simulations

The grids are made suitable for other drift angles by rotating the vessel inside the grids using a deform grid algorithm. Both the simulation and model test results of the forces in X- and Y-direction are plotted in figure 6. The numerical uncertainties of $\beta = 15°$ are applied to all other drift angles. Figure 6 shows that the trends are captured well. The force in X-direction shows an increase in comparison error with an increase in drift angle. This effect is expected to be partially due to the asymmetric flow pattern originating from turbulence tripping strips. The comparison error for the force in Y-direction decreases with an increase of drift angle and is for the last $\beta = 30°, 45°$ and $90°$ between 1-7%.

6   Conclusions

Verification and validation of free surface simulations with the KSKL turbulence model for the a tug has been performed to obtain a reliable prediction method for the force curves next to model tests.
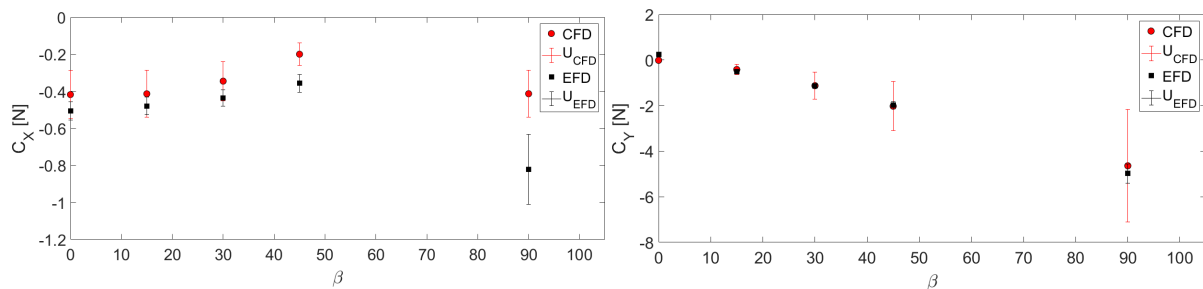
Fig. 6: Integral quantities vs. drift angle (uncertainty percentages based on $\beta = 15$ deg results)

It has been found that both the EFD and CFD have high computed uncertainties for the prediction of the hydrodynamic forces of the tug and also the comparison error of the finest grid is 12% for F_X and 25% for F_Y at $\beta = 15°$. Using other turbulence models did not improve the comparison error yet and deserves further investigation. Even though the uncertainties were high the force curves show similar trends to model tests, especially for the forces in Y-direction, which leads to the expectation that the computed uncertainty at $\beta = 15°$ is very conservative for the prediction of the other angles.

7   Acknowledgement

References

J. Brouwer, J. Tukker, and M. Van Rijsbergen. Uncertainty Analysis of Finite Length Measurement Signals. *AMT'13*, 2013.

H. Dol, J. Kok, and B. Oskam. Turbulence modeling for leading-edge vortex flows. *AIAA Journal*, (January), 2002.

L. Eça and M. Hoekstra. Verification of turbulence models with a manufactured solution. *European Conference on Computational Fluid Dynamics*, pages 1–14, 2006a.

L. Eça and M. Hoekstra. On the Influence of the Iterative Error in the Numerical Uncertainty of Ship Viscous Flow Calculations. *26th Symposium on Naval Hydrodynamics*, (October 2004):17–22, 2006b.

M. Gritskevich, A. Garbaruk, J. Schütze, and Fl. Menter. Development of DDES and IDDES formulations for the k-ω shear stress transport model. *Flow, Turbulence and Combustion*, 88(3):431–449, 2012.

ITTC. ITTC – Recommended Procedures and Guidelines - Example for uncertainty analysis of resistance tests in towing tanks. 7.5-02-02-02.1 (Revision 00). *Recommended Procedures and Guidelines ITTC*, page 11, 2014.

M. Thanyamanta W. Molyneux D. Jahra, F. Islam. Investigation of Hydrodynamic Loads and Flow Patterns Near an Escort Tug in Oblique Flows. *OMAE*, pages 1–8, 2015.

F. Menter, M. Kuntz, and R. Langtry. Ten Years of Industrial Experience with the SST Turbulence Model. *Turbulence Heat and Mass Transfer*, 4:625–632, 2003.

F. Menter, J. Schutze, K. Kurbatskii, M. Gritskevich, and A. Garbaruk. Scale-Resolving Simulation Techniques in Industrial CFD. *AIAA Journal*, 2011-3474(June):1–12, 2011.

J. Schot, J. de Jong, and R. van Koperen. Using CFD in the Design of Modern Ship Handling Tugs at Damen. In *Tugnology*, Rotterdam, 2017.

B. Smoker, B. Stockdill, and P. Oshkai. Escort Tug Performance Prediction Using Computational Fluid Dynamics. 45(1):1–12, 2016.

F. Stern, S. Bhushan, P. Carrica, and J. Yang. Large Scale Parallel Computing and Scalability Study for Surface Combatant Static Maneuver and Straight Ahead Conditions Using CFDShip-Iowa. *Parallel Computational Fluid Dynamics: Recent Advances and Future Directions*, 2009.

(ASME) The American Society of Mechanical Engineers. *Standard for Verification and Validation in Computational Fluid Dynamics and Heat Transfer*. The American Society of Mechanical Engineers, V&V 20, 2009.

S. L. Toxopeus. *Practical application of viscous-flow calculations for the simulation of manoeuvring ships*. PhD thesis, Delft University of Technology, 2011.

G. Vaz, F. Jaouen, and M. Hoekstra. Free-Surface Viscous Flowcomputations. Validation of URANS Code FRESCO. *ASME 28th International Conference on Ocean, Offshore and Arctic Engineering*, pages 1–13, 2009.

Validation of Wind Loads on a Slender Vessel using CFD

Jonathan W. Vogt[*], Marco Bovio[§], and Benoit Mallol[‡]

[*]Damen Shipyards, Singapore, [§]Damen Shipyards, Gorinchem/Netherlands, [‡]NUMECA International, Brussels/Belgium

jonathan.vogt@damen.com

1 Introduction

The IMO regulation 749.18, 'Severe wind and rolling criterion (weather criterion)', ensures a vessel has sufficient transversal stability to resist over-rolling in severe side winds. For some long, slender vessels, however, it can be difficult to comply with the empirical requirements of this regulation. To account for such difficulties, the regulation allows for the demonstration of compliance by means of model scale experimental measurements – from both a towing tank and wind tunnel campaign. In so doing, the hydrodynamic and aerodynamic lever arms, under side wind conditions, can be determined for various heeling angles and assessed as to whether the vessel is compliant and able to operate unrestricted.

Due to the necessarily conservative nature of the regulation (enabling it to be broadly applicable to a multitude of vessels), slender vessels like the DAMEN Fast Crew Support (FCS) 3307 have difficulties in satisfying the empirical requirements of the regulation, thus necessitating expensive experimentation in order to demonstrate the vessel's compliance with the regulation. In order to reduce the cost of proving compliance, DAMEN is developing, in partnership with its Computational Fluid Dynamics (CFD) code supplier NUMECA International, a CFD methodology that can be used in lieu of experimentation. This validation project has been undertaken with the intention of being able to demonstrate compliance to the satisfaction of classification societies.

The CFD methodology described here is focused on the prediction of the aerodynamic forces only. As the motivation for using the CFD approach is primarily cost and time related, it is imperative that the methodology be both sufficiently accurate but also with as low as possible computational cost and total turnaround time. The methodology reflects these aims.

The establishment of robust procedures in the literature for the accurate numerical modelling of wind loads over maritime vessels, is lacking. A small number of researchers have simulated flow over wind-exposed hulls and superstructures of various forms, with differing approaches and levels of fidelity. Validation for these cases (comparing either velocity probe or force data) was generally quite good in qualitative terms, while sometimes insufficient in quantitative terms (Polsky, 2002; Wnęk and Guedes Soares, 2015; He, *et al.* 2016).

A thoroughly and successfully validated investigation was undertaken by Forrest and Owen (2010), who performed full-scale Detached-Eddy Simulations (DES) of the flow field over a navy frigate in order to predict the flow field encountered at the helicopter landing pad on the vessel's rear deck. The model was validated against model-scale experimental hot-probe velocity data. The scale difference between the simulation and experiment was disregarded as the scale effect was demonstrated to be minor. Using an unstructured mesh of 7.4×10^6 cells, a relatively large normalised timestep $\Delta t^* = 0.0188$ (normalised by wind speed and vessel beam) and the k-ω SST turbulence model, good qualitative agreement was seen for the time-averaged flow field over the landing pad and in the Power Spectral Density (PSD) comparisons of velocity, at various points on the ship.

The present paper reports the results of a CFD validation campaign where a wind tunnel test of the DAMEN FCS3307 vessel was numerically replicated. The vessel and wind tunnel CFD domain is shown in Fig. 1.

2 Experiment

The experiment was undertaken at the University of Southampton wind tunnel using a 1:18 scale model of the 33m long FCS3307 vessel. The institute provided the 3D geometry of the testing facility, in order to allow a realistic reproduction of the environmental test conditions in the CFD model. The testing was conducted at various heading and heeling angles and also with and without containers on the rear deck of the vessel, to take account of the different operating configurations of this unit. The model was kept

at a constant longitudinal (zero) trim while maintaining the same displacement at different heeling angles. The model and sting were mounted in a small pool of water around the model (with the waterline flush with the floor of the tunnel), to avoid air recirculation under the model. The tests were all performed at a freestream velocity of approximately 7m/s, maintaining the flow above the critical Reynolds number (Re), (about 2.7×10^5, based on the vessel beam). Additionally, turbulence was introduced to the tunnel through screens which further raised the effective Reynolds number. The boundary layer profile at the test section was measured (without the model installed) and this was used to calibrate the CFD model. The results, against which the CFD model was compared, were corrected for tare drag (less than 2% of the measurements, in all cases) but were not corrected for blockage effects, allowing for a like-for-like comparison with the CFD model.
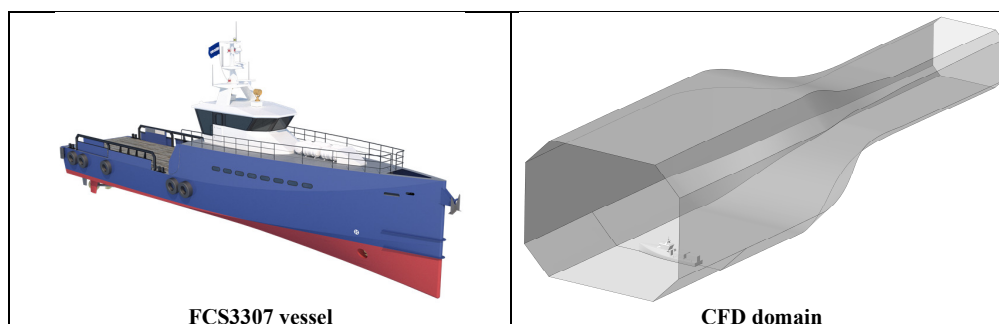

FCS3307 vessel   **CFD domain**

Fig. 1: Vessel and CFD domain.

3 Conceptual Model and Numerical Mesh

The computational domain reproduced the test-section and downstream contraction of the University of Southampton wind tunnel. This arrangement allowed for the faithful reproduction of flow field and blockage conditions apparent in the experiment. Turbulence screens upstream of the test section increased the turbulence and also straightened the flow after a 90° corner in the tunnel circuit.

Measurements taken in the empty tunnel showed a semi-developed and highly turbulent boundary layer. It has been shown in the literature that correctly reproducing the atmospheric boundary layer profile is essential for modelling accuracy (Polsky, 2002; Forrest and Owen, 2010). To correctly reproduce the boundary layer velocity profile, the numerical model required a distance of approximately 3m to the centre of the test section, employing a Turbulence Intensity (TI) of 10%. This value was determined through trial-and-error as the experimental TI was not recorded. To correctly characterise the profile, it was necessary to fully resolve the boundary layer on the floor of the tunnel, from the inlet to the installed model. A comparison of the measured and simulated boundary layer velocity profiles (at the test section, without the model) is shown in Fig. 2.

With a view to facilitating the quickest and simplest model preparation, the water pool in the wind tunnel was not included in the CFD model. Rather, the model was simply truncated at the solid tunnel floor with the submerged portion of the model disregarded. The resulting solid surfaces of the model do not form a sealed volume (with an opening at the tunnel floor), leading to a significant imbalance in the resultant vertical force acting the on model. This was accounted for in the CFD model by applying a vertical correction force acting at the centroid of the model-tunnel floor cross-section. The correcting force was defined as the ambient pressure in the domain, multiplied by the cross-sectional area. This vertical force vector also provided corrections for pitch moment and heeling moment.

The numerical mesh was generated with the mesher Hexpress Hybrid, by Numeca, which is a general purpose script-based automatic mesher that generates hex-dominant unstructured meshes about arbitrary and complex geometry. An initial mesh sensitivity study using a URANS solver,
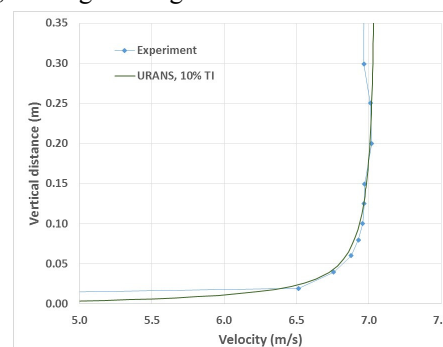

Fig. 2: Boundary layer velocity profile.

testing meshes between 8×10^6 and 182×10^6 cells, informed an initial mesh density that ultimately produced meshes between $10\text{-}13\times10^6$ cells, depending on the model arrangement.

The mesh concentrated spatial refinement on the model and wind tunnel surfaces. Two refinement boxes were used around the vessel and in its wake, to capture the flow details with more fidelity. All sharp edges on the model had increased refinement. The wind tunnel floor had a fully resolved boundary layer mesh from the inlet to the model, with a y^+ of approximately 0.4. The remainder of the wind tunnel walls used wall functions and had y^+ values of approximately 28. Due to the bluff nature of the ship model and the expectation of separation at sharp corners, the model boundary layer mesh also used wall functions, with a thickness of only three cells and y^+ less than 30. The viscous component of the forces acting on the model were expected to be extremely small, and with no smooth surface separation or opportunity for boundary layer development, there was no need for a detailed boundary layer mesh. The mesh is shown in Fig. 3.
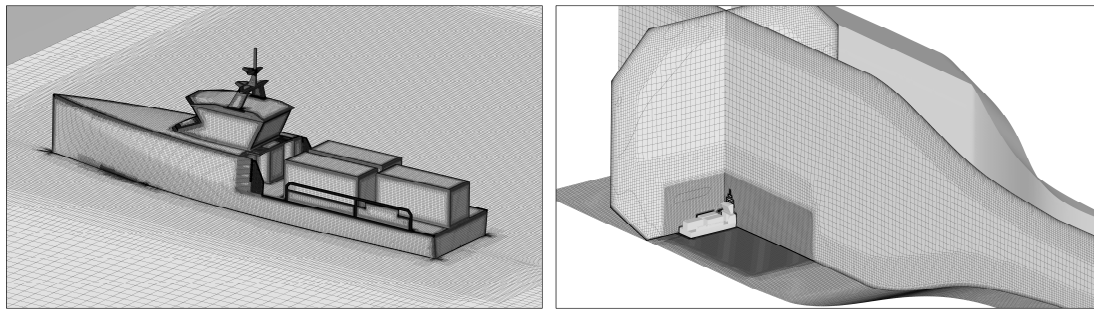

Fig. 3: Numerical mesh, heading = 90°, heel = 0°.

4 Numerical Settings

The solver FINE/Marine v6.1, by Numeca, was used for all simulations. It utilises the finite-volume method for the solution of the incompressible Navier-Stokes equations. It is an unstructured, face-based, segregated solver and its fully unsteady solver utilising an implicit 2nd-order accurate temporal discretisation scheme.

The mesh was prepared with the intention to compare the effectiveness of both the Unsteady Reynolds-Averaged Navier-Stokes (URANS) solver approach and the DES approach. DES has the advantage of being able to explicitly resolve the large scales of turbulence, which is particularly advantageous for large scale separation off bluff bodies. The DES model switches between an explicit resolution of the larger turbulent scales or a turbulence model calculation, based on the local mesh cell size. If the cell is not small enough to capture the larger scales, the DES model will be inactive and effectively behaves as a URANS solver.

The for URANS solver, the convective terms were discretised using the AVLSMART scheme (Pržulj and Basara, 2001), which is based on the 3rd-order QUICK scheme. For the DES solver, the convective terms were discretised using a blended scheme between 1st-order upwinding and central-differencing, with a 5% weighting to upwinding. The turbulence model used was the Explicit Algebraic Stress Model (EASM), which is based on the $k\text{-}\omega$ SST model but better accounts for the rotational component of turbulent flows.

A constant velocity $V = 6.98$m/s was applied at the inlet. With development of the boundary layer, the freestream velocity reaches 7m/s at the ship model. The turbulent quantities at the inlet were set to $k = 2.1565\times10^{-7}$ m^2/s^2 and $\omega = 14.0$ /s ($= V_{ref}/L_{ref}$), which corresponds to a TI = 10%. The tunnel outlet was set to a constant pressure outlet. The tunnel floor from the inlet to the model was set to a no-slip wall with fully resolved boundary layer. The ship model and remaining tunnel walls were set to no-slip walls, employing a wall function. The domain was initialised with zero velocity components and the same turbulence quantities as at the inlet.

Timestep sensitivity studies were undertaken for both URANS and DES approaches. The present mesh was temporally independent with a timestep of $\Delta t_{URANS} = 0.1$s for URANS. For the DES solver, no change in the temporally-averaged forces and moments were observed with a timestep smaller than

$\Delta t_{DES} = 0.01$s. This was considered quasi-temporal independence for the DES solver. When normalised in the same way as Forrest and Owen (2010), $\Delta t_{DES}* = 3.67\times10^{-3}$, which is only one-fifth of the normalised timestep employed in that study. The URANS cases solved 10 iterations per timestep, while the DES cases solved 15 iterations per timestep. DES was tested with 20 iterations per timestep, but this was shown to have negligible effect on the averaged forces.

In order to approach the solution as quickly as possible and reduce the overall solution time, an initial steady-state RANS simulation was conducted for just 100 iterations. This short simulation was sufficient to develop the flow field to a point such that it was a good starting point for both the DES and URANS models. This saved significant flow development time for both solution strategies.

The URANS cases, initialised from the steady state run, computed between 700 and 1500 timesteps, depending on the model arrangement. The simulation was run until the forces, moments and residuals had settled to a constant value. The DES cases were first computed for 150 timesteps to overcome the transient phase and achieve quasi-steadiness. A data averaging simulation was then initialised from this run and computed for about 1000 more timesteps (180 flow times across the model beam).

The simulations conducted are shown in Table 1, indicating the heading and heel angles and whether or not the containers on the deck were included. A heading angle of zero represents a bow into the wind condition, 90° is wind onto the portside. A positive heel angle represents the ship leaning away from the wind. The model including the containers increased the frontal area of the model (at heading of 90°) by 19%. A full sweep of heading angles were simulated with and without containers with the URANS solver and, at full side wind (heading of 90°), three different heeling angles were also simulated with the URANS solver. The DES solver was used for selected container cases at zero heel angle.

5 Results and Discussion

The results for the zero-heel cases, alongside the experimental results, are shown in Fig. 4. They are presented in terms of the forward (to bow), side (to starboard) and vertical (upward) forces, and the pitching, heeling and yaw moments. Very good qualitative agreement

Table 1: Simulated cases.

Heading (°)	Heel (°)				
	-10	0		20	40
	w. cont.	w. cont.	w/o. cont.	w. cont.	w. cont.
30		URANS, DES	URANS		
60		URANS	URANS		
90	URANS	URANS, DES	URANS	URANS	URANS
120		URANS, DES	URANS		
150		URANS, DES	URANS		

is found, both with and without containers. The agreement at the 90° heading case (side-on to the wind) is the most favourable – the side force is predicted within 12% without containers and within 4% with containers. For all headings, the solved forces generally achieved a lower percentage error than did the moment results, but the discrepancy was very similar in absolute terms. The CFD model tended to be further from the experimental results at heading angles increasingly distant from 90°, in both directions. This may be due to the increasing non-alignment of the freestream mesh cells with the ship model and the resulting complex tetrahedral mesh that is imposed near the ship surface.

The DES results in Fig. 4 indicate that, in general, the DES solver is slightly superior to the URANS solver, in terms of the calculation of forces and moments. The side force prediction, in particular, is significantly improved with the DES solver. It produced a less accurate result for the vertical force and relatively unchanged or slightly better for the forward force and the three moments.

The results for the heeled case are shown in Fig 5. The qualitative agreement is again very good, however, the correlation generally deteriorates at heel angles increasingly distant from zero and, again, in both directions. With the current, limited mesh refinement, discretisation errors may be contributing to the errors seen on the more extreme cases.

The URANS solver was not able to capture the inherent highly turbulent nature of the flow field, which is demonstrated quantitatively in Fig. 6 and qualitatively in Fig. 7. Both figure compare a URANS result against an instantaneous DES result. The URANS solution shows no evidence of time-dependant turbulent eddies, whereas the DES solution shows significant turbulent behaviour and a very high level of mixing. Although there is some local variation in the forces acting on the vessel (see Fig. 6), the position of the centre of pressure varied very little, not exceeding $0.01L_{pp}$.
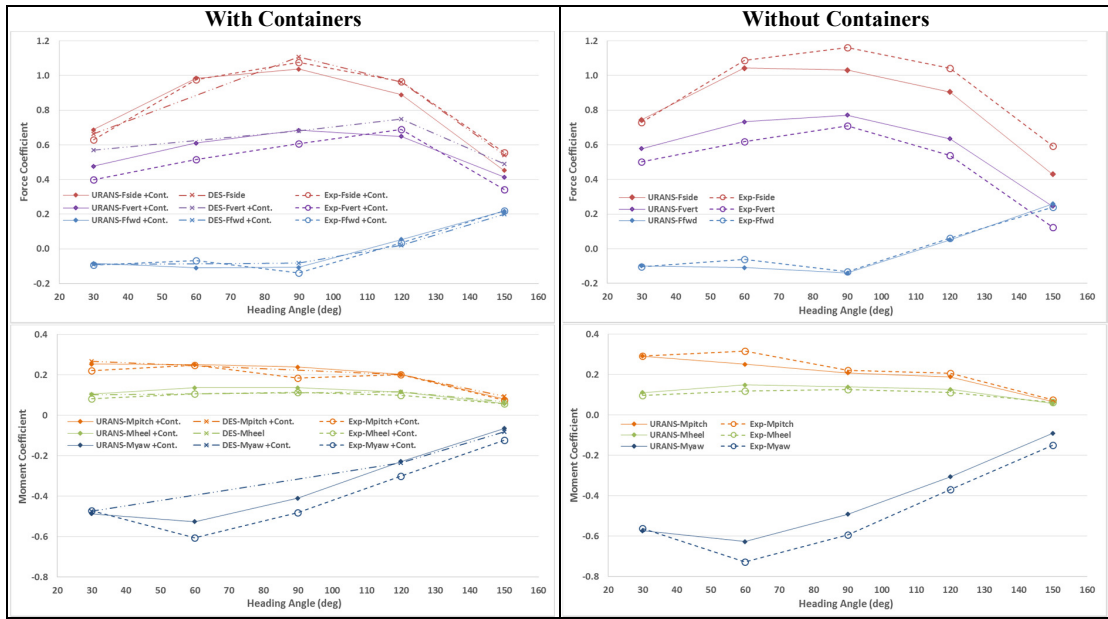
Fig. 4: Force and moment results for zero-heel cases, with and without containers.
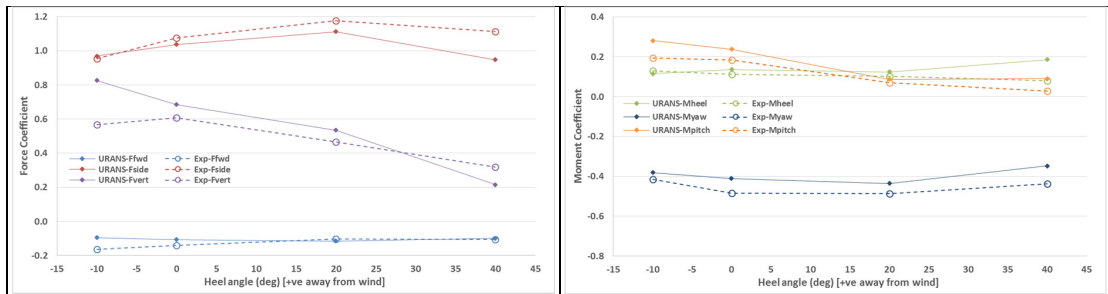
Fig. 5: Force and moment results for heeled cases, heading angle = 90°, with containers.

The DES solution is clearly capable of capturing more of the physical character of the flow and so could be beneficial in the determination of frequency domain information about the flow's interaction with the vessel, or perhaps useful statistical information about the loads and moments on the vessel. However, for obtaining the averaged force and moment data only, the URANS solver would appear to be an adequate approach, and slightly more cost effective than DES.

Fig. 6: Side force distribution; heading 90°, heel 0°.

6 Conclusion

A CFD validation study was undertaken to develop an affordable numerical modelling methodology that may be used for the determination of wind loads on model ships, without the need for expensive wind tunnel experiments. Both URANS and DES approaches were investigated. The CFD model reproduced the validation wind tunnel experiment and tunnel apparatus and achieved good correlation for forces and moments at various heading and heeling angles. The DES methodology was favourable in terms of its ability to capture the flow features. It also achieved slightly better correlation with the experimental data. The URANS solution, though unable to capture the temporal character of the flow, was able to predict the forces and moments with good accuracy and was also slightly cheaper to run than the DES solver. Given the highly turbulent nature of this bluff-body separation problem, prediction

of full-scale loads should be quite reliable. Future work will seek to adapt this methodology to full-scale prediction, with only minor changes anticipated.

a) Pressure on ship and floor, velocity magnitude on vertical cut at y = -0.4m

b) As (a) but with iso-surface of zero x-velocity.

c) Pressure on ship, velocity magnitude on vertical cut at y = -0.4m and horizontal cut near model ship deck
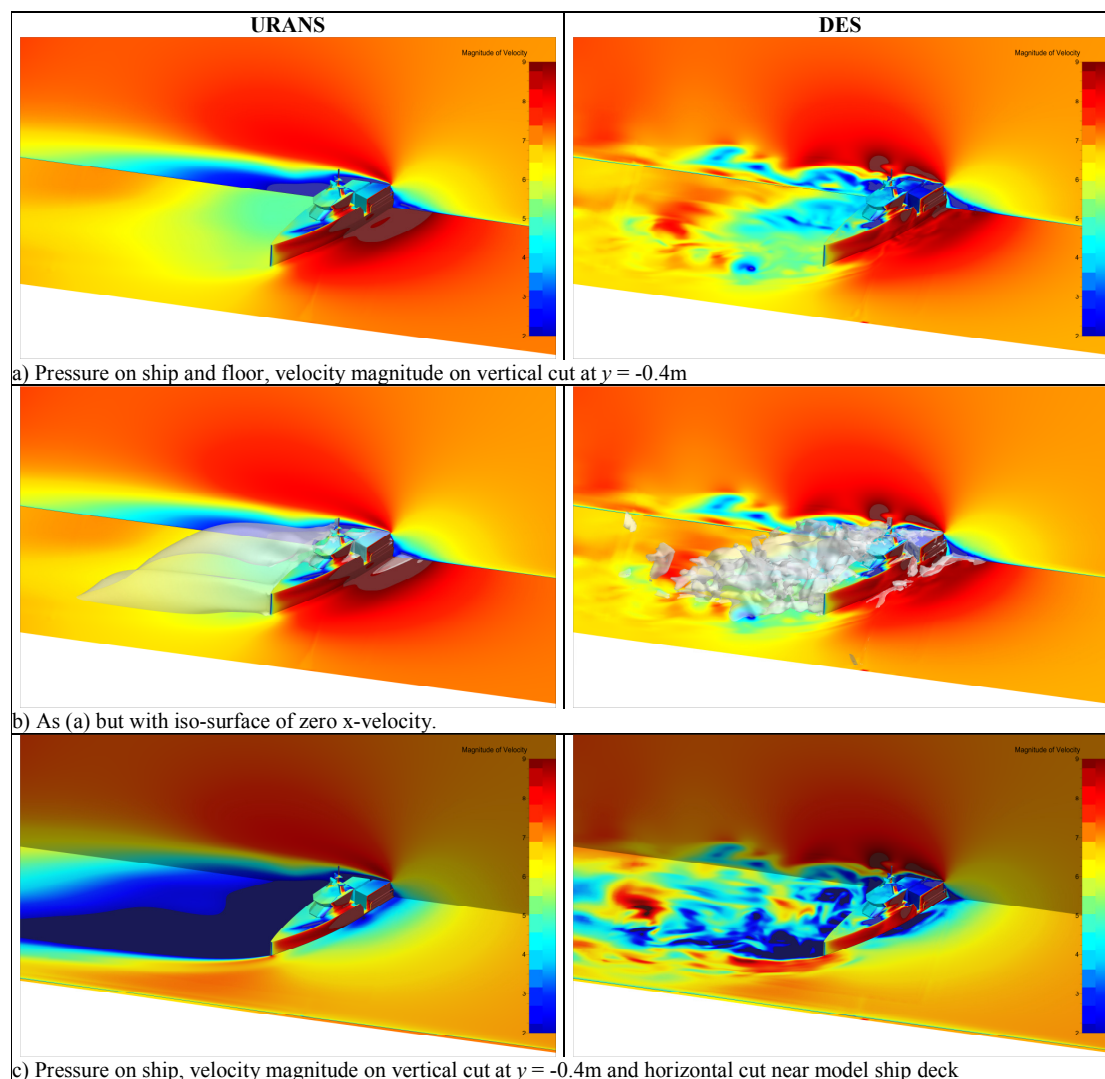
Fig. 7: Qualitative comparison of flow field; heading 120°, heel 0°.

References

J.S. Forest and I. Owen (2010). An investigation of ship airwakes using Detached-Eddy Simulation, *Computers and Fluids*, **39**, 656-673.

N.V. He, K. Mizutani and Y. Ikeda (2016). Reducing air resistance acting on a ship by using interaction effects between the hull and accommodation, *Ocean Engineering*, **111**, 414-423.

S.A. Polsky (2002). A computational study of unsteady ship airwake. Proceedings of 40th AIAA Aerospace Sciences Meeting & Exhibit, Reno, USA.

V. Pržulj and B. Basara (2001). Bounded Convection Schemes for Unstructured Grids. Proceedings of AIAA Computational Fluid Dynamics Conference, Anaheim, USA.

A. D. Wnęk and C. Guedes Soares (2015). CFD assessment of the wind loads on an LNG carrier and floating platform models, *Ocean Engineering*, **97**, 30-36.

Linearized Free Surface URANS Approach for Ship Hydrodynamics

Vuko Vukčević, Inno Gatin and Hrvoje Jasak
University of Zagreb, Zagreb/Croatia, {vuko.vukcevic, inno.gatin hrvoje.jasak}@fsb.hr

1 Introduction

The Computational Fluid Dynamics represents an active and rapidly expanding area of research in ship hydrodynamics, where researchers have focused on resolving detailed physics that include the effects of: vorticity, viscosity, nonlinearity, free surface, turbulence, *etc.* (see [Larsson et al., 2015] for state–of–the–art CFD ship hydrodynamics simulations). Such high–fidelity simulations are extremely accurate and provide valuable insight on flow phenomena in research and industry, however, they still require significant computational resources for everyday industrial use.

A common simplification in early days of numerical ship hydrodynamics has been the linearization of the free surface boundary condition. The linearization can yield an efficient set of tools, however, most of them rely on potential flow theory with severely limited success to certain ship hydrodynamic flows. Recently, Woolliscroft and Maki [Woolliscroft and Maki, 2016] introduced a Reynolds Averaged Navier–Stokes (RANS) CFD model with linearised kinematic and dynamic free surface boundary conditions, in order to reduce the CPU time, while retaining the necessary accuracy required for manoeuvring predictions in the design phase of the ship. The method has been successfully applied to steady resistance and pure yaw predictions, where a significant speed–up compared to fully nonlinear and two–phase CFD methods.

This work presents an extension of the original linearised free surface model by Woolliscroft and Maki [Woolliscroft and Maki, 2016] in order to be able to calculate general seakeeping of a ship, including the wave–ship interaction. The mathematical and numerical models implemented in OpenFOAM are first briefly discussed, followed by preliminary results regarding: steady resistance, diffraction, seakeeping and manoeuvring with overset grids.

2 Mathematical and Numerical Modelling

The mathematical model of an incompressible, single–phase, turbulent flow with linearised free surface boundary conditions is presented, followed by details on the numerical model based on the arbitrary polyhedral Finite Volume (FV) method [Jasak, 1996] for pressure, velocity and turbulence and the Finite Area (FA) method [Tuković and Jasak, 2012] for surface elevation equation.

2.1 Mathematical Model

RANS governing equations for a single–phase, incompressible and turbulent flow read:

$$\nabla{\cdot}\mathbf{u} = 0 \,, \quad \mathbf{x} \in \Omega \,, \tag{1}$$

$$\frac{\partial \mathbf{u}}{\partial t} + \nabla{\cdot}\big((\mathbf{u} - \mathbf{u}_g)\mathbf{u}\big) - \nabla{\cdot}(\nu_e \nabla \mathbf{u}) = -\frac{1}{\rho}\nabla p_d \,, \quad \mathbf{x} \in \Omega \,, \tag{2}$$

where $\mathbf{u}$ is the velocity field, $\mathbf{u}_g$ is the relative velocity due to the grid motion, ν_e is the effective kinematic viscosity, ρ is a constant fluid density and p_d is the dynamic pressure. Ω is the fluid domain, extending only up to calm free surface due to linearization of the free surface boundary conditions, while $\mathbf{x}$ is the radii vector. Effective viscosity ν_e is obtained by utilizing the $k - \omega \, SST$ model with standard wall functions. The gravitational acceleration is lumped inside the dynamic pressure using the following decomposition of pressure into hydrostatic and dynamic components:

$$p = p_d + \rho \mathbf{g}{\cdot}\mathbf{x} \,, \tag{3}$$

where $\mathbf{g}$ is the gravitational acceleration and $\mathbf{x}$.

In addition to RANS equations for the fluid flow, the free surface is described with a single–valued wave elevation function η with the following governing equation arising from kinematic boundary condition:

$$\frac{\partial \eta}{\partial t} + \nabla{\cdot}\big(\mathbf{u}_{fs} - \mathbf{u}_{gfs}\big)\eta = \mathbf{u}_{fs}{\cdot}n_{fs} \,, \quad \mathbf{x} \in \Gamma_0 \,, \tag{4}$$

where $\mathbf{u}_{fs}$ is the velocity field at the free surface, $\mathbf{u}_{gfs}$ is the free surface velocity field due to possible grid motion and n_{fs} is the normal vector to the calm free surface Γ_0. As the free surface boundary condition is linearised [Woolliscroft and Maki, 2016], the calculated elevation defines the pressure boundary condition for the RANS flow field:

$$p = \rho|\mathbf{g}|\eta. \tag{5}$$

Hence, a direct coupling between velocity field $\mathbf{u}$, surface elevation field η and pressure field is present ($\mathbf{u} \rightarrow \eta \rightarrow p$).

Since the final goal of the model is to efficiently simulate seakeeping of a ship in mild waves, we introduce:

- Implicit relaxation zones [Jasak et al., 2015] for wave generation and absorption, where the momentum equation Eq. (2) and surface elevation equation Eq. (4) are blended with the corresponding relaxation equation based on a given wave theory (see Jasak *et al.* [Jasak et al., 2015] for additional details),

- Six Degrees–of–Freedom (6 DOF) rigid body motion equations.

2.2 Numerical Modelling

RANS equations, Eq. (1) and Eq. (2) are discretised with arbitrary polyhedral FV framework within foam–extend–4.0, a community driven fork of the open source software OpenFOAM [Weller et al., 1998]. The time derivative term is discretised using either first order accurate Euler implicit scheme for calm water resistance simulations or with second order accurate backward scheme for wave related simulations (wave diffraction and seakeeping). The convection term in the momentum equation is discretised with Guass' theorem using linear upwind interpolation while diffusion terms (in momentum and pressure equation) are also discretised with Gauss theorem using central differencing and over–relaxed approach to non–orthogonal correction [Demirdžić, 2015].

Free surface elevation equation, Eq. (4) is discretised directly at the boundary faces using the Finite Area (FA) approach [Tuković and Jasak, 2012] available in foam–extend–4.0. The time derivative term is discretised either with Euler or with backward scheme (for calm water resistance and wave simulations, respectively), while the convection term is discretised using second–order accurate linear upwind scheme.

A strong coupling between $\mathbf{u} \rightarrow \eta \rightarrow p$ is resolved using a segregated solution algorithm based on a combination of SIMPLE and PISO algorithms. The algorithm for a single time step is presented in 1. First, the 6 DOF equations are solved and the ship motion and the grid are updated. The surface elevation equation is solved next, followed by a momentum equation. The pressure equation is then formed and solved multiple times in order to converge the pressure–velocity–6 DOF fields without under–relaxation. Note that the enhanced coupling procedure as presented by Gatin *et al.* [Gatin et al., 2017] is used to update the rigid body motion equations after the solution of each pressure equation. The procedure is repeated until convergence.

Algorithm 1 Segregated solution algorithm for a time step.

---

    while SIMPLE not converged **do**
        Update rigid body motion and move grid
        Solve surface elevation equation, Eq. (4)
        Solve momentum equation, Eq. (2)
        Update pressure boundary condition at the free surface, Eq. (5)
        while PISO not converged **do**
            Solve pressure equation, Eq. (1)
            Update rigid body motion
        end while
    end while

---

3 Calm Water Resistance

Calm water resistance simulations for the Japan Bulk Carrier (JBC) [tok, 2015] is considered first. The model is $L_{PP} = 7$ meters long, at design speed corresponding to the Froude number $F_n = 0.142$ and is free to heave and pitch. Note that the present model is suitable for low Froude numbers due to linearised free surface boundary condition. Three grids are used to perform a grid convergence study:

- Coarse grid: 93 411 cells,

- Medium grid: 170 159 cells,

- Fine grid: 256 721 cells.

Details of the fine grid are presented in Figure 1. All grids extend: 1 L_{PP} in front of the ship, 1.5 L_{PP} after the ship, 1 L_{PP} towards the side and 1 L_{PP} towards the bottom. CFD results presented in Table 1 compare

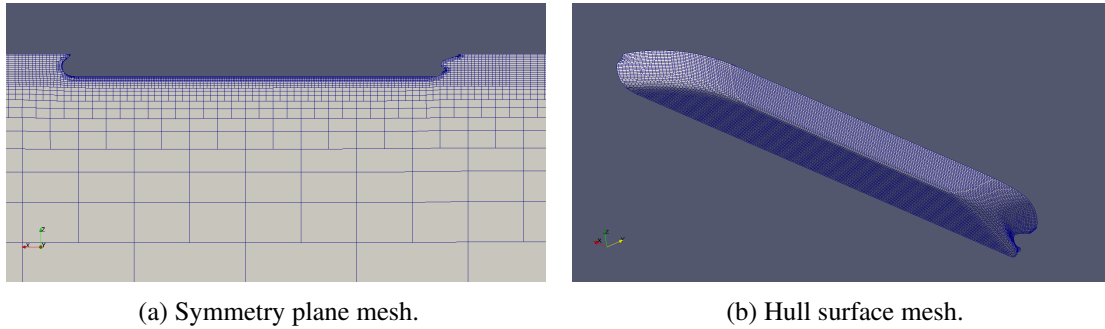(a) Symmetry plane mesh. (b) Hull surface mesh.

Fig. 1: Fine grid details (256 721 cells).

well with the available experimental data from the Tokyo 2015 Workshop [tok, 2015]. In addition, the frictional force is compared to the ITTC'57 correlation line, where it can be seen that the CFD results slightly under–predict the frictional resistance. The pressure force is lowered with grid refinement. Sinkage compares well with the experimental data, considering very small measured values ($\approx$ 6 millimetres). Furthermore, very small trim angle ($\approx 0.1°$) is well predicted with the current model.

Overall, the results show good agreement with experiments considering the lower fidelity of the present model due to the linearisation of the free surface and coarse grids. The main benefit of the current model is the CPU time, where the simulation on fine grid took approximately four hours on four Intel Core i7-4820K @ 3.70GHz cores. The convergence of the total resistance for all three grids is presented

Table 1: Results for the calm water resistance for the JBC hull.

	EXP	ITTC'57	GRID 1	GRID 2	GRID 3
$C_F \times 10^3$	N/A	3.159	3.086	3.108	3.109
$C_P \times 10^3$	N/A	N/A	1.536	1.272	1.126
$C_T \times 10^3$	4.289	N/A	4.622	4.380	4.235
$\sigma, \%L_{PP}$	-0.086	N/A	-0.112	-0.109	-0.108
$\tau, \%L_{PP}$	-0.180	N/A	-0.206	-0.192	-0.194

in Figure 2a, where the converged solution is reached at approximately $t = 70$s (after 7 000 iterations with $\Delta t = 0.01$ s). The convergence of sinkage for all grids is presented in Figure 2b.

4 KVLCC2 Wave Diffraction

In order to validate wave diffraction, a full scale KVLCC2 model is considered [tok, 2015] at zero forward speed. Five incident wave frequencies are considered: 0.2, 0.3, 0.4, 0.5 and 0.6 rad/s, while the
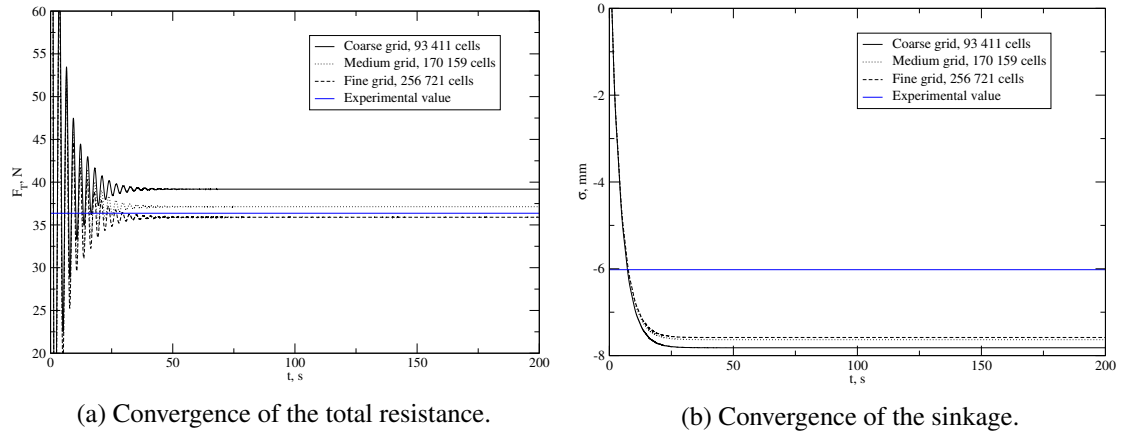
| (a) Convergence of the total resistance. | (b) Convergence of the sinkage. |

Fig. 2: Convergence of CFD simulations using three grids.

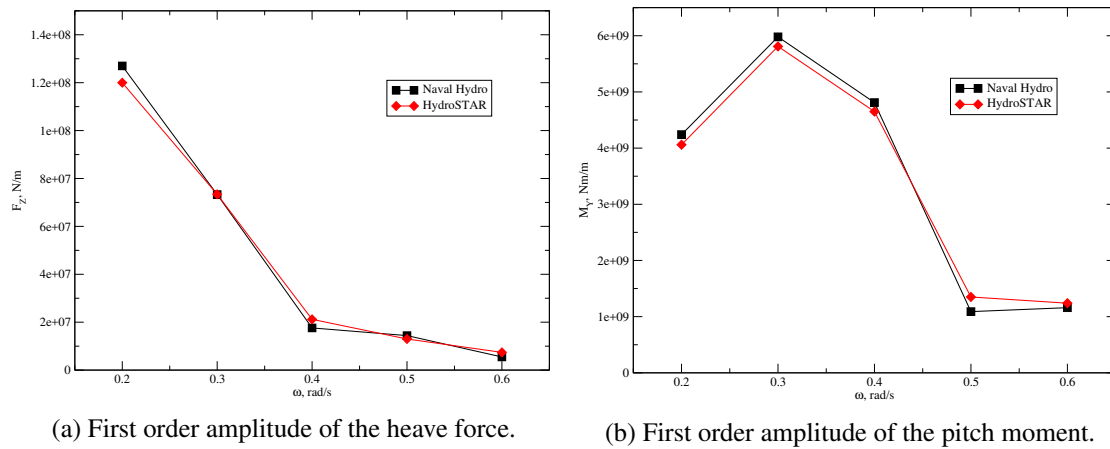| (a) First order amplitude of the heave force. | (b) First order amplitude of the pitch moment. |

Fig. 3: First order amplitudes for KVLCC2 wave diffraction.

wave steepness is $ka = 0.05$, where k is the deep water wave number and a is the wave amplitude. Small steepness is used in order to remain within the validity region of linear free surface waves. A single mesh consisting of 800 000 cells is used for all wave frequencies.

The first order amplitude of the heave (vertical) force and pitch moment are presented in Figure 3a and Figure 3b, comparing well with the linearised, potential flow, frequency domain solver HydroStar. The first order phases for the same items are presented in Figure 4a and Figure 4b, both showing good agreement with HydroStar. It is important to note that the CFD simulations have been run for ten periods and the final solution is obtained by taking an average of the Moving Window FFT during last five periods.

5 KVLCC2 Seakeeping at Design Speed

Seakeeping simulations are performed for the KVLCC2 ship in model scale at design speed, with $L_{PP} = 3.2$ m (see [got, 2010] for details). Three cases are considered for the present study: $\lambda/L_{PP} = 0.5$, 1.1 and 2.0, where three grids are used correspondingly: 298K, 305K and 350K cells. Heave, pitch and mean value of resistance are compared to experimental data by Park *et al.*parkEtAl2015.

The comparison of heave and pitch first order amplitudes with the experimental data is presented in Figure 5a and Figure 5b. The CFD results compare well with experiments, except for the heave motion for $\lambda/L_{PP} = 2.0$, where the heave amplitude is higher than the theoretical limit $\eta/a = 1$ for long waves. This indicates that wave reflection occurred and needs to be investigated further.

The mean value of resistance is presented in Figure 6a, where it can be observed that the present results do not agree well with experiments. This is probably caused by the innate disability of the model

to take into account nonlinear effects such as added resistance in waves, or it might be related to post processing errors. Both possibilities shall be investigated in future. A perspective view of the free surface is presented in Figure 6b, indicating the ability of the model to take into account weakly nonlinear interaction between wave system generated by forward speed of the ship and incident, radiated and diffracted wave systems.

(a) First order phase of the heave force.

(b) First order phase of the pitch moment.
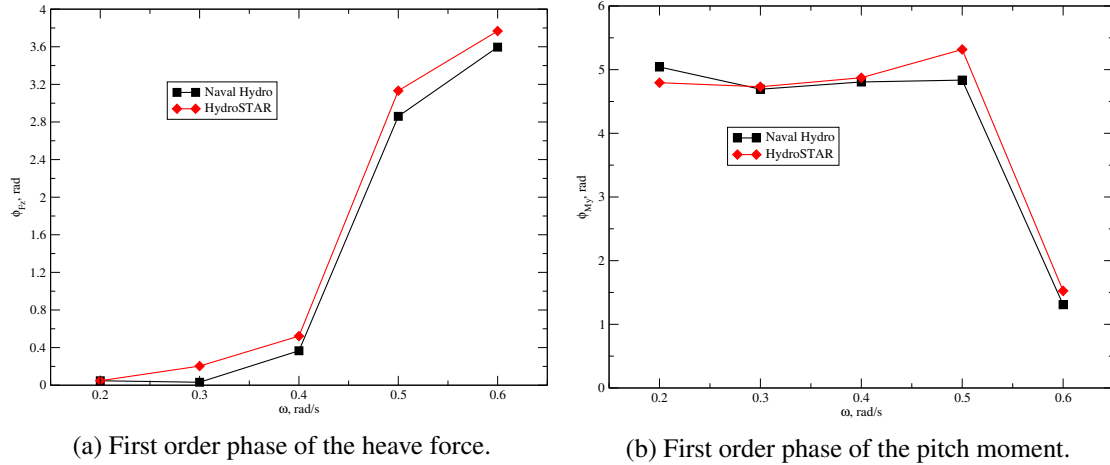
Fig. 4: First order phases for KVLCC2 wave diffraction.

(a) First order heave amplitudes.

(b) First order pitch amplitudes.
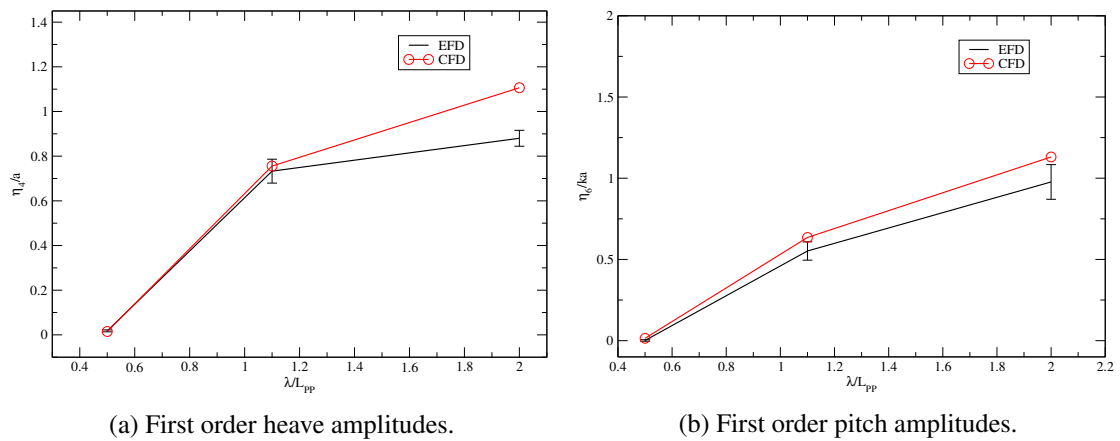
Fig. 5: Comparison of first order motions for the KVLCC2 model.

(a) Mean value of the total resistance.

(b) Perspective view of the $\lambda/L_{PP} = 1.1$ simulation.
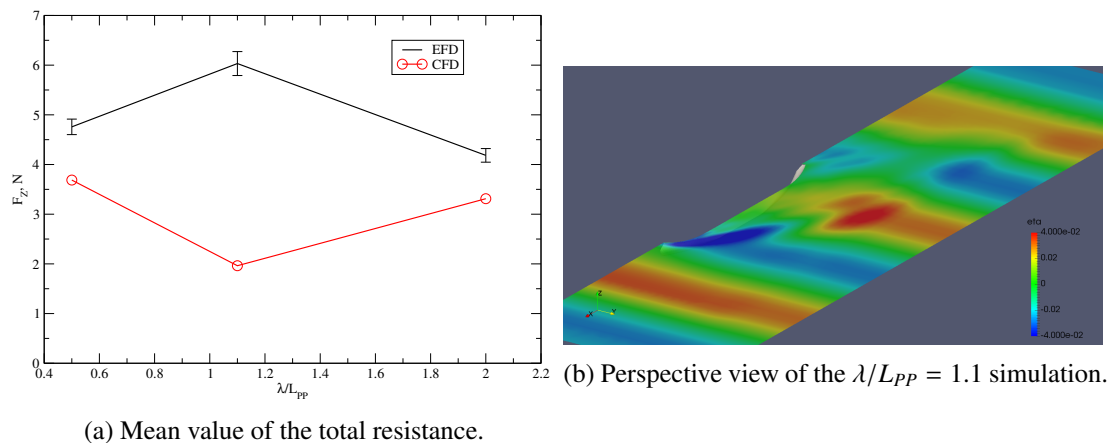
Fig. 6: Total resistance and free surface view for the KVLCC2 model.

6 Conclusion

This paper presents the linearised free surface URANS model for surface wave related problems such as wave diffraction and seakeeping of ships. The nonlinearity in the RANS equations is retained, while the free surface kinematic and dynamic boundary conditions are linearised, allowing us to consider single–phase flows without deforming the computational grid at the free surface.

The developed method is validated for calm water resistance and wave diffraction, showing good results compared to experiments and other numerical tools. The test cases indicate that the model is indeed suitable for cases where the free surface does not exhibit significant nonlinear behaviour (*i.e.* steep waves). The comparison of seakeeping tests with experimental data indicate the inability of the model to accurately predict the mean value of resistance in head waves at design speed. This problem shall be investigated further in future publications. Nevertheless, heave and pitch motions compare reasonably well with experiments.

The most important advantage of the model is its efficiency. Since the volume grid extends up to calm free surface, only part of the domain is meshed, thus saving the CPU time. All simulations have been carried out in parallel using four cores on a personal computer, which is hard to achieve with high–fidelity CFD models taking into account all the nonlinearities.

References

(2010). Gothenburg 2010: A Workshop on CFD in Ship Hydrodynamics. `http://www.insean.cnr.it/sites/default/files/gothenburg2010/index.html`. [Online; accessed 20 August 2015].

(2015). Tokyo 2015: A Workshop on CFD in Ship Hydrodynamics. `http://www.t2015.nmri.go.jp/`. [Online; accessed 20 August 2015].

Demirdžić, I. (2015). On the Discretization of the Diffusion Term in Finite–Volume Continuum Mechanics. *Numer. Heat Transfer, Part B*, 68:1–10.

Gatin, I., Vukčević, V., Jasak, H., and Rusche, H. (2017). Enhanced Coupling of Solid Body Motion and Fluid Flow in Computational Fluid Dynamics. *Revised manuscript under review: Ocean Eng.*

Jasak, H. (1996). *Error Analysis and Estimation for the Finite Volume Method with Applications to Fluid Flows*. PhD thesis, Imperial College of Science, Technology & Medicine, London.

Jasak, H., Vukčević, V., and Gatin, I. (2015). Numerical Simulation of Wave Loads on Static Offshore Structures. In *CFD for Wind and Tidal Offshore Turbines*, pages 95–105. Springer Tracts in Mechanical Engineering.

Larsson, L., Stern, F., Visonneau, M., Hirata, N., Hino, T., and Kim, J., editors (2015). *Tokyo 2015: A Workshop on CFD in Ship Hydrodynamics*, volume 3, Tokyo, Japan. NMRI (National Maritime Research Institute).

Tuković, Z. and Jasak, H. (2012). A moving mesh finite volume interface tracking method for surface tension dominated interfacial fluid flow. *Comput. Fluids*, 55:70–84.

Weller, H. G., Tabor, G., Jasak, H., and Fureby, C. (1998). A tensorial approach to computational continuum mechanics using object oriented techniques. *Comput. Phys.*, 12:620–631.

Woolliscroft, M. O. and Maki, K. J. (2016). A fast-running CFD formulation for unsteady ship maneuvering performance prediction. *Ocean Eng.*, 117:154–162.

Unsteady Behaviour in RANS Simulation of the JBC and KVLCC2

Jeroen Wackers, Emmanuel Guilmineau, and Michel Visonneau

LHEEA, Ecole Centrale de Nantes / CNRS-UMR 6598, 1 rue de la Noë, Nantes, France

jeroen.wackers@ec-nantes.fr

1 Introduction

Recently, using the adaptive grid refinement method in the flow solver ISIS-CFD developed by our group (Wackers et al. (2012), Queutey and Visonneau (2007)), we observed unsteady flow behaviour for RANS simulations of the Japan Bulk Carrier. Further analysis showed that Detached Eddy Simulation produces this unsteady behaviour also on non-adapted grids, in good agreement with measurements (Queutey et al. (2016)). However, the validity of our RANS simulations remains uncertain, since all published RANS results for the JBC are steady. Furthermore, to our surprise, a computational setup similar to the JBC has produced unsteady RANS flow even for the KVLCC2!

The goal of this paper is to determine whether these simulations using adapted grids are valid, or if the unsteadiness observed comes from numerical perturbations due to the grid adaptation technique. Therefore, the paper studies how our simulations can be unsteady, while steady results have been obtained for the same cases. Specifically, if a flow is physically unsteady but yields a steady simulation result, it may be forced to steadiness by (a) numerical diffusion, (b) a steady flow solver, or (c) forced symmetry through a vertical symmetry plane. On the contrary, if a flow is physically steady but its simulation is unsteady, then spurious energy is added to the flow numerically. A probable source of this energy would be (d) adaptive grid refinement.

These four aspects are tested through systematic variation of the simulation parameters. After a description of the two test cases (section 2), the paper presents a series of computations in which the factors listed above are modified one by one, in order to determine their effect (section 3). Then, section 4 discusses the physics of the unsteady flows to further analyse the cause of the unsteadiness. The paper ends with a conclusion.

2 Test cases and numerical setup

The KVLCC2 and JBC are simulated in double-model conditions using ISIS-CFD. Model scale is used with hull lengths $L = 5.71m$ for the KVLCC2 and $L = 7.00m$ for the JBC. Reynolds numbers are $Re = 4.60 \cdot 10^6$ and $Re = 7.46 \cdot 10^6$ respectively. Velocity is imposed on the inflow and side boundaries, while pressure is imposed for the outflow. The hull is modelled either with a low-Reynolds (no-slip) boundary condition or with a wall law, which means that the flow in the near-wall boundary layer is not simulated but approximated through the boundary condition. Turbulence is modelled with RANS and the anisotropic EASM model.

A 'baseline' simulation approach is defined as follows. No vertical symmetry plane is used so the entire flow is computed. Unsteady flow is solved using second-order accurate time integration. The grid is adapted with the FCH criterion (Wackers et al. (2017)) and refinement thresholds equal to 1.0 for the KVLCC2 and 2.4 for the JBC, which gives fine meshes with similar densities. A minimum cell size of $2.7 \cdot 10^{-4}L$ is imposed for the refinement. Initial meshes for the grid adaptation are created with HEXPRESS^{TM}. For low-Reynolds (LR) boundary conditions, these grids have $y^+ = 1$ in the first near-wall layer; for the wall law (WL) this is $y+ = 30$. Table 1 gives the number of cells in each grid.

Table 1: Numbers of cells (in millions).

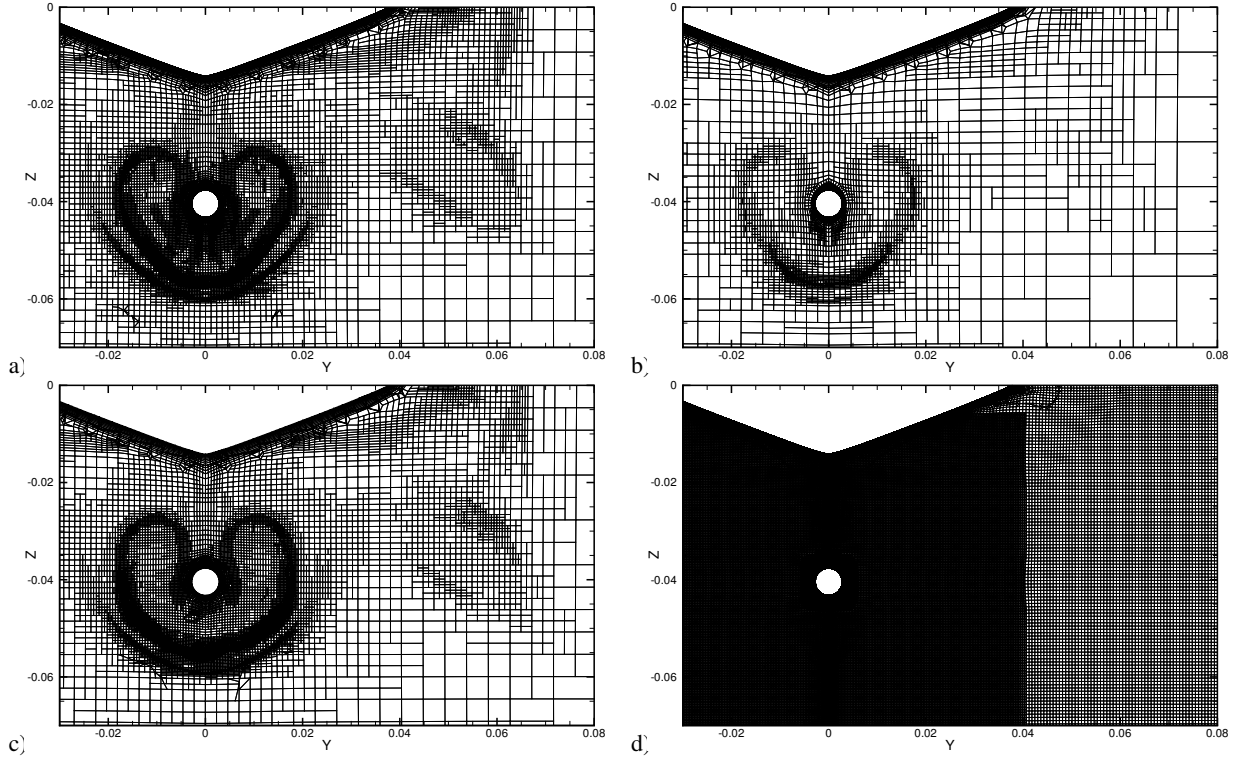| Case	Initial mesh	Baseline	Coarse	y-symm.	Non-adapted
KVLCC2 LR	0.48	16.66	3.51	9.40	–
KVLCC2 WL	0.29	10.59	1.49	4.74	–
JBC LR	0.63	24.45	6.37	11.04	90.6
JBC WL	0.29	8.17	2.34	3.98	63.0

Fig. 1: Cuts of the mesh at the plane S4, for the JBC. Baseline case with LR walls (a), coarser adapted grid with LR (b), baseline with WL (c), and fine non-adapted LR mesh (d).

3 Systematic variation of simulation parameters

A systematic variation of the numerical setup in section 2 is performed with five computations:

1. Baseline settings,
2. Unsteady time integration replaced by a steady solver,
3. Simulation of half the hull, with a y-symmetry condition in the the xz centre plane,
4. Twice coarser mesh (obtained by doubling the refinement threshold, see Wackers et al. (2017)),
5. Adaptive refinement replaced by a fine non-adapted mesh.

Examples of the meshes are found in figure 1, which shows the JBC cut plane S4 (corresponding to $x/L = 0.9843$). The number of cells in each mesh is given in table 1. The coarser grid (figure 1b) is, as expected, about twice coarser than the baseline grid, while a significant difference between LR and WL boundary treatment is evident in the adapted meshes (figures 1a and c). The fine non-adapted grid uses boxes of fine cells in the wake region (figure 1d); the size of the finest cells corresponds to the smallest cell sizes found in the shear layer on the coarse grid 1b.

The results are presented in the S4 plane for the JBC and in the propeller plane $x/L = 0.9825$ for the KVLCC2 (figure 2). Only the axial velocity is shown here; the other flow parameters behave similarly.

3.1 Low-Reynolds boundary conditions

When LR boundary treatment is used, the result at the end of the baseline simulation is indistinguishable from the averaged flow over the last 1000 of 3000 time steps (figures 2a and d). Furthermore, the solutions obtained with a steady solver are identical to the baseline solutions which use second-order time integration, even though these two computations are completely separate. Thus, the baseline LR simulations are steady and the result is independent of the solution method.

A comparison with the solutions that use a y-symmetry plane (mirrored in figure 2b to reproduce a full solution, shown only for JBC), shows that the difference between the baseline and y-symmetry simulations is negligible. Therefore, the flow physics is not modified by a symmetry plane.
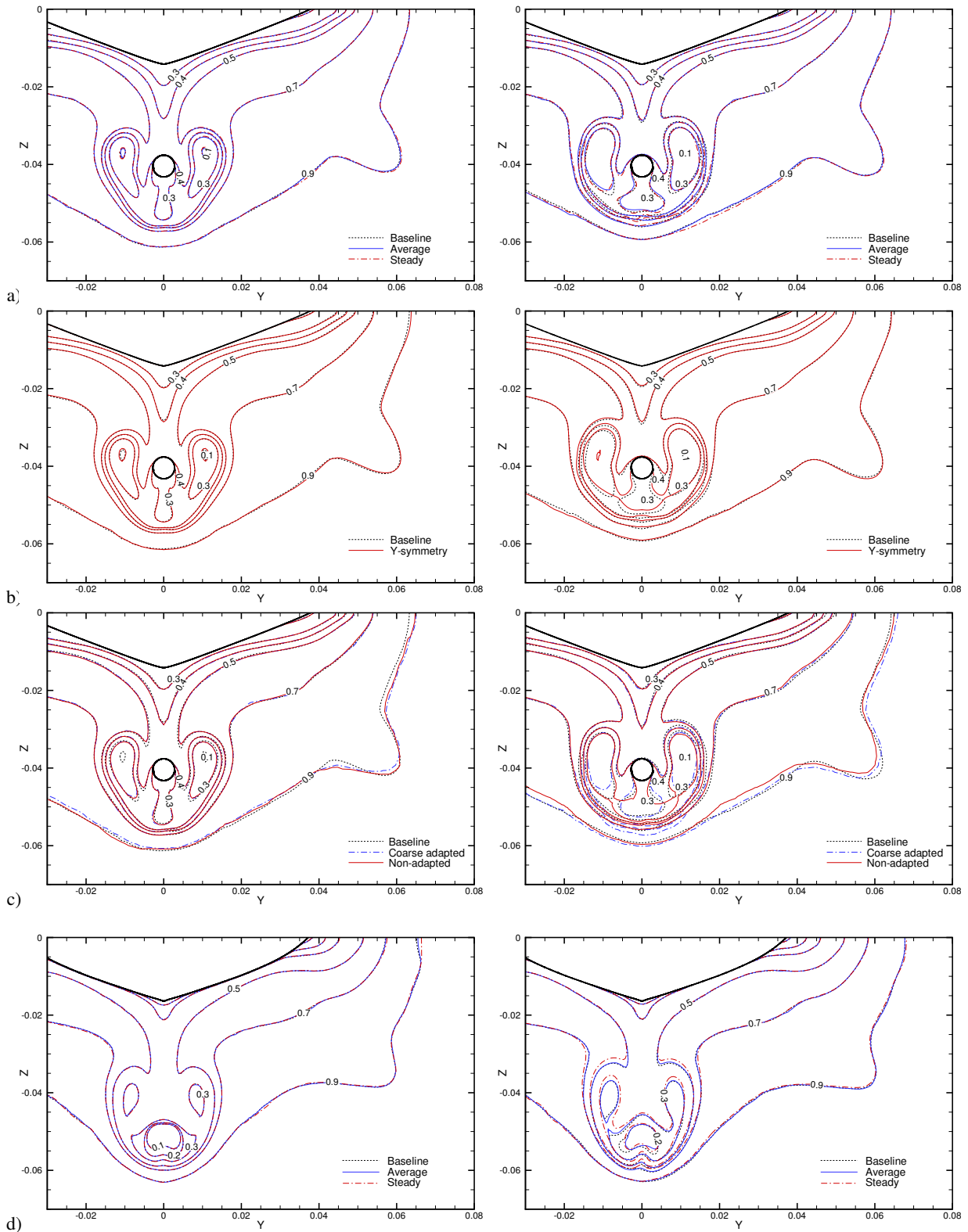
Fig. 2: Dependence of the axial velocity on the simulation parameters. JBC (S4 plane): modification of the temporal treatment (a), the vertical symmetry plane (b), and the mesh resolution (c). KVLCC2 (propeller plane): modification of the temporal treatment (d); further KVLCC2 results are not shown but are similar to the JBC. Left: LR boundary conditions, right: WL conditions.

As expected, the solutions on coarse grids are different from the baseline, due to the greater numerical diffusion (figure 2c shows the JBC). However, the solutions are similar so the baseline solutions are nearly grid converged. Finally, the solution computed for the JBC on a very fine non-adapted mesh corresponds well with the adapted meshes (figure 2c); it almost coincides with the coarse-grid solution. This shows that the grid adaptation does not introduce any major perturbation of the solutions for LR.

3.2 Wall-law boundary conditions

Compared to the LR boundary treatment, the wall law radically changes the results. For both ships, the baseline instantaneous and average solution do not coincide (figures 2a and d), so the baseline solution is unsteady. However, the flow is different for the two cases: the KVLCC2 has unsteadiness in the centre plane, below the propeller axis ($z = -0.05$), while the JBC shows wiggles in the shear layer around the main vortices. This shear layer is thicker in the average solution than in the instantaneous result, so its position is oscillating during the computation. The KVLCC2 average flow is non-symmetric, which means either that the dominant flow is asymmetric or that the averaging period was not long enough.

The steady solver does not produce a result which coincides with the average of the baseline. For the JBC (figure 2b) the tell-tale wiggles in the shear layer are present for the steady resolution. Thus, a steady solver does not stabilise the flow. The y-symmetry solution for the JBC has wiggles and the instantaneous flow does not correspond to its average (not shown), so even the symmetric solution is unsteady. Finally, the coarse-grid solution is more perturbed than the baseline. However, even our 'coarse' grid is locally quite fine compared with other studies so it is possible that real coarse grids stabilise the flow.

While the solution on a non-adapted fine grid for the JBC differs from the baseline (figure 2c), it too shows signs of unsteadiness. Some wiggles are present in the shear layer and the 0.3-isoline is asymmetric: the line around the main vortex is larger on the left side. Thus, the unsteady behaviour depends on the mesh but its main cause is not the adaptive refinement.

4 Physical analysis of the unsteady flow

From the previous section, it appears that the unsteady flow behaviour is related to the use of wall functions. Therefore, we study if the unsteadiness can be explained by the physical behaviour of the wall function. For this boundary condition, the flow in the viscous sublayer very close to the wall is not present in the simulation, but replaced by a wall law model. Since this model is based on attached, two-dimensional boundary layers, it is inaccurate for strong shear flow or separation.

For the JBC, unsteadiness appears in the shear layer which is created when the flow on the bottom of the ship flows upwards around the aft part of the ship and separates (figure 3c, mark A). Since the wall law solution does not contain the low-velocity sublayer close to the wall, while the actual separation of the fluid takes place in this sublayer, there is not enough low-velocity fluid after the separation: the dead-water zone above the separation is too small and the shear layer is thicker than for the LR solution.

The thicker shear layer has an effect on the turbulence model: the production of turbulence kinetic energy, which depends on the gradients of the velocity, is reduced near the wall. Thus, the turbulence intensity in the shear layer (figure 3d, B) is less for the WL solution. As a result, the flow damping due to turbulent viscosity is reduced, which allows the shear layer to become unsteady.

This phenomenon resembles the effect of a DES turbulence model, where the modelled turbulence is intentionally reduced in order to simulate the largest scales of the turbulence. Indeed, DES simulation for the JBC produces similar unsteadiness of the shear layer (Queutey et al. (2016)). However, for RANS this destabilisation is erroneous.

This mechanism is absent for the KVLCC2. While the dead-water zone above the separation is slightly more developed for the LR case (figure 3a, C), this has no influence on the turbulence kinetic energy (figure 3b, D) so the shear layer remains stable even for WL. However, the flow becomes unsteady below the propeller axis, where a second separation appears (figure 3a, E). Figure 4 shows that for the WL solution, there is no fluid with a velocity lower than 0.7 below the hull. Thus, when the flow separates, the WL solution cannot produce a stable dead-water zone with low velocity like LR. On the contrary, it contains a re-entrant jet of high-velocity fluid which destabilises when it touches the hull. This explains the appearance of unsteady flow below the propeller axis.
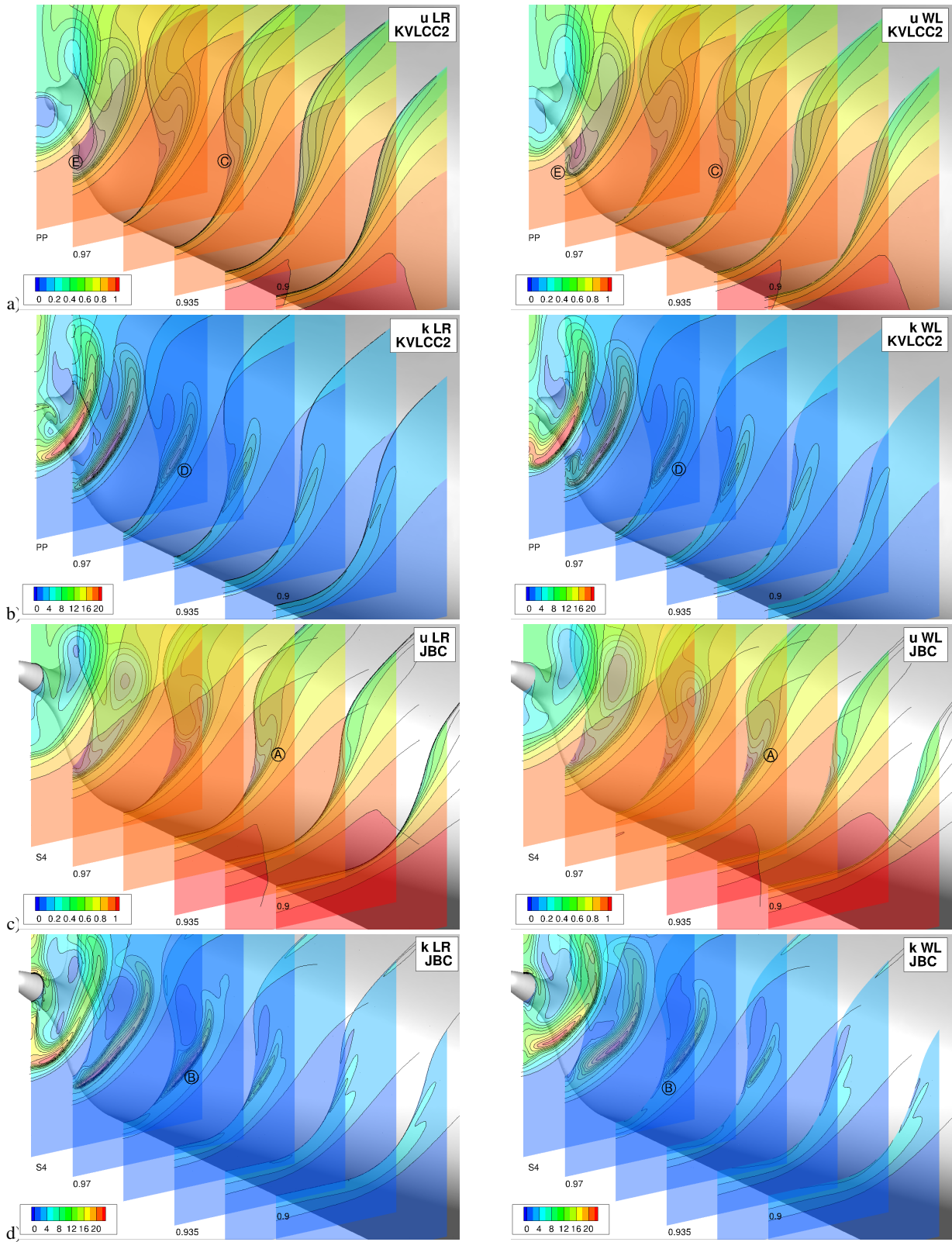
Fig. 3: Cut planes showing the axial velocity (a, c) and the turbulence kinetic energy (b, d) around the aftship of the KVLCC2 (a, b) and the JBC (c, d). Marks 'A' to 'E' on the figures are referenced in the text. The planes 'PP' (a, b) and 'S4' (c, d) represent the cuts of figure 2.
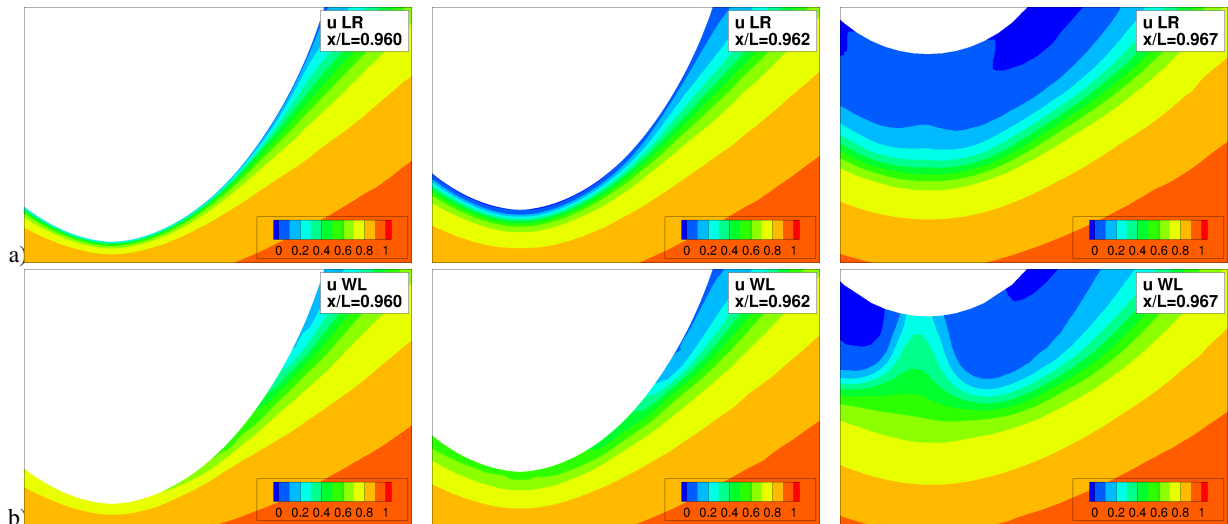
Fig. 4: KVLCC2: axial velocity in cut planes below the aft part of the hull, which show the different mechanisms of separation for low-Reynolds (a) and wall law (b) boundary conditions.

Thus, the approximative modelling of separated flow by the wall law boundary condition explains the apparition of unsteadiness both for the KVLCC2 and for the JBC. This confirms that the wall law model is the cause of the unsteady flow.

5 Conclusions

Systematic variation studies for the simulation of the KVLCC2 and the JBC show that with low-Reynolds (wall-resolved) boundary conditions on the hull, unsteady simulations on adaptively refined grids produce steady solutions. Stabilising mechanisms such as the use of a steady flow solver, a coarser grid, or a vertical symmetry plane, do not modify the solution. Furthermore, a solution on a fine non-adapted grid is very close to the adaptive-refined solutions. Thus, low-Reynolds solutions for both cases are steady.

With wall laws, solutions are unsteady both on adapted and on fine non-adapted grids. Coarser grids and a vertical symmetry plane do not reduce the instability for the JBC. In both cases, the properties of the wall law explain the unsteadiness: the JBC has insufficient production of turbulence close to the wall, while for the KVLCC2 there is a lack of low-velocity fluid close to the wall in a separation.

Thus, there is no evidence that the unsteadiness observed is an artefact due to the use of adaptive grid refinement. On the contrary, grid adaptation allows to predict the unsteadiness on grids which have 3 to 25 times less cells than the fine non-adapted grids in this study.

References

P. Queutey and M. Visonneau. An interface capturing method for free-surface hydrodynamic flows. *Comput Fluids*, **36**(9), 1481–1510.

P. Queutey, E. Guilmineau, M. Visonneau, J. Wackers, and G.B. Deng (2016). RANS and Hybrid RANS-LES simulations around the Japan Bulk Carrier of the Tokyo 2015 CFD Workshop. *NuTTS 2016*, St Pierre d'Oléron, France.

J. Wackers, G.B. Deng, A. Leroyer, P. Queutey, and M. Visonneau (2012). Adaptive grid refinement for hydrodynamic flows. *Comput Fluids*, **55**, 85–100.

J. Wackers, G.B. Deng, E. Guilmineau, A. Leroyer, P. Queutey, M. Visonneau, A. Palmieri, and A. Liverani (2017). Can adaptive grid refinement produce grid-independent solutions for incompressible flows? *J Comp Phys*, **344**, 364–380.

Extended CFD Guidelines for Zigzag Simulations in Self-propulsion Conditions at Low Froude Number

Anastasia Zubova, Alvaro del Toro Llorens, Benoit Mallol, Charles Hirsch
NUMECA International, Brussels/Belgium
anastasia.zubova@numeca.be, alvaro.deltorollorens@numeca.be, benoit.mallol@numeca.be,
charles.hirsch@numeca.be

1 Introduction

The present publication is following the work in progress on ship manoeuvrability prediction using CFD techniques embedding self-propulsion and standard zigzag manoeuvring simulations. Based on the Duisburg Test Case (DTC) and considering the earlier results by Zubova et al. (2016), new guidelines and clarifications are suggested. The current study is focused on the analysis of the complex flow around the stern of the hull resulting from the changing drift angle and the hull-propeller-rudder interaction. The behaviour of this flow dramatically influences the ship manoeuvrability and drives the ship's course keeping ability, hence its accurate prediction becomes the final goal of the present studies. Taking into consideration the earlier observed ship speed under-prediction and associated difference in manoeuvring time when compared to the experimental data, main attention is drawn to the rudder inflow velocity, self-propulsion modeling and the interaction effects. The complexity of the flow around the rudder, the influence of the propulsion and correlated interaction between the rudder, propeller and hull are all assessed to be of equal importance. Due to the low Reynolds number, an extensive mesh convergence assessment is performed while diskussing several mesh generation techniques, also including the adaptive grids technology. An in-depth analysis of the impact of the propulsion modeling on the ship manoeuvrability has been carried out, where an actuator disk model is confronted with a fully resolved propeller. The effect of the free surface on the ship manoeuvrability for a very low Froude number (Fn = 0.052) is considered. It has been investigated by comparing monofluid (3 DOF) and multifluid (6 DOF) simulations. Turbulence modeling has been investigated on the multifluid simulation case using the k-w (SST) and EASM turbulence models. An extensive numerical investigation has been performed with the FINE[TM]/Marine software, using unstructured mesh generation. Their results have been assessed in order to find a computation setup, which is a compromise between the adequate accuracy and minimal possible CPU cost. All results are validated by comparison of the ship yaw motion time histories to the results provided by Potthoff et al. (2016).

2 Computational mesh studies

A preliminary mesh convergence study for the isolated ship and rudder has shown a good convergence of forces and moments after 9000 non-linear iterations on the fine grid. Details of this study are summarized in the Tab. 1, which corresponds to a

Table 1: Mesh sensitivity study.

Mesh	Ship domain		Rudder domain	
	Nb of cells, MLN	Fx [N]	Nb of cells, MLN	Fx [N]
Coarse	4.96	1.64	1.46	0.0426
Medium	9.77	1.62	3.57	0.0428
Fine	20.57	1.65	7.44	0.0408

Reynolds number equal to $2 \cdot 10^6$ for the hull and $4.64 \cdot 10^4$ for the rudder. The Fine mesh for the overset rudder domain has been selected, whereas for the ship domain the Coarse mesh has been chosen considering the CPU costs. To assess the numerical solution error, additional simulations in monofluid have been performed applying the adaptive grid refinement technology. Second order spatial derivatives have been employed. Due to its tensor-based directional refinement nature both for the pressure and the velocity, this criterion is known to be effective for accurate representation of

wake flows and boundary layers. Verification procedure has been based on the studies considering the criterion application zone, minimum allowed cell size in adapted mesh area and the frequency of the adaptive criterion calls during the unsteady simulation. Considering the main target of pressure-dominated forces prediction, this criterion has been localized around the hull stern-propeller-rudder interaction zone and also including the full length of the hull, allowing the normal direction refinement inside the viscous layers mesh. Details of the study are summarized in the Tab. 2.

Table 2: Grid adaptation results.

Mesh	Nb of cells, MLN	Zone of application	Minimum cell size allowed, [m]	Frequency of call	Average difference on Rz [%]	Average time for 1 TS execution [min]
Initial mesh	6,4	-		-	-	0.7
Mesh 1	11	Stern-rudder	Lref/1000	Every 2 TS	2	1.569
Mesh 2	8.9	Stern-rudder	Lref/1000	Once	1	0.86
Mesh 3	42	Stern-rudder	Lref/2000	Every 2 TS	0.7	8.22
Mesh 4	7.4	Stern-rudder	Lref/2000	Once	0.7	1.04
Mesh 5	36.1	Hull-rudder	Lref/1000	Every 2 TS	9	5.35

Here, the Lref – the Lpp of the DTC hull; TS – simulation time step value; Rz – calculated yaw motion of the hull.

Considering the idea of flow adapted mesh generation, the Fine mesh of the rudder mentioned before has been relaxed in the far field mesh area, but preserving the same viscous layers insertion parameters. This explains the difference in the total mesh cell counts. Results with the adaptive grid refinement are compared to the non-adapted Initial mesh and have shown a maximum reduction of 2% of the comparison error, except the full hull and rudder region adaptation case (Mesh 5) showing the 9% Based on this result, a new study for the y+ influence on the hull forces prediction has been conducted, while adaptation in viscous layers is forbidden in the normal to solid. Since the present simulation has the ship hull y+ value in the range of 15 to 30, it could introduce the numerical error to the viscous part of the total hull resistance calculation. Thus, a new set of simulations has been conducted with the y+ falling into the range of 30 to 50. Both studies are employing the wall-function and the k-w (SST) turbulence model. Provided investigations has shown similar results regarding the maximum reduction of 2.5% compared to the non-adapted mesh calculation, also for limited to stern-rudder and full length hull-rudder being cases. Therefore, it has generally proved that an acceptable level of mesh convergence already has been reached before applying the adaptive grid technology. The mesh having the y+ of 50 on the ship hull and y+=0.7 on the rudder for the manoeuvring prediction have been generally improved and verified by the grid adaptation study. The adaptive grid technology has performed as an effective tool for the numerical error assessment. Considering the studied parameters of the grid adaptation, it has been shown that calling the procedure once can be sufficient for acceptable results accuracy and supports more efficient simulations regarding the time and setup complexity. For the rudder performance the numerical accuracy of the Overset grid technology used for the rotating rudder domain has been considered. To keep the high order least square interpolation type, an adaptive criterion has been applied during all the validation and manoeuvrability studies.

3 Rudder torque and lateral force calculation

The precise determination of the rudder torque (Q_R) and side force (Y_R) when operating at a ship drift angle (β) is a necessary condition for the accurate modeling of the ship manoeuvring. The prediction of the hydrodynamic torque caused by the action of the flow over the rudder requires an exact

assessment of factors such as hull wake, propeller rate and effective rudder angle (α_E) as the hull rotates. Knowing that the normal to the ship's centreline Y_R force is the main contribution of the rudder to the ship manoeuvring, it is thought that its possible under prediction is the source of the differences observed between the computations and the experiments. Based on the mesh convergence study summarized in Tab. 1, more insight into the impact of viscous layer formation of the rudder on the overall performance has been investigated. At this stage the tested conditions are the rudder behind the ship at a straight ahead and at 20° constant angle. Earlier studies by Ladson (1988) have shown that increasing the Re number reduces the mesh impacts on the lift and drag coefficients. Later studies towards the evaluation of the effects of the rudder performance prediction on ship's manoeuvrability by Liu et al. (2015) have shown that the lack of accuracy in the prediction of the rudder drag is less important than that of the lift. In Tab.3 results of the viscous layers investigations are summarized.

Table 3: Rudder VL parameters and overall performance assessment

Mesh	Y+	Number of layers	Min orthogonality	Max expansion ratio	Fx [N]	Fy [N]	Lift/Drag ratio(L/D)
Fine	1	7	10.03	11.68	0.04239	0.02231	0.526
Fine 2	0.7	9	9.32	11.55	0.04095	0.03807	0.929

Considering the resulting L/D ratio, the improvements from mesh involved in the Fine 2 mesh resulted in a higher Y_R value prediction and a better rudder performance compared to the under prediction observed during the earlier studies.

4 Propulsion modeling

It has been argued by Molland and Turnock (2007) that for a propeller upstream of a rudder, a good approach to model the physics is to treat the rudder and propeller as a combined unit. The influence of drift angle can then be applied in the form of velocity and flow straightening inputs to the basic isolated model of the rudder-propeller combination. Application of CFD methods can provide better insights into to the complex interaction of the hull-propeller and model the flow straightening effect directly through the manoeuvrability simulation. The self-propulsion methodology as explained in Zubova et al. (2016) has been improved, and now the ship is able to reach and keep the target speed in self-propulsion conditions at 0.4 m/s without manoeuvring and nearly at 0.362 m/s after the 1st overshoot of the manoeuvre. Considering a target speed of 0.387 m/s, this means an over prediction of nearly 3% at self-propulsion and a drop of the speed around 11% during the manoeuvre. These results can be linked to the following: unsteady effects related to propeller side force are not really included in the actuator disk model, but may play a relevant role on the dynamic response of the ship; the flow straightening effect causing the strong non-uniformity of the wake flow including the backflow occurrence delivered to the rudder.

Studies performed by Abramowski (2015) have also proved the importance of the wake flow resolution. In Fig. 1, relative velocity volume streamlines show the non-uniform flow coming from the hull at a drift angle of nearly 20°. The computations performed considering the real propeller inside a sliding grid have not shown a very significant improvement of the ship speed prediction before and during the manoeuvring.
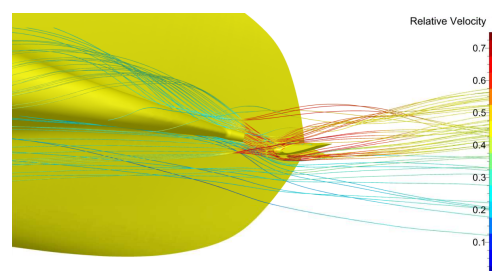

Fig. 1: Relative velocity streamlines at 1st Overshoot, $\delta = +20^o$.

Before the first rudder execution, the difference for the ship speed in self-propulsion conditions is less than 1% difference with respect to the experiments, and less than 3% during the manoeuvring. Comparison of received results can be observed in following Fig. 2, 3.
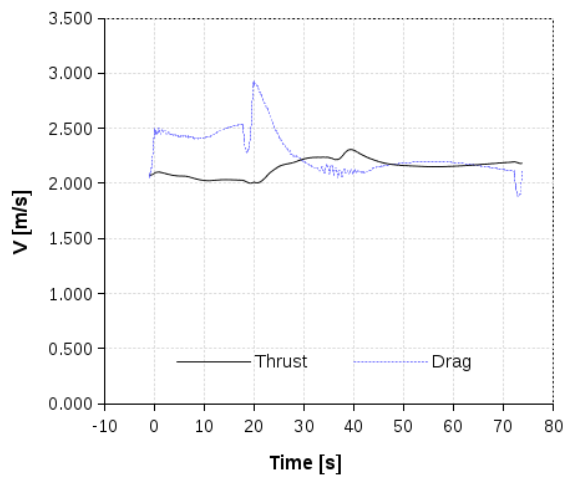

Fig. 2: Total Drag to propeller Thrust with enriched actuator disk model.
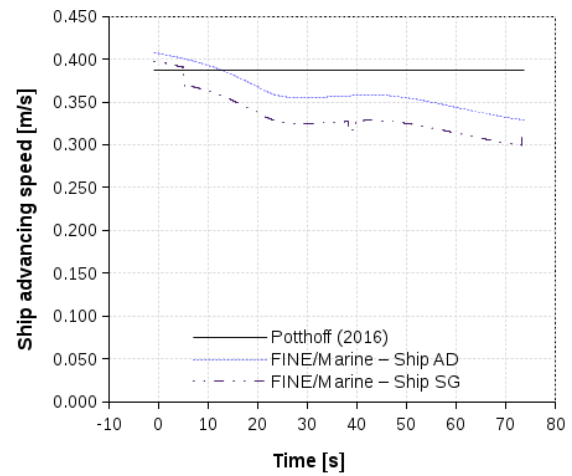

Fig. 3: Ship advancing speed in self-propulsion conditions while zigzag manoeuvre.

Following the experimental setup, the constant RPM approach has been applied and considering the obtained results for the self-propulsion before starting the manoeuvring, it shows a good correlation with the expected speed of the ship. Although a speed loss up to 20% of the target speed has been observed, the value is dependent on the stage of the zigzag manoeuvre. This effect is similar for the actuator disk model and the propeller in the sliding grid simulations. The observed effect is leading to the delay in the ship response regarding the yaw motion and a following longer phase for each rudder execution. These observations have led the research towards the idea of the thorough assessment of the added masses and the hull inertia parameters. Current simulations are performed with the ones provided by the experimental facilities, based on the real geometry and mass distribution of the model scale. The authors should conduct verification of this data.

5 Zigzag simulations in calm water conditions

This paragraph provides the results obtained for the zigzag manoeuvre with the monofluid and multifluid computations while compared to the results presented by Potthoff et al. (2016).

It should be noted that though the 1st overshoot angle and the time needed to reach it is in good agreement with experiments, the ship response after this point starts to differ showing a lower steering speed, and on the 3rd overshoot angle it shows the good agreement until reaching the maximum of -

20° for the rudder. Fig. 4 illustrates the ship response in time, where the simulation is compared with the experimental data and SHOPERA Workshop participants.
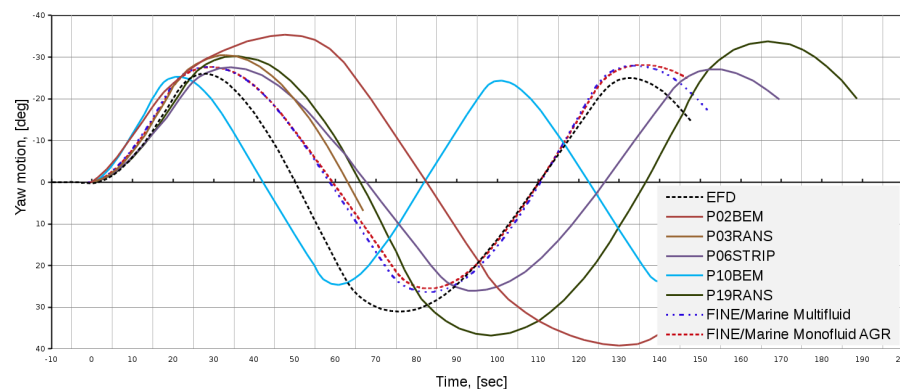

Fig. 4: Comparison between simulation and SHOPERA Workshop by Potthoff et al. (2016).

Considering provided results and numerical studies explained in the previous paragraphs, observed differences of the calculated and experimentally measured yaw motions could be also linked to the inertial parameters measurement uncertainty. Thus, the future investigations will be focused on the inertia matrix calibration. Considering the inertia matrix diagonal terms, it can be done with the simplified sequential simulations allowing only one DOF and also by means of the static drift angle simulations.

Influence of the turbulence modeling have been investigated based on the multifluid (6 DOF) simulation and includes studies with the k-w (SST) and EASM models available in the flow solver.

Obtained results have shown that the EASM model provides the larger modeling error when compared to the experimental data and should not be recommended for the similar manoeuvrability calculations. This error can be linked to the poor model performance in the field of the detached flows calculations. Comparison of the obtained results can be found in Fig. 5.
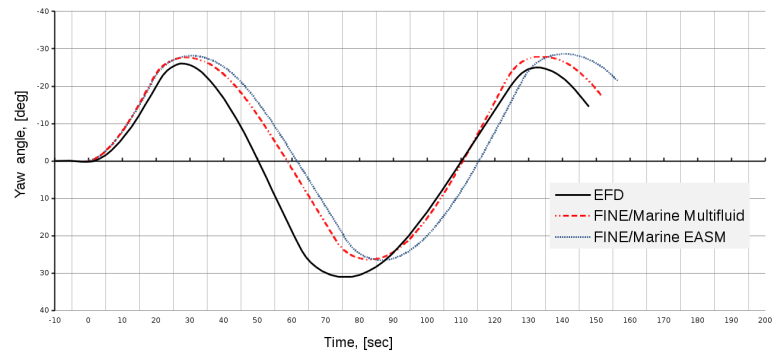

Fig.5: Turbulence modelling results.

6 Conclusions

The main goal of the carried investigations was to assess the effectiveness of the rudder, self-propulsion and stern flow prediction from the numerical accuracy viewpoint. The other target was to provide the solution within the minimum possible simulation costs. Thus, the following conclusions can be drawn:

- The Y_R under prediction has been generally improved with better mesh parameters in the viscous layers particularly using the Fine level of converged mesh (Tab. 3). Further improvements have been achieved by using the adaptive grid refinement technology on the local flow characteristics.
- The impact of the actuator disk model limitations is minimized by the hull flow straightening effect observed during the simulation and known from experimental studies. The self-propulsion target speed of 0.387 m/s has been reached within the accuracy limit. Results of the propeller in sliding grid simulations did not show a significant difference compared to enriched actuator disk regarding the self-propulsion simulations. This conclusion can be limited to the studied Froude and Reynolds numbers conditions.
- Actuator disk model enriched with the open water curve has shown a positive impact on the simulation time compared to the propeller in sliding grid. This effect is directly linked to the absence of the propeller mesh and the data transfer through the non-matching sliding boundaries requirement. It has resulted in faster simulation by the factor 2.
- Considering the Forces and Yaw moment prediction, the drop of the speed after the 1st rudder execution can be also linked to the observed rudder stall effect. The rudder also causes an upward turbulence (upwash) towards the propeller plane that challenges the turbulence modeling. Studied turbulence models, k-w (SST) and EASM, has shown that EASM model is less efficient for the manoeuvrability studies, mainly due to the underestimation of the flow detachment effects appearing here.
- Simulation results have showed the complex features of the stern flow. Rudder stall phenomenon is identified with the high frequency oscillations of forces. The manoeuvring effectiveness of the rudder is strongly dependent on the prediction of the flow coming from the propeller and mutual

interaction effects. Low Reynolds number flow poses a great challenge in the selection of a turbulence model for the manoeuvrability simulation, being this choice still under investigation.
- The impact of the unsteady effects related to the ship added masses is not fully clarified at the moment, and must be further investigated.
- Results present in the Fig. 4 show that the difference between mono- and multifluid simulations is relatively small and reaches it maximum difference at the extremities of the yaw angle. This can be linked to the growth of the magnitude of the numerical error present into the solution. With the monofluid simulation this effect has been reduced by the use of the grid adaptation.

Results comparison shows adequate prediction of the 1st and 3rd overshoot angle, whereas the 2nd overshoot angle is over predicted (Fig. 4). Based on the carried out validation studies and observed speed loss effects, it is most likely the ship inertial parameters dominant effect, rather than the numerical inaccuracies.

7 Perspectives

The following perspective directions for the research can be defined to enlarge the results:
- The manoeuvrability in waves should be assessed in the further research stage based on the current observations.
- Part of the conducted simulations benefit from the algebraic multigrid solver performance, resulting in up to 20% of the simulation time reduction compared to the classical solver, thus more investigations should be performed here mainly focusing on the studies including waves.
- Influence of the turbulence modelling should be investigated further with the DES mode, to verify the predictive capabilities of turbulence models in highly separated region.

References
A. Zubova, A. del Toro, B. Mallol and C. Hirsch, (2016) Progress towards CFD guidelines for zigzag simulation in waves, Proceedings of NuTTS 2016, Nantes, France.
R. Potthoff, B. el Moctar, A. Papanikolau, (2016) Presentation of Benchmark results, SHOPERA Benchmark Workshop, London.
P. Queutey and M. Visonneau (2007). An interface capturing method for free-surface hydrodynamic flows. Computers and Fluids, 36, 1481–1510.
C. Ladson, (1988), "Effects of independent variation of Mach and Reynolds numbers on the low-speed aerodynamic characteristics of the NACA 0012 airfoil section", Langley Research Center, Hampton, Viginia: National Aeronautics and Space Administration.
J. Liu, F. Quadvlieg, R., (2015) Impact of Rudder Profiles on Ship Manoeuvrability, Proceedings of MARSIM2015, Newcastle, UK.
A.F Molland, S.R. Turnock, (2007). Marine rudders and control surfaces: principles, data, design and applications, Oxford, UK, Butterworth-Heinemann.
T. Abramowski, (2005). Prediction of propeller force during ship maneuvering, Journal of theoretical and applied mechanics 43, 1, pp. 157-178, Warsaw, Poland.

CALL FOR PAPERS

21ˢᵗ Numerical Towing Tank Symposium (NuTTS'18)

Cortona, Italy, 30 September – 2 October 2018

Topics:

- Nonlinear flows around marine structures (LES, RANSE, Euler with or w/o free surface)
- Free-surface flows around marine structures (3-d ship seakeeping, free-surface viscous flows)
- Related topics (validation experiments, numerical techniques, grid generation, etc)

Deadlines:	Early feedback (optional):	30 March 2018
	Extended Abstracts received:	30 June 2018
	Payment received:	15 July 2018

You are invited to participate in the above event. The objective of the event is to provide a forum for informal discussions among experts in the field and to disseminate latest results. Younger workers and Ph.D. students are especially encouraged to participate. The event will be held at the Oasi Neumann near Marseille. All participants stay and have meals together to maximize interaction and discussion.

The extended abstracts of the proposed talk will be directly reproduced in pdf proceedings. Work in progress, encountered problems, etc. should be discussed in an open, informal atmosphere (no ties!) among colleagues. The first page of the extended abstract should be headed with the title and authors' names, affiliation and email address in a compact form to economize on space. Academic titles and page numbers shall be omitted. The extended abstract shall neither contain an abstract of the abstract, nor keywords, nor further headers. Font size shall not be less than 10pt Times New Roman. Extended abstracts should be limited to 6 pages in A4 format with 2.5 cm margin. An early reply will help us in organizing the event better. For the early feedback, a tentative title or topic will suffice.

Following the tradition of previous NuTTS events, the fees will be kept low to allow a maximum number of scientists to attend. The fees including accommodation (3 nights) and all meals during the symposium will be:

350 Euro PhD candidates and students
400 Euro authors
450 Euro other participants

Contact: Volker Bertram
              volker.bertram@dnvgl.com

Sponsors: tbd